

**ANALYTICAL AND EXPERIMENTAL INVESTIGATION OF A
1/8-SCALE DYNAMIC MODEL OF THE
SHUTTLE ORBITER**

Volume II — Technical Report

by

P. W. Mason, H. G. Harris, J. Zalesak, and M. Bernstein

May 1974

Final Report — Prepared Under Contract No. NAS 1-10635-12

by

Grumman Aerospace Corporation
Bethpage, New York 11714

Langley Research Center
Hampton, Virginia 23665

NATIONAL AERONAUTICS AND SPACE ADMINISTRATION

**ANALYTICAL AND EXPERIMENTAL INVESTIGATION OF A
1/8-SCALE DYNAMIC MODEL OF THE
SHUTTLE ORBITER**

Volume II – Technical Report

Prepared under Contract NAS 1-10635-12

for the

Langley Research Center
National Aeronautics and Space Administration
Hampton, Virginia 23365

by

P. W. Mason, H. G. Harris, J. Zalesak, and M. Bernstein

Grumman Aerospace Corporation
Bethpage, New York 11714

May 1974

Section 1
INTRODUCTION

**ANALYTICAL AND EXPERIMENTAL
INVESTIGATION OF A 1/8-SCALE DYNAMIC
MODEL OF THE SHUTTLE ORBITER**

Volume II - Technical Report

By P. W. Mason, H. G. Harris, J. Zalesak, and M. Bernstein

**GRUMMAN AEROSPACE CORPORATION
Bethpage, New York 11714**

1 - INTRODUCTION

1.1 OVERVIEW AND SUMMARY

The Space Shuttle configuration has more complex structural dynamic characteristics than previous launch vehicles, primarily because of the high modal density at low frequencies, and the high degree of directional coupling in the pitch plane. An accurate analytical representation of these characteristics is a primary means for treating structural dynamics problems during the design phase of the Shuttle program. The 1/8-scale model program was developed to explore the adequacy of available analytical modeling technology, and to provide the means for investigating problems which are more readily treated experimentally. The basic objectives of the 1/8-scale model program are to

- Provide early verification of analytical modeling procedures on a Shuttle-like structure
- Demonstrate important vehicle dynamic characteristics of a typical Shuttle design
- Disclose any previously unanticipated structural dynamic characteristics
- Provide for development and demonstration of cost-effective prototype testing procedures.

As listed in the FOREWORD, this four-volume report covers the analytical and experimental results relating to the Orbiter structure. The analytical studies pertaining to the External Tank (ET) and Solid Rocket Booster (SRB) are covered in References 9-1 and 9-2, respectively.

The mathematical modeling of the Orbiter began in January 1973. Consistent with the concepts of testing substructuring capability in NASTRAN level 15.5 (using ALTERS where needed), the structure was divided into five components: fuselage, fin, cargo doors, payload, and wing.

All skin material in the initial NASTRAN model (Model I) was considered to be nonbuckled, i. e., fully effective. This approach is consistent with the design of the full-scale Shuttle Orbiter where any wrinkling of the skins would loosen the bonded thermal protection system (TPS).

After a series of static and dynamic tests of the experimental Orbiter model, it was concluded that the NASTRAN model should be modified to account for initial imperfections and poor joint designs. These changes in the finite element model (NASTRAN Model II) accounted for additional flexibility in six major areas

- Fin/fuselage supports
- Forward/mid-fuselage splice
- Cargo door attachments
- Wing carry-through structure
- Effective width of fuselage and wing skins
- Payload attachment.

The effects of revising the NASTRAN model were substantial. The agreement between the second analysis and test is very good for the low frequencies, and as generally expected, discrepancies between theory and test become larger for the higher modes. Also, the static test data reported herein has a $\pm 10\%$ error in reproducibility. It is felt, however, that the agreement of Model II results with test data is sufficiently close such that a full coupling analysis may be pursued.

In NASTRAN Model I the CQDMEM2 element was used to model a fully effective structure. The major cause for lack of correlation was traced to the ineffectiveness of the skin panels due to the presence of initial bows. Model II used bars and shear panels to represent the behavior of the physical model. Here, effective bar areas and an effective shear modulus were used. It is felt that this type of modeling is more descriptive of the actual characteristics of the structure. The

effectiveness factors were obtained through the use of a computer program that solved the large deflection problem of in-plane loading of plates with initial imperfections. Little information exists in published form that contain the parameter range and type of loading of interest to the present study. Work was done by NASA some 20 years ago. It is recommended that this work be updated to cover a broad range of aspect ratios, initial imperfections and loadings. Publication of these data in chart form would be beneficial to modeling efforts on many structural projects.

Some remodeling of major joints could have been made in the analysis. However, for some joints such as the fin-to-fuselage connection, only static tests could give the exact behavior no matter how careful an analysis was made.

The original analysis plan for the 1/8-scale model required that all components (Orbiter, ET and two SRB's) be coupled to determine mated vehicle modes. This combined hydro-visco-elastic analysis is theoretically possible within the present NASTRAN system, but from a practical stand point it is not. Although modes were successfully calculated for the individual components, it was impracticable to couple these components and analyze the total (mated) vehicle due to extremely large computer time requirements. Note that the lack of correlation of the Orbiter analytical and test modes for Model I is not a fault of NASTRAN. This lack of agreement did, however, cause a shift of emphasis from studying the coupling problem to examining the Orbiter correlation by the use of Model II. Coupling is still a major problem. Two approaches seem feasible:

- Modal coupling in lieu of static coupling to reduce the size of the final problem
- Incorporation into NASTRAN of approximate reduction schemes, such as FEER (Reference 9-3), that employ an automatic tridiagonal reduction algorithm.

Master Agreement NAS 1-10635, Task 21 will pursue the modal coupling approach by making the appropriate ALTERS to the NASTRAN rigid formats.

The analysis of the 1/8-scale model was viewed as a pilot study of the use of NASTRAN on realistic aerospace projects. Therefore, some comments extend past specific application to the 1/8-scale model. Many areas must be considered in attempting to judge the NASTRAN system, some of which are not necessarily concerned with NASTRAN itself.

One of the prime reasons for Grumman's interest in NASTRAN is the work that NASA is doing in attempting to establish NASTRAN as the industry standard. For multicorporation aerospace projects, standardization is a necessity. Standardization of computer programs, type of data, etc., is important from a contractual point of view, where subcontractors interface with prime contractors and the prime contractors interface with the principal agency. However, with standardization there must be sufficient technical flexibility - in this regard NASTRAN has room for improvement. Some overall comments concerning NASTRAN (Section 8 contains additional detail) are as follows:

- The learning period required to become proficient with the NASTRAN system is lengthy
- The five Orbiter substructures were coupled using NASTRAN level 15.5. No great difficulties were encountered in using NASTRAN to do this. However, the column partitioning vectors required in the MERGE instruction are somewhat awkward. The equilibrium checks that were incorporated in the analysis proved helpful in finding numerical errors in the stiffness and mass matrixes and in giving a high level of confidence that there are no extraneous constraints. For the 1/8-Scale Orbiter Model, five substructures were combined to give the total structure. Multilevel substructuring does not appear to present any technical difficulties
- Existing eigenvalue routines in NASTRAN are inadequate to handle the large size problems that are associated with the coupled structure
- Regardless of many objections, a Government/industry standard like NASTRAN is a necessity.

1.2 SYMBOLS AND ABBREVIATIONS

Symbols

δ	deflection, in.
δ_{ij}	influence coefficient, i.e., deflection of point i due to unit load at point j., in./lb
f_m	frequency of model, Hz

f_p	frequency of prototype, Hz
L_m	length of model
L_p	length of prototype
t	skin thickness of model, in.

Abbreviations

ALARM	}	computer programs to solve eigenvalue problems of very large size
FEER		
ALTER		modification of NASTRAN rigid formats
CBAR	}	finite elements in the NASTRAN program used in analysis of Orbiter structure
CROD		
CSHEAR		
CTRMEM		
CQDMEM2		
CQUAD2		
DOF		degrees of freedom
ET		external Tank
GLOW		gross liftoff weight
LH_2		liquid Hydrogen
LO_2		liquid Oxygen
MPC		multiple point constraint - NASTRAN
NASTRAN		NASA Structural Analysis System
SPC		single point constraint - NASTRAN
SRB		Solid Rocket Boosters
TPS		thermal protection system

Section 2
DESCRIPTION OF PHYSICAL MODEL

2 - DESCRIPTION OF PHYSICAL MODEL

2.1 DESIGN OBJECTIVE

The 1/8-Scale Shuttle Dynamic Model is based on Grumman's proposed Design 619 parallel-burn Space Shuttle, shown schematically in Fig. 2-1. Figure 2-2 shows a mockup of the 1/8-Scale Shuttle Model basic configuration; Fig. 2-3 shows the detailed structural arrangement of the prototype Orbiter. In simplifying the 1/8-scale model design, a major objective was to keep model fabrication cost within target, while retaining as many of the significant structural dynamic characteristics as possible. The allotted funds did not permit fabrication of an exact or "replica" model at the small scale necessary for testing in the existing NASA/Langley facilities. Thus, only the general characteristics of the major Orbiter components have been simulated; there has been no attempt to model local details. Figure 2-4A is an external view of the 1/8-Scale Orbiter Model. Figure 2-4B shows the model with nonstructural plastic fairings mounted.

2.2 DESIGN CONSIDERATIONS

2.2.1 SIMILITUDE REQUIREMENTS

A first step in the modeling procedure was to determine the major factors that influence the response of the prototype being studied. For the Shuttle structure, this was accomplished under Task 4 of the Master Agreement Program (Reference 9-4).

Table 2-1 summarizes pertinent scaling relationships that must exist between the model and the prototype. These follow directly from a dimensional analysis of the various parameters that influence the dynamic behavior of the structure, and from the choice of the model material. Extrapolating prototype behavior from model test data is accomplished by directly using these scaling relationships. Note, however, that because of design expediency some of the scaling rules have been compromised. For example, the local skin stiffness on the model is less than the required skin scaled value of the prototype to prevent buckling. Liberty has also been taken in modeling the stiffness characteristics by some necessary lumping to avoid the large expense of exact scaling of very small dimensions. Thus stiffeners, although lumped to some extent, have not been eliminated completely. If they were

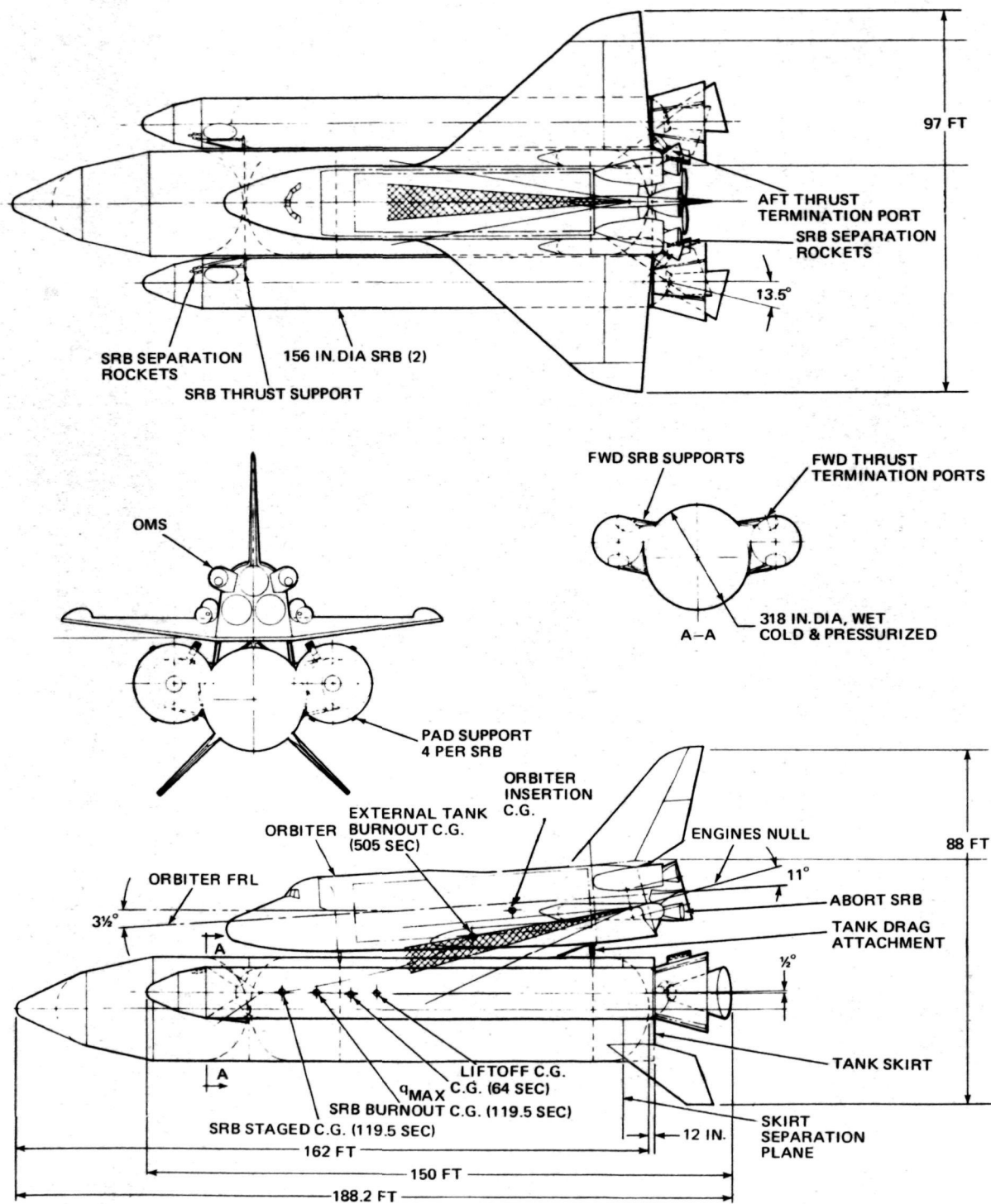


Fig. 2-1 Grumman Parallel-Burn Space Shuttle Design 619 Used as Reference Prototype for 1/8-Scale Model Design

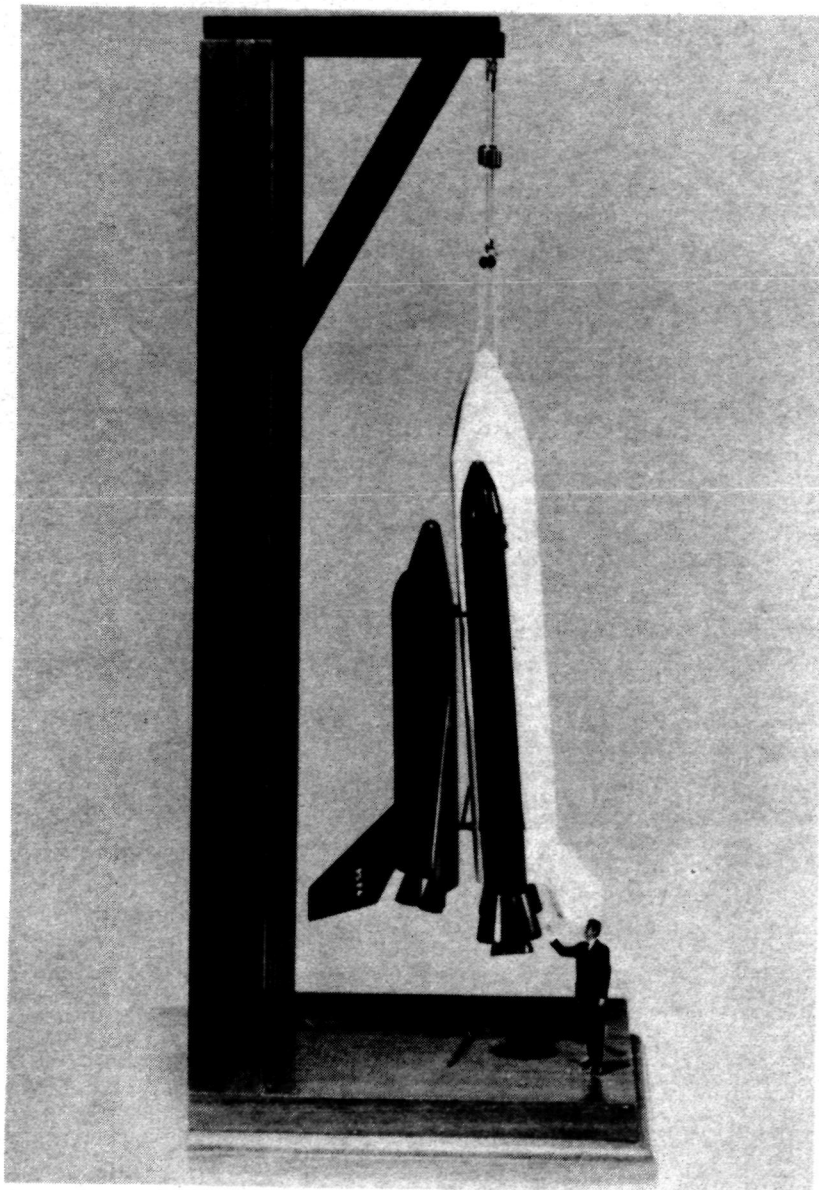


Fig. 2-2 Mockup of 1/8-Scale Shuttle Model Basic Configuration

S-3

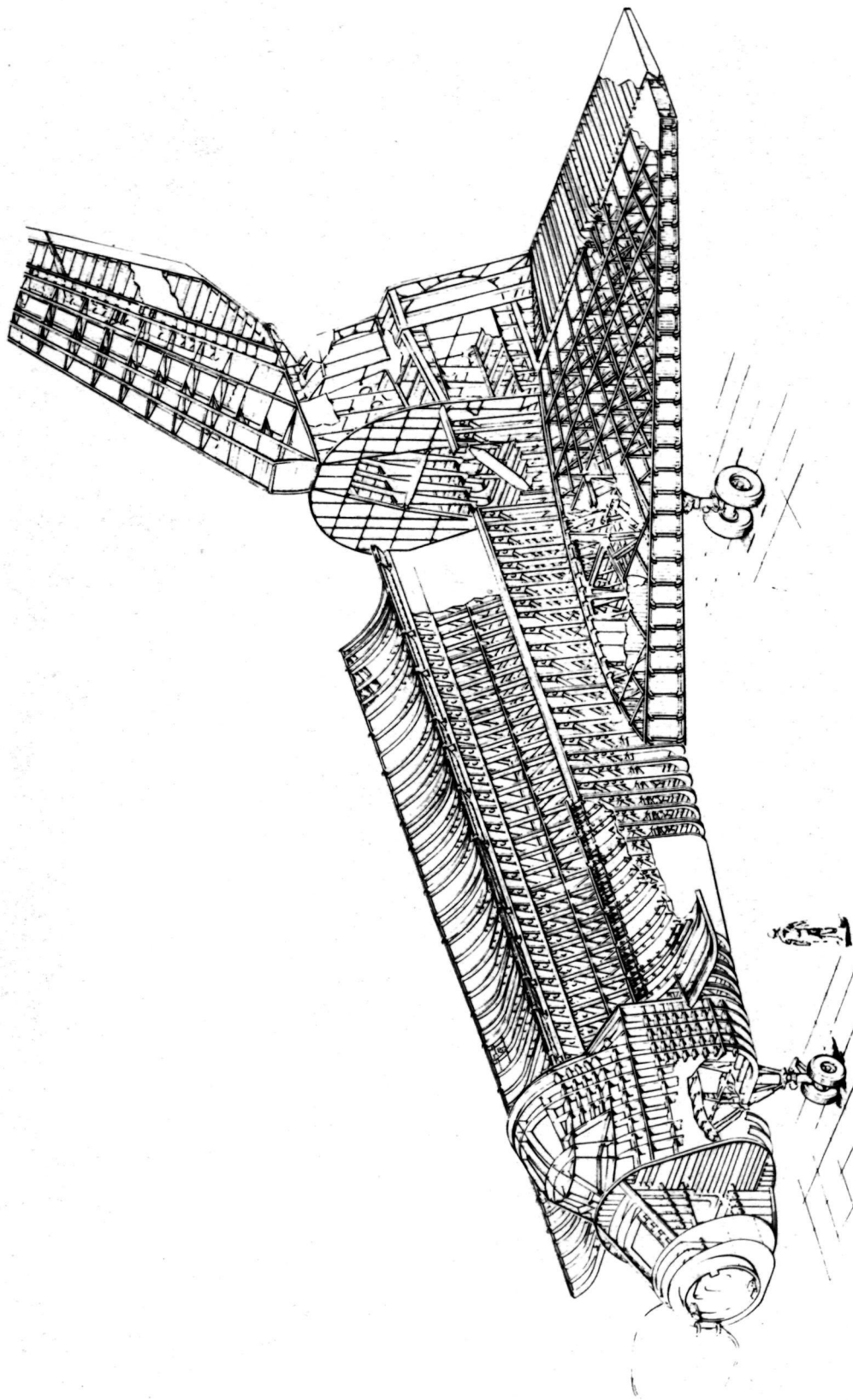
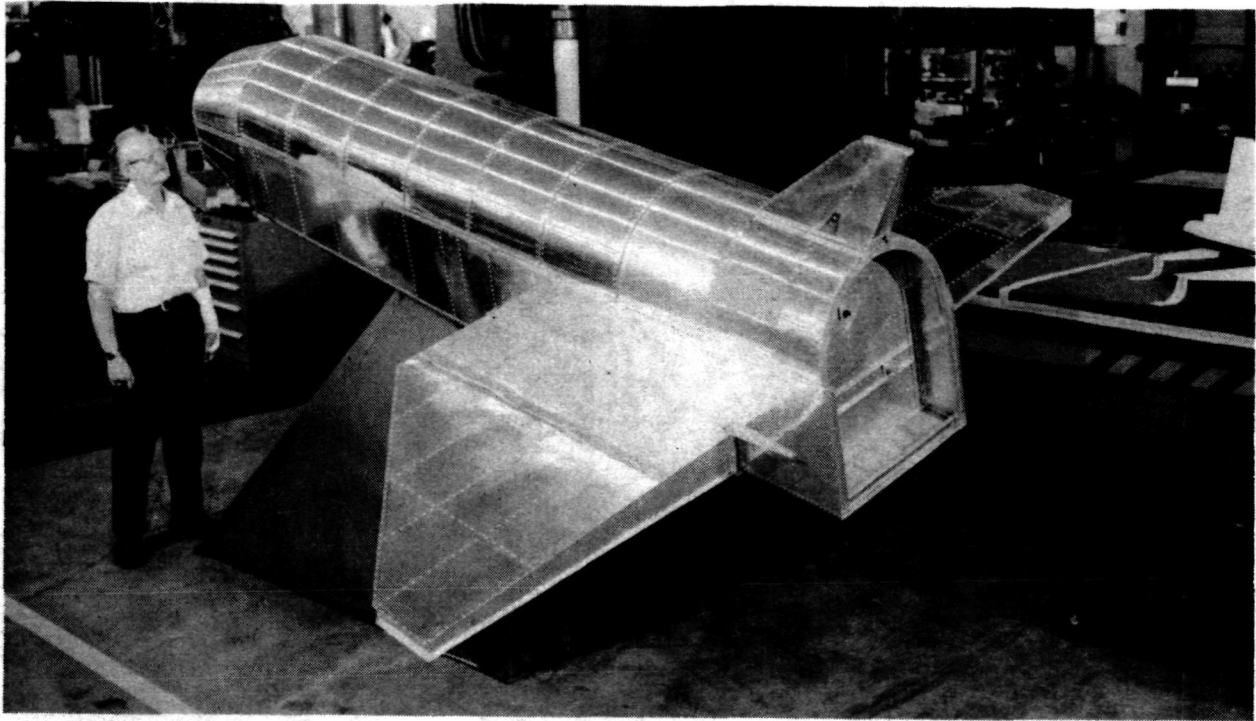
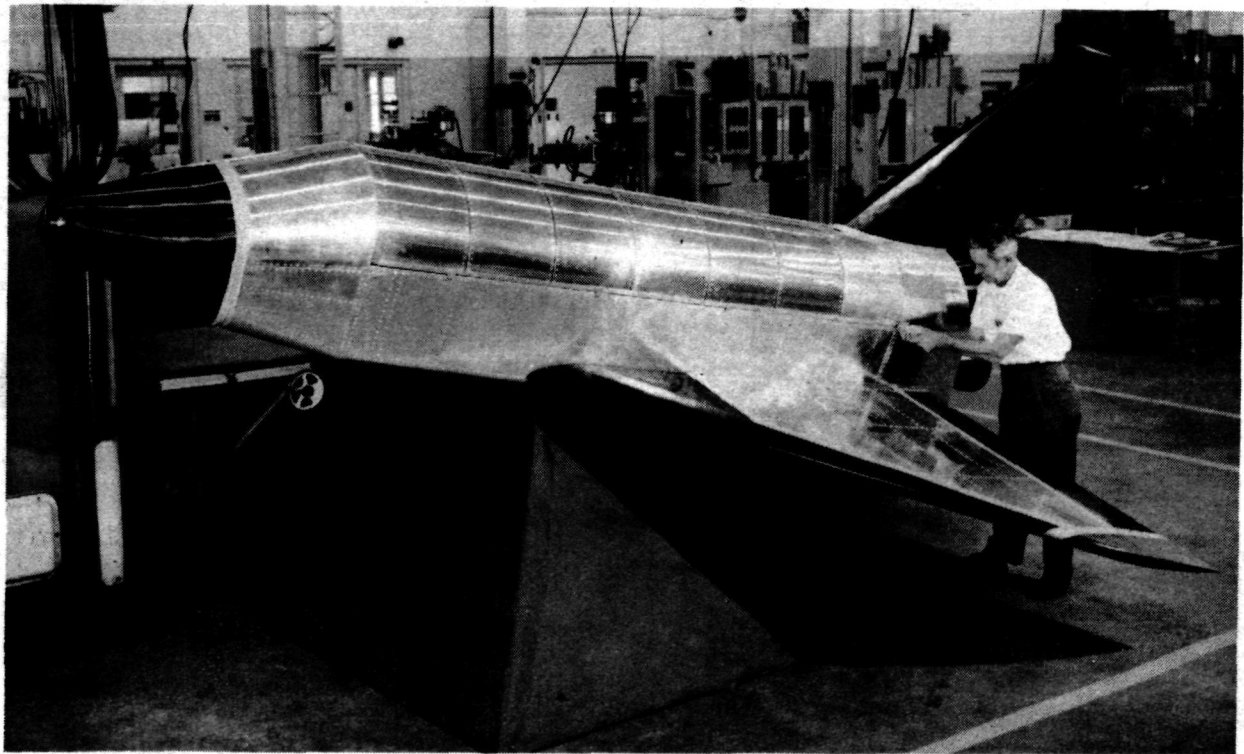


Fig. 2-3 Prototype Orbiter (Grumman Design 619) Structural Arrangement



T-1

A. Structural Configuration



T-2

B. Model With Fairings

Fig. 2-4 Views of Finished 1/8-Scale Orbiter Model

completely eliminated, then the local stiffness of the skins would not be duplicated, and premature buckling would occur.

While accurate modeling of the prototype was desirable for extrapolating basic Shuttle dynamic characteristics, another prime study object was an evaluation of the NASTRAN dynamic analysis and its correlation with model test data. A complete static and dynamic analysis was made using NASTRAN with the structure modeled to a degree of refinement considered sufficient for preliminary design purposes. Thus, the need for direct scaling of the prototype design to obtain an exact model in every detail was not considered to be crucial. Note also that the Shuttle design was still in a state of flux at the beginning of this study, hence any attempt to model the then current vehicle exactly would not be overly beneficial to the Shuttle project.

Table 2-1 Pertinent Scaling Relationships for the 1/8-Scale Model

Physical Quantity	Magnitude ^(a)	Physical Quantity	Magnitude ^(a)
Length and displacements	$\frac{L_m}{L_p} = \frac{1}{8}$	Stress ($\sigma = E\epsilon$)	$\sigma_m = \sigma_p$
Poisson's ratio, ν	$\nu_m = \nu_p$	Force ($F = \sigma A$)	$\frac{F_m}{F_p} = \left(\frac{1}{8}\right)^2 = \frac{1}{64}$
Mass density	$\frac{\rho_m}{\rho_p} = 1$	Longitudinal stiffness, EA	$\frac{(EA)_m}{(EA)_p} = \left(\frac{1}{8}\right)^2 = 1/64$
Modulus of elasticity, E	$\frac{E_m}{E_p} = 1$	Bending stiffness, EI	$\frac{(EI)_m}{(EI)_p} = \left(\frac{1}{8}\right)^4 = 1/4096$
	$\epsilon_m = \epsilon_p$	Torsional stiffness, GJ	$\frac{(GJ)_m}{(GJ)_p} = \left(\frac{1}{8}\right)^4 = 1/4096$
Area	$\frac{A_m}{A_p} = \left(\frac{1}{8}\right)^2 = \frac{1}{64}$	Weight ($W = \rho V$)	$\frac{W_m}{W_p} = \left(\frac{1}{8}\right)^3 = \frac{1}{512}$
Area moment of inertia, I	$\frac{I_m}{I_p} = \left(\frac{1}{8}\right)^4 = \frac{1}{4096}$	Acceleration ($F = ma$)	$\frac{a_m}{a_p} = \frac{8}{1}$
Mass moment of inertia, I'	$\frac{I'_m}{I'_p} = \left(\frac{1}{8}\right)^5 = \frac{1}{32,768}$	Natural Frequency, ω	$\frac{\omega_m}{\omega_p} = \frac{8}{1}$

TT-1

^aSubscript "m" refers to the model; subscript "p" refers to prototype.

2.2.2 LOADS

LOAD FACTORS

Table 2-2 summarizes the principal load factors used in the design of the 1/8-scale Orbiter Model. No attempt was made to limit the lateral and transverse loads during the vibration mode surveys.

LOADS INDUCED BY HANDLING

The handling load conditions were assumed critical in the design of the 1/8-Scale Orbiter Model because of the low overall stiffness of the structure. Table 2-2 lists the load factors used in the design for the handling conditions. All raising and lowering of the model was accomplished with the model in a vertical orientation, supported from integral nose fittings. These stipulations were necessary to prevent permanent buckling in the lower skins.

Table 2-2. - Summary of Load Factors Used in 1/8-Scale Model Design

Condition	Load Factors	
	Limit, g	Ultimate, g
Impact during fabrication and assembly	$n_x = 2$	3
Cable and hoist fitting and attachments	$n_x = 2$	3
During raising and lowering model ^(a)	$n_x = 1.5$	2.25
During mode surveys ^(b)	$n_x = 1.2$	1.8
Lateral forces during handling ^(c)	$n_y = n_z = 0.5$	0.75

^aSelected to account for dynamic effects during starting and stopping of the hoist system.

^bSelected to provide a 20% envelope on body bending and shears and local interface loads due to dynamic loading.

^cValue for lateral (Y) and transverse (Z) load factors was selected to account for handling forces.

TT-2

2.2.3 MASS AND STIFFNESS DISTRIBUTION

Table 2-3 lists the Orbiter design weight distribution for one-half of the model structure. A schematic "stick figure" representation of the fuselage mass distribution (for one-half of the structure) is shown in Fig. 2-5. Note that, as stated in Table 2-3, the fuselage weight of 100.91 lb contains the aft OMS ballast of 26.15 lb and the cabin ballast of 29.2 lb per one-half structure. The abort SRB (Fig. 2-1) is not included in the model.

Table 2-3 Design Weight Distribution for One-half of the 1/8-Scale Orbiter Model Structure

Substructure	Weight, lb	Weight, %
Fuselage	100.91 ^(a)	48.34
Wing	32.86	15.74
Cargo doors	6.52	3.12
Fin	3.85	1.84
Payload	64.62	30.96
Total	208.76 ^(b)	100.00

^aThe fuselage weight of 100.91 lb contains the aft OMS ballast of 26.15 lb and the cabin ballast of 29.2 lb (per half structure)

TT-3 ^bThe actual measured weight was 420 lb for the Orbiter model

Figure 2-6 compares the total axial cross-sectional areas of the 1/8-Scale Orbiter Model with the scaled prototype Design 619. A similar comparison is made in Fig. 2-7 for the area moments of inertia about the Y-axis (vertical bending). Curve "A" represents the values used in NASTRAN Model I. Curve "B" represents the effect of removing the door longeron. Curve "C" represents NASTRAN Model II with partially effective skin and no door longeron. The drop in values from "B" to "C" is due to the presence of initial out-of-plane bows in the skin panels. The actual value of the inertia in Model II is higher due to the door longeron, but the change is not as great as the difference between curves "A" and "B". This is because the door longeron is only partially effective, due in some part to the cargo door attachments. Curve "D" represents the prototype Design 619 values scaled by the ratio of 4096.

Dead load shear, axial load, and moment diagrams (for the one-half Orbiter Structure) supported at the interstage are shown in Fig. 2-8; Fig. 2-9 presents axial dead-load diagrams for the half orbiter suspended from nose fittings.

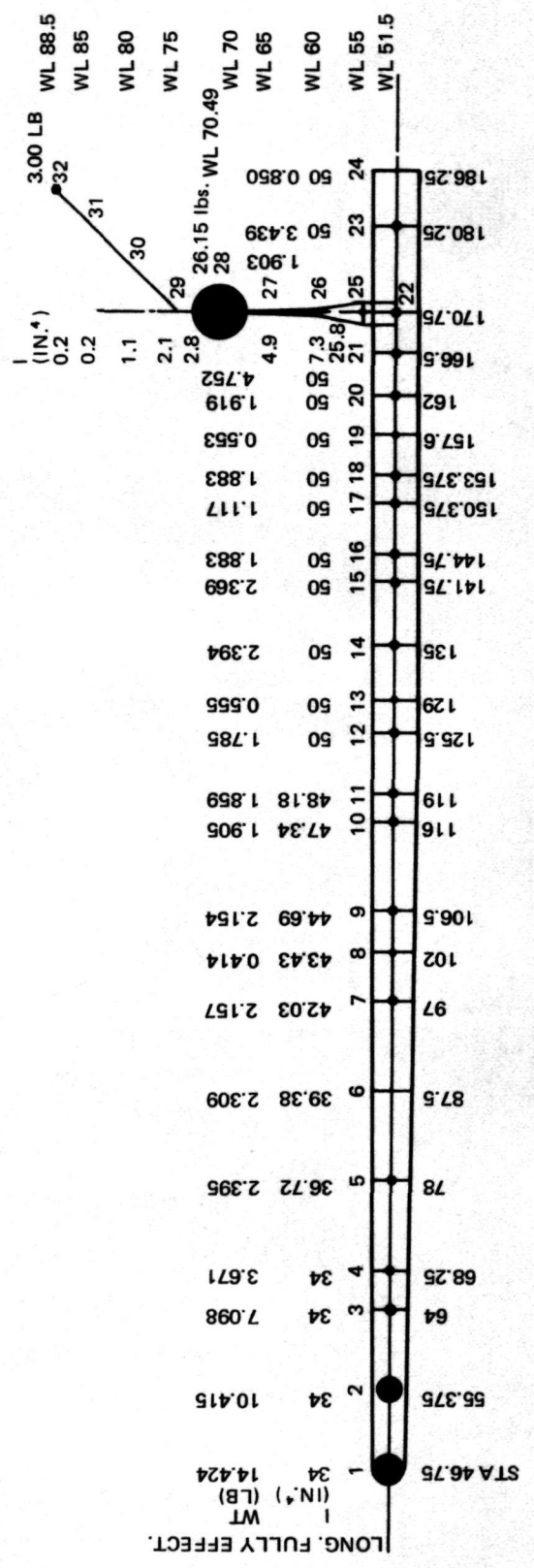
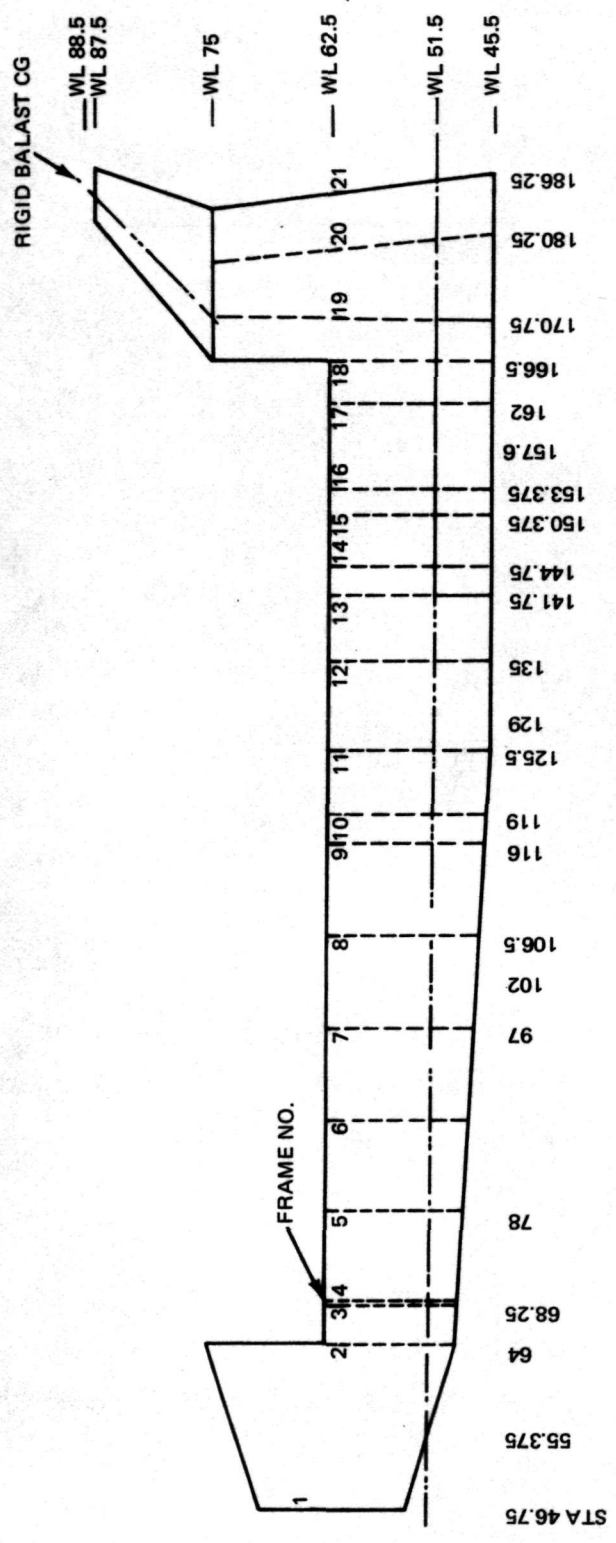


Fig. 2-5 Fuselage "Stick Model" Mass Distribution (One-Half Structure)

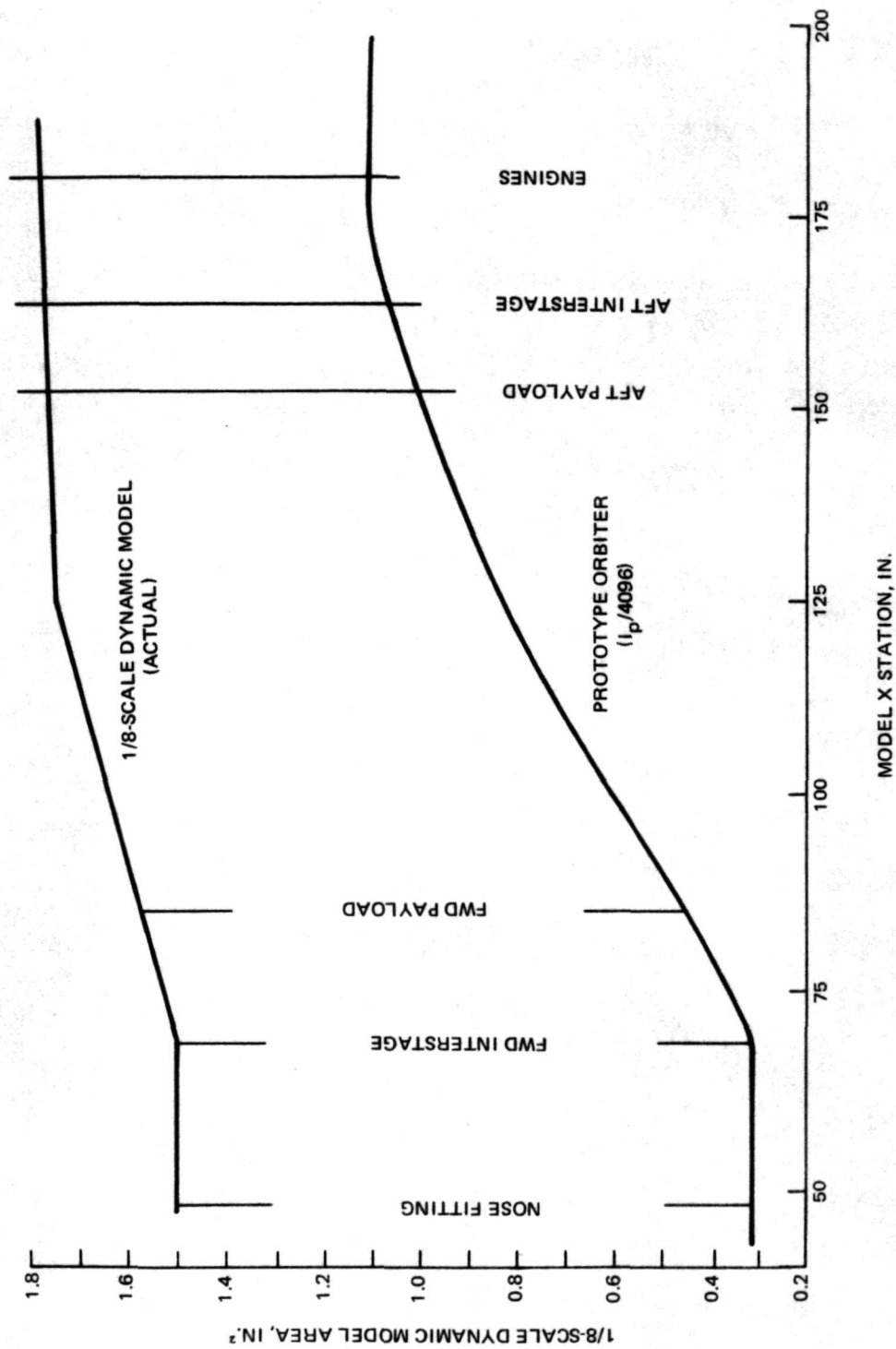


Fig. 2-6 Comparison of Cross-Sectional Areas of Prototype and 1/8-Scale Orbiter Model

T-4

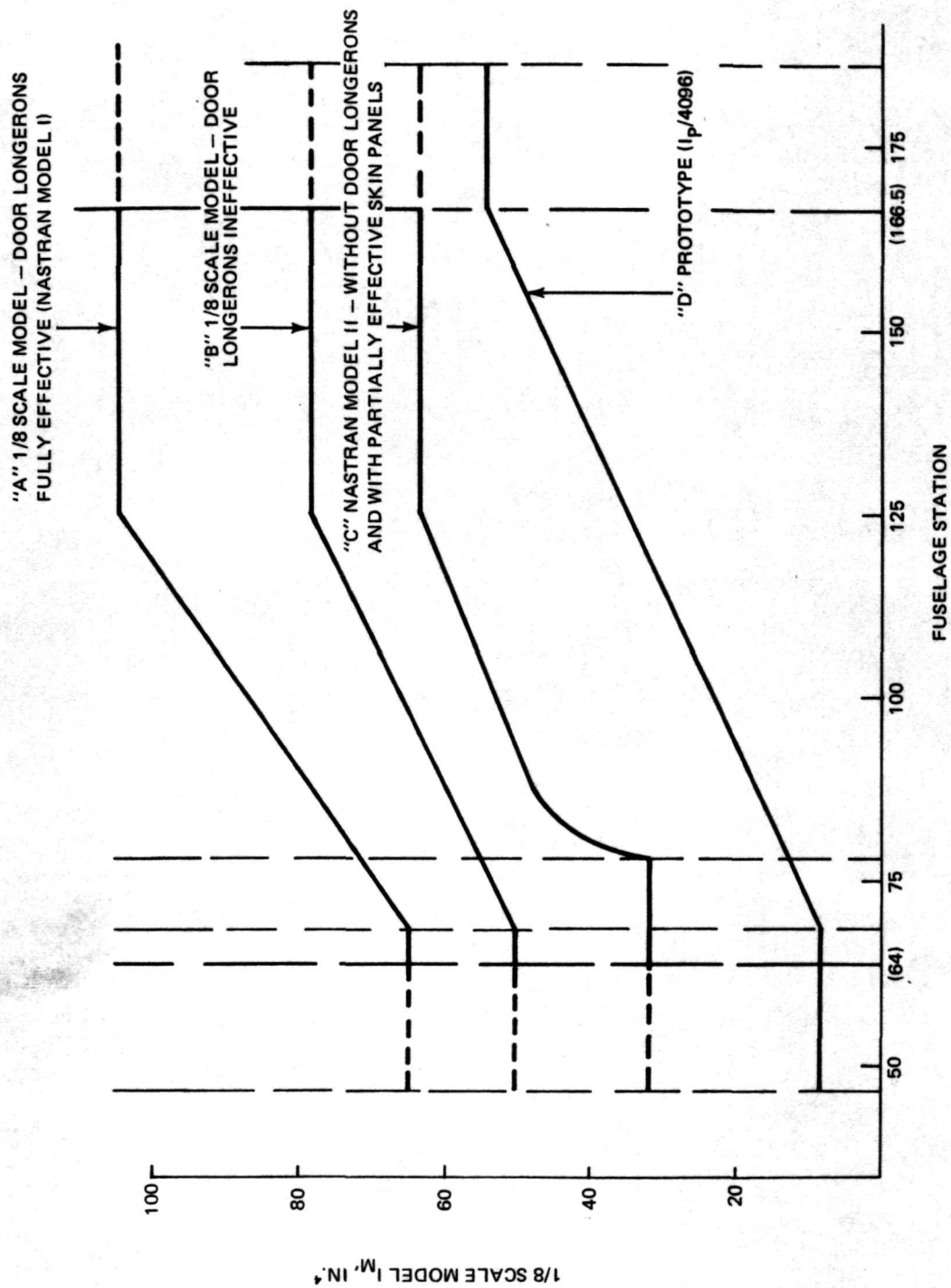


Fig. 2-7 Comparison of Fuselage Moments of Inertia of Prototype and 1/8-Scale Orbiter Model

T-5

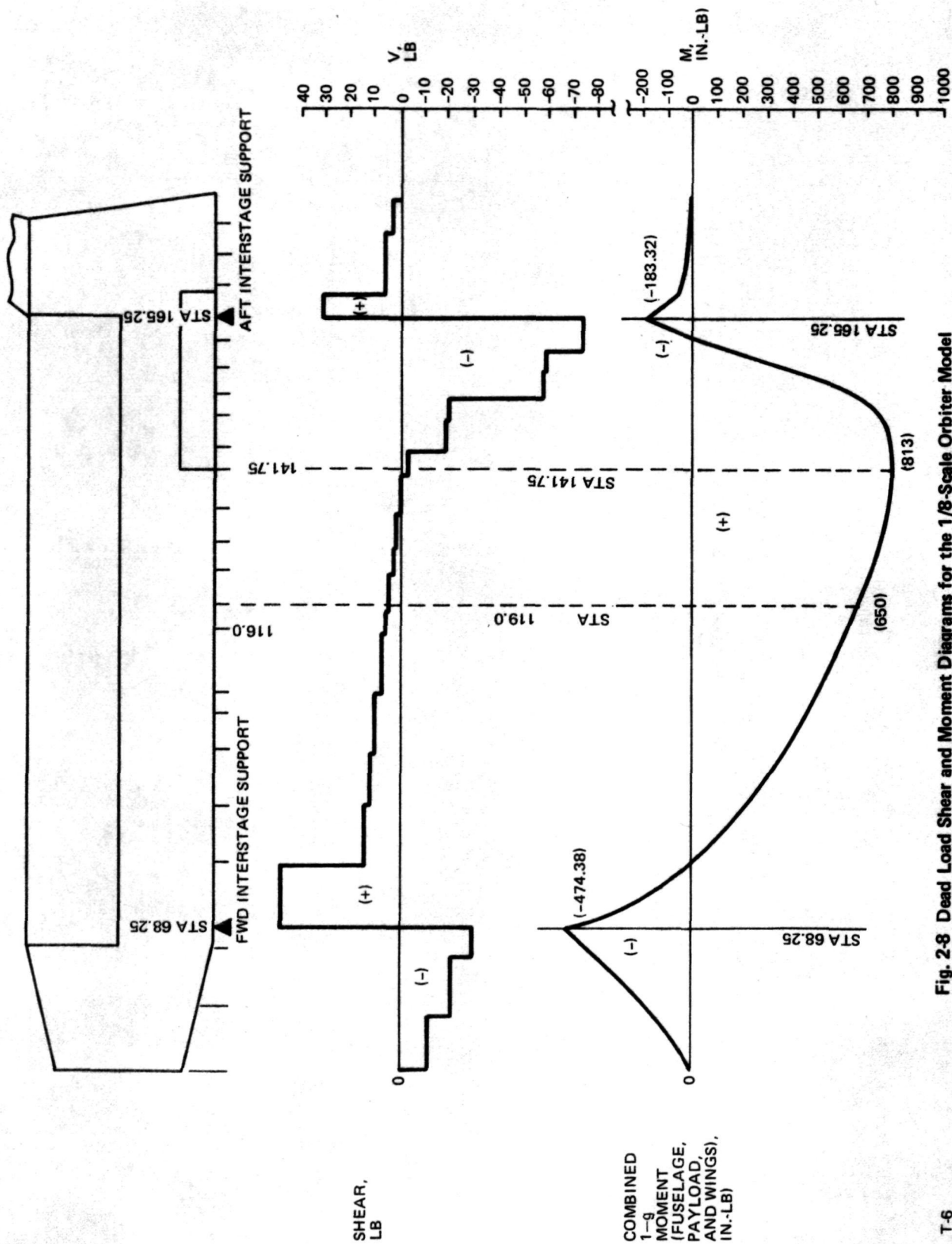


Fig. 2-8 Dead Load Shear and Moment Diagrams for the 1/8-Scale Orbiter Model Supported at the Interstage (Half Orbiter Values)

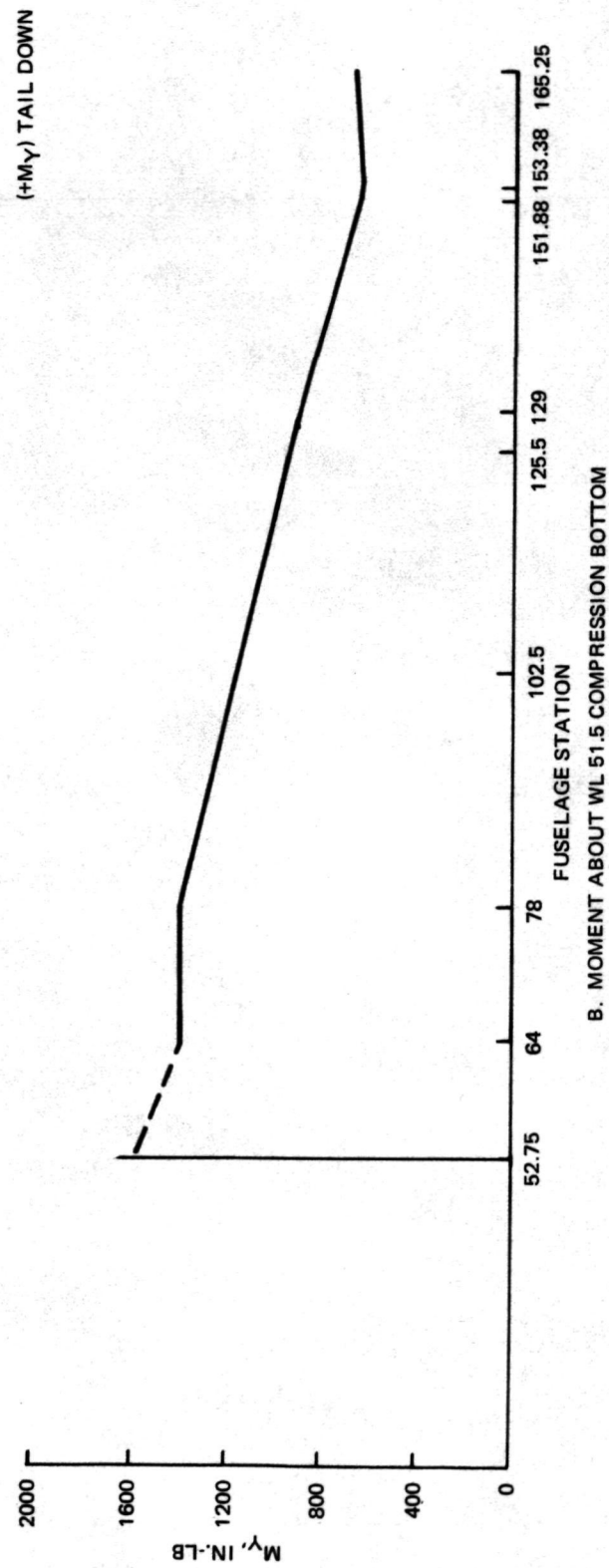
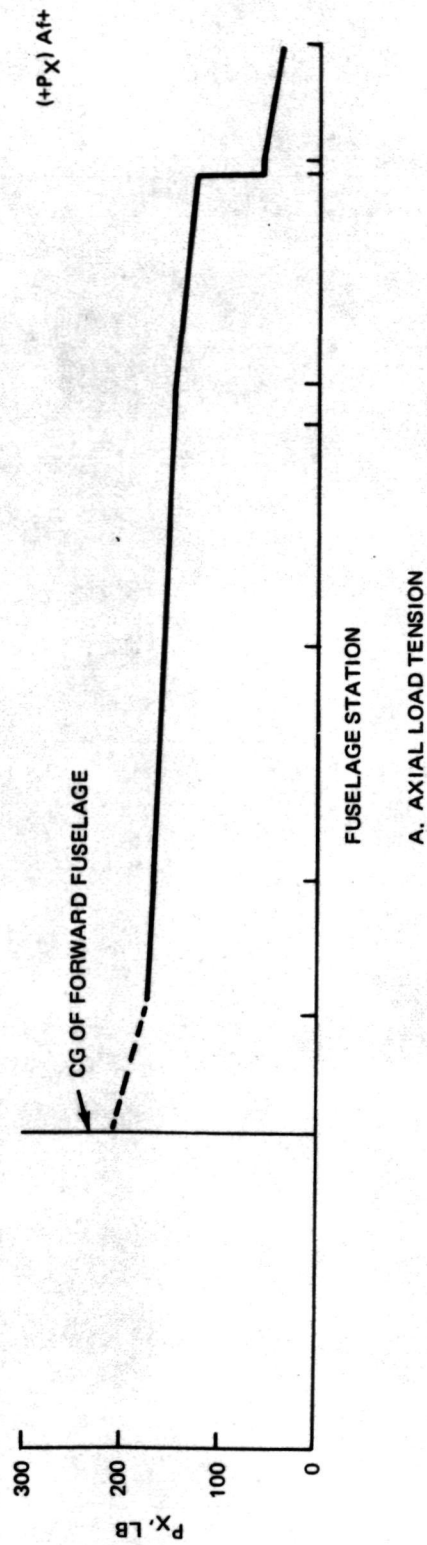


Fig. 2-9 Axial Load and Moment Diagrams for the 1/8-Scale Orbiter Model Hung from Nose Fitting (Half Orbiter Values)

T-7

2.3 FABRICATION DETAILS

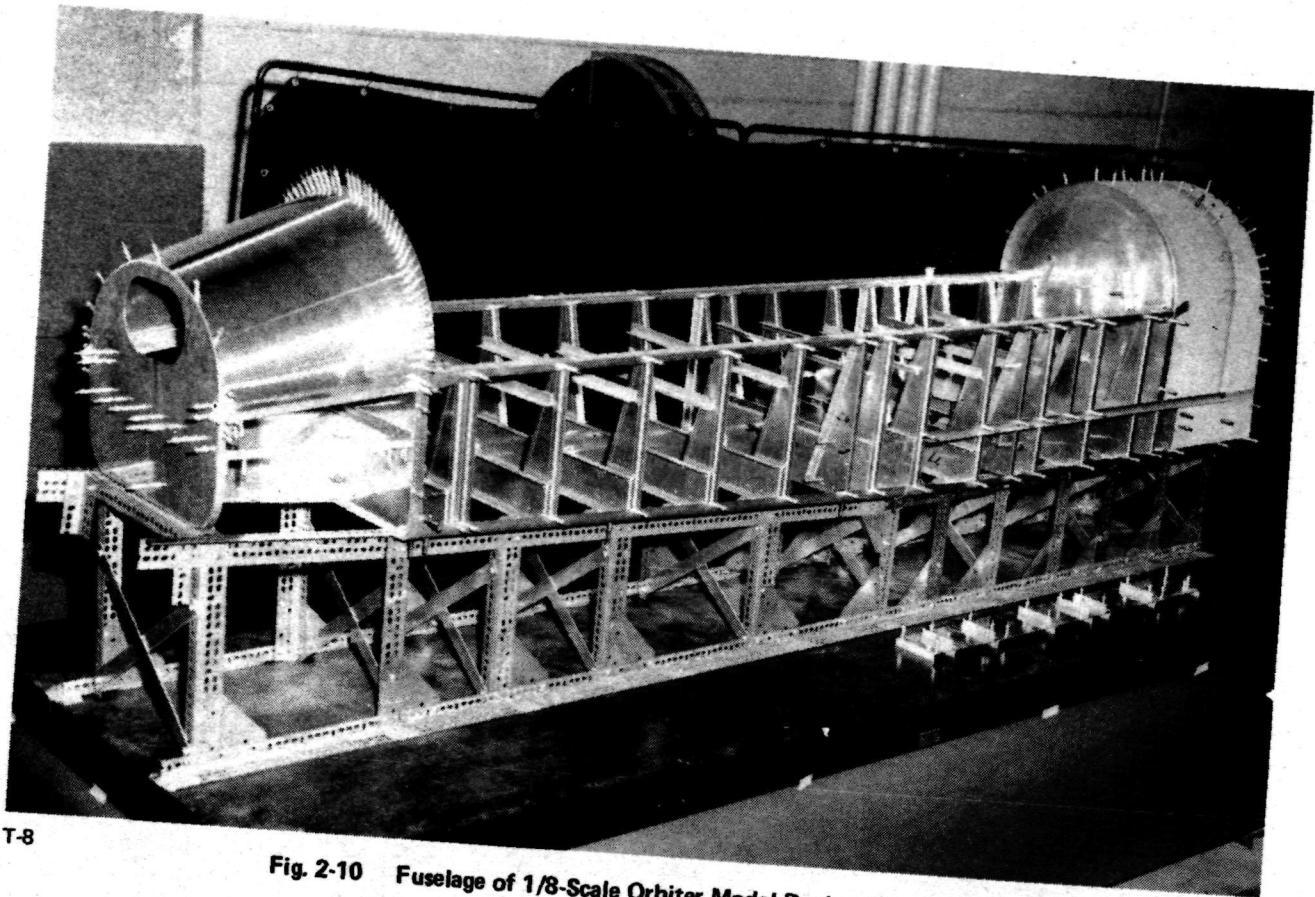
2.3.1 FUSELAGE

The external lines of the 1/8-Scale model were simplified to reduce fabrication cost, hence more flat side and bottom skins are used in the model than were employed in the design prototype. The model fuselage has been fabricated as three modules: a forward section, having a tapered non-circular stiffened shell; a U-shaped stiffened mid-fuselage section, with straight sides and bottom deck; and an aft section, with shell geometry similar to the prototype. (See Fig. 2-10.)

The forward fuselage (Fig. 2-11) contains attachments for supporting ballast weights that simulate the mass of the forward equipment. The hoisting "pick ups" are attached to longerons which, in turn, are spliced to the mid-fuselage upper longeron at Station 64.0. Figure 2-12 shows the forward-to-mid-fuselage interface.

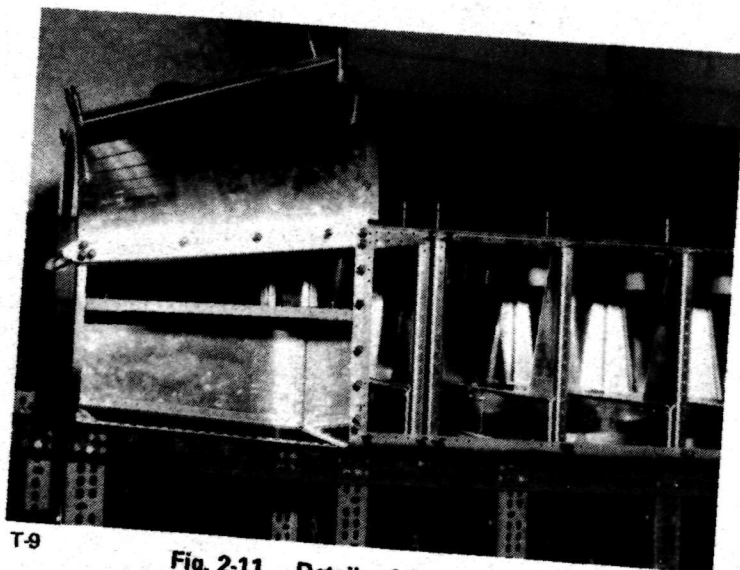
The fuselage mid-section of the prototype consists of closely spaced frames covered by corrugation stiffened skin carrying TPS tiles. The model has similar (but simplified) geometry and structural arrangement, consisting of a series of U-shaped frames spaced at approximately 10 in. apart. The model skin thickness is 0.020 in. on the side and 0.025 in. on the bottom. This thickness is enough to prevent buckling under static load (if the sheet is perfectly flat), but it results in a larger overall section area and moment of inertia than the scaled prototype values (as shown in Fig. 2-6 and 2-7). Payload support attachments are provided to permit four variations in the payload configuration. The longerons are designed to furnish the proper scaled area for the aft end of the fuselage, and are kept constant in area for the entire length of the fuselage to limit fabrication costs. To simulate the prototype weight, a distribution of about 0.8 lb/in., including the structural weight, was required; it was obtained by increasing the thickness of the frame webs where stiffness is not a factor.

The aft fuselage, Fig. 2-13 and 2-14, is geometrically similar to the prototype, but contains only two full bulkheads, one aft frame, and two intermediate frames. Neither the abort SRB's, nor the cutouts for them and for the OMS in the prototype, were modeled. The cross-sectional areas of the struts between the lower engines and the aft interstage fittings (Fig. 2-13) are scaled directly from the prototype areas.



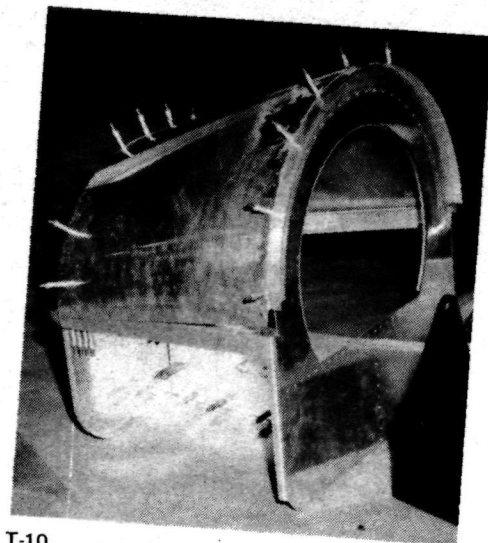
T-8

Fig. 2-10 Fuselage of 1/8-Scale Orbiter Model During Fabrication



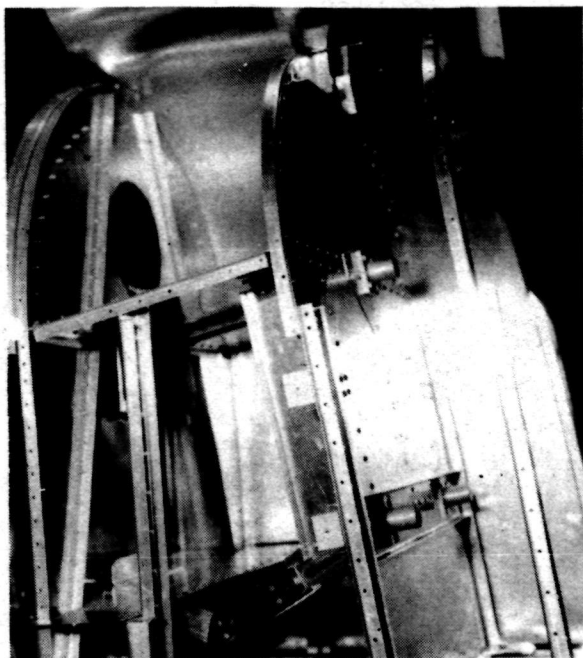
T-9

Fig. 2-11 Details of Forward Fuselage Module

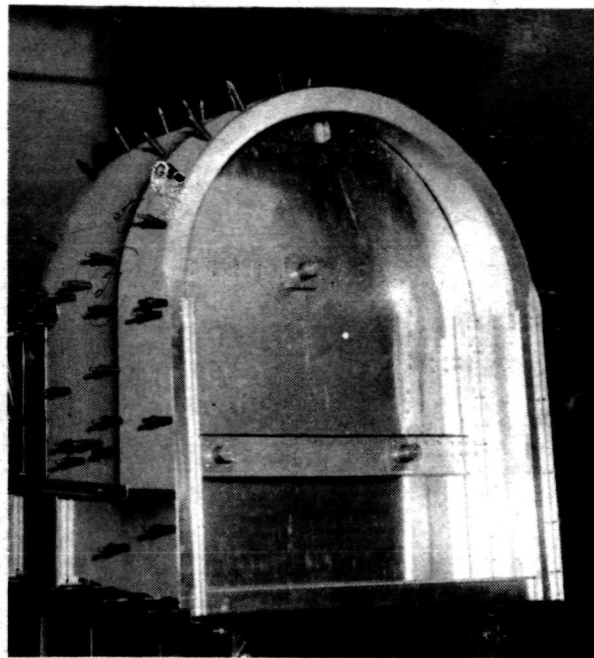


T-10

Fig. 2-12 Forward-To-Mid-Fuselage Interface



T-11 Fig. 2-13 Aft Fuselage Details

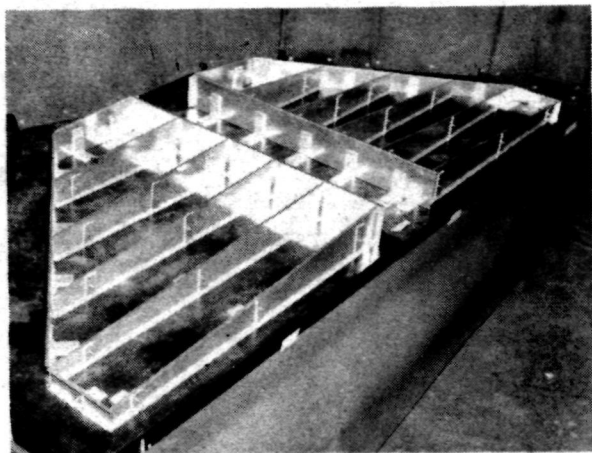


T-12 Fig. 2-14 Aft Fuselage — Engine Mounts

The fuselage frames in the cargo bay region are constructed of aluminum sheet bent to form a channel section. The tapered side wall channel section and the lower portion are attached back-to-back to form a U-shaped frame (Fig. 2-10). The material used to form the frames is sufficiently thick to ease fabrication and to avoid buckling. In addition, the frames are heavy enough to simulate some of the non-structural weight in the prototype. The details of the prototype bulkheads were not scaled to avoid excessive costs, and because these details are not significant in establishing the primary structural dynamic characteristics of the model. Figure 2-14, the aft fuselage during assembly, shows the three simulated engine mounts.

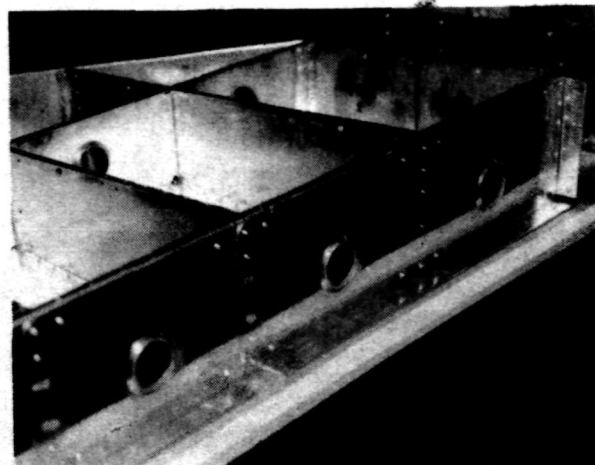
2.3.2 WINGS

The delta wings, shown under construction in Fig. 2-15 and 2-16, consist of six spars and four ribs formed from .032-in. 2024 aluminum sheet. The covers are 0.020 in. thick, constant over both upper and lower surfaces. The wing tapers in depth from 2.5 in. at the tip (BL 61.58) to 6.0 in. at the root (BL 13.75), with the top cover at a constant elevation (WL 51.5). Shear fittings connect the closure rib at BL 13.75 to the fuselage frames (the side wall of the fuselage is at BL 12.5). The bottom cover is spliced to the fuselage bottom skins and the upper cover is spliced to the fuselage carry-through deck extending from station 144.75 to Station 170.75.



T-13

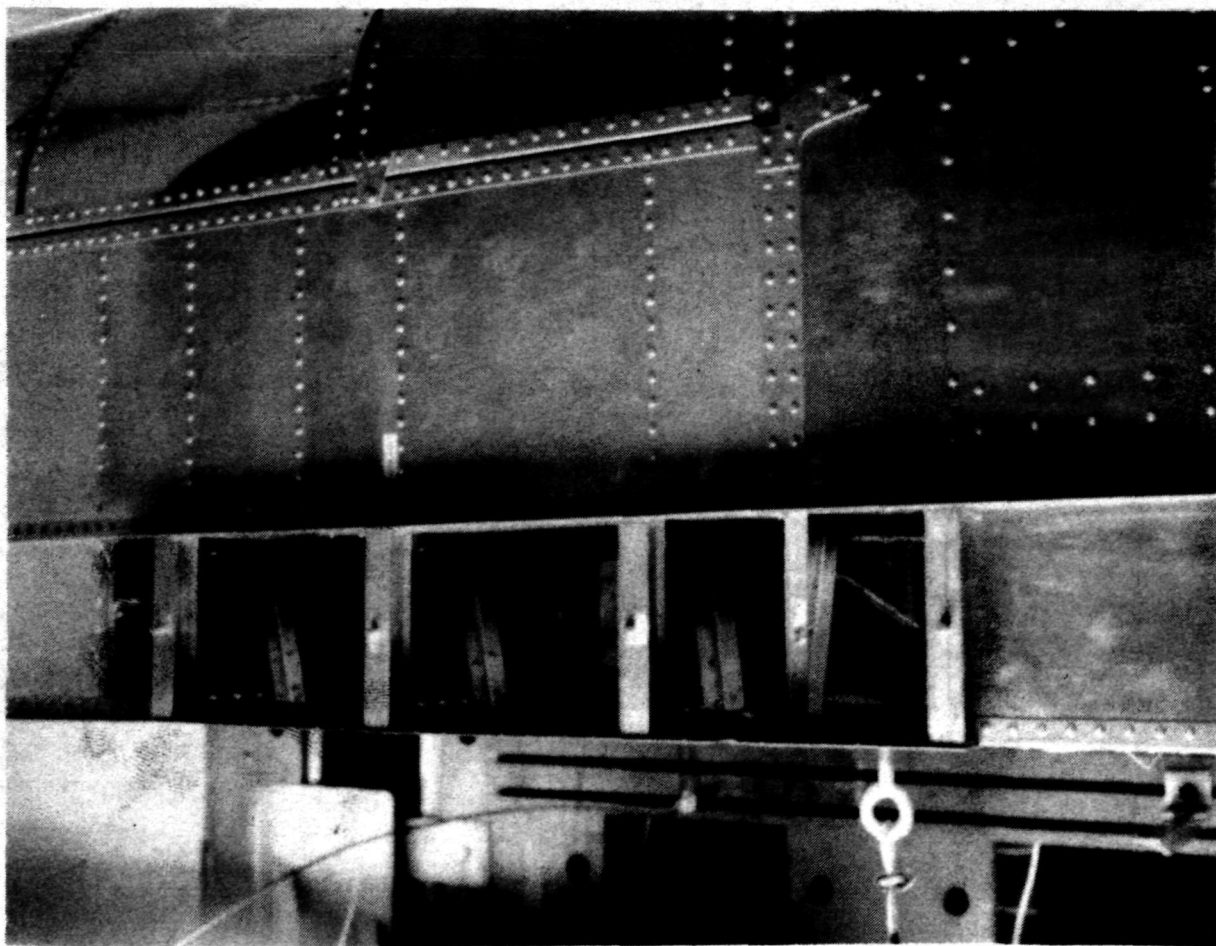
A. Wings During Assembly



T-14

B. Wing Rib and Spar Details

Fig. 2-15 Construction of 1/8-Scale Orbiter Model Wing



T-15

Fig. 2-16 Fuselage Side Wall and Wing Shear Attachments

This means that full bending continuity exists only between the last four spars in the wing. To some extent, this simulates the behavior of the prototype where the wheel well in the forward portion of the wing requires a large cut-out in the lower surface. Thus, although the wing is a delta planform, it tends to act more like a high aspect ratio structure. The proper weight distribution on the wing has been obtained by adding steel ballast plates to the rib and spar webs.

2.3.3 VERTICAL FIN

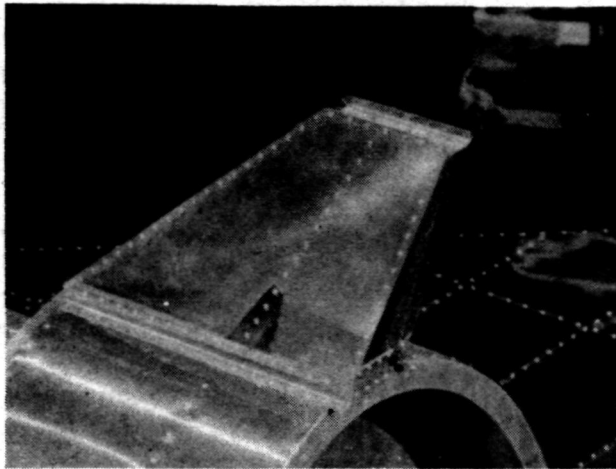
The vertical fin, Fig. 2-17 and 2-18, contains three spars and a closure rib that supports the fin ballast weight. The ballast weight is located at the scaled prototype center of gravity, hence the model fin is much smaller in planform than would be required if the total fin were modeled. The spar webs are 0.032 in. thick, and the covers are 0.020 in. thick. The forward spar is connected to the fuselage bulkhead at Station 166.5 by a 0.040-in. thick angle fitting. The aft spar is connected by a similar angle fitting to the fuselage closure frame which is relatively flexible, compared to the two bulkheads that support the forward and mid-spars. The central spar is connected to the engine support bulkhead through gusset panels from the spar flanges to clips attached to an angled doubler.

2.3.4 CARGO DOORS

The cargo doors (Fig. 2-19) consist of a removable seven-segment semicircular cylindrical shell. The semicircular frames at the ends of each segment have a common lower flange and independent upper flanges attached to adjacent shell segments. These V-shaped frames allow the door segments to breathe in the fore-aft direction, yet act in resisting shear forces. The door segments and frames are connected to the door longeron which, in turn, is attached to the fuselage upper longeron by four keystone shaped fittings (see Fig. 2-20). The door shell segments are 0.016-in. thick, compared to a scaled prototype value of 0.00325 in. The heavier gage is required to prevent buckling.

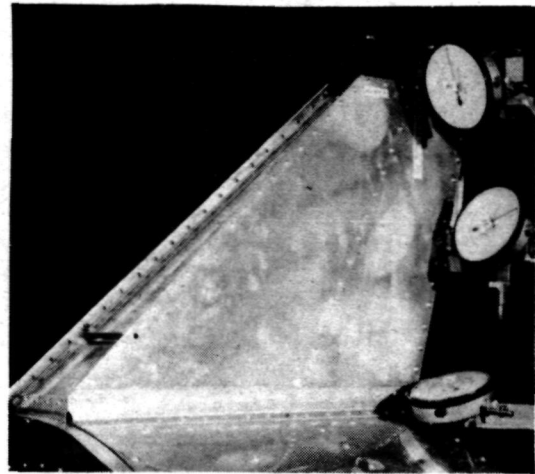
2.3.5 PAYLOAD, BALLAST WEIGHTS, ATTACHMENTS AND OTHER DETAILS

The payload (Fig. 2-21 and 2-22) consists of two channels intermittently welded together at the flanges to form a closed box. Fittings were then attached to this box to support it in a statically determinate fashion within the cargo bay area of the fuselage. The model is constructed to accommodate four types of payload; however, only the full-up

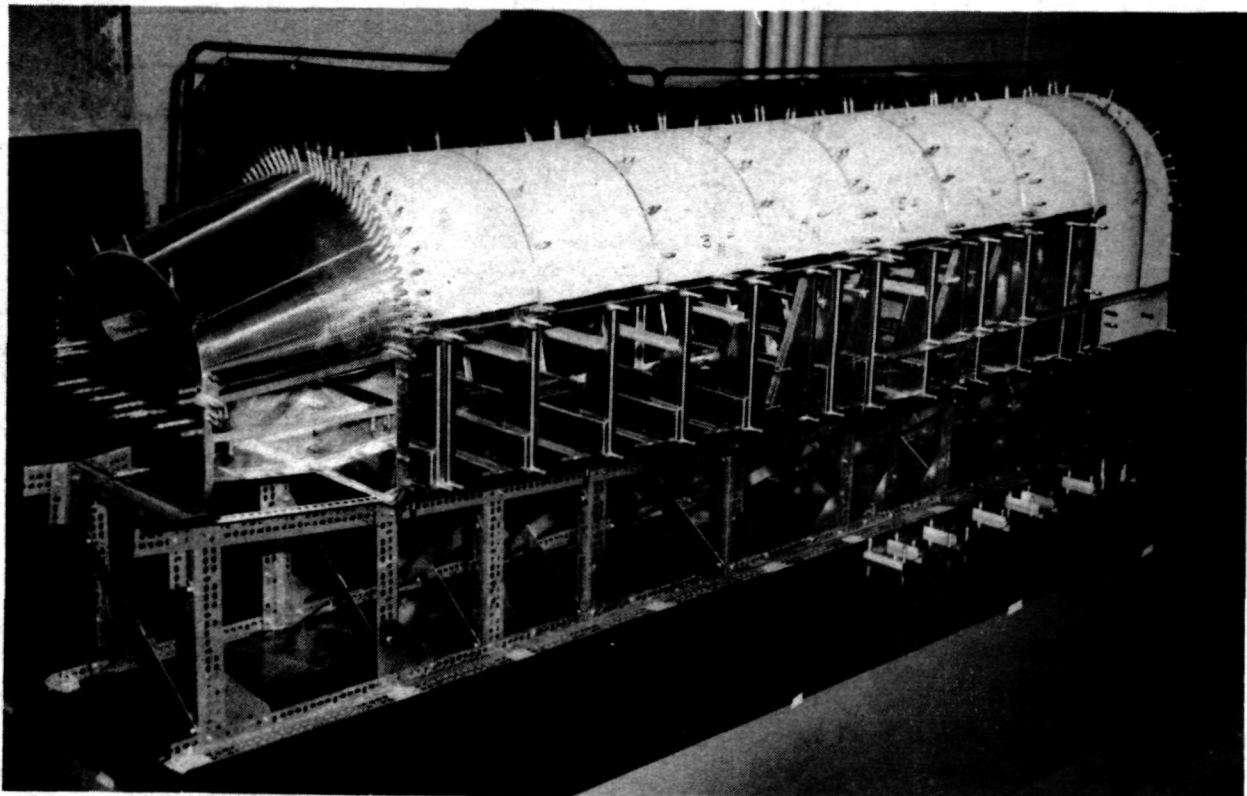


T-16

Fig. 2-17 Fin Structure

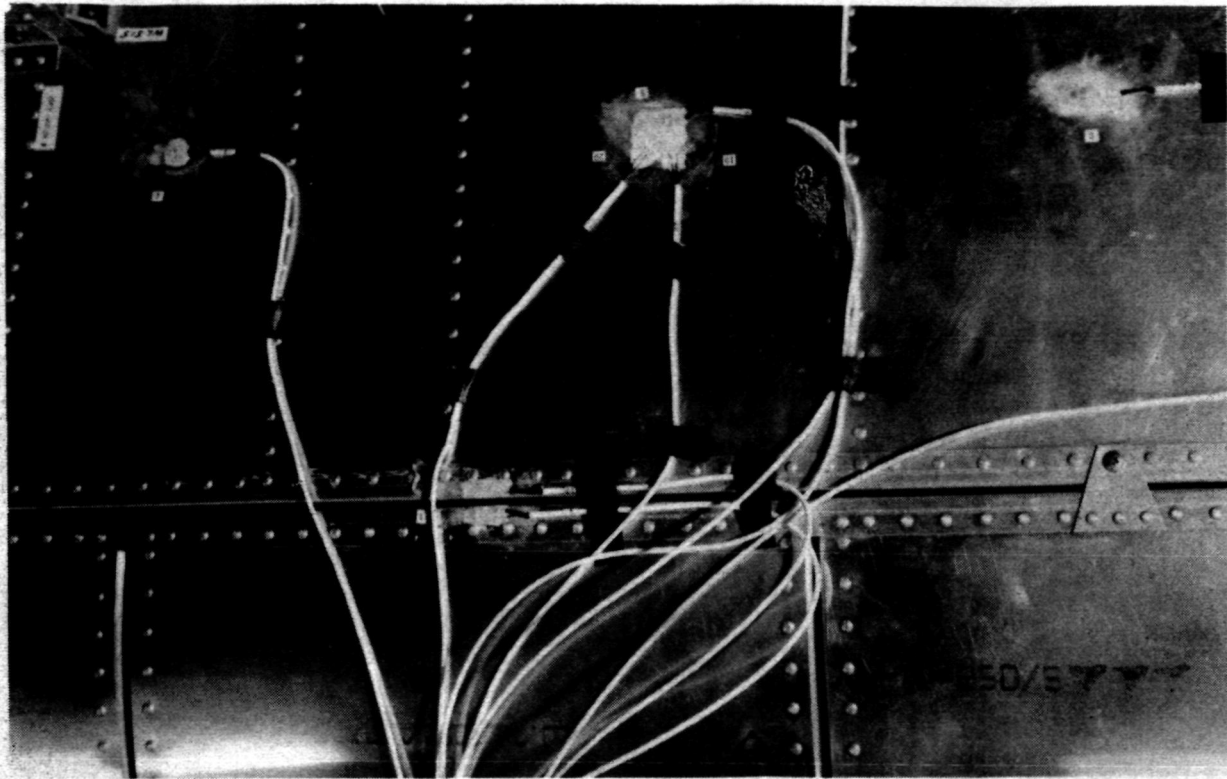


T-13 Fig. 2-18 Fin Forward Attachment Detail



T-18

Fig. 2-19 Cargo Doors During Assembly



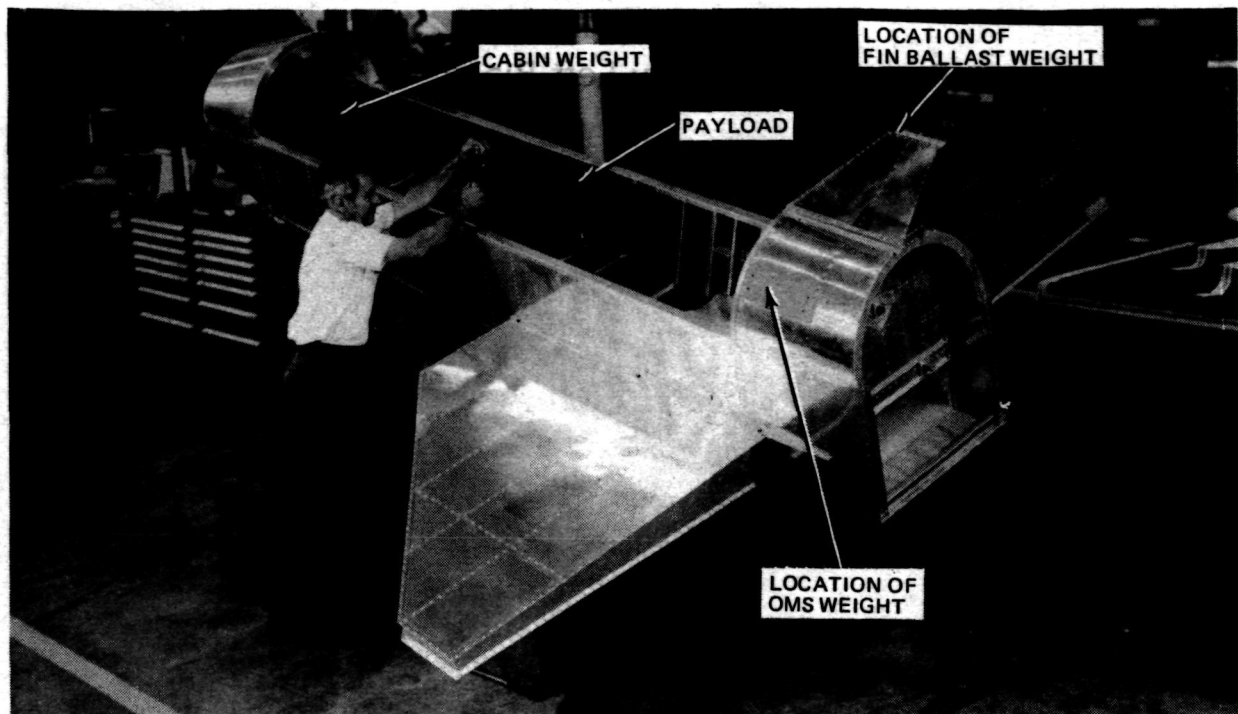
T-19

Fig. 2-20 Cargo Door Attachment Details

payload case (equivalent to 65,000 lb in the prototype) was analyzed. For this condition, the forward payload support (FS 78.0) provides vertical and side load reactions. At the aft end, outrigger brackets provide two vertical supports connecting the payload to the fuselage sidewall at FS 151.875, BL \pm 10.125. Drag and side load are taken out at the aft end of the payload on the center line. Typical payload attachments are shown in Fig. 2-22.

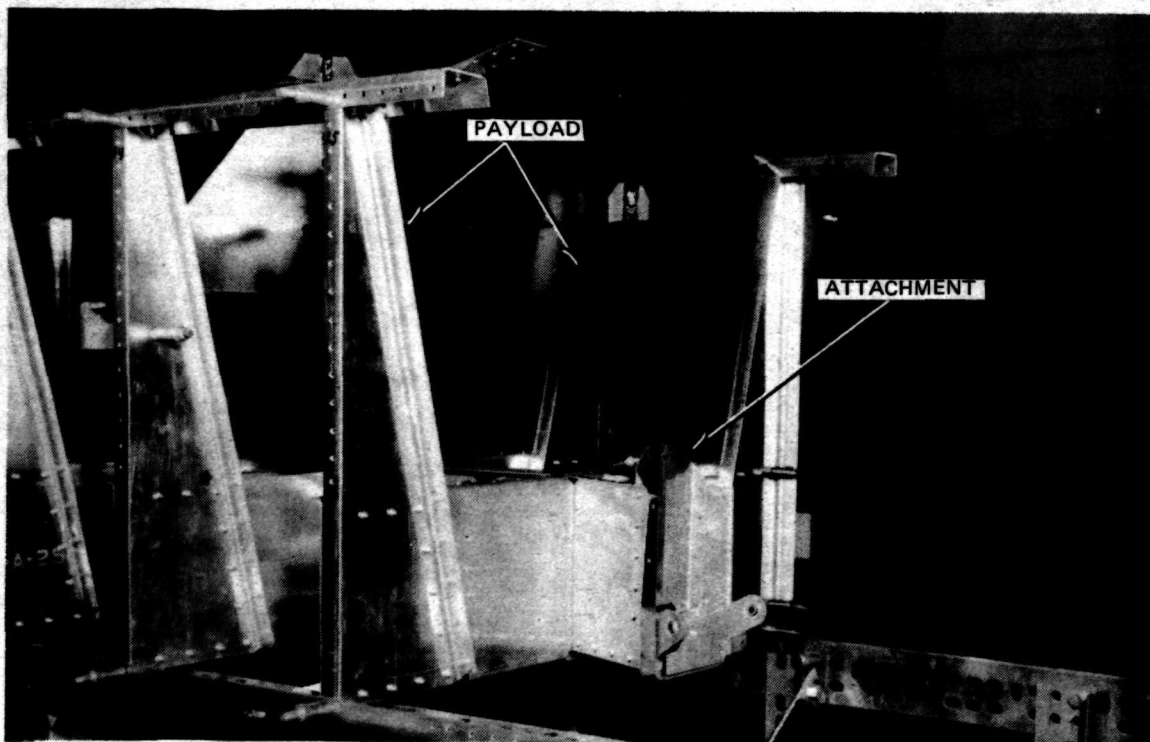
Major ballast weights (Fig. 2-21) consist of the cabin ballast, of 58.4 lb; two OMS ballast weights, 29.2 lb each; and the fin ballast, 6.0 lb.

A difficult task in designing a scaled model is the simulation of the behavior of fittings and connections to the proper scale. In the 1/8-Scale Orbiter Model, joints and attachments have been simplified primarily to reduce fabrication costs. Basically, it is believed that the model joints are stiffer than the prototype, except in certain locations such as the fin-fuselage connection, the forward-mid-fuselage splice, and the forward payload attachment. Analytical modeling of the cargo door attachments proved to be rather subtle. The torsional stiffness of the fuselage depends greatly on the behavior of these attachments.



T-20

Fig. 2-21 Location of Main Ballast Weights



T-21

NOTE

This configuration not used in tests to date. Presented to show typical details only.

Fig. 2-22 Payload Typical Attachment Details

Section 3
FINITE ELEMENT ANALYSIS PROCEDURES

3 - FINITE ELEMENT ANALYSIS PROCEDURES

3.1 BASIC PHILOSOPHY

The following guide lines were established in setting up the finite element model and analysis procedures:

- (1) The entire vehicle would be analyzed using NASTRAN.
- (2) The model would be of sufficient refinement to adequately predict overall dynamic behavior. No attempt would be made to try to predict local panel motions.
- (3) The modeling detail would be of sufficient refinement to allow for the prediction of internal load distributions that would be adequate for preliminary design of the structure. Although there was no intention of computing internal loads, the analysis was considered to be representative of an actual prototype design situation. Interest, therefore, existed in evaluating how NASTRAN would blend into a design environment.
- (4) The total structure would be analyzed by employing substructuring techniques to again evaluate how well NASTRAN could handle these procedures in a design environment. NASTRAN could, in principle, handle the entire Shuttle as a single unit; realistically it can not. The total vehicle contains the Orbiter, External Tank (ET) and two Solid Rocket Boosters (SRB's). This combined hydro-visco-elastic problem required far too much computer time to be considered as a single unit. The Orbiter by itself could have been considered as a single unit, but again, this did not represent a realistic situation.
- (5) Analyses of the ET and SRB's would be performed under separate contract to investigate the hydro-elastic and visco-elastic capabilities of NASTRAN (References 9-1 and 9-2). All four bodies (Orbiter, ET, and SRB's) would be coupled using static substructuring techniques to obtain an analytical model of the launch configuration.

(6) The NASTRAN weight analysis capability would be used to calculate the individual component and total weights for the nonfluid portions of the model. A supplementary weight check would be conducted and the NASTRAN results adjusted where necessary. Structural grid points would be used as dynamic mass points using the Guyan reduction method as required. Note that this procedure differs from Grumman's usual practice, which is to establish a weights model independent of the structural model. In this approach, unit loads on the weights model mass points are then beamed to appropriate structural node points. The dynamic model is thus the same as the weights model or a subset of it. This procedure inherently results in a smaller dynamic model and additional reduction schemes are not necessary. The equivalent reduction takes place in the beaming of unit loads from the weights model to the structural model. This method was not used because

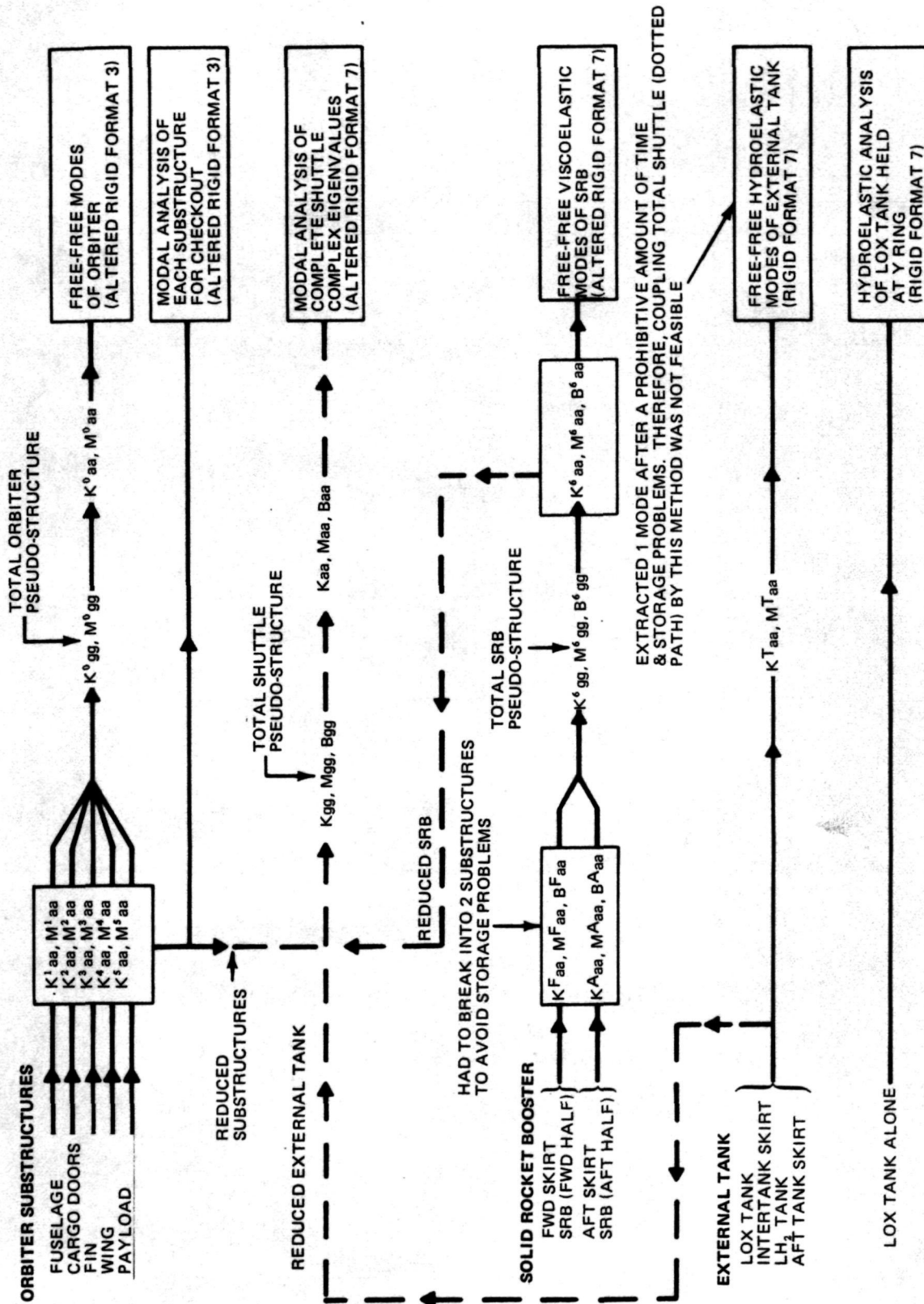
- More extensive alters to the NASTRAN rigid formats would have been required
- The NASTRAN weight analysis capability would not have been used
- Basic mode data would have been produced at nonphysical points which might hinder test correlation.

3.2 OVERALL ANALYSIS FLOW

The overall analysis flow, Fig. 3-1, represents the originally proposed analysis for the combined total vehicle. The Orbiter was divided into five substructures: fuselage, cargo doors, fin, wing and payload. The ET was divided into two substructures: the LOX tank and the aft portion of the external tank (consisting of the inter-tank skirt, LH₂ tank, and aft tank skirt). The SRB was to be handled as a single unit (consisting of the forward skirt, propellant cylinder and propellant, and the aft skirt).

Several technical problems arose during the study which prevented the completion of the proposed overall analysis, namely:

- The Orbiter analysis was completed at the same time that initial test results were made available. A rather poor correlation was shown to exist for the Orbiter alone



- Separate analyses were performed for the following SRB and ET structures:
 - LOX tank alone
 - Total ET, comprising the LOX and LH₂ tanks coupled with the intertank and aft tank skirts
 - SRB alone.

The SRB had to be divided into two substructures, and then coupled using an "ALTERed" Rigid Format 7. Storage problems were encountered in attempting to analyze the total SRB. Analysis of the total tank structure using the ALTERed Rigid Format 7 uncovered the practical inadequacy of NASTRAN in solving large hydroelastic problems. One mode was obtained after using what was considered to be an extremely large amount of computer time.

The two major problems encountered (lack of correlation of analysis and test data for the orbiter; excessive computer time requirements for coupling the total vehicle) forced a decision to abandon the original overall analysis flow. Consequently, basic effort was redirected to rectifying the Orbiter analysis to obtain correlation with test results; also a separate study (Contract NAS 1-10685-21 with Grumman) was initiated to find a means for improving the efficiency of the hydro-elastic analysis. Upon completion of this parallel study, current plans are to couple the components of the total vehicle using modal coupling procedures, rather than the standard type static procedures indicated in Fig. 3-1.

In the context of this report, the original Orbiter analytical model is designated "Model I"; the modified analytical model, which reflects test behavior, is referred to as "Model II." The analytical procedures used for both models were the same, except where noted.

Referring to the Orbiter portion of Fig. 3-1, observe that each of the five Orbiter substructures was analyzed to produce reduced mass and stiffness matrices for selected dynamic degrees of freedom (DOF's) and interface attachment points. Modes for these substructures were then obtained with the interfaces held - an exception is the fuselage, which was analyzed in a free-free condition. This approach aided in checking and understanding the behavior of the combined Orbiter vehicle. Next, the five substructure stiffness and mass matrices were merged to form the total Orbiter

mass and stiffness matrices. These matrices were again reduced to yield final stiffness and mass matrices that were used in the modal analysis.

3.3 SUBSTRUCTURING PROCEDURE

The basic substructuring procedure for combining substructures as presented in the NASTRAN User's Manual were followed, but with some minor changes in the assumptions used, and with more extensive DMAP ALTERS. These ALTERS were written for Rigid Format 3 to provide for a more reliable substructuring procedure.

The analysis was performed in two phases, as shown in Fig. 3-2. In NASTRAN Phase 1, each substructure was analyzed and checked separately. The output from this phase was then assembled onto a copy tape for the symmetric and antisymmetric cases, and coupled in NASTRAN Phase 2. The same set of ALTERS are used for both phases, the particular phase being determined by an input parameter.

The following assumptions were used in formulating this substructuring procedure:

- Any external supports present are included in the Analysis Set (a-set)
- Any zero stiffness DOF's and symmetric or antisymmetric boundary constraints at the model plane of symmetry are included in the Single Point Constraint Set (SPC-set). No other DOF's are included in this set
- Masses which are associated with zero stiffness DOF's will be lost unless these DOF's are "beamed" to adjacent points using Multipoint Constraints (MPC's)
- The interface DOF's may be sequenced differently and in different coordinate systems in any two substructures to be coupled. The MPC's are used to relate the appropriate DOF's irrespective of local coordinate systems or initial sequencing
- Grid points, rather than scalar points, were used in Phase 2. This allowed total Orbiter mode plots to be obtained in this phase, rather than obtaining substructure mode plots in a NASTRAN Phase 3 run. PLOTTEL elements were used to define the Phase 2 Orbiter pseudo structure

- The grid cards used in Phase 2 were the same as the grid cards used in Phase 1 that contained any a-set DOF. Any DOF's not in the Phase 1 a-set were removed by SPC cards. Each substructure had a unique set of grid identification numbers, and referenced a common basic coordinate system.

Although the general theory presented in the NASTRAN User's Manual for substructuring is correct, it does not provide analysis checks at various critical points in the procedure. Consequently, the following checks were incorporated in the Model I analysis by means of DMAP ALTERS:

- A rigid body check was made in Phase 1 after the generation of the reduced stiffness and mass matrices. Temporary rigid body supports were included in the deck as "support" cards for this purpose
- The structural transformation matrixes G_m , G_o , and D were used to generate equilibrium matrices for the various constraint sets, except SPC's. These equilibrium matrices represent resultants about a chosen origin due to unit applied loads at the appropriate DOF's
- Provision was made to compute either free-free modes, or modes with the substructure held at the interface. This is necessary if each substructure is to be checked independently in Phase 1
- A rigid body mass matrix relative to the basic origin was computed. This was compared with the general mass matrix calculated by the Grid Point Weight Generator (GPWG). This check verified that no mass had been lost in the reduction process.

The DMAP statements to perform these functions for Rigid Format 3 were presented in Volume IIIB, Appendix B1, of this report.

In the Model II analysis, a revised ALTERED Rigid Format 3 was used. The new alters provide more convenient checks including an SPC check. These ALTERS require a revision in the GPWG module (refer to Volume IIIA, Appendix A4) to obtain a transformation matrix that is generated from geometric data. This matrix expresses the resultant loads in terms of unit G-set loads about a chosen origin that is defined by the GRDPNT parameter.

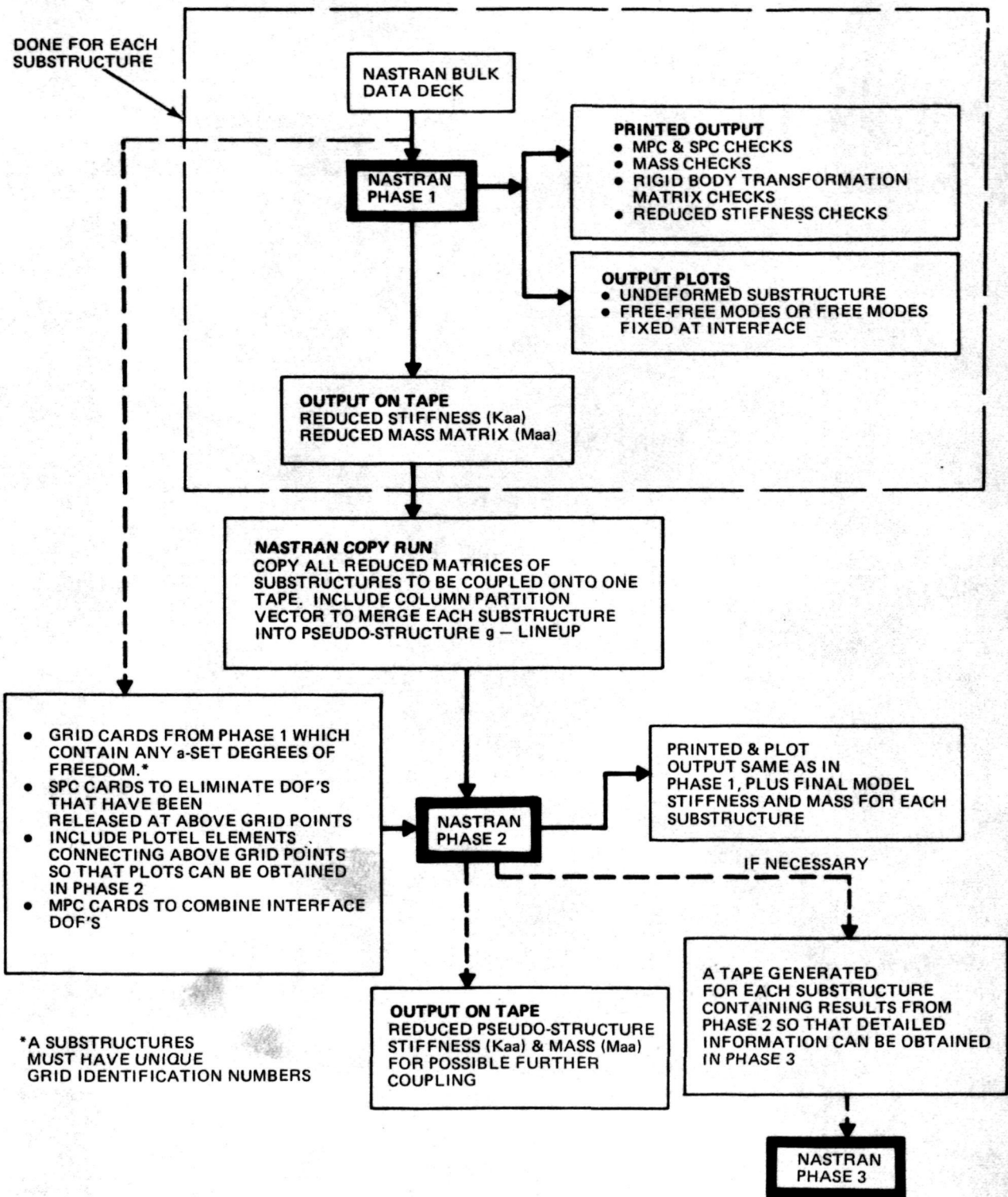


Fig. 3-2 Flow Diagram for NASTRAN Substructuring to Obtain Normal Modes

The rigid body error ratio was removed since the support card could be used to define temporary supports to obtain restrained modes. This eliminated the necessity of inputting a column partitioning vector to remove the temporary supports from the a-set DOF's. It was felt that the reduced stiffness check and the incorporated rigid body transformation checks were more helpful in pin-pointing errors. The rigid body transformation matrices G_m , G_o , and D were related to the rigid body motions of the origin and similar independently derived matrices were subtracted to give rigid body transformation checks.

A rigid body mass matrix was generated from the reduced mass matrix M and compared with the M_o matrix that is output from the GPWG. This approach ensured that no weight had been lost in the DOF reduction process.

The revised ALTERS to Rigid Format 3 are given in Volume IIIA, Appendix A4.

3.4 FINITE ELEMENT MODEL I

Table 3-1 shows the number of grid points and types of finite elements used in Model I for the five Orbiter substructures. Sketches of the finite element model are presented in Appendix A of this volume. These drawings were prepared to establish the finite element model geometry and member data. In the discussion that follows, reference to these sketches is implied.

NOTE

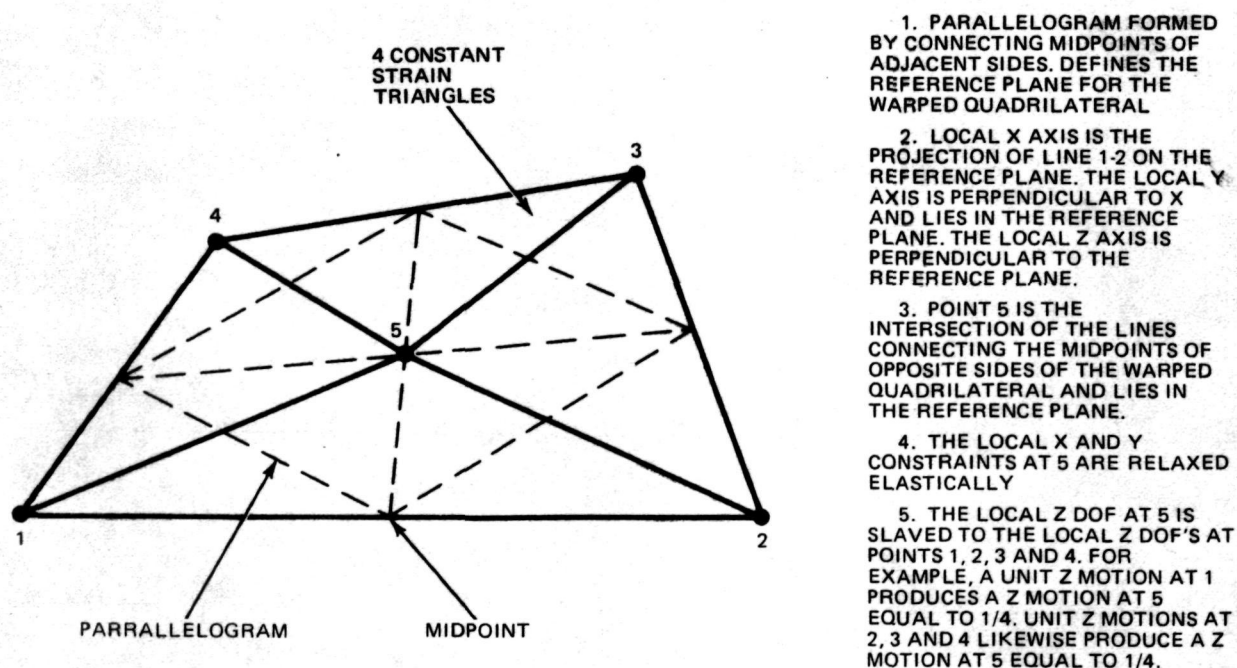
Appendix A includes a list of the sketches it contains. The summary list included here augments the general drawing titles in terms of discussion specifics. Readers should consult these "background" sketches as they may desire, even though the text does not, in every case, cite specific Appendix A illustrations.

- Orbiter general arrangement, Fig. A-1
- Fuselage frames (total of 21), Fig. A-2 through A-4
- Fuselage sidewall (skin), bottom deck, keel, and wing carry-through; also, cargo door frames, and shell segments, Fig. A-5
- Orbiter wing, Fig. A-6
- Fin and payload idealizations, Fig. A-7.

Table 3-1 Statistical Description of 1/8-Scale Orbiter — Model I

Substructure	No. grid points	No. CBAR	No. CODMEM2	No. CSHEAR	No. CROD	No. CTRMEM	No. CQUAD2	Total No. of members	Symmetric Case		Antisymmetric Case	
									DOF after SPC & MPC	DOF after Guyan	DOF after SPC & MPC	DOF after Guyan
Payload	12	8	—	—	—	—	—	8	24	24	26	26
Fin	59	—	24	22	65	—	—	111	101	25	99	24
Wing	192	—	149	81	187	8	—	425	531	183	531	183
Doors	134	9	20	64	178	—	16	287	396	26	384	26
Fuselage	537	93	336	172	616	7	—	1224	1417	246	1368	222
Total (1/2 Orbiter Structure)	934	110	529	339	1046	15	16	2055	2469	504	2408	481
Orbiter Analysis TT-4	215	Contains 125 Plotel elements							400	339	378	324

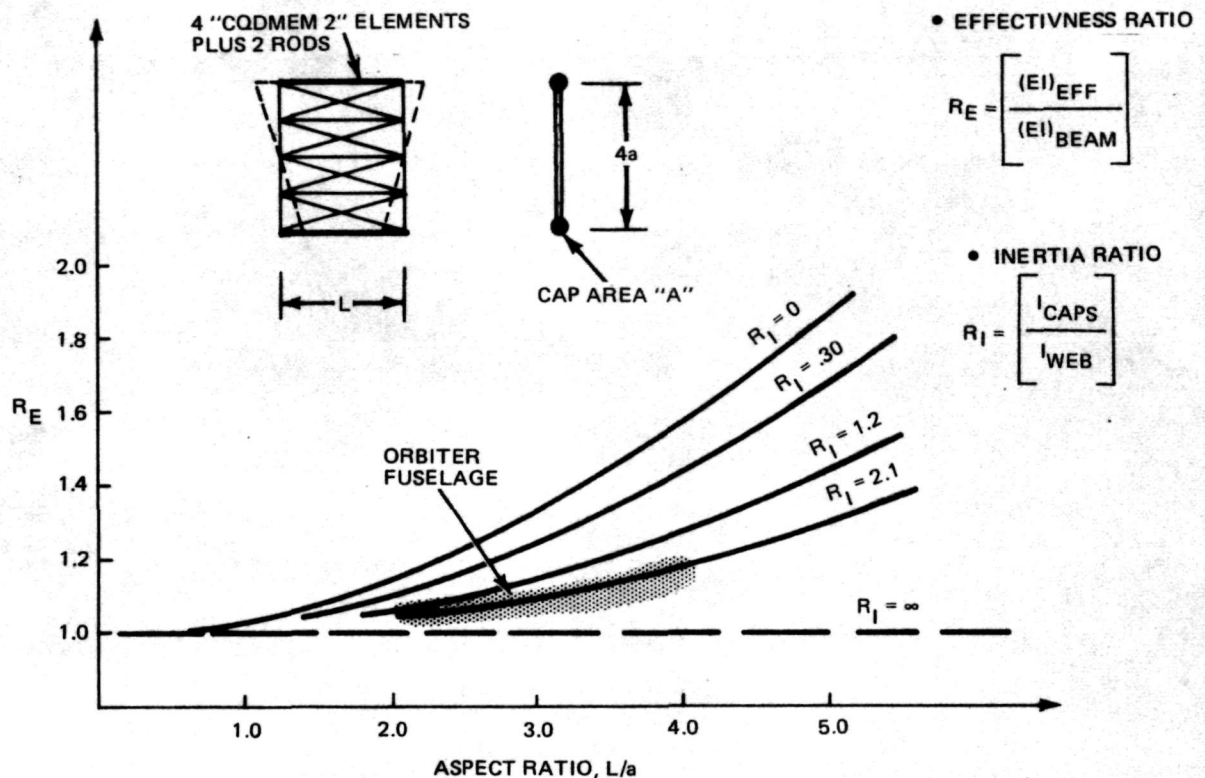
The fuselage shell structure was modeled using CQDMEM2 elements - a new element in NASTRAN, but one that has been used widely at Grumman. As Fig. 3-3 shows, it is a warped quadrilateral composed of four constant strain triangles having a common central node defined by the intersection of lines that connect the midpoints of the opposite sides of the quadrilateral. Figure 3-4 illustrates the suitability of this element to represent the fuselage side wall. The curves in this figure compare the effective stiffness of a composite beam segment subjected to pure bending with the conventional beam formula, $EI = \frac{ML}{\theta}$. In these calculations the node displacements along the sides have been constrained to remain linear by MPC's. With no caps, the error in stiffness becomes larger with increasing aspect ratio. When caps are added, they tend to dominate the bending behavior and reduce the error. The dotted region represents the locus of beam segments for the fuselage side wall. (A single CQDMEM2 element of aspect ratio 1 is 70% too stiff in pure bending, and hence should not be used to idealize the web of a spar or rib.) Note that Fig. 3-4 implies that the expected error for the fuselage side wall should be in the neighborhood of 10% or less. But the curve in Fig. 3-4 is only indicative of the behavior of a composite beam segment. Calculations performed on the fuselage section at Station 116 indicate that the finite element model is only 1.2% stiffer than the actual EI value. (Note also that the finite element model contains more segments than used in developing Fig. 3-4, and the neutral axis is not at the midheight of the section.)



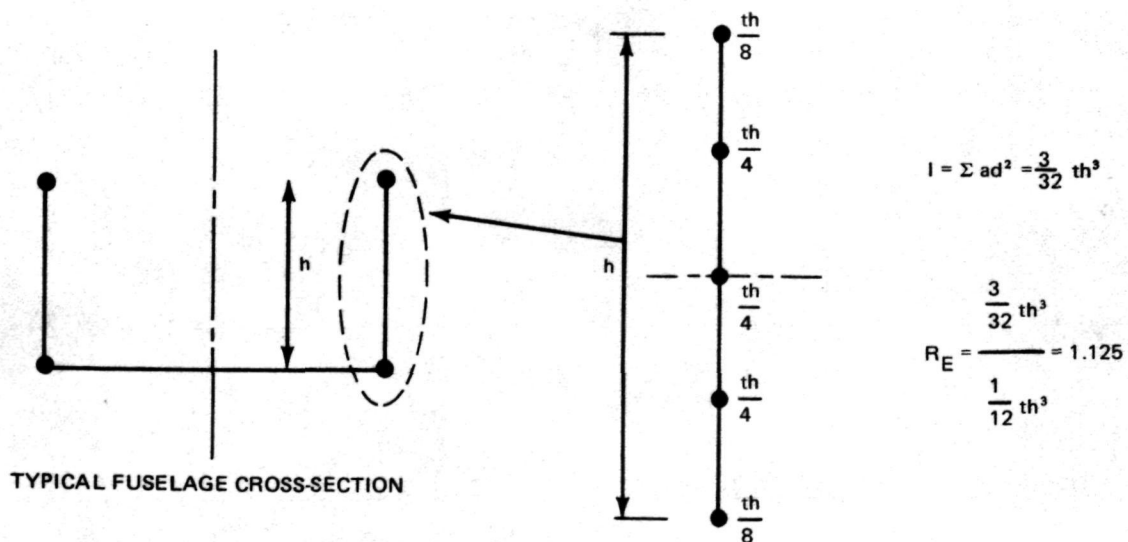
T-24

Fig. 3-3 Basic Assumptions Used in Developing the Warped Quadrilateral "CQDMEM 2" Finite Element

Figure 3-5 is an alternate rod/shear panel idealization. Here, the side wall has been modeled with five rods and four shear panels, wherein the areas of the rods represent the "lumped" adjacent material in the web. A simple calculation indicates that this model overestimates the bending inertia by 12.5%. This error is greater



T-25 Fig. 3-4 Behavior of a Beam Segment Composed of Four "CODMEN 2" Elements and Two Rods



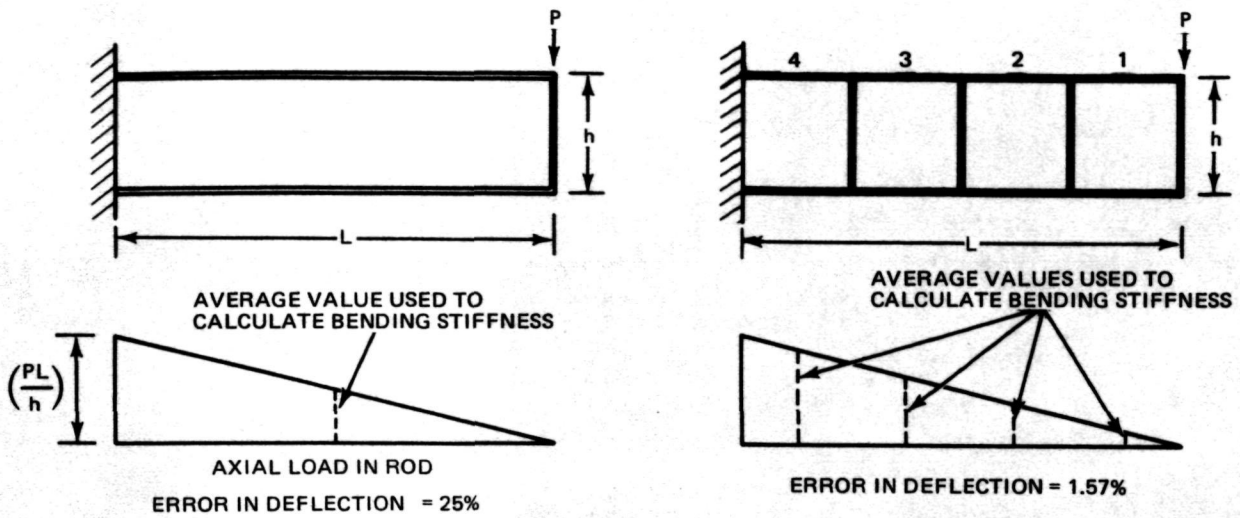
T-26

Fig. 3-5 Alternate Rod and Shear Panel Idealization For Fuselage Side Wall

than the error associated with 4 CQDMEM2 elements of aspect ratio 1 with no cap material. One might be tempted to adjust the areas of the rod and panel idealization to obtain the correct inertia; however, care must be taken in doing this or else the axial stiffness and lateral inertia will be incorrect. With these guide lines in mind, the CQDMEM2 elements were used for modeling the sidewalls. Note that in the foregoing discussion, there is a tacit assumption that the material is unbuckled and fully effective. As pointed out earlier, this assumption follows from the criteria used for the prototype design.

The U-shaped fuselage frames and the keel were idealized using CROD and CSHEAR elements. Here, effective cap areas were calculated for the CROD elements to represent the appropriate bending behavior.

In idealizing bending members with rods and panels, some thought must be given to the refinement of the model. As an example, consider the simple cantilever beam illustrated in Fig. 3-6 where one-sixth of the cross-sectional area (th) of the bending material has been "lumped" into each of two equivalent caps (CROD elements) to preserve the inertia, and the shear material has been idealized as a shear panel. The CROD element uses the average shear load in evaluating the stiffness rather than a linear varying distribution. Figure 3-7 shows the error associated with this approach. This figure compares the strain energy of a constant stress bar with the strain energy for a linearly varying stressed bar (an element usually associated with a force method bar and panel idealization). For this simple case the ratio, R , is zero; from the curve the error is 25 %. This means that the bending deflection is actually 33 % greater ($\frac{\epsilon}{1-\epsilon}$ where ϵ is the percent error from the curve). The only means for improvement, without using a different element, is to further refine the model as shown in Fig. 3-6. The ratio, R , for each of the four top cap rods is 0, 1/2, 2/3 and 3/4 for rod numbers 1, 2, 3 and 4, respectively; the errors are 25, 3.6, 1.3 and 0.68 %, respectively. The combined error is only 1.57 % because the fourth element contributes the most to the strain energy. Note that the shear deformation is the same for either one large panel or the summation of four smaller panels. Thus, in terms of idealizing beam bending behavior, the limitation placed on the aspect ratio of a panel is predominately in terms of a control on the number of rods, and not so much on the shape of a panel.



T-27

Fig. 3-6 Error Associated With Coarseness of Grid

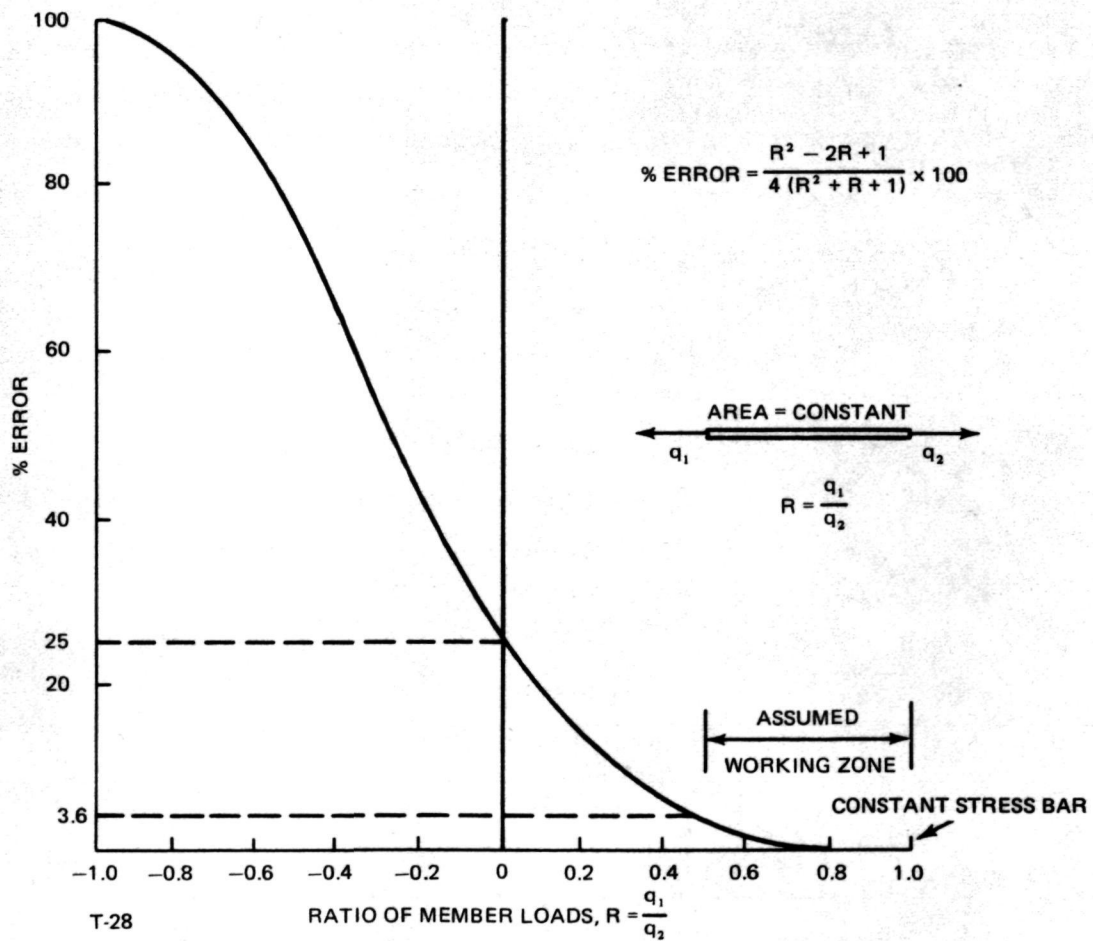


Fig. 3-7 Error in Strain Energy by Assuming Constant Stress in Cap Members

As indicated previously, CQDMEM2 elements should not be used to idealize beam webs - they are too stiff in undergoing this type of behavior. Since CQDMEM elements are even stiffer, the same comment applies. It is advisable not to use a CQDMEM1 (isoparametric element) to represent the web of a beam, even if the direct stress properties are set to zero in attempting to simulate a shear panel. The isoparametric element under these conditions does not behave in the same fashion as the conventional Garvey shear panel (element CSHEAR).

CBAR elements were used to represent thin-ring type of frames, such as the engine compartment closure frame (Appendix A, Fig. A-4). These elements, with offsets, were also used to represent the fuselage upper longeron.

The rib and spar webs of the wing and fin (fabricated from bent sheet) were idealized with CSHEAR elements. Again the effective rib and spar bending material was incorporated into CROD elements located in the covers. The covers themselves were represented by CQDMEM2 elements and, in the case of the wing, some CTREM elements located at the leading edge. Intermediate node lines were established for the wing and fin to further refine the grid. For the wing, the geometry of these node lines was established by the location of fuselage frames.

The shell portion of the cargo bay doors was idealized using CQDMEM2 elements, except for a few CQUAD2 elements that were required for local stability at Stations 102.12 and 129.0. The door frames were idealized with CSHEAR and CROD elements. Note that these frames contain two webs (Fig. 3-8), one common lower cap, and two upper caps that connect to the forward and aft shell segments. This allows the doors to "breathe" in the longitudinal direction. The door frames and shell segments were connected to the door longeron represented by CBAR elements. The longeron was, in turn, connected to the fuselage at four discrete points with MPCs. In Model II, the details of this region were changed; the door longeron was set at WL 62.81, while the fuselage longeron remained at WL 62.5.

The payload was idealized as a series of CBAR elements extending from Station 76.0 to 151.875. The fore and aft fittings that support the payload were assumed to be rigid. (Data for the MPC's is given in Appendix A, Fig. A-7.)

NASTRAN plots of the finite element model are shown in Fig. 3-9 through 3-14.

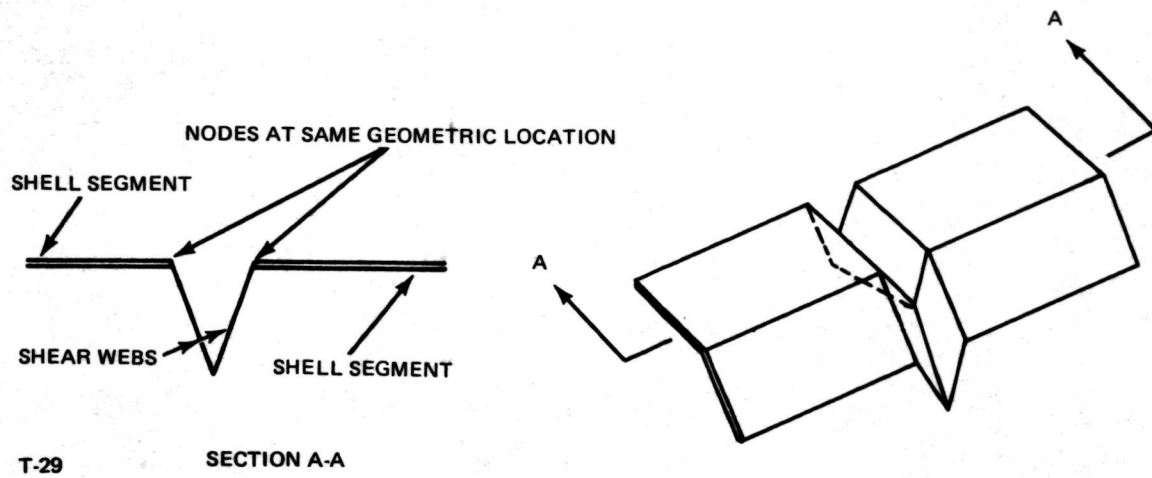
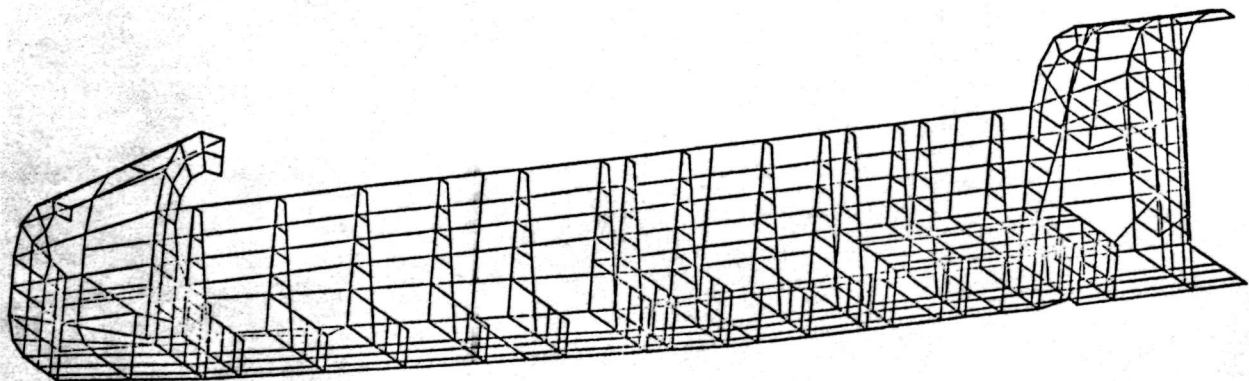
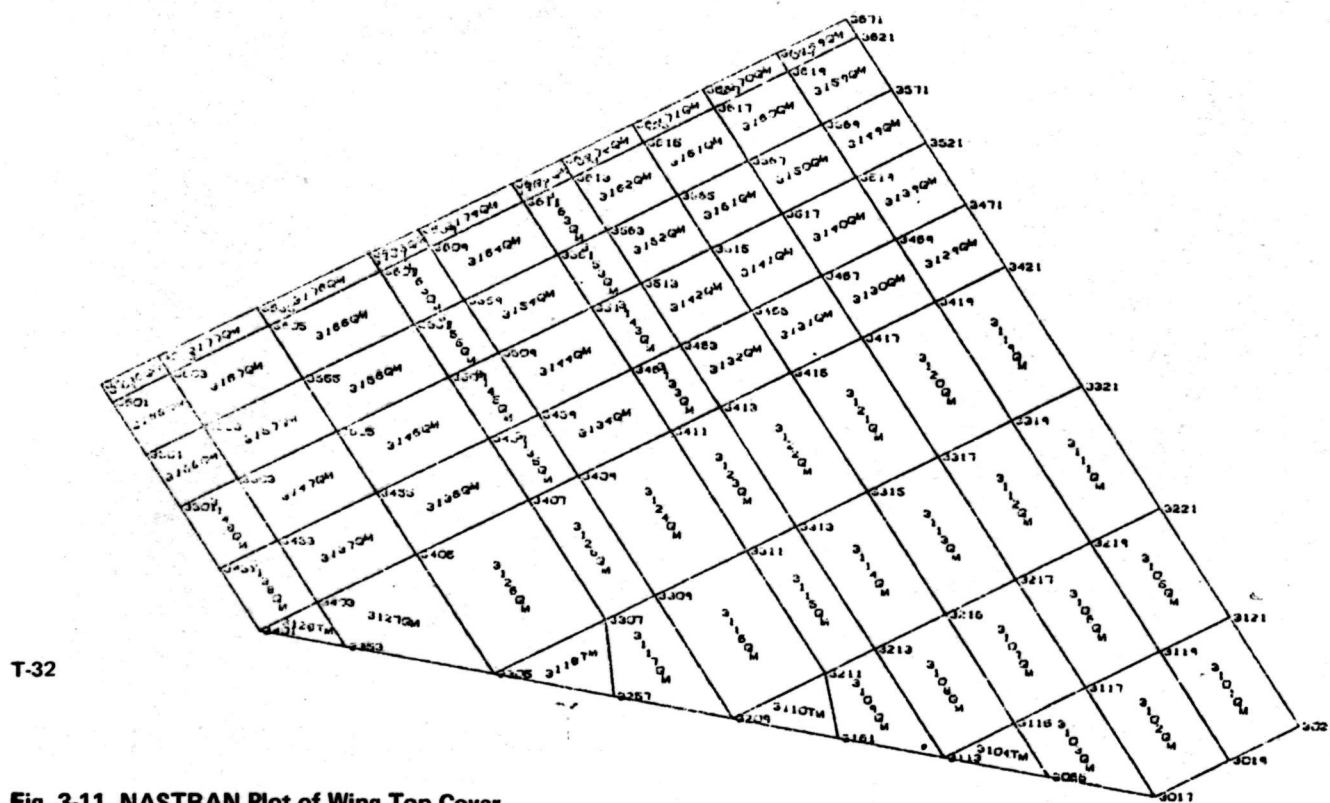
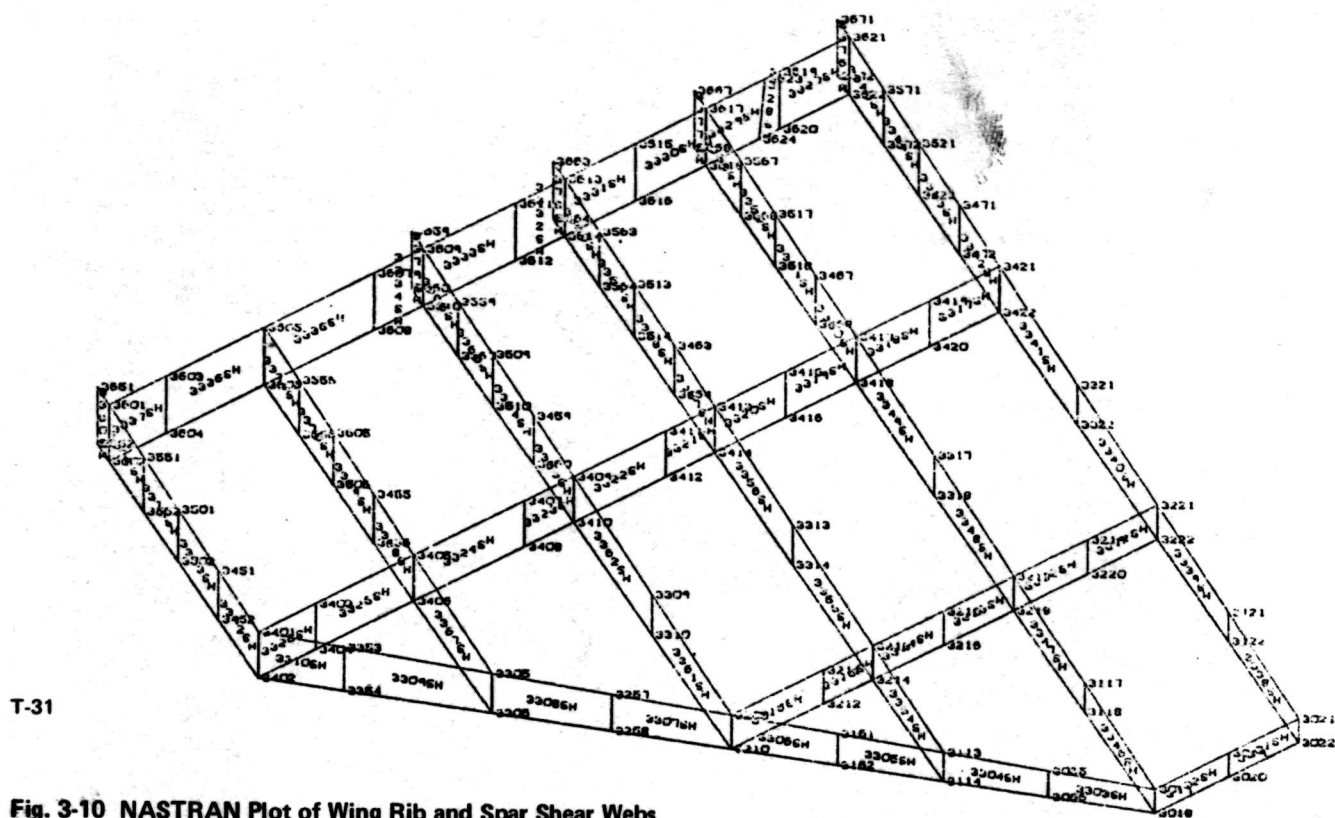


Fig. 3-8 Schematic of Cargo Door Frames



T-30

Fig. 3-9 NASTRAN Plot of Orbiter Fuselage



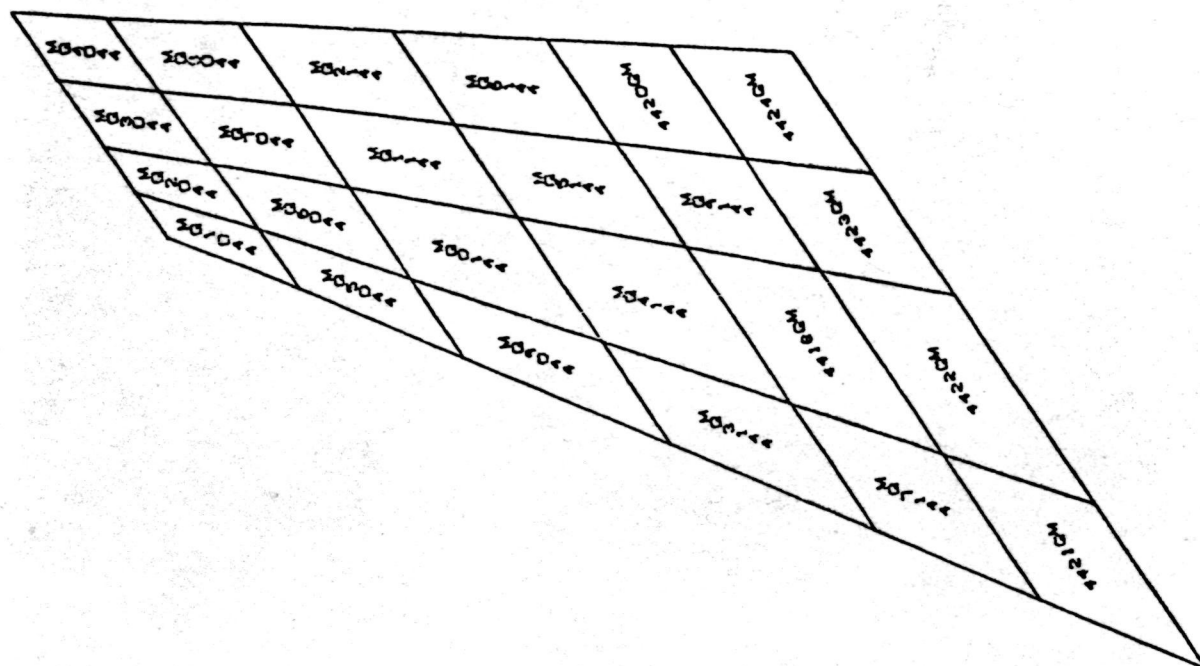


Fig. 3-13 NASTRAN Plot of Fin Cover

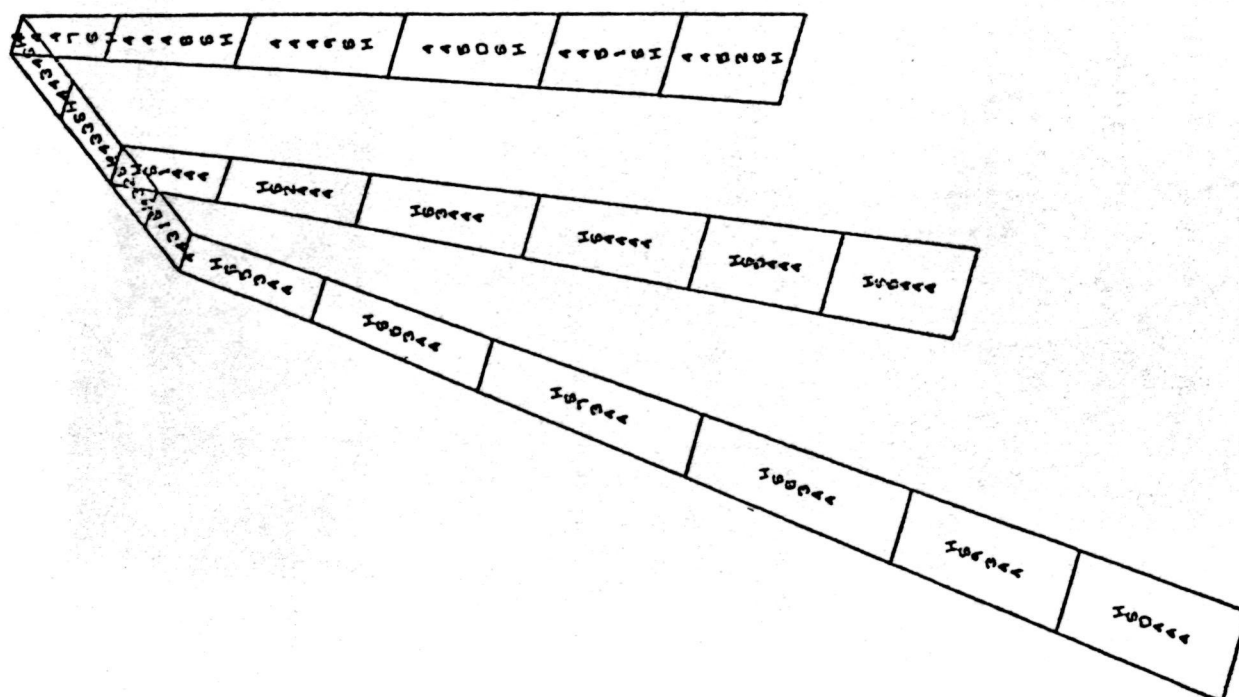


Fig. 3-12 NASTRAN Plot of Fin Webs

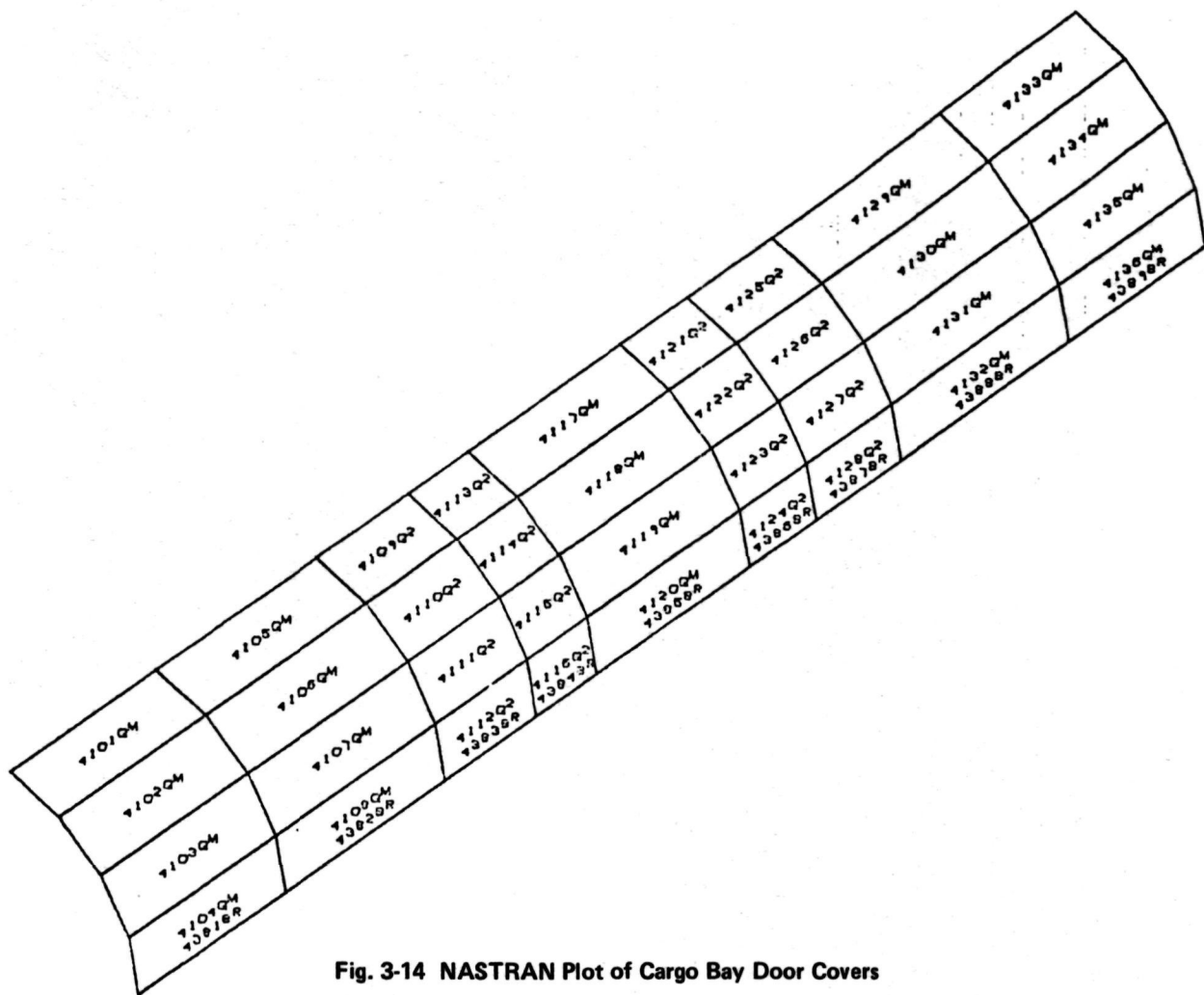


Fig. 3-14 NASTRAN Plot of Cargo Bay Door Covers

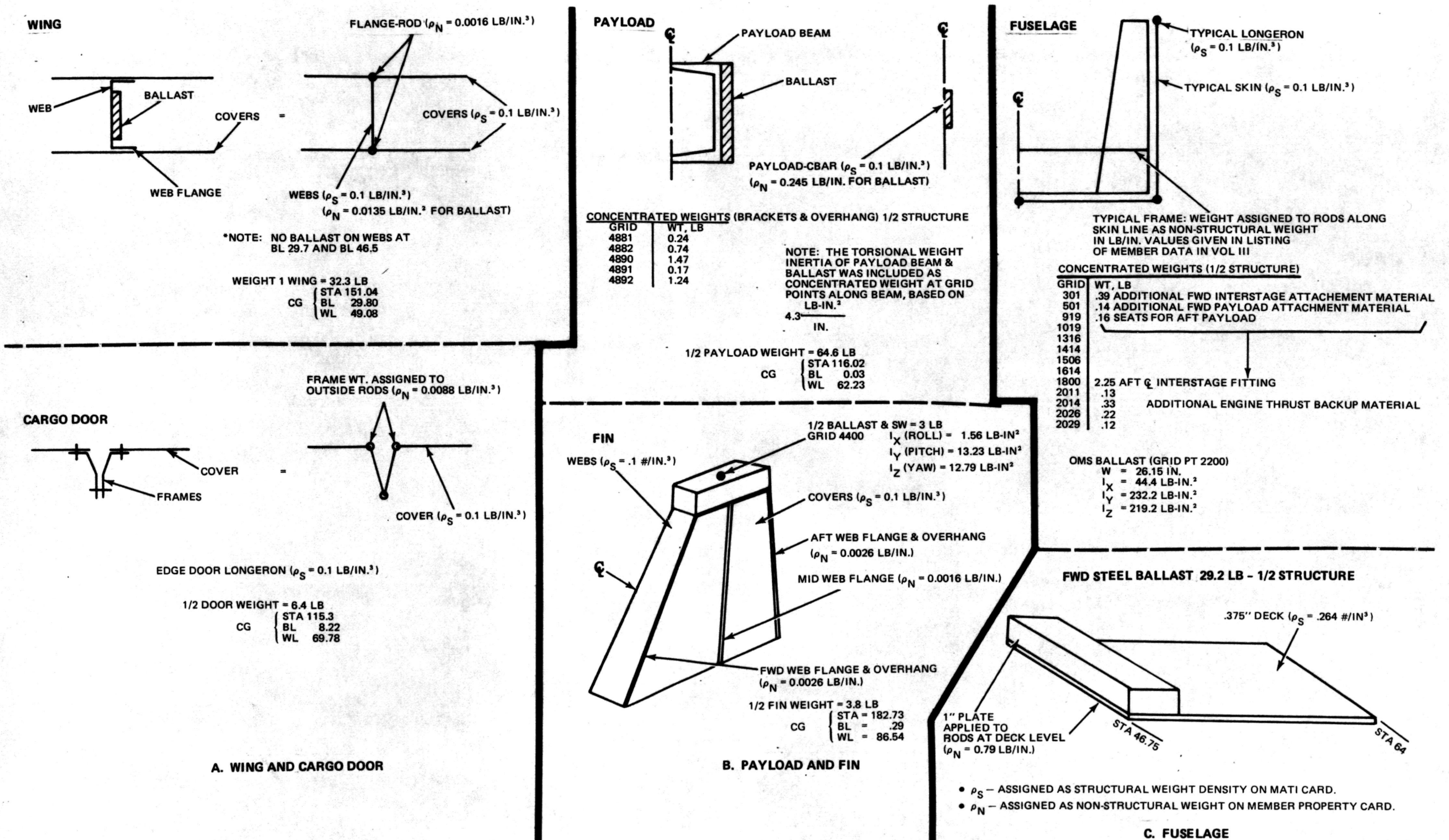
T-35

3.5 MASS DATA

A mass matrix was generated by NASTRAN for each of the substructures using weight data in three forms

- Assigned as structural weight density on MAT1 cards
- Assigned as nonstructural weight on member property cards
- Lumped into concentrated weights.

The sketches in Fig. 3-15 illustrate how the weight was distributed to the various structural grid points. Table 3-2 gives the half-structure Orbiter weights and centers of gravity of the various substructures. Table 3-1 indicates the number of DOF's for



A. WING AND CARGO DOOR

B. PAYLOAD AND FIN

C. FUSELAGE

- ρ_S - ASSIGNED AS STRUCTURAL WEIGHT DENSITY ON MATI CARD.
- ρ_N - ASSIGNED AS NON-STRUCTURAL WEIGHT ON MEMBER PROPERTY CARD.

Table 3-2 NASTRAN Model Weights and Center-of-Gravity Locations

Substructure	Weight, lb (a)	Center of Gravity		
		X	Y	Z
Fuselage	100.8	116.36	8.43	58.37
Wing	32.3	151.04	29.80	49.08
Cargo door	6.4	115.30	8.22	69.78
Payload	64.6	116.02	—	62.23
Fin	3.8	182.73	—	86.54
Total (1/2 Orbiter)	207.9	122.94	—	59.05

TT-5 ^aSubstructure weights are for half structure (including ballast)

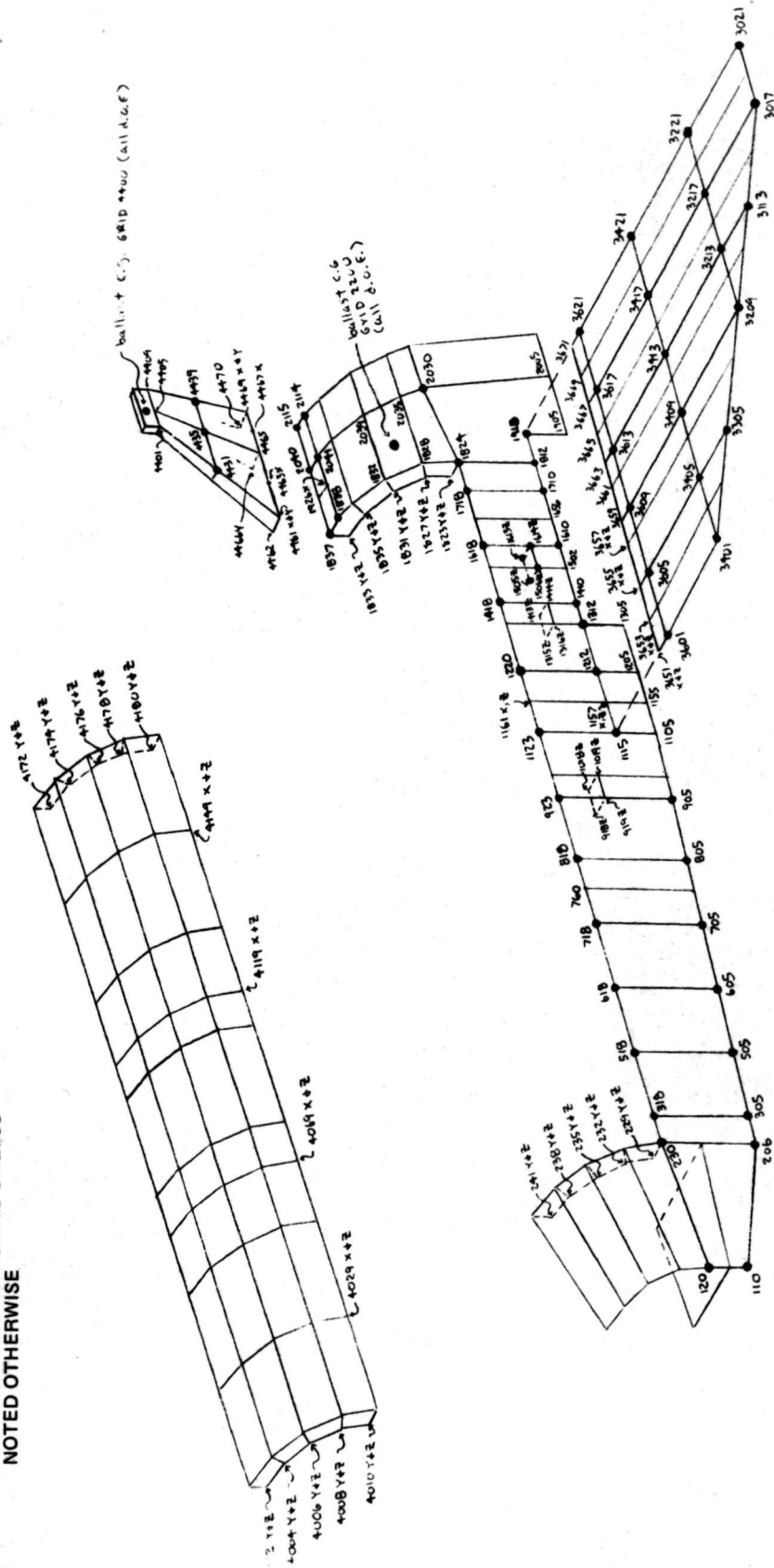
the various substructures after SPC's and MPC's have been applied, and after the Guyan reduction. The final number of DOF's for the symmetric and antisymmetric cases were 339 and 324, respectively. Figure 3-16 illustrates the location of the retained DOF's that were used in the dynamic analysis (Model I).

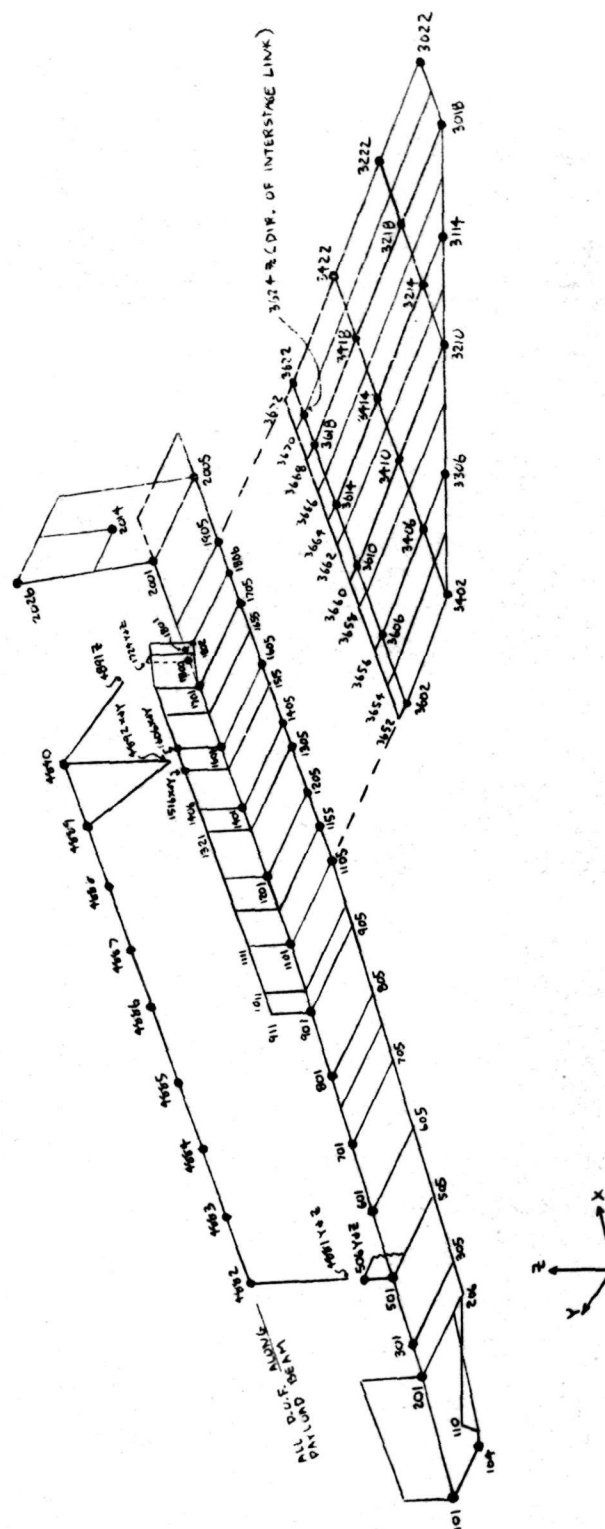
3.6 COMPONENT RESULTS FOR MODEL I

The results for the individual substructures were obtained from the Phase 1 analyses. This output was generated to facilitate understanding the behavior of the substructures and the total vehicle. Subsection 5.5 discusses the use of the fuselage modes in conjunction with a simple beam model to aide in rationalizing the behavior of the total vehicle. Modes were calculated for the substructures either restrained at their interconnection, or in a free-free state, whichever seemed more appropriate. The substructure modes also helped in uncovering input errors, such as an incorrect constraint specification. An additional output from Phase 1 consisted of the weight and center-of-gravity location. This helped to ensure that all mass data was included prior to analyzing the total vehicle. In this regard, it should be noted that although an SPC can properly constrain a nonstrainable DOF in the stiffness matrix (such as motion normal to a bulkhead), any mass located at this DOF will be lost. Mass should not be placed at these DOF's and MPC's should be used to constrain the motion. Obtaining the substructure weight and center-of-gravity data from the substructure mass matrix, using rigid body transformations, thus provides a valuable check.

The lowest frequencies for the various substructures are indicated in Table 3-3 with the corresponding support and boundary conditions. Of particular interest are the values for the fuselage. These were checked by alternate means (described in Section 5) to ensure their validity.

- GENERAL NOTES
- 1) • INDICATES GRID POINTS RETAINED FOR DYNAMIC DOF'S
 - 2) X, Y & Z DOF'S ASSUMED AT GRID POINTS UNLESS NOTED OTHERWISE





T-37(B)

Fig. 3-16 Orbiter Phase 2 Degrees-of-Freedom -- Model I (Sheet 2 of 2)

Table 3-3 Lowest Frequencies for Orbiter Substructures — Model I

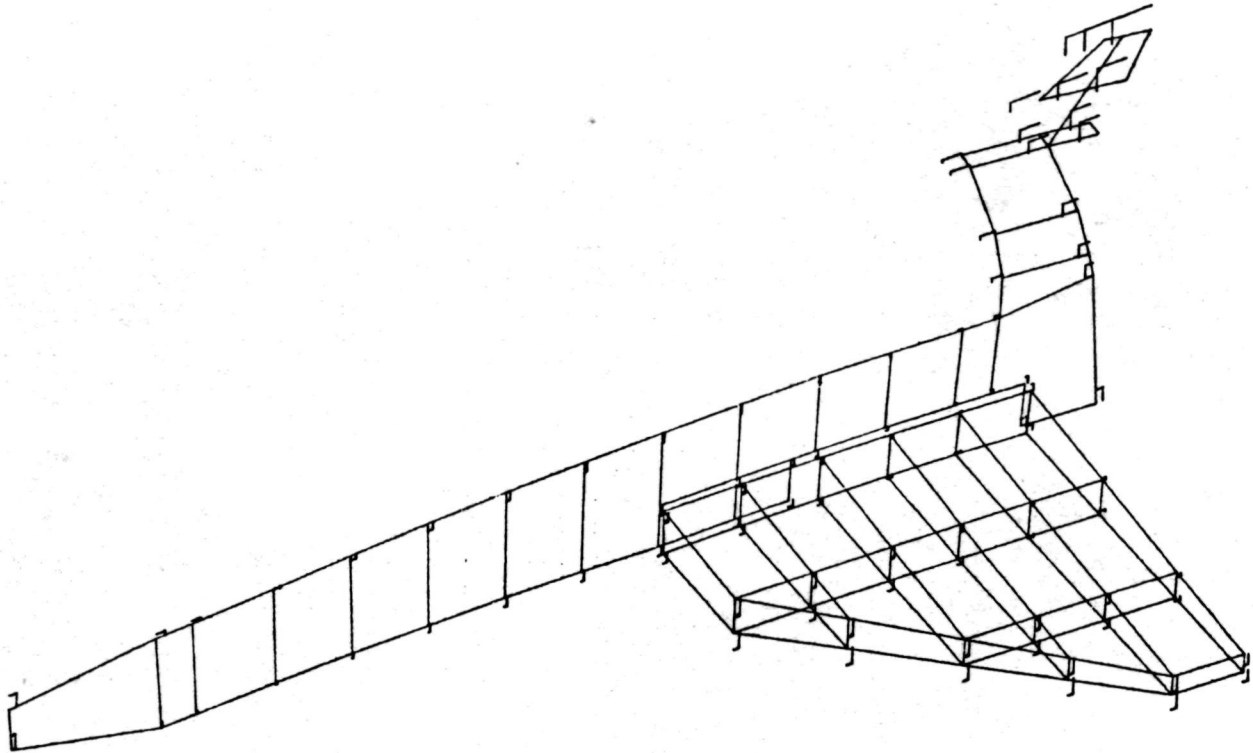
Substructures	Frequency, Hz		
	1st	2nd	3rd
● Fuselage			
— Free, Symmetric	62.2	129.9	
— Free, Antisymmetric	28.7	89.1	128.3
● Payload			
— Restrained, Symmetric	81.2	268.5	627.7
— Restrained, Antisymmetric	68.6	175.4	462.8
● Cargo doors			
— Free, Symmetric	4.6	10.7	17.6
— Restrained, Antisymmetric	156.4	622.2	1054.6
● Wing			
— Restrained	77.6	158.3	259.9
● Fin			
— Restrained, Symmetric	264.2	841.3	1263.3
— Restrained, Antisymmetric	107.8	407.2	1018.7

TT-6

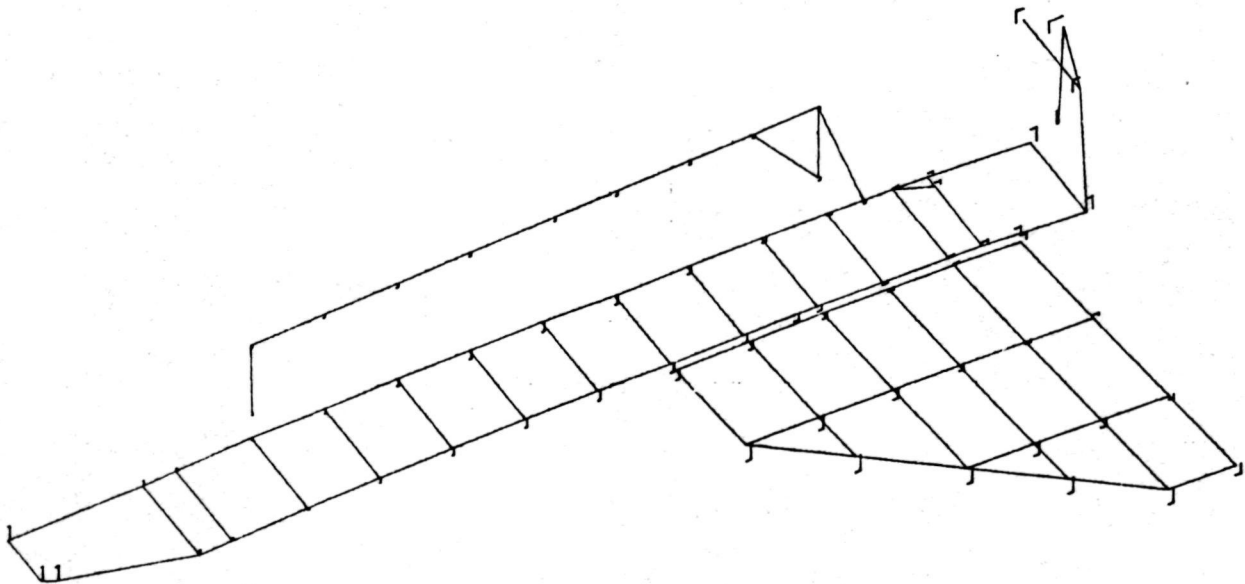
3.7 ORBITER RESULTS FOR MODEL I

In Phase II of the coupling analysis, the five Orbiter substructures were coupled and modes were calculated. PLOTTEL elements were used to connect the reduced dynamic grid points for plotting purposes. Figures 3-17 and 3-18 are NASTRAN plots of the first two symmetric modes. These plots show the deformed structure together with the X, Y and Z displacement components measured from the undeformed position. The first mode (at 53.2 Hz) exhibits fuselage vertical bending, fin pitching, and wing motion. Most of the wing motion is due to bending in the root region; the outer portion remained almost linear. Note that the point of maximum deflection is at the fin tip.

The second mode (at 62.6 Hz) consists principally of wing bending together with some payload and fuselage vertical bending. (Additional plots of higher modes are shown in Volume IIIB, Appendix B19.) Frequencies for the symmetric and antisymmetric cases are given in Table 3-4.

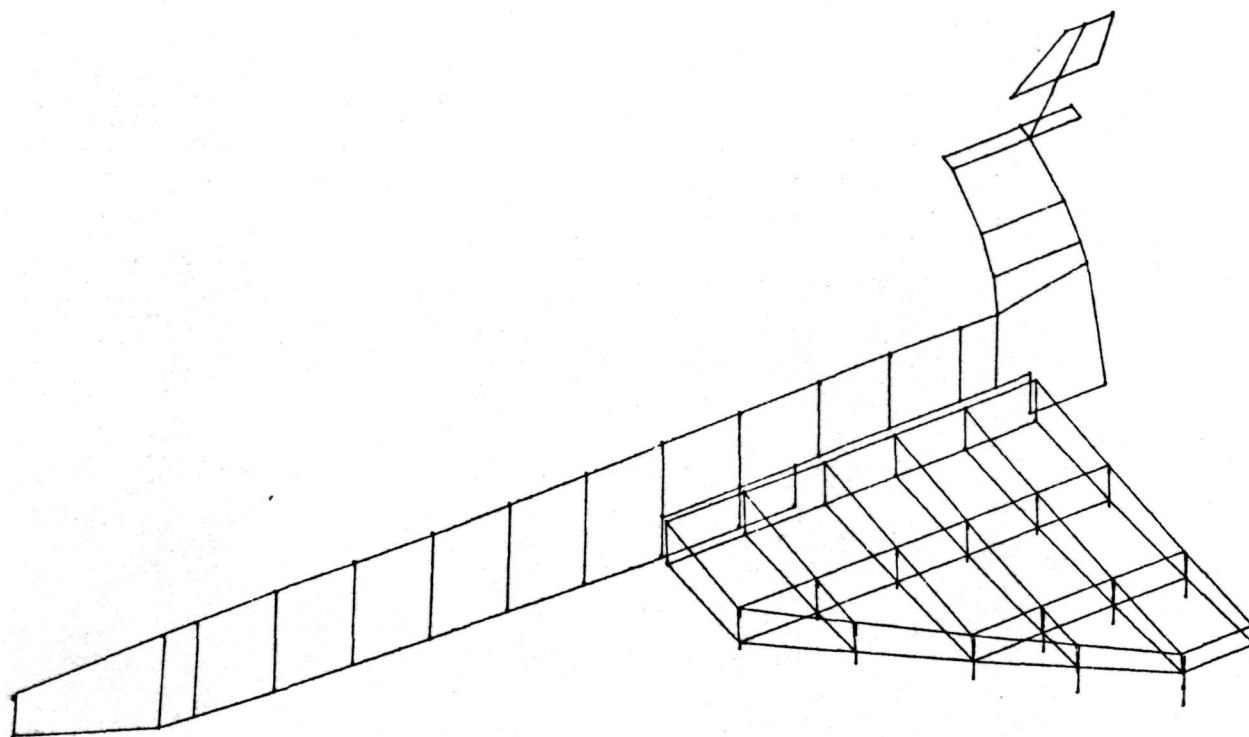


A. $f_1 = 53.2$ Hz Fuselage Side Wall, Wing and Fin

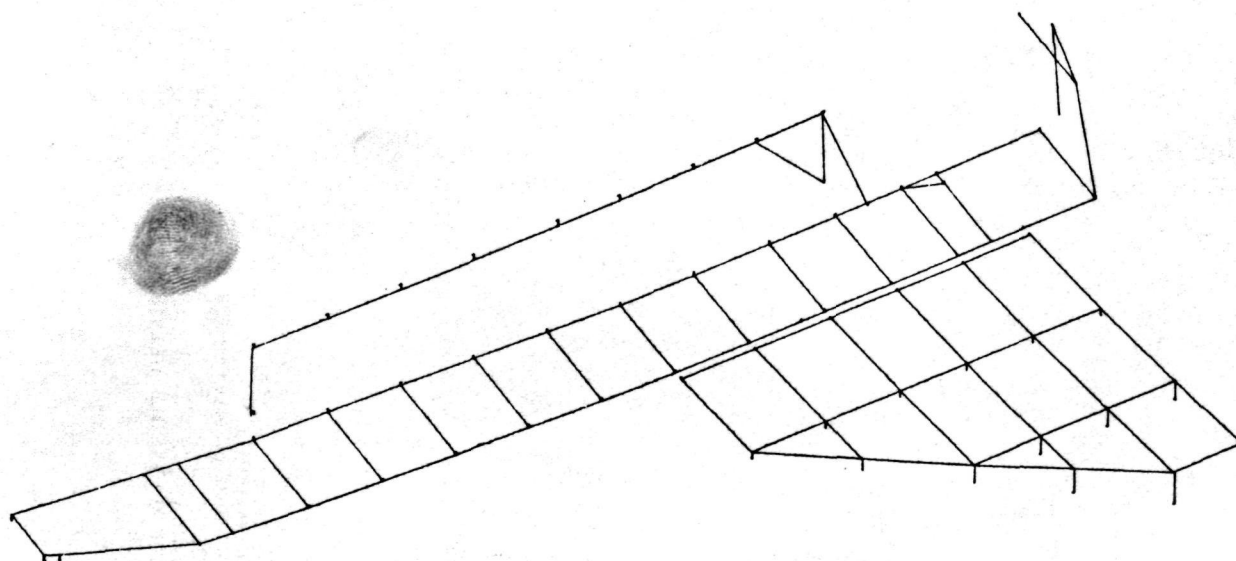


B. $f_1 = 53.2$ Hz Fuselage Bottom Deck, Wing Lower Cover, and Payload

Fig. 3-17 First Symmetric Mode



A. $f_2 = 62.6$ Hz Fuselage Side Wall, Wing and Fin



B. $f_2 = 62.6$ Hz Fuselage Bottom Deck, Wing Lower Cover, and Payload

Table 3-4 Frequencies for Symmetric and Antisymmetric Modes – Model I

Mode	Frequency, Hz (Symmetric Case)	Frequency, Hz (Antisymmetric Case)
1	53.2	52.9
2	62.6	72.6
3	75.2	85.1
4	108.5	92.0
5	133.7	101.5
6	156.3	135.3
7	162.2	—
8	175.2	—
9	216.4	—

TT-7

The coupled Phase 2 stiffness matrix formed for dynamic analysis was also used to calculate static deflections for comparison with data measured during the horizontal static test. This was accomplished by inverting the stiffness matrix restrained at the test support points and calculating the deflections for loads applied at the test locations. The DMAP ALTER statements to do this are presented in Volume III, pages A21-38 and A21-39.

Section 4
EXPERIMENTAL INVESTIGATION

4 - EXPERIMENTAL INVESTIGATION

4.1 TESTING PROCEDURES

All static and dynamic testing has been conducted at the NASA/Langley Research Center. Three series of tests have been performed to date on the 1/8-Scale Orbiter Model, and this series forms the basis for the correlation discussed in this report. Additional tests of the 1/8-Scale model are planned on a time-shared basis with on-going tests of other components (ET and SRB).

The main objective of the first series of tests was to determine the symmetric free-free modes and frequencies. For these tests, the model was suspended horizontally and inverted on soft springs attached to the interstage fittings (Fig. 4-1 and 4-2.)

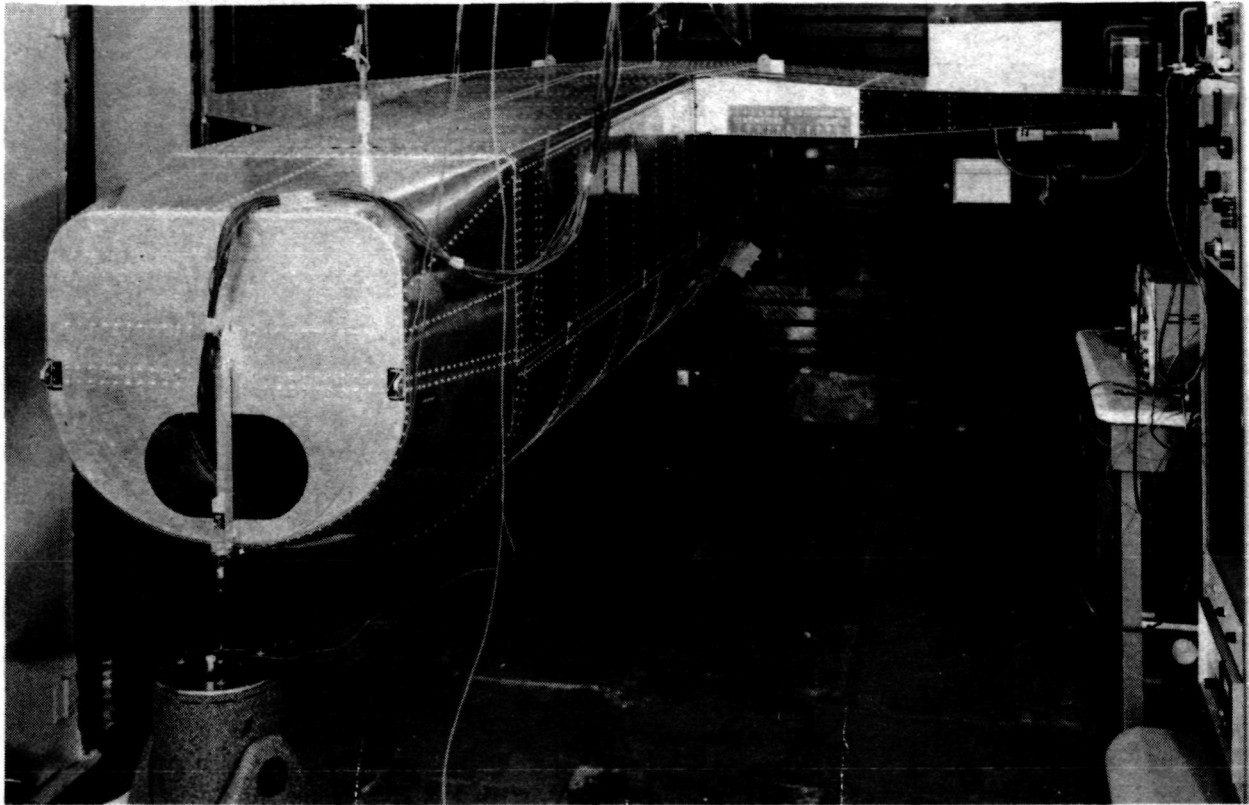
In the second series of tests, the model was suspended vertically from two integral nose fittings. A "wiffle tree" arrangement was used to apply an axial preload to the model through the lower engine thrust structure and the fuselage bottom skin (Fig. 4-3 through 4-5.) Strain measurements were made to determine the behavior of selected typical panels under the effect of the axial preload (Fig. 4-6). The second series of mode surveys was conducted to determine the effect of the model dead weight and preload on the natural frequencies.

The last of the three series of tests was performed with the model in a horizontal position, right-side up, and supported at the interstage fittings. The model was loaded incrementally with statically applied loads at a number of locations. Deflection measurements were made over the whole model (Fig. 4-7) for each applied load during loading and unloading. This data was used to obtain influence coefficients for comparison with the analytical results. The analytical results are presented in Appendix B of this volume.

Details on the testing procedures are given in Reference 9-5.

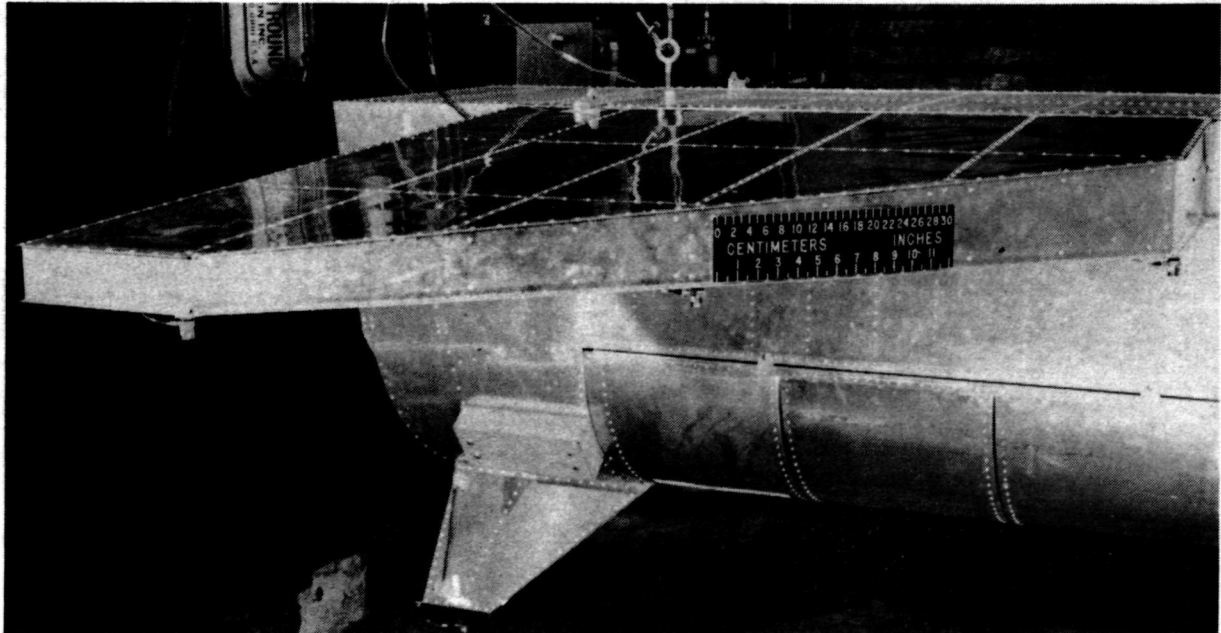
4.2 MODE SURVEY WITH ORBITER MODEL SUSPENDED HORIZONTALLY AT INTERSTAGE POINTS

Symmetric free-free modes and frequencies were obtained while the vehicle was suspended in a horizontal and inverted position, with soft springs attached to the interstage points (Fig. 4-1). The shaker was mounted at the nose bulkhead and oriented to produce an exciting force in the transverse ($\pm Z$) direction. Thirty nine components



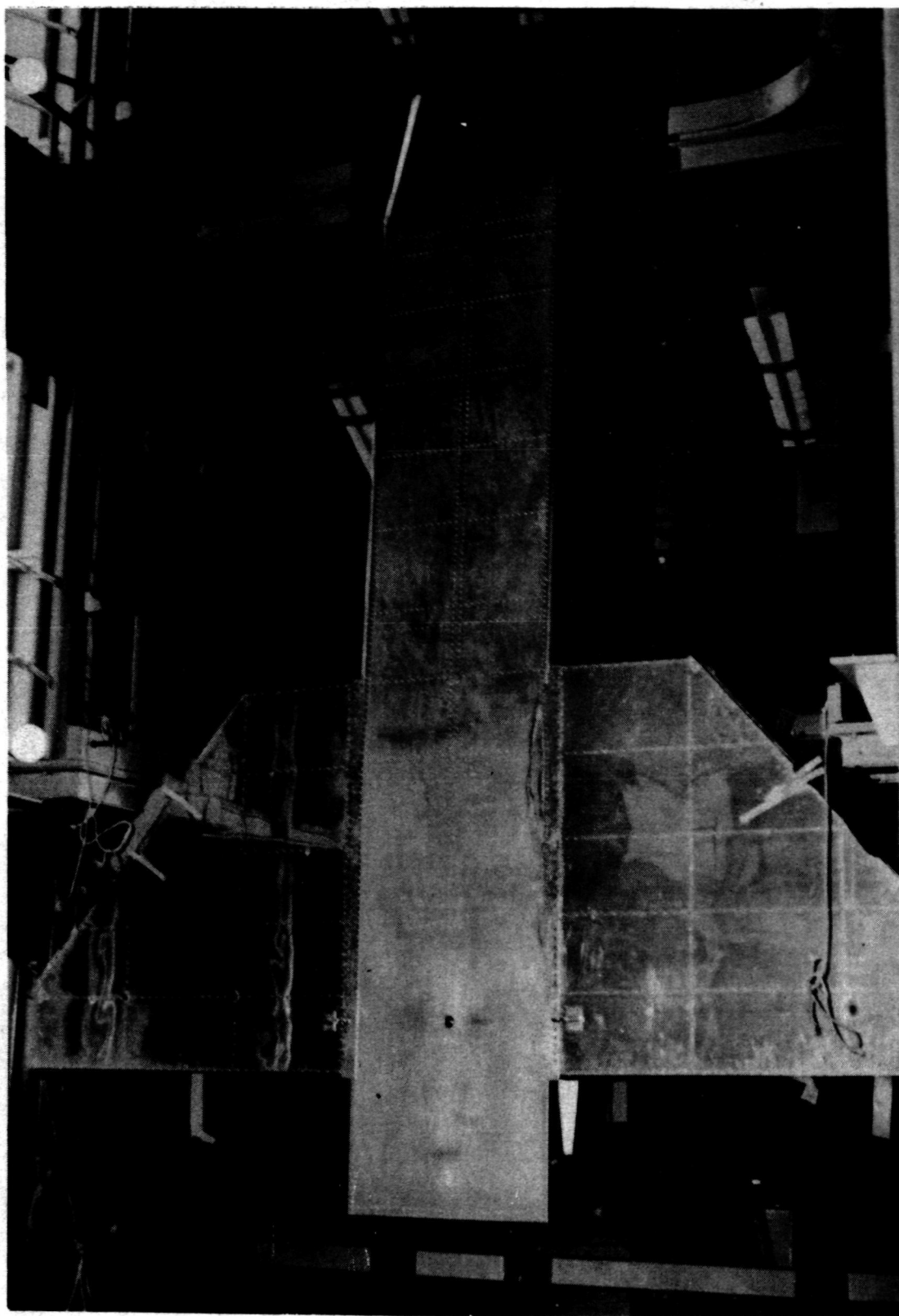
T-39

Fig. 4-1 Orbiter Model Suspended in Horizontal Inverted Attitude for Vibration Tests – Forward View



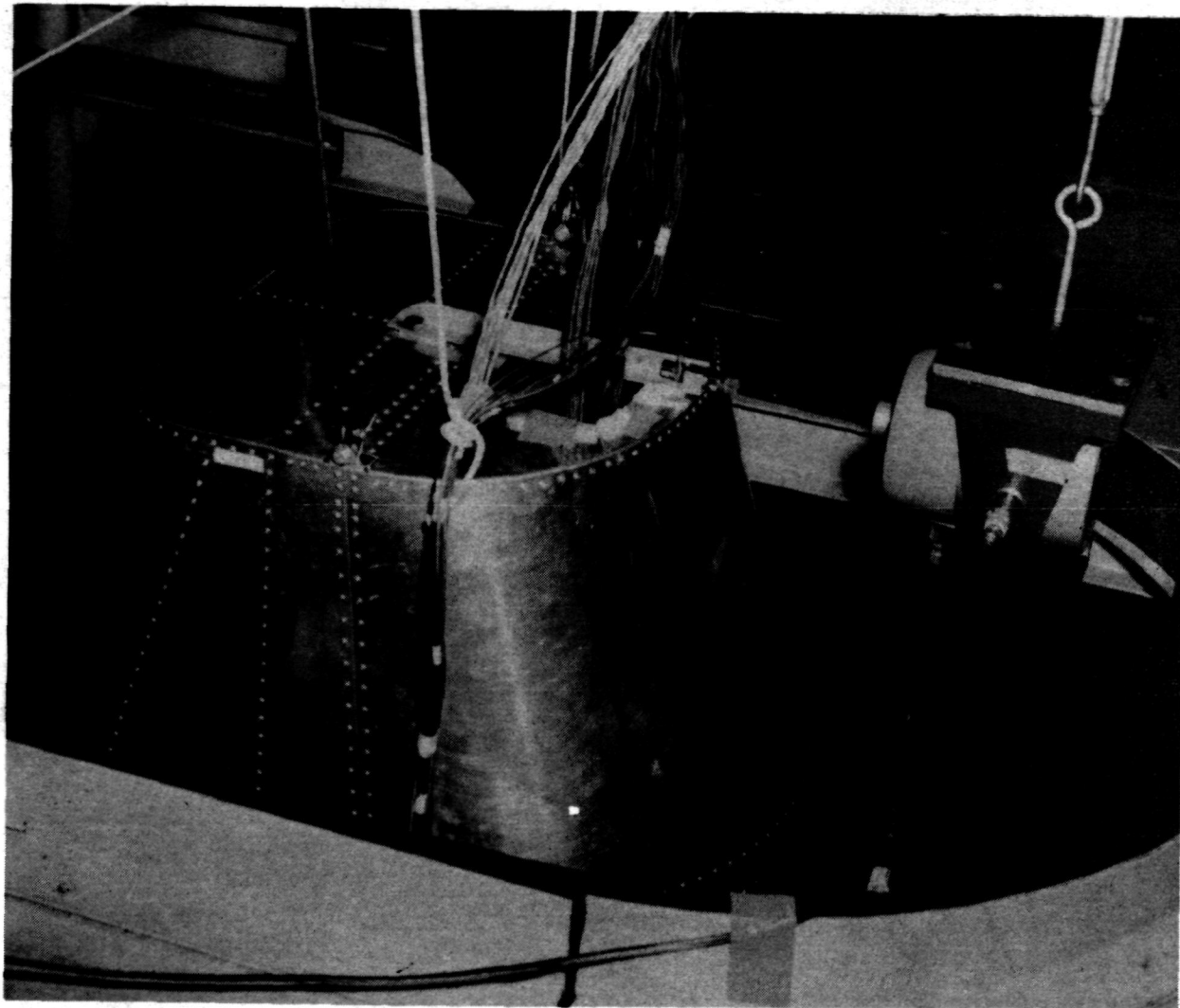
T-40

Fig. 4-2 Orbiter Model Suspended in Horizontal Inverted Attitude for Vibration Tests – Aft View



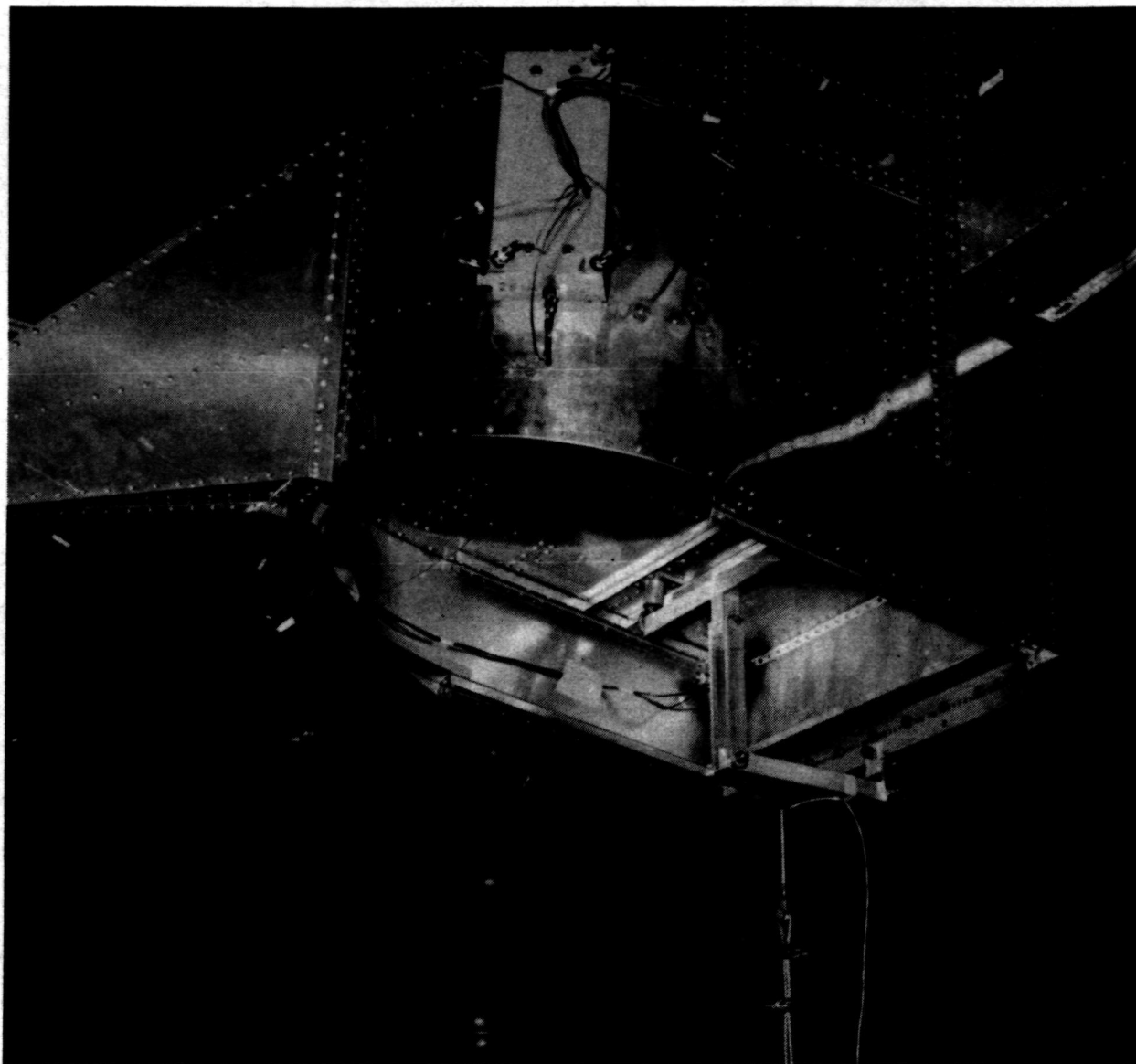
T-41

**Fig. 4-3 Orbiter Model Suspended in Vertical Attitude for
Vibration Tests With Axial Preload**



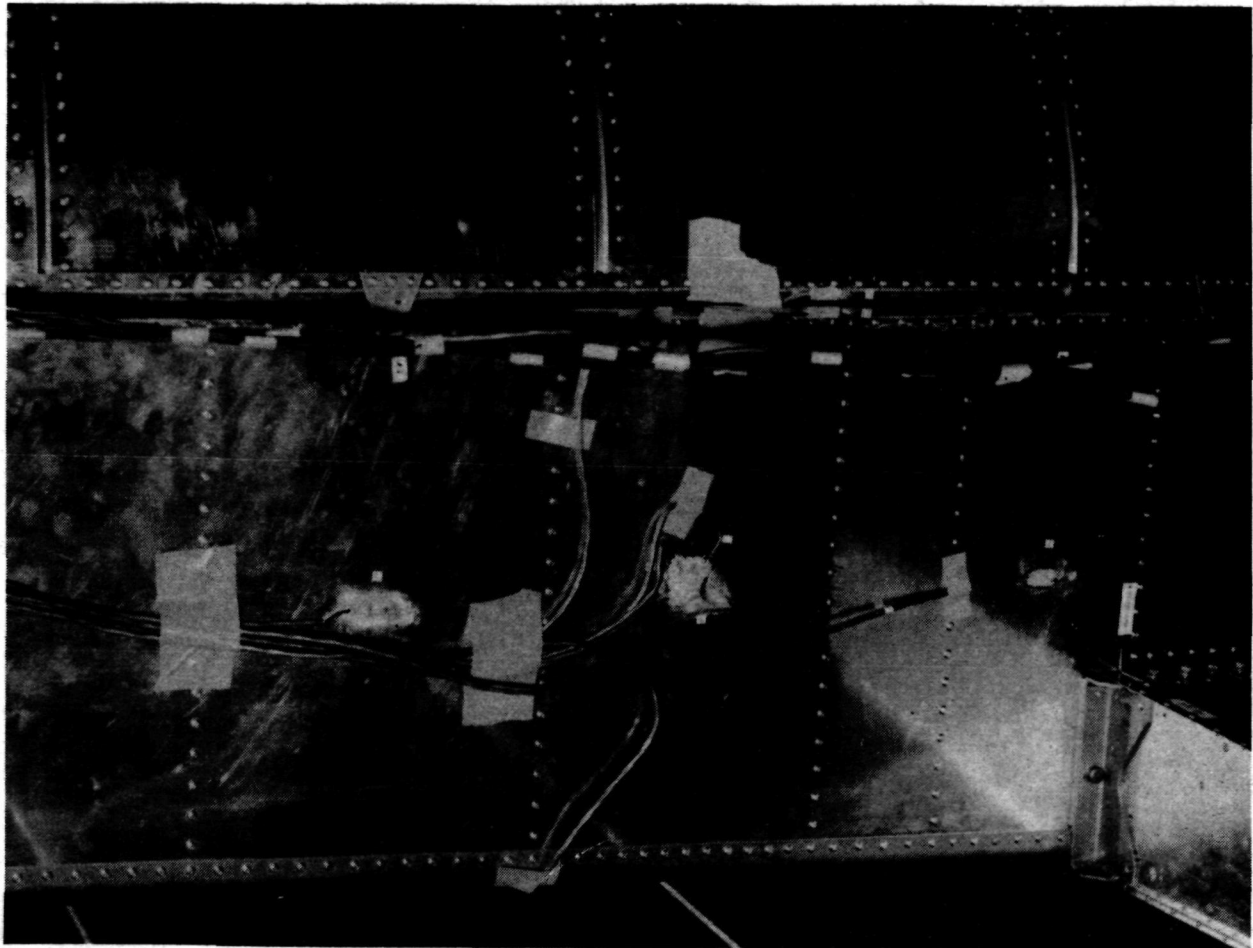
T-42

Fig. 4-4 Suspension Cable Connections and Typical Shaker Installation Used for Vibration Tests of Orbiter Model in Vertical Attitude



T-43

Fig. 4-5 Linkage for Applying Axial Preload to Fuselage During Vibration Tests of Orbiter Model Suspended in Vertical Attitude



T-44

Fig. 4-6 Typical Strain Gage Installation on Orbiter Model Fuselage Side Wall Panels and Longerons

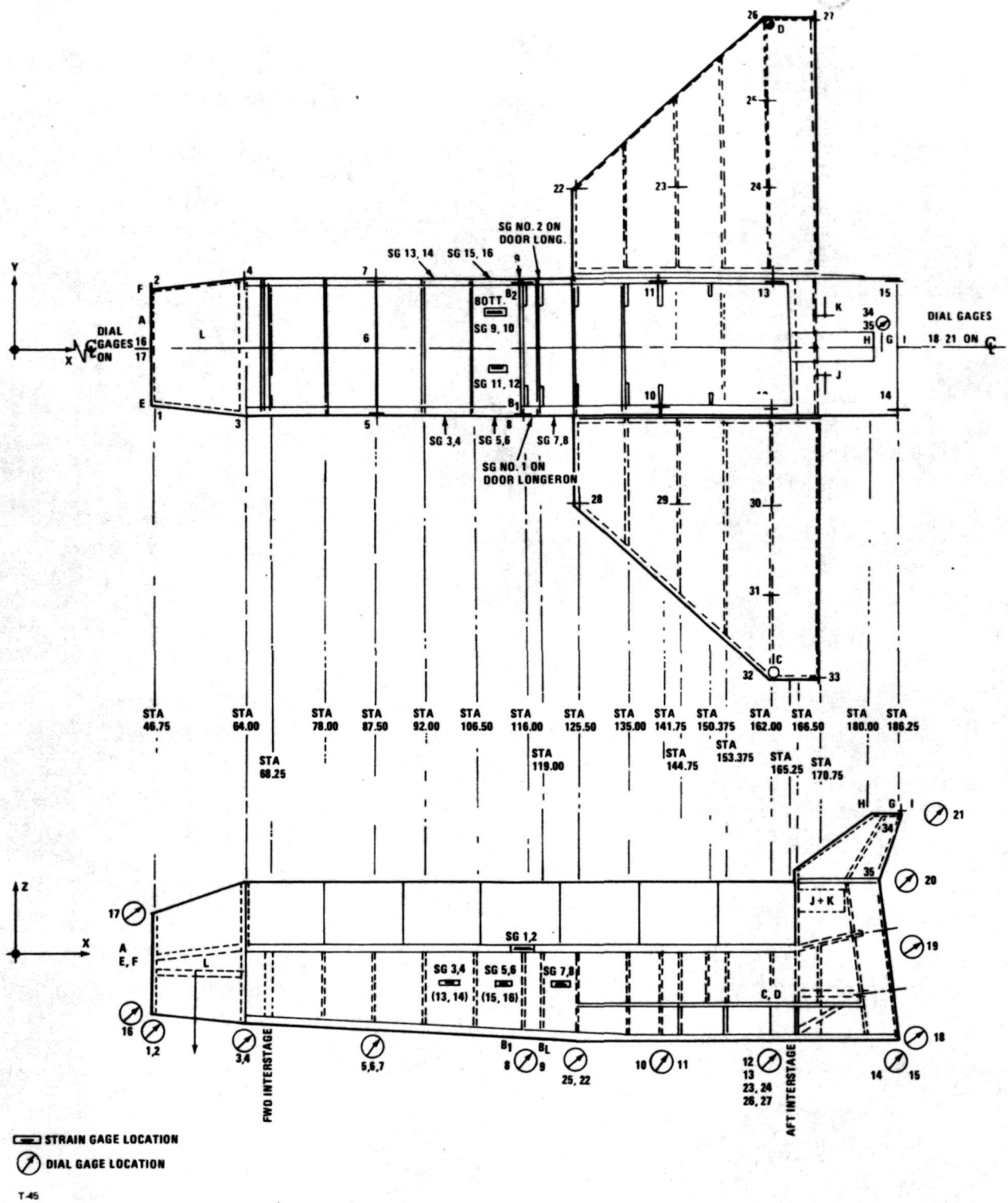


Fig. 4-7 Location of Strain and Dial Gages for Static Tests

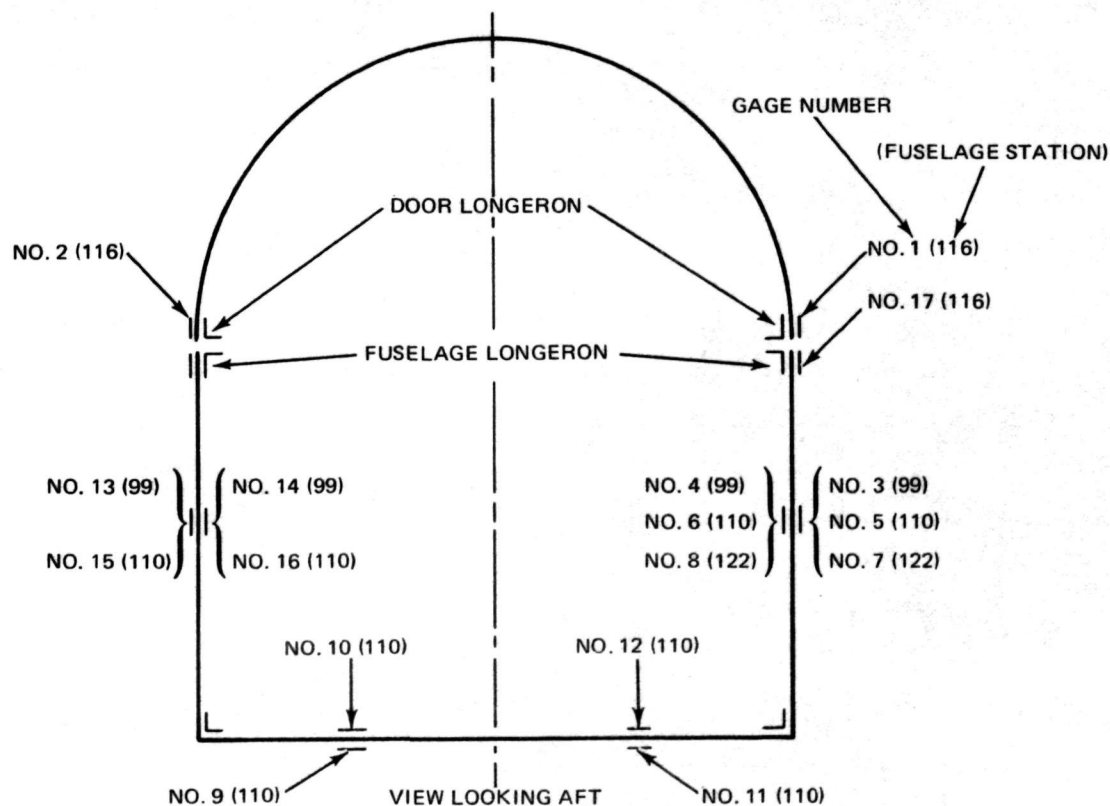
Table 4-1 Summary of Measured Symmetric Free-Free Modes (Horizontal Inverted Orientation)

Mode No.	Frequency, Hz	Mode Description
1	43.6	Fuselage 1st Bending
2	52.7 (avg of 51.2 & 54.2)	Wing 1st Bending (vs Payload Vertical)
3	58.2	Wing 1st Bending (vs Aft Fuselage Vertical)
4	80.1	Fin Fore-Aft
5	95.7	Payload Fore-Aft (vs Fwd Fuselage-Fore-Aft)
6	104.1	Wing 1st Torsion
7	107.0	Payload Aft Vertical

TT-8

Table 4-2 Variation of Fundamental Frequency with Axial Preload

Axial Load, lb (a)	Measured Frequency, Hz
0	43.67
200	43.86
400	44.05
600	44.25

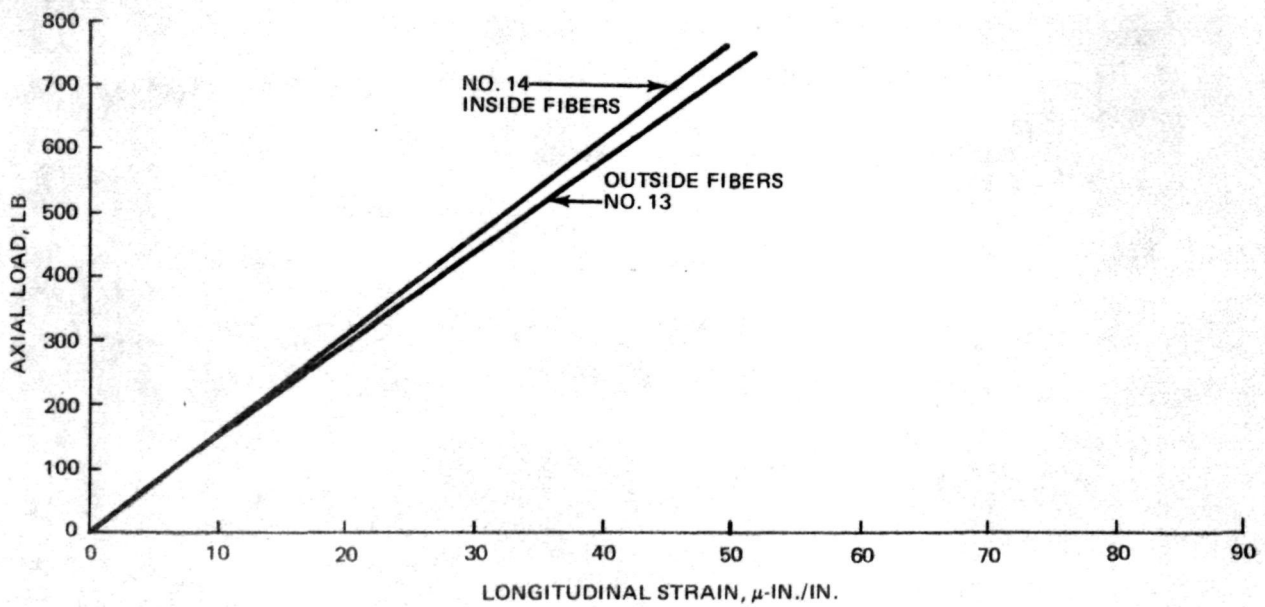
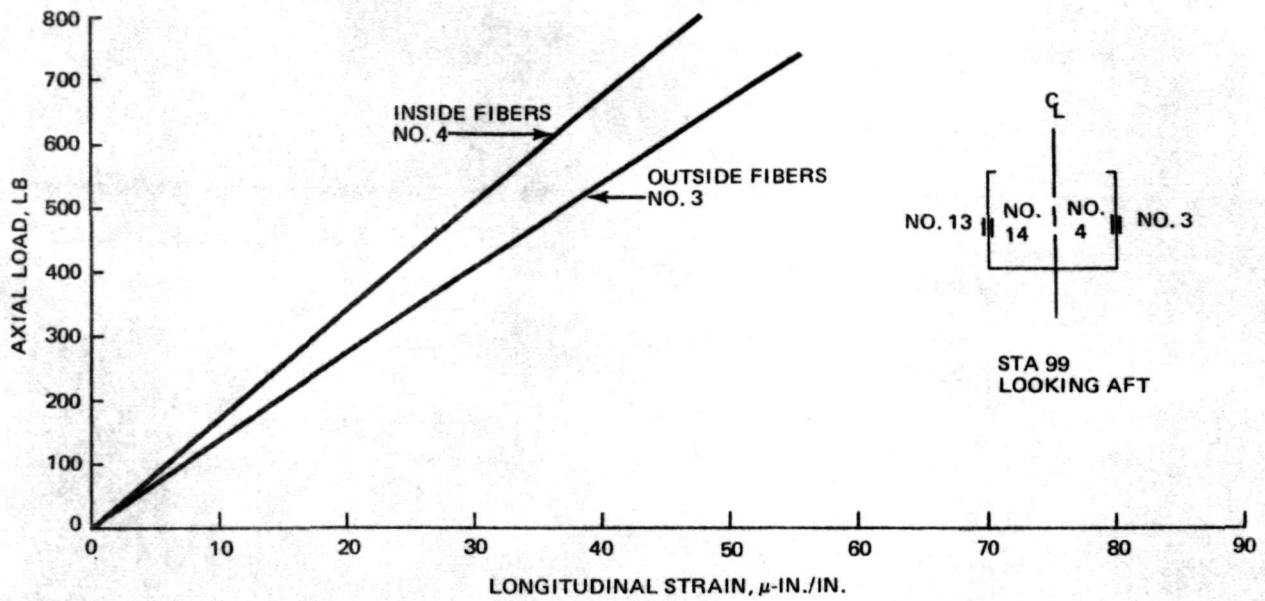
TT-9 ^aThe axial preload is in addition to the model dead load**Fig. 4-8. Location of Strain Gages – Section View**

of acceleration were monitored during the test to obtain data for plotting mode shapes. Figure 4-2 shows the aft portion of the vehicle and some of the accelerometers. (Note the accelerometers bonded to the wing and fin ballast weight.) Seven symmetric free-free modes and frequencies were measured as listed in Table 4-1. Plots of the measured mode shapes are given in Appendix C of this volume.

4.3 MODE SURVEY WITH ORBITER MODEL SUSPENDED AT FUSELAGE NOSE

For this series of tests the model was suspended from cables attached to the nose lugs (Fig. 4-3 and 4-4). Both static and vibration tests were performed with the Orbiter in this position. This test was initiated after the horizontal test at a point where it was perceived that the results did not correlate with the NASTRAN Model I analysis. At this point, the ineffectiveness of the skins was believed to be a major contributor to the lack of correlation. Consensus indicated that by preloading the vehicle a quantitative value could be obtained for the skin effectiveness factors that should be applied in the analysis. Consequently, a simple two-tier "whiffle tree" arrangement was attached to the aft end of the model for applying axial load (see Fig. 4-5). Loading in increments of 200 lb up to a total of 600 lb was applied with the frequencies being measured for each load level. These values are shown in Table 4-2. The small change in frequency due to the applied preload indicated that the 600-lb load was not sufficient to eliminate the initial imperfections.

Static strains were also measured with the vehicle in the nose-up position. Strain gages were attached at 20 locations (Fig. 4-6 through 4-8.) (Note that Fig. 4-7 also shows the location of dial gages used in the horizontal static test.) Strains were measured for increments of axial load, some of which are shown plotted in Figures 4-9 through 4-13. As indicated in Fig. 4-8, gages were mounted on both the inside and outside of the fuselage skins at a given station. For example, gages No. 3 and 4, on the left side wall at Station 99, are attached to the outside and inside, respectively. The difference in the inner and outer gages, divided by two, is the bending strain which was then used to estimate the change in the central deflection of the panel for the specified load range. With increasing load the curves should become parallel. The largest difference between the two curves is shown on Fig. 4-12 for gages No. 7 and 8. (Methods that were used for analyzing this data are discussed in Section 5.)



T-47

Fig. 4-9 Load-Strain Curves for Side Wall Panels (Sta 99.0)

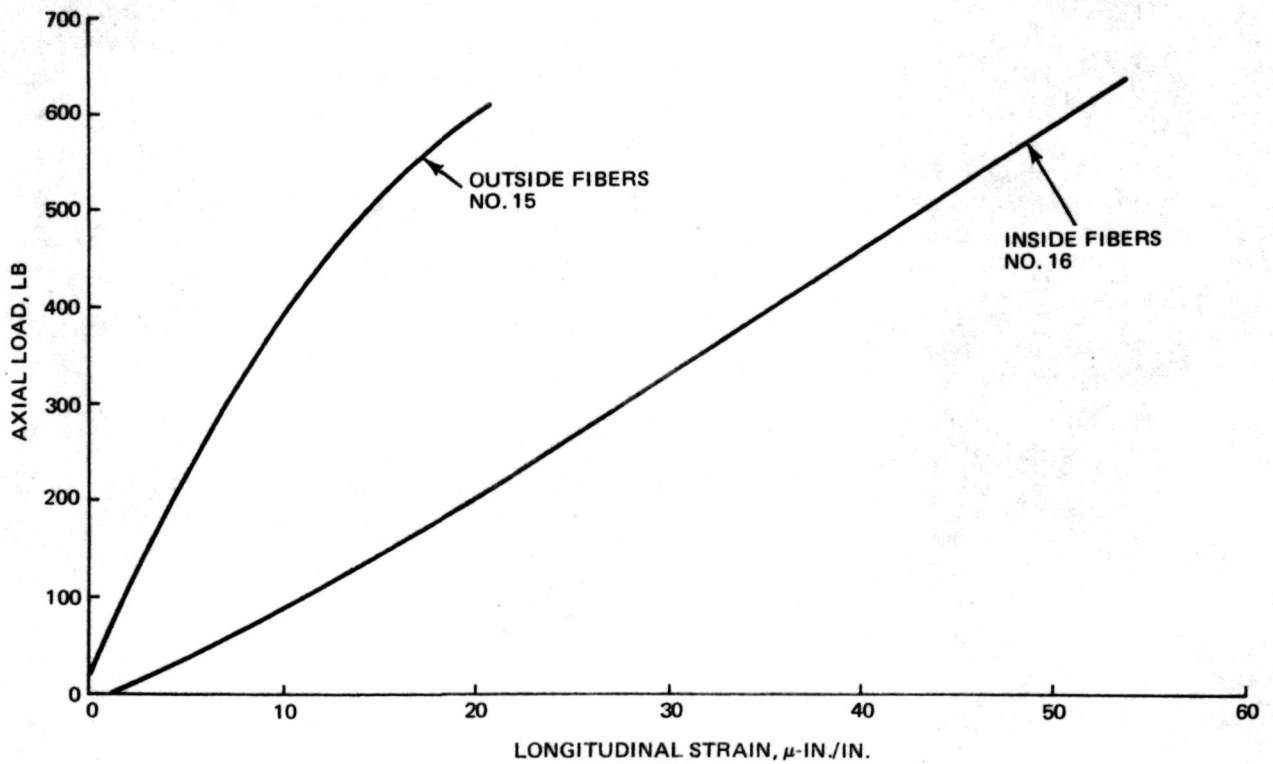
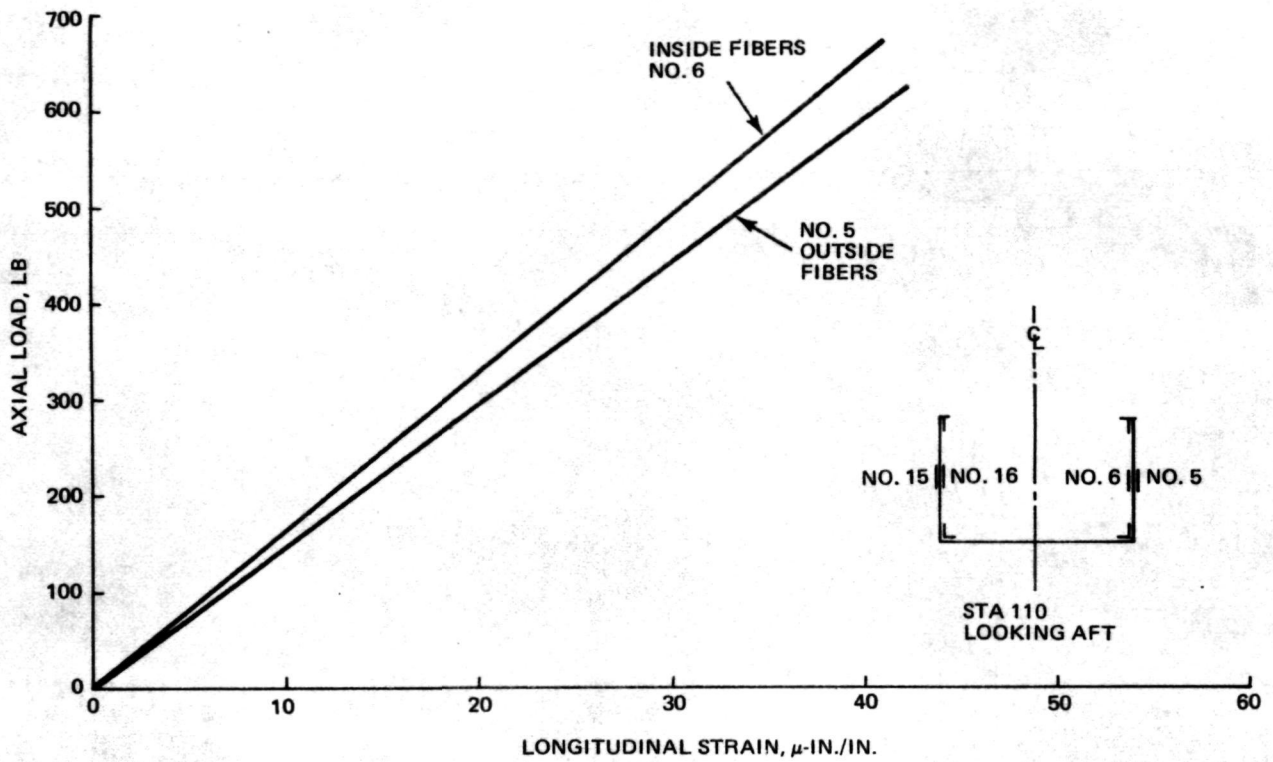


Fig. 4-10 Load-Strain Curves for Side Wall Panels (Sta 110.0)

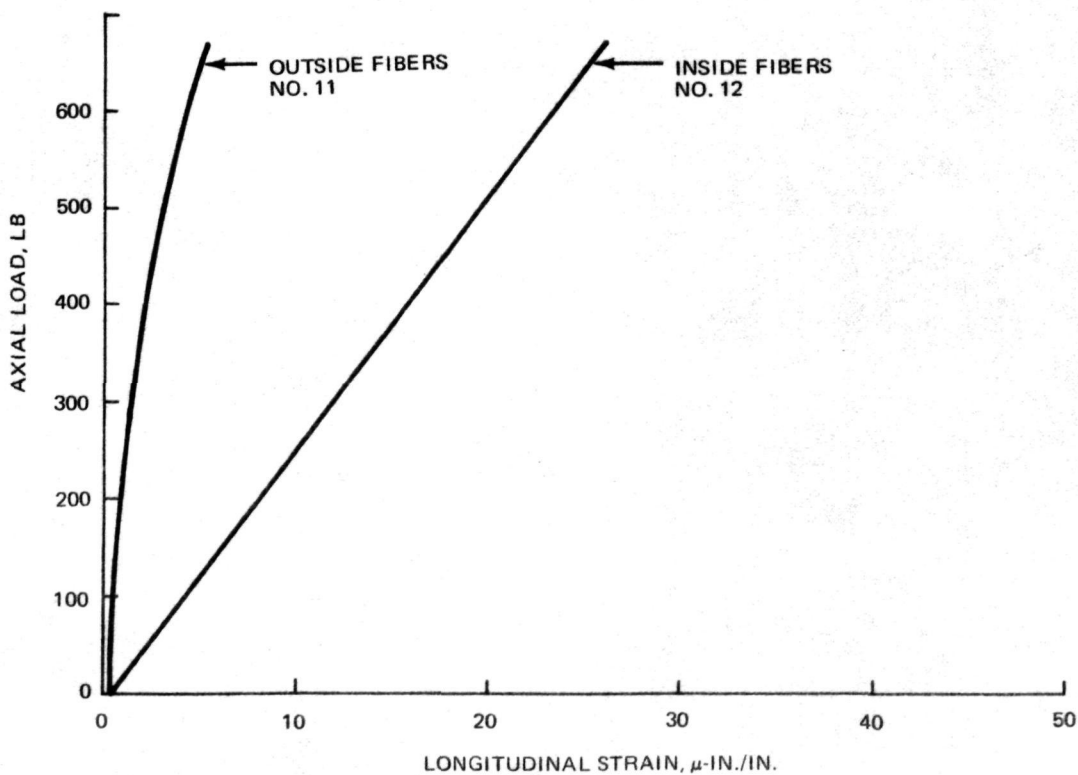
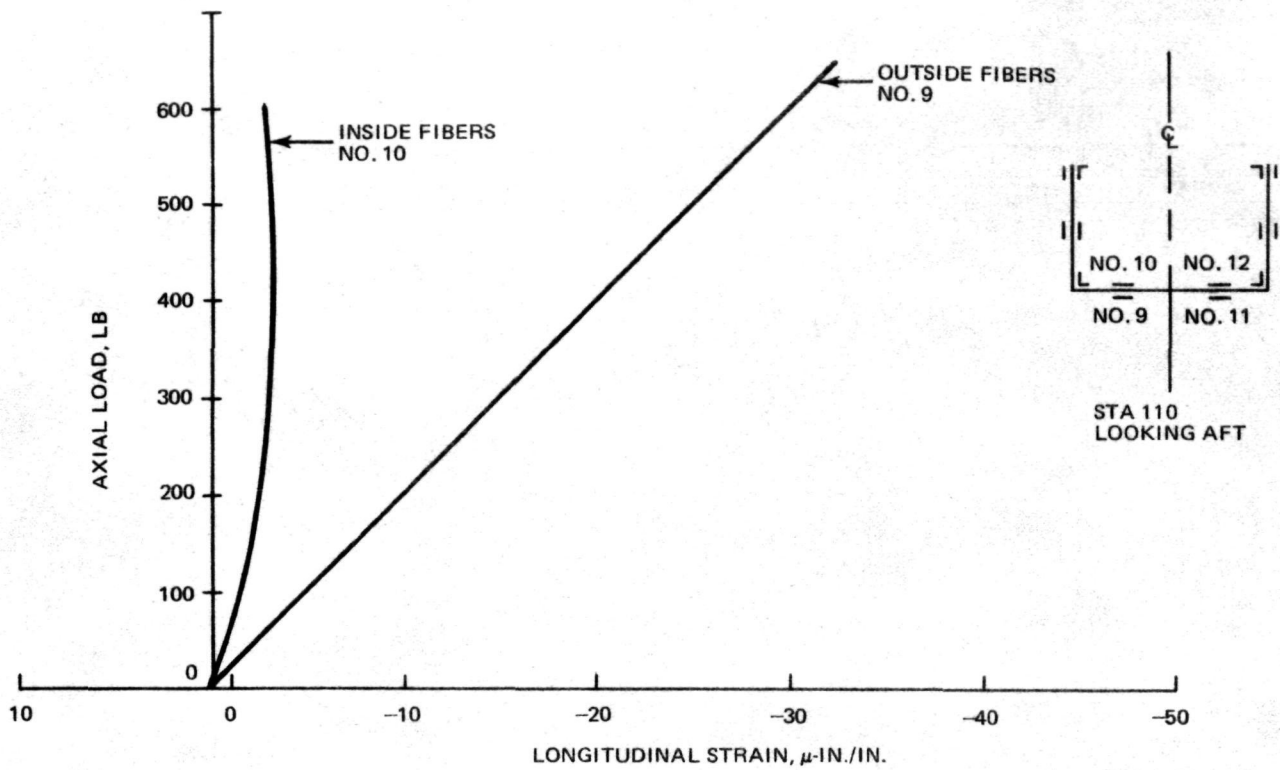


Fig. 4-11 Load-Strain Curves for Bottom Deck Panels (Sta 110.0)

In Fig. 4-13, the strains are plotted for gages No. 1, 2, 17 and 18, which were attached to the fuselage upper longerons and door longerons at Station 116. An important point is that the fuselage and door longerons are not straining the same amount. This is because there is an ineffectiveness factor associated with the door longeron due to the manner in which the door is connected to the fuselage.

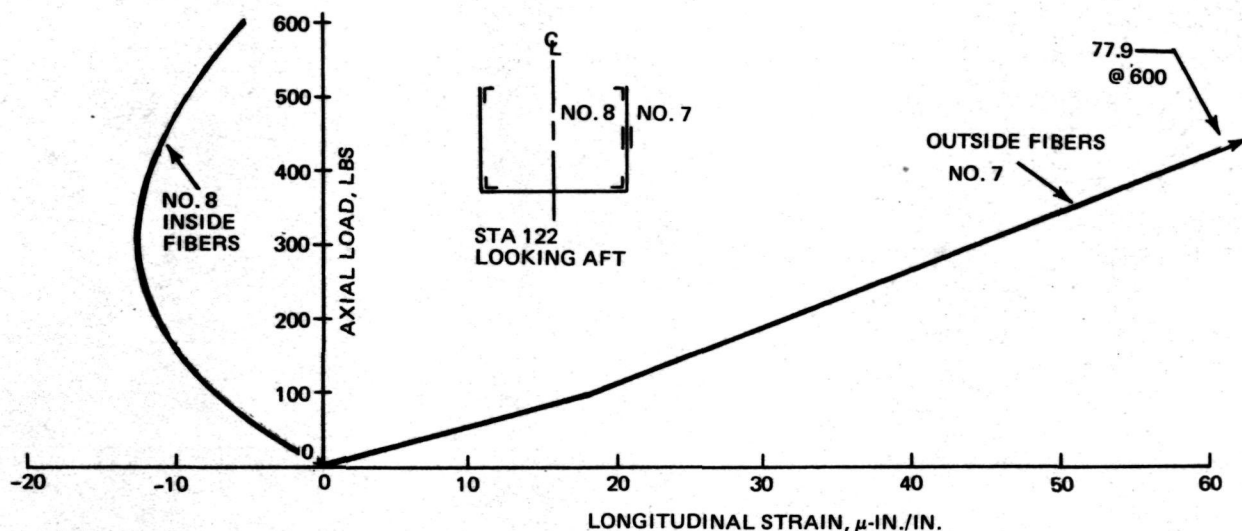


Fig. 4-12 Load-Strain Curves for Side Wall Panel (Sta 122.0)

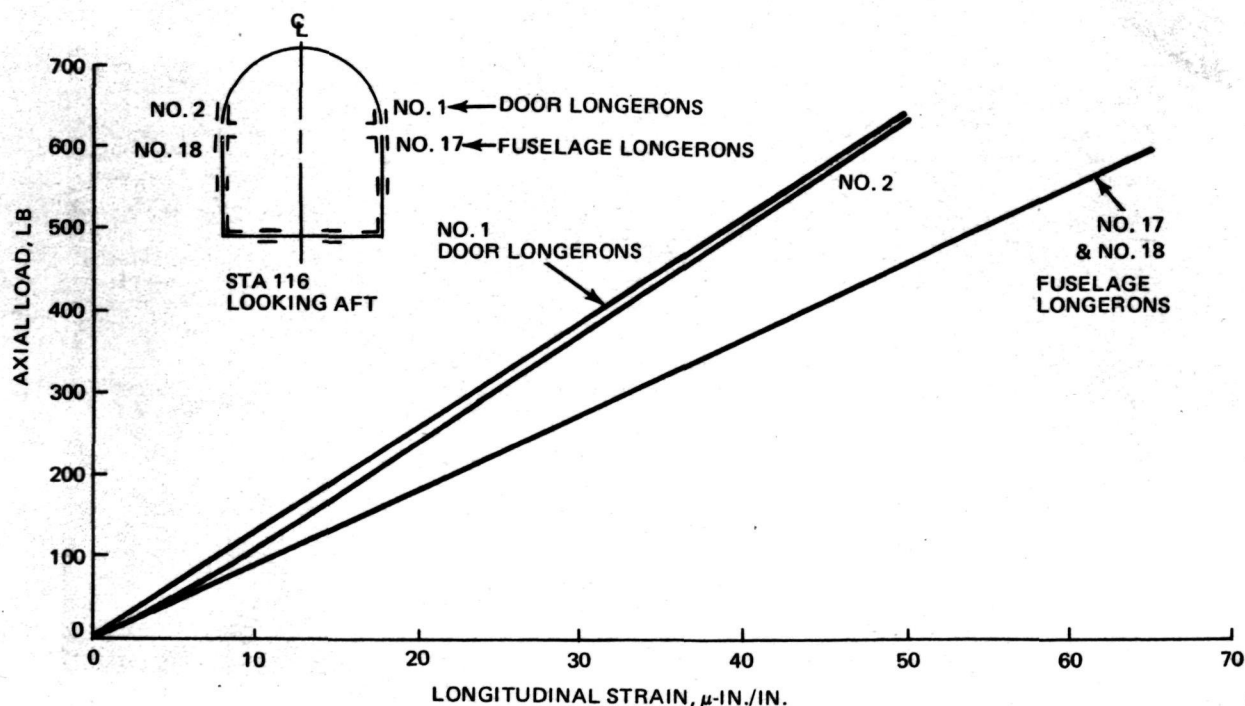
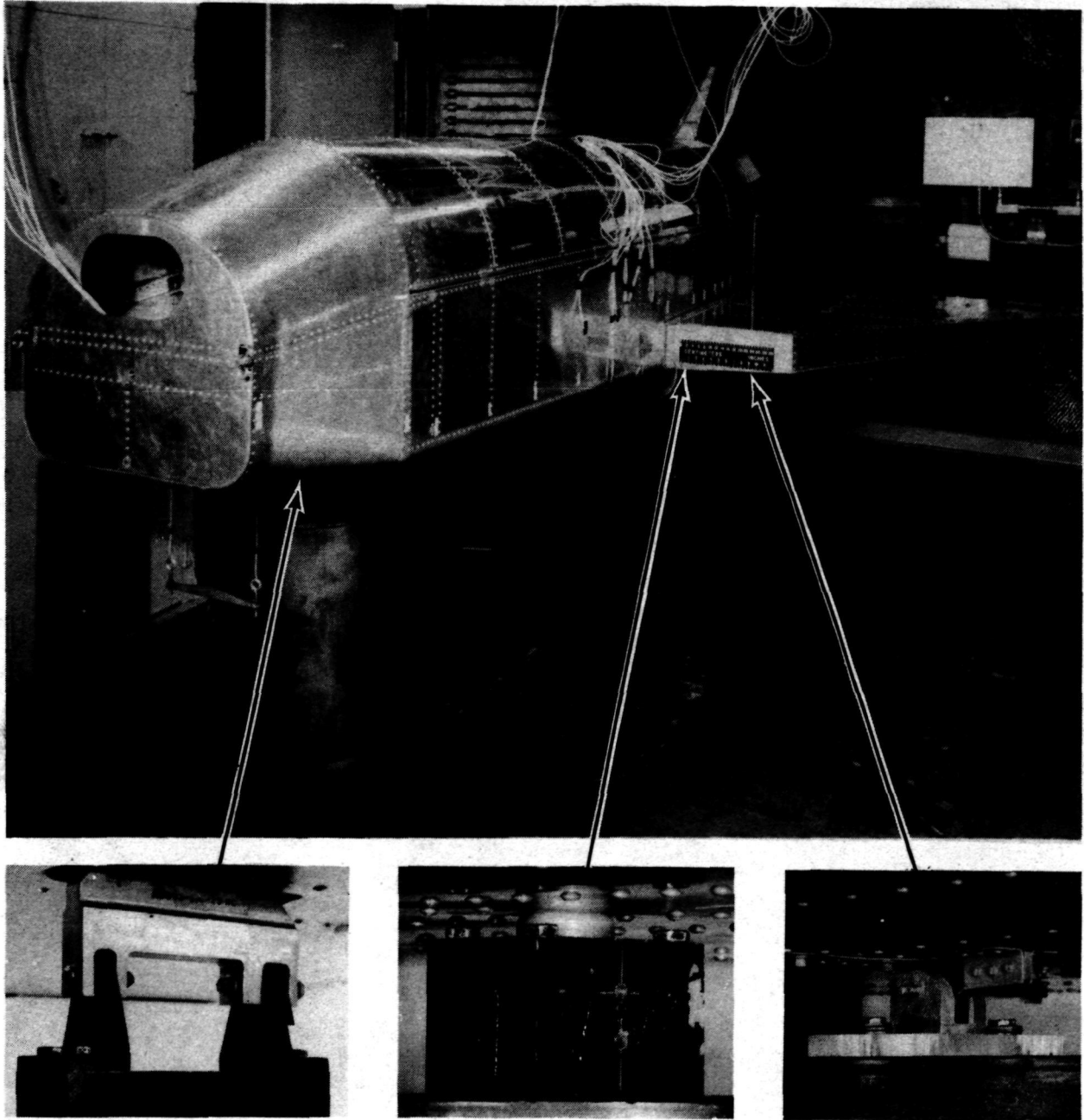


Fig. 4-13 Load-Strain Curves for Longerons (Sta 116.0)

4.4 STATIC TESTS

Static testing was conducted with the model setup shown in Fig. 4-14 through 4-18. The model was supported at the interstage points by fittings that rested on pylons. The pylons were approximately two feet high, and were bolted directly to the test floor. Loading was applied in increments by means of dead weights (see Fig.

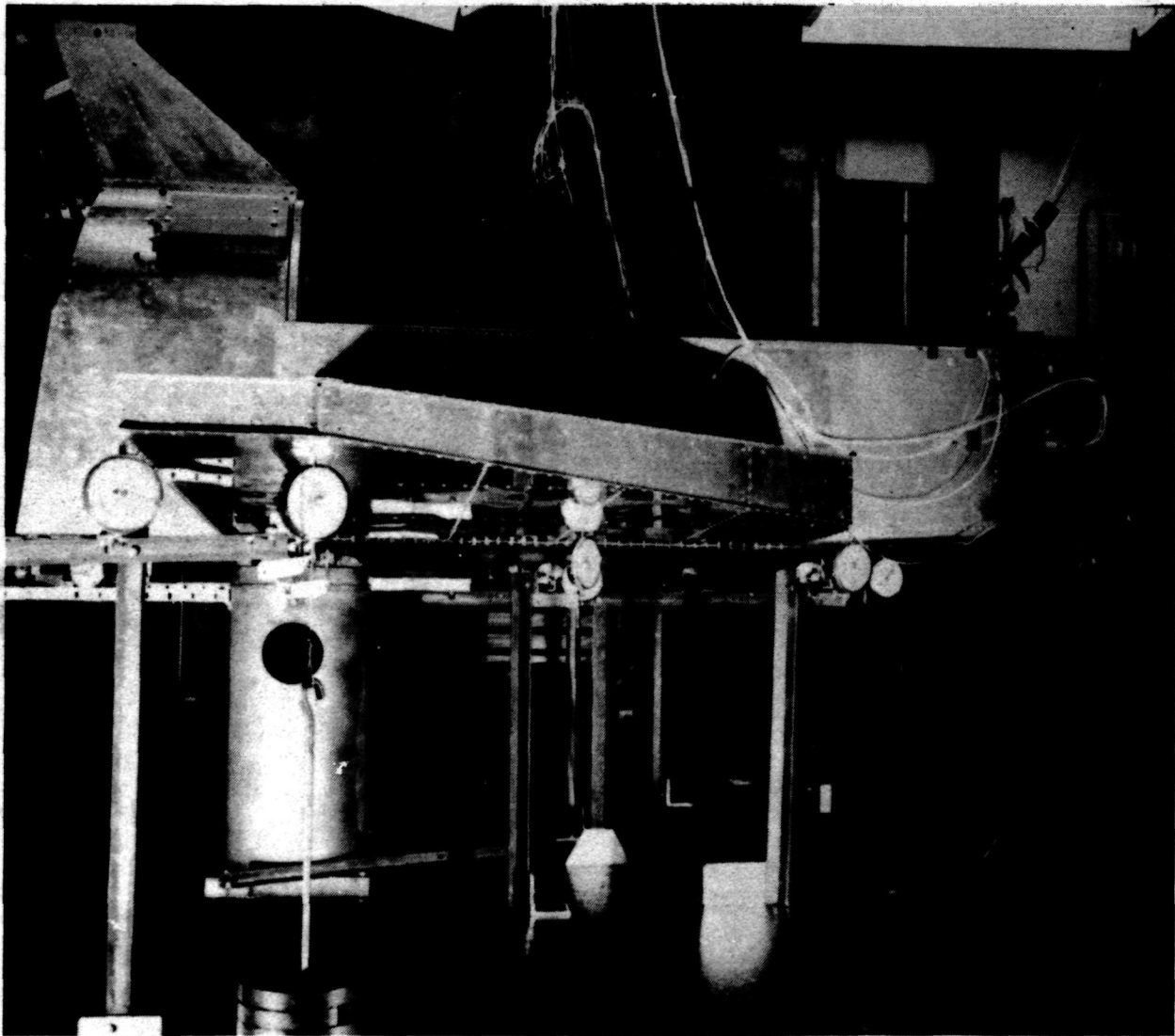


T-52

Fig. 4-14 Details of Model Support for Static Tests

4-15 through 4-17). Deflections were measured by dial gages, most of which had an accuracy of ± 0.0001 in. Influence coefficients were obtained from the measured load-deflection curves for comparison with calculated values. The tests and type of loading are indicated in Table 4-3; plotted test data is given in Volume IIIA, Appendix A3.

Figure 4-17 shows the aft portion of the model during the application of a longitudinal (+X) force to the OMS ballast center of gravity. Loads were applied to the ballast weights to investigate the local flexibility of the attachments of these relatively heavy masses. Figure 4-18 shows a closeup of the cabin ballast weight instrumenta-



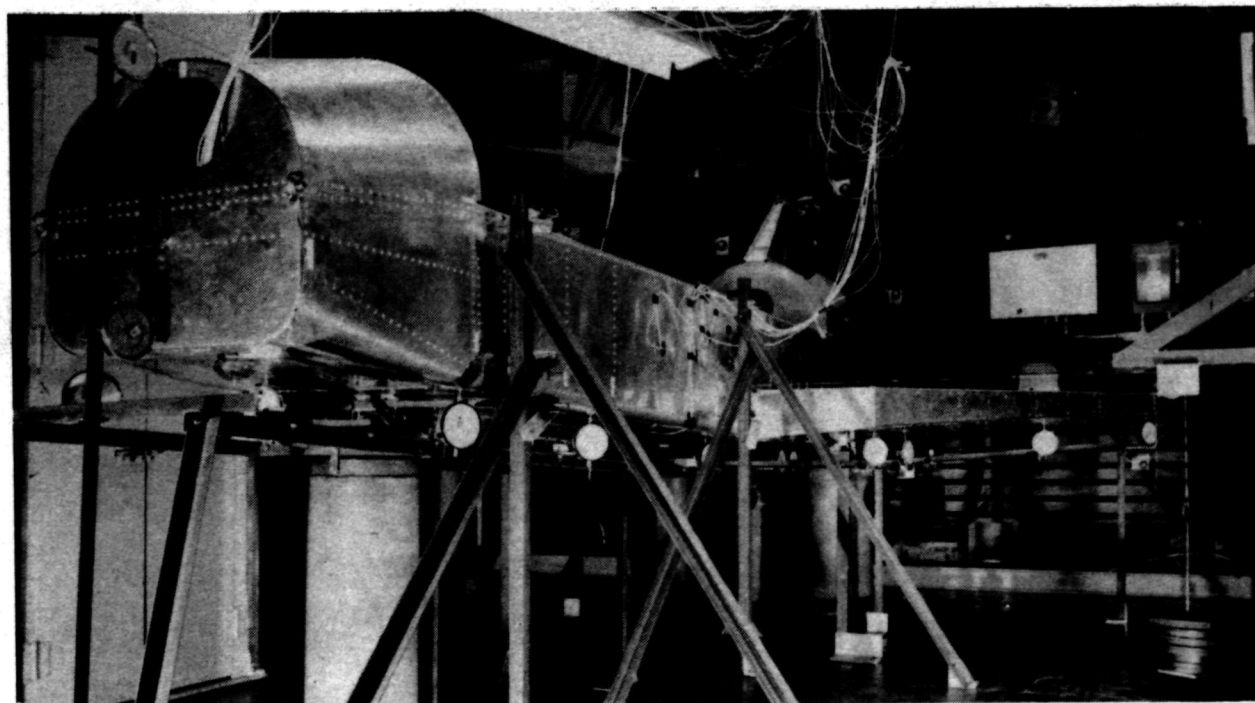
T-53

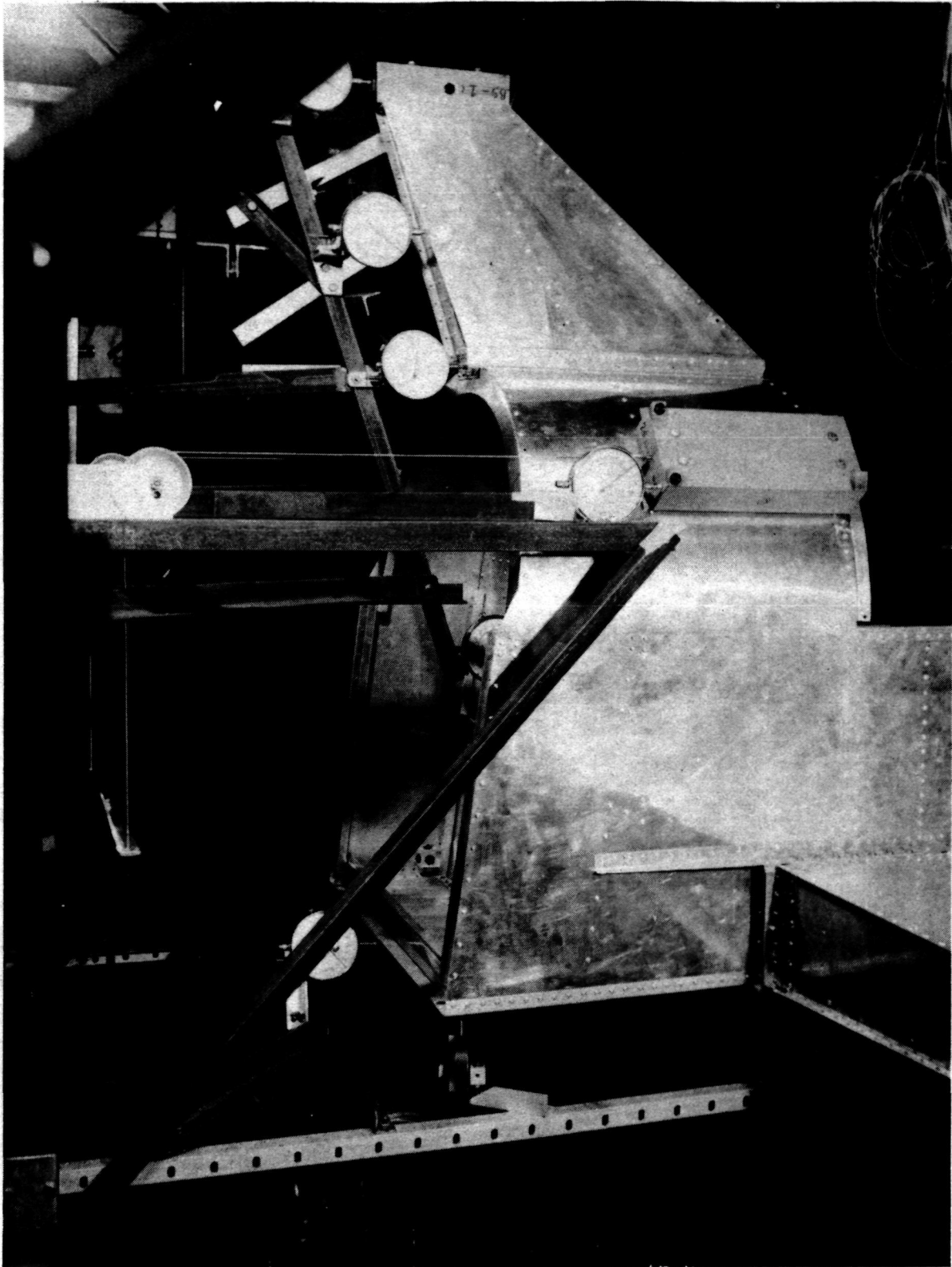
Fig. 4-15 Static Test Setup (Side View)

tion during static test. From a physical point of view, all static testing was kept as simple as possible using only available instrumentation. This was done to control both the cost and the time schedule.

Influence coefficients as shown in Table 4-4 were obtained by averaging the loading and unloading plots for both downloads (-Z) and uploads (+Z) (Fig. 4-19 and 4-20). Note that Figure 4-19 shows the deflections measured at two symmetrically placed gages (dial gages No. 1 and 2) during tests with the cargo doors off and load applied at the nose of the model. A similar set of load deflection curves is shown in Figure 4-20 for the mid-fuselage region. For the latter case, the dial gages for the +Z loading were moved aft because of interference of the gages with the loading wires.

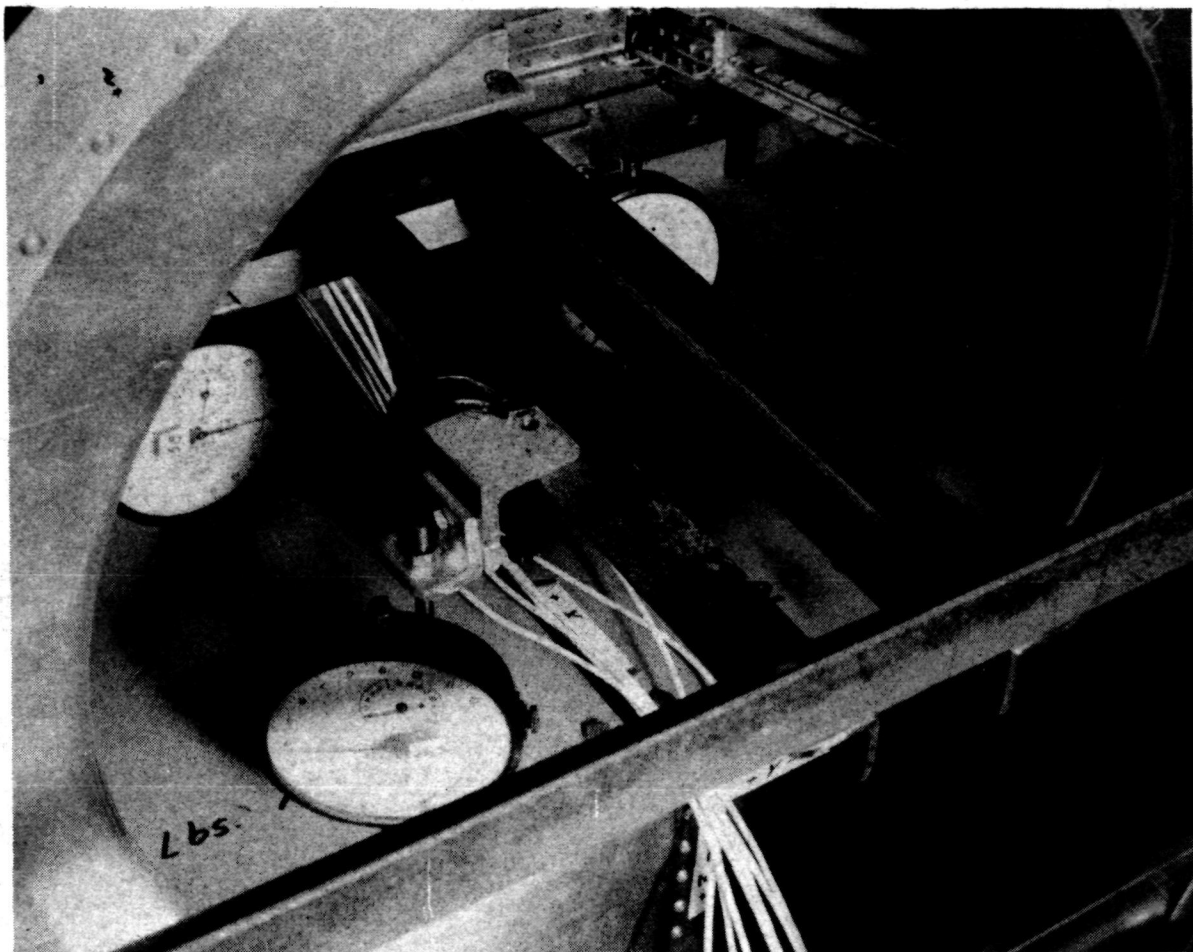
The average of gages No. 1 and 2 for loading and unloading in the -Z direction at the nose with the cargo doors off (test No. 7) is 74.0×10^{-6} and 87.5×10^{-6} in./lb. The average of these two values is 80.75×10^{-6} . Similarly, for test No. 8 (+Z loading at the nose), these values are 84.5×10^{-6} and 86.2×10^{-6} , and the average is 85.35×10^{-6} . The NASTRAN Model I analysis gave 55.4×10^{-6} . All seven numbers appear in Table 4-4, columns 16 through 22 for the δ_{11} coefficient. The average of





T-55

Fig. 4-17 Apparatus for Loading and Measurement at Aft End of Fuselage During Static Tests



T-56

Fig. 4-18 Dial Gages Used for Measurement of Forward Cabin Ballast Deflection During Static Tests

Table 4-3 Static Tests

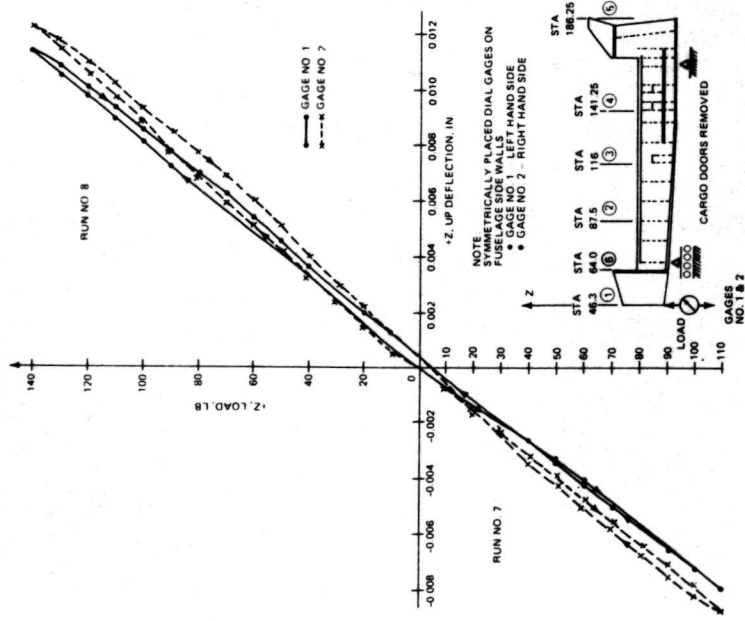
Test No.	Loading Condition	Payload Doors	Load	
			Direction	Application
4	• Mid Fuselage – Normal Symmetric	On	+Z	FS 116
3	– Normal Symmetric	On	-Z	FS 117.5
14	– Normal Symmetric	On	-Z	FS 117.5
5	– Normal Symmetric	Off	+Z	FS 116
6	– Normal Symmetric	Off	-Z	FS 117.5
15	– Normal Symmetric	Off	-Z	FS 117.5
35	– Lateral Antisymmetric	Off	-Y	FS 117.5
17	– Lateral Antisymmetric	Off	-Z	FS 117.5
7	• Fuselage Nose – Normal Symmetric	Off	-Z	FS 46.8
8	– Normal Symmetric	Off	+Z	FS 46.8
30	– Torsion Antisymmetric	On	$+\theta_X$	BL \pm 11.5
29	– Torsion Antisymmetric	Off	$+\theta_X$	BL \pm 11.5
9	• Wing Tip – Normal Symmetric	On	+Z	FS 162
13	– Normal Symmetric	On	-Z	FS 162
10	– Normal Symmetric	Off	-Z	FS 162
11	– Torsion Antisymmetric	On	$+\theta_X$	FS 162
12	– Torsion Antisymmetric	Off	$+\theta_X$	FS 162
18	• Fin Ballast – Long. Symmetric	Off	+X	Fin cg
19	– Long. Symmetric	Off	-X	Fin cg
20	– Long. Symmetric	Off	-X	Fin cg
??	– Long. Symmetric	On	+X	Fin cg
21	– Long. Symmetric	On	-X	Fin cg
31	– Lateral Antisymmetric	Off	-Y	Fin cg
22	• OMS Ballast – Long. Symmetric	Off	+X	OMS cg
23	– Long. Symmetric	Off	-X	OMS cg
25	• Payload – Normal Symmetric	Off	+Z	FS 117.5
26	– Normal Symmetric	Off	-Z	FS 117.5
28	– Torsion Antisymmetric	Off	$+\theta_Y$	+Z @ 117.5, -Z @ 78.0
32	• Cabin Ballast – Normal Symmetric	Off	-Z	FS 55.4

TT-10

Table 4-4 1/8-Scale Orbiter (Model I) Measured and Calculated Influence Coefficients

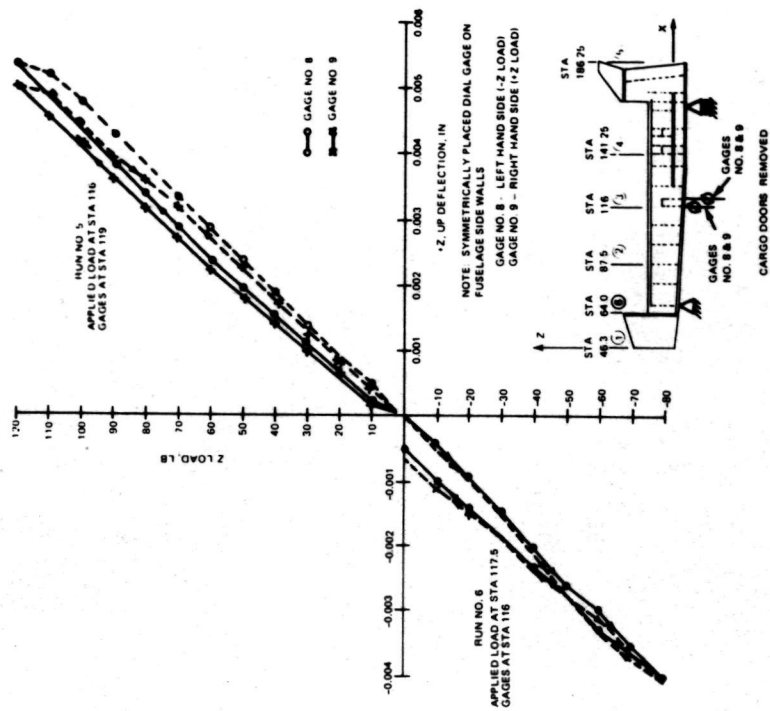
[illegible]

Note: Values are based on slopes determined from preliminary data. Variations of approximately 10% are possible in interpreting the raw data and in repeating the tests.



T-47

Fig. 4-19 Load-Deflection Curves for $\pm Z$ Loading on Nose Bulkhead (Sta 46.75)



T-58

Fig. 4-20 Load-Deflection Curves for $\pm Z$ Loading at Mid-Fuselage (Sta 119)

all the test values, both download (-Z) and upload (+Z), is 83.05×10^{-6} . Comparing the analysis with this averaged test value gives

$$\frac{\delta_{11} \text{ (Model I)}}{\delta_{11} \text{ (Test)}} = \frac{55.4}{83.05} = 66.6 \% \quad (4-1)$$

For the mid-fuselage region, using test No. 5 and 6 the same type comparison gives

$$\frac{\delta_{33} \text{ (Model I)}}{\delta_{33} \text{ (Test)}} = \frac{35.61}{45.87} = 78 \% \quad (4-2)$$

Both of the previous values are for the condition with the cargo door off. Comparing the analysis values for the door-on condition with the door-off condition

$$\frac{\delta_{33} \text{ (Model I - Door On)}}{\delta_{33} \text{ (Model I - Door Off)}} = \frac{31.0}{35.61} = 87 \% \quad (4-3)$$

and with comparable test data

$$\frac{\delta_{33} \text{ (Test - Door On)}}{\delta_{33} \text{ (Test - Door Off)}} = \frac{40.7}{45.87} = 88.5 \% \quad (4-4)$$

which indicates about the same percentage effect of the door. In the analysis the skins were assumed to be fully effective, while Equation 4-2 indicates that the test model fuselage inertia is only 78 % of the analytical value. If

I_{FA} = analytical value of the moment of inertial of the fuselage

I_{DA} = analytical value of the moment of inertia of the doors about the combined neutral axis

I_{FT} = test value of the fuselage inertia

I_{DT} = test value of the inertia of the doors about the combined neutral axis

then, from the above ratios,

$$\frac{I_{FT}}{I_{FA}} = 0.78 \quad (4-5)$$

$$\frac{I_{FA}}{I_{FA} + I_{DA}} = 0.87 \quad (4-6)$$

$$\frac{I_{FT}}{I_{FT} + I_{DT}} = 0.885 \quad (4-7)$$

Combining Equations 4-5 through 4-7, then

$$\frac{I_{DT}}{I_{DA}} = 0.694 \quad (4-8)$$

In Model I, the door longeron is not fully effective because it is attached to the fuselage at only four locations. In Subsection 5.12, the effectiveness factor associated with Model I is estimated to be 0.75. This factor being defined by $I_D = kA_D d^2$, where k is the effectiveness factor, A_D is the area of the door longeron, and d is the distance from the door longeron to the combined neutral axis. This means that the contribution of the door longeron to the combined inertia is only 52 % of the conventional section property value ($0.75 \times 0.694 = 0.516$). The loss in effectiveness given by Equation 4-8 is due to the fact that Model I does not account for local bending or shear deformation in the straps and door longerons.

Section 5
ANALYTICAL MODEL INVESTIGATION

5 - ANALYTICAL MODEL INVESTIGATION

5.1 BACKGROUND

Section 5 contains a series of separate analytical model investigations conducted at Grumman. The relationship between these separate subtasks is illustrated in Fig. 5-1. After evaluating the generalized mass and stiffness for the five Orbiter substructures (Subsection 5.2), a number of possibilities were suggested for explaining the differences between the Model I analysis and the test results. Consequently, separate studies were initiated to:

- Investigate the adequacy of the CQDMEM2 element used in a major portion of the finite element model (Subsection 5.3)
- Establish a simplified independent beam model of the fuselage and calculate frequencies (Subsections 5.4 and 5.5)
- Evaluate the Guyan reduction procedure (Subsection 5.6)
- Investigate the modeling in the forward region of the fuselage (Subsection 5.7)
- Evaluate the stress distributions due to 1 g and dynamic loads and check these stresses against linear buckling values (Subsections 5.8 and 5.9).

While these studies were being performed, additional tests were made at Langley (Subsections 4.3 and 4.4). These tests, especially the static test, confirmed some of the suspicions concerning the effectiveness of the fuselage skins and cargo door longerons. Test results lead to additional analytical tasks at Grumman to:

- Study the effect of initial imperfections on the stiffness characteristics of panels loaded in tension and compression (Subsection 5.10)
- Evaluate the test data to determine experimental effectiveness factors and estimate the amount of initial imperfection that existed in the 1/8-scale model panels (Subsection 5.11)
- Analytically study the effectiveness of the cargo door attachments (Subsection 5.12).

While these studies were being performed at Grumman, additional analytical and experimental work was performed at Langley. This effort included:

- A study of the effects of varying the panel aspect ratios in a finite element model on the predicted frequencies
- Examining the wing carry-through region and studying the local effects of the cutouts
- Investigating the wing/fuselage shear ties
- Evaluating the effects of removing the direct stress capability in the fuselage panels on the frequencies of the Orbiter
- Studying various methods for modeling the cabin ballast
- Analytically investigating the fin-fuselage connection
- Investigating the effects of initial panel imperfections on the stiffness and frequency characteristics of a cantilevered beam constructed of bars and shear panels. (This investigation included the fabrication and testing of a separate built-up cantilever model that resembled the fuselage sidewall. Provision was made to "force in" known initial imperfections in the panels.)

The results of all these separate investigations led to a set of remodeling guidelines for establishing Model II. These guidelines are discussed in Section 6.

5.2 SUBSTRUCTURE CONTRIBUTIONS TO THE GENERALIZED MASS AND STIFFNESS

The contributions of each of the five major components to the generalized mass and stiffness were calculated and used to evaluate the Rayleigh quotient:

$$\omega^2 = \frac{\sum \{\phi_i\}^T [K_i] \{\phi_i\}}{\sum \{\phi_i\}^T [M_i] \{\phi_i\}} = \frac{K_G}{M_G} \quad (5-1)$$

	(Fuselage)	(Wing)	(Doors)	(Fin)	(Payload)
$= \frac{6299.78}{0.05629} \left[\begin{array}{cccccc} 0.748 & + & 0.101 & + & 0.130 & + & 0.015 & + & 0.006 \\ 0.548 & + & 0.156 & + & 0.024 & + & 0.224 & + & 0.048 \end{array} \right] \quad (5-2)$					

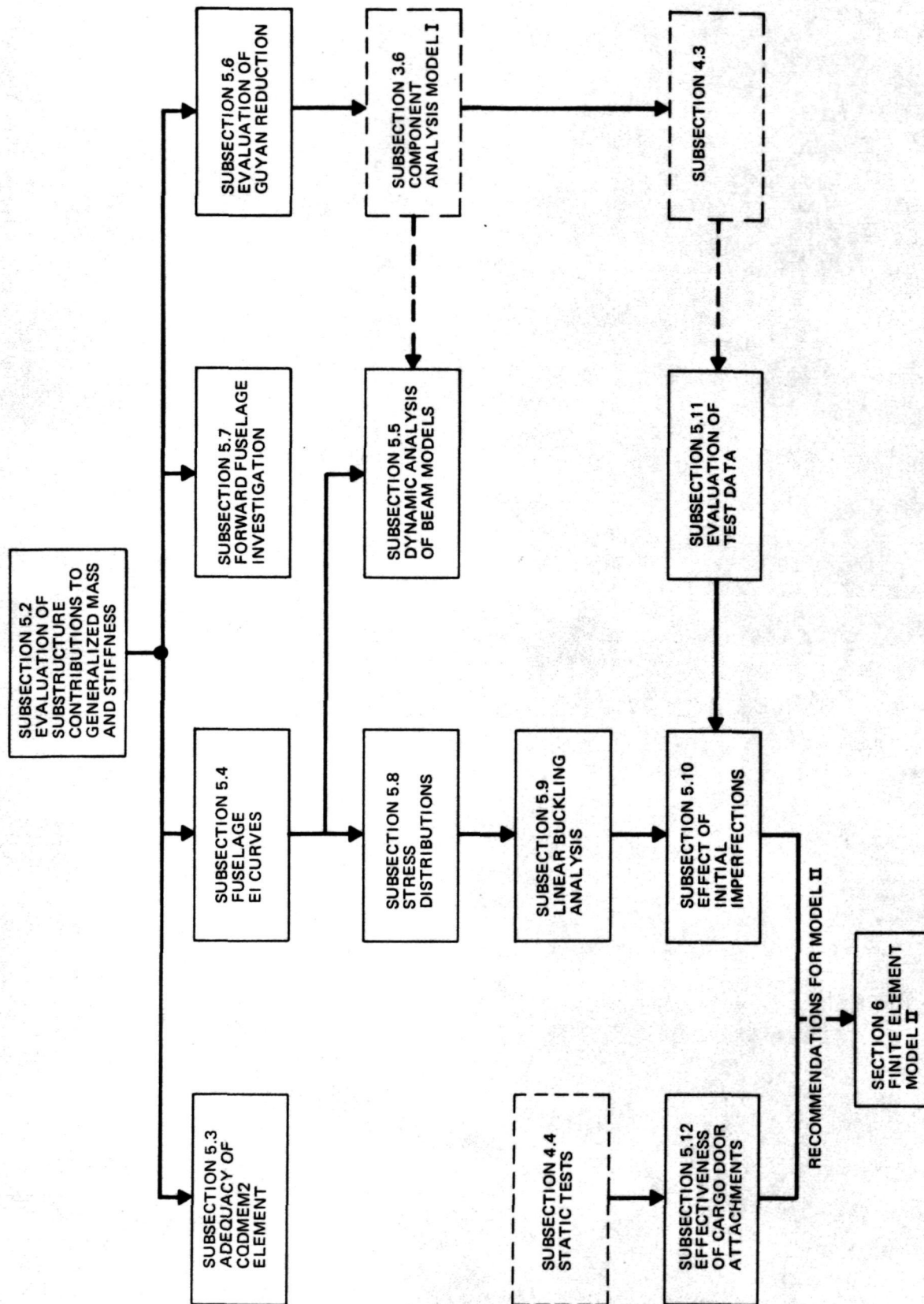


Fig. 5-1 Relationships Among Various Analytical Investigations Discussed in Section 5

where

$\{\phi_i\}$ = portion of modal vector for the i th component

$[K_i]$ = stiffness for i th component

$[M_i]$ = mass matrix for i th component.

The frequency is $f = \frac{\omega}{2\pi} = 53.2$ Hz.

The terms within the brackets are the values calculated for the fuselage, wing, doors, fin and payload, respectively, for the first symmetric mode. These values are arranged in tabular form in Table 5-1. Note that the fuselage accounts for approximately 75 % of the generalized stiffness. The fuselage weight of 100.91 lb includes the OMS ballast of 26.15 lb and the fuselage cabin ballast of 29.2 lb per half structure.

Table 5-1 Orbiter Substructure Contributions to First Symmetric Modal Mass and Stiffness (Model I)

Substructure	Weight		Modal Stiffness		Modal Mass	
	lb	%	Value	%	Value	%
Fuselage	100.91	48.34	4710.25	74.8	.03087	54.8
Wing	32.86	15.74	635.15	10.1	.00880	15.6
Door	6.52	3.13	822.34	13.0	.00131	2.4
Fin	3.85	1.84	97.03	1.5	.01260	22.4
Payload	64.62	30.95	35.01	0.6	.00271	4.8
Total	208.76	100.00	6299.78	100.00	.05629	100.00

TT-11

The fin, which weighs only 2 % of the total vehicle, accounted for 22 % of the generalized mass. On the other hand, the payload weighs 30 % of the total and accounted for only 5 % of the generalized mass.

Comparisons of the analytical Model I modes with test modes are presented in Section 7. For the first mode, both test and analytical values compare rather well except for the motion of the fin ballast. For this DOF, the ratio of the test value to the analysis value is approximately

$$\frac{\phi_{\text{Test}}}{\phi_{\text{Analysis}}} = 1.25. \quad (5-3)$$

An estimate on the analytical frequency that accounts for the additional flexibility of the fin can be obtained by using the Rayleigh quotient with a modified mode shape that reflects the test value. That is

$$\phi' = \phi_{\text{Analysis}} + \Delta \phi. \quad (5-4)$$

Since all points are in fair agreement, except the fin ballast, the only quantity in the quotient that needs to be modified is the fin generalized mass

$$(M_G')_{\text{Fin}} = (0.224) (1.25)^2 = 0.350. \quad (5-5)$$

The generalized stiffness for the fin is small compared to the total and, hence, any small additional stiffness due to the modified mode shape can be neglected. An estimate on the frequency is thus

$$\begin{aligned} f &= \frac{1}{2\pi} \left(\frac{6299.78}{0.05629} \right)^{1/2} \left(\frac{1}{1.0 - 0.224 + 0.350} \right)^{1/2} \\ &= (53.2) (0.89)^{1/2} = 50.2 \text{ Hz}. \end{aligned} \quad (5-6)$$

This value is still much higher than the measured value of 43.6 Hz and indicates that the "softness" of the fin supports is not the sole contributor to the lack of correlation. It might be suspected, however, that additional fin "softness", which had not been included in Model I, could account for approximately 30 % of the discrepancy.

If $\{\phi\}$ is a mode shape it must satisfy the equation

$$[K]\{\phi\} - \omega^2 [M]\{\phi\} = 0. \quad (5-7)$$

Differentiating this equation with respect to a design parameter, p_i (either a stiffness or mass parameter)

$$\begin{aligned} \left[\frac{\partial K}{\partial p_i} \right] \{\phi\} + [K] \left\{ \frac{\partial \phi}{\partial p_i} \right\} - \frac{\partial \omega^2}{\partial p_i} [M] \{\phi\} \\ - \omega^2 \left[\frac{\partial M}{\partial p_i} \right] \{\phi\} - \omega^2 [M] \left\{ \frac{\partial \phi}{\partial p_i} \right\} = 0 \end{aligned} \quad (5-8)$$

or

$$\left[\frac{\partial K}{\partial p_i} \right] \{\phi\} - \frac{\partial \omega^2}{\partial p_i} [M] \{\phi\} - \omega^2 \left[\frac{\partial M}{\partial p_i} \right] \{\phi\} + \left[[K] - \omega^2 [M] \right] \left\{ \frac{\partial \phi}{\partial p_i} \right\} = 0. \quad (5-9)$$

Multiplying Equation 5-9 by $\{\phi\}^T$, and transposing Equation 5-7, it can be seen that the last term in Equation 5-9 vanishes. Rearranging the result,

$$\frac{\partial \omega^2}{\partial p_i} = \frac{\{\phi\}^T \left[\frac{\partial K}{\partial p_i} \right] \{\phi\} - \omega^2 \{\phi\}^T \left[\frac{\partial M}{\partial p_i} \right] \{\phi\}}{\{\phi\}^T [M] \{\phi\}}. \quad (5-10)$$

If p_i is restricted to stiffness changes only, then;

$$\frac{\partial \omega^2}{\partial p_i} = \frac{\{\phi\}^T \left[\frac{\partial K}{\partial p_i} \right] \{\phi\}}{\{\phi\}^T [M] \{\phi\}}. \quad (5-11)$$

Equation 5-11 provides a means for judging the change in the frequency due to changing the stiffness of a given design parameter, p_i . If the design parameter p_i is taken to be a representative stiffness quantity of a given component (for example, a scalar multiplying the moment of inertia distribution of the fuselage) then the terms in the numerator of the Rayleigh quotient represent the relative values of the derivatives with respect to the scalar p_i . Thus, if the inertia distribution of the fuselage is scaled by p_F , then an estimate on the new frequency, ω_N , is

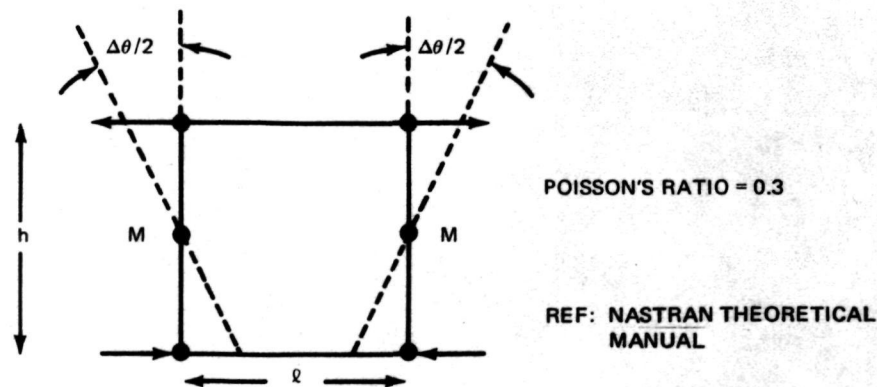
$$\omega_N^2 = \omega_0^2 + \left(\frac{\partial \omega^2}{\partial p_F} \right) p_F$$

where ω_0 represents the old frequency. Once a change is made, the mode shape will of course change, and new values of the derivatives should be calculated. For the particular set of design parameters represented by Model I, however, a change in the fuselage inertia will produce the largest change in frequency. The next item

of most importance is the cargo door stiffness. In accordance with these observations, separate investigations were initiated to study the fuselage EI distribution, the adequacy of the finite elements used in the fuselage, and the finite element representation around the cabin and OMS ballast. These investigations will be discussed in the next subsection.

5.3 ADEQUACY OF THE CQDMEM2 ELEMENT

Correct behavior of a finite element under in-plane bending is a rather severe test for adequacy of the element. A comparison of different NASTRAN elements under pure bending is given in Section 15 of the NASTRAN Theoretical Manual. For convenience, this data is reproduced in Fig. 5-2. Note that the CQDMEM2 element is 71 % too stiff ($\frac{1}{0.585} - 1 = 0.71$) using a Poisson's ratio of 0.3. The CQDMEM element is much worse, and the CQDMEM1 is not much of an improvement over the CQDMEM2 element. The results of "stacking" four CQDMEM2 elements to form a beam segment was discussed in Section 3. The effects of adding CROD elements to account for flange material was described, and it was noted that the behavior approaches beam theory with an increasing ratio of cap material. The neutral axis of the 1/8-scale model fuselage is not at mid-height, hence these curves do not strictly apply.



$\frac{\Delta\theta/M}{l/EI}$	Beam Theory	QDMEM	QDMEM1	QDMEM2
	1.000	.224	.675	.585

T-59

Fig. 5-2 Comparison of Flexibilities for a Pure Bending Couple Applied to Square Membrane Elements, $l = h$

Figure 5-3 illustrates a typical fuselage side wall section. It contains two CROD elements, the upper representing the upper fuselage longeron, and the lower representing the lower longeron and deck. The side wall was modeled with five CQDMEM2 elements having a thickness of 0.020 in. The moment of inertia, calculated from section properties, is 33.0. The ratio of cap to web inertia being

$$R_I = \frac{I_{\text{cap}}}{I_{\text{web}}} = \frac{22.87}{10.14} = 2.26.$$

(Note that the neutral axis is located 4.78 in. above the lower cap.) The heights of the five panels agree with the location of node lines at fuselage Station 116. A length of 10 in. was used for the composite segment, which is slightly larger than the maximum distance between frames in the fuselage. The sides of the element were con-

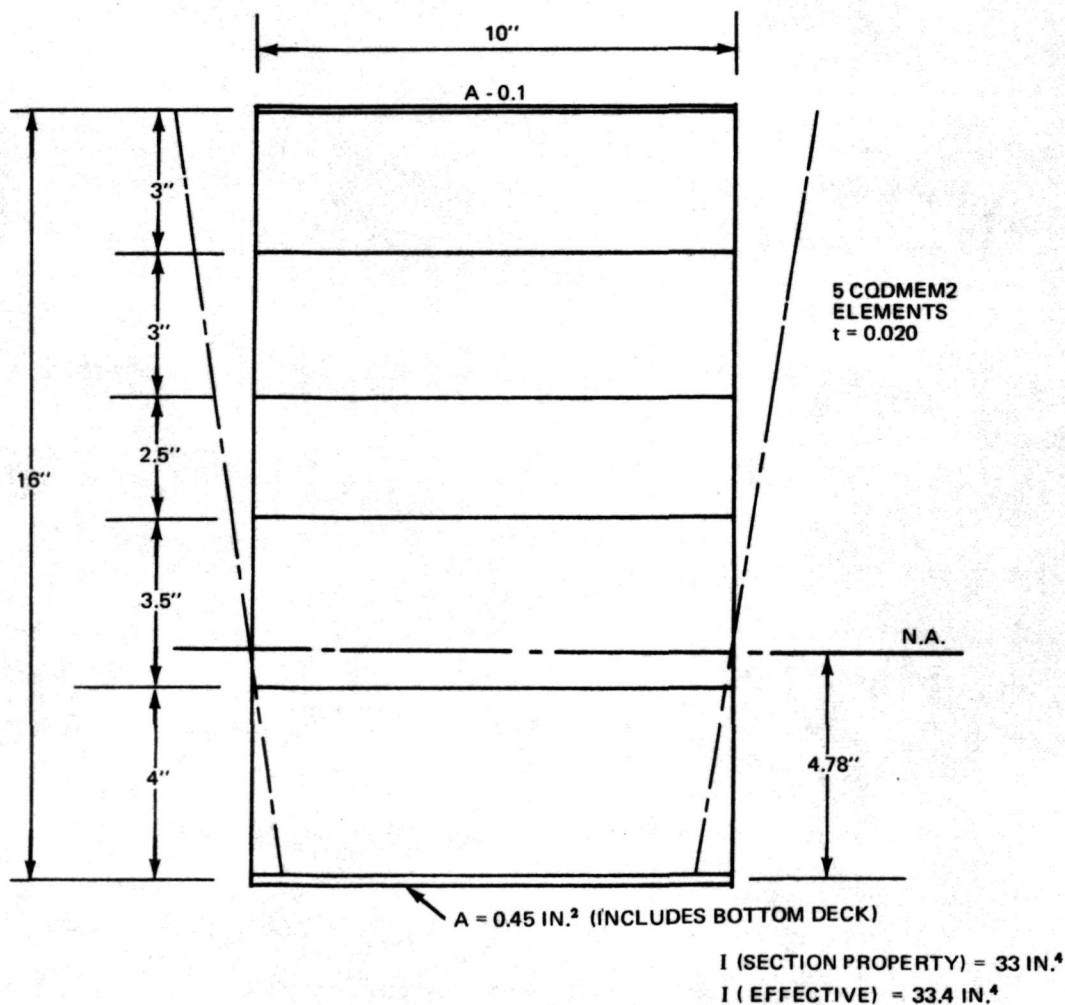


Fig. 5-3 Fuselage Side Wall in Pure Bending

strained by MPC's to produce pure bending, as shown in the figure. These calculations yielded an "effective inertia" value of 33.4. The error is, therefore

$$\frac{33.4 - 33.0}{33.0} = 1.21 \%$$

For shorter length segments the error would be less (as is indicated by the curves in Fig. 3-4). Thus it was felt that the idealization should work rather well, at least for predicting the frequencies of low modes. For high fuselage modes the number of transverse station cuts might not be sufficient, because of the more abrupt variations in the moment diagram for higher modes. However, before these effects become important, it was believed that other low mode effects not already included would become more important.

In all of this discussion it has been assumed that the section is fully effective - that is, non-buckled.

5.4 FUSELAGE EI CURVES

A beam equivalent model of the fuselage was created and analyzed by NASTRAN to check the validity of the finite element model. The simplified model is shown in Fig. 5-4 with section properties and lumped weights indicated at each station. The moments of inertia were obtained from section cuts and from deflections that were calculated using the finite element model. The fuselage vertical deflections (from the NASTRAN analysis) for a unit moment applied at the fin ballast are plotted in Fig. 5-5. The structure was supported at the interstage points (FS 68.25 and 166.5). As shown in the figure, a correction was made to account for the non-zero displacement at Station 68.25. This is because the forward support is on the centerline; hence, the local deformation of the frame produces a linear shift in the side wall displacements. These corrected deflections were then used to calculate the second derivatives by the formula

$$y_i'' = \frac{1}{h^2} (y_{i-1} - 2y_i + y_{i+1})$$

The values of EI were then computed from $(EI)_i = -\frac{M_i}{y_i''}$

where M_i is the moment at station i due to the unit moment at the fin ballast. The inertia values that were obtained are shown plotted as curve "B" in Fig. 5-6. Curves

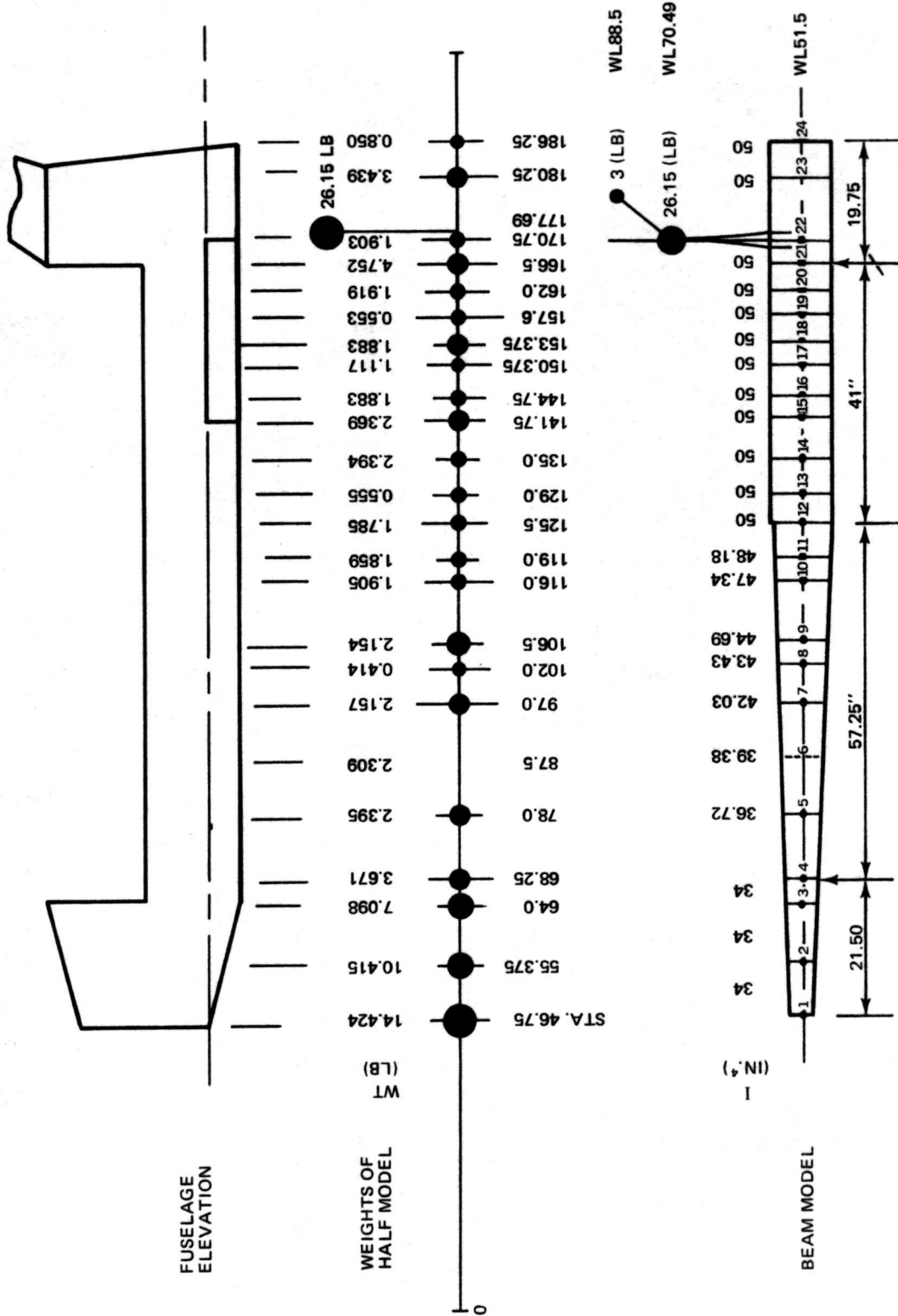


Fig. 5-4. 1/8 Scale Orbiter Fuselage Beam Model

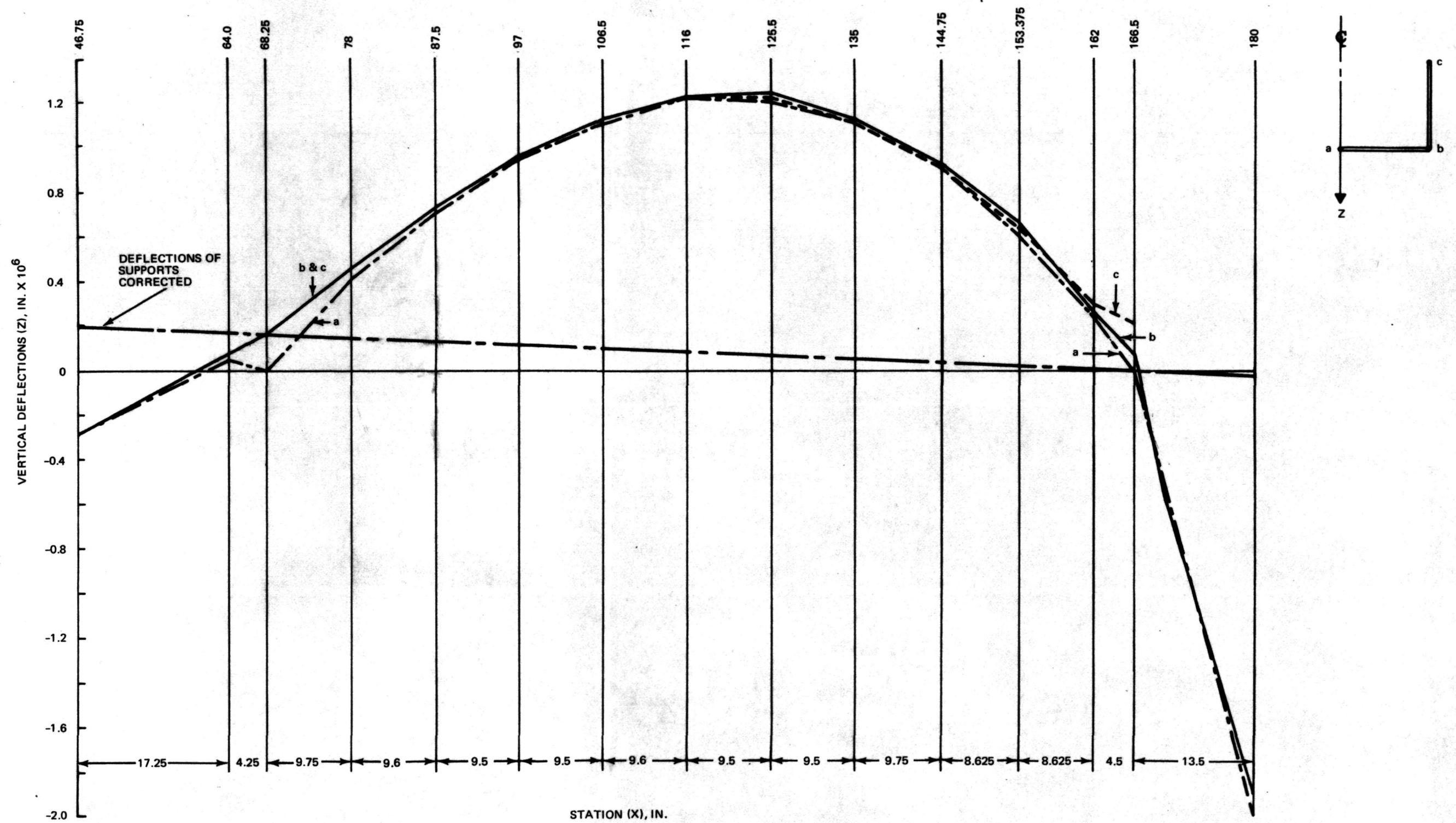


Fig. 5-5 1/8 Scale Orbiter Fuselage Vertical Deflections for Unit Moment at Fin Ballast Center of Gravity (Model I Analysis)

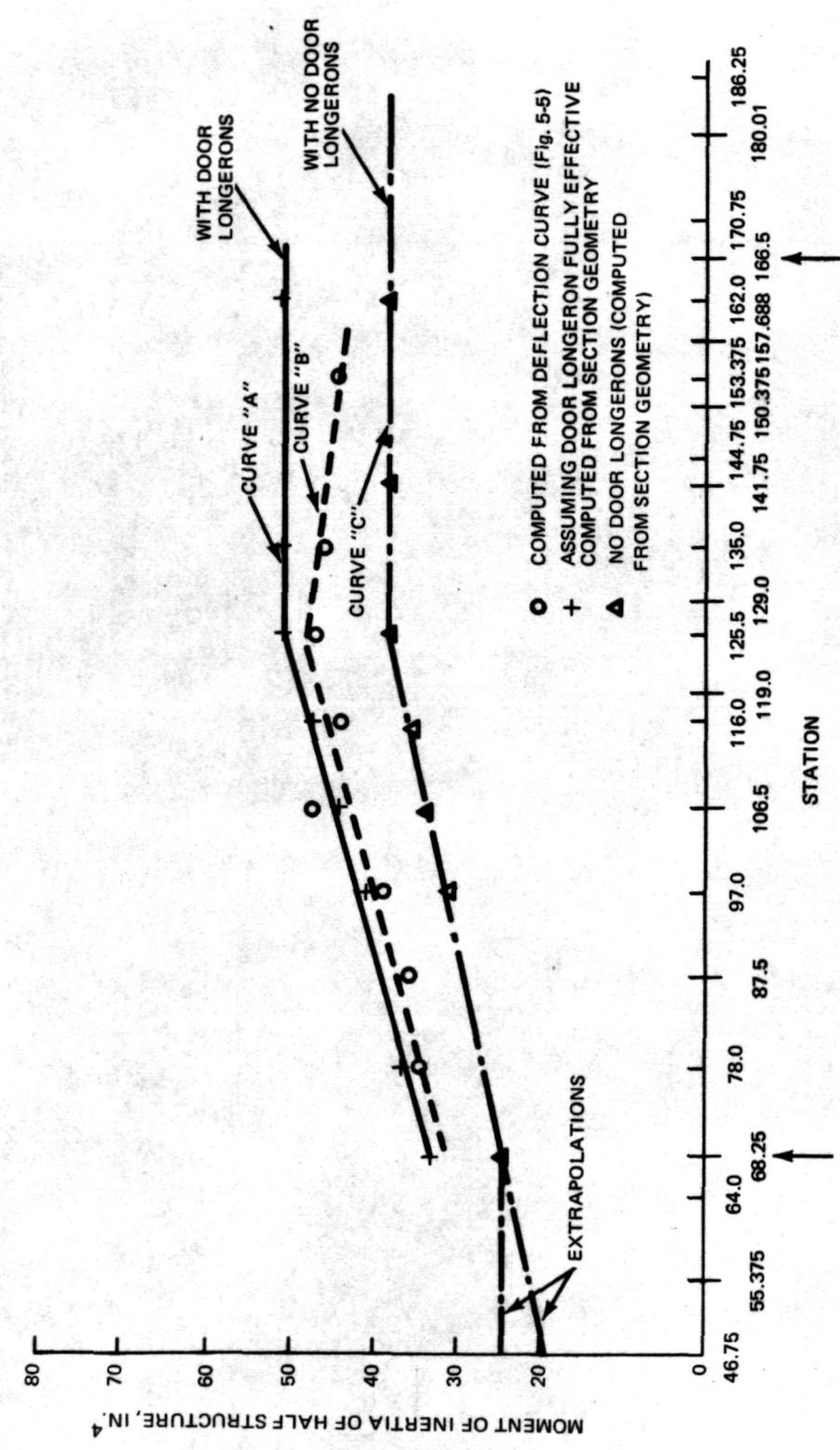


Fig. 5-6 1/8-Scale Orbiter Fuselage Model - Moment of Inertia

T-63

"A" and "C" were obtained from section cut calculations. Curve "A" assumes the door longeron to be fully effective, while curve "C" does not include the door longeron.

The position of the neutral axis was located by using the horizontal displacements calculated from the finite element model. These displacements were used to calculate average strains from which the neutral axis was located by assuming that plane sections remain plane during bending. The position of the neutral axis, plotted in Fig. 5-7, compares favorably with that obtained from section cuts. The location of the neutral axis does not appear to be influenced greatly by the wing except for a small effect near the aft end.

A similar procedure was used to determine the bending properties of the aft end of the fuselage and the fin. Figure 5-8 shows the aft fuselage and fin stub with a unit horizontal load applied at the fin ballast ($Z = 88.5$). The horizontal displacements, shown in Fig. 5-9, were used to calculate the equivalent moment of inertia distribution (also shown in Fig. 5-9). An elevation of $Z = 51.5$ was used as a zero reference for measuring all displacements.

5.5 DYNAMIC ANALYSIS OF BEAM MODELS

The EI curves discussed in Subsection 5.4 were used to create a stick model of the fuselage (Fig. 5-3). The model contained 32 nodes and 31 beam elements. The value of I that was used corresponded to curve "C" in Fig. 5-6 (section cut data - no door longeron). The neutral axis was assumed to be at a constant WL of 51.5. All mass data for the fuselage was lumped at the 32 node points. The wing, fin, payload, and cargo doors were not included. The MPC's were used to constrain the model such that no axial deformation was considered. The results for the first three symmetric free-free modes for the beam model are shown in column "A" of Table 5-2. Results are also shown from the Phase I finite element analysis for the Model I fuselage substructure. The first mode of the beam model was high by approximately 11 %. The beam model was modified to include axial deformation and the MPC's were removed. The results of this change are shown in column "B". Note that the effect is small on the first mode. Next, the location of the neutral axis was modified in the cabin region of the fuselage, and a more accurate distribution of the cabin ballast was used. The results for this change are shown in column "C". Finally, shear deformation was included by using the fuselage side wall as the shear area. The re-

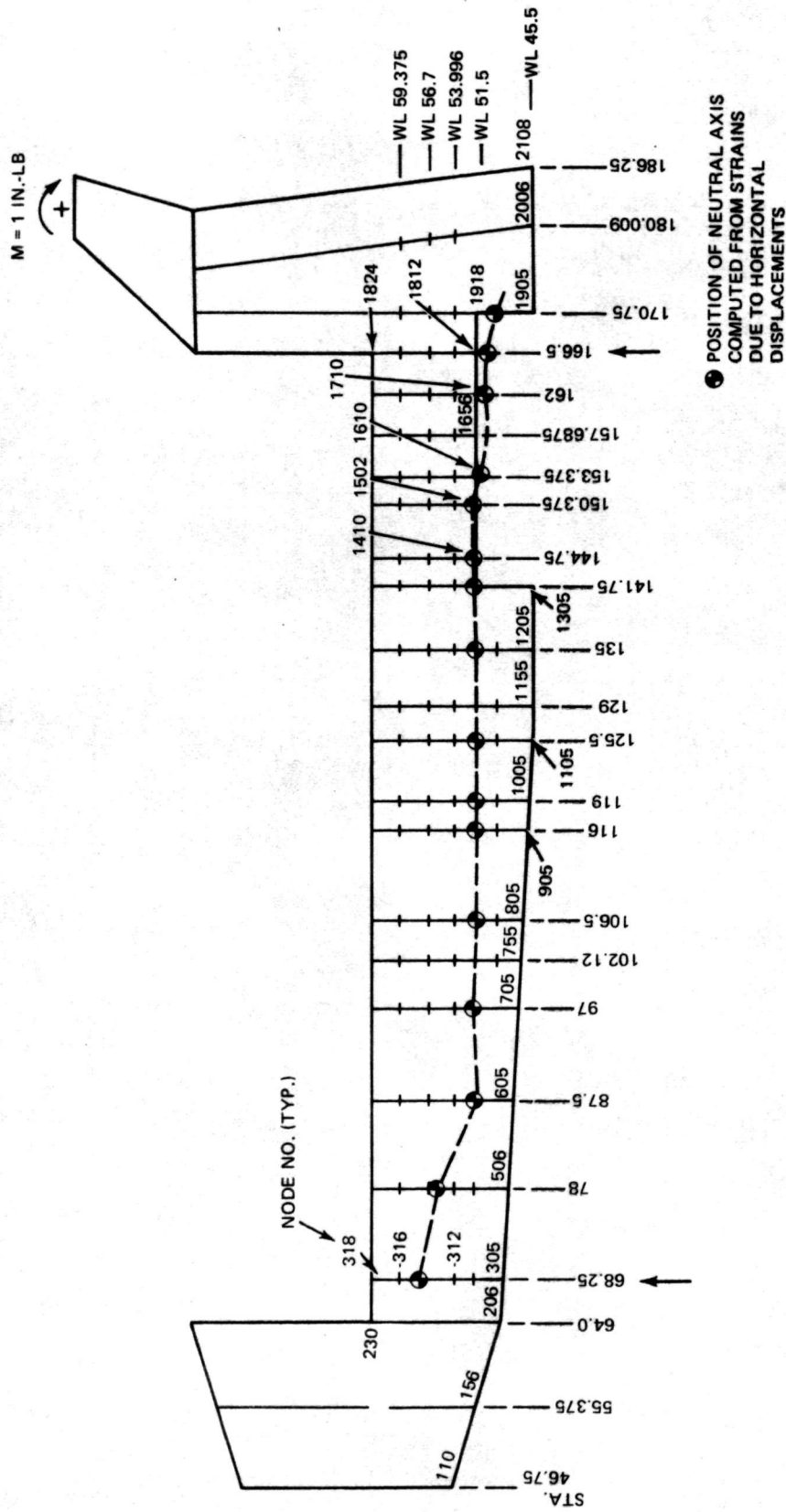
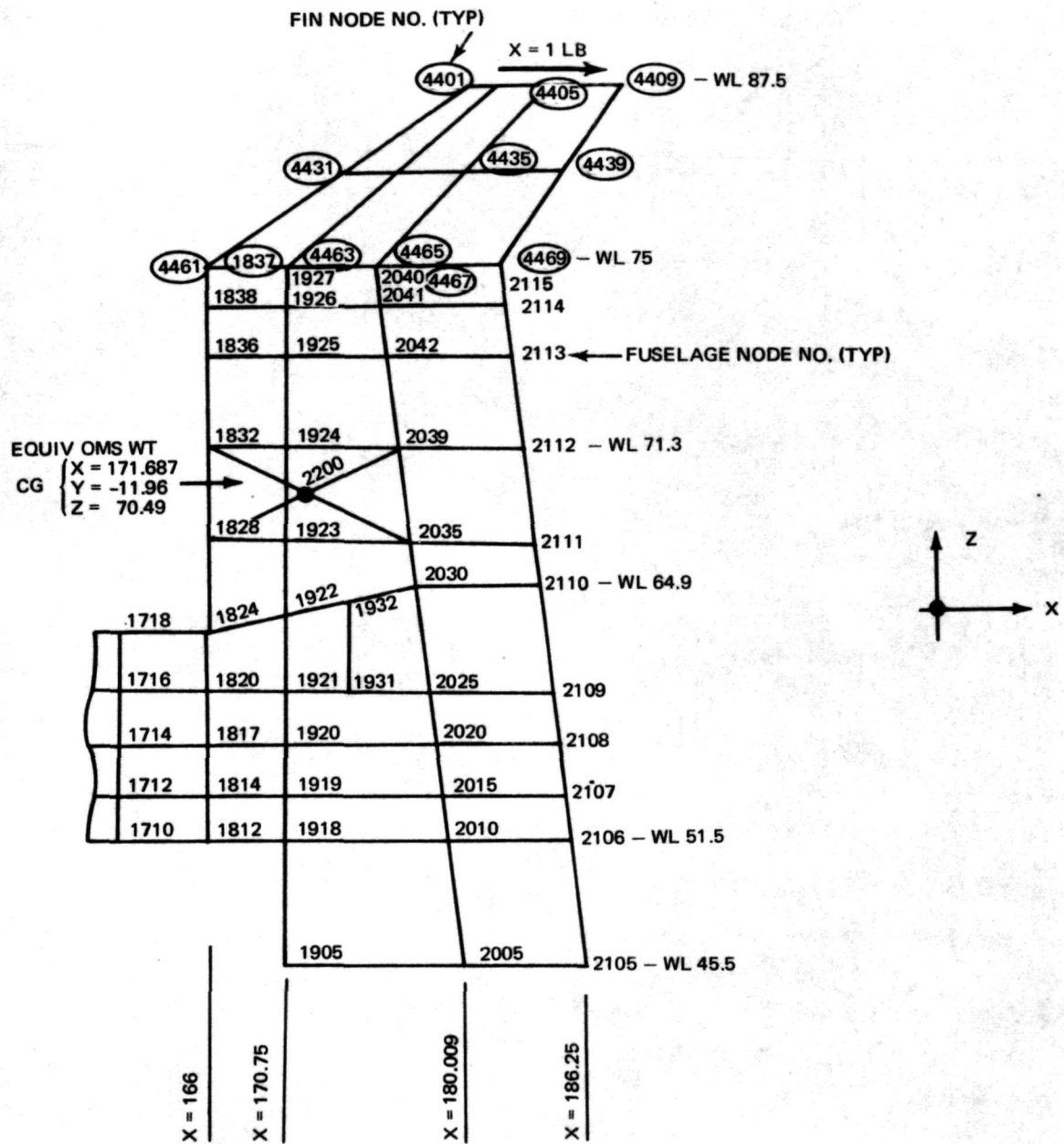


Fig. 5-7 1/8-Scale Orbiter Fuselage Model — Position of Computed Neutral Axis

T-79



T-64

Fig. 5-8 Elevation of Aft Fuselage and Fin

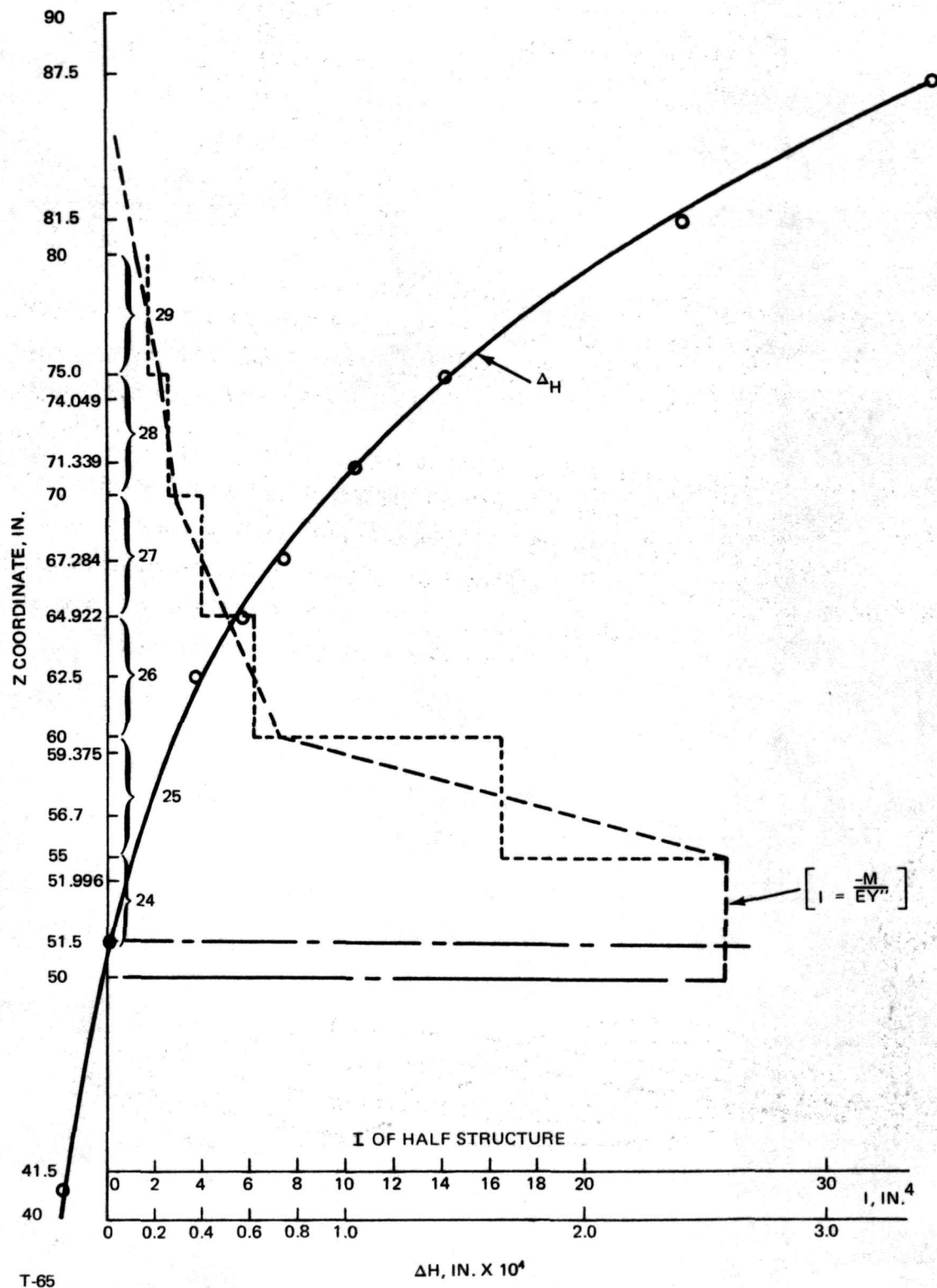


Fig. 5-9 1/8-Scale Aft Fuselage Model – Horizontal Deflections

Table 5-2 Results of Fuselage Beam Model Analyses

Mode	NASTRAN Finite El. Model I (Fuselage)	NASTRAN Beam Models			
		A Using MPC's	B No MPC's	C Neut. Ax. & Mass	D Shear Defl.
1	62.2	69	68.3	64.3	61.2
2	129.9	142.2	134.6	138.1	115.8
3	191.3	265.4	244.1	230.5	189.9
TT-12					

sults of this change are shown in column "D" of Table 5-2, and in Fig. 5-10. In this case, the first mode differed from the finite element model by only 1.6 %. The third mode differed by only 0.7 %, thus showing the effect of including shear deformation in calculating higher modes.

At this point in the analytical investigation, it became clear that no major errors had been made in the NASTRAN Model I analysis of the fuselage. The discrepancies between analysis and test were due either to error in the testing, or to a fundamentally different behavior between the 1/8-scale model and the basic assumptions used in establishing the finite element model.

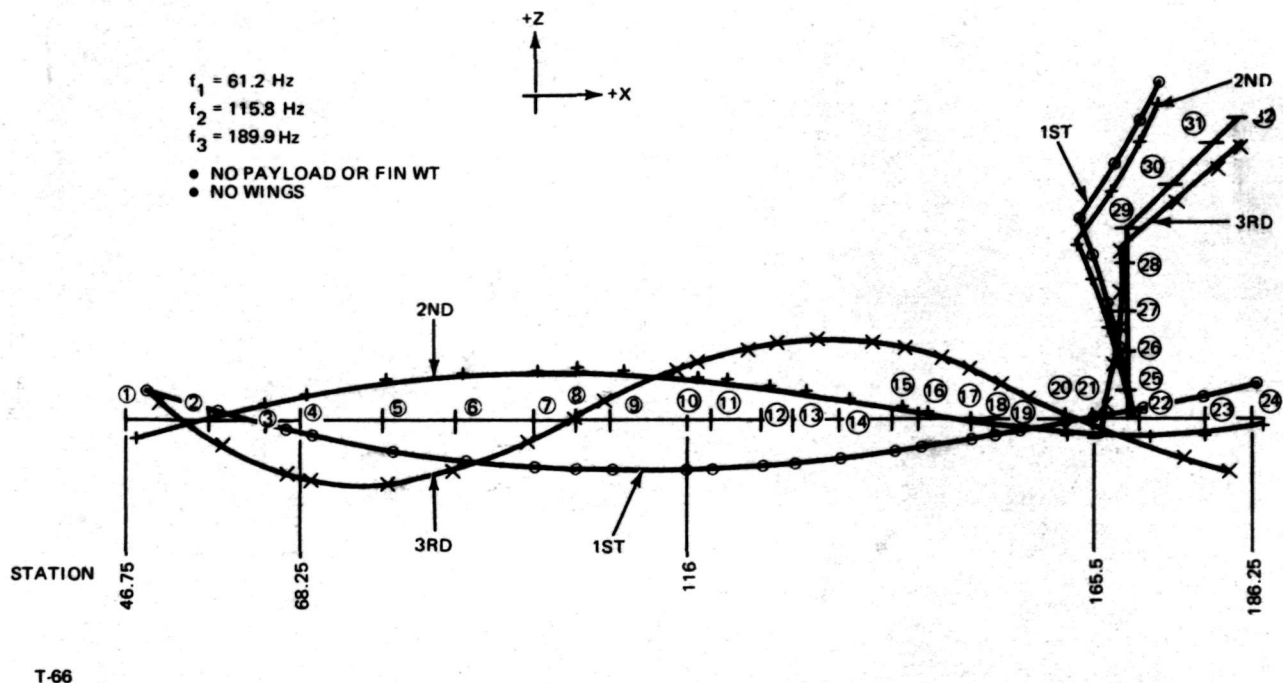


Fig. 5-10 1/8-Scale Shuttle Beam Model – First Three Modes for Fuselage Symmetric Case

Reproducibility of the test results for horizontal and vertical dynamic tests (Subsection 4.2 and 4.3) eliminated any suspicion of the testing procedures. Unfortunately, the schedule did not permit dismantling the 1/8-scale model and dynamic test of the individual components. Thus, no test data existed for the fuselage substructure to compare with the analytical results just discussed. Consideration was given to extending the beam model to represent the entire Orbiter. However, time required to perform other analytical investigations prevented this from happening. The advantage of a simple Orbiter model over the extensive finite element model would be that basic parameters could be investigated more easily to tune the model to the test results. Derivatives of frequency with respect to various stiffness parameters (such as the moment of inertia of the fuselage) could be easily obtained. This, of course, could be obtained by using the finite element model and slaving a large number of elements to represent a single parameter.

5.6 EVALUATION OF THE GUYAN REDUCTION PROCEDURE

The Guyan reduction involves an approximation in establishing the transformation that is used to reduce the number of DOF's in a problem. Initially, the inertia forces at the DOF's to be eliminated are neglected. This allows formulation of a transformation, based on statics, that expresses the DOF's to be eliminated in terms of those to be retained. The reduction of the mass and stiffness matrices follow from virtual work considerations. If harmonic motion is assumed then the equations of motion are

$$\{F\} = [K] \{\Delta\} - \omega^2 [M] \{\Delta\} \quad (5-12)$$

where

- $\{F\}$ = a vector of external forces
- $\{\Delta\}$ = a vector of node displacements
- $[K]$ = stiffness matrix
- $[M]$ = mass matrix
- ω = circular frequency.

Partitioning Equation 5-12 into parts yield

$$\begin{Bmatrix} F_1 \\ F_2 \end{Bmatrix} = \begin{bmatrix} K_{11} & K_{12} \\ K_{21} & K_{22} \end{bmatrix} \begin{Bmatrix} \Delta_1 \\ \Delta_2 \end{Bmatrix} - \omega^2 \begin{bmatrix} M_{11} & M_{12} \\ M_{21} & M_{22} \end{bmatrix} \begin{Bmatrix} \Delta_1 \\ \Delta_2 \end{Bmatrix} \quad (5-13)$$

where the subscript "1" refers to DOF's to be eliminated, and "2" refers to DOF's to be retained. Neglecting the inertia terms, $-\omega^2 M_{11}$ and $-\omega^2 M_{12}$, leads to

$$\{F_1\} = [K_{11}]\{\Delta_1\} + [K_{12}]\{\Delta_2\}. \quad (5-14)$$

If the external forces $\{F_1\}$ are zero,

$$\{\Delta_1\} = -[K_{11}]^{-1} [K_{12}]\{\Delta_2\}. \quad (5-15)$$

Using this relationship, the transformation, $[T]$, can be established

$$\begin{Bmatrix} \Delta_1 \\ \Delta_2 \end{Bmatrix} = \begin{bmatrix} -[K_{11}]^{-1} & [K_{12}] \\ 0 & I \end{bmatrix} \{\Delta_2\} = [T] \{\Delta_2\} \quad (5-16)$$

or

$$\{\Delta\} = [T] \{\Delta_R\} \quad (5-17)$$

where the subscript "R" indicates reduced degrees of freedom.

From virtual work considerations

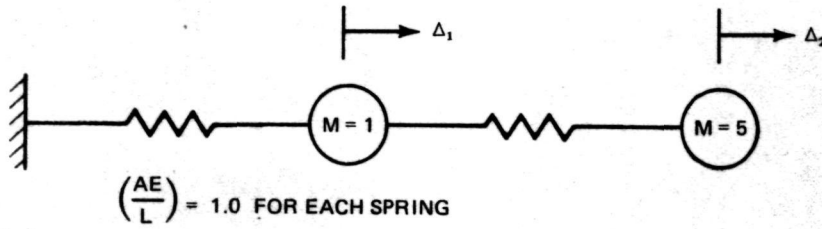
$$\{F_R\} = [T]^T \{F\}. \quad (5-18)$$

Combining equations 5-12, 5-17 and 5-18 yields

$$\begin{aligned} \{F_R\} &= [T]^T [K] [T] \{\Delta_R\} - \omega^2 [T]^T [M] [T] \{\Delta_R\} \\ &= \left[[K_R] - \omega^2 [M_R] \right] \{\Delta_R\} \end{aligned} \quad (5-19)$$

where $[K_R]$ and $[M_R]$ are the reduced stiffness and mass matrices, respectively.

The choice of which DOF's to eliminate becomes important because of the assumption involved in the transformation. To illustrate this point, and to discuss general methods for evaluating large systems, consider the simple two-DOF problem shown in Fig. 5-11. It consists of two masses and two springs. The values of the masses are 1 and 5, and the stiffness of the springs are both 1.0. Assuming harmonic motion, the equations of equilibrium are



T-67

Fig. 5-11. Simple Two-DOF Problem

$$\begin{Bmatrix} F_1 \\ F_2 \end{Bmatrix} \begin{bmatrix} 2 & -1 \\ -1 & 1 \end{bmatrix} \begin{Bmatrix} \Delta_1 \\ \Delta_2 \end{Bmatrix} - \omega^2 \begin{bmatrix} 1 & 0 \\ 0 & 5 \end{bmatrix} \begin{Bmatrix} \Delta_1 \\ \Delta_2 \end{Bmatrix} \quad (5-20)$$

If DOF No. 2 is eliminated, the transformation matrix, $[T]$, is

$$\begin{Bmatrix} \Delta_1 \\ \Delta_2 \end{Bmatrix} = \begin{bmatrix} - & - & - & \frac{I}{-} & - & - \\ -[K_{22}] & -1 & [K_{21}] \end{bmatrix} \{\Delta_1\} = [T] \{\Delta_1\} \quad (5-21)$$

$$= \begin{bmatrix} 1 \\ 1 \end{bmatrix} \{\Delta_1\} \quad (5-22)$$

The reduced mass and stiffness matrices for this case are

$$[K_R] = [T]^T [K] [T] = [1] \quad (5-23)$$

$$[M_R] = [T]^T [M] [T] = [6]. \quad (5-24)$$

Thus,

$$\{F_R\} = [1] \{\Delta_R\} - \omega^2 [6] \{\Delta_R\} = 0 \quad (5-25)$$

and hence,

$$\omega^2 = \frac{1}{6} = 0.1666.$$

On the other hand, if DOF No. 1 is eliminated, then the transformation, $[T]$, is

$$\begin{Bmatrix} \Delta_1 \\ \Delta_2 \end{Bmatrix} = \begin{bmatrix} -[K_{11}] & -1 & [K_{12}] \\ - & - & - \\ - & - & - \end{bmatrix} \{\Delta_2\} = [T] \{\Delta_2\} \quad (5-26)$$

$$= \begin{bmatrix} 1/2 \\ 1 \end{bmatrix} \{\Delta_2\} \quad (5-27)$$

II

from which

$$[K_R] = [1/2]$$

$$[M_R] = [5.25]$$

and

$$\omega^2 = 0.0952.$$

The exact solution is

$$\omega_1^2 = .09502 \text{ and } \omega_2^2 = 2.10498.$$

The mode for the lower frequency is

$$\begin{Bmatrix} \Delta_1 \\ \Delta_2 \end{Bmatrix} = \begin{Bmatrix} 0.5249 \\ 1.0 \end{Bmatrix}.$$

A method for evaluating the Guyan reduction procedure has been suggested (S. Goldenberg of Grumman) and consists of first evaluating the inertia forces associated with a unit value of the mode shape. Returning to the first case (DOF No. 2 eliminated),

$$\{F_I\} = -\omega^2 [M] [T] \{\phi\} \quad (5-28)$$

$$\begin{Bmatrix} F_{I1} \\ F_{I2} \end{Bmatrix} = -\omega^2 \begin{bmatrix} 1 & 0 \\ 0 & 5 \end{bmatrix} \begin{bmatrix} 1 \\ 1 \end{bmatrix} \{1\} = -\omega^2 \begin{Bmatrix} 1 \\ 5 \end{Bmatrix} \quad (5-29)$$

The scalar ω^2 may be neglected since only the shape of the distribution is of interest. Using these forces the static deflection shape is calculated from

$$\{\Delta\} = [K]^{-1} \{F_I\} \quad (5-30)$$

or

$$\begin{Bmatrix} \Delta_1 \\ \Delta_2 \end{Bmatrix} = \begin{bmatrix} 1 & 1 \\ 1 & 2 \end{bmatrix} \begin{Bmatrix} 1 \\ 5 \end{Bmatrix} = \begin{Bmatrix} 6 \\ 11 \end{Bmatrix} \quad (5-31)$$

This static deflection shape is now used in the Rayleigh quotient

$$\omega^2 = \frac{\{\Delta\}^T [K] \{\Delta\}}{\{\Delta\}^T [M] \{\Delta\}} \quad (5-32)$$

For the present case this gives $\omega^2 = 0.09516$. The static deflection shape $\begin{Bmatrix} 6 \\ 11 \end{Bmatrix}$ is equivalent to $\begin{Bmatrix} 0.5455 \\ 1 \end{Bmatrix}$

Repeating this procedure for the case when DOF No. 1 is eliminated yields

$$\omega^2 = 0.09501$$

$$\begin{Bmatrix} \Delta_1 \\ \Delta_2 \end{Bmatrix} = \begin{Bmatrix} 0.5238 \\ 1 \end{Bmatrix}$$

These results are summarized in Table 5-3. Although a rather extreme case, this shows that the results that are obtained by the Guyan reduction are heavily dependent on the DOF's being eliminated. Eliminating No. 2 is a poor choice, as would be suspected. Regardless of the choice, however, it is possible to judge the validity of the results by first calculating the inertia forces due to the "expanded" Guyan mode, and then using these forces to calculate static deflections. The frequency can then be obtained by using these static deflection shapes in the Rayleigh quotient. For the present example, the elimination of DOF No. 2 yielded an error in frequency of 75.3 %, which was improved by using the static deflection technique to being in error by only 1.47 %. The elimination of DOF No. 1 is in error by 1.89 %, and this was improved to being in error by only 0.01 %. For this simple case the exact solution is

Table 5-3 Summary of Calculations for Simple Two-DOF Problem

Calculation	ω^2	% Error	Mode Shape
(1) Guyan Elimination of No. 2	0.1666	75.3	1, 1
(2) Guyan Elimination of No. 1	0.0952	1.89	0.5, 1
(3) Using Static Shape From (1)	0.09516	1.47	0.5455, 1
(4) Using Static Shape From (2)	0.09501	.01	0.5238, 1
(5) Exact	0.09502	—	0.5249, 1

TT-13

known, hence an error can be calculated. Of course, for large problems this is not the case. Thus it becomes desirable to have procedures that can estimate the error or follow the convergence. Rewriting Equation (5-12).

$$\begin{Bmatrix} F_1 \\ F_2 \end{Bmatrix} = \begin{bmatrix} K_{11} - \omega^2 M_{11} & K_{12} - \omega^2 M_{12} \\ K_{21} - \omega^2 M_{21} & K_{22} - \omega^2 M_{22} \end{bmatrix} \begin{Bmatrix} \Delta_1 \\ \Delta_2 \end{Bmatrix} \quad (5-33)$$

$$= \begin{bmatrix} A_{11} & A_{12} \\ A_{21} & A_{22} \end{bmatrix} \begin{Bmatrix} \Delta_1 \\ \Delta_2 \end{Bmatrix} \quad (5-34)$$

Setting the external force $\{F_1\} = 0$ leads to

$$\{\Delta_1\} = -[A_{11}]^{-1} [A_{12}] \{\Delta_2\} \quad (5-35)$$

from which

$$\begin{Bmatrix} \Delta_1 \\ \Delta_2 \end{Bmatrix} = \begin{bmatrix} -[A_{11}]^{-1} [A_{12}] \\ I \end{bmatrix} \{\Delta_2\} = [T] \{\Delta_2\} \quad (5-36)$$

Using this transformation in conjunction with the full stiffness and mass matrices leads to

$$[K_R] = [T]^T [K] [T] \quad (5-37)$$

$$[M_R] = [T]^T [M] [T] \quad (5-38)$$

where $[K_R]$ and $[M_R]$ are the reduced stiffness and mass matrices. Here, however, the transformation $[T]$ is frequency dependent. Note that if ω is set to zero, $A_{11} = K_{11}$ and $A_{12} = K_{12}$, and the transformation is identical to the transformation used in the Guyan reduction. An iteration procedure can be used to evaluate the transformation $[T]$, assuming that only the first mode is of interest. Using this procedure on the previous problem where DOF No. 2 has been eliminated leads to the values shown in Table 5-4. Observe that convergence is occurring, although not as fast as the one-step static deflection procedure.

A shortcoming of the methods just discussed is that they do not give an error bound on the original calculations. For example, in the static deflection procedure,

**Table 5-4 Convergence of Frequency Using Frequency-Dependent
Reduction Transformation for Simple Two-DOF Problem**

Cycle	Assumed ω^2	Mode	Calculated ω^2	Change in ω^2
1	0	1, 1	0.16	—
2	0.16	0.20, 1	0.135	0.025
3	0.135	0.333, 1	0.109	0.026
4	0.109	0.4545, 1	0.0968	0.0122
5	0.0968	0.5163, 1	0.09504	0.0017
Exact	—	0.5249, 1	0.09502	—
TT-14				

a new mode and frequency must be calculated to estimate the improvement in the original value. There is no indication of the closeness of this second value to the exact value.

A procedure for predicting a frequency error bound has been suggested by I. U Ojalvo of Grumman (Reference 9-6). This method was used to determine the error bounds on the first three symmetric modes from the Model I fuselage Phase 1 analysis. This was done to determine if enough dynamic DOF's (or the correct ones) were retained after the Guyan reduction to ensure that this was not the cause of the discrepancy between the analysis and test results. The error bound formula (derived in Appendix D of this volume) is

$$\frac{\{U\}^T [M] \{U\}}{\{\bar{\varphi}\}^T [M] \{\bar{\varphi}\}} \geq \left(1 - \frac{\bar{\lambda} + \epsilon}{\lambda + \epsilon}\right)^2 \quad (5-39)$$

where

$$\{U\} = [K_M]^{-1} \{F\}$$

and

$$\{F\} = [K_M] \{\bar{\varphi}\} - (\bar{\lambda} + \epsilon) [M] \{\bar{\varphi}\}.$$

Here,

$\{\bar{\varphi}\}$ = expanded calculated mode obtained from

$$\{\bar{\varphi}\} = [T] \{\varphi_a\}$$

where $\{\varphi_a\}$ is the mode for the reduced dynamic DOF system, and $[T]$ is the reduction transformation.

Since $\{\bar{\varphi}\}$ is not exact, the full system of equations are not satisfied, that is $\{F\} \neq 0$.

$$\bar{\lambda} = \bar{\omega}^2 = \text{calculated eigenvalue (approximate)}$$

$$\lambda = \omega^2 = \text{exact eigenvalue}$$

ϵ = an increment added to the eigenvalue. This is used to convert the singular stiffness matrix $[K]$ to $[K_M]$ by

$$[K_M] = [K] + \epsilon [M]. \quad (5-40)$$

The results of the error bound calculations are summarized in Table 5-5. Note that the computed first symmetric mode, which is the first fuselage bending mode, has an accuracy of greater than 95%. The test and the analysis results, however, disagreed by approximately 20% for the first fuselage bending mode. Thus, it was concluded that the Guyan reduction was not the cause of the discrepancy.

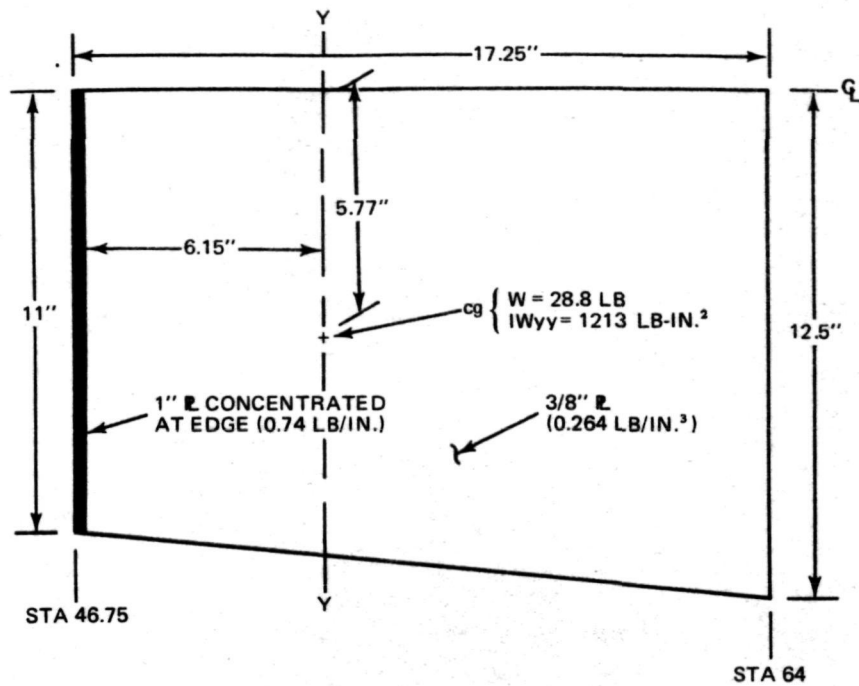
Table 5-5 Results of Error Bound Calculation for First Three Symmetric Fuselage Substructure Modes

Mode	Mode Description (Frequency, Hz)	Accuracy of Frequency (Greater than, %)
1	1st Bending (62.2)	95
2	2nd Bending (129.9)	82
3	3rd Bending (191.3)	71
TT-15		

5.7 FORWARD FUSELAGE INVESTIGATION

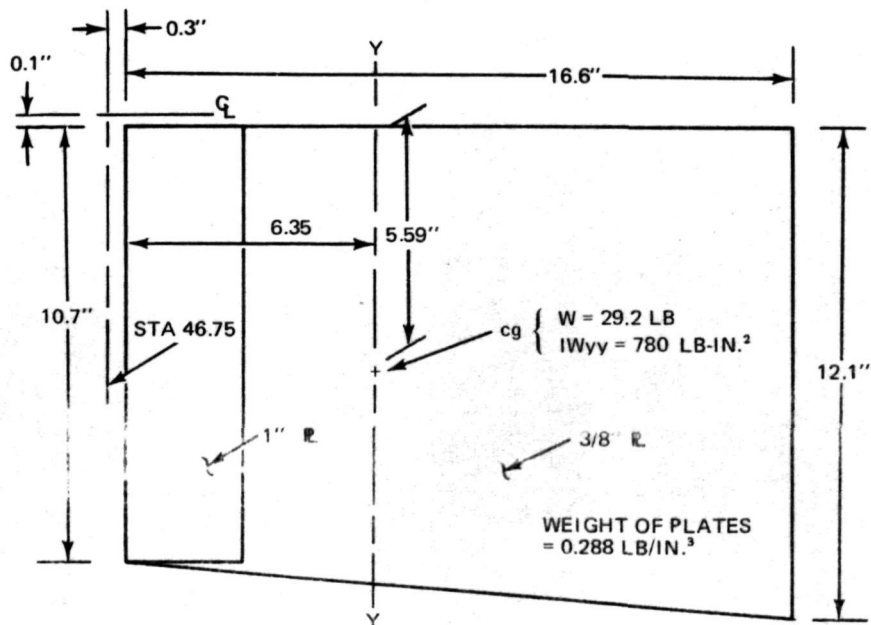
The forward fuselage, from Station 46.75 to 87.5 shown in Fig. 5-12 and 5-13, was investigated to determine the sensitivity of the modeling of the ballast deck and surrounding structure on the calculated frequency. Symmetric modes were calculated for three cases with the models cantilevered at Station 87.5.

CASE 1 - The Case 1 analysis was used as a basis of comparison for Cases 2 and 3. The structure and dynamic DOF were identical to the forward portion of Model I. Figure 5-14 shows the first mode results. The following calculations were performed to verify that these results were representative of the first symmetric Model I Orbiter mode. Initially, the idealized ballast center of gravity and weight were



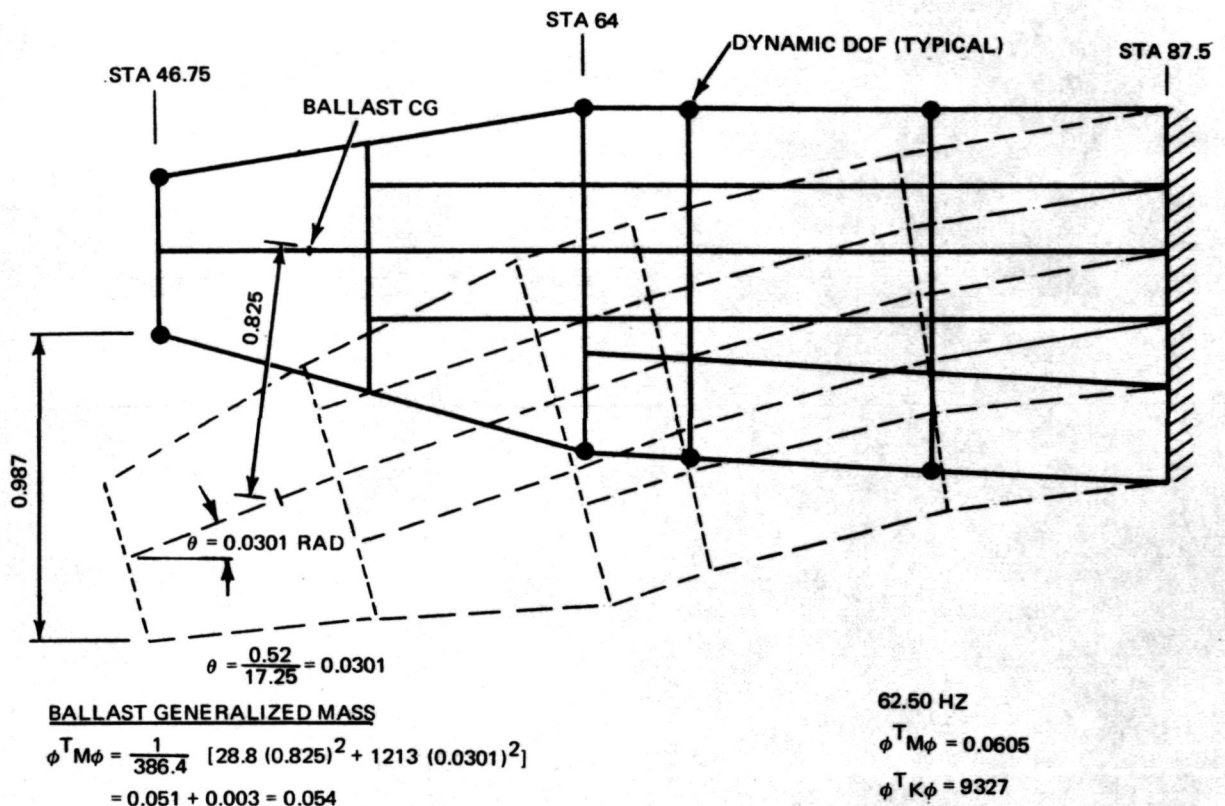
T-68

Fig. 5-12 Idealized Forward Steel Ballast



T-69

Fig. 5-13 Actual Forward Steel Ballast



T-71

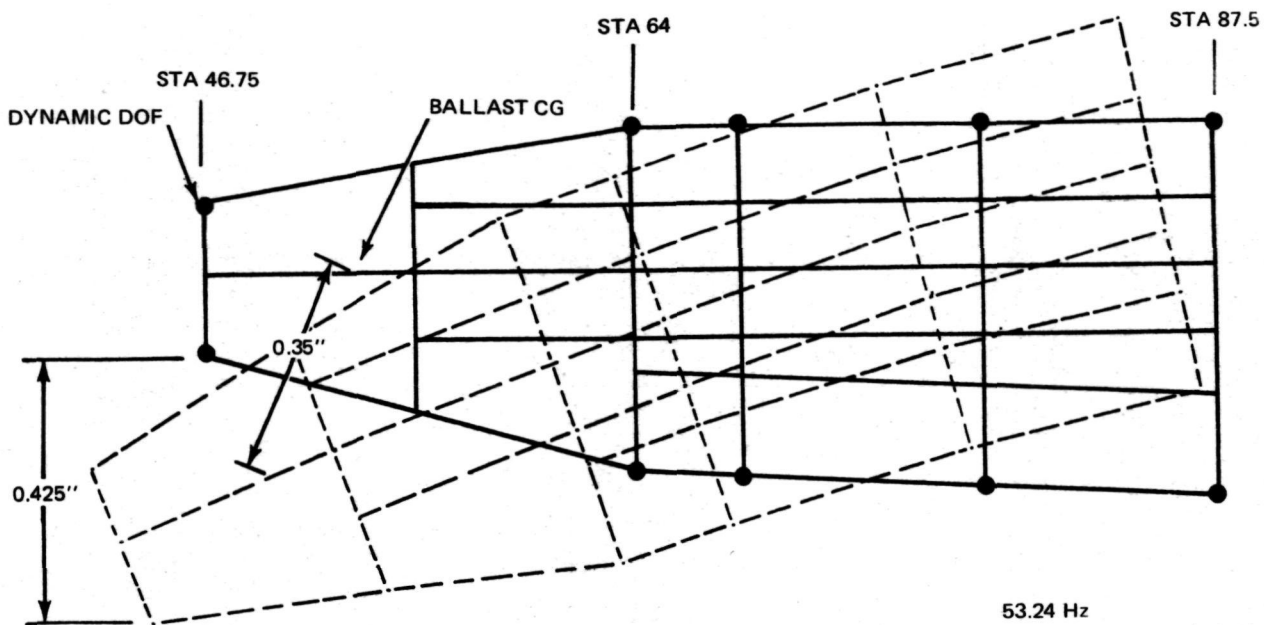
Fig. 5-14 Cantilevered Forward Fuselage (First Mode)

determined (Fig. 5-12). Then the generalized mass of the ballast was calculated by scaling the motion of the center of gravity (Fig. 5-14). This was compared with the value obtained by using the Model I Orbiter mode after adjusting the mode shape to account for the relative motion at Station 87.5. Figure 5-15 shows the forward portion of the fuselage and the Model I mode shape with that adjustment included. Figure 5-16 shows the same mode shape, but with the undeformed fuselage translated and rotated so as to align the fuselage Stations at Station 87.5. From Fig. 5-14, the ballast generalized mass is

$$M_G = \frac{1}{386.4} \left[28.8 (0.825)^2 + 1213 (0.0301)^2 \right]$$

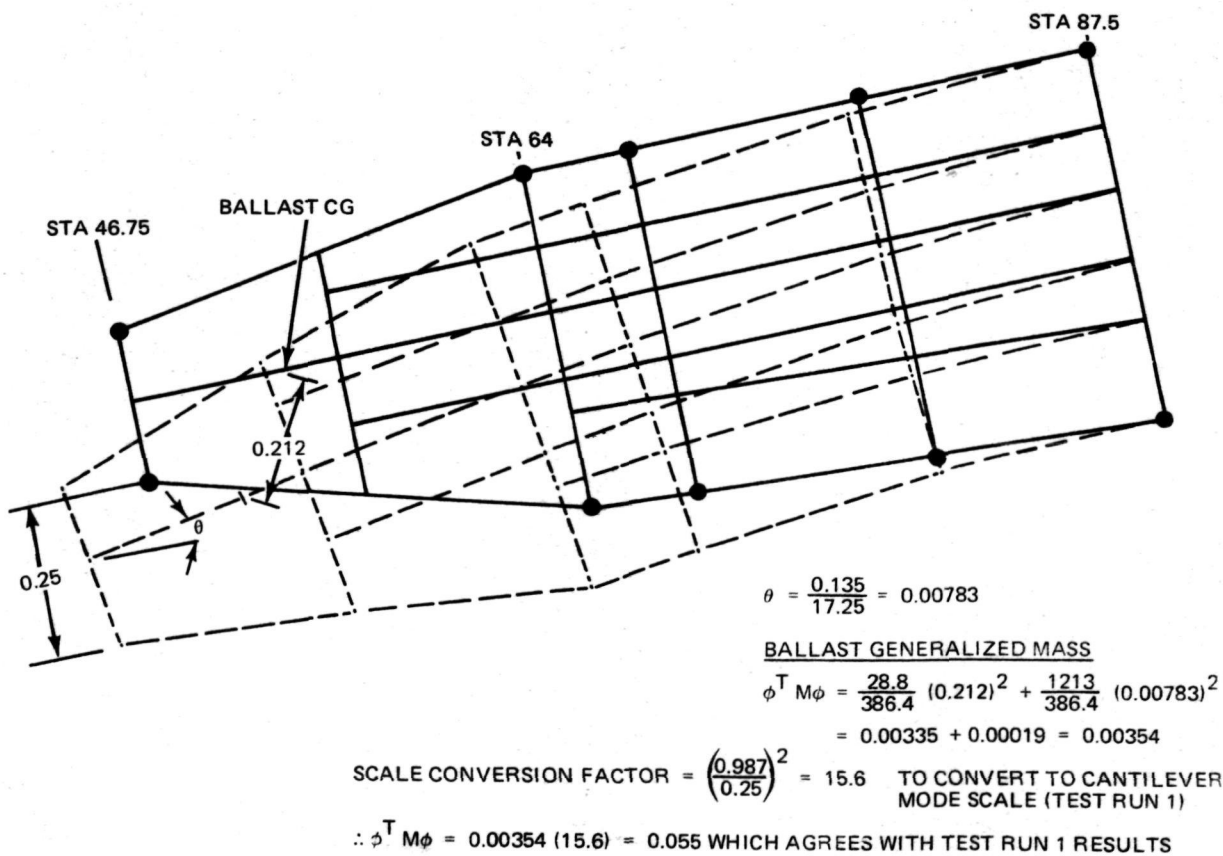
$$= 0.054$$

The first term in brackets is the contribution of the linear motion (0.825) of the ballast mass (28.8) while the second is that for the rotation (0.0301) of the ballast inertia (1213).



T-72

Fig. 5-15 Forward Fuselage First Symmetric Mode - Model I Orbiter Analysis



T-73

Fig. 5-16 Forward Fuselage First Symmetric Mode - Model I Orbiter Analysis Relative to Sta 87.5 (53.24 Hz)

Similarly, from Fig. 5-16, the ballast generalized mass is

$$M_G = \frac{1}{386.4} \left[28.8 (.212)^2 + 1213 (0.00783)^2 \right] \\ = 0.00354$$

Adjusting this value for the scaling in the mode shape yields

$$(0.00354) \left(\frac{0.987}{0.25} \right)^2 = 0.055$$

which agrees with the cantilevered case and verifies the use of the cantilevered model to adequately represent the behavior of this portion of the fuselage. Results of the calculations for Case 1 are tabulated in Table 5-6.

CASE 2 - This model is the same as Case 1, except that dynamic DOF's were retained at the corners of the ballast deck. The results (Refer to Table 5-6) indicated that additional DOF at the ballast deck will not alter the frequency of the first mode. The shape is plotted in Fig. 5-17.

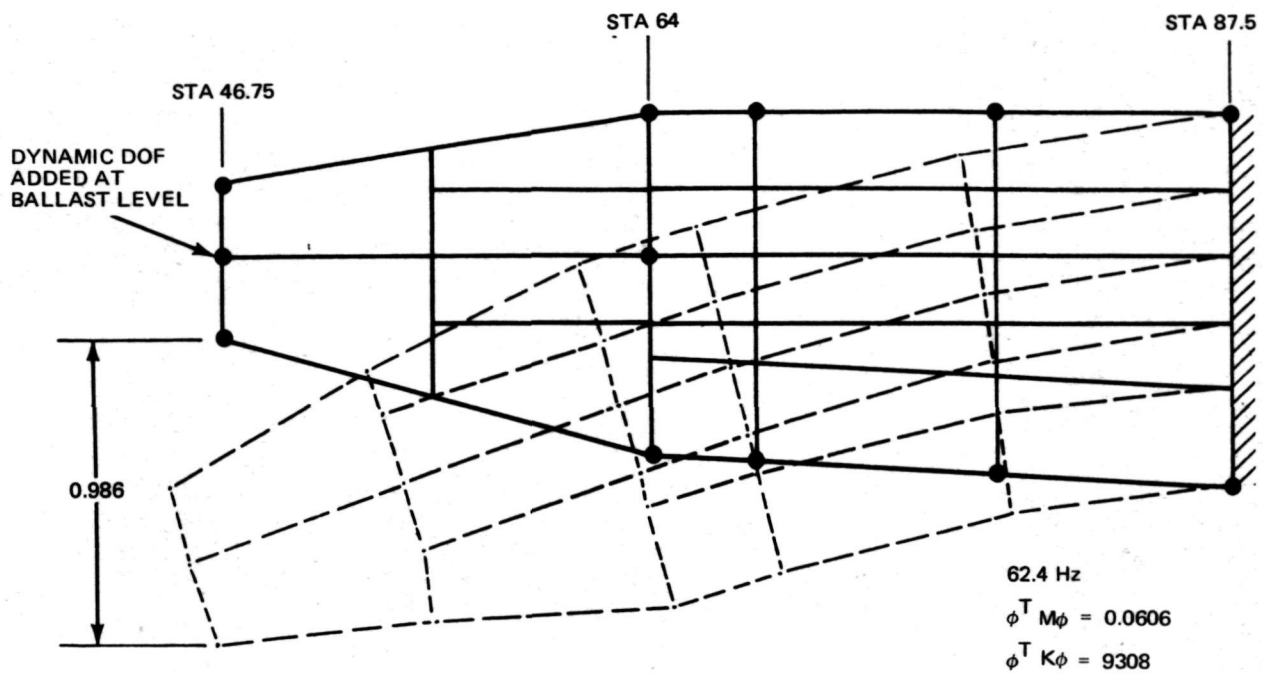
CASE 3 - The ballast deck was replaced with a rigid deck where the center of gravity and weight were determined from actual dimensions of the ballast (see Fig. 5-13). The DOF's at the center of gravity were retained with all deck ties described by MPC's. The shell structure from Station 46.75 to 64.0 was changed from CQDMEM2 elements to an equivalent CROD and CSHEAR arrangement. These changes also did not produce an appreciable change in the first mode results. (Refer to Table 5-6 and Fig. 5-18.)

The results of this investigation eliminated the ballast deck idealization and the selected DOF's around it as being a major cause for the discrepancy between the Model I analytical results and the test values.

Table 5-6 Summary of Forward Fuselage Analytical Investigations

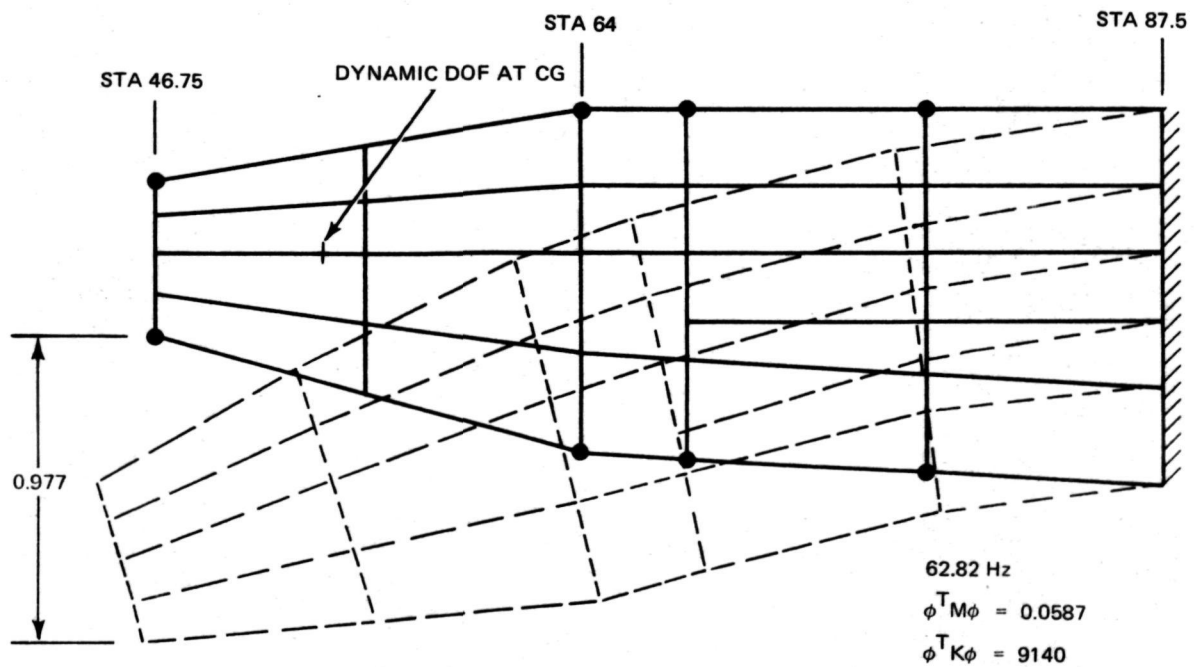
Mode	Case	Frequency, Hz	Generated Mass	Generated Stiffness
1	1	62.50	0.0605	9327
	2	62.39	0.0606	9308
	3	62.82	0.0587	9140
2	1	239.13	0.0428	96577
	2	228.15	0.0617	126752
	3	235.52	0.0768	168089
3	1	331.74	0.0517	224781
	2	301.28	0.0668	239450
	3	316.63	0.0324	128251

TT-16



T-74

Fig. 5-17 Cantilevered Forward Fuselage, Case 2 – First Mode



T-75

Fig. 5-18 Cantilevered Forward Fuselage, Case 3 – First Mode

5.8 STRESS DISTRIBUTIONS

5.8.1 1 g STRESSES

The 1 g stresses were calculated for the fuselage with the Orbiter supported horizontally at the interstage attachments. A moment diagram for the half structure (Fig. 5-19) was obtained by representing the weights as a system of "lumped" concentrated loads. At Station 119.0 the value of the 1 g moment is 650 in.-lb (for the half structure).

NASTRAN Model I stresses were obtained by using the reduced mass matrix with a 1 g acceleration. These stresses are illustrated in Fig. 5-20 for a fuselage section at Station 119.0. A summation of the cap loads at Station 119.0 gives an internal moment of 630 in.-lb. This compares rather well with the value of 650 in.-lb from the moment diagram, considering that the moment diagram is only an approximation.

A comparison of the 1 g Model I stresses with simple $\frac{Mc}{I}$ values is shown in Table 5-7 for the top and bottom longerons. Two values of the moment of inertia I_{yy} have been used; one for a fully effective section which is representative of Model I; the second for a partially effective section which is believed to be more representative of the actual 1/8-scale model. The values for the NASTRAN Model I analysis are within an acceptable range provided by the $\frac{Mc}{I}$ check. Here, the values of M and I are questionable.

5.8.2 DYNAMIC STRESSES

Dynamic stresses were estimated by multiplying the analytical amplitude for the first mode by that obtained in the test. For harmonic motion the displacement, δ_z , at any station, X, is related to the amplitude, Δ_z by

$$\delta_z = \Delta_z \sin \omega t \quad (5-41)$$

differentiating and substituting

$$\delta_z = - \frac{\ddot{\delta}_z}{\omega^2} \quad (5-42)$$

In the test, the RMS value for the accelerometer at Station 125.5 was 0.412 g for the first mode which has a frequency of 43.6 Hz. (The amplitude of the harmonic force was 3 lb applied in the transverse direction at the nose fitting). The maximum displacement δ_z max (at Station 125.5) is thus

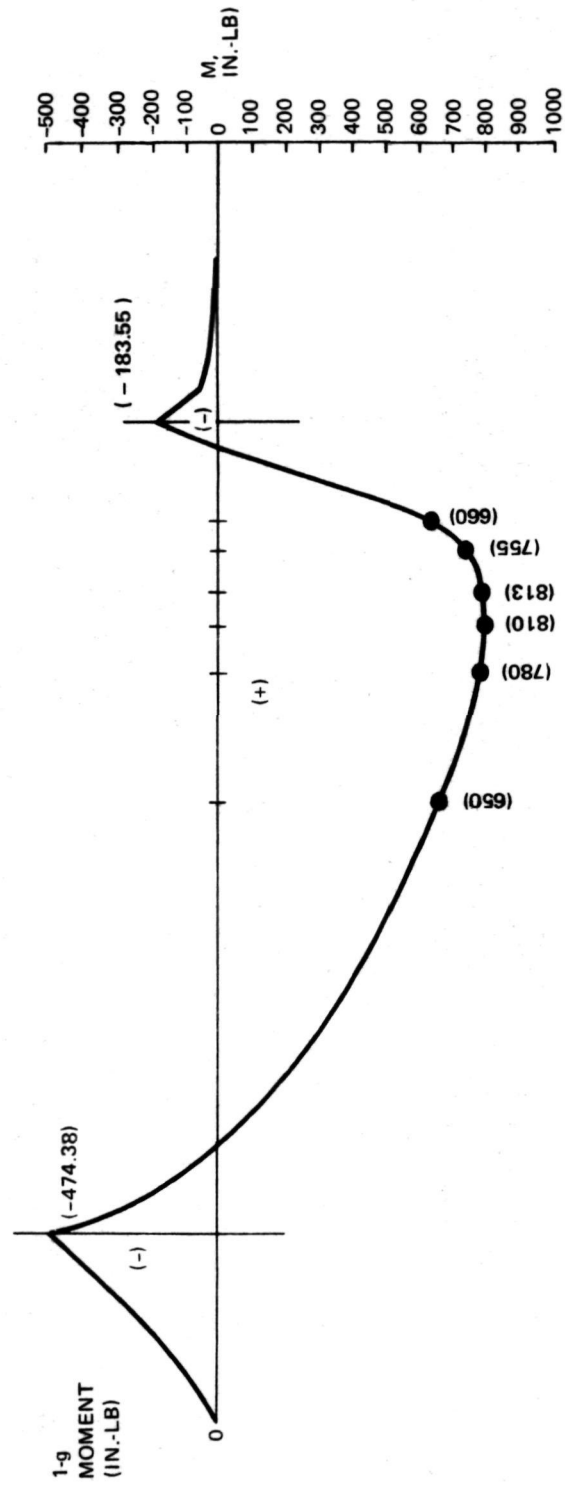
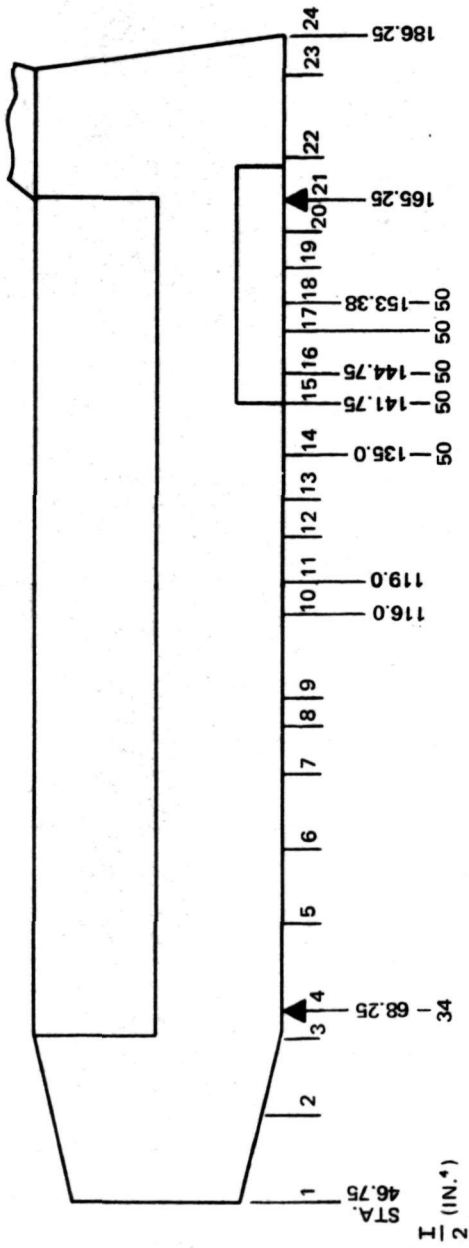
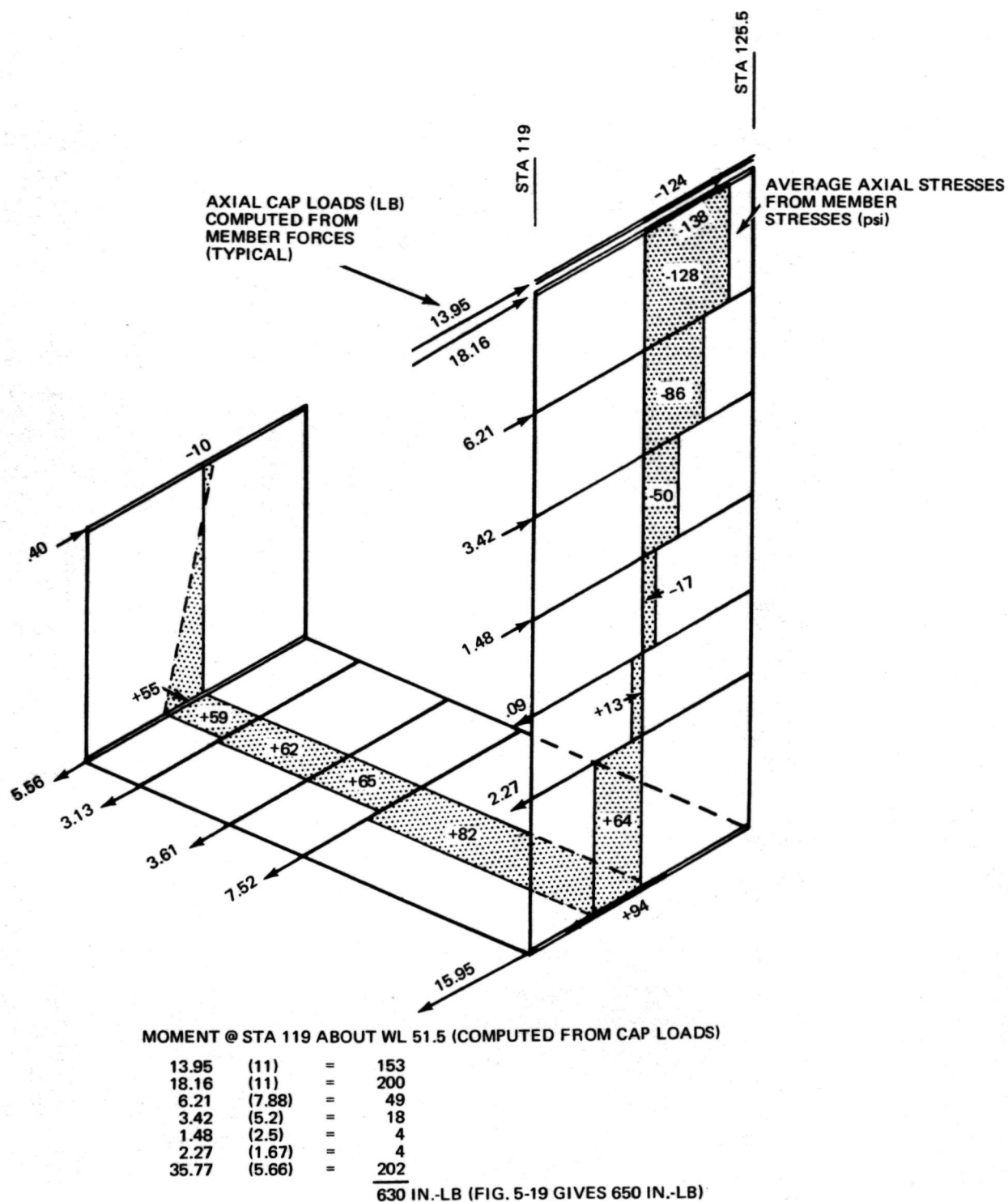


Fig. 5-19 Orbiter Model 1-g Moments Diagram (Half Structure Values)

T-80



T-76

Fig. 5-20 NASTRAN Model I 1-g Stresses and Cap Loads

Table 5-7 One-g Longer Stresses, Orbiter Supported Inverted and Horizontally From Interstage Attachments

Station	Longitudinal Stresses (from NASTRAN Model I)		Moment Half Structure, in.-lb	C ₁ (Top), in.	C ₂ (Bot.), in.	$\frac{1}{2}$ ivy (0.75 Effective Door Longerons), in. ²	Longeron Stresses from $\frac{M_c}{I}$ for Fully Effective Skins		Model II (0.5 Effectiveness Factor)				
	Top Longeron, psi	Bottom Longeron, psi					Top, psi	Bot., psi	$\frac{1}{2}$ ivy	C ₁ (Top), in.	C ₂ (Bot.), in.	Longeron Stresses from $\frac{M_c}{I}$	
												Top, (psi)	Bot., psi
i		3	4	5	6	7	8	9	10	11	12	13	14
64.0	-26.4	156.7	-350	9.55	4.35	28.7	.116	53	17.9	7.86	6.04	-154	118
68.5	-1.2	62.0	-450
78.0	-43.2	6.8	0	10.35	4.25	32.5	0	0	25.4	9.96	4.64	0	0
87.5	62.0	46.3	240
97.0	110.5	-49.5	390
102.5	103.9	-59.2	480
106.5	115.5	-66.9	520
116.0	132.2	-78.2	625	11.55	4.95	41.3	175	-75	33.2	11.15	5.35	210	-101
119.0	137.2	-90.0	650
125.5	144.1	-89.5	720	11.87	5.13	44.6	191	-83
129.0	142.1	-85.0	760	36.0	11.5	5.5	230	-110
135.0	137.2	-66.8	780
141.75	132.5	-71.0	810	11.39	5.61	43.0	214	-106	33.7	10.58	6.42	254	-154
144.75	99.9	-74.3	813
150.38	59.4	-64.0	755
153.38	75.4	-46.4	660
157.69	91.4	-35.0	430
162.0	32.9	11.4	50
166.5	-12.2	65.5	180

TT-17

$$\delta_z \text{ max} = \frac{(1.414) (0.412) (386)}{(2\pi \times 43.6)^2} = 0.003 \text{ in.}$$

The strains in the top fuselage longeron were obtained by taking the difference of the node displacements for the first mode. These values were then normalized to a unit value of the mode shape at Station 125.5. The normalized strain is relatively constant over the mid-portion of the fuselage indicating that deformation has an approximately constant radius of curvature for this region. For Model I, the normalized strain was calculated to be 0.0102 as shown in Table 5-8; a similar analysis performed later for Model II gave a value of 0.0112. Table 5-8 also lists other key information for Models I and II and the horizontal dynamic test.

Table 5-8 Selected Analysis and Test Results for First Free-Free Symmetric Mode

	Model I	Model II	Horiz. Dyn. Test
Frequency, Hz	53.2	44.2	43.6
ϵ_x (Top Longeron)	0.0102	0.0112	—
δ_z (Sta 125.5)	1.0	1.0	1.0
δ_x (Fin Ballast)	3.36	3.73	4.0
δ_z (Sta 116.0)	1.04	1.05	1.0+
δ_z (Wing Tip, Sta 162)	1.53	0.396	1.12

TT-18

The maximum dynamic stress in the longeron can be estimated by using the analytical strain for a unit deformation and the test value for the amplitude

$$\epsilon = (0.0102) (0.003) = 30.2 \times 10^{-6}$$

hence,

$$\begin{aligned} \sigma &= E\epsilon = (10.5 \times 10^6) (30.2 \times 10^{-6}) \\ &= 317 \text{ psi (top longeron) .} \end{aligned}$$

For a 16-in. deep section, the neutral axis is located approximately 6 in. from the bottom longeron. Thus the bottom longeron stress is approximately

$$\sigma = \frac{6}{10} (317) = 190 \text{ psi (bottom longeron).}$$

In the horizontal dynamic test the vehicle was suspended in an inverted position from the interstage points. The total maximum stresses between Stations 119 to 125.5 were thus estimated to be

$$\text{Total} = 1 \text{ g} \pm \text{dynamic}$$

$$\sigma(\text{bottom longeron}) = -94 \pm 190 \text{ psi}$$

$$\sigma(\text{top longeron}) = +137 \pm 317 \text{ psi.}$$

Hence, the maximum compressive stresses are,

$$\sigma(\text{bottom longeron}) = -284 \text{ psi}$$

$$\sigma(\text{top longeron}) = -180 \text{ psi.}$$

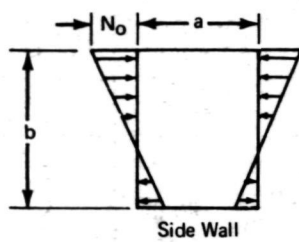
5.9 LINEAR BUCKLING ANALYSIS

Elastic buckling stresses for the side wall (in both the inverted and right-side up conditions) and bottom deck panels are given in Table 5-9. Buckling loads for typical panels in other parts of the model are given in Table 5-10. The coefficients, k , used in the buckling formulas, are based on the assumption that the panels are simply supported. The buckling stresses are plotted in Fig. 5-21 and 5-22 together with the 1 g stresses from Subsection 5.8. The lowest buckling stress was found to be 167 psi for a $9\frac{1}{2} \times 12\frac{1}{2}$ -in. bottom deck panel. This panel size and shape, which is typical of most of the panels in the lower deck, is also the most critical from a margin-of-safety point of view ($MS = 0.412$ for 1-g plus dynamic stresses).

The 1 g stress in the central portion of the lower longeron was calculated to -94 psi (Subsection 5.8). The stresses within the bottom deck panels are somewhat lower than the longeron stresses because of local shear lag effects (see Fig. 5-20), however, the longeron stress may be used as a representative value. In Subsection 5.8 the dynamic stress in the lower longeron was estimated to be 190 psi. This maximum amplitude value is almost constant throughout the central region of the fuselage. (The middle portion of the fuselage is basically a light beam connecting two heavy masses - one is the forward cabin region; the second is the aft thrust structure. This simple two-mass beam model has a constant bending moment along the beam for the first free-free mode).

Superimposing the harmonic dynamic stress and the static 1 g stress leads to the diagram shown in Fig. 5-23. The dynamic stress of 190 psi amplitude oscillates about the static stress of -94 psi with the total value exceeding the elastic buckling stress of 167 psi for approximately 4/10 of each cycle.

Table 5-9 Elastic Buckling Stresses for Simply Supported Side Wall and Bottom Deck Panels



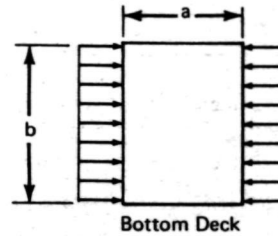
$$\sigma_{cr} = \frac{k \pi^2 D^*}{b^2 t}$$

$$N_x = N_0 \left(1 - \alpha \frac{y}{b}\right)$$

$$\alpha = 1.6$$

$$k = \left(\frac{b}{a} m + \frac{a}{bm}\right)^2$$

$$m = 1$$



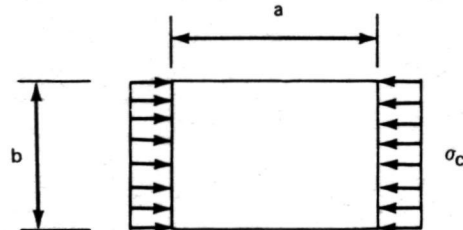
Fuselage Stations		a	Side Wall (Normal)					Bottom Deck				Side Wall (Upside Down)				
			α	b	(a/b)	k	σ_c , psi	b	(a/b)	k	σ_c , psi	α	b	(a/b)	k	σ_c , psi
Frame	7 Sta 97	9.5	1.6	16	0.594	17.9	270	12.5	0.76	4.33	167	2.67	16	0.594	35.3	533
	8 106.5	9.5	1.6	16	0.594	17.9	270	12.5	0.76	4.33	167	2.67	16	0.594	35.3	533
	9 116.0	3.0	1.6	16	0.187	—	—	12.5	0.24	19.4	755	2.67	16	0.187	—	—
	10 119.0	6.5	1.6	16	0.406	23.6	356	12.5	0.52	5.95	230	2.67	16	0.406	39.5	596
	11 125.5	9.5	1.6	16	0.594	17.9	270	12.5	0.76	4.33	167	2.67	16	0.594	35.3	533
	12 135	6.75	1.6	16	0.421	23	347	12.5	0.54	5.72	221	2.67	16	0.421	38.8	585
	13 141.75	3.0	1.6	16	0.187	—	—	12.5	0.24	19.4	755	2.67	16	0.187	—	—
	14 144.75															

*See Reference 9-8

TT-19

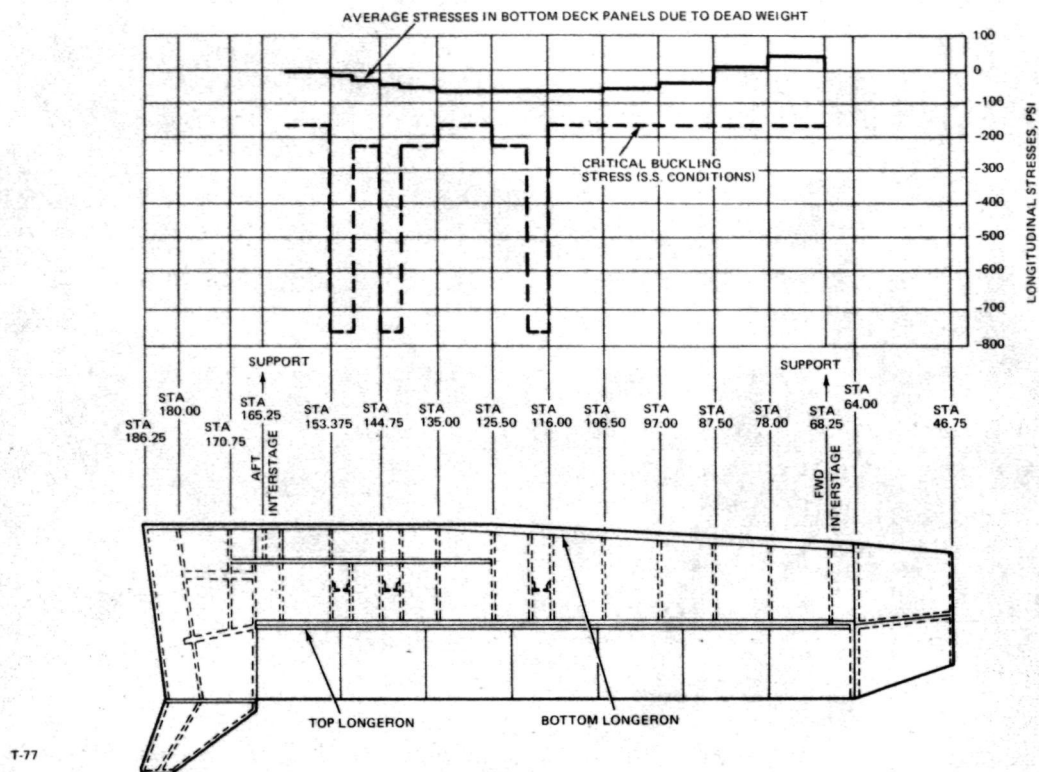
Table 5-10 Elastic Buckling Loads

$$P = \frac{\kappa \pi^2 D}{b}$$



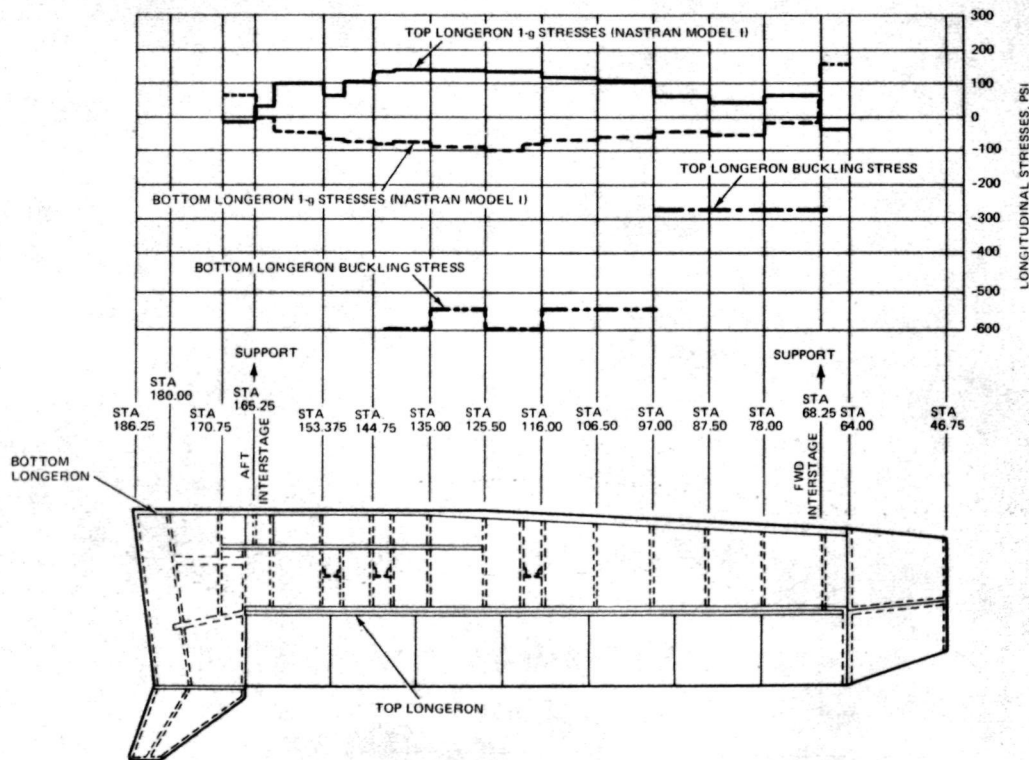
	t, in.	a, in.	b, in.	E, psi	ν	$\left(\frac{a}{b}\right)$	CLAMPED			SIMPLE SUPPORT		
							k	σ_c , psi	P_c , lb.	k	σ_c , psi	P_c , lb.
Wing Cover	0.020	16	8.7	10^7	0.3	1.835	8.0	381	66.4	4.03	192	33.4
Square Plate	0.020	10	10	10^7	0.316	1.0	10.07	367	73.4	4.00	146	29.2
Fuselage Side Wall	0.020	9.5	17	10^7	0.3	0.56	13.0	162	55.2	5.50	69	23.4
Fuselage Bot. Deck	0.025	9.5	12.5	10^7	0.3	0.760	11.6	417	30.5	4.31	155	11.3

TT-20



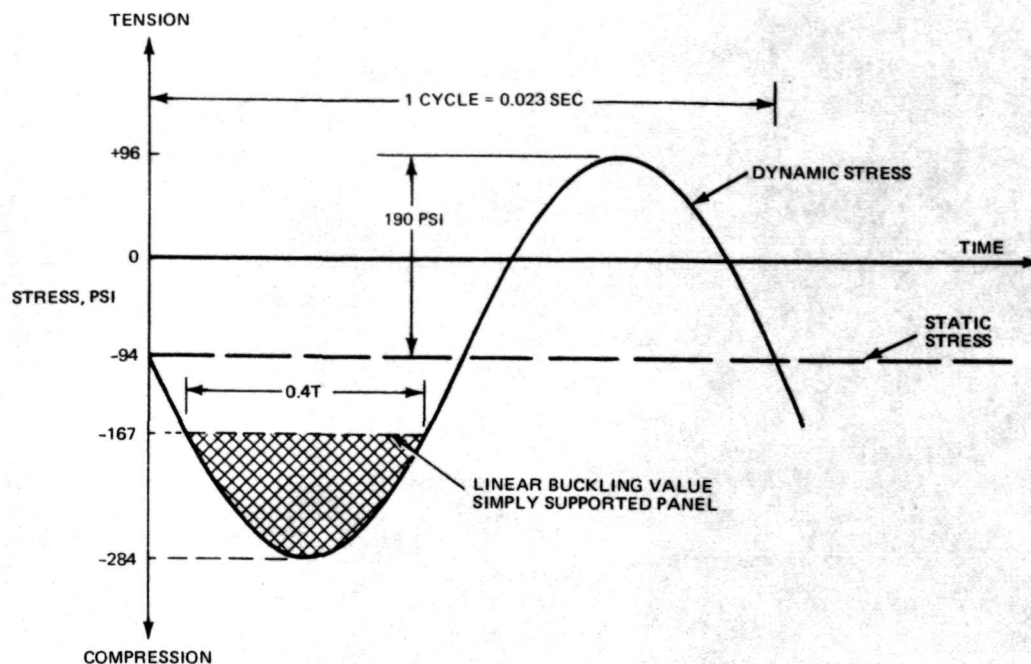
T-77

Fig. 5-21. Comparison of 1-g and Critical Buckling Stresses for Bottom Deck Panels — Orbiter Suspended Inverted from Interstage Fittings



T-78

Fig. 5-22 Comparison of 1-g and Critical Buckling Stresses of Fuselage Side Wall Panels — Orbiter Suspended Upside Down from Interstage Fittings



T-81

Fig. 5-23 Stress Variation in One Cycle for a 9- $\frac{1}{2}$ x 12- $\frac{1}{2}$ -Inch Bottom Deck Panel Located in the Mid-Fuselage Region

These results should be viewed qualitatively. The elastic buckling stress is based on the assumption that the panels are simply supported. A fully clamped panel with an aspect ratio of 0.75 would have a buckling coefficient, k , equal to 11.69 which is 2.7 times the simply supported value of 4.33. For this case, the buckling stress would be -450 psi, which is well above the maximum stress of -284 psi. The panels are certainly far from being clamped, and most likely the constraints are more represented by the simply supported condition. Any additional constraint will of course raise the buckling value. If the buckling value is exceeded, as indicated in Fig. 5-23, then theoretically the "effective" modulus of elasticity will immediately drop to one-half of the linear value. This assumes that the panel is initially flat. If the panel contains an initial imperfection, then the phenomenon is altered and the reduction of E to an effective E takes place more gradually and well before the elastic buckling load. This is discussed in more detail in the next subsection. Since there is ample evidence that the panels do contain initial imperfection (refer to Subsection 5.11), any concern about exceeding the elastic buckling value is somewhat academic. Of more interest is the fact that lower deck strains are oscillating about a static strain of -9.0×10^{-6} in./in. with an amplitude of approximately 18.0×10^{-6} in./in. These values set a bound on the range of the "Effective" modulus that will be selected in later sections.

5.10 EFFECT OF INITIAL IMPERFECTIONS ON PANEL STIFFNESS

Figure 5-24A illustrates a perfectly flat panel supported on all four sides and loaded uniformly on two opposite sides. The panel will behave in a linear fashion until the stress, σ , reaches σ_c where

$$\sigma_c = \frac{k\pi^2 E}{12(1-\nu^2)} \left(\frac{t}{b}\right)^2 \quad (5-43)$$

The term σ_c is the Euler buckling stress, and k is a constant that depends on the aspect ratio of the plate. If the load is increased past σ_c the center portion of the panel becomes ineffective (Fig. 5-24B), and results in a non-uniform distribution of stress. If, as suggested by Von Karman, this distribution is replaced by the distribution shown in Fig. 5-24C where $\left(\frac{b_e}{2}\right)$ is the effective width adjacent to each side, then Equation 5-43 may be modified to give

$$\sigma_e = \frac{k\pi^2 E}{12(1-\nu^2)} \left(\frac{t}{b_e}\right)^2 \quad (5-44)$$

where σ_e is the edge stress. (The rationale behind this is illustrated in Fig. 5-25 where the uniform stress, σ_e , acts on an equivalent plate of width b_e . The ineffective portion of the real plate simply ties the two strips together where each strip has deformed into a one-quarter sine wave.) In this expression, k is usually taken equal to 4.0 (long plate). Solving Equation 5-44 for b_e ,

$$b_e = \left\{ \frac{\pi}{\sqrt{3(1-\nu^2)}} \sqrt{\frac{E}{\sigma_e}} \right\} t = 1.925 \sqrt{\frac{E}{\sigma_e}} t \quad (5-45)$$

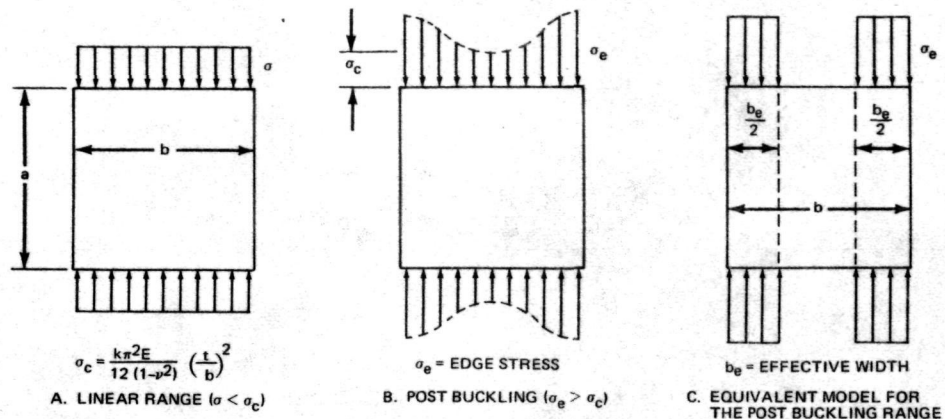
If the loading is increased until the edge stress approaches the yield value, then for aluminum (with $E = 10.5 \times 10^6$ and $\sigma_{\text{yield}} = 42,000$ psi) this expression equals

$$b_e = 1.925 \sqrt{\frac{10.5 \times 10^6}{42,000}} t = 30.4 t \quad (5-46)$$

which is the expression that is often used to "lump" sheet material into adjacent caps.

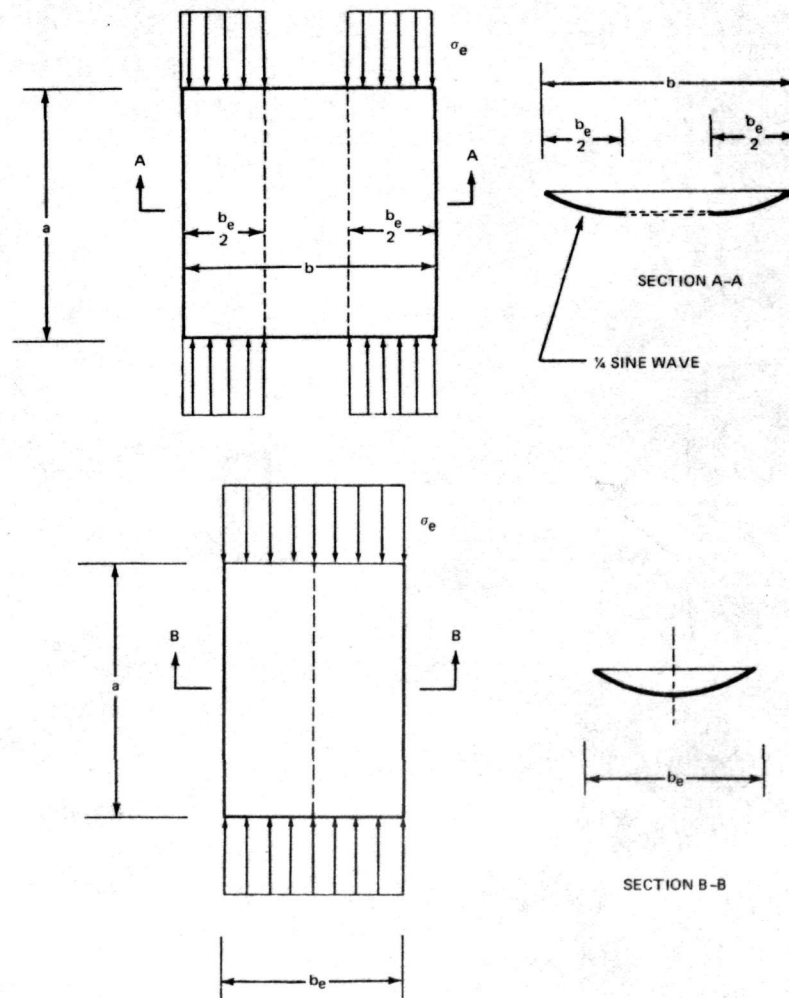
Equations 5-43 and 5-44 may be written as

$$\sigma_c b^2 = \frac{k\pi^2 E}{12(1-\nu^2)} t^2$$



T-82

Fig. 5-24 Plate Behavior Under Compressive Load



T-83

Fig. 5-25 Von Kármán Model of the Effective Width of a Post-Buckled Plate

II

or

$$\sigma_e b_e^2 = \frac{k \pi^2 E}{12 (1 - \nu^2)} t^2$$

from which

$$\sigma_c b^2 = \sigma_e b_e^2$$

or

$$b_e = b \sqrt{\frac{\sigma_c}{\sigma_e}} . \quad (5-47)$$

This is the commonly used expression for relating the effective width, b_e to the total width, b . The effective width, b_e , is load dependent, and must be obtained by an iteration procedure where it enters into the calculation of the overall moment of inertia.

If the total load on the sheet is P , then

$$P = \sigma_e t b_e . \quad (5-48)$$

Substituting Equation 5-47,

$$P = b t (\sigma_c \sigma_e)^{1/2} .$$

Defining the average stress by,

$$\sigma = \frac{P}{A} = \frac{P}{b t}$$

leads to

$$\sigma = (\sigma_c \sigma_e)^{1/2} . \quad (5-49)$$

The stress, σ_e , may be related to the overall strain, E , by

$$\sigma_e = E \epsilon .$$

Here, it is assumed that the plate is loaded by keeping the edges straight. The strain, ϵ , is thus equal to the end shortening divided by the original length. Substituting this into Equation 5-49,

$$\sigma = (\sigma_c E)^{1/2} \epsilon^{1/2} \quad (5-50)$$

Differentiating,

$$\frac{d\sigma}{d\epsilon} = \frac{1}{2} (\sigma_c E)^{1/2} \epsilon^{-1/2} = E'$$

and dividing by $E = \frac{\sigma}{\epsilon}$ gives

$$\frac{E'}{E} = \frac{\left(\frac{d\sigma}{d\epsilon}\right)}{\left(\frac{\sigma}{\epsilon}\right)} = \frac{1}{2} \left(\frac{\sigma_c}{E}\right)^{1/2} \epsilon^{-1/2}.$$

At buckling, $\epsilon = \epsilon_c$ and $\epsilon_c = E \epsilon_c$; hence

$$\frac{E'}{E} = \frac{1}{2}. \quad (5-51)$$

A plot of the stress strain curve is shown in Fig. 5-26. The curve is linear until the Euler stress is reached; at this point, the modulus drops immediately to one-half of the linear value. With increasing load the modulus continues to drop, but not as drastically as the sudden change in going past the Euler stress.

Gerard and Becker (Reference 9-7) have given formulas for the postbuckling behavior of elastically compressed flat plates, which are

For:

$$\frac{\sigma_e}{\sigma_c} < 3,$$

$$\frac{\sigma}{\sigma_e} = \beta + (1 - \beta) \frac{\sigma_c}{\sigma_e}$$

where

$$\beta = 0.50$$

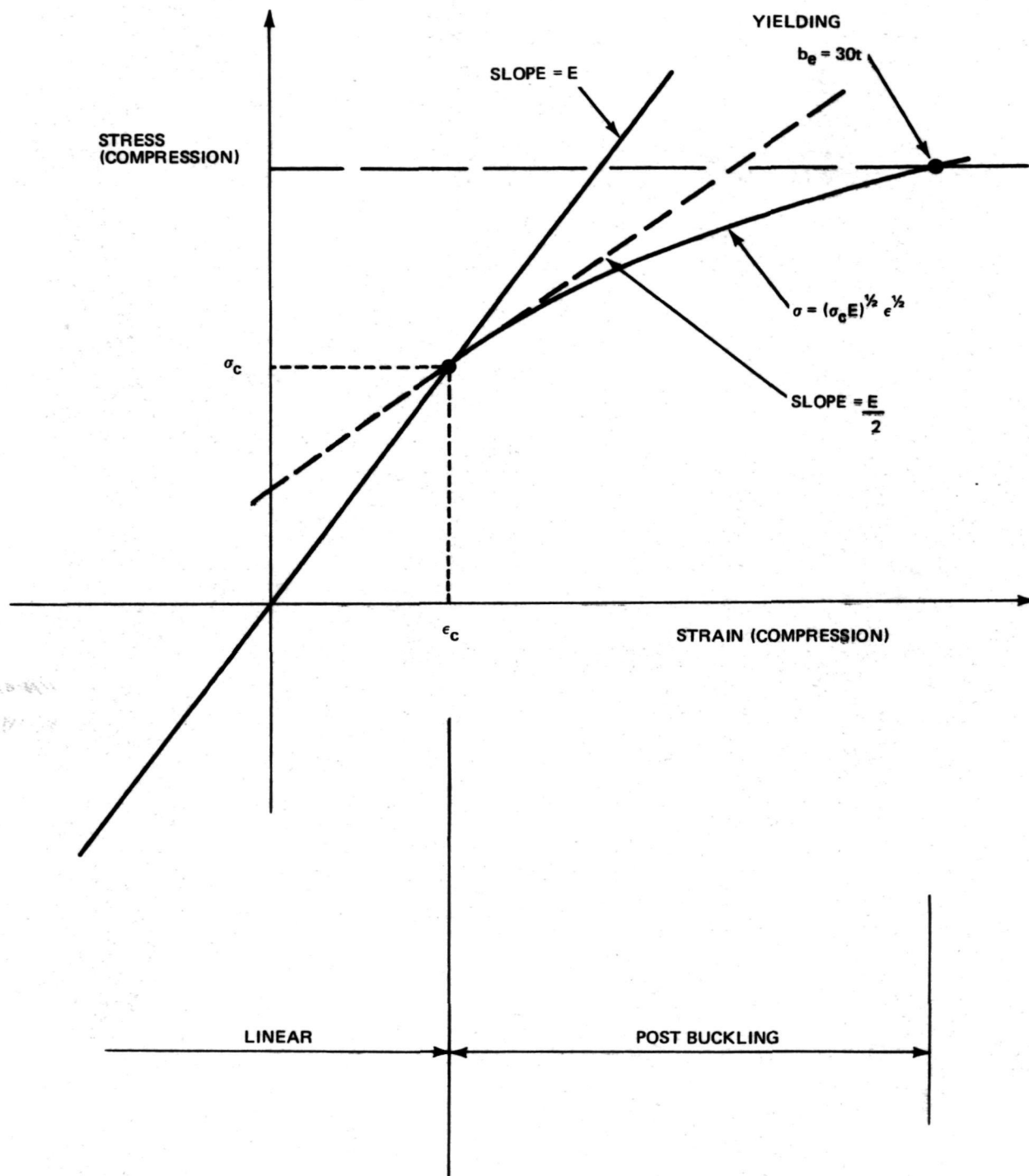
(When the unloaded edges are held straight but free to move laterally)

$$\beta = 0.746$$

(When the unloaded edges are held straight and restrained from moving laterally).

For

$$\frac{\sigma_e}{\sigma_c} > 3,$$



$$\frac{\sigma}{\sigma_e} = 0.19 + 0.81 \left(\frac{\sigma_c}{\sigma_e} \right)^{1/2} \quad (5-53)$$

(Long, simply supported plate - edge held straight, free to move laterally.)

Differentiating Equation 5-52

$$\frac{d\sigma}{d\epsilon} = \beta E . \quad (5-54)$$

For the case of no lateral restraint $\beta = 0.5$, which agrees with the previous expressions using the Von Kármán assumption; however, for lateral restraint $\beta = 0.746$, indicating that the elastic postbuckling stiffness is greatly dependent on the conditions of lateral restraint.

If the plate contains an initial imperfection, then the behavior illustrated in Fig. 5-26 is altered. In Appendix E of this volume, a large deflection analysis for axially loaded plates with an initial bow is formulated. The formulation follows closely the analysis given by Timoshenko (Reference 9-8), the addition being to include into the lateral deflection term the displacement function

$$w_o = \bar{W}_o \cos \frac{\pi x}{2a} \cos \frac{\pi y}{2b} \quad (5-55)$$

where \bar{W}_o is the maximum initial imperfection at the center of the plate. A computer program was written and used to solve the resulting equations for various plate aspect ratios and values of \bar{W}_o . The results are plotted in Fig. 5-27 through 5-30. In Fig. 5-27 compressive load-strain curves have been plotted for a square plate having various initial imperfections. The curves have been normalized to the elastic buckling load

$$P_c = 10.07 \frac{\pi^2 D}{a}, \text{ and critical strain}$$

$$\epsilon_c = \sigma_c \left(\frac{1 - \nu^2}{E} \right), \text{ with } \nu = 0.316 \text{ and } E = 10^7.$$

The end load, P , has been obtained by integrating the nonlinear end stress distribution while the strain, ϵ , is the end shortening divided by the original length. Note that the effect of the initial imperfection is to translate the conventional post buckling

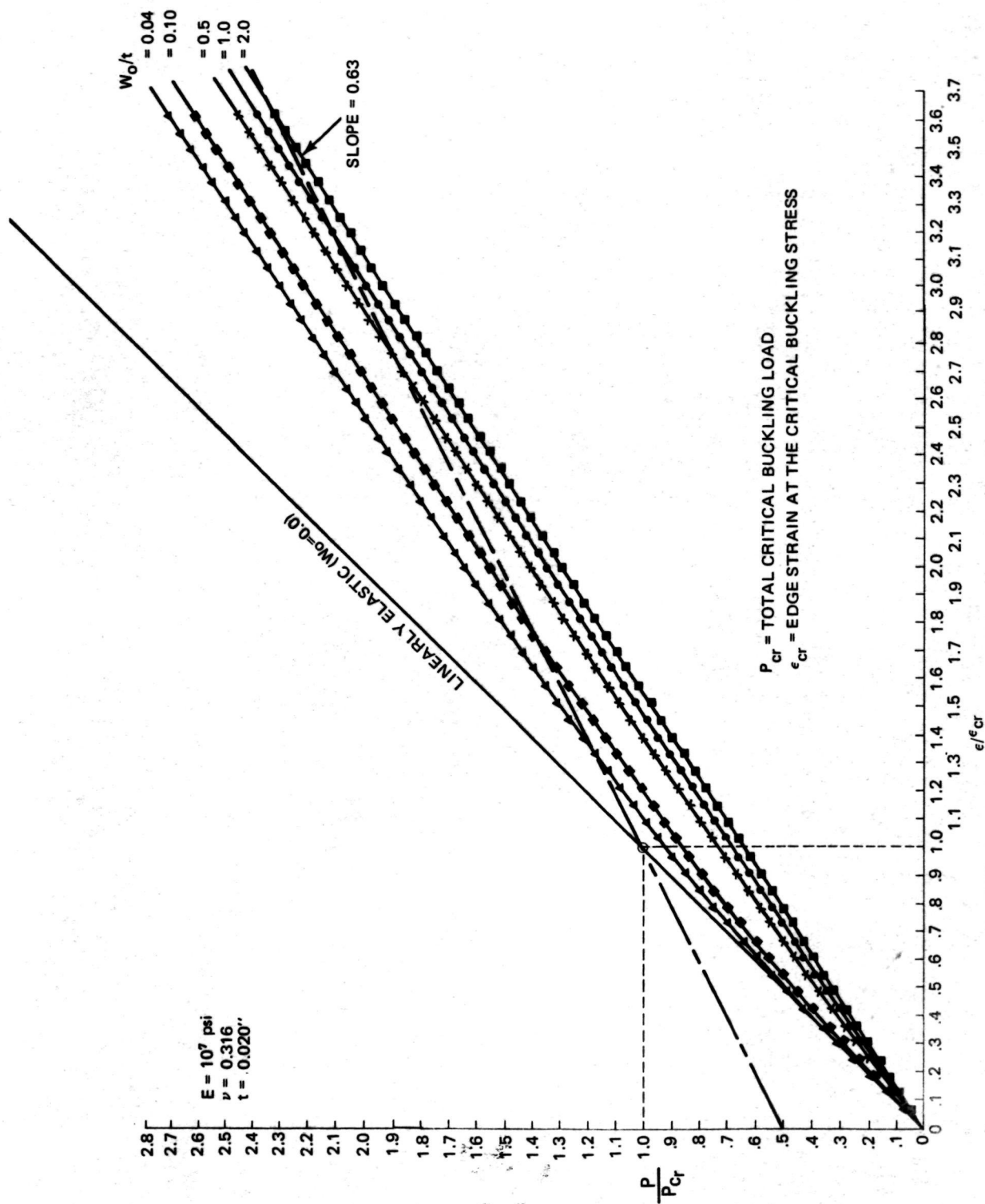


Fig. 5-27 Load - Strain Curves for Square Plate with Various Initial Imperfections

T-85

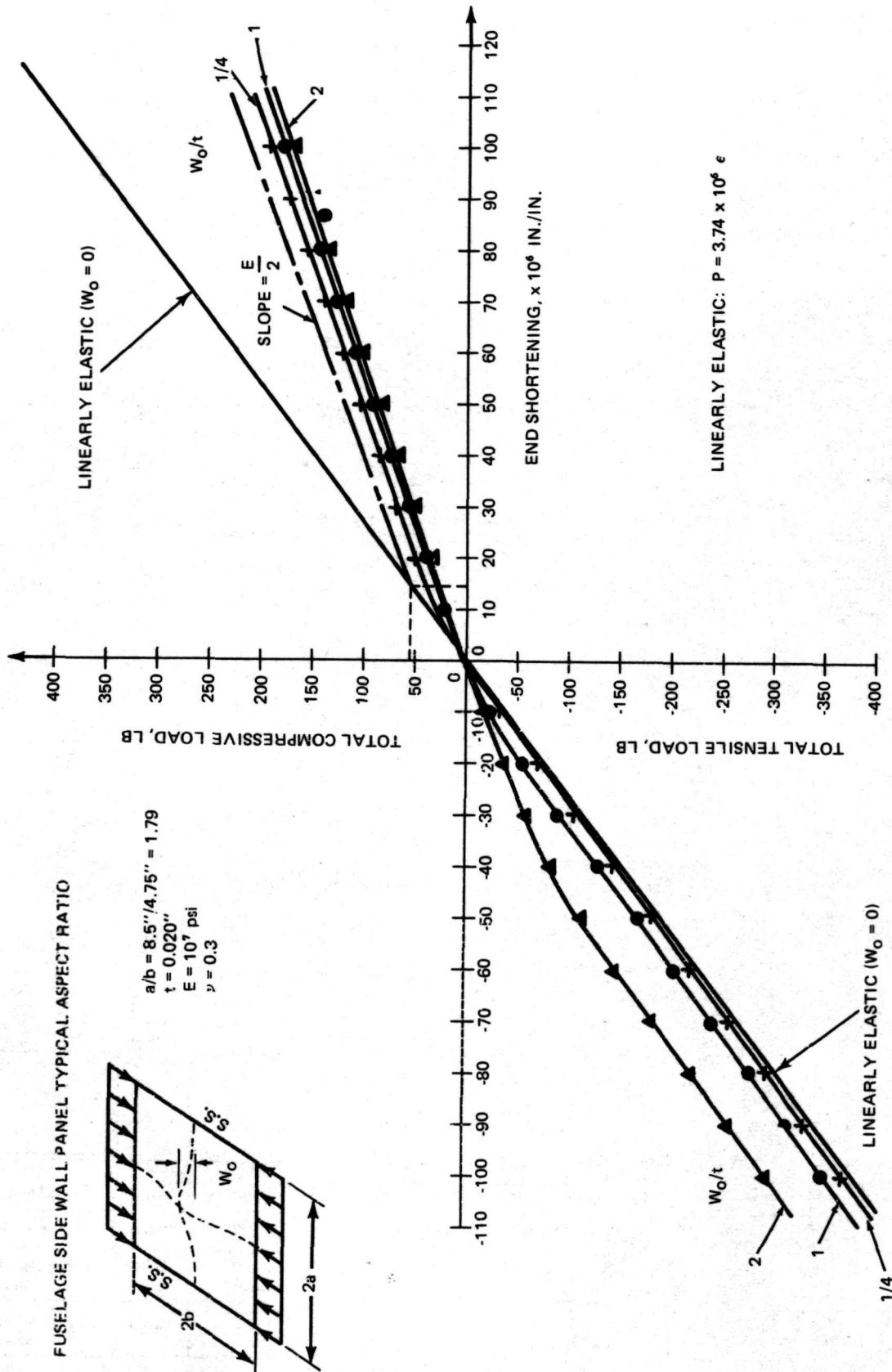


Fig. 5-28 Load vs End Shortening for Typical Side Wall Panel

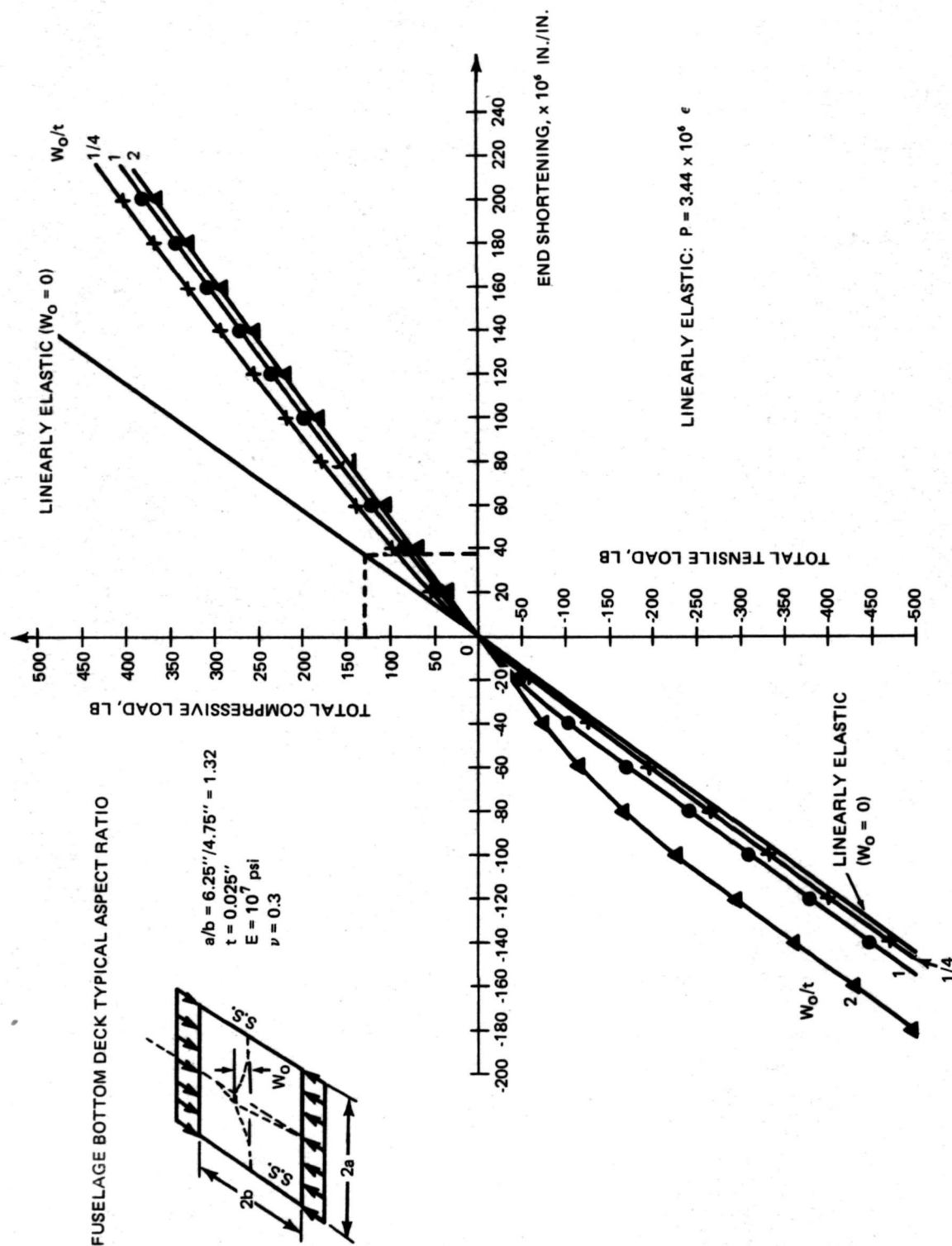


Fig. 5-29 Load vs End Shortening for Typical Bottom Deck Panel

T-87

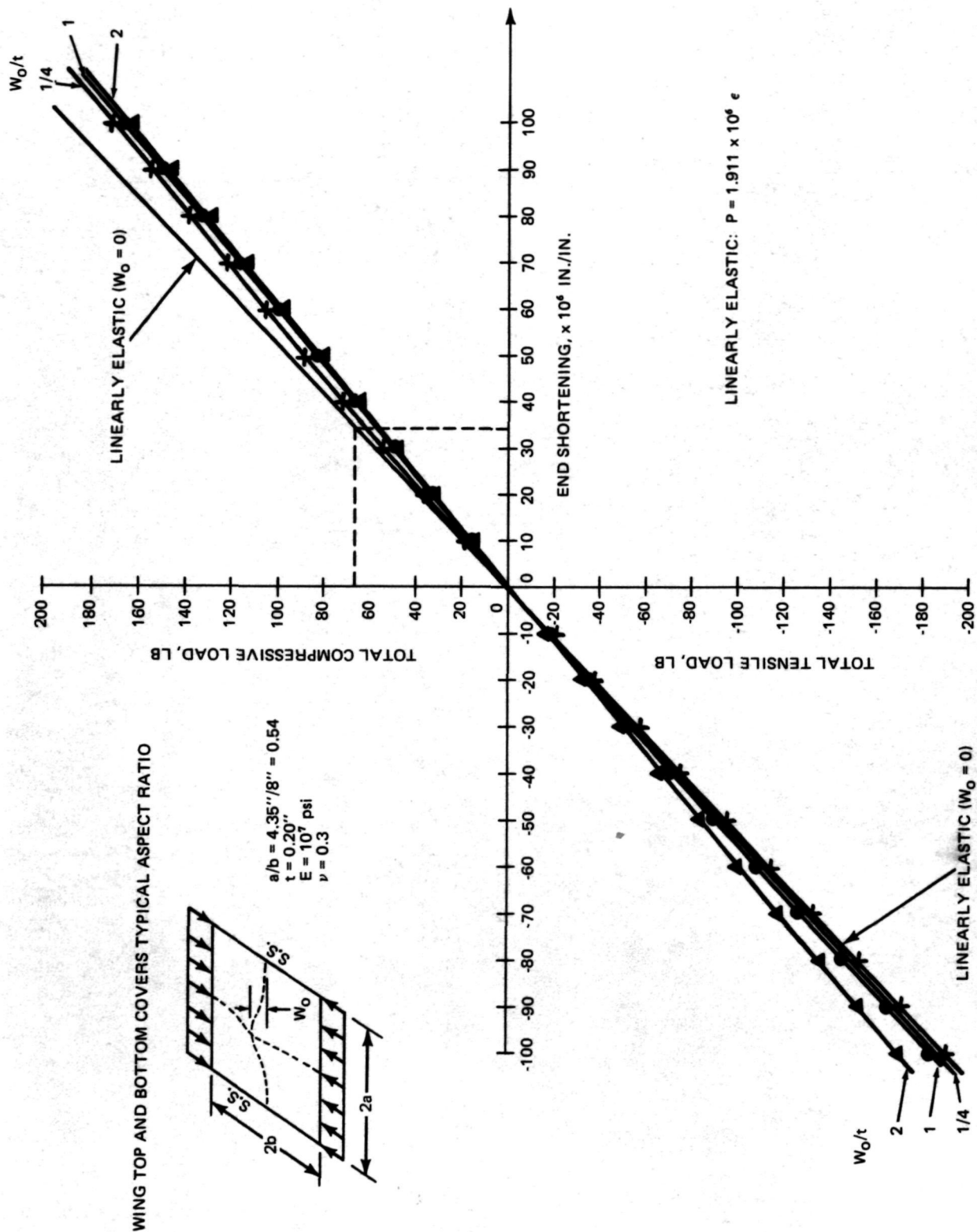


Fig. 5-30 Load vs End Shortening for Typical Wing Cover Panel

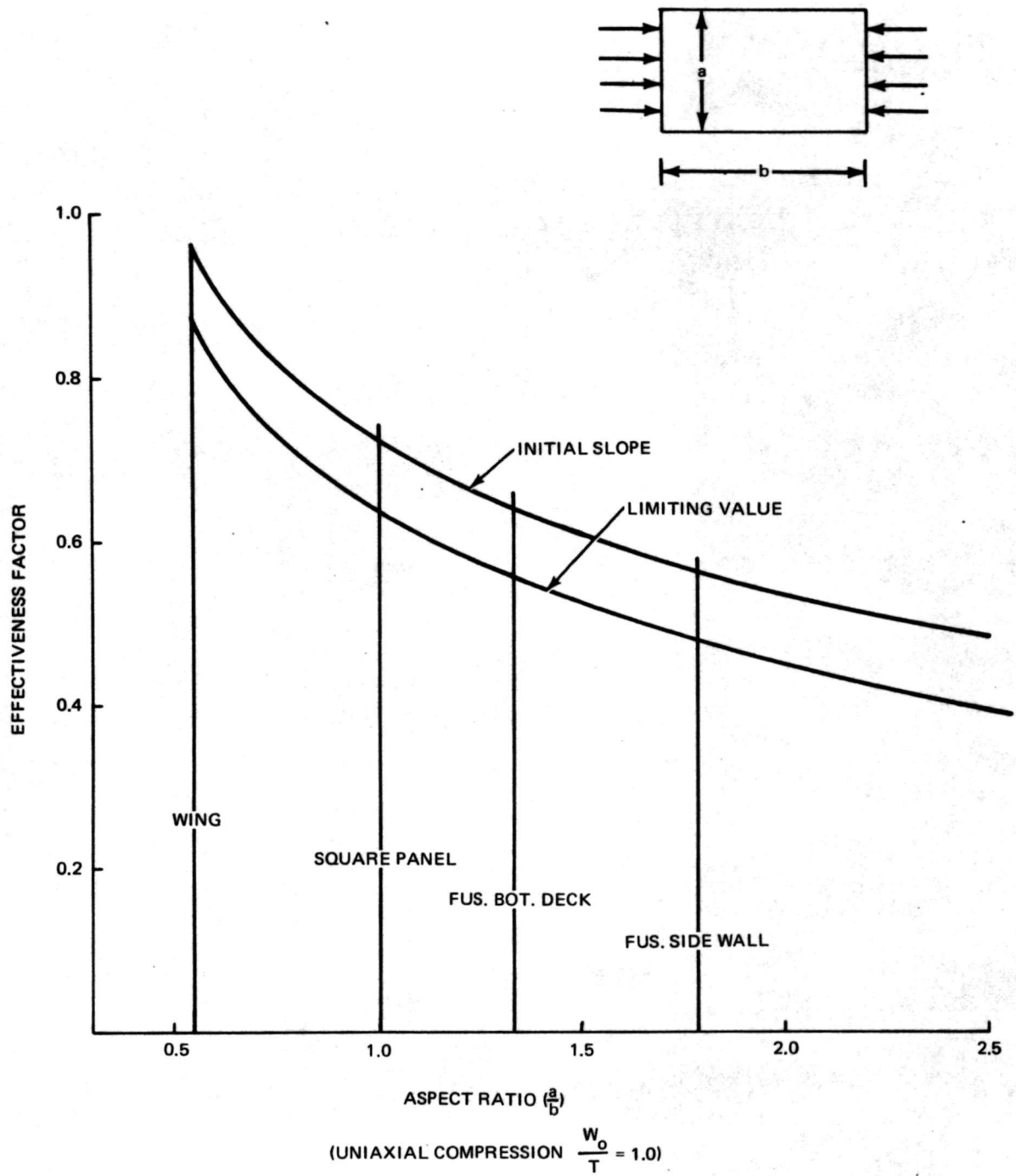
behavior into the elastic range (compare Fig. 5-26 and 5-27). For $\left(\frac{W_0}{t}\right)$ equal to 0.04, the slope of the curve at the critical strain is approximately 0.75; while for $\left(\frac{W_0}{t}\right)$ equal to 2.0, the value is approximately 0.64. The curves tend to become parallel at larger strains where the slope is approximately 0.63.

In Fig. 5-28 through 5-30, load strain curves are plotted for a typical fuselage side wall panel, bottom deck panel, and wing cover. These curves extend into both the tension and compression range. Considering Fig. 5-28, which represents a 17x9.5-in. fuselage sidewall panel, observe that the initial tension and compression slope is approximately one-half of the linear value for $\left(\frac{W_0}{t}\right)$ equal to 1.0. On the compressive side the curves are closely banded for a wide range of initial imperfections. For large compressive strains the slopes of these curves approach a value slightly under one-half. On the tension side the slopes of the curves approach the linear value, where the panels with smaller initial imperfection approach this value faster. The plots in Fig. 5-29 and 5-30 exhibit the same behavior, the shift in values being due to different aspect ratios. In Fig. 5-31, the results are cross-plotted for various aspect ratios. Two curves are shown representing the initial effectiveness factor and the limiting values that occur with large strains. As would be expected, the smallest effectiveness factor is associated with the panel having the largest aspect ratio (short, wide panel loaded along long edges).

Section 6 contains a discussion on the use of these results in combination with some practical considerations to remodel the fuselage and wing structures. Basically, the following effectiveness factors, e , were selected:

- Fuselage:
 - Axial and bending behavior in bottom deck and sidewall $e = 0.5$
 - Shear effectiveness factor $e = 2/3$
- Wing:
 - Axial behavior in top and bottom covers $e = 0.85$
 - Shear effectiveness in covers $e = 0.85$
 - Shear effectiveness in webs $e = 1.0$.

In Subsection 6.1.3, the rationale for selecting the shear and bending effectiveness factors (not covered in this section) is discussed. Appendix F contains detailed descriptions and calculations of these effectiveness factors.



5.11 EVALUATION OF TEST DATA

5.11.1 PRELOAD

As indicated in Subsection 4.3, the preload had a minor effect on the frequency. Considering a compact section, the natural frequency, f , varies with the axial load, P , according to the formula (Reference 9-9),

$$f^2 = f_o^2 \left(1 + \frac{P}{P_c} \right) \quad (5-56)$$

where f_o is the frequency with no preload and P_c is the Euler buckling load,

$$P_c = \frac{\pi^2 EI}{L^2} \quad (5-57)$$

If L is taken as 97 in. (distance between interstage attachments, also the approximate distance between node lines for the first mode) and I is assumed to be 85.2 in.⁴ (the fully effective value at Station 116) then $P_c = 940,000$ lb. Passing a parabola through this point and the calculated value of 53.20 Hz under no load, leads to curve "A" in Fig. 5-32. If an effectiveness factor of one-half is used in the wall and bottom deck panels, then the value of I at Station 116.0 is approximately 69.0 in.⁴, and $P_c = 810,000$ lb. Passing a parabola through this point and the zero preload frequency (obtained from the horizontal test) leads to curve "B" in Fig. 5-32. The average axial dead load is approximately 150 lb for the model half structure

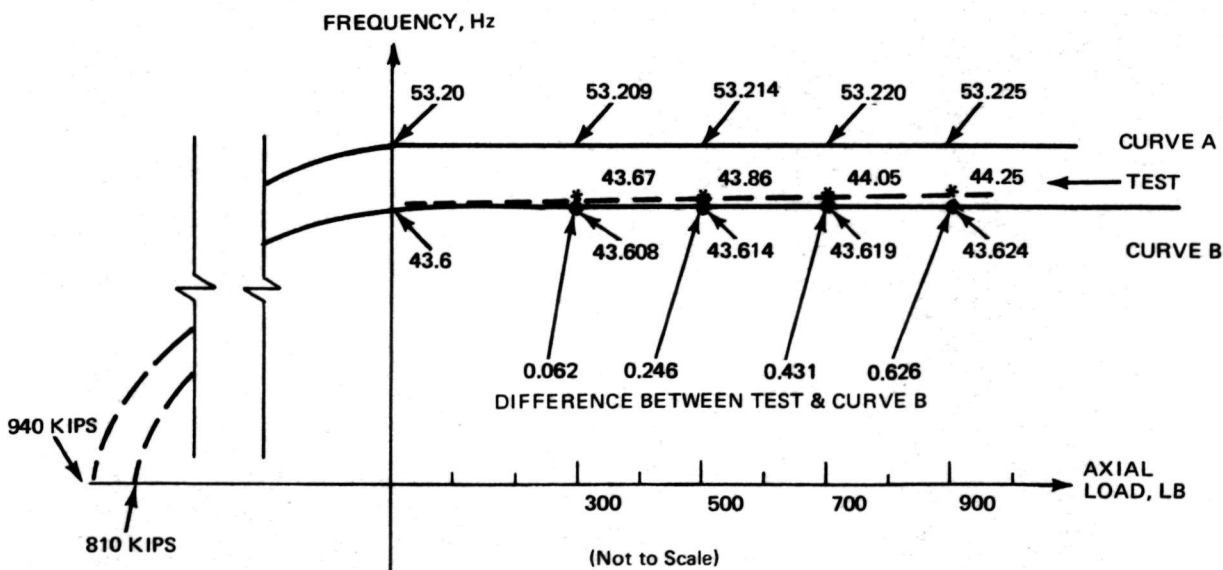


Fig. 5-32 Effective of Axial Load on Frequency

(see Fig. 2-9), and has been added to the preload to obtain the total value. The test values are shown plotted on Fig. 5-32, where it can be seen that they lie between curves "A" and "B", being very close to curve "B." Analytical values are shown for curves "A" and "B," and a comparison of these values with the test data indicates that a curve passed through the test data is drifting slowly from curve "B" (partially effective section) to curve "A" (fully effective section). Although one can question the accuracy of the test data for this type of plotting, and the validity of applying Equation 5-56 to this analysis, there is at least a qualitative trend to the results. Each test point having a different preload represents a section with a different effectiveness factor. Thus there is a family of parabolas bounded by the curves "A" and "B," where for any given parabola passing through a test point the effectiveness factor is constant.

Considering two parabolas "x" and "y", then,

$$f_x^2 = f_{ox}^2 \left(1 + \frac{P_x}{P_{cx}} \right) \quad (5-58a)$$

$$f_y^2 = f_{oy}^2 \left(1 + \frac{P_y}{P_{cy}} \right) \quad (5-58b)$$

The frequency at zero preload is proportional to the square root of the moment of inertia

$$f_{ox} = C_1 \sqrt{I_x} \quad (5-59a)$$

$$f_{oy} = C_1 \sqrt{I_y} \quad (5-59b)$$

while the Euler load is directly proportional to I

$$P_{cx} = C_2 I_x \quad (5-60a)$$

$$P_{cy} = C_2 I_y \quad (5-60b)$$

Therefore

$$P_{cx} = P_{cy} \left(\frac{I_x}{I_y} \right) \quad (5-61)$$

From Equations 5-59a and b,

$$I_x = I_y \left(\frac{f_{ox}}{f_{oy}} \right)^2 \quad (5-62)$$

Substituting Equation 5-62 into 5-61,

$$P_{cx} = P_{cy} \left(\frac{f_{ox}}{f_{oy}} \right)^2 \quad (5-63)$$

Substituting Equation 5-63 into 5-58a,

$$f_x^2 = f_{ox}^2 \left(1 + \frac{P_x}{P_{cy} \left(\frac{f_{ox}}{f_{oy}} \right)^2} \right) \quad (5-64)$$

Solving for f_{ox}^2 ,

$$f_{ox}^2 = f_x^2 - \left(\frac{P_x}{P_{cy}} \right) f_{oy}^2 \quad (5-65)$$

If parabola "y" corresponds to curve "B" and "x" corresponds to the parabola through the test value at 900 lb, then,

$$f_{ox}^2 = (44.25)^2 - \frac{900}{810,000} (43.60)^2$$

from which

$$f_{ox} = 44.226 \text{ Hz.}$$

Substituting into Equation 5-62 and 5-61,

$$I_x = \left(\frac{44.226}{43.600} \right)^2 I_y = 1.0289 I_y$$

and

$$P_{cx} = 1.0289 P_{cy} = 833,425 \text{ lb.}$$

The 3% increase in the moment of inertia requires a 10% increase in the effectiveness factor. Values of I for a fully effective section, half effective, and the condition just calculated, are shown in Table 5-11. For all values, the ratio of I

Table 5-11 Fuselage Moments of Inertia for Various Effectiveness Factors

Effectiveness Factor	Door On		Door Off		$\frac{(I_{\text{door off}})}{(I_{\text{door on}})}$
	I	$\frac{(I_{\text{partial}})}{(I_{\text{full}})}$	I	$\frac{(I_{\text{partial}})}{(I_{\text{full}})}$	
1.0	85.2	1.0	71.2	1.0	0.836
0.50	69.0	0.81	57.8	0.81	0.836
0.55	71.0	0.835	59.4	0.835	0.836

TT-21

(door off) to I (door on) has been kept constant. The preload thus caused a minor increase in the effectiveness factor for the section. A substantial increase would have required a prohibitive preload.

5.11.2 STRAINS

Measured strain data is shown in Fig. 4-9 through 4-13. The location of the strain gages is shown in Fig. 4-8. The strains for the gages mounted in pairs on the inside and outside may be split into axial and bending strains, ϵ_A and ϵ_B ,

$$\epsilon_A = \frac{\epsilon_1 + \epsilon_2}{2} \quad (5-66)$$

$$\epsilon_B = \frac{\epsilon_1 - \epsilon_2}{2} \quad (5-67)$$

where ϵ_1 and ϵ_2 represent the strains on the extreme fibers in the middle of a panel (see Fig. 5-33). Assuming plane sections remain plane before and after bending, the strain, ϵ_B , may be related to the curvature (see Fig. 5-34) by

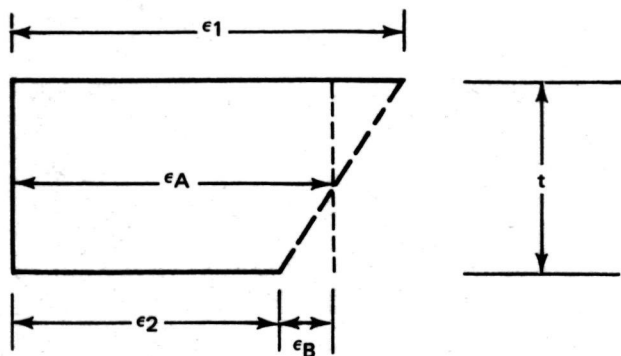
$$dx (1 + \epsilon_B) = (R + \frac{t}{2}) \frac{dx}{R},$$

therefore

$$\frac{1}{R} = \frac{2\epsilon_B}{t} \approx \frac{d^2 y}{dx^2} \quad (5-68)$$

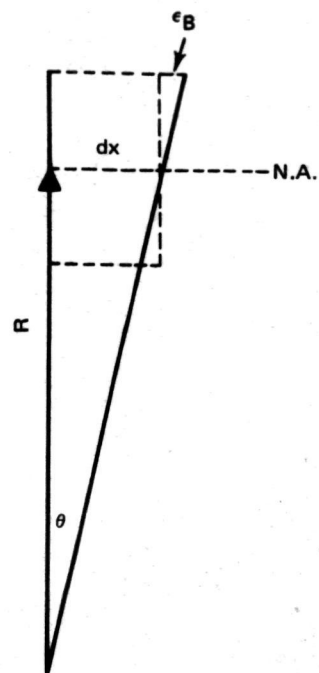
If it is assumed that the initial imperfection is in the form of a $(1 - \cos)$ wave and retains this shape under dead load and preload (see Fig. 5-35), then the change in deflection caused by the preload is

$$y = \frac{a_0}{2} \left(1 - \cos \frac{2\pi x}{l} \right) \quad (5-69)$$



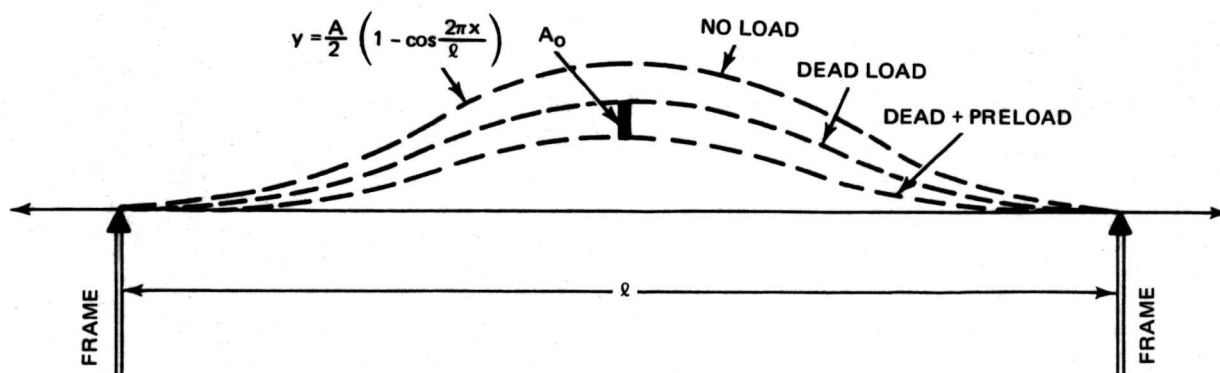
T-91A

Fig. 5-33 Axial and Bending Strains



T-91B

Fig. 5-34 Strain-Curvature Relations



T-92

Fig. 5-35 Assumed Shapes of Panel Imperfections

Table 5-12 Estimates of Panel Imperfections

Station	Gages	ℓ	$\left(\frac{x}{\ell}\right)$	$\cos \frac{2\pi x}{\ell}$	$\left(\frac{\ell}{\pi}\right)^2 \left(\frac{1}{\cos \left(\frac{2\pi x}{\ell}\right)}\right)$	$\epsilon_B \times 10^{-6}$	t	A_0	$\left(\frac{A_0}{t}\right)$
99	3 & 4 13 & 14	9.5	0.21	0.242	36.7	4.5	0.020	0.0083	0.42
						1.0	0.020	0.0018	0.09
110	5 & 6 15 & 16 11 & 12 9 & 10	9.5	0.368	0.682	13.6	2.0	0.020	0.0014	0.07
						16.0	0.020	0.0109	0.54
						10.0	0.025	0.0054	0.216
						13.0	0.025	0.0071	0.284
122	7 & 8	6.5	0.46	0.975	4.4	42.0	0.020	0.0092	0.47

TT-22

where a_o is the change in the maximum deflection at the center of the panel. Differentiating and substituting into Equation 5-68

$$\frac{2\epsilon_B}{t} = \frac{a_o}{2} \left(\frac{2\pi}{l} \right)^2 \cos \frac{2\pi x}{l}, \text{ hence} \quad (5-70)$$

$$a_o = \left(\frac{l}{\pi} \right)^2 \left(\frac{1}{\cos \left(\frac{2\pi x}{l} \right)} \right) \left(\frac{\epsilon_B}{t} \right) \quad (5-71)$$

This expression is somewhat conservative. If a sine wave were chosen ($y = a_o \sin \frac{\pi x}{l}$), where the bow is "out" in one panel and "in" in adjacent bays, then the value of a_o is twice that given by Equation 5-71. The ratios of $\frac{a_o}{t}$ for various panels are shown in Table 5-12. Values range from 0.07 to 0.54. Recognizing that these values are conservative; that they only represent the change due to preload; and that the preload has not straightened out the panel (since the plots of the inner and outer gages have not become parallel in Fig. 4-9 through 4-12); it is safe to conclude that the initial imperfections are equal to or greater than the panel thicknesses for a large number of panels.

5.11.3 INFLUENCE COEFFICIENTS

The procedure for obtaining influence coefficients was discussed in Subsection 4.4. Table 4-4 is a summary of the influence coefficients obtained from plots of the loading and unloading curves in both positive and negative directions. Typical load deflection curves are shown in Fig. 4-19 and 4-20. (Additional plots are given in Volume IIIA, Appendix A3.)

For the mid-fuselage (Station 116), the ratio of analytical and test influence coefficients for the door-off condition is

$$\frac{\delta_{33} \text{ (Model I)}}{\delta_{33} \text{ (Test)}} = \frac{35.61}{45.87} = 78 \%$$

This ratio is in good agreement with the ratio of I for an effectiveness factor of one-half compared with I for a fully effective section (Table 5-10).

$$\frac{I \text{ (1/2 effectiveness factor)}}{I \text{ (fully effective)}} = \frac{69.0}{85.2} = 81 \%$$

The deflection coefficient ratio for the nose is

$$\frac{\delta_{11} \text{ (Model I)}}{\delta_{11} \text{ (Test)}} = \frac{55.4}{83.05} = 66.6 \%$$

The larger disagreement for this case has been attributed to the additional flexibility of the forward mid-fuselage splice of the test model.

The deflection coefficient ratio for the wing tip is

$$\frac{\delta \text{ (Wing Tip - Model I, Symm)}}{\delta \text{ (Test)}} = \frac{290.}{362} = 80 \%$$

With the structure supported on the interstages, loads on the wing tip do not produce appreciable bending in the fuselage. Hence the 20% discrepancy between analysis and test has been attributed to the initial imperfections in the test model wing skins and the additional flexibility associated with cutouts in the wing carry-through structure.

Deflection data for the fin is given in Appendix G of this volume. For a horizontal load at the fin ballast the ratio of fin rotations with respect to the fuselage interface is

$$\frac{\theta \text{ (Model I)}}{\theta \text{ (Test)}} = \frac{534.0 \times 10^{-6}}{1751.0 \times 10^{-6}} = 30.4 \%$$

This large discrepancy has been attributed to the flexibility of the forward fin-fuselage attachment of the test model.

The ratio of deflection coefficients for the payload with respect to the interstage attachments is

$$\frac{\delta \text{ (Model I)}}{\delta \text{ (Test)}} = \frac{27.1}{42.4} = 64 \%$$

This discrepancy has been attributed in part to fuselage effectiveness, but mostly to local flexibility associated with the payload support structure. An intermediate analysis correcting all items except the payload yielded a payload deflection coefficient of 30.8×10^{-6} . This represents an increase of 13.5 %. It is not as large as the mid-fuselage discrepancy because the payload supports are rather close to the interstage attachments; hence, less fuselage bending is involved.

5.12 EFFECTIVENESS OF CARGO DOOR ATTACHMENTS

5.12.1 SYMMETRIC BENDING CASE

The door shell is primarily ineffective for symmetrical loading because of the breather joints. However, the edge longeron, which is connected to the fuselage at four stations, is partially effective. The effectiveness of the door longeron can be determined through the use of some simple analytical models. The NASTRAN Model I static load analysis with a unit load at Station 116.0 can be approximated with a simple beam having a unit load at its mid-point. The length of the beam is 97 in., which corresponds to the distance between the interstage attachments (points of support for the Model I static analysis and for the static test). Assuming the beam properties to be constant and equal to the values at Station 116.0, the deflection at the mid-point is

$$\delta = \frac{PL^3}{48 EI} + \frac{PL}{4 A_s G} \quad (5-72)$$

Substituting $L = 97$, $P = 1$, $G = \frac{E}{2.6}$ and $E = 10.5 \times 10^6$ yields

$$\delta = \left(\frac{1810}{I} + \frac{6}{A_s} \right) 10^{-6} \quad (5-73)$$

With the cargo doors off, the fully effective section properties are

$$I = 71.4 \text{ in.}^4$$

$$A_s = 0.66 \text{ in.}^2$$

where the shear area, A_s , is taken as the cross-sectional area of the side walls. Using these values, $\delta = 34.3 \times 10^{-6}$ which agrees rather well with the Model I analysis where $\delta = 35.61 \times 10^{-6}$.

In Subsection 6.1.3 following it is reasoned that the fuselage skins are approximately one-half effective for direct stress, and two-thirds effective for resisting shear. For this case, the reduced section properties are

$$I = 57.8 \text{ in.}^4 \text{ (refer to Appendix F of this volume)}$$

$$A_s = \frac{2}{3} (.66) = 0.44 \text{ in.}^2$$

Substituting these values into Equation 5-73, $\delta = 44.9 \times 10^{-6}$, which is in rather good agreement with the static test result, $\delta_{33} = 45.87 \times 10^{-6}$ (refer to Subsection 4.4).

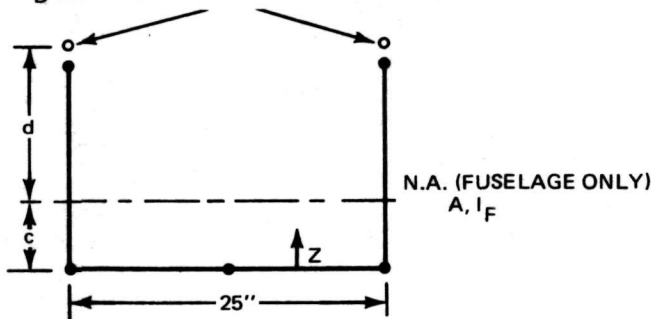
Figure 5-36 shows the effect on the moment of inertia when the door longeron is added. Since the door longeron shifts the neutral axis by only a small amount, compared to the total height of the section (see Table 5-13), the following approximate expression can be used for the moment of inertia:

$$I = I_F + 2 A_D (d)^2 . \quad (5-74)$$

Substituting this expression into Equation 5-74 and solving for A_D

$$A_D = \frac{1}{2 d^2} \left\{ \left(\frac{1810}{\delta \times 10^6 - \frac{6}{A_S}} \right) - I_F \right\} . \quad (5-75)$$

A_D (EFF. DOOR LONGITUDINAL AREA)



$$\Sigma A = A + 2 A_D$$

$$\Sigma A \times Z = A \times c + 2 A_D (d + c)$$

$$N. A. (FULL SECT) = \bar{Z} = \frac{\Sigma A \times Z}{\Sigma A} = \frac{A \times c + 2 A_D (d + c)}{A + 2 A_D}$$

$$I (FULL SECT) = I = I_F + A (\bar{Z} - c)^2 + 2 A_D (d + c - \bar{Z})^2$$

$$IF \bar{Z} - c \text{ SMALL, } \bar{Z} = c$$

$$APPROX. I (FULL SECT) = I_F + 2 A_D (d)^2$$

T-93

Fig. 5-36 Moment of Inertia for Fuselage and Effective Door Longeron at Sta 116.0

Table 5-13 Moment of Inertia Using Exact and Approximate Formulas for Sta 116.0

	I_F	A	A_D	C	Z	I		I Approx
						Exact	Approx	I Exact
100% Eff. Fus 0% Eff. a_d	71.4	1.766	0	4.95	—	71.4	—	—
100% Eff. Fus 100% Eff. a_d	71.4	1.766	.06	4.95	5.73	87.1	88.2	1.02
50% Eff. Fus 0% Eff. a_d	57.8	1.124	0	5.35	—	57.8	—	—
50% Eff. Fus 100% Eff. a_d	57.8	1.124	.06	5.35	6.47	72.6	71.9	0.99

TT-23

Equation 5-75 is approximate and yields results which are about 5 % lower than the correct values when the shift in the neutral axis is appropriately accounted for.

Substituting into Equation 5-74 the following values:

$$\delta = 31.0 \times 10^{-6} \text{ (Model I deflection with cargo door attached)}$$

$$I_F = 71.4 \text{ in.}^4 \text{ (Estimated fully effective Model I fuselage)}$$

$$A_s = .66 \text{ in.}^2 \text{ (Estimated fully effective shear area)}$$

$$d = 11.55 \text{ in. (Refer to Appendix F of this volume)}$$

yields $A_D = 0.042 \text{ in.}^2$. The actual door longeron area used in Model I is 0.056 in.^2 , hence, the effectiveness factor is

$$\frac{0.042}{0.056} = 75 \%$$

The door longeron is not fully effective, even in Model I, because it is not attached continuously.

The effectiveness of the door longeron in the static test can be estimated by substituting the following into Equation 5-75:

$$\delta = 40.7 \times 10^{-6} \text{ } (\delta_{33} \text{ from static test with the cargo door on})$$

$$I_F = 57.8 \text{ in.}^4 \text{ (I for 1/2 effective skins)}$$

$$A_s = 0.44 \text{ in.}^2 \text{ (2/3 effectiveness factor on shear area)}$$

$$d = 16.5 - 5.35 + 0.31 = 11.15 \text{ (refer to Appendix F; the addition of 0.31 is to account for the offset between the fuselage and door longerons)}$$

from which $A_D = 0.035 \text{ in.}^2$. Hence the effectiveness factor for the door longeron in the static test is

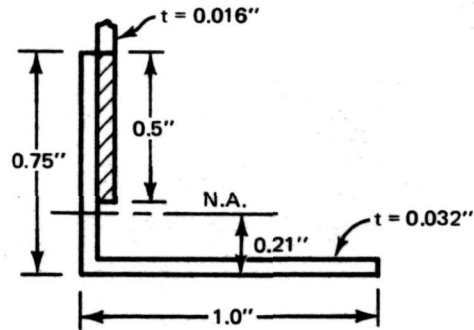
$$\frac{0.035}{0.063} = 55 \%$$

The area of 0.063 is a revised value for the door longeron (see Fig. 5-37).

To verify these results a separate, small, simplified model (Fig. 5-38) was analyzed using NASTRAN. The model consists of an assemblage of CBAR elements which incorporate the changes that were eventually made in Model II. Figures 5-37, 5-39, and 5-40 show the details of the revised door longeron, door strap, and

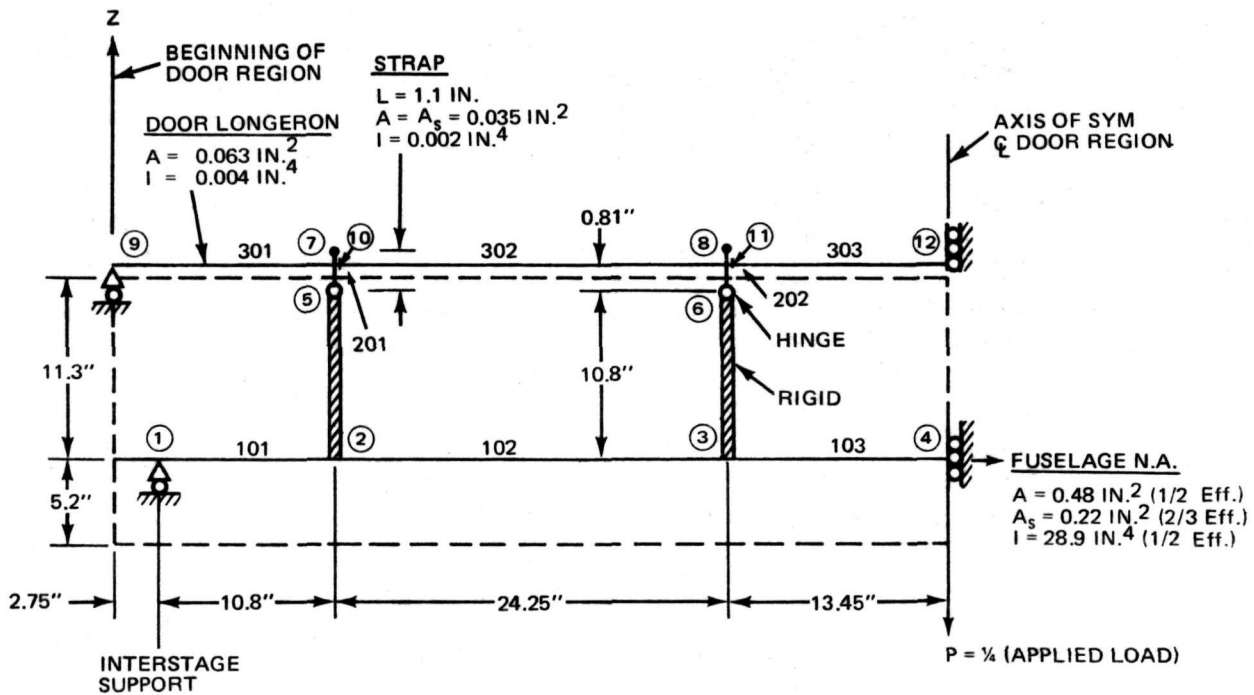
$$A = 0.063 \text{ in.}^2$$

$$I = 0.004 \text{ in.}^4$$



T-94

Fig. 5-37 Door Longeron Properties



MPC EQUATIONS

$$\begin{aligned}\Delta 5X &= \Delta 2X + 10.8 \theta 2Y \\ \Delta 5Z &= \Delta 2Z \\ \Delta 6X &= \Delta 3X + 10.8 \theta 3Y \\ \Delta 6Z &= \Delta 3Z \\ \Delta 7X &= \Delta 10X + 0.29 \theta 10Y \\ \Delta 7Z &= \Delta 10Z \\ \theta 7Y &= \theta 10Y \\ \Delta 8X &= \Delta 11X + 0.29 \theta 11Y \\ \Delta 8Z &= \Delta 11Z \\ \theta 8Y &= \theta 11Y\end{aligned}$$

SPC'S (REACTIONS)

$$\begin{aligned}F1Z \\ F4X, M4Y \\ F9Z \\ F12X, M12Y\end{aligned}$$

T-97

Fig. 5-38 Simplified NASTRAN Model Incorporating Changes to Model I
(One-Quarter of Door Region Shown)

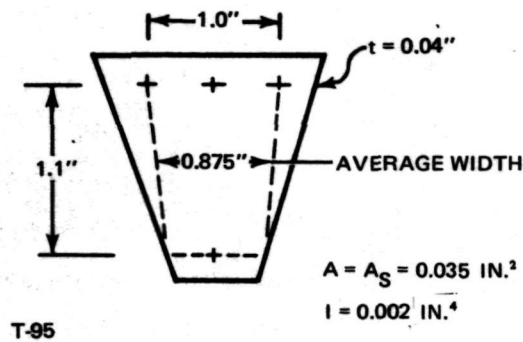


Fig. 5-39 Door - Fuselage Strap

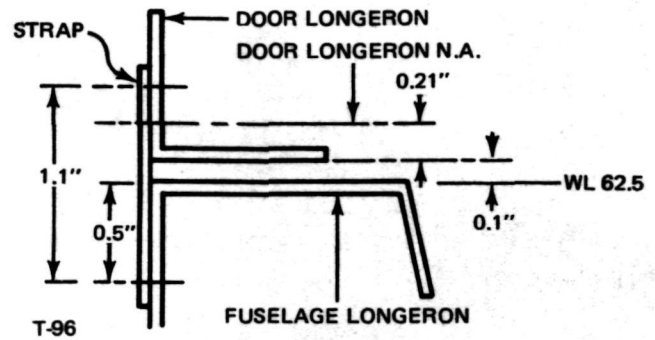


Fig. 5-40 Door - Fuselage Connection

door-fuselage connections, respectively. The results of the NASTRAN analysis are shown in Fig. 5-41. The center deflection $\delta = 41.24 \times 10^{-6}$ agrees closely with the test value of 40.7×10^{-6} . Substituting the calculated deflection and the properties of the simplified model ($\delta = 41.24 \times 10^{-6}$, $I_F = 57.8 \text{ in.}^4$, $A_S = 0.44 \text{ in.}^2$ and $d = 11.61$) into Equation 5-75 gives $A_D = 0.029 \text{ in.}^2$ and, therefore, the effectiveness factor for the door longeron is

$$\frac{0.029}{0.063} = 46 \%$$

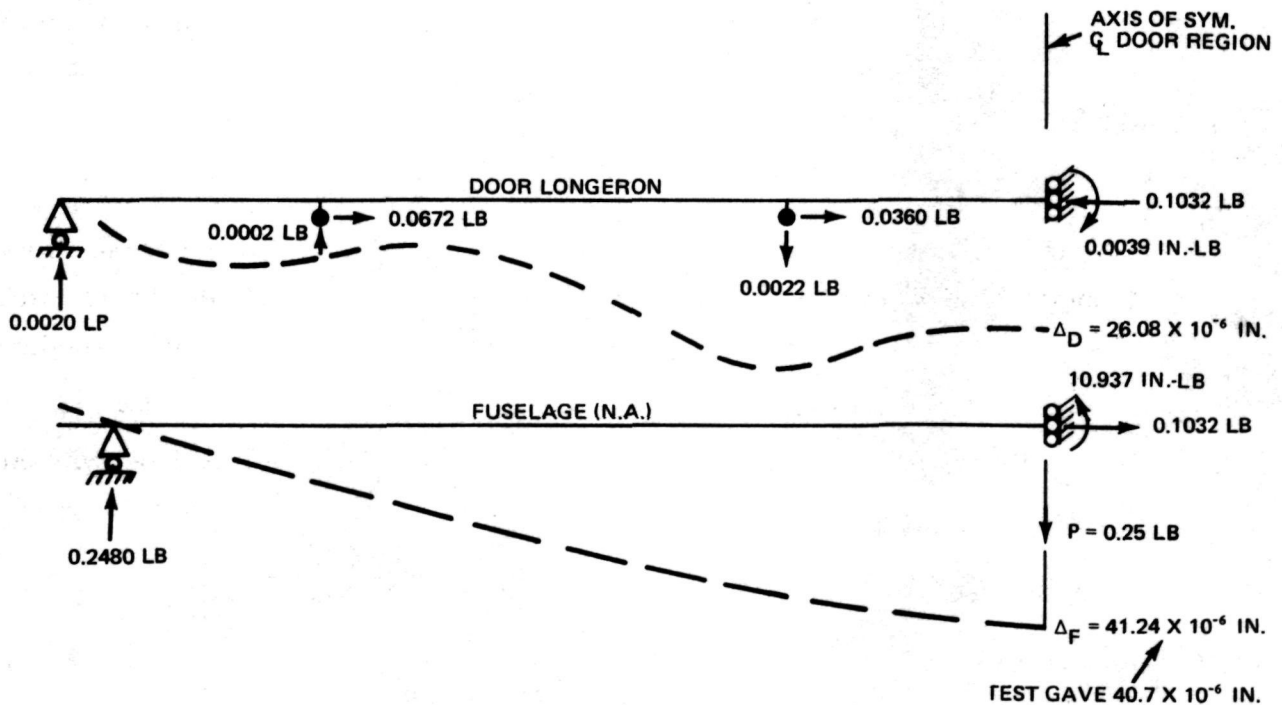


Fig. 5-41 Simplified NASTRAN Model Results

The reduction in the effectiveness factor is due to inclusion of the cargo door connection details.

5.12.2 ANTISYMMETRIC BEHAVIOR CASE

The torsional stiffness of the fuselage is greatly dependent on the local flexibility of the door attachments. If these attachments are rigid (for example, the door longeron is continuously connected to the fuselage upper longeron by a rigid shear panel), then the combined "U" shaped fuselage and circular cargo door form a closed cell. If, however, the connections are very flexible, then the behavior of the combined section will approach the behavior of an open channel and the torsional stiffness will drop significantly. To study this effect, a typical fuselage section was considered (Fig. 5-42). The factors k_1 , k_2 , k_3 , and k_4 represent thickness effectiveness factors. In Model I, points "a" and "b" (Fig. 5-42) are common, and the door extends from point "b" on one side to point "b" on the opposite side as a segmented arc. In Model II, points "a" and "b" are separated by 0.31 in. on both sides, and straps were inserted to connect the cargo door to the fuselage at four discrete points along the length of the door. For Model I, $k_1 = k_3 = k_4 = 1.0$, and k_2 represents the effectiveness due to discrete attachments although the connection was made at the same water line. In Model II, $k_1 = 1.0$, $k_3 = k_4 = 2/3$, and k_2 represents the additional flexibility due to separating the longerons by a distance of 0.31 in. and including bending and shear in the straps and longerons.

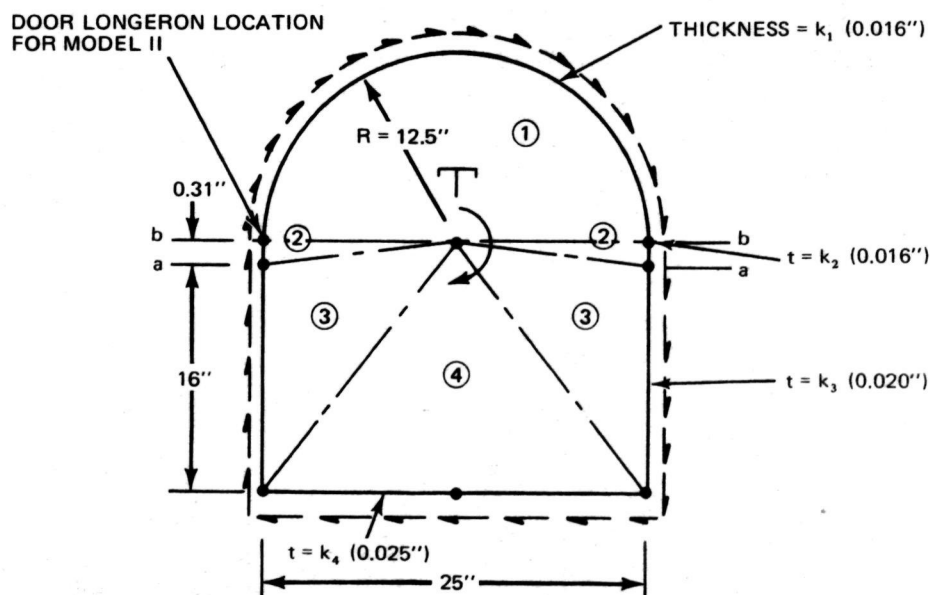


Fig. 5-42. Torque Cell Representation of Typical Fuselage Section

For a closed cell, the constant shear flow, q , is given by

$$q = \frac{T}{2A} = \frac{T}{\sum_i 2A_i} \quad (5-76)$$

and the rotation, θ , due to q is given by

$$\theta = \frac{qL}{2A} \sum_i \frac{S_i}{G_i \bar{t}_i} \quad (5-77)$$

where

- A = enclosed area
- \bar{t}_i = effective thickness of segment i
- S_i = length of segment i
- G_i = effective shear modulus
- L = length of torque cell.

With the effectiveness factors, k , associated with the thickness and not the shear modulus, Equations 5-76 and 5-77 may be combined to give the rotation, θ , for a unit torque

$$\theta = \frac{L}{4 A^2 G} \sum_i \left(\frac{S_i}{k_i \bar{t}_i} \right) \quad (5-78)$$

Substituting the values given in Table 5-14 gives

$$\theta = 14.95 \times 10^{-12} \left\{ \frac{2460}{k_1} + \frac{40}{k_2} + \frac{1600}{k_3} + \frac{1000}{k_4} \right\} \quad (5-79)$$

In this expression, $L = 103$ in. (the length of the cargo door), and $G = 4.04 \times 10^6$. As mentioned previously for Model I, $k_1 = k_3 = k_4 = 1.0$. The value of k_2 was ob-

Table 5-14 Parameters for Simple Torque Cell Calculations

Segment	$2 A_i$	S_i	t_i	S_i/t_i
1. Door Shell	491	39.3	.016	2460
2. Interface Region	7.75	.62	.016	40
3. Side Wall	400	32.0	.020	1600
4. Bottom Deck	407.75	25.0	.025	1000
Σ	1306.5	—	—	—

tained by equating the strain energy of an equivalent shear panel to the strain energy of the axial loads in the door and fuselage longerons plus the energy in an additional shear panel required to extend the door region (see Fig. 5-43).

Thus,

$$U_{(\text{Equivalent Panel})} = U_{(\text{Shear Panel})} + U_{(\text{Longerons})}. \quad (5-80)$$

The shear flow of q lb/in. is transferred across the door connection by four fittings (Fig. 5-44), each assumed to carry equal shear forces

$$H = \frac{qL}{4} = 25.75 q. \quad (5-81)$$

The axial force in the longerons thus builds and drops in a "saw tooth" pattern, Fig. 5-45. The axial energy, U , is,

$$U = \frac{1}{2} \int_0^L \frac{S^2}{AE} dx. \quad (5-82)$$

Evaluating this integral for the total length, $L = 103$ in., for both the door and fuselage longerons gives

$$U = \frac{1}{2} \left\{ \frac{1}{E} \left(\frac{1}{A_D} + \frac{1}{A_F} \right) 5775 \right\} q^2 \quad (5-83)$$

where

$$\begin{aligned} A_D &= \text{door longeron area} \\ A_F &= \text{fuselage longeron area.} \end{aligned}$$

The strain energy for the shear panel is

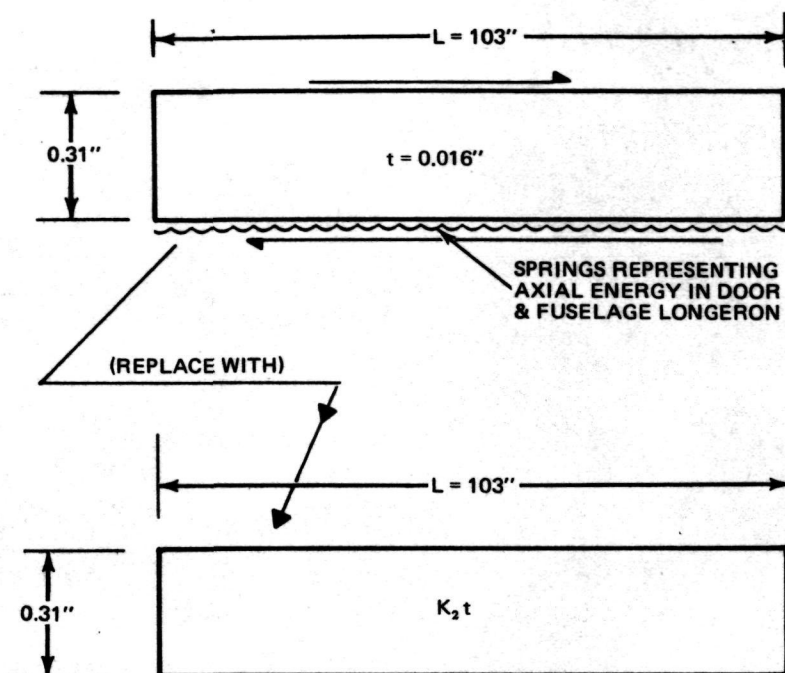
$$U = \frac{1}{2} \left(\frac{A}{Gt} \right) q^2. \quad (5-84)$$

Adding Equations 5-83 and 5-84 and equating to the strain energy of the equivalent panel

$$\frac{1}{2} \left(\frac{A}{G k_2 t} \right) q^2 = \frac{1}{2} \left(\frac{A}{Gt} \right) q^2 + \frac{1}{2} \left\{ \frac{1}{E} \left(\frac{1}{A_D} + \frac{1}{A_F} \right) 5775 \right\} q^2. \quad (5-85)$$

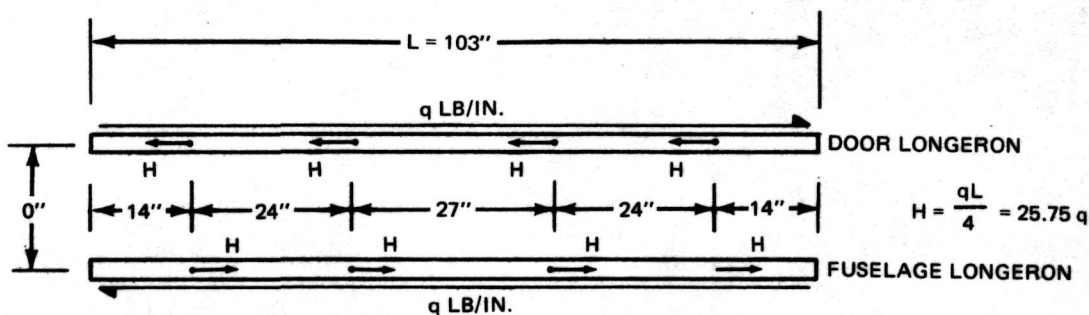
From which

$$k_2 = \frac{A}{\left\{ A + \frac{Gt}{E} \left(\frac{1}{A_D} + \frac{1}{A_F} \right) 5775.0 \right\}}. \quad (5-86)$$



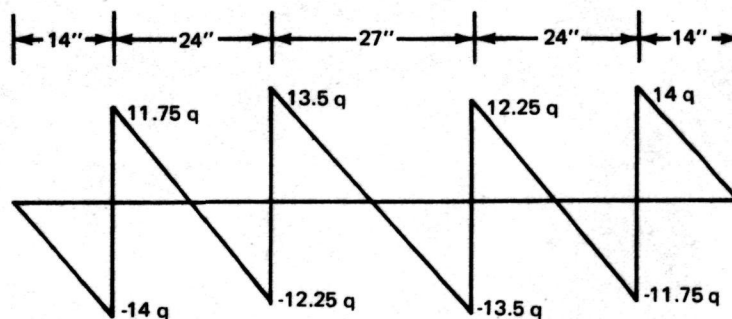
T-100

Fig. 5-43 Equivalent Shear Panel to Represent Energy in Door and Fuselage Longerons Plus Physical Door Shell Extension (Model I Simulation)



T-101

Fig. 5-44 Assumed Shear Transfer Between Door and Fuselage for Model I



Door Longerons Shown — Fuselage Longerons Equal and Opposite

T-102

Fig. 5-45 Axial Load Distribution in Door and Fuselage Longerons

With $A = (0.31)(103) = 32.6$, $t = 0.016$, $A_D = 0.056$, $A_F = 0.1$, and $\frac{E}{G} = 2.6$, Equation 5-86 gives $k_2 = 0.032$.

Returning to Equation 5-79

$$\begin{aligned}\theta &= 14.95 \times 10^{-12} \left\{ \frac{2460}{1.0} + \frac{40}{0.032} + \frac{1600}{1.0} + \frac{1000}{1.0} \right\} \\ &= 0.095 \times 10^{-6} \text{ radians.}\end{aligned}\quad (8-87)$$

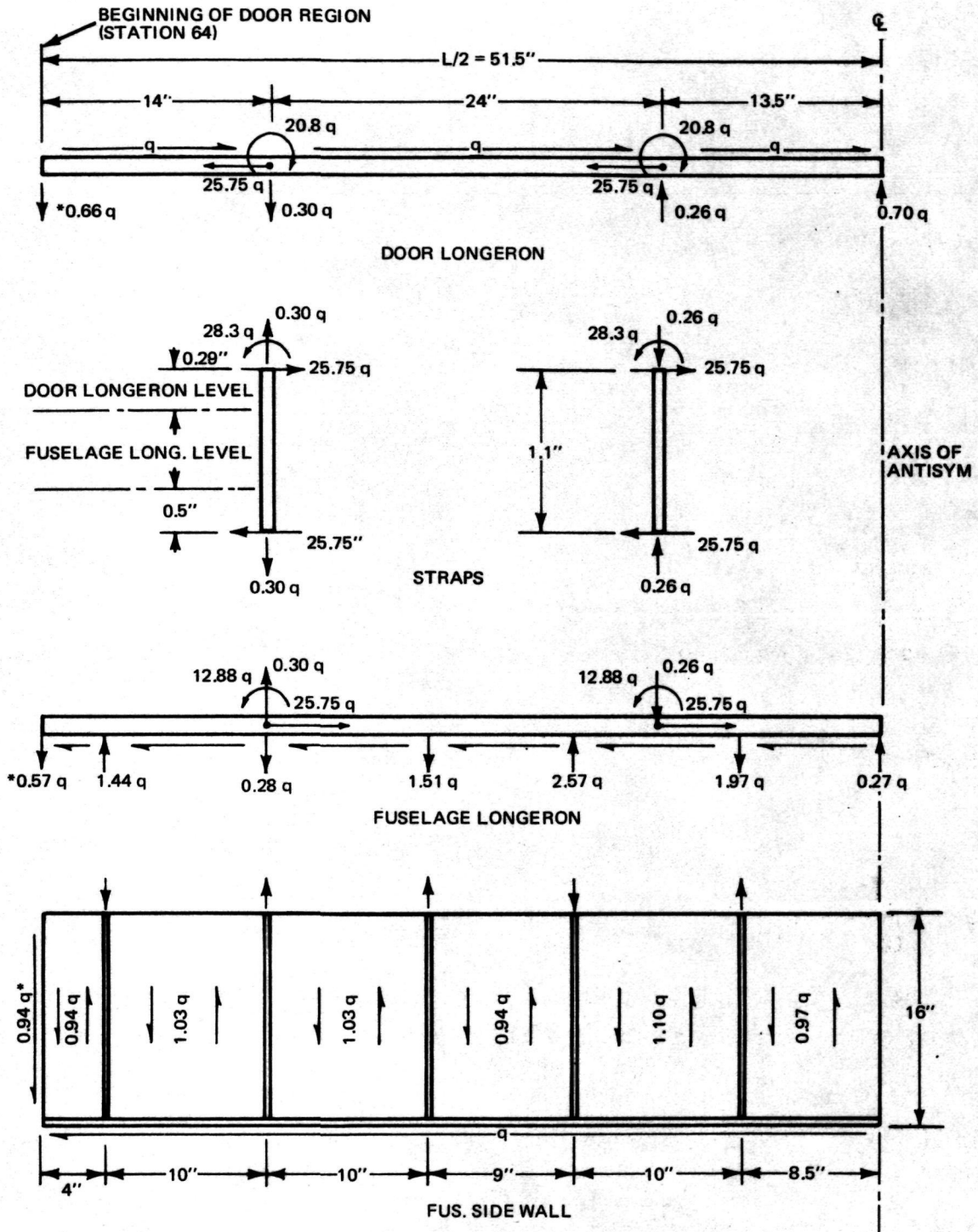
For Model I, the relative twist between Stations 64.0 and 166.5 is 0.10×10^{-6} radians. Comparing these two results

$$\frac{\theta(\text{simple torque cell})}{\theta(\text{Model I})} = \frac{0.095}{0.100} = 95 \%. \quad (5-88)$$

From test data, the relative twist between Stations 64.0 and 166.5 is $\theta = 0.17 \times 10^{-6}$ radians. Substituting this value, and $k_1 = 1.0$, $k_3 = k_4 = 2/3$ into Equation 5-79 and solving for k_2 , yields $k_2 = 0.008$. This value is one-quarter of the value of k_2 predicted by Model I analysis.

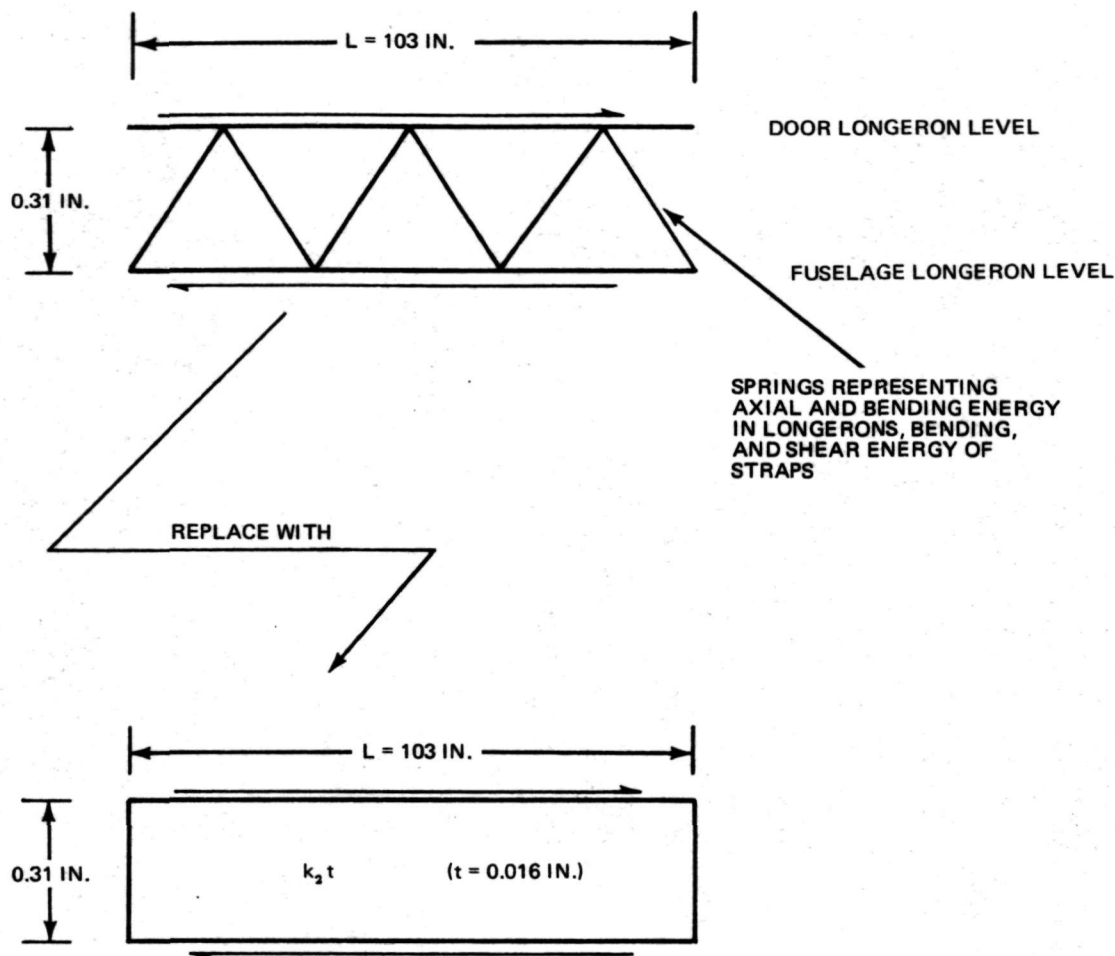
The Model II analysis described in Section 6, predicted a twist θ equal to 0.32×10^{-6} radians (approximately twice the test value) for a unit torque applied at the nose fittings. The following analyses were performed to understand the deficiencies that still lie in Model II. A simplified model (Fig. 5-46) was devised and analyzed making the following assumptions.

The shear flow, q (assumed to be constant), is transferred from the door to the fuselage through the four straps. Taking advantage of antisymmetry only half of the door region was analyzed. The straps are assumed to carry equal shear and are pinned on the fuselage side, although offset from the fuselage longeron, and moment-connected to the door longeron. The vertical interface forces on the door longeron caused by the "strap tie moments" were obtained by assuming the longeron to be a continuous beam on rigid supports. The results of the hand analysis are shown in Fig. 5-46. Note that the vertical interface forces on the side wall produced a minor change in the shear that was assumed in Equation 5-79, and hence was neglected. The k_2 value for Model II was obtained by equating the strain energy of an equivalent panel to the combined strain energy (see Fig. 5-47) of the following:



T-104

Fig. 5-46 Assumed Shear Transfer Between Door and Fuselage for Model II



T-105 Fig. 5-47 Equivalent Shear Panel to Represent Strain Energy in Straps and Longerons

- Axial energy in the door and fuselage longerons, same expression as Equation 5-83
- Bending energy in the door and fuselage longerons
- Bending and shear energy in the straps (the axial energy is negligible).

The bending energy in the longerons and straps is

$$U_b = \frac{1}{2} \int \frac{M^2 dx}{EI} = \frac{1}{2} \left\{ \frac{1}{E} \left(\frac{3700}{I_D} + \frac{1173}{I_S} + \frac{734}{I_F} \right) \right\} q^2. \quad (5-89)$$

The shear energy in the straps is

$$U_s = \frac{1}{2} \int \frac{V^2 dx}{A_s G_s} = \frac{1}{2} \left\{ \frac{1}{G_s} \left(\frac{2920}{A_s} \right) \right\} q^2. \quad (5-90)$$

Adding Equations 5-83, 5-89, and 5-90 yields

$$U = \frac{q^2}{2E} \left[\left(\frac{1}{A_D} + \frac{1}{A_F} \right) 5775 + \left(\frac{3700}{I_D} + \frac{734}{I_F} + \frac{1173}{I_S} \right) \right] + \frac{q^2}{2G_S} \left[\frac{2920}{A_S} \right] \quad (5-91)$$

Equating this expression to the equivalent shear panel energy given by the left side of Equation 5-85

$$k_2 = \frac{(A/t)}{\left[\frac{G}{G_S} \left(\frac{2920}{A_S} \right) + \frac{G}{E} \left(\frac{5775}{A_D} + \frac{5775}{A_F} + \frac{3700}{I_D} + \frac{734}{I_F} + \frac{1173}{I_S} \right) \right]} \quad (5-92)$$

Substituting the following into Equation 5-92:

$$\begin{aligned} G &= G_S \\ E/G &= 2.6 \\ A_S &= \text{shear area of straps} = 0.035 \text{ in.}^2 \\ A_D &= \text{area of door longeron} = 0.063 \text{ in.}^2 \\ A_F &= \text{area of fuselage longeron} = 0.16 \text{ in.}^2 \text{ (includes equivalent skin area)} \\ I_D &= \text{inertia of door longeron} = 0.004 \text{ in.}^4 \\ I_F &= \text{inertia of fuselage longeron} = 0.002 \text{ in.}^4 \\ I_S &= \text{inertia of strap longeron} = 0.002 \text{ in.}^4 \\ A &= \text{area of equivalent shear panel} = (0.31)(103) = 32.6 \text{ in.}^2 \\ t &= \text{thickness of equivalent shear panel} = 0.016 \text{ in.,} \end{aligned}$$

yields $k_2 = 0.0024$. Substituting this value of k_2 into Equation 5-79 with $k_1 = 1.0$ and $k_3 = k_4 = 2/3$ yields

$$\begin{aligned} \theta &= 14.95 \times 10^{-12} [2,460 + 16,660 + 2,400 + 1,500] \\ &= 0.344 \times 10^{-6} \text{ radians.} \end{aligned} \quad (5-93)$$

Comparing this value with Model II results

$$\frac{\theta (\text{Simple Model})}{\theta (\text{Model II})} = \frac{0.344}{0.320} = 1.07. \quad (5-94)$$

The rather good agreement lends credibility to the assumptions employed in the simplified model as shown by Table 5-15. Note that the k_2 term in Equation 5-93 contributes 72% to the twist, θ . If Equation 5-92 is normalized, then

$$k_2 = \frac{2040}{854980} \left[\frac{1}{0.098 + 0.041 + 0.016 + 0.416 + 0.165 + 0.264} \right] \quad (5-95)$$

strap shear _____
 axial, door longeron _____
 axial, fuselage longeron _____
 bending, door longeron _____
 bending, fuselage longeron _____
 bending, strap _____

Here it can be seen that the bending terms dominate the denominator. If the inertia of the door longeron is increased because of including more effective shell material, then k_2 will be smaller and the calculated twist will be more in line with test data.

Table 5-15 Torque Cell Effectiveness Factors and Rotations for a Unit Nose Torsion

	Model I	Model II	Test
k_1	1.0	1.0	1.0 (assumed)
k_2 (calc)	0.032	0.0024	0.008
k_3	1.0	2/3	2/3 (assumed)
k_4	1.0	2/3	2/3 (assumed)
θ (Analysis-Test)	0.100×10^{-6}	0.32×10^{-6}	0.170×10^{-6}
θ (Calculated)	0.095×10^{-6}	0.344×10^{-6}	—

TT-25

Section 6
FINITE ELEMENT ANALYSIS FOR MODEL II

SECTION 6

6 - FINITE ELEMENT ANALYSIS FOR MODEL II

6.1 FINITE ELEMENT MODEL II

6.1.1 GENERAL

The second finite element model was constructed using information obtained from

- Behavior of Model I (Section 3)
- Experimental results (Section 4)
- Separate analytical investigations (Section 5).

Various methods are available for tuning the parameters of a finite element model so that the analytical results are forced to agree with test data. If the number of individual parameters (areas and gages) is too large, then it is possible to "slave" groups of parameters into a fewer number of unknowns. This was not done because on a typical large aerospace project, the finite element model is the chief source of a large variety of information - including data such as: static deflections due to applied loads; thermal distortions; internal loads due to flight maneuvers, landings, taxing and take offs; thermal stresses; and influence coefficients for flutter analysis, transient dynamic analyses, and aeroelastic corrections. An attempt to "tune" a finite element model to accurately predict one type of behavior might jeopardize its ability to predict other types of behavior, thus degrading the overall usefulness of the model. The alternative is to create several "tuned" models; clearly this is not desirable, at least in the design phase of a project.

Note that at this stage, a good deal of thought was given to modifying the 1/8-scale experimental model. No amount of analytical effort can change basic undesirable behavior; only by changing the actual design can the situation be rectified. After reviewing a number of proposed changes it was decided not to incorporate any physical model changes because modification would have produced too drastic a schedule slippage for the project to tolerate.

With the foregoing considerations as prime factors, the following course was decided:

- Not to change the 1/8-scale model
- Not to "tune" the analytical model to specific test data

- To establish a second finite element model that would recognize test results and incorporate the findings obtained in the separate analytical studies.

In the next subsection overall remodeling guide lines are discussed. These are elaborated on in the ensuing detailed subsections covering modifications to the individual components.

6.1.2 REMODELING GUIDE LINES

The guiding rules described in the following paragraphs for modifying Model I were established and observed in developing the second finite element model (Model II).

FUSELAGE - A bar and shear panel idealization was used in place of the grid of direct stress elements. The areas of the bars include actual areas plus lumped effective skin material. An effective shear modulus was used in place of the actual material value. This accounts for additional shear flexibility due to the presence of initial imperfections. A typical effective width and effective shear modulus was used throughout the main portion of the fuselage, instead of attempting to use separate values for each panel based on test or measurements. It was felt that this represented a more realistic design approach.

The flexibility of the forward fuselage strap (refer to Volume III, Appendix A, pg A1-1; see part AD 383-526-41 on view C-C) was included by double noding Station 64.0 and inserting an axial spring between the nodes. The spring constant was determined using test data.

WING - The wing carry through was modified to more accurately account for cut-outs. A bar and panel idealization was used on the wing covers, where the cover panel effective widths were lumped into equivalent bar areas. An effective shear modulus was used in modeling the rib and spar webs.

FIN - Springs were added between the fin and the fuselage to account for the flexibility of the connections in the 1/8-scale model. The values for these springs was based on static test data. No attempt was made to refine the model in this region. Early in the project, but after the model was constructed, this connection detail was recognized to be rather poor from a flexibility point of view. An alternate design was developed but not implemented on the constructed model.

CARGO DOOR - The door longeron was shifted to the actual 1/8 scale model location. In Model I, the door longeron had been set at the same water line as the fuselage upper longeron. Additional modeling detail was also added to more accurately account for the flexibility of the door-fuselage connections.

PAYLOAD - Springs were added at the payload supports to account for the local flexibility of the connections. These values were determined by test data.

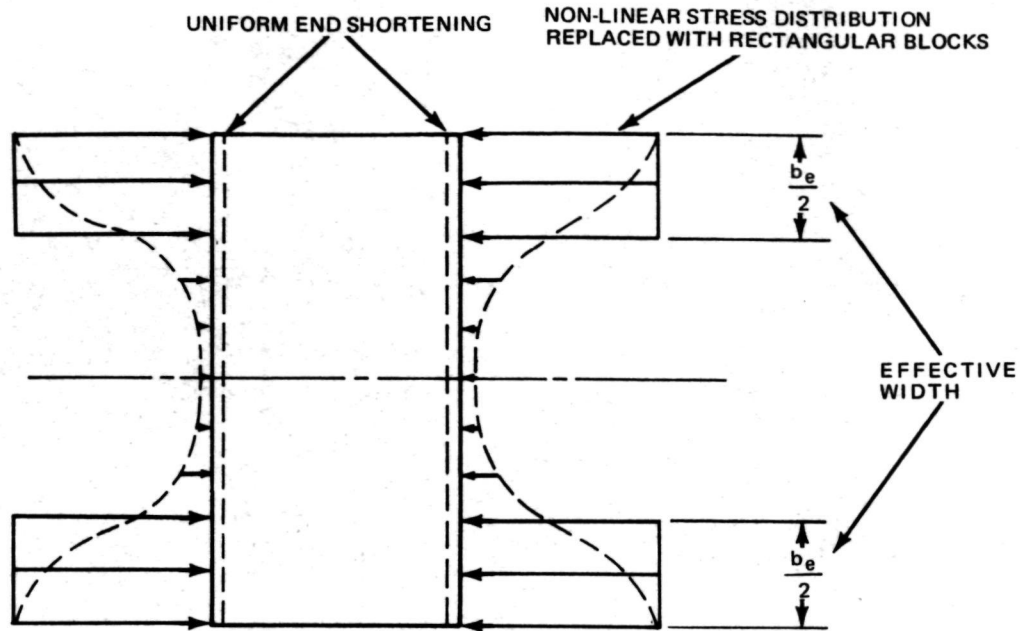
6.1.3 FUSELAGE

In Subsection 5.10 the effective width for uniformly strained panels containing initial imperfections was discussed. Time prevented the extension of this study to include bending and shear. For a fuselage section containing many longerons the uniaxial straining case is sufficient. The conventional procedure is to lump adjacent skin effective widths with the longeron areas using an effective width formula

$$b_e = b \left(\frac{\sigma_{ci}}{\sigma_i} \right)^n \quad (6-1)$$

where σ_{ci} is the Euler stress for the i th panel and σ_i is the bending stress obtained from $\sigma_i = \frac{My_i}{I}$. The moment of inertia, I , is dependent on the lumped areas, hence the procedure is iterative. Since the stress depends on the sign and value of the bending moment, the moment of inertia is load-condition dependent. When the constant n equals one-half, the formula is of the form suggested by Von Kármán. Marguerre suggested using two-thirds for the constant. Many other formulas have been suggested for calculating effective widths; however, again they are based on the uniaxial case. Where there are relatively few longerons the conventional effective width concept must be modified because a large stress gradient will exist across a given panel. The mid-section of the 1/8-scale model fuselage contains five longerons (two upper, two lower, and one on the center line). Thus, for the symmetric case a bending stress distribution exists in the sidewall skins; for the antisymmetric case, a bending stress distribution exists in the bottom deck.

The following rationale has been used to develop an effective amount of material to be considered as working in bending. In Fig. 6-1, the effective width is illustrated for a plate subjected to uniform end shortening. The stress drops off



T-106

Fig. 6-1 Stress Distribution Due to Uniform End Shortening

rapidly a short distance from the edge. Figure 6-2 illustrates an assumed stress distribution due to bending strains (the ends remain straight after bending). Again the stress is assumed to drop off from the linear $\left(\frac{My}{I}\right)$ distribution such that the inner portion becomes ineffective in resisting bending. The non-linear stress distribution is replaced with two trapezoidal blocks each having a height $\left(\frac{b_e}{2}\right)$ such that the moment of the trapezoidal blocks about the neutral axis is equal to the moment of the nonlinear distribution. The moment of the inertia of the partially effective rectangular section is

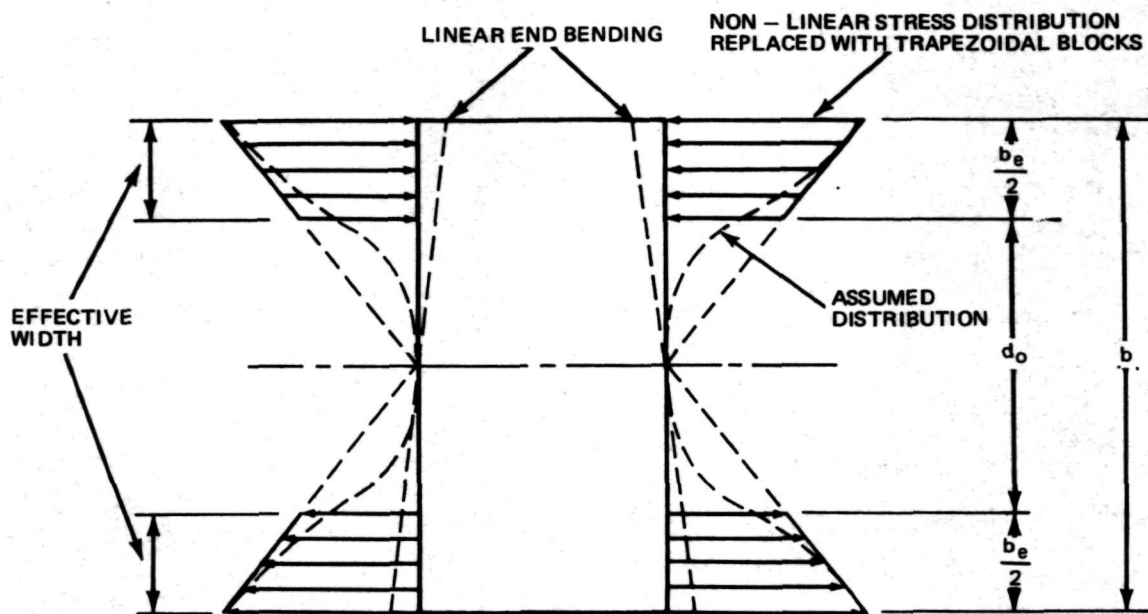
$$I = \frac{t}{12} \left(b^3 - d_o^3 \right) \quad (6-2)$$

where $d_o = (b - b_e)$ is the height of the ineffective material. Since the effectiveness factor is

$$e = \left(\frac{b_e}{b} \right) \quad (6-3)$$

then the ratio of the effective I_e to the fully effective value I_o is,

$$\left(\frac{I_e}{I_o} \right) = 1 - (1 - e)^3 .$$



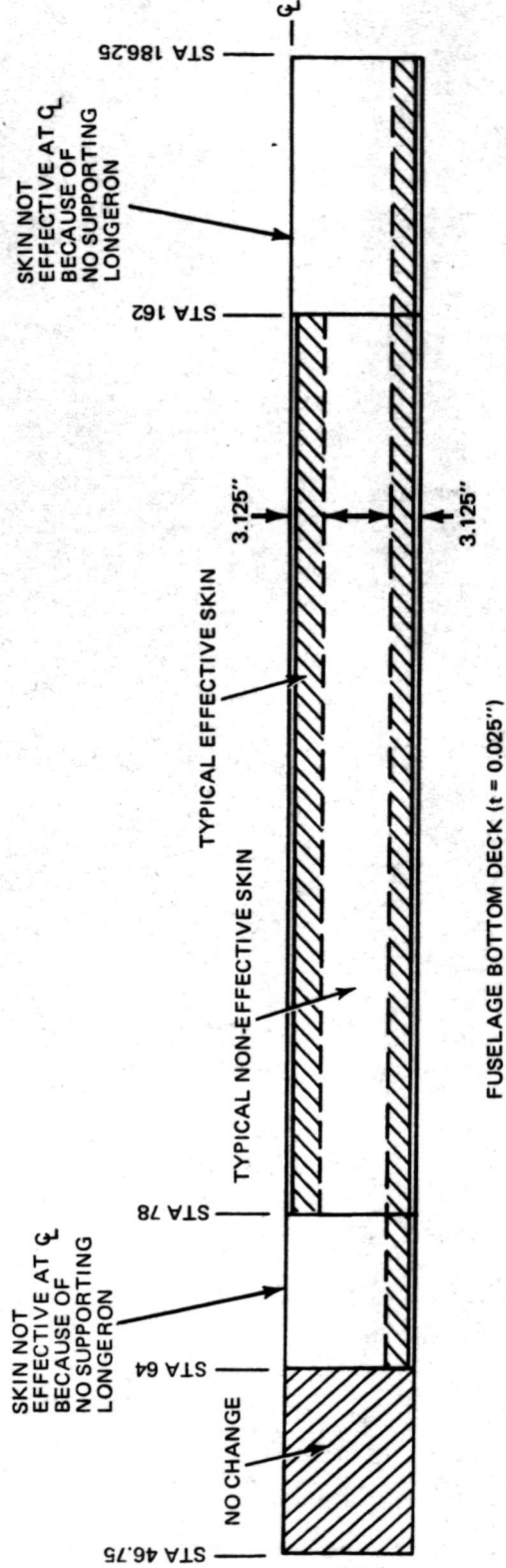
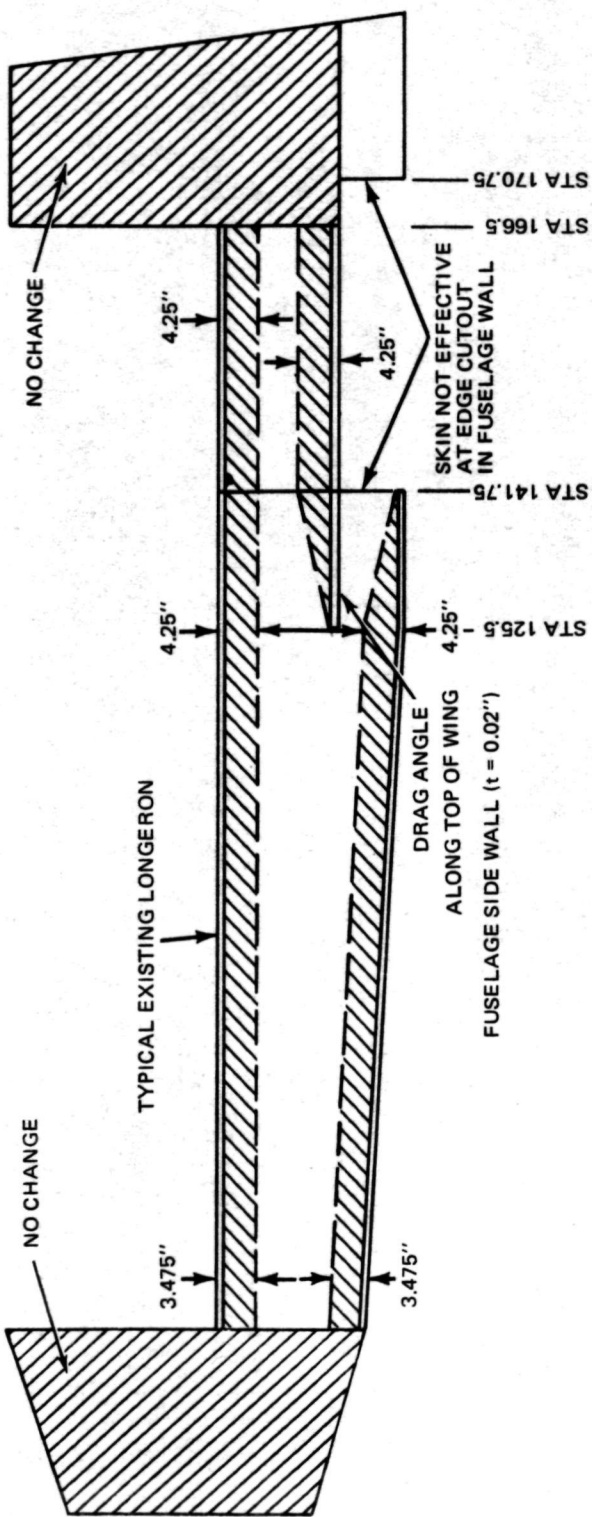
T-107

Fig. 6-2 Assumed Stress Distribution Due to Linear End Bending

This ratio is relatively insensitive for values of e above one-half as can be seen here:

e	(I_e/I_o)
0.4	0.784
0.5	0.875
0.6	0.936
0.7	0.973

It was decided to choose a common effectiveness factor for both the sidewall and bottom deck. This was done to simplify the situation and also recognize the fact that the symmetric and antisymmetric cases will produce reversed behavior in the side wall and bottom deck. (For the symmetric case, the bottom deck is loaded axially and the side wall is in bending; for the antisymmetric case, the side walls are loaded axially and the bottom deck is in bending). The common effectiveness factor leads to one overall model for representing both types of boundary conditions. From the analytical work discussed in Section 5 the common effectiveness factor was chosen to be one half. Applying this factor to the center of the fuselage, and projecting it along the length, resulted in the distribution of effective material shown crosshatched in Fig. 6-3 (Note that the wide crosshatch in the forward and aft regions



T-108

Fig. 6-3 Fuselage Effective Skin Widths

indicates that no change was made between Model I and Model II. These areas were left as an assemblage of direct stress elements). Since there is no center longeron between Stations 64 and 78, and 162 to 186.25, no effective material has been included in the bottom deck central strip. A transition in the sidewall effective material strips was provided between Stations 125.5 and 141.75 to recognize the sidewall cutout where the wing is attached, and the start of the angle attaching the top of the wing to the fuselage at WL 51.5.

Figure 6-4 shows a typical fuselage mid-section and illustrates how the effective widths were lumped into equivalent caps. In the NASTRAN model, the actual longerons were kept separate from the equivalent bar areas designated a_1 , a_2 and a_3 to facilitate possible future adjustment. The values of these areas were determined by solving three equations: the first equated the I_{yy} of the total equivalent section (Fig. 6-4A) to I_{yy} of the partially effective section (Figure 6-4B) the second equation preserved the location of the neutral axis; and the third employed an assumption,

$$a_2 = (a_1 + a_3).$$

This assumption is based upon an even proportioning of the effective width material. The lateral moment of inertia, I_{zz} , of the equivalent section was then checked against the I_{zz} of the partially effective section. For an effectiveness factor $e = 0.5$ this disagreement is approximately 10%.

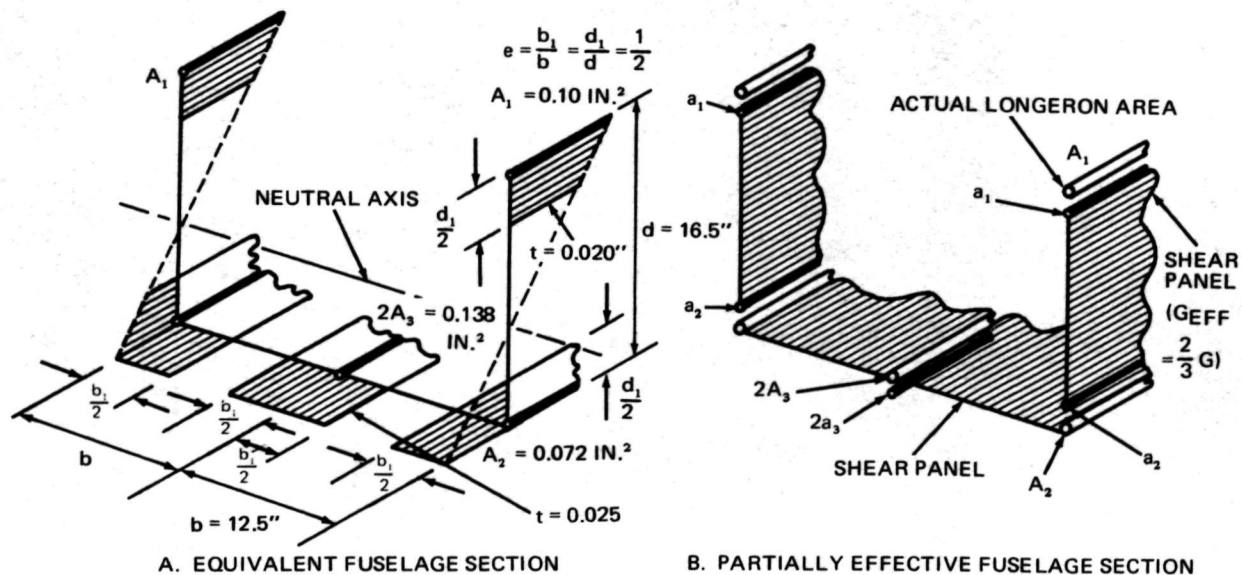


Fig. 6-4 Method for Lumping Effective Panel Widths into Equivalent Caps

If an attempt is made to preserve the I_{zz} , in lieu of the assumption that was employed, then a_2 becomes much larger and a_3 drops significantly. The results of three methods for calculating a_1 , a_2 , and a_3 are shown in Table 6-1. It was felt that to preserve both I_{yy} and I_{zz} required too drastic a shift in material; since this approach would introduce extraneous local shear lag effects, it was not used. Curves and tables in Appendix F of this volume give section properties at various fuselage stations for ranges in the effectiveness factor, e .

The value of I_{yy} for $e = 0.5$ is 57.8 (not including the doors); the fully effective value is 71.2. The ratio is

$$\frac{I_{yy}(e = 0.5)}{I_{yy}(\text{Fully Effective})} = \frac{57.8}{71.2} = 0.81$$

From Subsection 4.4, the ratio of mid-fuselage influence coefficients was

$$\frac{\delta_{33}(\text{Model I})}{\delta_{33}(\text{Test})} = \frac{35.61}{45.87} = 0.78$$

The rather good agreement tends to lend credibility to the analytical work and reasoning used in determining the effectiveness factor.

A shear effectiveness factor of two-thirds was used on all shear panels in the mid-fuselage region. This value is recommended in References 8, 9-10 and 9-11. Test results (Reference 9-12) on very thin diagonal tension beams gave ratios of G_{eff}/G ranging from 0.45 to 0.7, with an average of 0.6 for 12 tested panels. This substantiated to some extent the analytical result of two-thirds recommended by Stein (Reference 9-11). Although the aspect ratios of the tested panels differ from the 1/8-scale model, the value of two-thirds is believed to be representative of the actual behavior.

Model II contains the same fuselage grid refinement as Model I. Thus, a single shear panel was not used to cover the entire side wall or half of the lower deck. Phantom members having an area of 0.001 in.² were used as intermediate rod elements between the panels since the use of multiple panels permits variation in load at each corner attachment. Subdividing the shear panels allows for a more correct interaction

Table 6-1 Typical Fuselage Section Properties at Sta 116.0
(No Doors, Effectiveness Factor $e = 0.5$)

	Method 1 1. I_{yy} Preserved 2. N.A. Preserved 3. Assume $A_2 = (A_1 + A_3)$	Method 2 1. I_{yy} Preserved 2. N.A. Preserved 3. I_{zz} Preserved Not Used	Method 3 Summation of Effective Width X Thickness Not Used
A_1	0.057	0.061	0.083
A_2	0.121	0.166	0.161
A_3	0.064	0.027	0.078
I_{yy}	57.8	57.8	—
I_{zz}	109.6	124.6	—

TT-26

with the frames. However, when this is done, rods must be placed around the panels for stability. Of course, MPC's could have been used in lieu of the phantom rods, but experience shows that using rods is more convenient.

The fuselage was double-noded at Station 64.0, and a spring inserted in the axial direction to account for the flexibility of the joint (refer to Volume IIIA, Appendix A2). The value for the spring constant of 148,000 lb/in. was back-calculated from static test data. This value is approximately equal to a joint effectiveness factor of 70 %.

6.1.4 WING

Remodeling of the wing followed, in principle, the procedures used on the fuselage. A sketch of the wing effective material strips is shown in Fig. 6-5. A direct stress effectiveness factor of $e = 0.85$ was used in both the rib and spar directions for the upper and lower covers. This effectiveness factor is in line with the value obtained in Subsection 5.10 for a panel having an initial imperfection of $\left(\frac{W_0}{t}\right) = 1.0$. An effective shear modulus of $G_{eff} = 0.85 G$ was also used in the covers. The top and bottom covers were thus replaced with a rod and shear panel idealization. The equivalent rod areas were obtained by simply adding the effective cover material to the actual spar and rib caps.

A fully effective value of G was used for the spar and rib shear panels. Here, it was felt that the wing ballast weights (which are attached to the webs, at the midpoints,) would tend to minimize any initial imperfection, and also would act to prevent any out of plane deformation (panel bowing) when the structure is loaded.

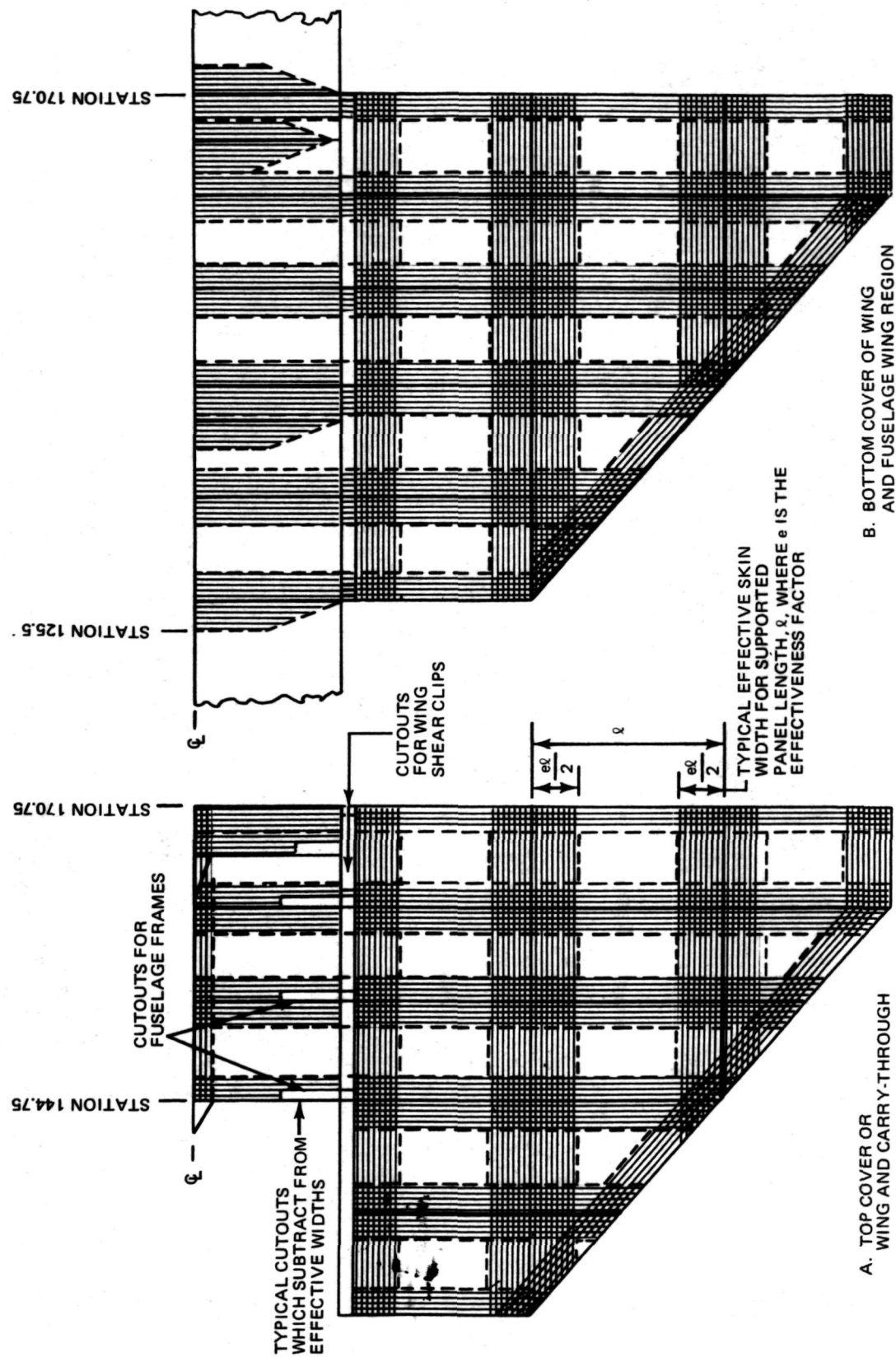


Fig. 6-5 Effective Wing Skin Widths

T-111

T-110

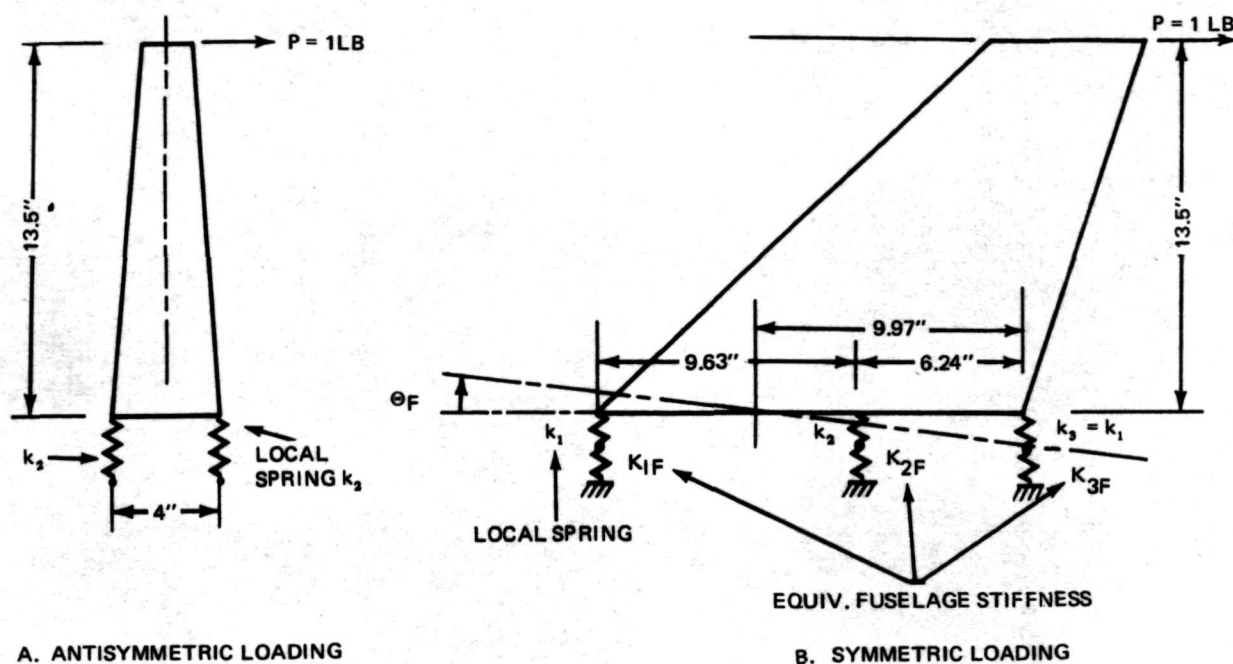
The grid system for Model II is much coarser than for Model I, with the mesh being set by the location of ribs and spars.

The wing effective width strips were extended into the carry-through structure as shown in Fig. 6-5. These widths were reduced where appropriate to account for cutouts. Note that the top cover of the carry-through does not contain an effective width strip along the fuselage side wall in the longitudinal direction. Here, the cutouts for the fuselage frames completely destroy the longitudinal continuity of the deck.

Static test results for loading at the wing tip were discussed in Subsection 5.11. There the ratio of Model I to test data was calculated to be 0.80. This is in good agreement with the theoretical initial imperfection calculations which indicate that an effectiveness factor of 0.85 would be used for Model II. The difference between 0.80 and 0.85 can be attributed to additional flexibility in the fuselage and wing carry-through not present in Model I, but being accounted for in Model II.

6.1.5 FIN

Springs were inserted between the fin and the fuselage to account for the local flexibility associated with the fin/fuselage connection. The values for the spring constants were based on the difference between static test and analytical values calculated using Model I. In Fig. 6-6, the local springs are identified as k_1 , k_2 , and k_3 . The equivalent fuselage spring constants K_{1F} , K_{2F} and K_{3F} were obtained by evaluating the fin fuselage interaction forces for a unit load applied at the fin ballast. This loading produces a local angular distortion, θ_{FA} (see Fig. 6-7), of the fuselage interface equal to 5.34×10^{-6} radians. Using this value the fuselage spring constants were found to be $K_{1F} = 18,150$ lb/in., $K_{2F} = 18,600$ lb/in., and $K_{3F} = 3,770$ lb/in. The difference in magnitude between points 1 or 2 and 3 indicates the relative softness of the aft frame. In the test, the relative angle, θ_{FT} , was found to be 17.51×10^{-6} radians. The difference between these two angles is a measure of the local springs that were added. To evaluate this redundant system the springs k_1 , k_2 and k_3 were placed in series with K_{1F} , K_{2F} and K_{3F} and the total angle, θ_{FT} , used to relate the applied force and the rotation and the combined spring system. This yielded one equation with three unknowns. The second equation was obtained by performing the same analysis, but for antisymmetric loading and assuming that all load was taken by the middle support. For the antisymmetric case, the local lateral analytical rotation was calculated to be 17.5×10^{-6} radians, while the static test gave a value of 43.3×10^{-6} radians. The



A. ANTISYMMETRIC LOADING

B. SYMMETRIC LOADING

T-112

Fig. 6-6 Local Springs to Account for Fin Connection Flexibility

final equation assumed the local springs k_1 and k_3 to be equal. Values of the various spring constants are shown in Table 6-2 where the third column gives values for the revised equivalent local fuselage springs, including the flexibility of the connection. Observe that a rather large change has been made to the forward connection (approximately 80 %).

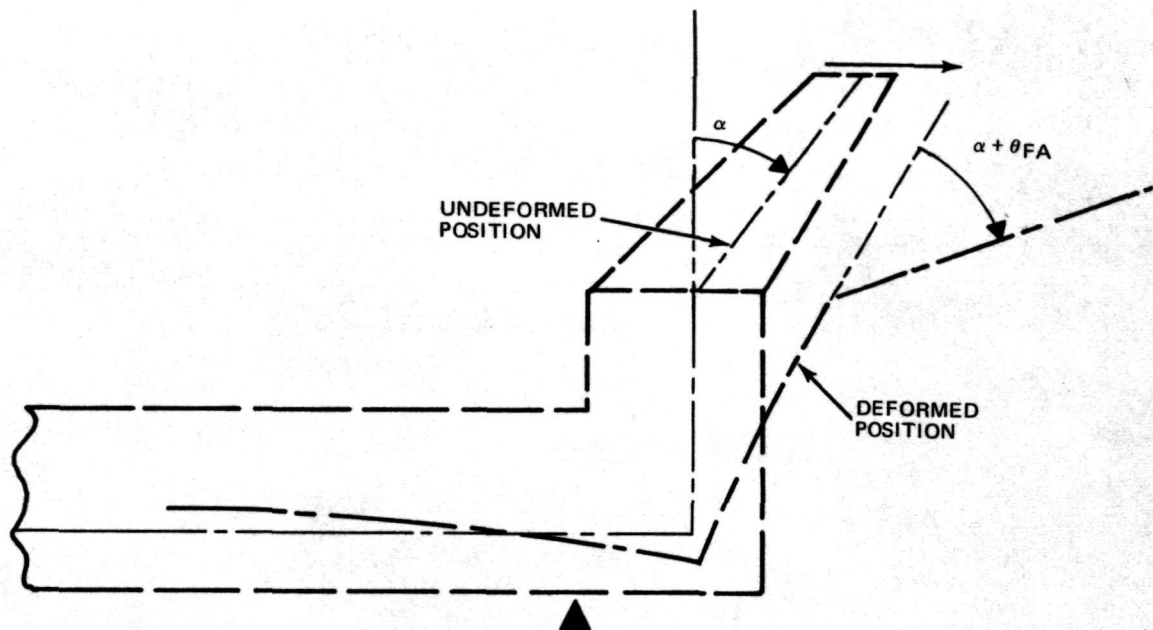
Recommendations for changing the design of the forward attachment were made early in the study. However, as mentioned previously, these suggestions were not

Table 6-2 Local Spring Constants to Account for Fin Connection Flexibility

Equivalent Local Fuselage Springs (Model I)	Local Springs Added to Model I	Equivalent Local Fuselage Spring Including Connection(a)
$K_{1F} = 18,150$	$k_1 = 4,350$	$K_{1C}^{(a)} = 3,500$
$K_{2F} = 18,600$	$k_2 = 65,500$	$K_{2C} = 14,500$
$K_{3F} = 3,770$	$k_3 = 4,350$	$K_{3C} = 2,020$

TT-27

$${}^a K_{iC} = \frac{1}{\left(\frac{1}{K_{iF}} + \frac{1}{k_i} \right)}, i = 1, 2, 3$$



T-113

Fig. 6-7 Local Fuselage Angular Distortion, θ_{FA}

implemented because the workload in Langley shops indicated a large slippage in testing schedule would result. On balance, it was decided that more productive information could be obtained from continued tests of the existing experimental model to uncover other possible sources of disagreement.

A side investigation (not reported in Section 5) entailed analytically "cutting" the forward fin connections. The effect of doing this was to drop the frequency of the first fuselage bending mode from 53.2 Hz to 48.05 Hz. Analytically "cutting" the aft connection produced a minor change in the frequency.

Thought was also given to modeling the connection in detail (again as a side study) to obtain equivalent spring constants to incorporate in the overall analysis. This idea was also abandoned because of joint nonlinearities. The simplest and most straightforward approach was to use the test data.

6.1.6 CARGO DOORS

In remodeling the cargo door region, particular attention was paid to the actual location of the fuselage and door longerons and the details of the straps that connect the door to the fuselage. These details are shown in Fig. 5-37, 5-39 and 5-40. These changes added greatly to the flexibility of the cargo-door/fuselage interface as discussed previously in Subsection 5.12.

6.1.7 PAYLOAD

Static test No. 26 (a Z load on the payload at Station 117.5) revealed relative motion between points A and B (Fig. 6-8) on the payload and points A' and B' on the fuselage. The absolute and relative deflections are shown in Table 6-3 for a unit load at point C on the payload. Note that Model I did not account for this relative motion. To account for the discrepancy, it was decided to add vertical springs equal to $2k_1$ at the forward support (k_1 for the half structure) and k_2 at each of the aft supports. Since the payload is determinately supported, a load, P, at Station 117.5 produces reactions of $0.46 P$ and $0.54 P$ at stations 78.0 and 151.88, respectively.

The values of the spring constants are thus:

$$k_1 = \frac{0.46}{(2)(0.99 \times 10^{-5})} = 23,150 \text{ lb/in. and } k_2 = \frac{(\frac{1}{2})(0.54)}{(0.84 \times 10^{-5})} = 32,250 \text{ lb/in.}$$

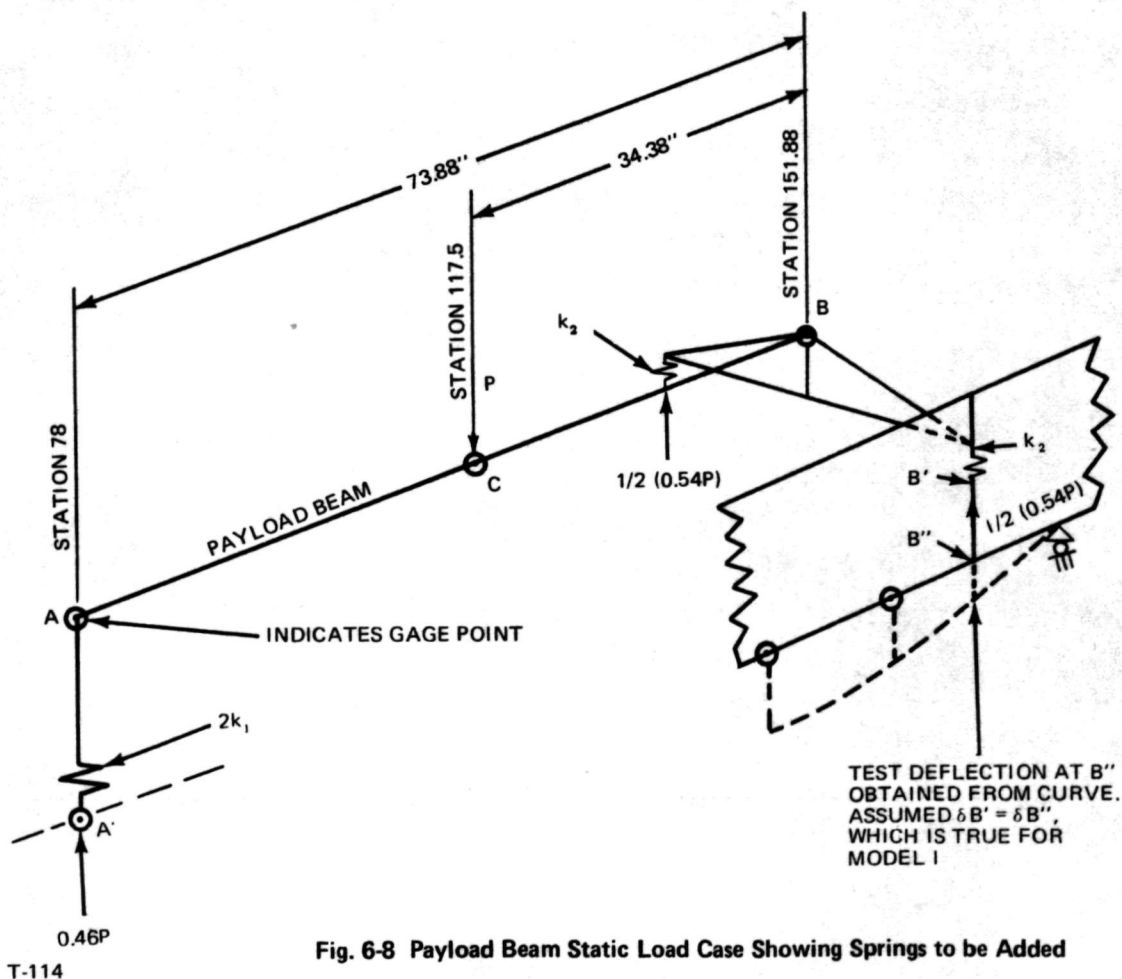


Fig. 6-8 Payload Beam Static Load Case Showing Springs to be Added

Table 6-3 Comparison of Analytical and Experimental Deflections

Point	P = 1 lb Vertical Deflection in.		Payload Deflection Relative To Fuselage, in.	
	Test	Model I	Test	Model I
A	3.03×10^{-5}	1.39×10^{-5}	0.99×10^{-5}	0
A'	2.04×10^{-5}	1.39×10^{-5}	0	0
B	1.87×10^{-5}	0.69×10^{-5}	0.84×10^{-5}	0
B'	1.03×10^{-5}	0.69×10^{-5}	0	0
C	4.24×10^{-5}	2.71×10^{-5}	2.74×10^{-5}	1.69×10^{-5}

TT-28

6.2 NASTRAN ANALYSIS FOR MODEL II

6.2.1 COMPONENT RESULTS

The NASTRAN analysis of Model II followed the procedures outlined in Subsection 3.3, except that the springs between the payload and fuselage, and the fin and fuselage, were added in Phase II of the analysis. The frequencies of the first three modes for the various components are given in Table 6-4 together with the results obtained using Model I.

Table 6-4 Frequencies for Orbiter Structures — Comparison of Models I and II

Substructure	Frequency Hz					
	1 st Mode		2 nd Mode		3 rd Mode	
	I	II	I	II	I	II
Fuselage						
• Free, Symmetric	62.2	55.2	129.9	109.9	191.3	154.3
• Free, Antisymmetric	28.8	25.1	89.1	73.8	128.3	110.0
Payload						
• Restrained, Symmetric	81.2	81.2 ^(a)	268.5	268.5 ^(a)	627.7	627.7 ^(a)
• Restrained, Antisymmetric	68.6	68.6 ^(a)	175.4	175.4 ^(a)	462.8	462.8 ^(a)
Cargo Doors						
• Free, Symmetric	4.6	4.3	10.7	10.9	17.6	19.9
• Restrained, Antisymmetric	156.4	151.7	622.2	319.8	1054.6	384.3
Wing						
• Restrained	77.6	74.5	158.3	148.7	259.9	254.5
Fin						
• Restrained, Symmetric	264.2	281.2 ^(b)	841.3	852.2 ^(b)	1263.3	1269.4 ^(b)
• Restrained, Antisymmetric	107.8	137.5 ^(b)	407.2	462.7 ^(b)	1018.7	1307.1 ^(b)

^aSprings Added in Phase 2^bSupports Changed, Springs Added in Phase 2

TT-29

6.2.2 ORBITER RESULTS

The frequencies for the total symmetric and antisymmetric Orbiter are given in Table 6-5 together with the results obtained using Model I. These results and a comparison with test data will be discussed in Section 7.

Table 6-5 Frequencies for Symmetric and Antisymmetric Modes for Models I and II

Mode	Frequency, Hz Symmetric Case		Frequency, Hz Antisymmetric Case	
	Model I	Model II	Model I	Model II
1	53.2	44.2	52.9	42.2
2	62.6	54.4	72.6	57.0
3	75.2	63.0	85.1	58.6
4	108.5	80.2	92.0	71.6
5	133.7	103.5	101.5	78.9
6	156.3	115.9	135.3	103.5
7	162.2	121.6	—	120.3
8	175.2	139.7	—	146.5
9	216.4	170.9	—	159.2
10	—	185.0	—	196.1

TT-30

Section 7
CORRELATION OF ANALYTICAL AND
EXPERIMENTAL RESULTS

SECTION 7

7 - CORRELATION OF ANALYTICAL AND EXPERIMENTAL RESULTS

7.1 STATIC TEST CORRELATION

The static testing procedure was described in Section 4, together with some limited correlation with the Model I results. A list of the various static tests is given in Table 4-3 and the location of the dial gages that were used to measure deflections is shown in Fig. 4-7. Table 7-1 indicates the static tests used as the basis of correlation between test data and both Model I and Model II analytical results. Deflection plots of the structure, obtained from test and analysis, are shown in Fig. 7-1 through 7-10. Individual load deflection plots are contained in Volume IIIA, Appendix A3, and Appendix G of this volume.

Stresses in the fuselage panels at the upper longeron, lower longeron, and bottom deck are also plotted in Fig. 7-1 through 7-7. The stresses have been calculated using $\left(\frac{Mc}{I}\right)$ where a reduced value of the moment of inertia has been used. The values of the moment of inertia, extreme fiber distances c_1 and c_2 , and the reciprocal of the section modulus $\left(\frac{c}{I}\right)$, are plotted in Fig. 7-11. The following nomenclature has been used in Fig. 7-1 through 7-8:

- σ_T (D.L.) = bending stress at top longeron level $\left(\frac{Mc}{I}\right)$, due to 1-g Load
- σ_T (L.L.) = bending stress at top longeron level $\left(\frac{Mc}{I}\right)$, due to Live Load
- σ_T (TOT) = bending stress at top longeron level $\left(\frac{Mc}{I}\right)$, due to 1-g and Live Load
- σ_B (D.L.) = bending stress at bottom deck level $\left(\frac{Mc}{I}\right)$, due to 1-g Load
- σ_B (L.L.) = bending stress at bottom deck level $\left(\frac{Mc}{I}\right)$, due to Live Load
- σ_B (TOT) = bending stress at bottom deck level $\left(\frac{Mc}{I}\right)$, 1-g and Live Load
- σ_c (Bot. Deck) = elastic buckling stress of bottom deck
- σ_c (Sidewall-Top) = elastic buckling stress of side wall for positive bending
(compression top)
- σ_c (Sidewall-Bot.) = elastic buckling stress of side wall for negative bending
(compression bottom)

Table 7-1. Static Test Correlation

Loading Condition	Static Test No.	Cargo Doors	Reference (Fig. No.)	Load-Deflection Plots	Influence Coeff. $\times 10^6$, in./lb			Remarks
					Test	Model I	Model II	
• Mid Fuselage $P_z = -80$ lb @ 117.5 $P_z = +120$ lb @ 116.0 $P_z = +120$ lb @ 116.0 $P_z = -80$ lb @ 117.5	3 4 5 6	On On Off Off	7-1 7-2 7-3 7-4	A3-1 Thru A3-5 A3-6 Thru A3-10 A3-11 Thru A3-15 A3-16 Thru A3-20	40.9 40.6 44.75 47.0	31.0 31.0 35.61 35.61	44.82 44.82 — —	Buckling - Top Sidewall (87.0 \rightarrow 150) No Buckling No Buckling Buckling - Top Sidewall (87.0 \rightarrow 150)
• Forward Fuselage $P_z = -110$ lb @ 46.8 $P_z = +140$ lb @ 46.8 Nose Torsion	7 8 30	Off Off On	7-5 7-6 G-11	A3-21 Thru A3-22 A3-23 Thru A3-26 G8 Thru G10	80.75 85.35 0.243	55.4 55.4 0.150	72.97* 72.97* 0.37	Buckling - Bottom Deck (68 \rightarrow 87) Buckling - Top Sidewall (68 \rightarrow 150)
• Wing Tip $P_z = -25$ lb @ FS 162, BL 61.6	13	On	7-8, 7-9	A3-32 Thru A3-35	340.0	290.0	341.4	Buckling of Bottom Cover (See Fig. 7-8)
• Fin Ballast $P_x = +65$ lb @ Ballast $P_y = -45$ lb @ Ballast $P_x = -45$ lb @ Ballast	18 31 21	Off Off On	G-4 G-7 7-7	G1 Thru G3 G5 Thru G6 ---	388.0 695.0 380.0	186.8* 286.0* 186.8	360.1* 567.6* 360.1	Buckling - Top Sidewall (103 \rightarrow 162)
• Payload	26	Off	7-10	G12 Thru G14	42.4	27.9	39.2*	

* Model II with Cargo Door On

TT-191

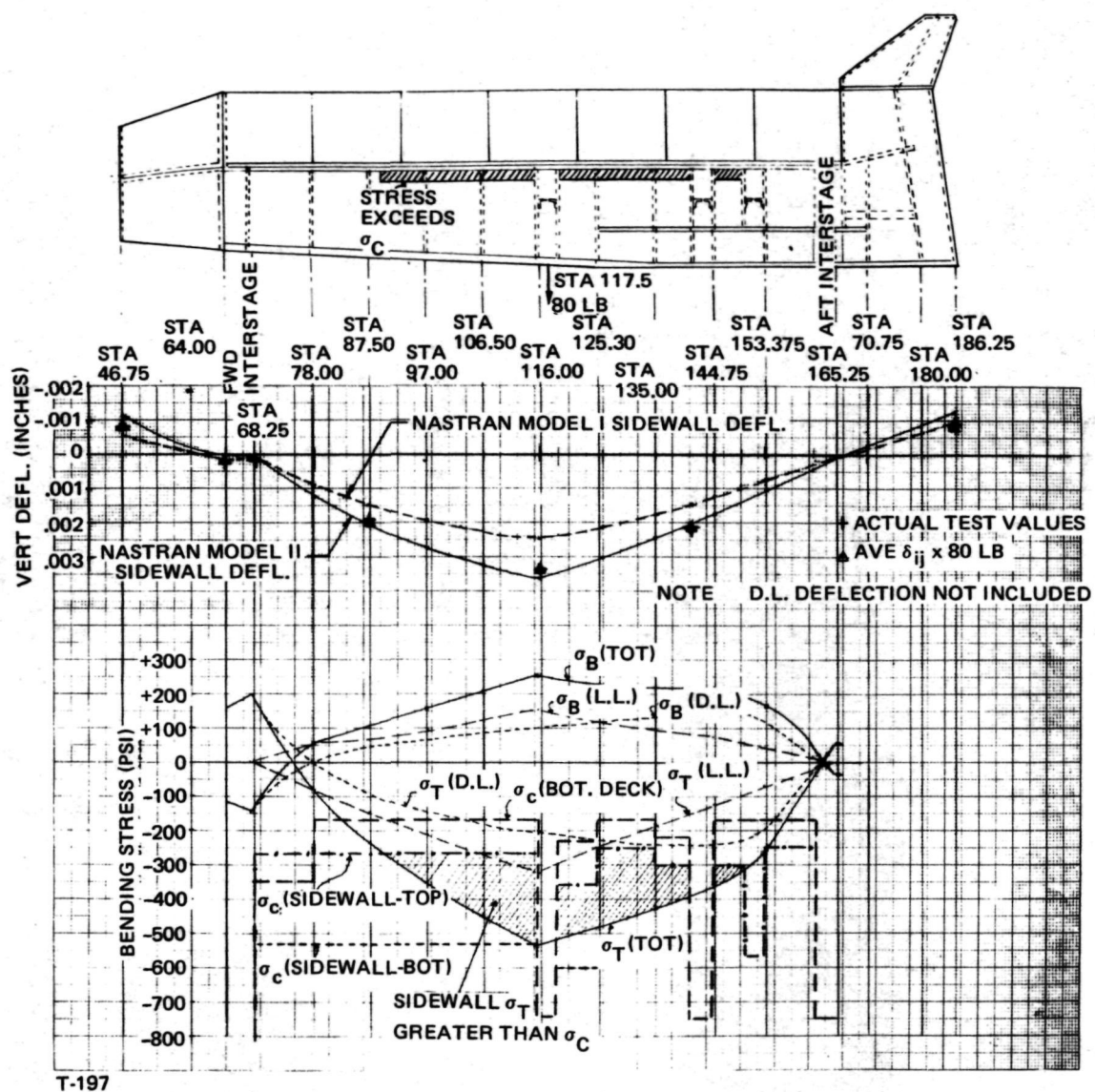


Fig. 7-1 Static Test No. 3 – Stress and Deflection Correlation

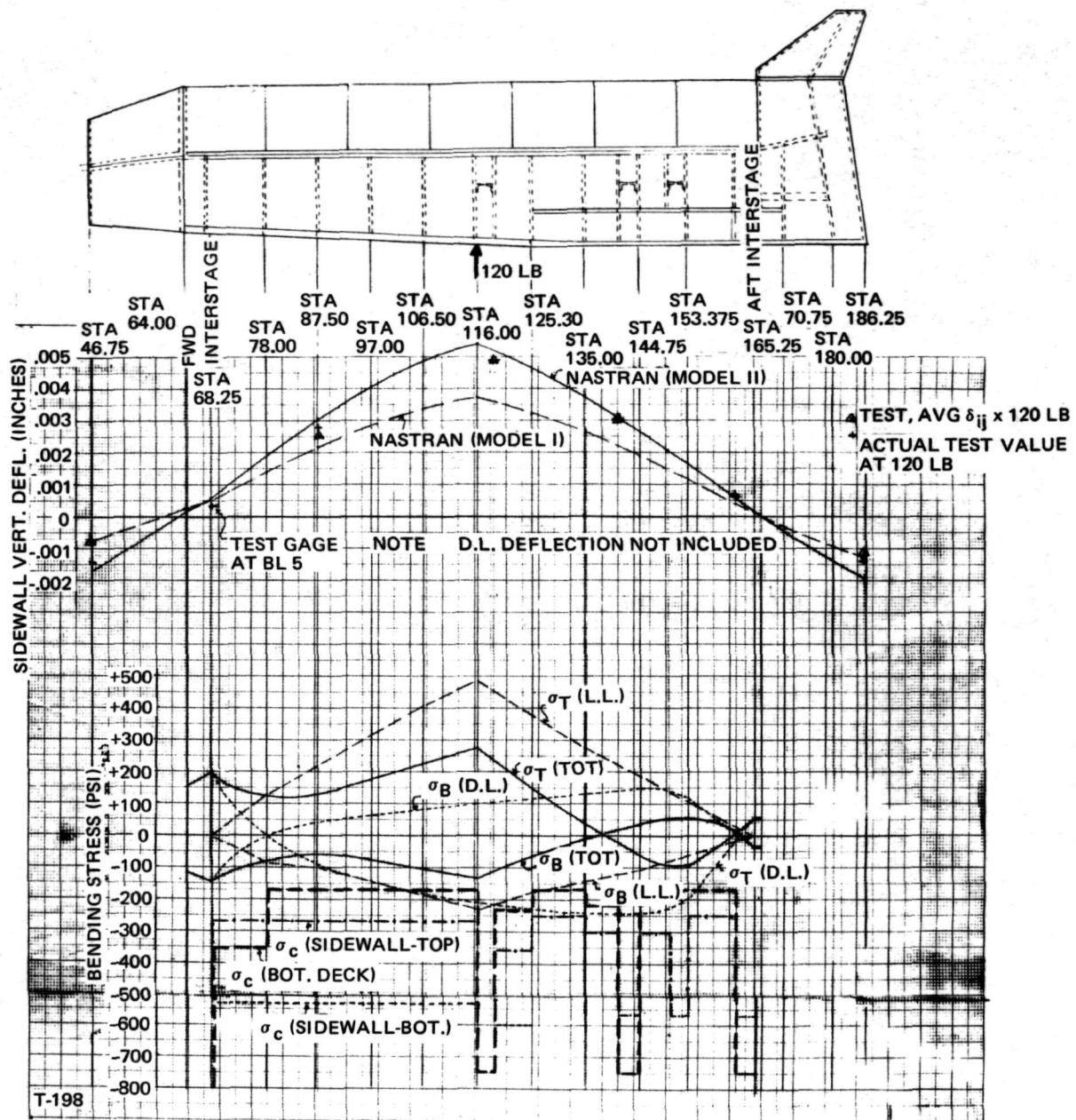


Fig. 7-2 Static Test No. 4 – Stress and Deflection Correlation

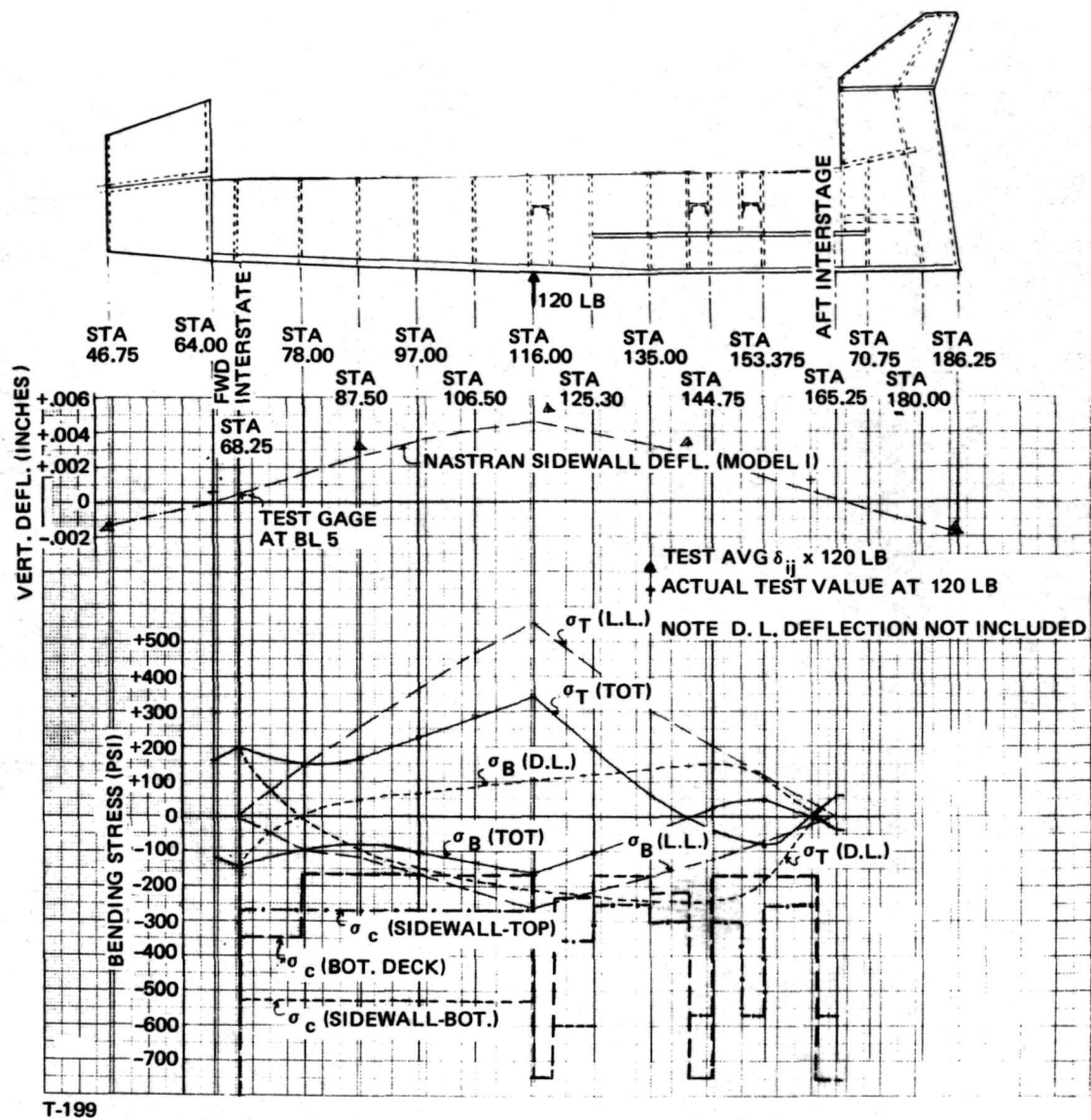


Fig. 7-3 Static Test No. 5 – Stress and Deflection Correlation

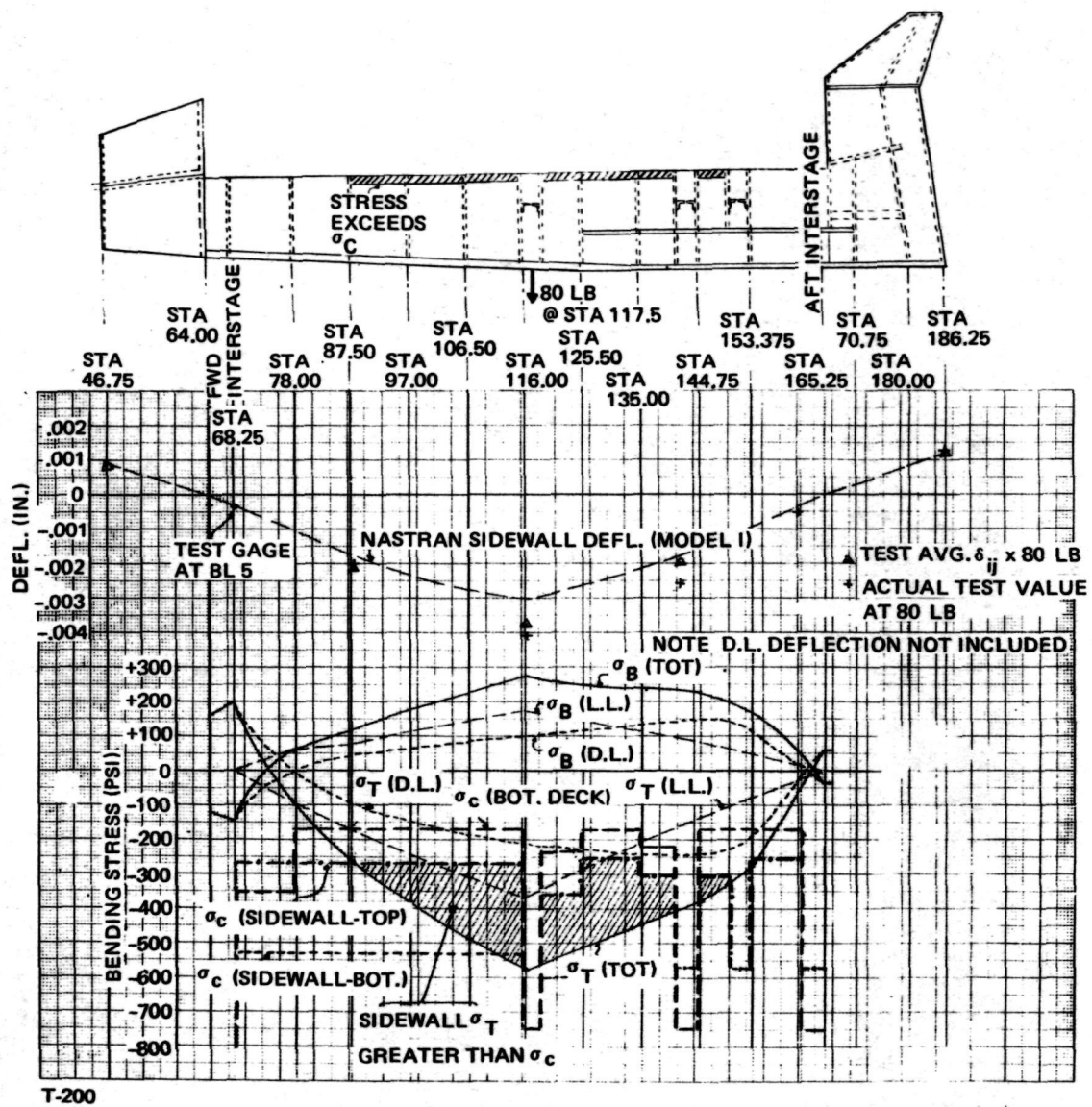


Fig. 7-4 Static Test No. 6 – Stress and Deflection Correlation

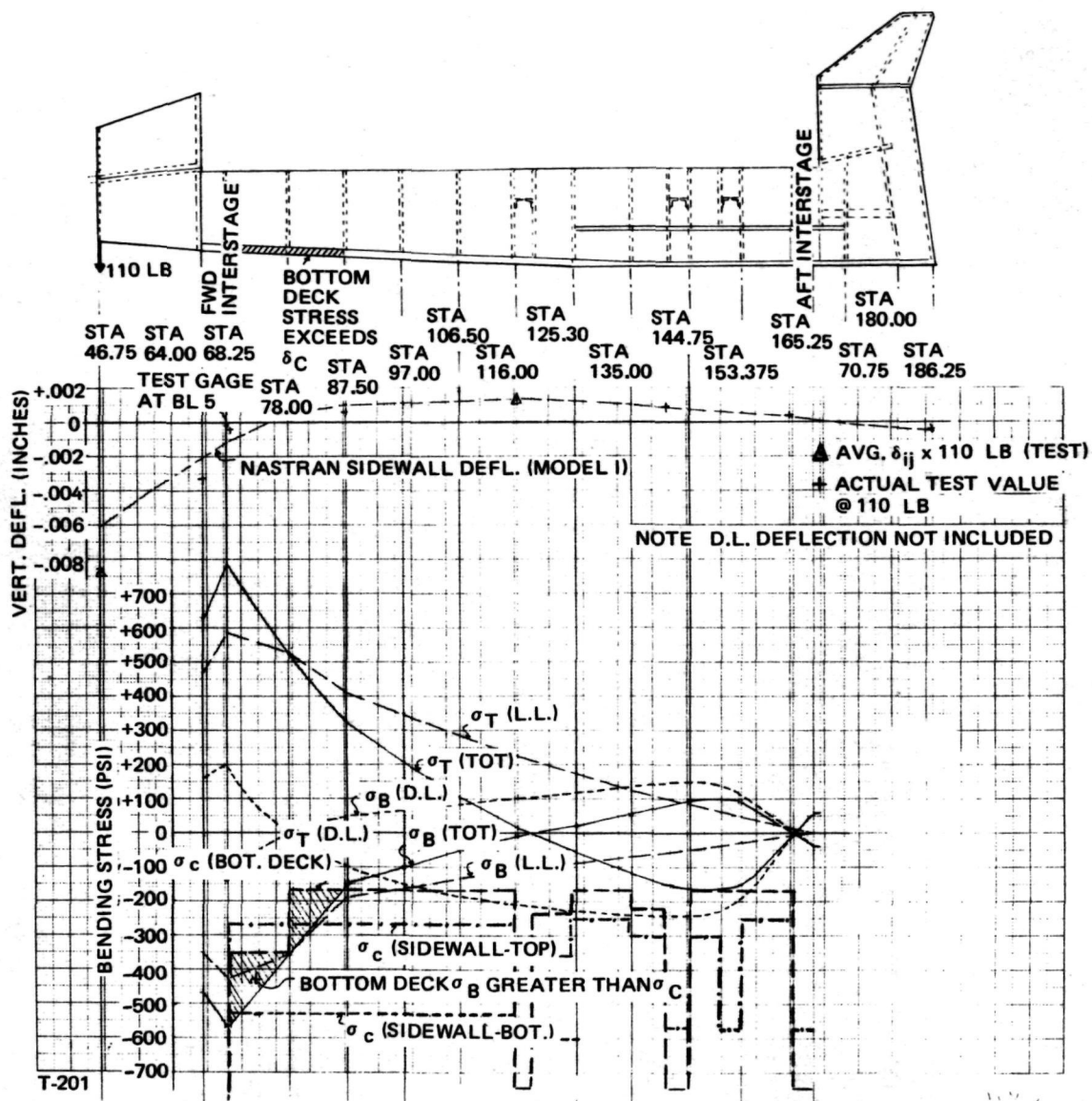


Fig. 7-5 Static Test No. 7 – Stress and Deflection Correlation

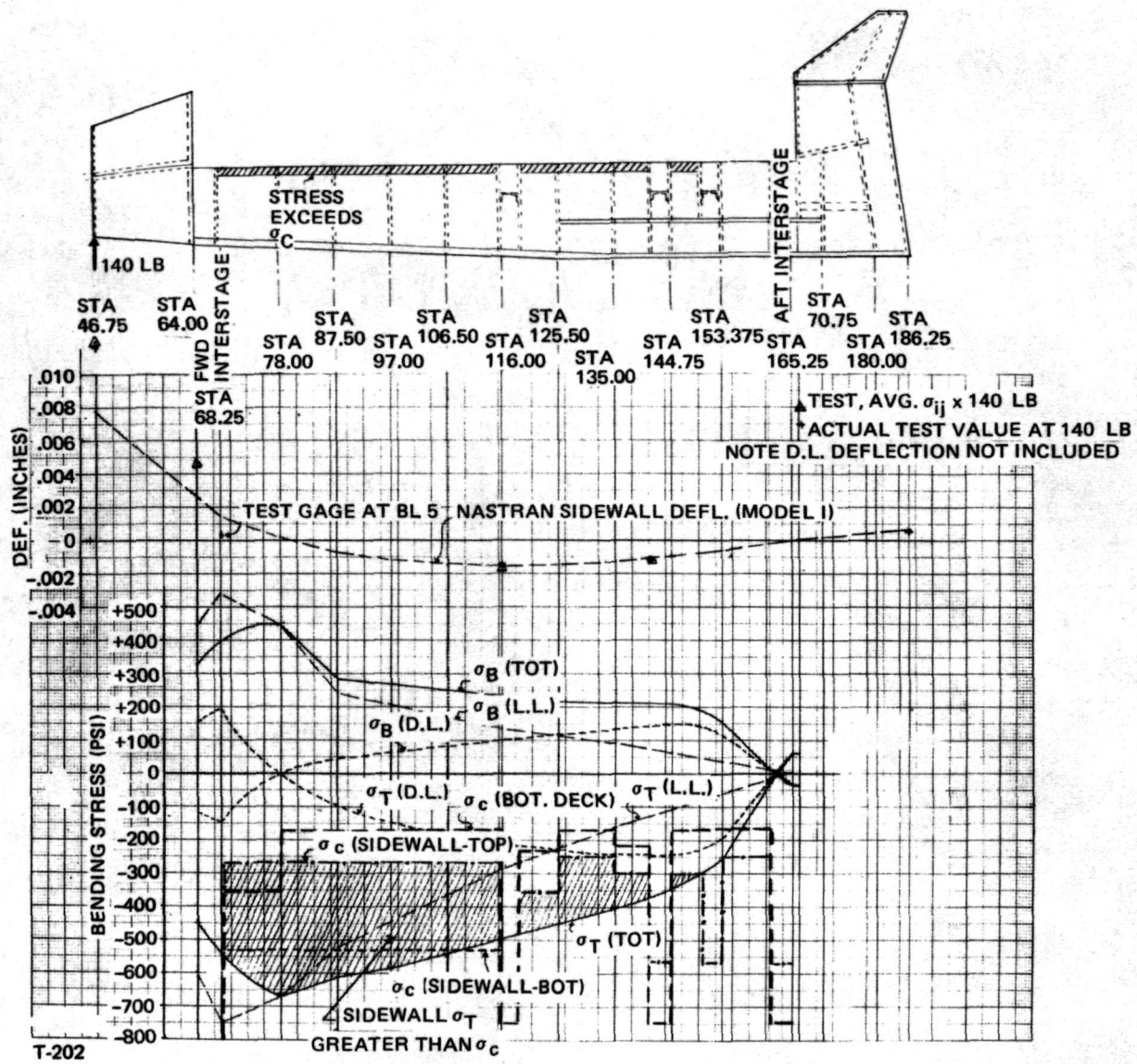


Fig. 7-6 Static Test No. 8 – Stress and Deflection Correlation

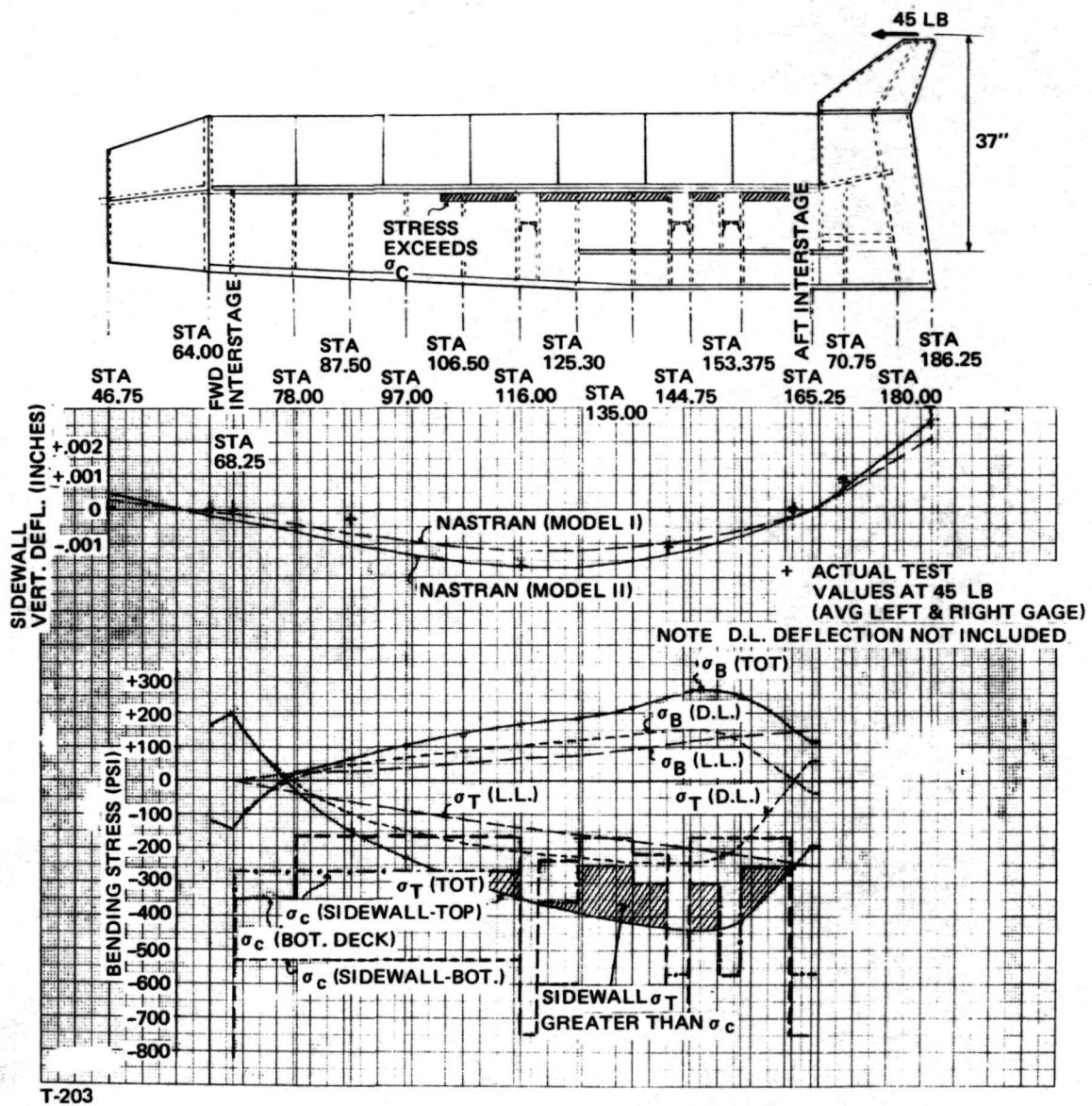


Fig. 7-7 Static Test No. 21 – Stress and Deflection Correlation

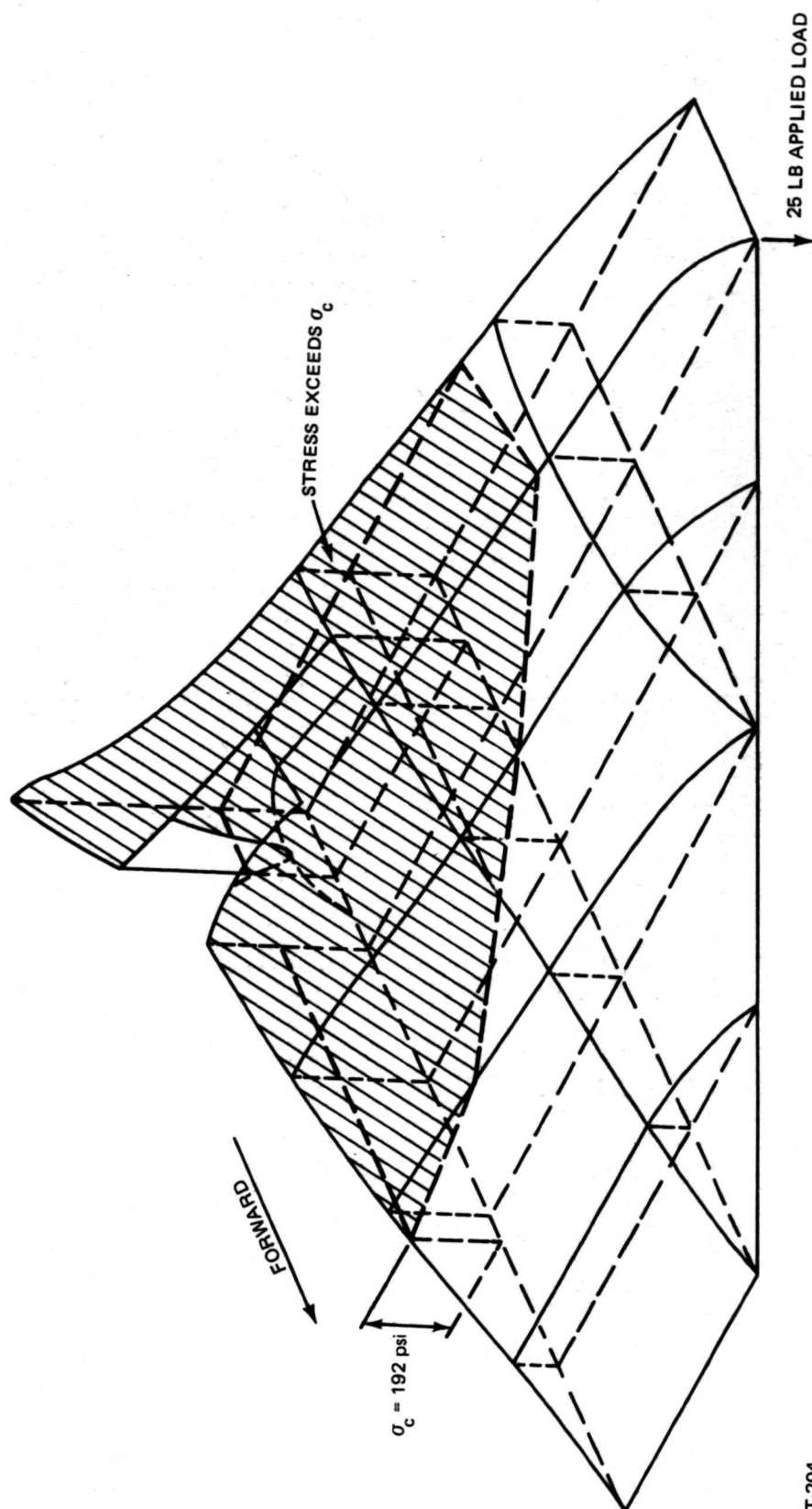


Figure 7-8 Wing Bottom Cover Compressive Bending Stress (Model 1) (Dead Load Included)

T-204

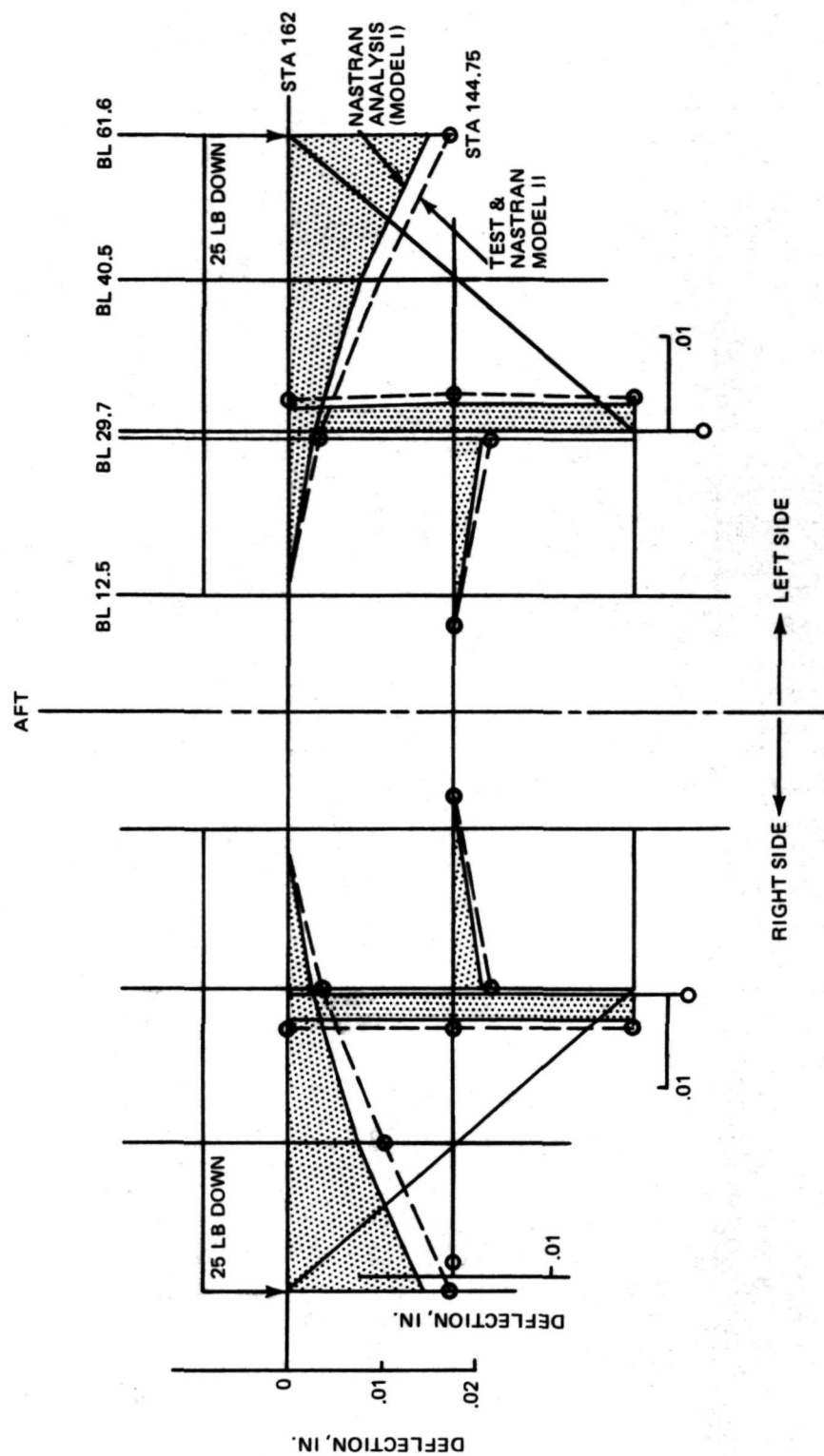


Fig. 7-9. Wing Static Deflections - (Run 13) Test and Analysis Comparison

T-205

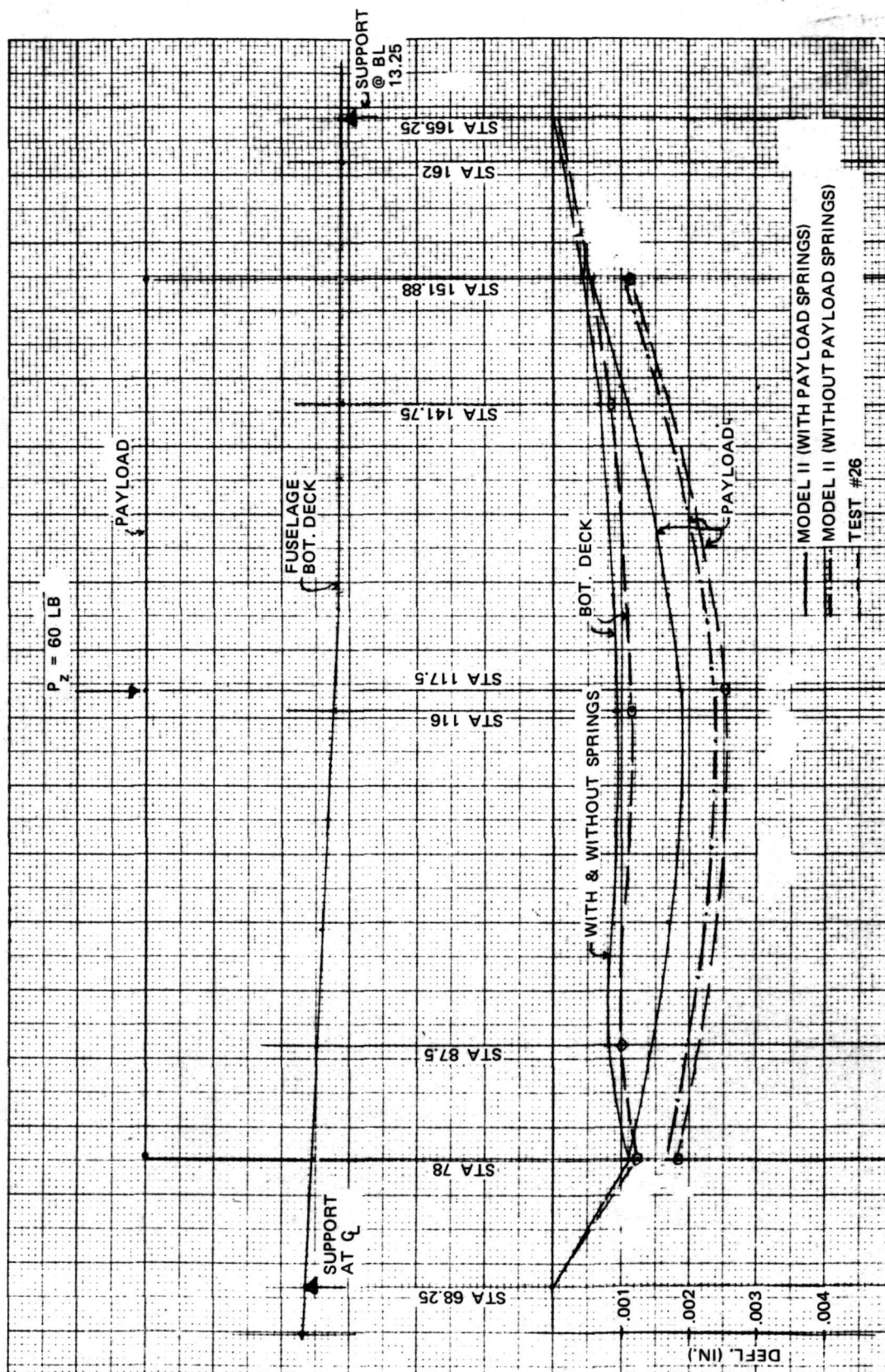


Fig. 7-10. Correlation of Payload Deflections - Static Test No. 26

T-206

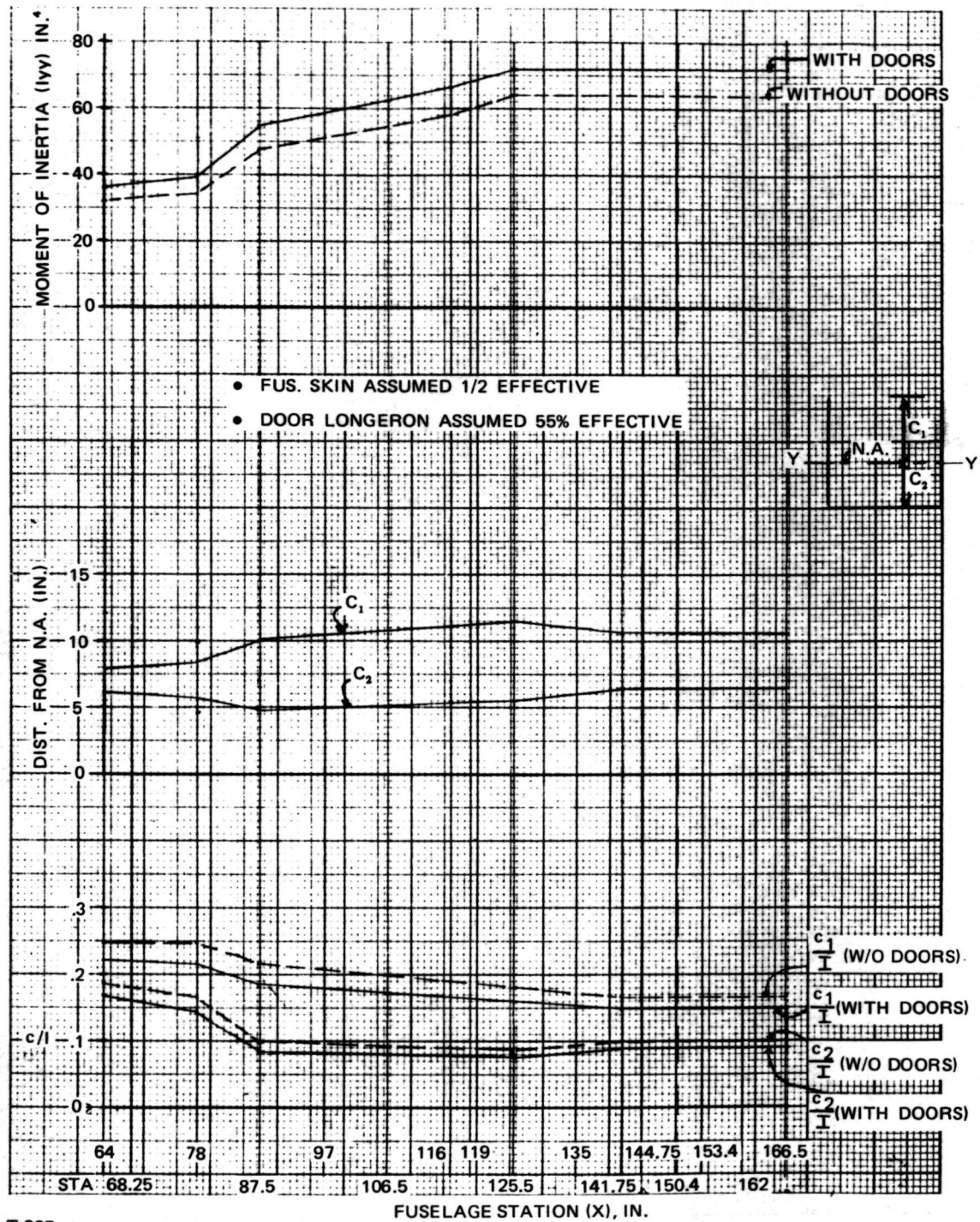
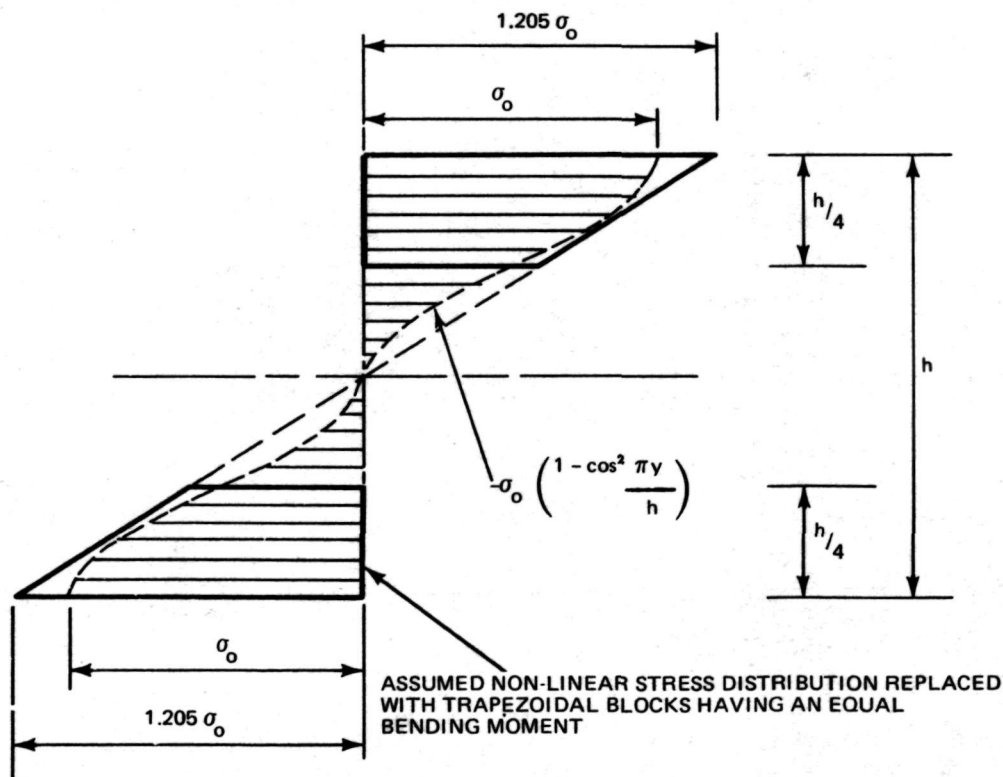


Fig. 7-11. Fuselage Section Property Curves

The critical stresses, σ_c , are based on linear elastic values given in Tables 5-9 and 5-10. The cross hatched regions in Fig. 7-1 through 7-8 indicate where the values of σ (Total) = $\sigma(1_g) + \sigma$ (Live Load) exceed the linear elastic critical stresses. The $\left(\frac{Mc}{I}\right)$ stresses are perhaps 20 % larger than the actual values as indicated in Fig. 7-12. Here, it is assumed that the actual stress varies as $\sigma = \sigma_o \left(1 - \cos^2 \frac{\pi y}{h}\right)$ because of the presence of an initial bow. If the nonlinear distribution is replaced with trapezoidal blocks having an equal bending moment, then the linear $\left(\frac{Mc}{I}\right)$ value, represented by the trapezoidal distribution, will exceed the maximum nonlinear value by 20 %. The critical stresses are based on the assumption that the panels are simply supported; therefore, any restraint provided by the frames will increase these values. The crosshatched regions thus tend to over-estimate the behavior, although they do indicate a basic softening of the structure that is reflected in the values of the influence coefficients obtained by the method illustrated in Fig. 7-13. The lower portion of the load deflection curves (Fig. 7-13) between zero and 50 % of the maximum was used to determine the loading influence coefficient, δ_{ij}^L , and the unloading influence coefficient, δ_{ij}^u . Note that the load deflection curves exhibit hysteresis effects (refer to Volume IIIA, Appendix A3),



T-208 Fig. 7-12 Equivalent Trapezoidal Stress Blocks for an Assumed Nonlinear Stress Distribution

and that the plots for the gages at the point of load application are more nearly linear. The deflection plots for Model II (cargo doors on) agree rather well with test data (Table 7-2), as can be seen from Fig. 7-1, 7-2, 7-7, 7-9, and 7-10.

Figure 7-8 illustrates the wing bottom cover bending stress distribution. These values were obtained by fairing curves through panel average stresses. The drop in the aft portion of the cover stress is due to the redistribution caused by the cutout provided for the interstage fitting. The wing deflections for Model II agree closely with test measurements as shown in Figure 7-9.

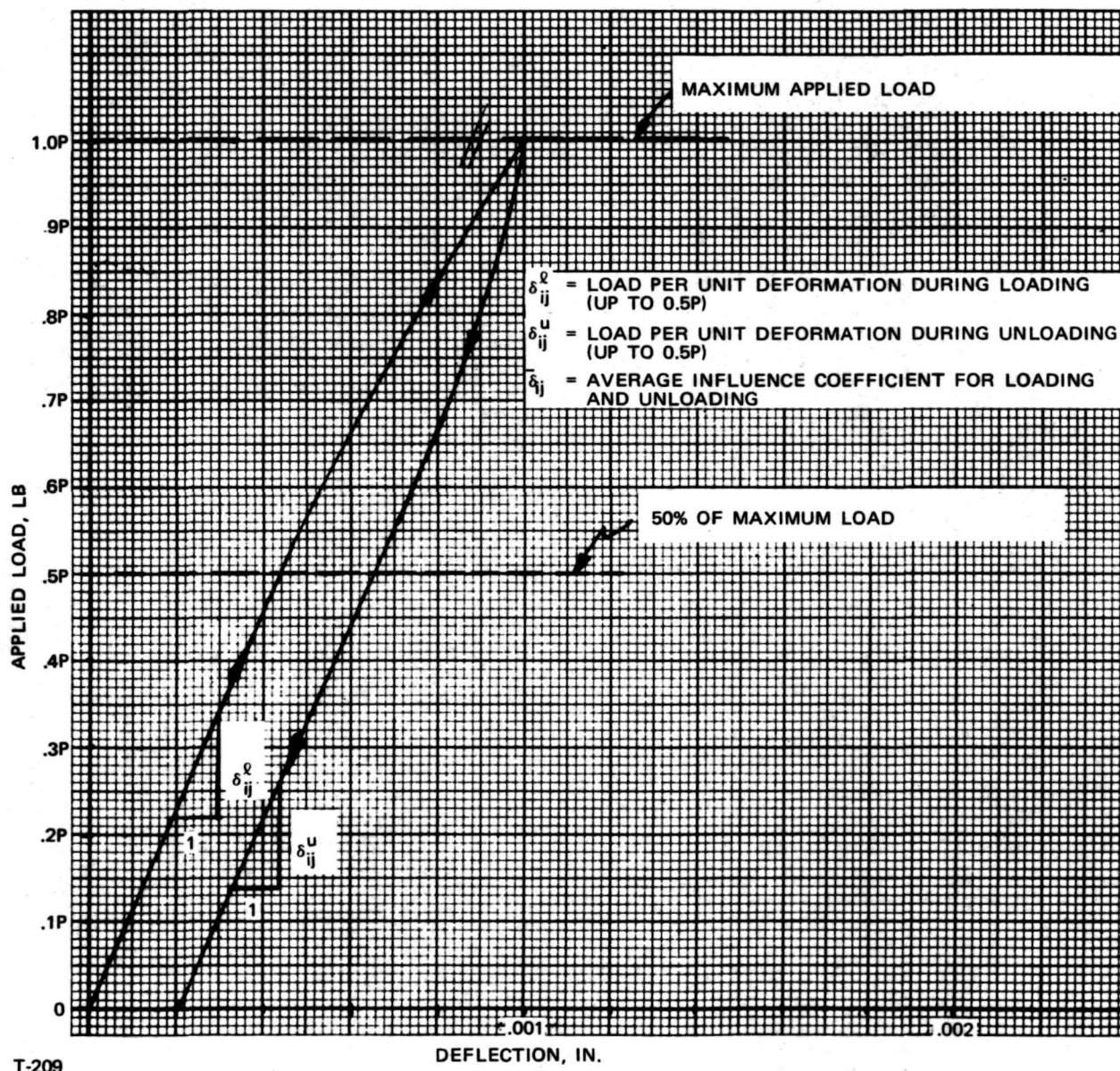


Fig. 7-13. Method Used to Obtain Experimental Influence Coefficients

Table 7-2. Fuselage Influence Coefficient Correlation

Influence Coeff, In./lb	Mid-Fuselage Load, Cargo Doors On						Mid-Fuselage Load, Cargo Doors Off						Nose Load, Cargo Doors Off									
	Test Run 3, Down Load Sta 117.5			Test Run 4, Up Load Sta 116			Test Run 6, Down Load Sta 117.5			Test Run 5, Up Load Sta 116			NASTRAN Anal. Value		Test Run 7, Down Load Sta 46.8		Test Run 8, Up Load Sta 46.8					
	Model I	Model II	Avg	Loaded	Un- loaded	Avg	Loaded	Un- loaded	Avg	Loaded	Un- loaded	Avg	Loaded	Un- loaded	Model I	Model II	Loaded	Un- loaded	Avg			
	2	3	4	5	6	7	8	9	10	11	12	13	14	15	16	17	18	19	20	21	22	23
1																						
δ_{13}	-6.82	-14.19	-11.0	-8.9	-9.95	-7.4	-5.4	-6.4	-11.37	-10.1	-10.4	-10.25	-10.6	-14.0	-12.3							
δ_{23}	18.14	25.76	24.7	23.8	24.25	21.3	20.8	21.05	22.03	26.2	27.9	27.05	24.6	27.0	25.8							
δ_{33}	31.0	44.82	41.4	40.4	(40.9)	40.7	40.5	(40.6)	35.61	50.7	43.5	(47.0)	42.0	47.5	(44.75)							
δ_{43}	17.94	25.32	26.3	26.0	26.15	27.0	23.8	25.4	21.99	28.0	24.0	26.0	26.5	28.8	27.65							
δ_{53}	-11.28	-10.98	-11.28	-10.5	-10.95	-10.0	-8.5	-9.25	-15.04	-16.6	-13.0	-14.8	-10.4	-14.8	-12.6							
δ_{11}																						
δ_{21}																						
δ_{31}																						
δ_{41}																						
δ_{51}																						
δ_{61}																						
						</																

Note: Values are based on slopes determined from preliminary data. Variations of approximately 10% are possible in interpreting the raw data and in repeating the tests.

7.2 DYNAMIC TEST CORRELATION

Analytical and experimental results for the first five symmetric modes are shown plotted in Fig. 7-14 through 7-18. Table 7-3 contains a comparison of the analytical and experimental frequencies for these same modes. Note that Table 7-3 is aligned in ascending order of the Model II analytical results. Descriptions of the basic behavior of these analytical results were developed, then correlated with a test mode having the same behavior, and its frequency was entered in the table. The mode corresponding to the test frequency of 104.1 Hz is somewhat questionable, being very similar to the 106.8-Hz mode. The 104.1-Hz mode was not measured in the second (vertical suspension) mode survey. Note, also, that two modes were measured for the wing first bending mode. The 51.2-Hz frequency corresponds to resonance of the left wing, while the 54.2-Hz frequency corresponds to that of the right wing. Mode survey data is contained in Appendix C of this volume; additional experimental data is contained in Reference 9-5.

Referring to Table 7-3, the analytical results for the first five symmetric free-free frequencies of Model II are within an error of 8.3 % of the experimental results, and four of these frequencies agree within an error of 3.2 % or less. Table 7-3 also indicates the large improvement between Model I and Model II results when compared with test data.

The mode shapes are presented in Fig. 7-14 through 7-18. In reviewing these figures it may be noted that there is fairly good agreement between analysis and test.

Table 7-3. Comparison of Analytical and Experiment Frequencies for the Symmetrical Free-Free Normal Modes

Mode	Model I Freq, Hz	Model II Freq, Hz	Test Freq, Hz	Model I to Test % Error	Model II to Test % Error	Description
1	53.2	44.2	43.6	+22.0	+ 1.4	Fuselage 1st bending
2	62.6	54.4	51.2 } 54.2 }	+18.8	+3.2	Wing 1st bending (vs payload vertical)
3	75.2	63.0	58.2	+39.2	+ 8.3	Wing 1st bending (vs aft fuselage vert)
4	108.5	80.2	80.1	+35.4	+ 0.1	Fin fore-aft
5	—	103.5	104.1 ^(a) } 106.8 }	—	— 3.1	Payload - aft vertical
6	133.8	115.9	—	—	—	Payload fore-aft (vs fwd fuselage fore-aft)
7	162.3	121.5	—	—	—	Aft fuselage pitch
8	133.8	139.7	—	—	—	Wing 1st torsion (vs fwd fuselage fore-aft)
9	175.3	170.9	—	—	—	Fuselage 2nd bending & wing fore-aft
10	216.5	185.0	—	—	—	Wing fore-aft bending

^aQuestionable mode; very similar to 106.8 Hz mode, also not measured during the second survey on 1-3-74.

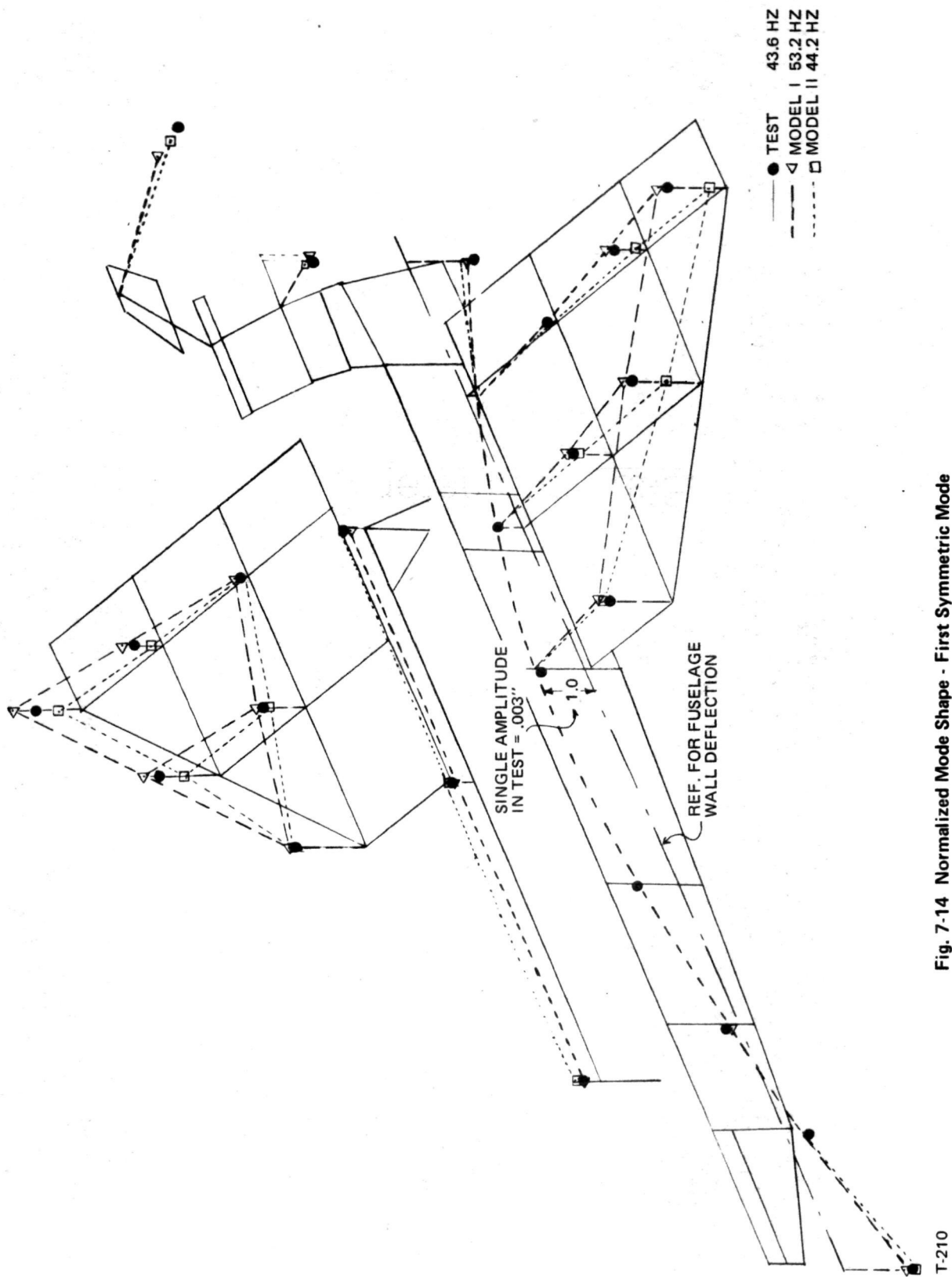
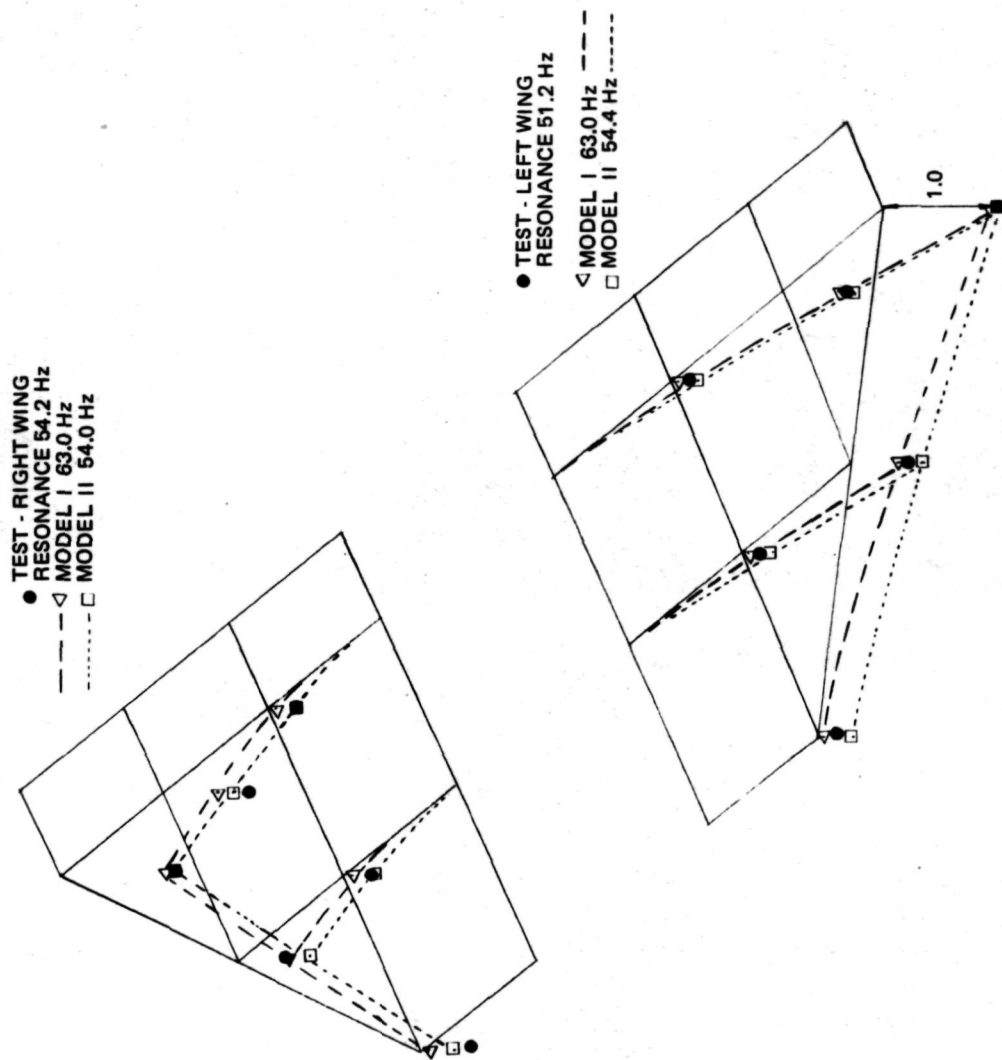


Fig. 7-14 Normalized Mode Shape - First Symmetric Mode



T-211 Fig. 7-15 Normalized Mode Shape - Second Symmetric Mode

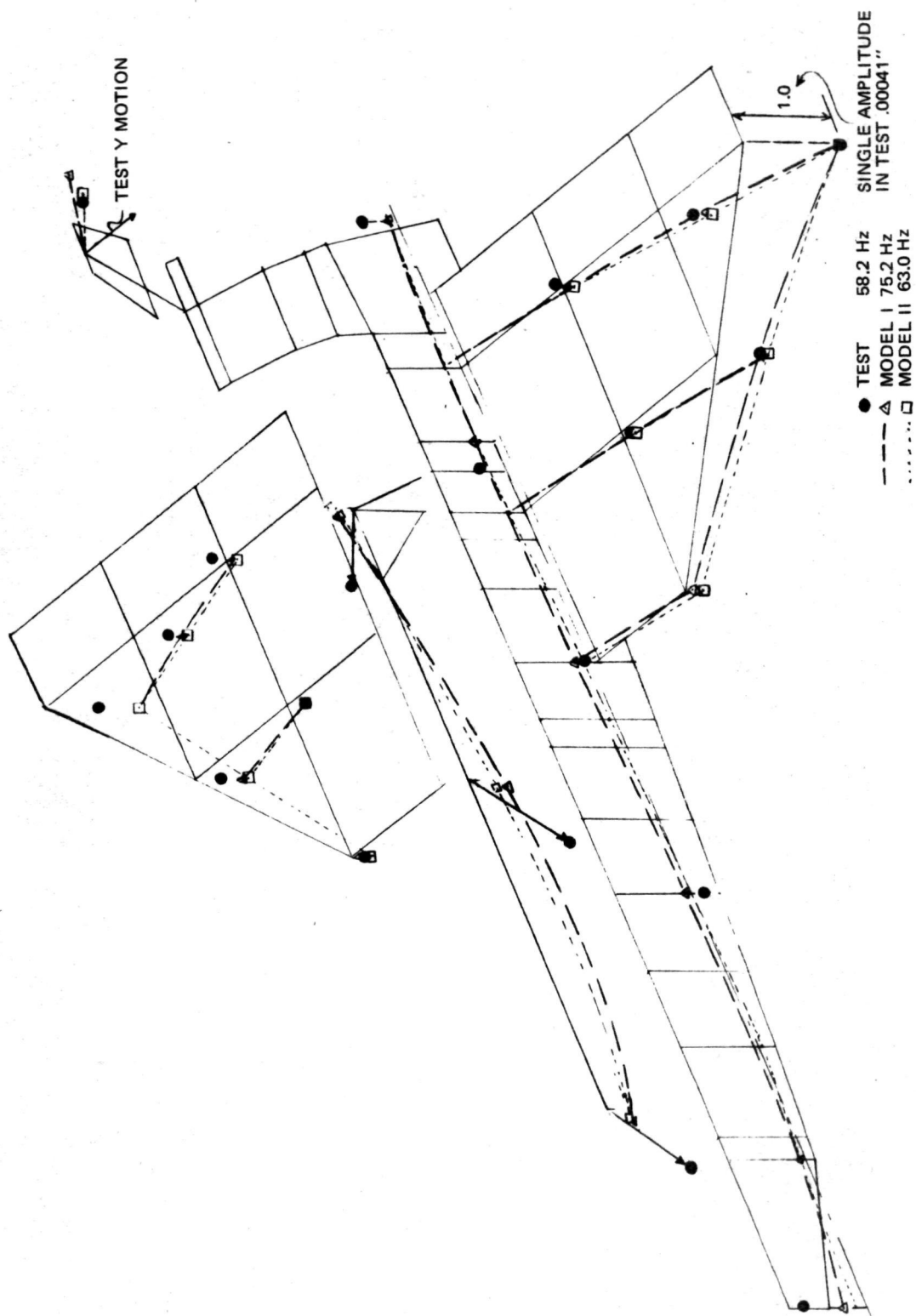


Fig. 7-16. Normalized Mode Shape - Third Symmetric Mode

T-212

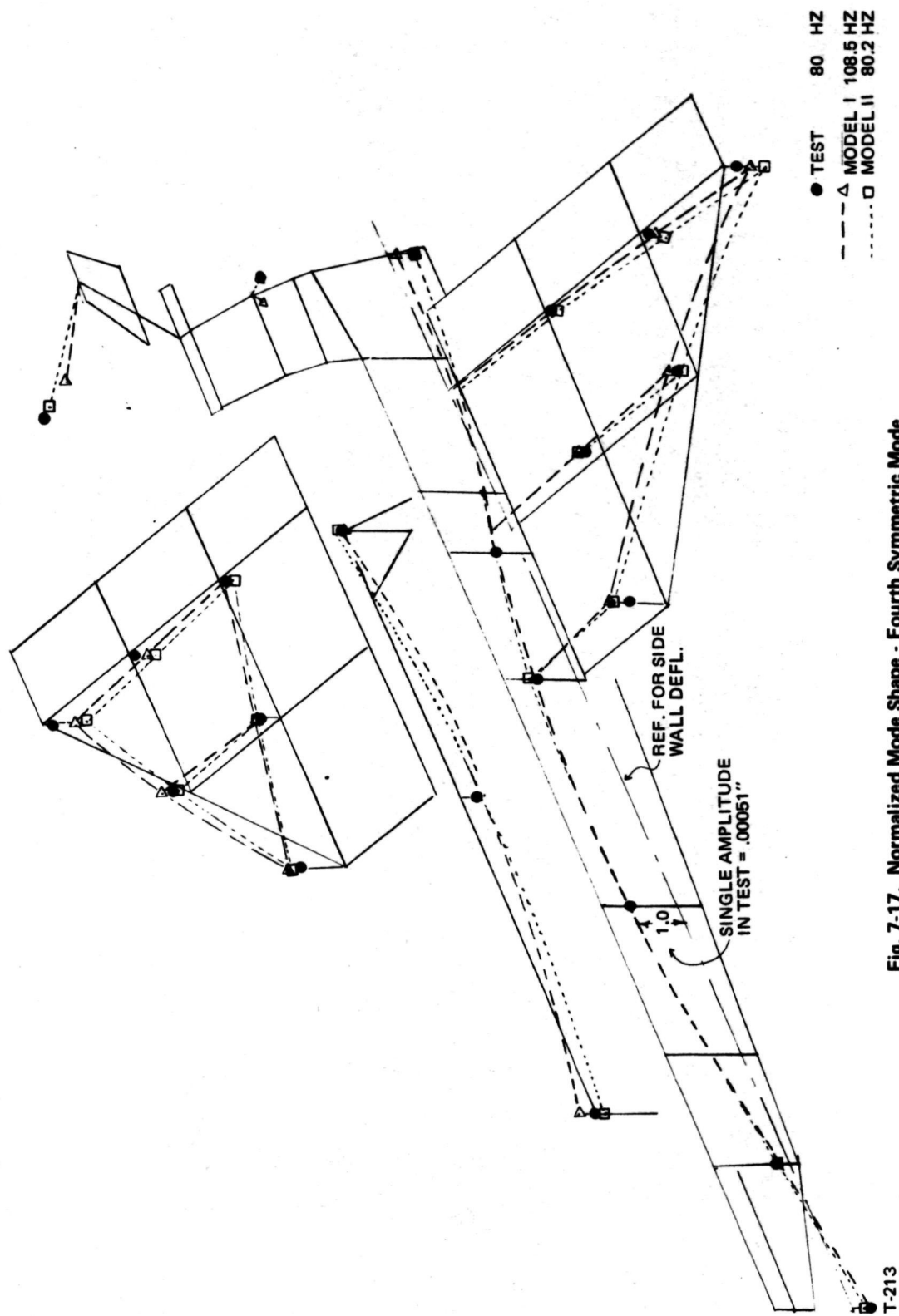


Fig. 7-17. Normalized Mode Shape - Fourth Symmetric Mode

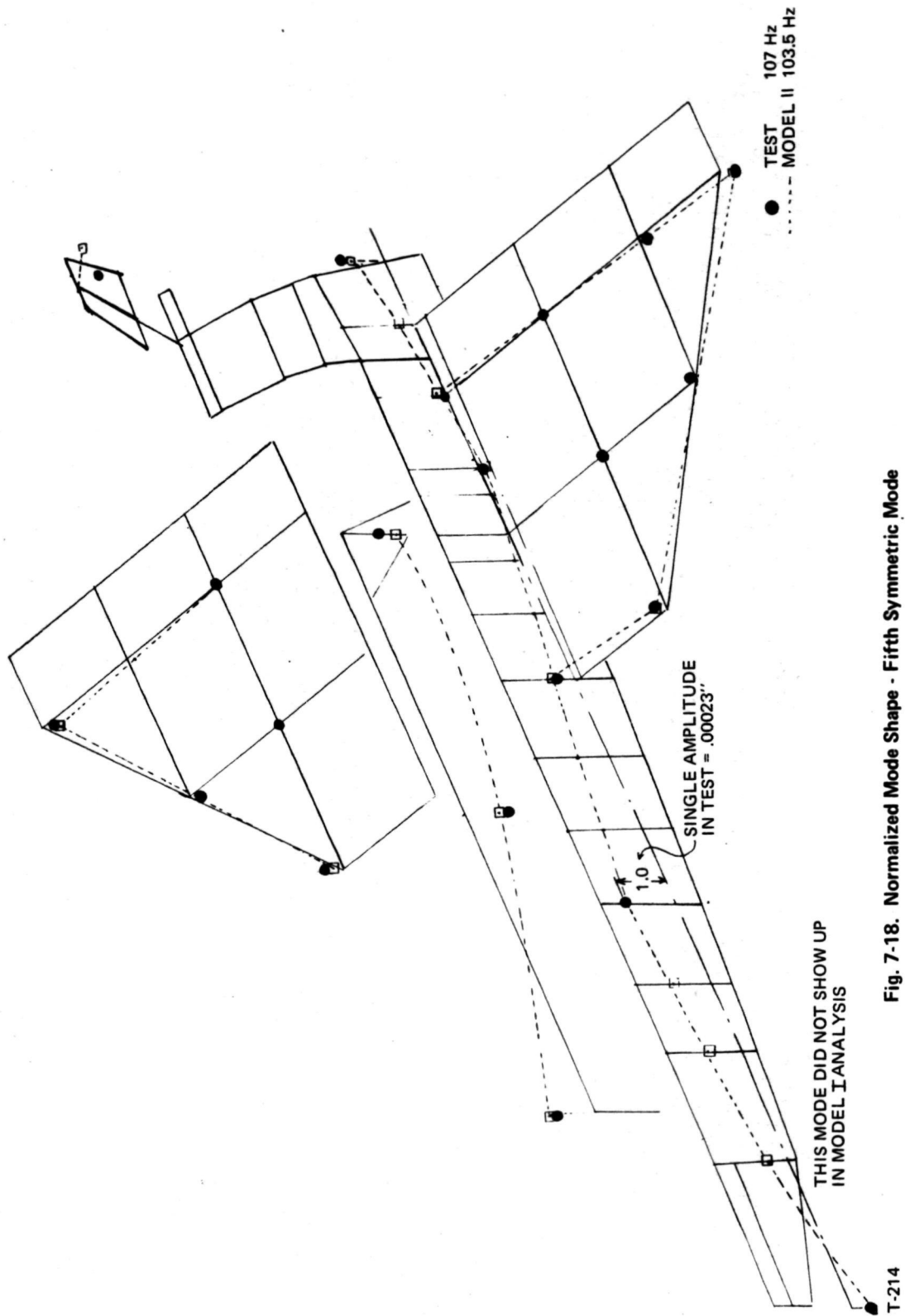


Fig. 7-18. Normalized Mode Shape - Fifth Symmetric Mode

Table 7-4. Substructure Contributions to the Z Component of Momentum for the First Free- Free Mode for Model I and Model II

Substructure	Weight	%	Model I		Model II	
			$(M\phi)_z$	% +	$(M\phi)_z$	% +
Fuselage	100.91	48.34	-0.1219	—	-0.1180	—
Payload	64.62	30.96	+0.0661	46.6	+0.0970	69.5
Wing	32.86	15.74	+0.0675	47.5	+0.0367	26.3
Cargo Doors	6.52	3.12	+0.0084	5.9	+0.0061	4.2
Fin	3.85	1.84	-0.0201	—	-0.0218	—
Σ	208.76	100.00	0.0	100.0	0.0	100.0

TT-194

These mode shapes have been normalized to the most representative displacement component. Thus, the first mode has been normalized to a unit motion of the mid-fuselage (Station 125.5), and not to the maximum displacement which occurs at the fin ballast. From Fig. 7-14 observe that the first mode for Model I agreed closely with test data, the exception being the fin ballast motion, although the frequency was in error by 22.0%. The mode shape for Model II agrees rather well with test data for the fuselage, has better agreement for the fin, but shows less agreement for the wing tip. The Z components of the momentum for the five substructures are tabulated in Table 7-4 for Model I and II. Although the fuselage displaces up through the center portion, the total fuselage momentum is negative because almost all of the mass is concentrated at the ends (see Fig. 5-4), which displace down. The fin adds slightly to the negative momentum of the fuselage, and this is balanced by the positive momentum of the payload, wing and cargo doors which in Model I contribute 46.6, 47.5, and 5.9 %, respectively, to the total positive momentum. In Model II the negative momentum of the fin and fuselage, which is approximately the same as Model I because of the similarity of the mode shape, is balanced by different percentages for the other three substructures, predominantly the payload and wing (refer to Table 7-4). The moment of inertia of the fuselage for Model II is approximately 80 % of the inertia for Model I, while the Model II wing moment of inertia is approximately 85 % of the Model I value (refer to Subsections 6.1.3 and 6.1.4). Springs calculated from static deflection data were added to the Model II payload support structure (Subsection 6.1.7) which were not present in Model I. Thus, on a relative basis, the Model II wing is stiffer than the Model I wing, while the Model II payload is softer compared to the respective fuselage stiffnesses. Because the pay-

Table 7-5. Estimated Stresses for Static and Dynamic Tests

Location		Horizontal Suspension Dynamic Test*				Static Test No. 3			Static Test No. 4			Static Test No. 13		
		1g	Dyn	Max +	Max -	1g	P _z = -80	Total	1g	P _z = +120	Total	1g	P _z = -25	Total
Fuselage	Upper Longeron Sta 116 $\sigma_c = -270$	+200	±321	+521	-121	-200	-320	-520	-200	+490	+290	X	X	X
	Lower Longeron Sta 116 $\sigma_c = -533$	-100	±193	+ 93	-293	+100	+150	+250	+100	-230	-130			
	σ_c (Bot Deck) = -167													
Wing	Upper Cover Sta. 153, B.L. 21 $\sigma_c = -192$	- 80	± 71	- 9	-151	X	X	X	X	X	X	+80	+240	+320
	Lower Cover Sta. 153, B.L. 21 $\sigma_c = -192$	+ 80	± 71	+151	+ 9							-80	-200	-280

*3 lb Harmonic Force at Nose Fitting - 1st Symmetric Mode
TT-195

load weight is twice the wing weight, a small change in the payload motion must be offset by a larger change in the wing motion. There is evidence that the payload springs and the wing stiffness have not been correctly "tuned" to produce the correct behavior.

Table 7-5 lists estimated stresses for the static and dynamic tests for the fuselage longerons and wing cover. In the inverted dynamic test, the dynamic and maximum stresses in the bottom deck exceeded critical stresses. In static test No. 3, the stress in the upper portion of the side wall panel due to the applied load exceeds the critical stress of -270 psi. The applied load in static test No. 4 was not large enough to produce a net compressive stress in the bottom deck in excess of the linear elastic critical values. Hence, there is some question on the suitability of static test data for determining actual dynamic elastic characteristics and, in the case of the fuselage, some questions as to whether static tests fully covered the range of dynamic behavior. For the wing, results of static test No. 13 appear to have adequately covered the dynamic test range. All of the static applied load and 1 g stresses in Table 7-5 have been estimated using $\left(\frac{Mc}{I}\right)$ with a reduced value for the moment

of inertia. The dynamic stresses were obtained by multiplying NASTRAN strains by the test amplitude. The static load deflection plots do not show an abrupt change in stiffness that would be expected for linear buckling; they do show a slight "bending over" as might be expected for a bowed panel. In addition hysteresis is present in the loading and unloading cycle.

Table 7-6 lists numerical values for strain and deflections for both analysis and test results for the first free-free symmetric mode. These values verify the good agreement noted previously.

**Table 7-6 Selected Analysis and Test Results
for First Free-Free Symmetric Mode**

	Model I	Model II	Test
Frequency	53.2	44.2	43.6
ϵ_x (Top Longeron)	0.0102	0.0112	—
ϵ_y (Wing Top Cover) Sta 153.4 (BL 21)	-0.00302	-0.00098	
δ_z (Sta 125.5) Node 1105	1.0	1.0	1.0
δ_x (Fin Ballast) Node 4400	3.36	3.73	4.0
δ_z (Sta 116) Node 905	1.04	1.05	1.0
δ_z Wing Tip Sta 162 Node 3017	1.53	0.40	1.1
δ_z Payload Mid-Point Node 4886	0.44	0.63	0.5
δ_z (Nose) Node 110	-1.43	-1.60	-1.5
δ_z (OMS Ballast) Node 2200	-0.76	-0.64	-0.85 \pm
δ_x (OMS Ballast) Node 2200	1.18	0.97	1.1 \pm
δ_z (Approx. Wing CG) Node 3413	0.69	0.28	0.55 \pm

TT-196

Section 8
CONCLUSIONS AND RECOMMENDATIONS

8 - CONCLUSIONS AND RECOMMENDATIONS

Comments and recommendations concerning the analysis and correlation fall within three basic categories: modeling procedures, correlation, and experiences with NASTRAN.

8.1 MODELING PROCEDURES

In NASTRAN Model I, the CQDMEM2 element was used to model a fully effective structure. Lack of correlation should not be attributed to the behavior of this element or to NASTRAN. The major cause for lack of correlation was traced to the ineffectiveness of the skin panels due to the presence of initial bows. Model II used bars and shear panels to represent the behavior of the physical model. Here, effective bar areas and an effective shear modulus were used. It is felt that this type of modeling is more descriptive of the actual characteristics of the structure. The effectiveness factors were obtained through the use of a computer program that solved the large deflection problem of in-plane loading of plates with initial imperfections. Little information exists in published form that contain the parameter range and type of loading of interest of the present study. Work was done by NASA some 20 years ago. It is recommended that this work be updated to cover a broad range of aspect ratios, initial imperfections and loadings. Publication of this data in chart form would be beneficial to modeling efforts on many structural projects.

Some remodeling of major joints could have been made in the analysis. However, for some joints such as the fin/fuselage connection, only static tests could give the exact behavior - no matter how careful an analysis was made.

Consistent mass concepts tend to lose their significance for structures that do not behave in a linear, fully effective fashion. In fact, for structures of this type, it becomes desirable to control the mass and stiffness properties independently.

8.2 CORRELATION

- The results of the vibration tests reported here are limited in scope, and have not been fully completed
- The static test data have a $\pm 10\%$ error in reproducibility
- It is felt that the agreement of Model II results with test data is sufficiently close to pursue a coupling analysis.

8.3 COMMENTS ON AND EXPERIENCES WITH NASTRAN

The analysis of the 1/8-scale model was viewed as a pilot study of the use of NASTRAN on realistic aerospace projects. Therefore, some of the comments extend past specific application to the 1/8-scale model. Many areas must be considered in attempting to judge the NASTRAN system, some of which are not necessarily concerned with NASTRAN itself.

One of the prime reasons for Grumman's interest in NASTRAN is the work that NASA is doing in attempting to establish NASTRAN as the industry standard. For multicorporation aerospace projects, standardization is a necessity. Standardization of computer programs, type of data, etc, is important from a contractual point of view, where subcontractors interface with prime contractors and the prime contractor interfaces with the principal agency. However, with standardization there must be sufficient technical flexibility - in this regard NASTRAN has room for improvement.

8.3.1 FLEXIBILITY OF THE NASTRAN SYSTEM

NASTRAN contains a number of rigid formats that allow for specific types of problems to be solved. Where these formats do not fit the specific application, the rigid format may be changed with ALTERS. In analyzing the 1/8-Scale Orbiter Model, numerous ALTERS to Rigid Format 3 were made. The system was modified to handle substructuring using level 15.5. It was found that, although the basic system can be modified, it requires an extensive learning period to become sufficiently proficient with the system to make use of ALTERS. After making a series of extensive ALTERS, the modified program must then be checked; if altered again, it must be rechecked. Because this procedure is cumbersome, it tends to produce a small group of NASTRAN experts. Our own in-house system (COMAP ASTRAL; Reference 9-13) contains no rigid formats; only one structural command generates all the required matrices (or those that are requested) to solve the problem. All matrix operations are coded in a simple, interpretive language that may be learned in a few hours. This system requires that the engineer understand the physics of the problem. Altering NASTRAN, on the other hand, requires a good understanding of the systems aspects of NASTRAN. Thus, there is diversion of engineering talent from engineering problem-solving to overcoming NASTRAN system complexities.

8.3.2 CAPABILITY OF NASTRAN

The original analysis plan for the 1/8-scale model required that all components (Orbiter, ET and two SRB's) be coupled to determine mated vehicle modes. This combined hydro-visco-elastic analysis is theoretically possible within the present NASTRAN system, but from a practical stand point it is not. Although modes were successfully calculated for the individual components, it was not possible to couple these components and analyze the total (mated) vehicle due to extremely large computer time requirements. Note that the lack of correlation of the Orbiter analytical and test modes for Model I is not a fault of NASTRAN. This lack of agreement did, however, cause a shift of emphasis from studying the coupling problem to examining the Orbiter modeling, design, and fabrication in more detail. Although the Orbiter correlation has been cleared up by the use of Model II, coupling is still a major problem. Two approaches seem feasible:

- Model coupling in lieu of static coupling to reduce the size of the final problem
- Incorporation into NASTRAN of approximate reduction schemes that employ the automatic tri-diagonal reduction algorithm. (For example, FEER (Reference 9-3; or ALARM, being developed by Grumman under Master Agreement NAS 1-10635, Task 17. FEER and ALARM would have to be extended to handle complex modes).

Master Agreement NAS 1-10635, Task 21, will pursue the model coupling approach by making the appropriate ALTERS to the NASTRAN rigid formats.

Many complaints of NASTRAN are associated with the form of the stress output. Average stresses in elements are of little use to the engineer in the design mode. Traditional cap loads and shear flows are preferable. At this stage the designer is looking for the best load paths, and will rearrange the framing to the best of his ability to obtain it. The elements of the structure are proportioned to withstand the load imposed on them using allowable stresses, therefore the average stress in an element is not a convenient quantity. NASTRAN level 15.5 produces element corner forces which may be used as input to a post processor to produce equivalent cap loads and shear flows. The Grumman post processor produces listings of member loads not only by condition, but by critical condition ranking as well.

Table 8-1 1/8-Scale Model Orbiter NASTRAN Analysis Computing Statistics

Anal.	Description	Method	No. of Modes		Debugging			Good Runs		
			Free	Restr.	CPU Min	Sys Min	No. of Runs	CPU Min	Sys Min	No. of Runs
Original Model	1. Wing - Phase I	INV	-	3	32	110	8	6	23	1
	2. Cargo Doors - Phase I (Symmetric Case)	GIV	26	-	14	49	7	3	9	1
	(Antisymmetric Case)	GIV	-	9	8	28	6	2	7	1
	3. Payload Beam - Phase I (Symmetric Case)	GIV	-	21	2	8	4	1	4	1
	(Antisymmetric Case)	GIV	-	23	2	5	2	1	4	1
	4. Fin - Phase I (Symmetric Case)	GIV	-	12	5	15	3	2	7	1
	(Antisymmetric Case)	GIV	-	12	2	8	2	2	7	1
	5. Fuselage - Phase I (Symmetric Case)	INV	6	-	146	528	10	25	89	1
	(Antisymmetric Case)	INV	6	-	100	355	5	23	84	1
	6. Orbiter - Phase 2 (Symmetric Case)	INV	11	-	12	42	7	36	193	2
	(Antisymmetric Case)	INV	14	-	17	89	4	62	370	3
					340	1237	58	163	797	14
	Total Time Used							503	2034	72
	(Took 2½ mo. calendar time starting from uncorrected data)									
Model I	1. Wing - Phase I (Not Run, Same as Original Model)	-	-	-	-	-	-	-	-	-
	2. Cargo Doors - Phase I (Symmetric Case)	GIV	-	21	1	3	3	1	4	1
	(Antisymmetric Case)	GIV	-	23	-	-	-	1	5	1
	4. Fin - Phase I (Symmetric Case)	GIV	-	12	1	2	4	2	6	1
	(Antisymmetric Case)	GIV	-	12	-	-	-	2	6	1
	5. Fuselage - Phase I (Symmetric Case)	INV	6	-	25	74	3	26	100	1
	(Antisymmetric Case)	INV	6	-	-	-	-	23	83	1
	6. Orbiter - Phase 2 (Symmetric Case)	INV	12	-	-	-	-	40	230	1
	(Antisymmetric Case)	INV	9	-	-	-	-	41	237	2
					27	79	10	136	671	9
	Total Time Used (1 week)							163	750	19
Model I Investigation	6. Symmetric Orbiter - Phase 2 (Fwd Fin Support Cut)	INV	10	-	-	-	-	50	296	2
	(Aft Fin Support Cut)	INV	10	-	-	-	-	45	177	1
	Total Time Used (1 week)							95	473	3
Model II	1. Wing - Phase I (Skin 50% Eff)	INV	-	4	4	19	4	3	19	1
	(Skin 85% Eff)	INV	-	4	-	-	-	2	12	1
	2. Cargo Doors - Phase I (Symmetric Case)	GIV	26	-	7	28	5	2	11	1
	(Antisymmetric Case)	GIV	-	4	2	9	3	1	7	1
	3. Payload Beam - Phase I (Symmetric Case)	GIV	-	21	-	-	-	1	5	1
	(Antisymmetric Case)	GIV	-	23	-	-	-	1	5	1
	4. Fin - Phase I (Symmetric Case)	GIV	-	12	-	-	-	2	8	1
	(Antisymmetric Case)	GIV	-	12	-	-	-	1	6	1
	5. Fuselage Phase I - G = 50% Eff (Symmetric Case)	INV	8	-	29	141	7	18	93	1
	(Antisymmetric Case)	INV	-	-	2	9	1	-	-	-
	Fuselage Phase I-G = 2/3 Eff (Symmetric Case)	INV	8	-	-	-	-	18	102	1
	(Antisymmetric Case)	INV	9	-	-	-	-	17	93	1
	6. Orbiter - Phase 2 (Symmetric Case)	INV	13	-	-	-	-	42	292	2
	(Antisymmetric Case)	INV	13	-	-	-	-	22	142	1
					44	206	20	130	795	14
	Total Time Used							174	1001	34
	(Took 3 mo. calendar time which includes extensive data revision)									
Total Time Used For Orbiter Mode Analyses								935	4258	128

TT-191

8.4.3 COMPARISON OF COMPUTER RUNNING TIMES

A complete record of the amount of computer time needed to debug and analyze the various Orbiter models using NASTRAN is presented in Table 8-1. Table 8-1 shows the NASTRAN computing statistics for obtaining the Orbiter symmetric and antisymmetric dynamic modes by the substructuring method of analysis. An original NASTRAN analysis of the 1/8-scale Orbiter (prior to minor structural changes), and two revised analyses known as Model I and Model II, are shown. In addition, two Phase 2 analyses of Model I were made. The NASTRAN Rigid Format 3 which included extensive DMAP ALTERS for checking purposes was used throughout. For each item in Table 8-1, undeformed and deformed plots were also obtained. The original analysis, as expected, used up most of the debugging time. The model I analysis profited considerably from the availability of the corrected input data generated in the original analysis, as can be seen in Table 8-1, since only minimal changes were made. Model II had extensive data revisions and thus a somewhat larger debugging time than Model I. In all of the foregoing three analyses however, production run times were about the same. This is because there was no major change in idealization size or number of dynamic DOF's in the three analyses.

A summary of the total amount of computing time used on the NASTRAN analysis is, therefore, 411 CPU (1522 System) minutes for 88 debugging runs, and 524 CPU (2736 System) minutes for 40-good runs. In addition time to develop ALTERS for Rigid Format 7 (for the ET and SRB analyses took 40CPU (310 System) minutes.

Section 9
REFERENCES

9 - REFERENCES

Cited
References

- 9-1 Bernstein, M., Coppolino, R., Zalesak, J., and Mason P.W., "Development of Technology Fluid/Structure Interaction Modeling of a 1/8-Scale Dynamic Model of the Shuttle External Tank," NASA CR-132459, Grumman Aerospace Corporation, Bethpage, New York, August 1974.
- 9-2 Levy, A., Zalesak, J., Bernstein, M., Mason, P. W. "Development of Technology for Modeling of a 1/8-Scale Dynamic Model of the Shuttle Solid Rocket Booster (SRB)", NASA CR-132492, Grumman Aerospace Corporation, Bethpage, New York, July 1974.
- 9-3 Newman, M. and Pipano, A., "Fast Modal Extraction Via the FEER Computer Program," Paper presented at the Third NASTRAN User's Colloquium, NASA/Langley Research Center, Hampton, Virginia, September 11-12, 1973; also NASA TMX 2893, September 1973, pp 485-506.
- 9-4 Anonymous, "Preliminary Shuttle Structural Dynamics Modeling Design Study," NASA CR-112196, Grumman Aerospace Corporation, Bethpage, New York, November 1972.
- 9-5 Pinson, L.D., Coordinator, "Analytical and Experimental Vibration Studies of a 1/8-Scale Shuttle Orbiter," Prospective NASA TN L-9806, National Aeronautics and Space Administration, Langley Research Center, Hampton, Va.
- 9-6 Ojalvo, I.U., "An Error Bound For Approximate Modes and Frequencies", Grumman Memorandum No. STMECH 73.66 (November 1973).
- 9-7 Gerard, G., Handbook of Structural Stability, Part IV, "Failure of Plates and Composite Elements" NACA TN 3784, August 1957.
- 9-8 Timoshenko, S.P., and Gere, J.M., Theory of Elastic Stability, Second Edition, McGraw-Hill Book Co., New York, 1961, pp 411-418.
- 9-9 Rogers, G.L., An Introduction to the Dynamics of Framed Structures, John Wiley and Sons, Inc., New York, 1954 pp 216-218.

- 9-10 Kuhn, P., Stresses in Aircraft and Shell Structures, McGraw-Hill Book Co. Inc., New York, 1956, Chapter 3.
- 9-11 Stein, M. and Starnes, J.H. Jr., "Numerical Analysis of Stiffened Shear Webs in the Postbuckling Range", Numerical Solutions of Non-linear Structural Problems, R. H. Hurtung, Ed., Publication AMD Vol. 6, American Society of Mechanical Engineers, United Engineering Center, New York, 1973.
- 9-12 Tsongas, A.G. and Ratay, R.T., "Investigation of Diagonal-Tension Beams With Very Thin Stiffened Web", NASA Report No. CR-101854, Manned Spacecraft Center, Houston, Grumman Aerospace Corp., Bethpage, New York, July 1969.
- 9-13 Grumman Aerospace Corporation "IDEAS" Manual, Vol IIA, 1969.

Supplemental

References

Bernstein, M., Mason, P. W., Zalesak, J., Gregory, D.J., and Levy A., "NASTRAN Analysis of the 1/8-Scale Space Shuttle Dynamic Model", Paper presented at the Third NASTRAN User's Colloquium, NASA/Langley Research Center, Hampton Va., September 11-12, 1973; also published as NASA TMX-2893, September 1973, pp 169-241; also presented at the Proceedings of the ESRO/CERS Third Testing Symposium on Large Structures for Manned Spacecraft, "Frascati, Italy, 22-26 October 1973, and published as ESRO SP-99, March 1974.

Karman T., Sechler, E.E. and Donnell L.H. in Trans. Am Soc Mech Eng Vol 54 pp 53 1932.

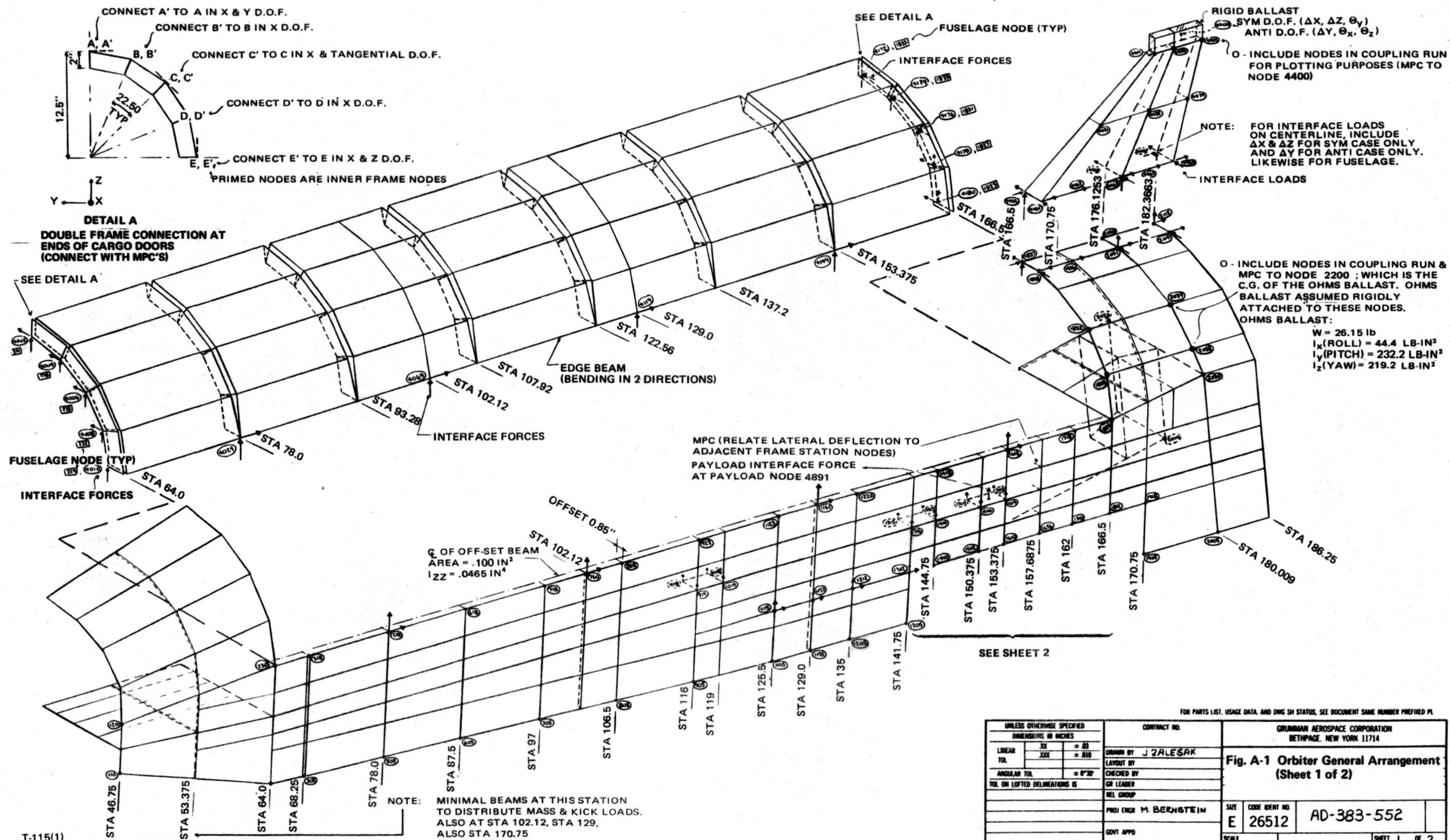
Appendix A
FINITE ELEMENT MODEL I

TABLE OF CONTENTS

NOTE

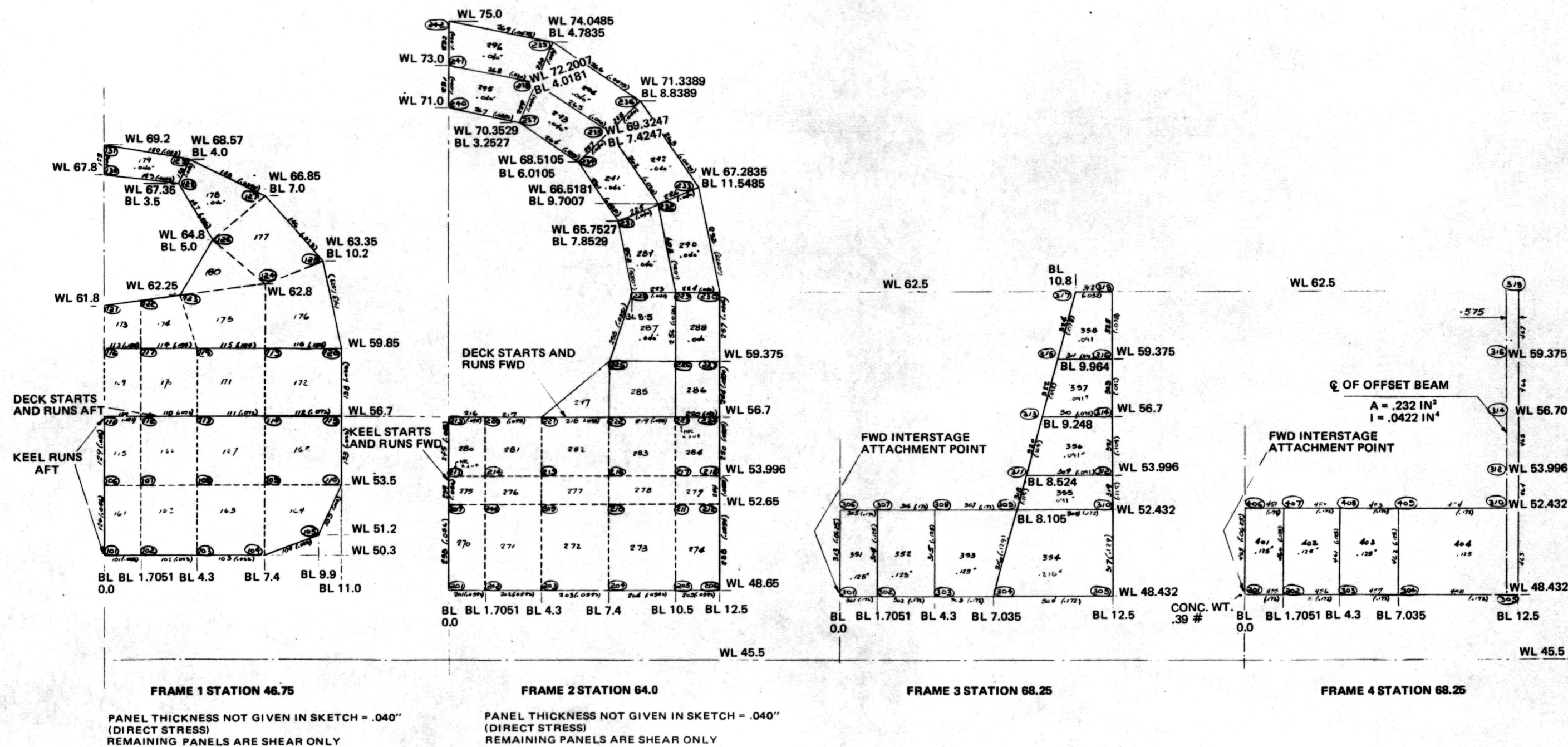
Appendix A consists of
the following illustrations:

<u>Figure</u>		<u>Page</u>
A-1	Orbiter General Arrangement	A-2
A-2	Orbiter Fuselage-Frames 1 thru 7	A-4
A-3	Orbiter Fuselage-Frames 8 thru 12	A-6
A-4	Orbiter Fuselage Frames 15 thru 21	A-8
A-5	Orbiter Fuselage-Skin, Deck and Keel Structure	A-10
A-6	Orbiter Wing	A-12
A-7	Orbiter Fin and Payload	A-14



FOR PARTS LIST, USAGE DATA, AND DWG SH STATUS, SEE DOCUMENT SAME NUMBER PREFIXED PL

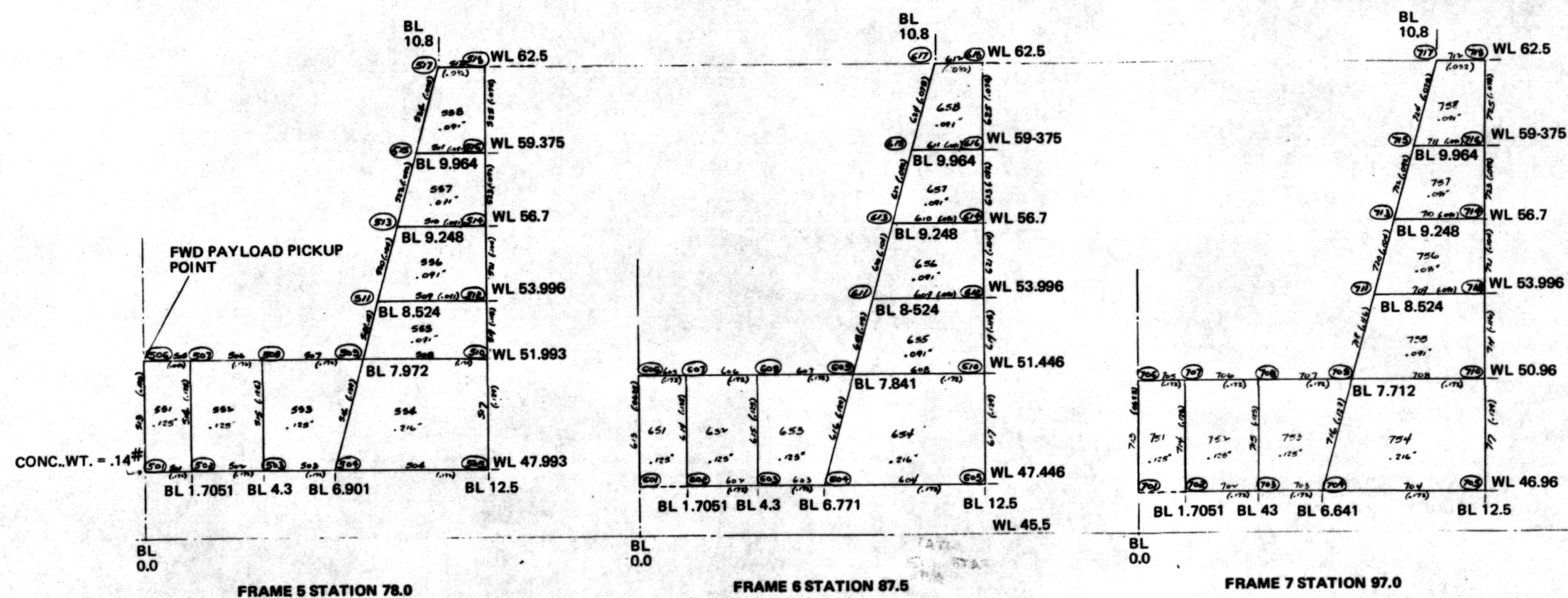
UNLESS OTHERWISE SPECIFIED DIMENSIONS IN INCHES		CONTRACT NO.		GRUMMAN AEROSPACE CORPORATION BETHPAGE, NEW YORK 11714	
LINEAR TOL.	XXX	DRAWN BY J ZALESK		Fig. A-1 Orbiter General Arrangement (Sheet 1 of 2)	
	XXX	LAYOUT BY			
ANGULAR TOL.	± 0°30'		CHECKED BY		
	± 0°30'		GR LEADER		
TOL. ON LOFTED DELINEATIONS IS		REL GROUP		SIZE E CODE IDENT NO. 26512 AD-383-552 SHEET 1 OF 2	
		PROJ ENGR M. BERNSTEIN			
		GOVT APPD			



T-116(1)

UNLESS OTHERWISE SPECIFIED DIMENSIONS IN INCHES		CONTRACT NO.		GRUMMAN AEROSPACE CORPORATION BETHPAGE, NEW YORK 11714	
LINEAR TOL.	XX XXX	± .03 ± .010	DRAWN BY LAYOUT BY	D. GREGORY	Fig. A-2 Orbiter Fuselage Frames 1 Thru 7 (Sheet 1 of 2)
ANGULAR TOL.	XX XXX	± 0°30'	CHECKED BY		
TOL. ON LOFTED DELINEATIONS IS			GR LEADER		
			REL GROUP		
			PROJ ENGR	M. BERNSTEIN	SIZE E
			GOVT APPD		CODE IDENT NO. 26512
					AD-383-553
					SCALE 1/2
					SHEET 1 OF 2

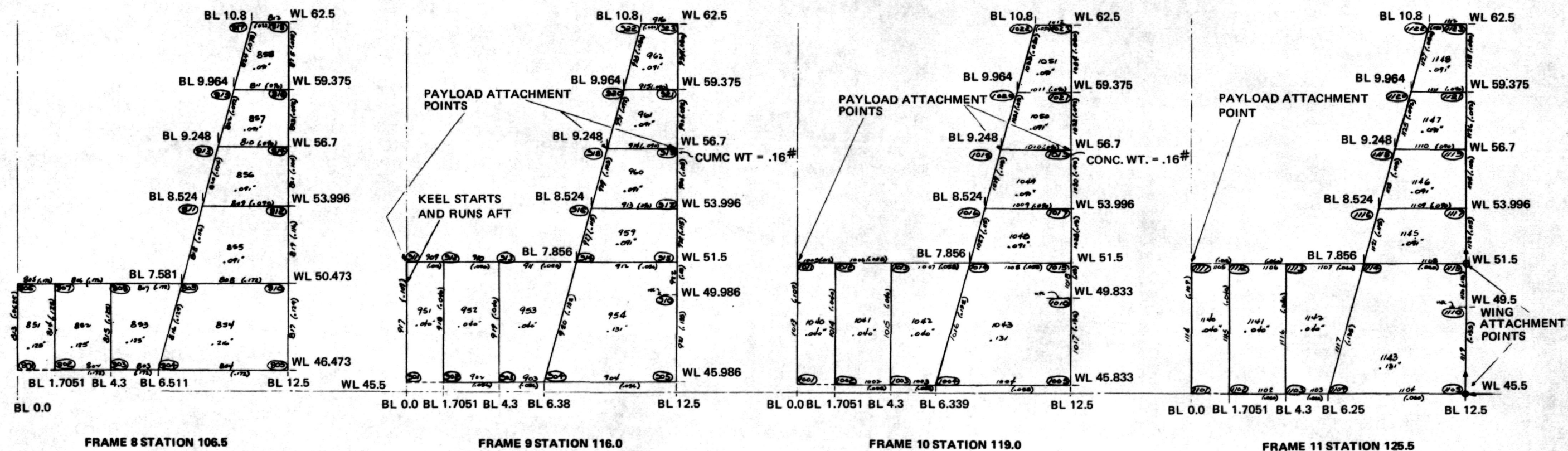
REVISIONS						
ZONE	LYN	DESCRIPTION	EFF CODE	MODEL	DATE	APPROVED



T-116(2)

FOR PARTS LIST, USAGE DATA, AND DRG SH STATUS, SEE DOCUMENT SAME NUMBER PREFIXED PL

UNLESS OTHERWISE SPECIFIED			CONTRACT NO.		GRUMMAN AEROSPACE CORPORATION BETHPAGE, NEW YORK 11714		
DIMENSIONS IN INCHES					Fig. A-2 Orbiter Fuselage Frames 1 Thru 7 (Sheet 2 of 2)		
LINEAR	XX	± .03	DRAWN BY D. GREGORY				
TOL	XXX	± .010	LAYOUT BY				
ANGULAR TOL		± 0°30'	CHECKED BY				
TOL ON LOFTED DELINEATIONS IS			GR LEADER				
			REL GROUP				
			PROJ ENGR M. BERNSTEIN		SIZE	CODE IDENT NO	
					E	26512	AD-383-553
			GOVT APPD		SCALE	1/2	SHEET 2 OF 2

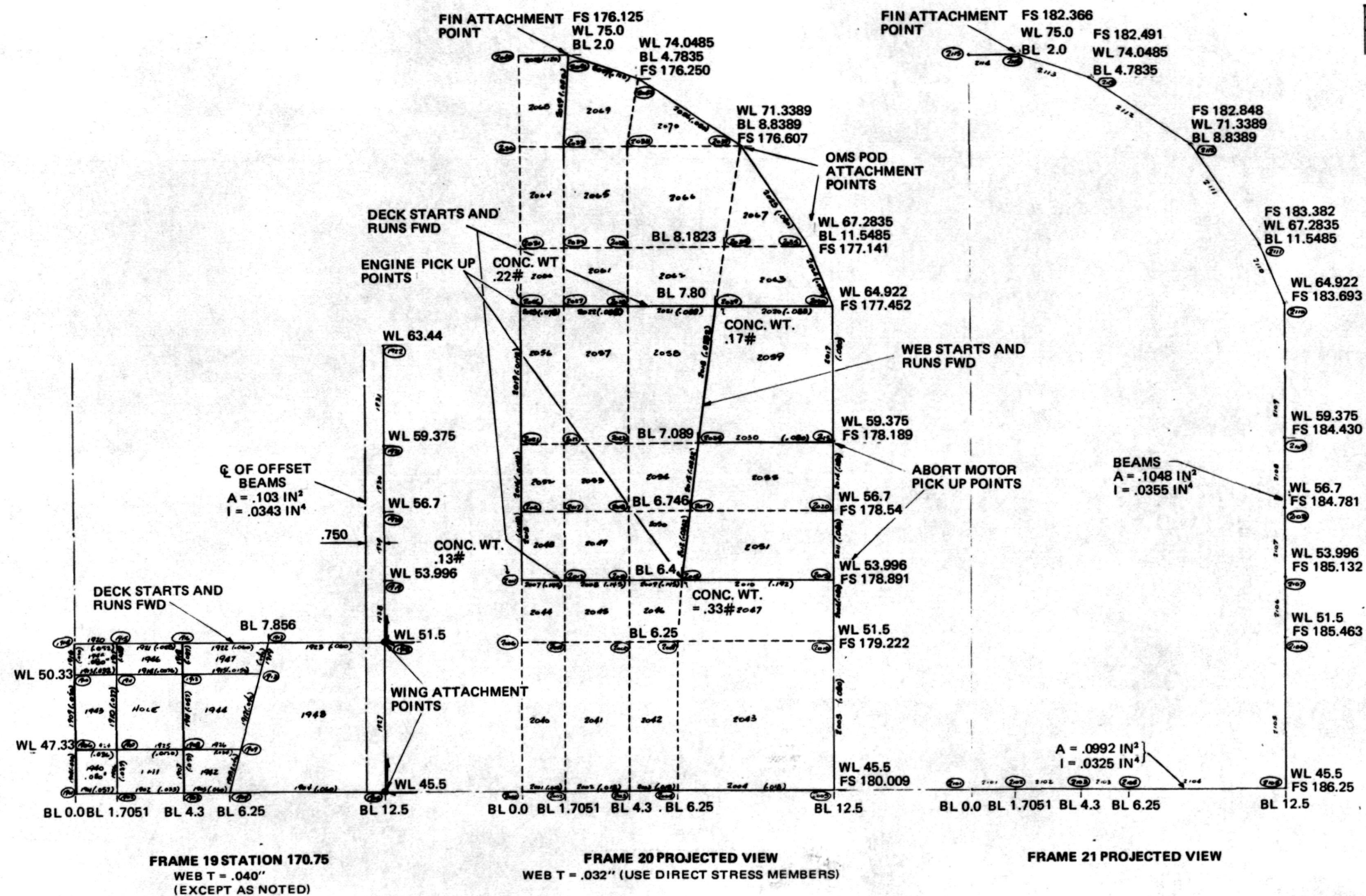


ALL BL DIMENSIONS ARE IN -Y DIRECTION

FOR PARTS LIST, USAGE DATA, AND DWG SH STATUS, SEE DOCUMENT SAME NUMBER PREFIXED PL

UNLESS OTHERWISE SPECIFIED DIMENSIONS IN INCHES		CONTRACT NO.		GRUMMAN AEROSPACE CORPORATION BETHPAGE, NEW YORK 11714	
LINEAR	XX ± .03	DRAWN BY	D. GREGORY	Fig. A-3 Orbiter Fuselage Frames 8 Thru 11 (Sheet 1 of 2)	
TOL	XXX ± .010	LAYOUT BY			
ANGULAR TOL	± 0°30'	CHECKED BY			
TOL ON LOFTED DELINEATIONS IS		GR LEADER			
		REL GROUP		SIZE	CODE IDENT NO.
		PROJ ENGR M. BERNSTEIN		E	26512
		GOVT APPD		SCALE	AD-383-554
				1/2	SHEET 1 OF 2

T-116(3)

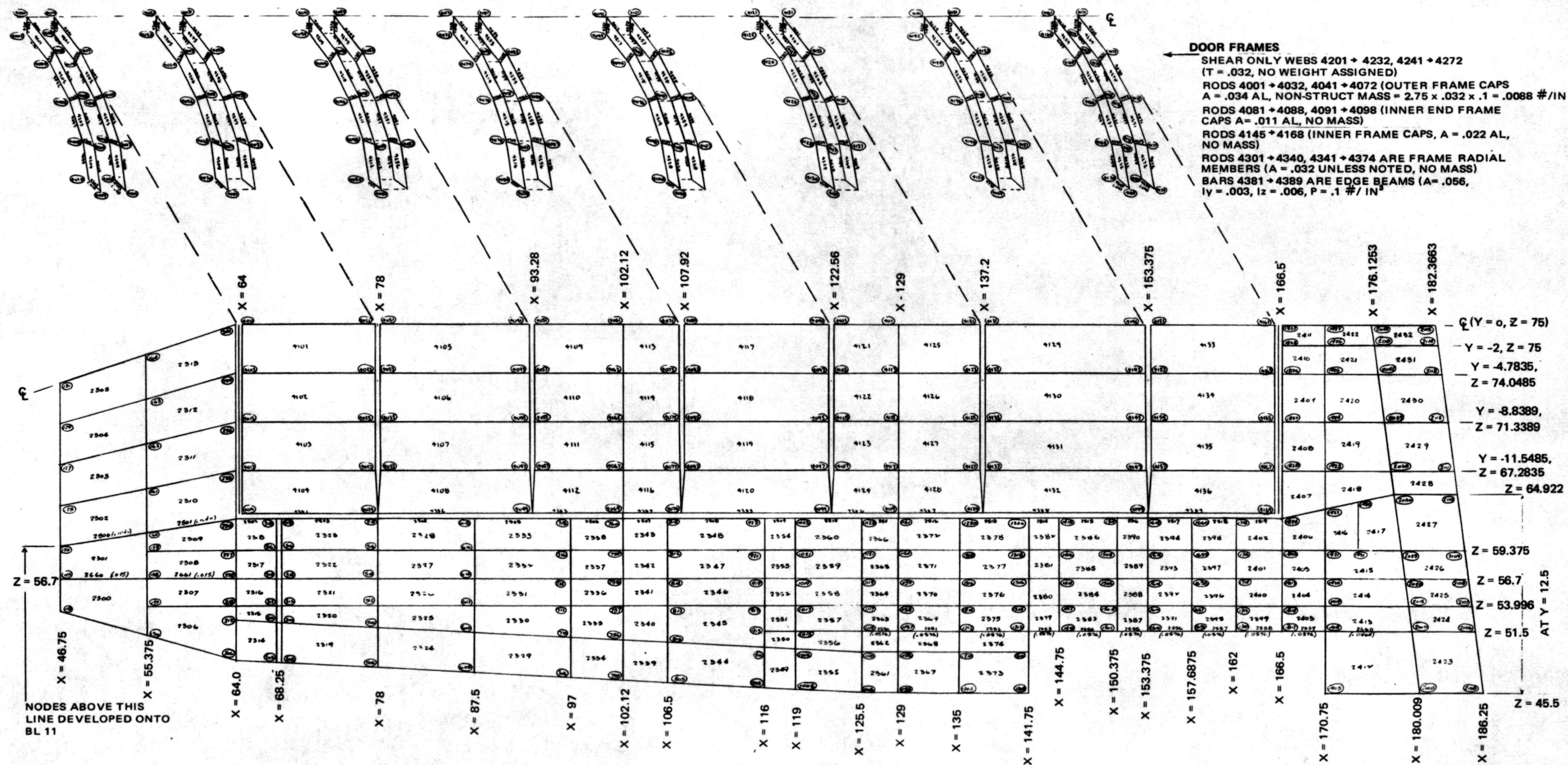


REVISIONS					
DATE	BY	DESCRIPTION	OFF CODE	MODEL	APPROVED

T-116(6)

FOR PARTS LIST, USAGE DATA, AND DWG SH STATUS, SEE DOCUMENT NUMBER PREFIXED UN

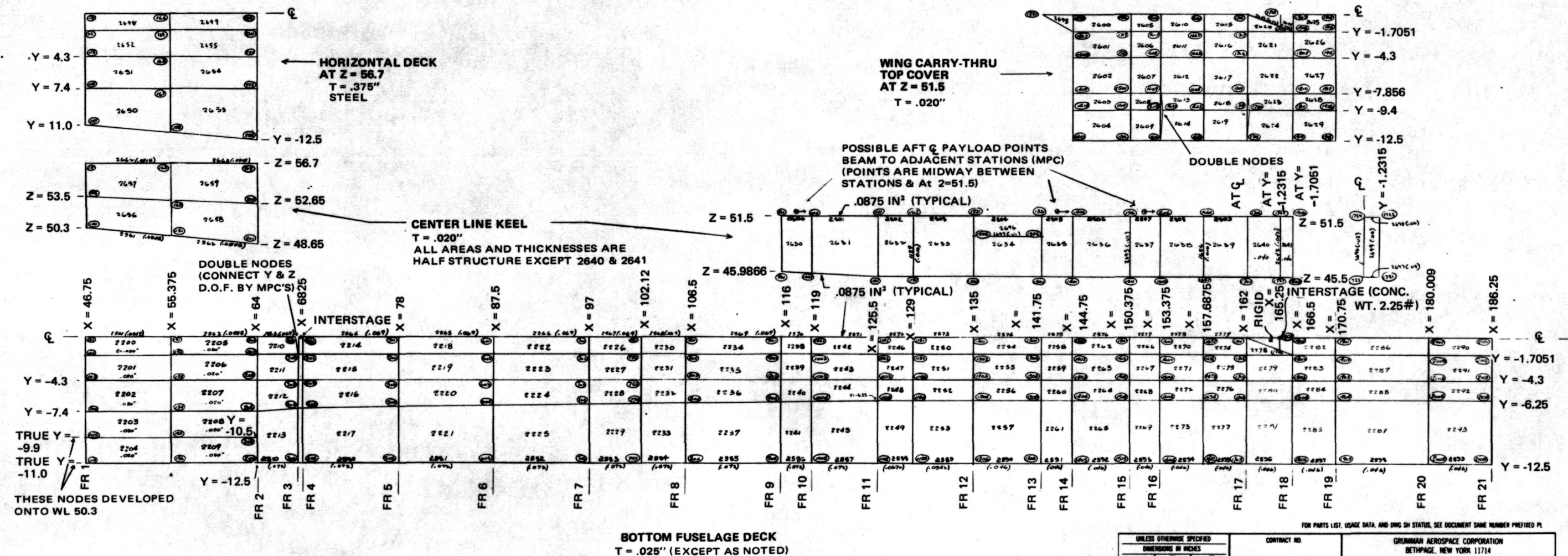
UNLESS OTHERWISE SPECIFIED DIMENSIONS IN INCHES		CONTRACT NO.		GRUMMAN AEROSPACE CORPORATION BETHPAGE, NEW YORK 11714	
LINEAR TOL	XX	± .01	DRAWN BY D. GREGORY	<div style="font-size: 1.2em; font-weight: bold;">Fig. A-4 Orbiter Fuselage Frames 19 Thru 21 (Sheet 2 of 2)</div>	
	XXX	± .010			
ANGULAR TOL	± 0°30'		LAYOUT BY		
TOL. ON LIFTED DELINEATIONS IS			CHECKED BY		
			OR LEADER		
			REL GROUP		
			PROJ ENGR M. BERNSTEIN	SIZE E	CODE IDENT NO. 26512
			GOVT APPD	AD-383-555	
			SCALE 1/2	SHEET 2 OF 2	



UNLESS OTHERWISE SPECIFIED			CONTRACT NO.		GRUMMAN AEROSPACE CORPORATION BETHPAGE, NEW YORK 11714	
DIMENSIONS IN INCHES						
LINEAR TOL	XX	± .03	DRAWN BY J. ZALESK		Fig. A-5 Skin, Deck and Keel Structure Orbiter Fuselage (Sheet 1 of 2)	
	XXX	± .010				
ANGULAR TOL	± 0°30'		CHECKED BY OR LEADER			
TOL ON LOFTED DELINEATIONS IS						
			REL GROUP			
			PROJ ENGR M. BERNSTEIN		SIZE CODE IDENT NO.	
			GOVT APPD		E 26512	
					AD-383-556	
					SCALE 1/4" SHEET 1 OF 2	

T-117(1)

REVISIONS						
DATE	BY	DESCRIPTION	EFF CODE	MODEL	DATE	APPROVED



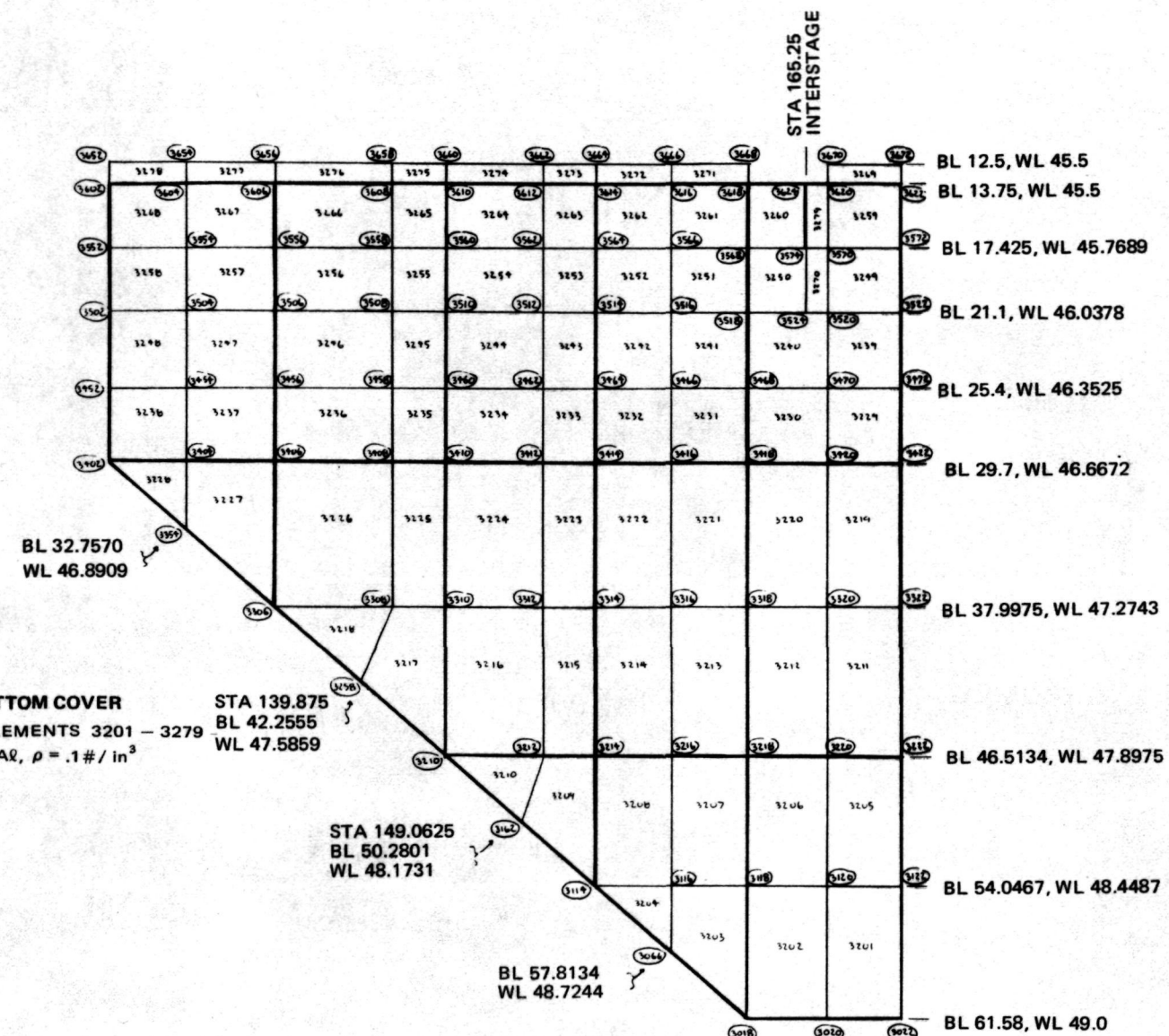
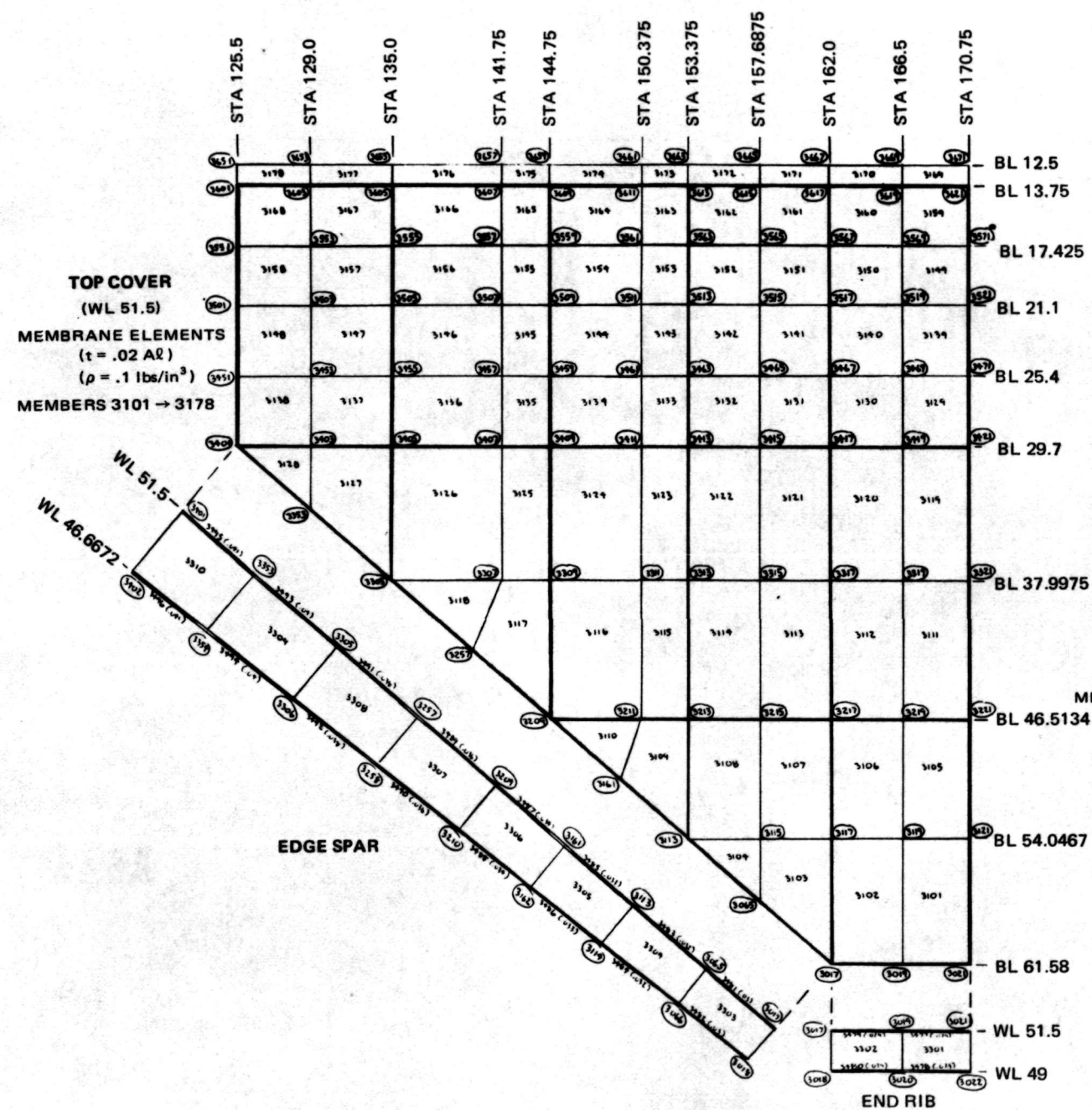
NOTE: BEAMS ALONG THIS STATION TO DISTRIBUTE KICK LOADS & MASS

BOTTOM FUSELAGE DECK
T = .025\" (EXCEPT AS NOTED)

FOR PRINTS LIST, SPECIAL WORK AND SPECIAL, SEE DOCUMENT ORIGIN NUMBER PRINTED PL

UNLESS OTHERWISE SPECIFIED DIMENSIONS IN INCHES			CONTRACT NO.		GRUMMAN AEROSPACE CORPORATION BETHPAGE, NEW YORK 11714	
LINEAR TOL	XX	± .03	DRAWN BY J. ZALESK		Fig. A-5 Skin, Deck and Keel Structure Orbiter Fuselage (Sheet 2 of 2)	
	XXX	± .010	LAYOUT BY			
ANGULAR TOL		± 0°30'	CHECKED BY			
TOL ON LOFTED DELINEATIONS IS			OR LEADER			
			REL GROUP			
			PROJ ENGR M. BERNSTEIN		SIZE	CODE IDENT NO.
					E	26512
			GOVT APPD		AD-383-556	
					SCALE	1/4"
					SHEET 2 OF 2	

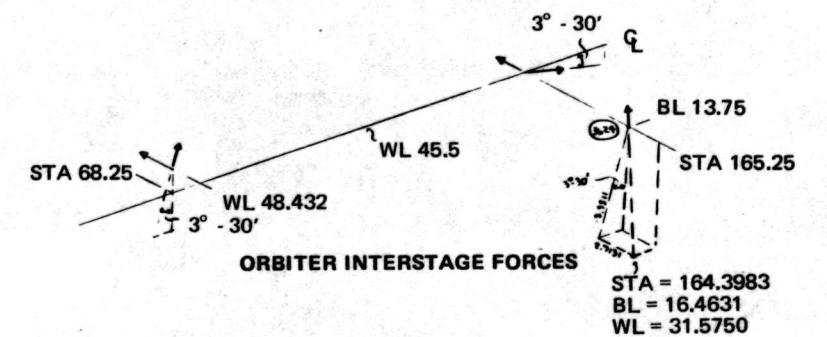
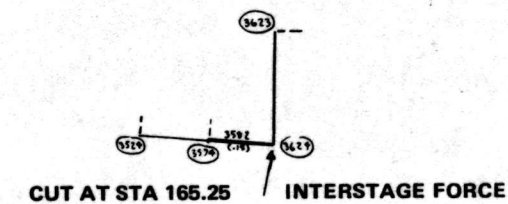
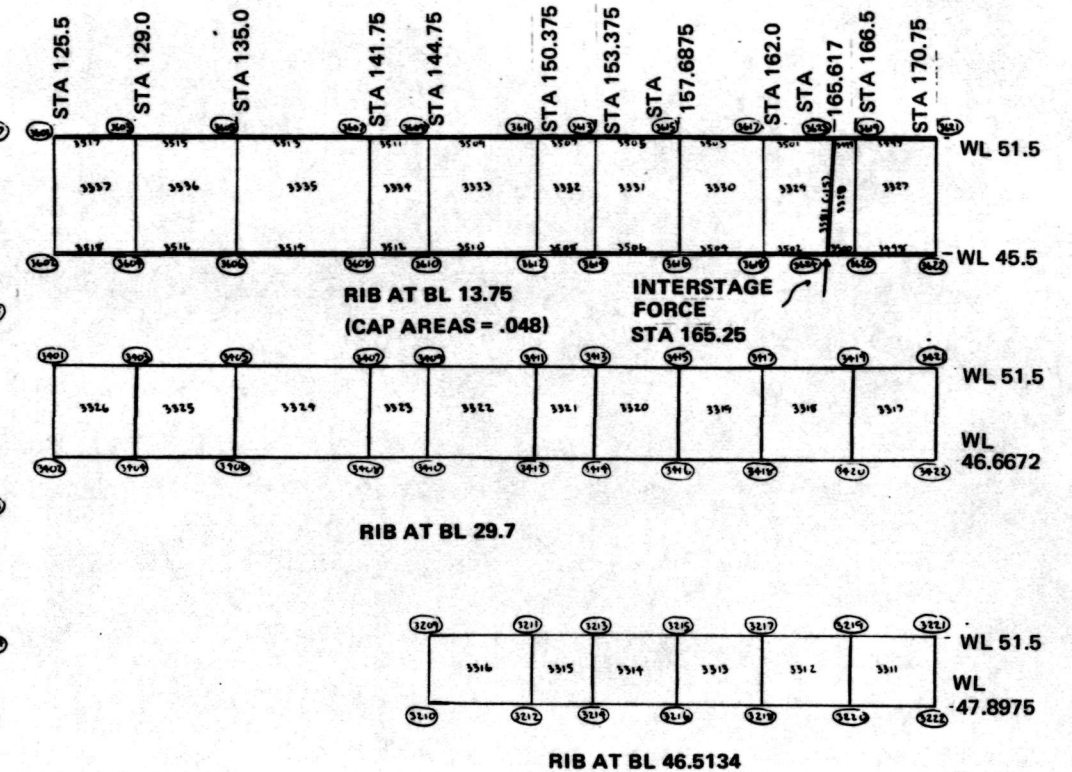
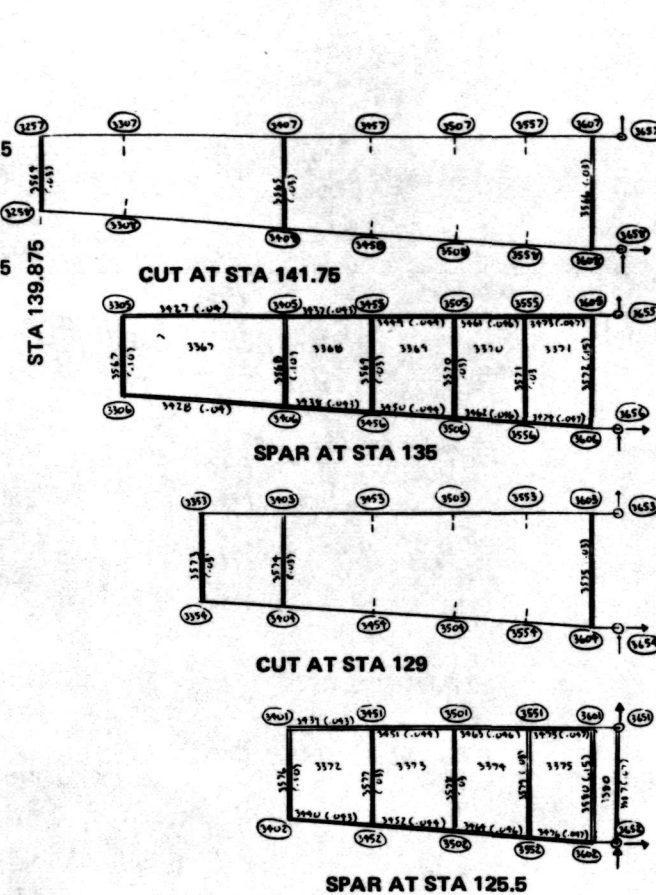
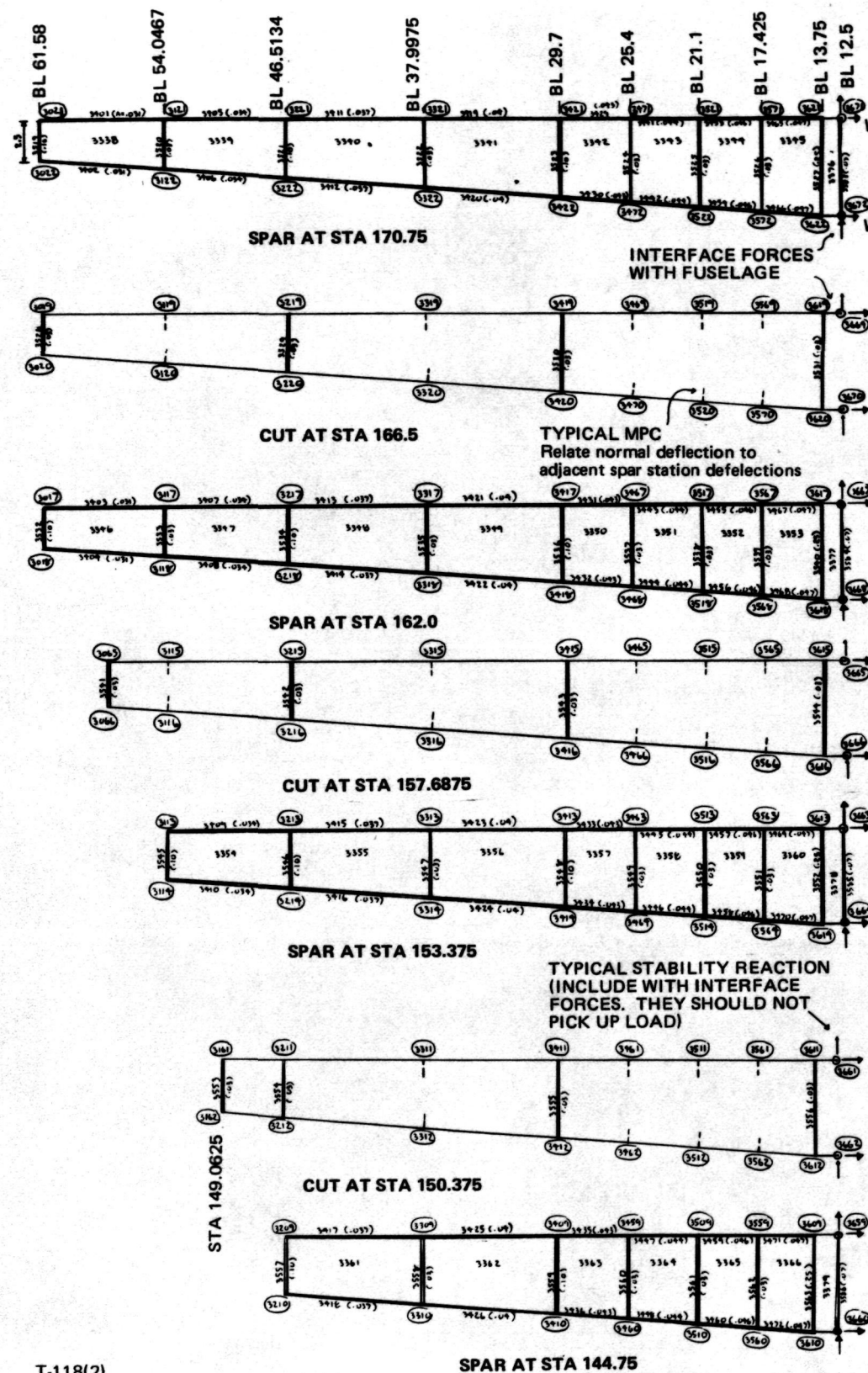
T-117(2)



T-118(1)

FOR PARTS LIST, USAGE DATA, AND DWG SH STATUS, SEE DOCUMENT SAME NUMBER PREFIXED BY

UNLESS OTHERWISE SPECIFIED		CONTRACT NO.		GRUMMAN AEROSPACE CORPORATION	
DIMENSIONS IN INCHES		DRAWN BY J. ZALESK		BETHPAGE, NEW YORK 11714	
LINEAR TOL.	XX	LAYOUT BY		Fig. A-6 Orbiter Wing (Sheet 1 of 2)	
	XXX	CHECKED BY			
ANGULAR TOL.	GR LEADER		SIZE E 26512 AD-383-557		
TOL. ON LOFTED DELINEATIONS IS	REL GROUP				
		PROJ ENGR M. BERNSTEIN		SCALE 1/4	
		GOVT APPD			
				SHEET 1 OF 2	



NOTES

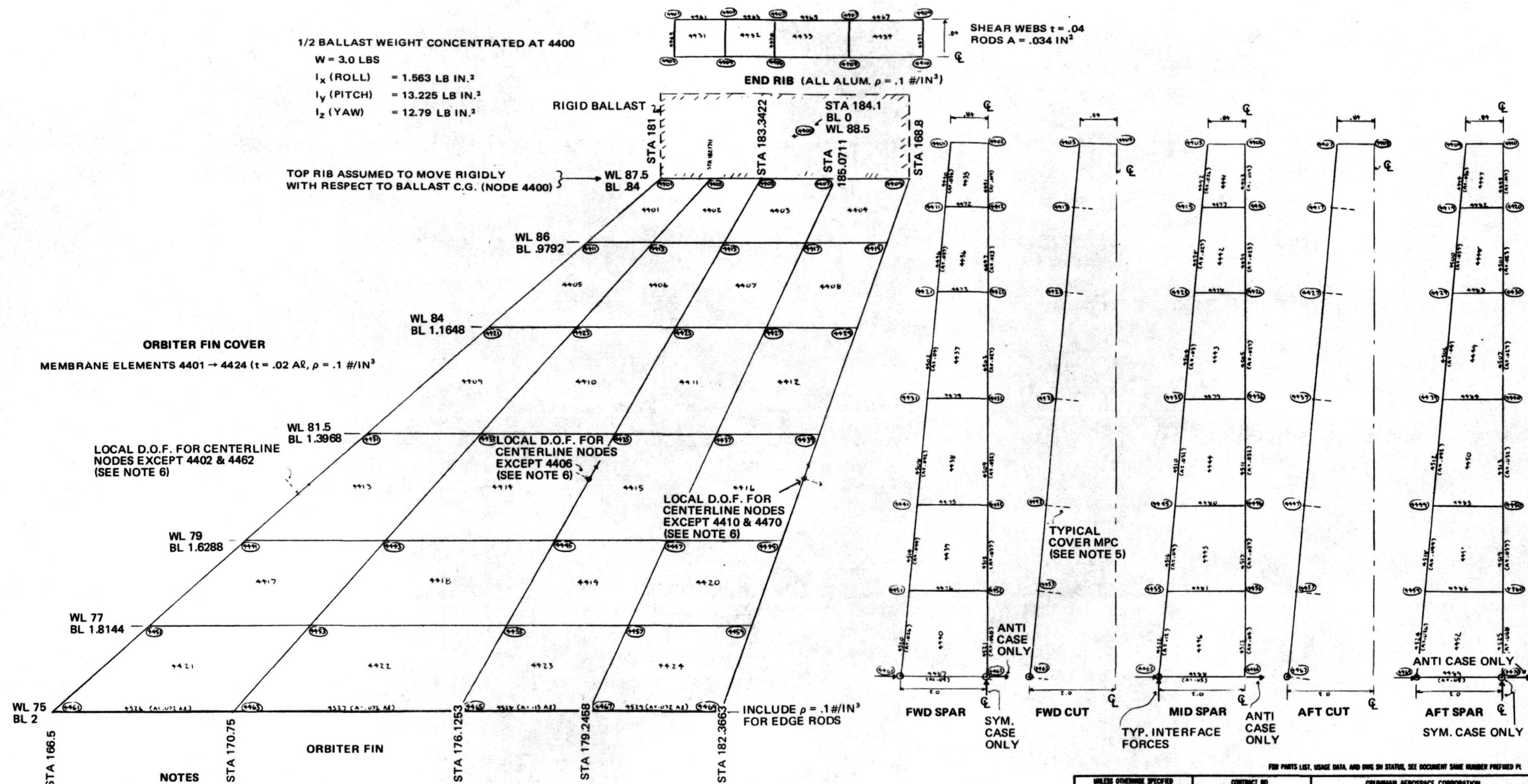
- All Spar and Rib webs are shear only elements (members 3301 → 3379). Structural density $\rho = .1 \text{ \#/in}^3$. Thickness = .032 A2 except members 3376 → 3380 which is $t = .125 \text{ A2}$. Ballast non-structural weight of .0135 \#/in^2 have been assigned to the webs, except along BL 29.7 and BL 46.5134 and member 3376 → 3380.
- Rods 3401 → 3518 are rib and spar caps. The cap areas are equivalent areas to give the correct moment of Inertia of the actual web channel. The flange mass has been included as non-structural mass of .0026 \#/in .
- Rods 3519 → 3580, 3583 → 3587 are vertical web bars. They represent actual web connection angles, or if none, represent fictitious members to transfer load into shear panels. No mass assign to these members, since ballast was assumed to cover whole webs.
- Rods 3581 and 3582 represent Interstage connection Lug.

REVISIONS					
ZONE	LTR	DESCRIPTION	EFF CODE	MODEL	DATE

FOR PARTS LIST, USAGE DATA, AND DRWG SH STATUS, SEE DOCUMENT SAME NUMBER PREFIRED PL

UNLESS OTHERWISE SPECIFIED			CONTRACT NO.		GRUMMAN AEROSPACE CORPORATION		
DIMENSIONS IN INCHES					BETHPAGE, NEW YORK 11714		
LINEAR TOL	XX	± .03	DRAWN BY J. ZALESK		Fig. A-6 Orbiter Wing (Sheet 2 of 2)		
	XXX	± .010	LAYOUT BY				
ANGULAR TOL		± 0°30'	CHECKED BY				
			GR LEADER				
TOL ON LOFTED DELINEATIONS IS			REL GROUP				
			PROJ ENGR M BERNSTEIN				
					SIZE	CODE IDENT NO	
					E	26512	AD-383-557
			GOVT APPD		SCALE	1/4	SHEET 2 OF 2

T-118(2)



NOTES

- 1) ALL SPAR WEBS ARE SHEAR ONLY ELEMENTS ($t = .032$ AL, $\rho = .1$ #/IN³)
- 2) OUTER SPAR CAP AREAS ARE EQUIVALENT AREAS TO GIVE CORRECT MOMENT OF INERTIA OF ACTUAL CHANNEL. NO DENSITY ρ ASSIGNED TO THESE RODS ONLY NON-STRUCTURAL WEIGHT TO INCLUDE FLANGES AND OTHER NEGLECTED MATERIAL.
- 3) RODS 4472 → 4486 REPRESENT FICTITIOUS RODS TO TRANSFER LOAD INTO SHEAR PANELS (A = .034 AL, NO ρ)

- 4) CENTERLINE SPAR CAPS ARE EQUIVALENT AREAS SO THAT WHEN ADDED TO OUTER CAPS, GIVE THE CORRECT CROSS SECTION AREA OF CHANNEL. NO WEIGHT ASSIGNED TO THESE RODS.
- 5) COVER MPC'S RELATE DEFLECTIONS NORMAL TO COVER TO ADJACENT SPAR DEFLECTIONS.
- 6) FOR SYM. CASE ONLY, THE LOCAL D.O.F. NORMAL TO PLANE OF SPAR WILL BE MPC'ed TO OUTER SPAR NODE D.O.F.

FOR PARTS LIST, USAGE DATA, AND DWG SW STATUS, SEE DOCUMENT SAME NUMBER PREFIXED PL

UNLESS OTHERWISE SPECIFIED		CONTRACT NO.		GRUMMAN AEROSPACE CORPORATION	
DIMENSIONS IN INCHES				BETHPAGE, NEW YORK 11714	
LINEAR TOL	XX	± .03	DRAWN BY J. ZALESK	Fig. A-7 Orbiter Fin and Payload (Sheet 1 of 2)	
	XXX	± .010			
ANGULAR TOL	± 0°30'		CHECKED BY		
			OR LEADER		
TOL ON LOFTED DELINEATIONS IS		REL GROUP			
		PROJ ENGR M. BERNSTEIN		SIZE	CODE IDENT NO.
				E	26512
		GOVT APPD		AD-383-558	
				SCALE	FULL
				SHEET 1 OF 2	

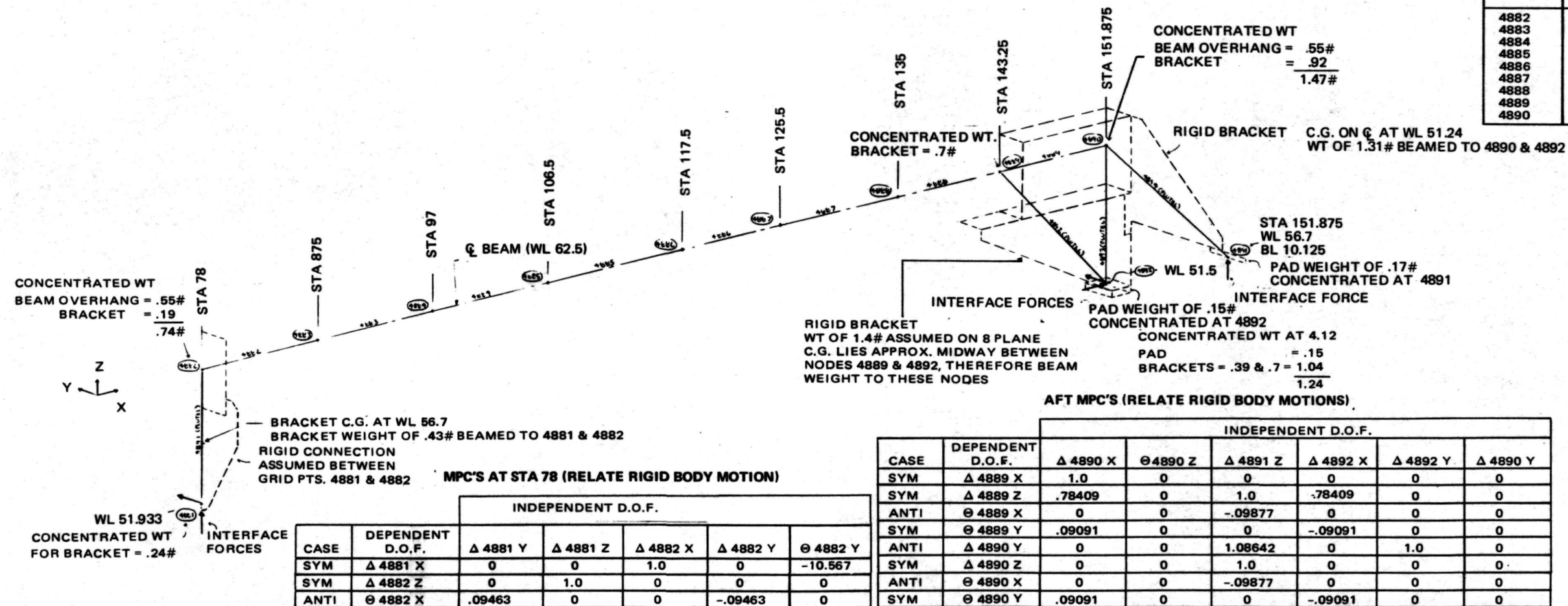
T-119(1)

REVISIONS						
ZONE	LTN	DESCRIPTION	REV CODE	MODEL	DATE	APPROVED

NOTES

- 1) ORBITER PAYLOAD BEAM REPRESENTED BY BEAMS 4882 → 4889 (ALUMINUM)
SECTION PROPERTIES ARE FOR 1/2 STRUCTURE ($A = 5.775 \text{ IN}^2$, $I_{yy} = 23.23 \text{ IN}^4$, $I_{zz} = 21.87 \text{ IN}^4$, $J = 31.0 \text{ IN}^4$)
- 2) STRUCTURAL DENSITY OF $P = .1 \text{ #/IN}^3$ WAS USED. THE 1/2 BALLAST WEIGHT OF 18.1 LBS WAS DISTRIBUTED AS NON STRUCTURAL WT OF .245 #/IN.
- 3) ALL SUPPORT BRACKETS, ASSUMED RIGID, THEIR WEIGHTS WERE DISTRIBUTED AS CONCENTRATED WEIGHTS AS SHOWN IN SKETCH
- 4) THE TORSIONAL WEIGHT INERTIA OF PAYLOAD BEAM & BALLAST WAS INCLUDED AS CONCENTRATED MASS. THIS MASS, AT EACH NODE BASED ON 4.3 #/IN^2

NODE	TORSIONAL MASS (# IN ²)
4882	25.13
4883	40.85
4884	40.85
4885	44.08
4886	40.85
4887	37.63
4888	38.16
4889	36.28
4890	23.24



ORBITER LONG. PAYLOAD

T-119(2)

UNLESS OTHERWISE SPECIFIED DIMENSIONS IN INCHES		CONTRACT NO.		GRUBMAN AEROSPACE CORPORATION BETHPAGE, NEW YORK 11714	
LINEAR TOL	XXX ± .010	DRAWN BY J. ZALESK	LAYOUT BY	Fig. A-7 Orbiter Fin and Payload (Sheet 2 of 2)	
ANGULAR TOL	± .03°	CHECKED BY	OR LEADER		
TOL ON LOFTED DELINEATIONS IS		REL GROUP			
		PROJ ENGR M. BERNSTEIN	SCALE	CODE IDENT NO	AD-383-558
		GOVT APPD	SCALE FULL		SHEET 2 OF 2

Appendix B
ORBITER STATIC TEST CASES - ANALYTICAL DEFLECTIONS FOR
MODEL I SUPPORTED ON INTERSTAGES

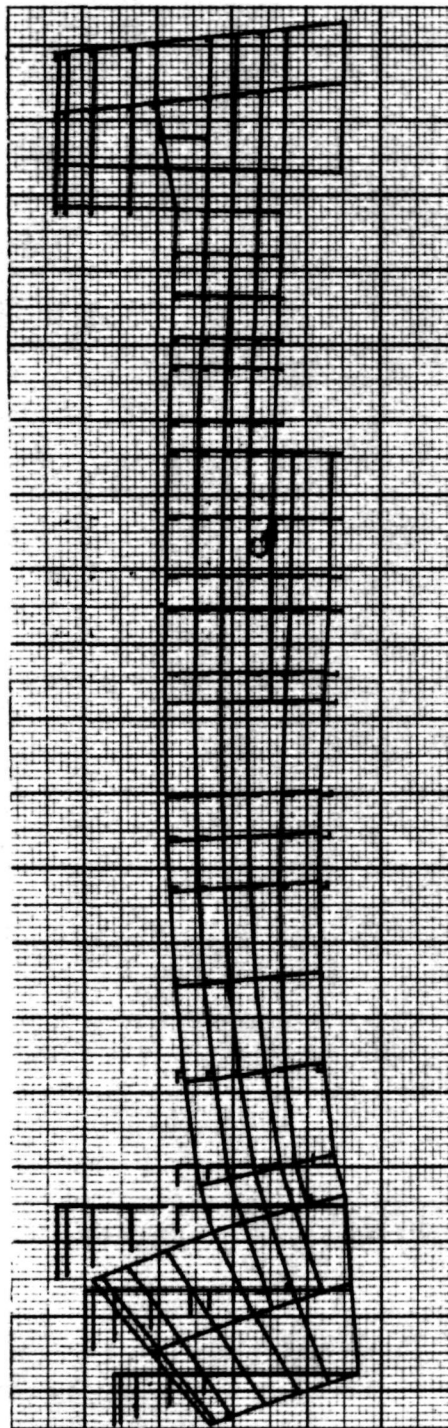
TABLE OF CONTENTS

NOTE

Appendix B consists of the
following illustrations:

<u>Figure</u>		<u>Page</u>
B-1	Fuselage Load - Sta 46.75, Grid 120	B-2
B-2	Fuselage Load - Sta 116.0, Grid 906	B-3
B-3	Wing Tip Load - Grid 3017.	B-4
B-4	Fin Ballast Load - Grid 4400	B-5
B-5	OMS Ballast Load - Grid 2200	B-6
B-6	Payload Load - Sta 117.5, Grid 4885	B-7
B-7	Payload Moment - Sta 117.5, Grid 4886.	B-8
B-8	Orbiter Fuselage - Dead Load Down	B-9

1 12/14/73 MAX-DEF. = 5.31948-05

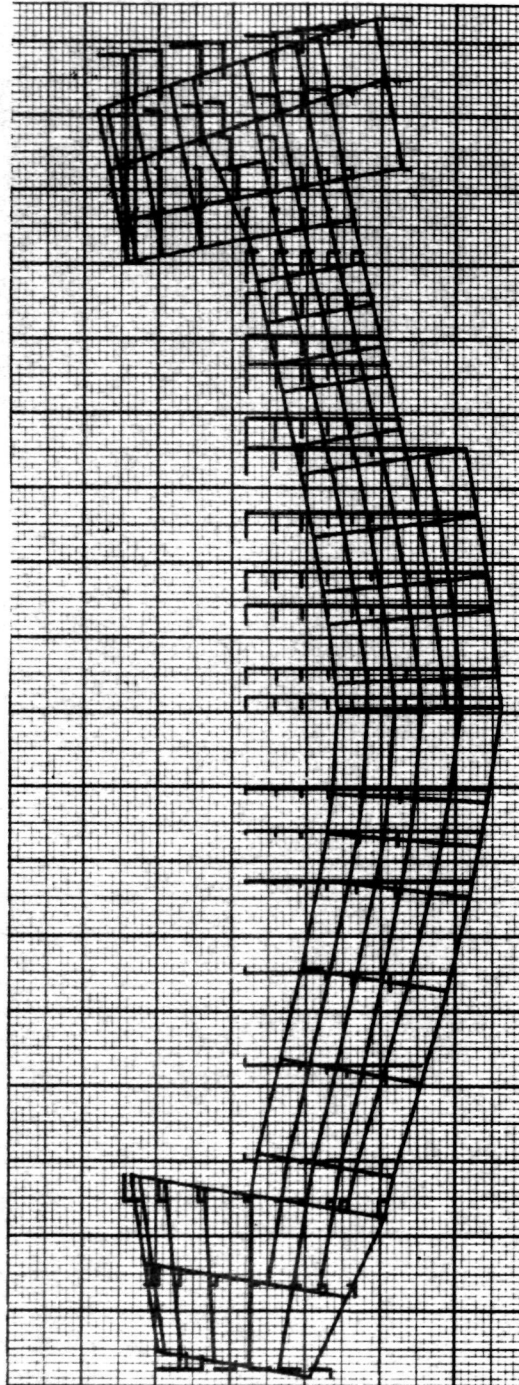


ORBITER STATIC TEST CASES ON INTERSTAGE SUPPORTS
ORBITER FUSELAGE, SYM CASE
UNIT PZ DOWN ON FULL ORBITER (FUS. LOAD AT STA 46.75-GRID 120)
STATIC DEFOR. SUBCASE 1

T-120

Fig. B-1 Fuselage Load - Sta 46.75, Grid 120

2 12/14/73 MAX-DEF. = 3.10005-06

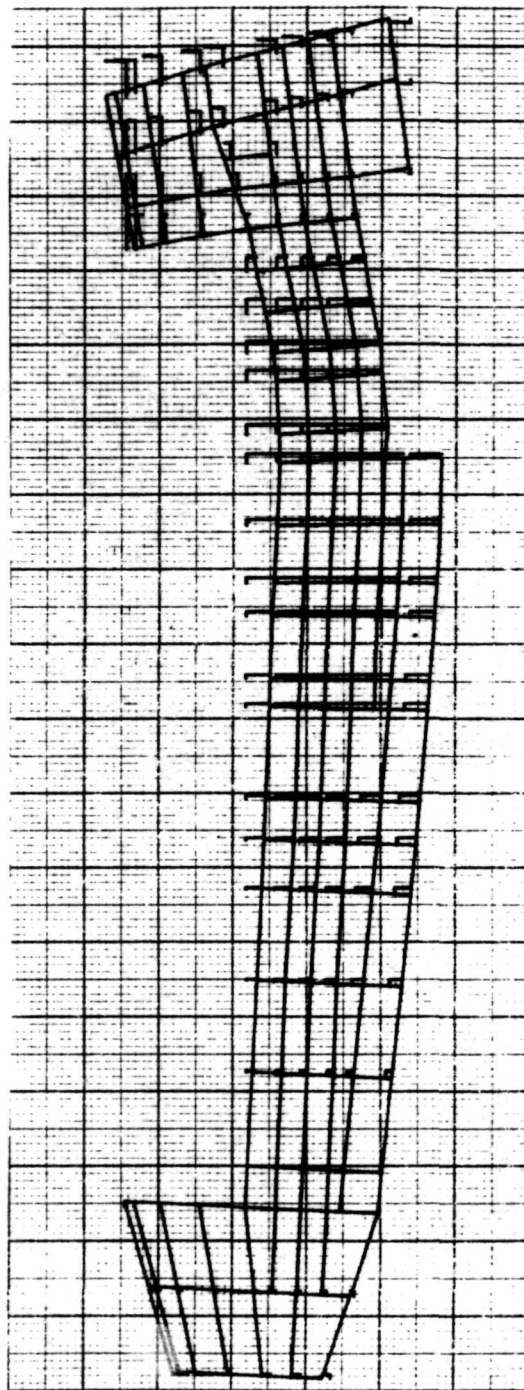


ORBITER STATIC TEST CASES ON INTERSTAGE SUPPORTS
ORBITER FUSELAGE, SYM CASE
UNIT PZ DOWN ON FULL ORBITER (FUS. LOAD AT STA 116.0-GRID 906)
STATIC DEFOR. SUBCASE 2

T-121

Fig. B-2 Fuselage Load - Sta 116.0, Grid 960

3 12/14/73 MAX-DEF. = 1.78167-05

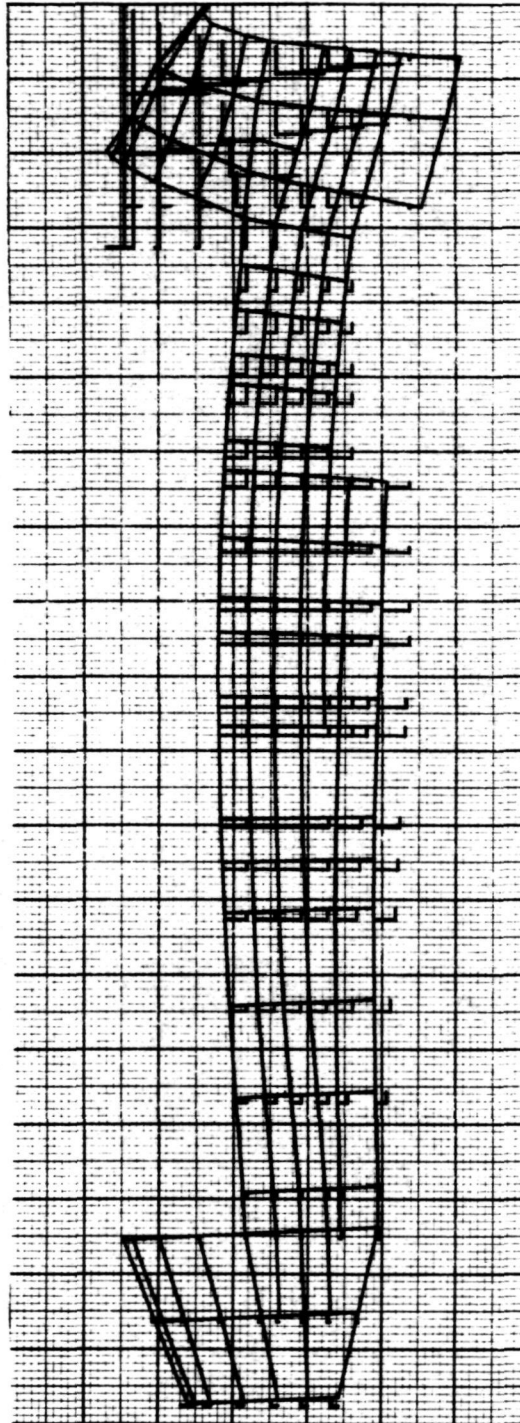


ORBITER STATIC TEST CASES ON INTERSTAGE SUPPORTS
ORBITER FUSELAGE, SYM CASE
UNIT P2 ON FULL ORBITER (WING TIP LOAD-GRID 3017)
STATIC DEFOR. SUBCASE 3

T-122

Fig. B-3 Wing Tip Load - Grid 3017

4 12/14/73 MAX-DEF. = 8.78577-05

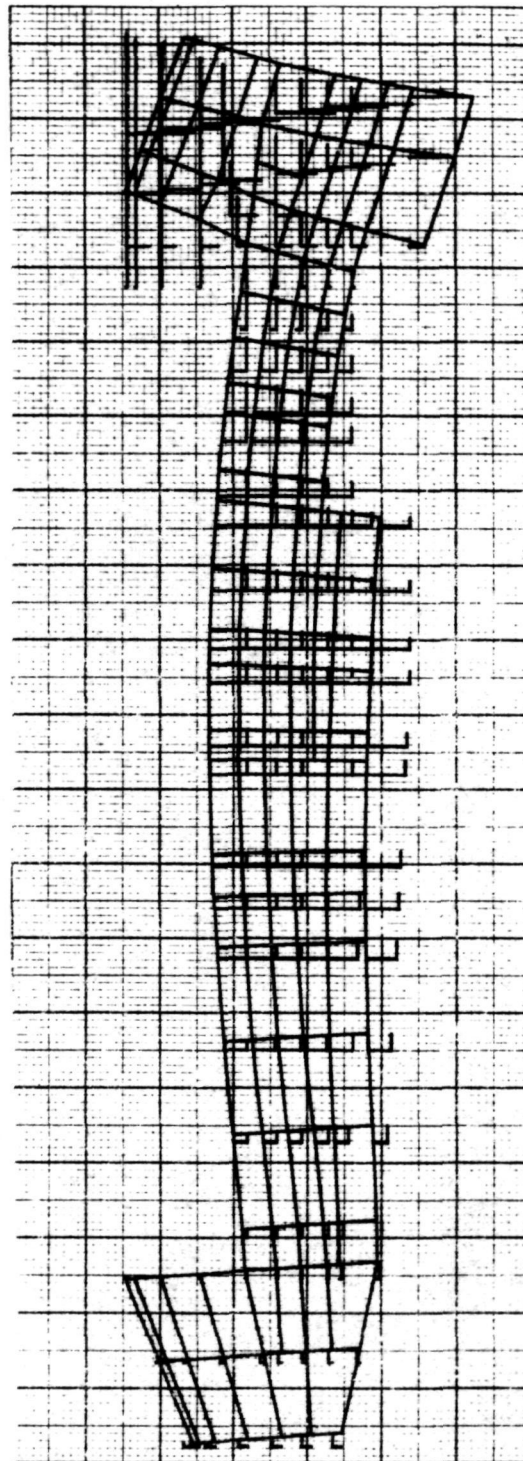


ORBITER STATIC TEST CASES ON INTERSTAGE SUPPORTS
ORBITER FUSELAGE, SYM CASE
UNIT PX AFT ON FULL ORBITER (FIN BALLAST LOAD - GRID 4400)
STATIC DEFOR. SUBCASE 4

Fig. B-4 Fin Ballast Load - Grid 4400

T-123

5 12/14/73 MAX-DEF = 3.64883-05

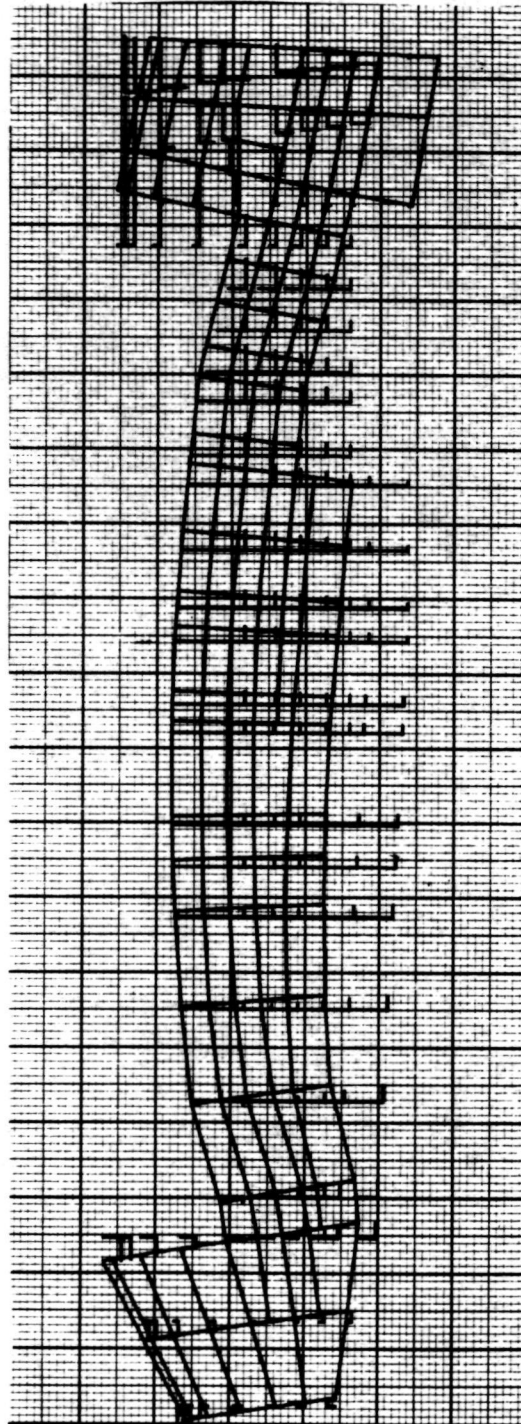


ORBITER STATIC TEST CASES ON INTERSTAGE SUPPORTS
 ORBITER FUSELAGE, SYM CASE
 UNIT PX AFT ON FULL ORBITER (OMS BALLAST LOAD - GRID 2200)
 STATIC DEFOR. SUBCASE 7

T-124

Fig. B-5 OMS Ballast Load - Grid 2200

6 12/14/73 MAX-DEF. = 1.39090-05

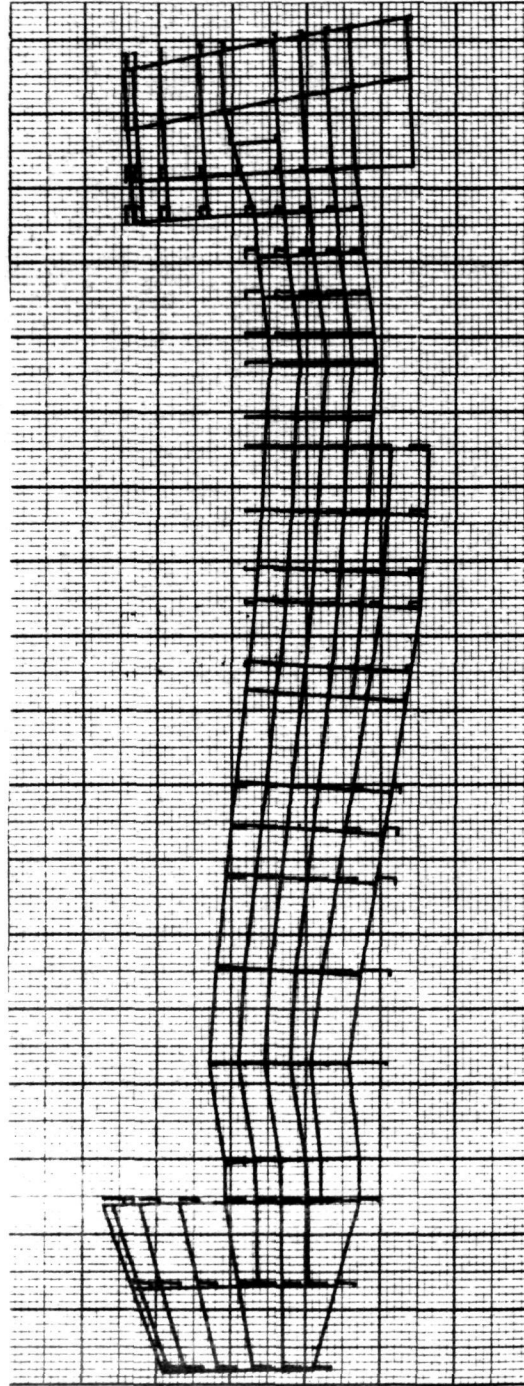


ORBITER STATIC TEST CASES ON INTERSTAGE SUPPORTS
ORBITER FUSELAGE, SYM CASE
UNIT PZ UP ON FULL ORBITER (PAYLOAD LOAD STA 117.5-GRID 4885)
STATIC DEFOR. SUBCASE 8

T-125

Fig. B-6 Payload Load - Sta 117.5, Grid 4885

7 12/14/73 MAX-DEF. = 3.09988-07

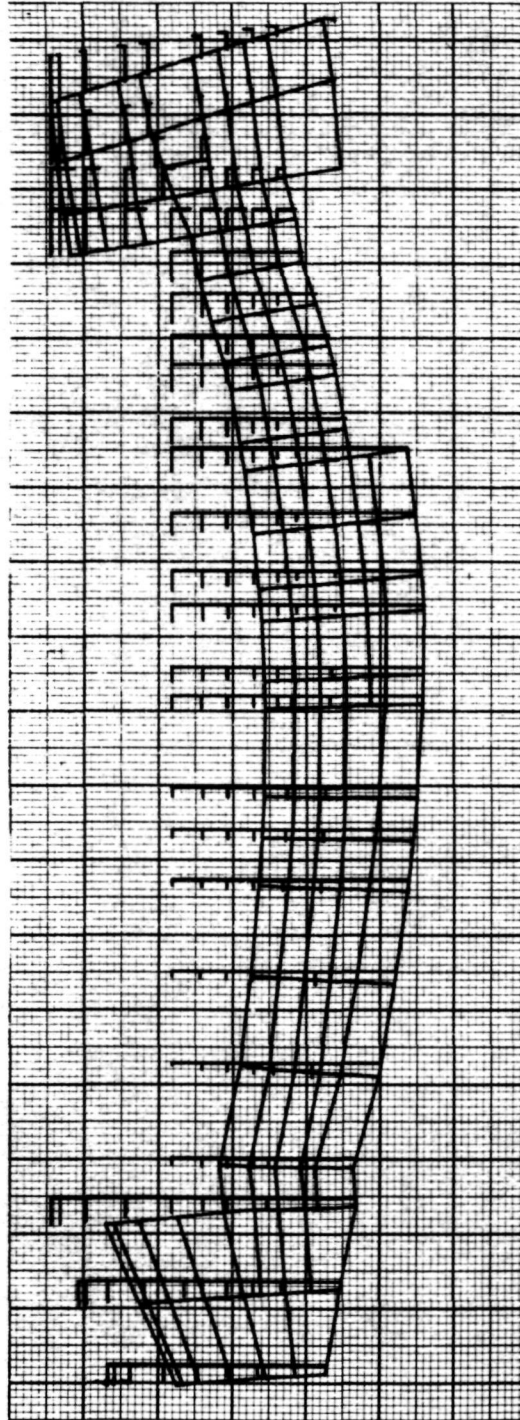


ORBITER STATIC TEST CASES ON INTERSTAGE SUPPORTS
 ORBITER FUSELAGE, SYM CASE
 UNIT MY MOM. ON FULL ORBITER (PAYLOAD MOM. STA 117.5-GRID 4886)
 STATIC DEFOR. SUBCASE 9

T-126

Fig. B-7 Payload Moment - Sta 117.5, Grid 4886

8 12/14/73 MAX-DEF. = 0.0293260



ORBITER STATIC TEST CASES ON INTERSTAGE SUPPORTS
ORBITER FUSELAGE, SYM CASE
DEAD LOAD DOWN
STATIC DEFOR. SUBCASE 12

T-127

Fig. B-8 Orbiter Fuselage - Dead Load Down

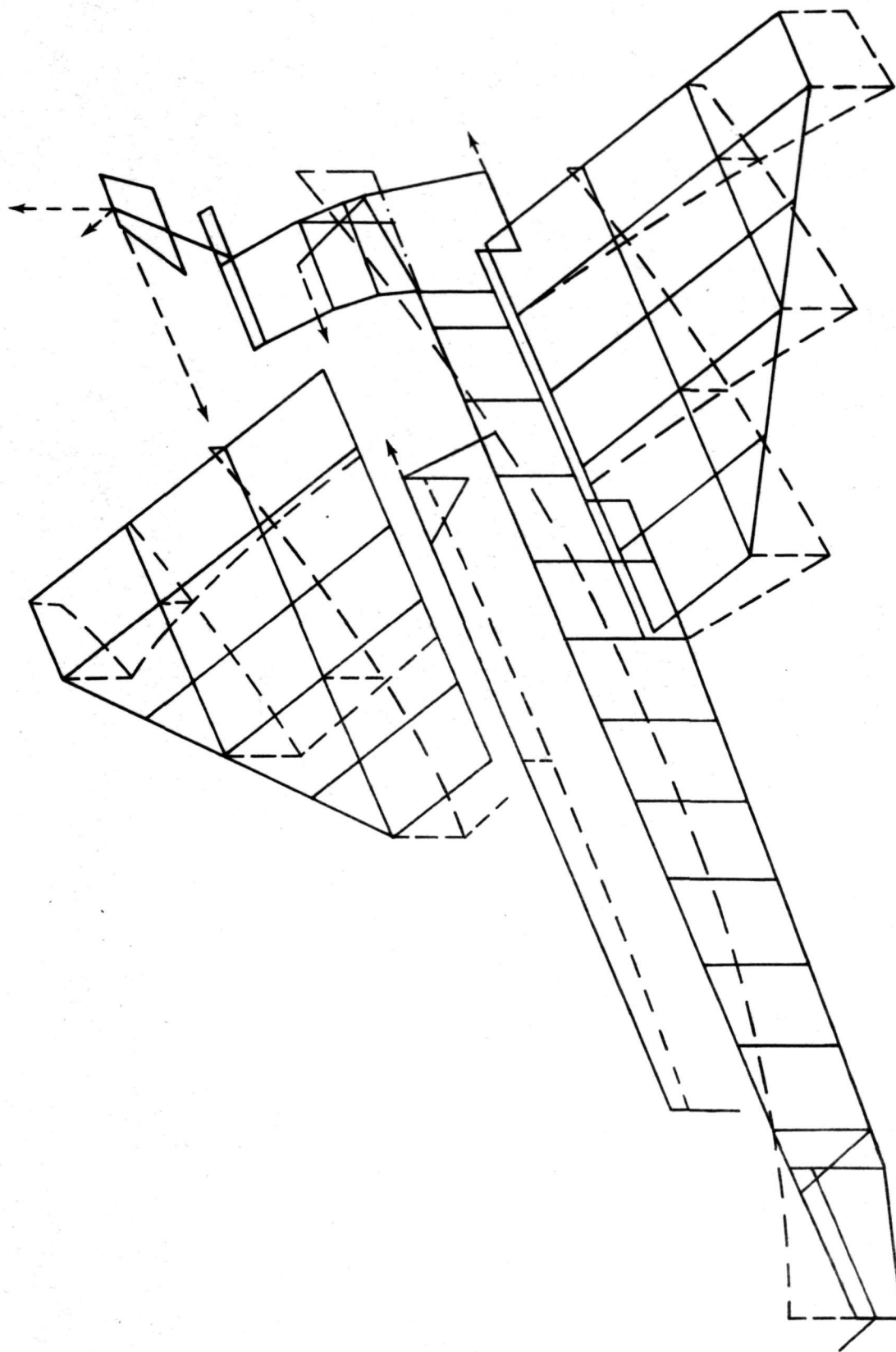
Appendix C
MODE SURVEY DATA

TABLE OF CONTENTS

NOTE

Appendix C consists of
the following illustrations:

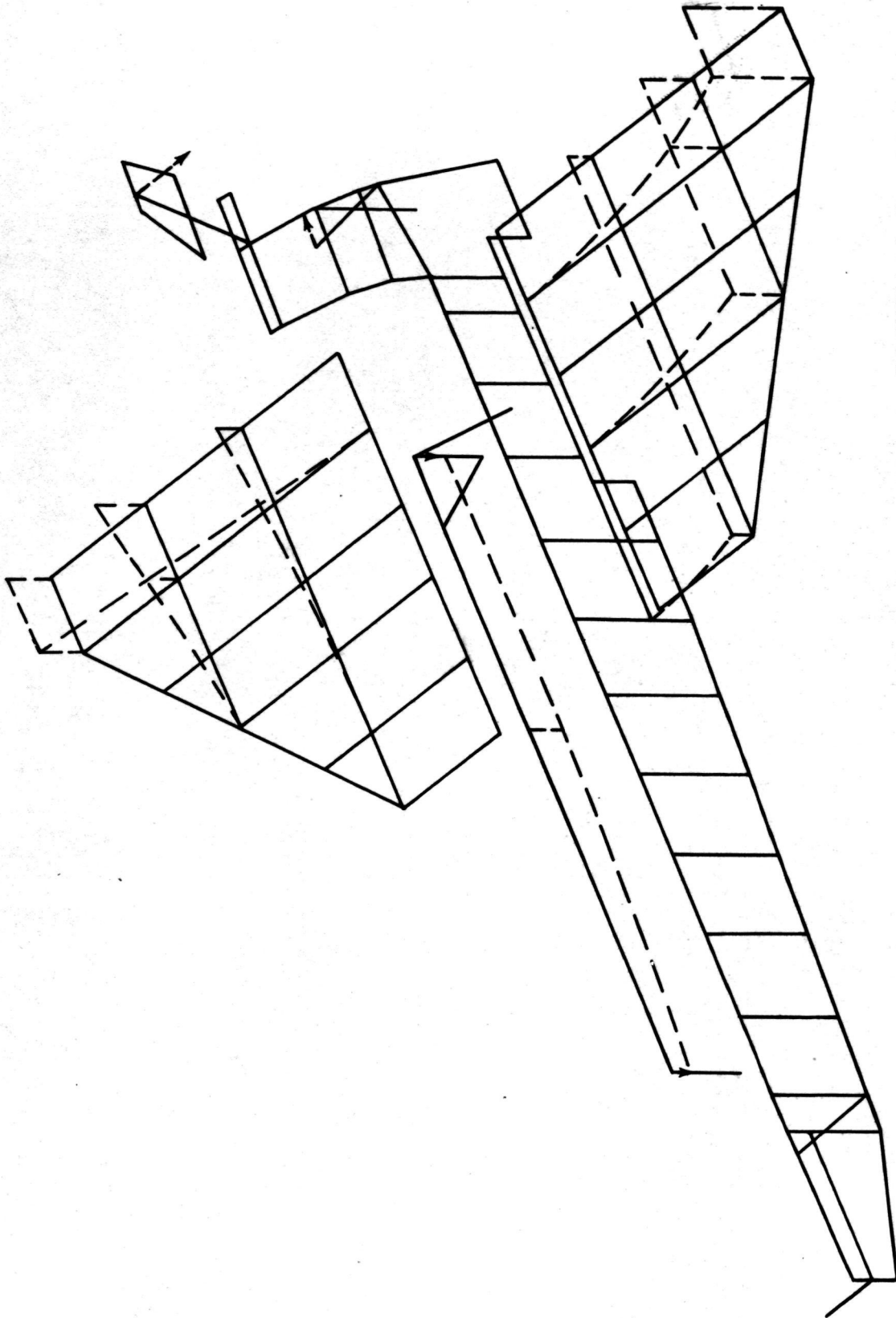
<u>Figure</u>		<u>Page</u>
C-1	Preliminary Mode Survey Data (7-12-73), $f = 43.6$ Hz Symmetric Z-Excitation	C-2
C-2	Preliminary Mode Survey Data (7-13-73), $f = 51.2$ Hz (LH Wing Resonance) Symmetric Z-Excitation	C-3
C-3	Preliminary Mode Survey Data (7-13-73), $f = 54.2$ Hz (RH Wing Resonance) Symmetric Z-Excitation	C-4
C-4	Preliminary Mode Survey Data (7-12-73), $f = 58.2$ Hz Symmetric Z-Excitation	C-5
C-5	Preliminary Mode Survey Data (7-12-73), $f = 80.1$ Hz Symmetric Z-Excitation	C-6
C-6	Preliminary Mode Survey Data (7-12-73), $f = 95.7$ Hz Symmetric Z-Excitation	C-7
C-7	Preliminary Mode Survey Data (7-12-73), $f = 104.1$ Hz Symmetric Z-Excitation	C-8
C-8	Preliminary Mode Survey Data (7-12-73), $f = 107.0$ Hz Symmetric Z-Excitation	C-9
C-9	Preliminary Vertical Suspension Frequency Sweep, Effect of Preload	C-11
C-10	Preliminary Mode Survey Data (1-3-74) 0-lb Static Load, $f =$ 43.67 Hz Symmetric Z-Excitation	C-13
C-11	Preliminary Mode Survey Data (1-3-74), 0-lb Static Load, $f =$ 80.06 Hz Symmetric Z-Excitation	C-14
C-12	Preliminary Mode Survey Data (1-3-74), 600-lb Static Load, $f =$ 44.23 Hz Symmetric Z-Excitation	C-15
C-13	Preliminary Mode Survey Data (1-3-74), 600 lb Static Load, $f = 80.0$ Hz Symmetric Z-Excitation	C-16
C-14	Preliminary Mode Survey Data (1-3-74), 600-lb Static Load, $f = 96.85$ Hz Z-Excitation	C-17
C-15	Preliminary Mode Survey Data (1-3-74), 600-lb Static Load, $f = 106.84$ Hz Symmetric Z-Excitation	C-18
C-16	Preliminary Mode Survey Data (1-8-74), 0-lb Static Load, $f =$ 43.6 Hz Antisymmetric Y-Excitation	C-19



T-128

Ref: NASA Langley Research Center, Structural
Dynamics Research Laboratory

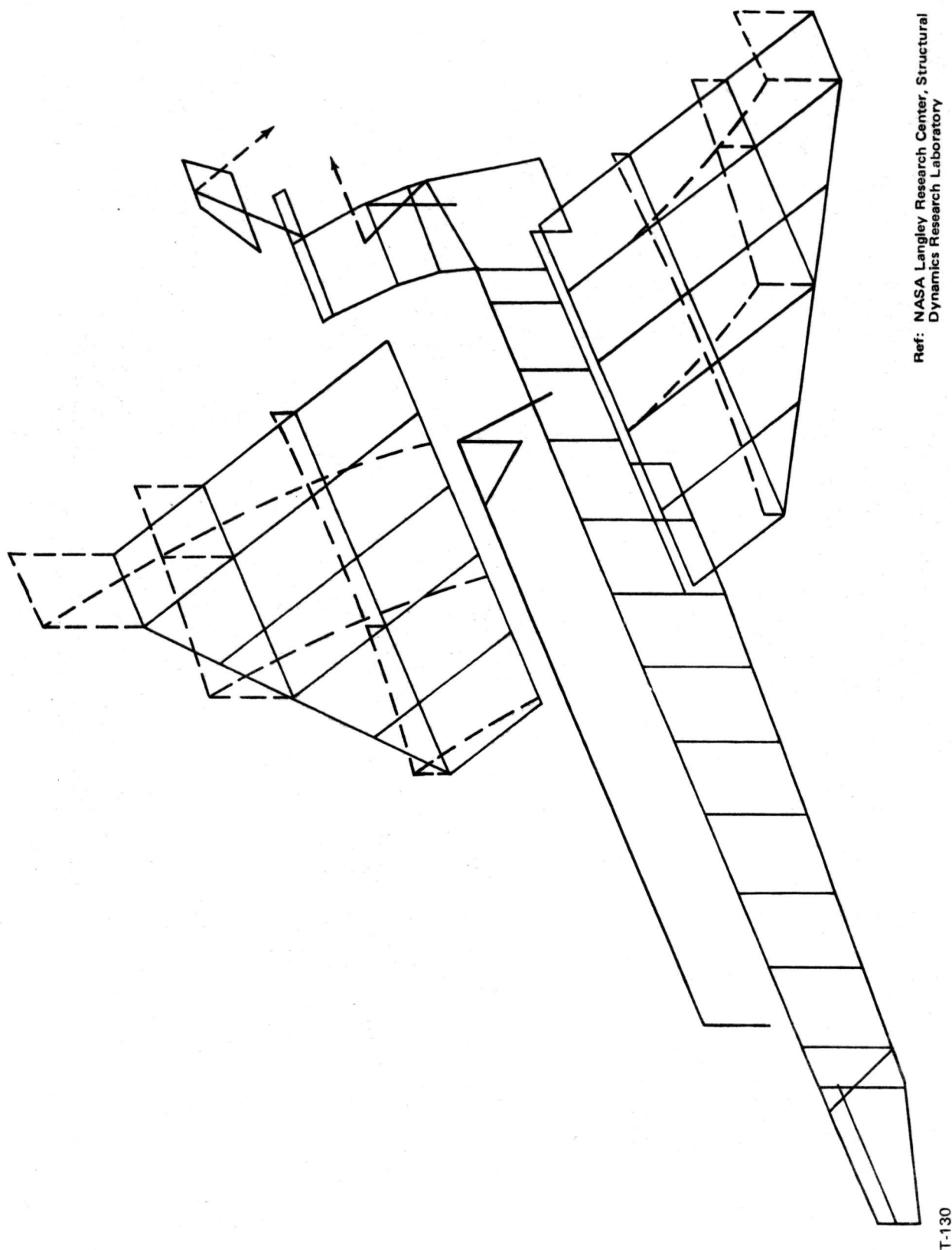
Fig. C-1 Preliminary Mode Survey Data (7-12-73), $f = 43.6$ Hz
Symmetric Z-Excitation



Ref: NASA Langley Research Center, Structural
Dynamics Research Laboratory

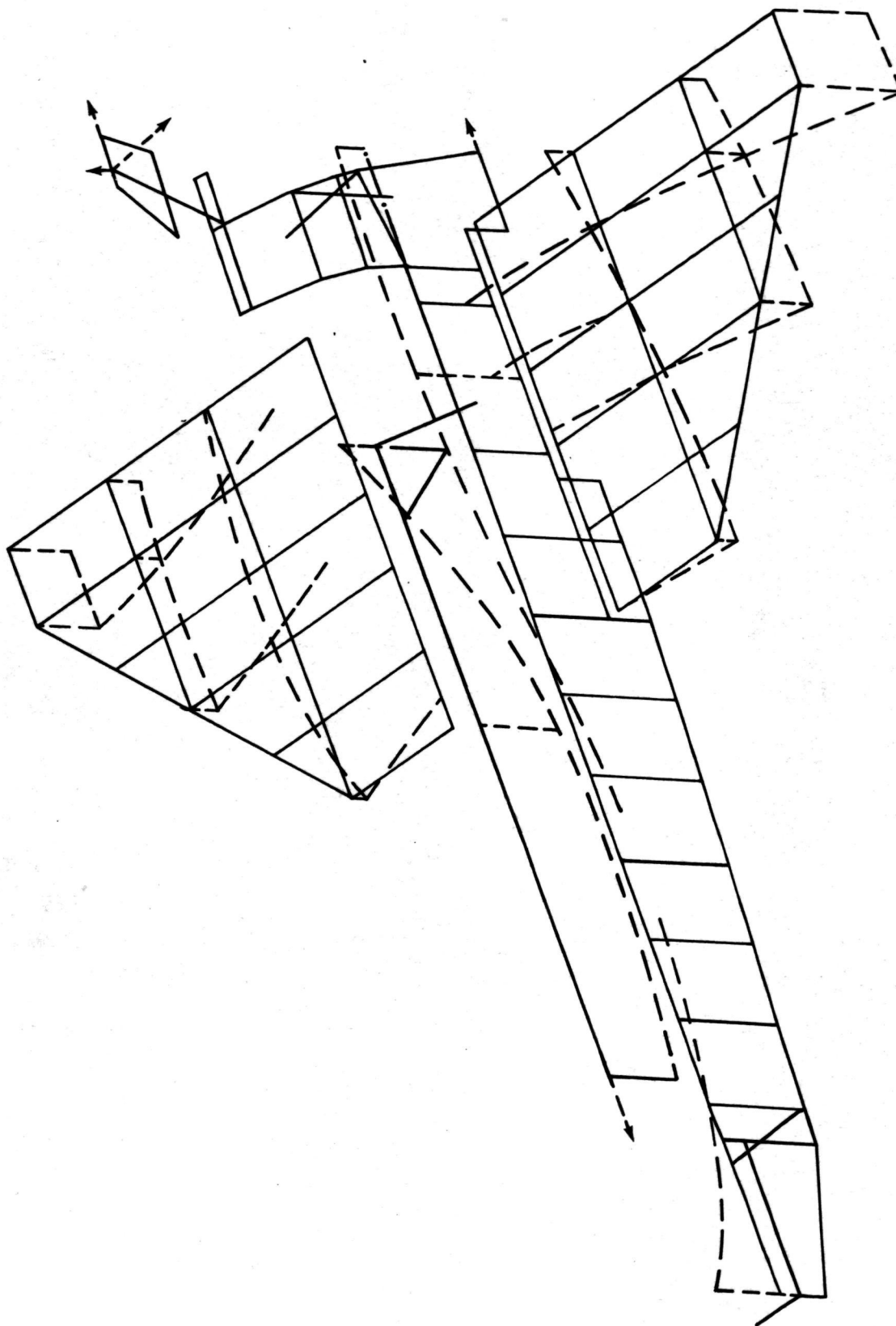
Fig. C-2 Preliminary Mode Survey Data (7-13-73), $f = 51.2$ Hz
(LH Wing Resonance) Symmetric Z-Excitation

T-129



Ref: NASA Langley Research Center, Structural
Dynamics Research Laboratory

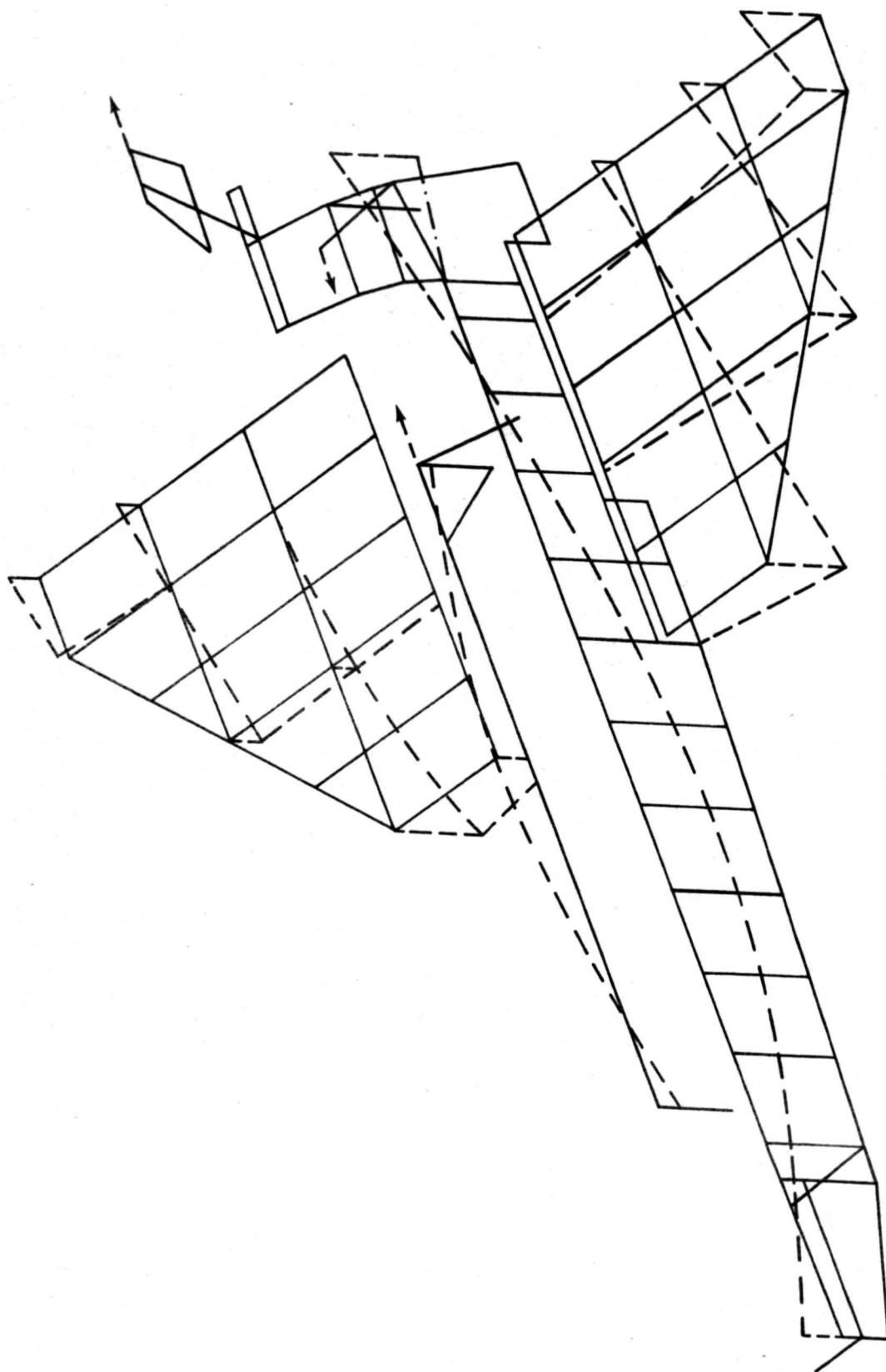
Fig. C-3 Preliminary Mode Survey Data (7-13-73), $F = 54.2 \text{ Hz}$
(RH Wing Resonance) Symmetric Z-Excitation



T-131

Ref: NASA Langley Research Center, Structural
Dynamics Research Laboratory

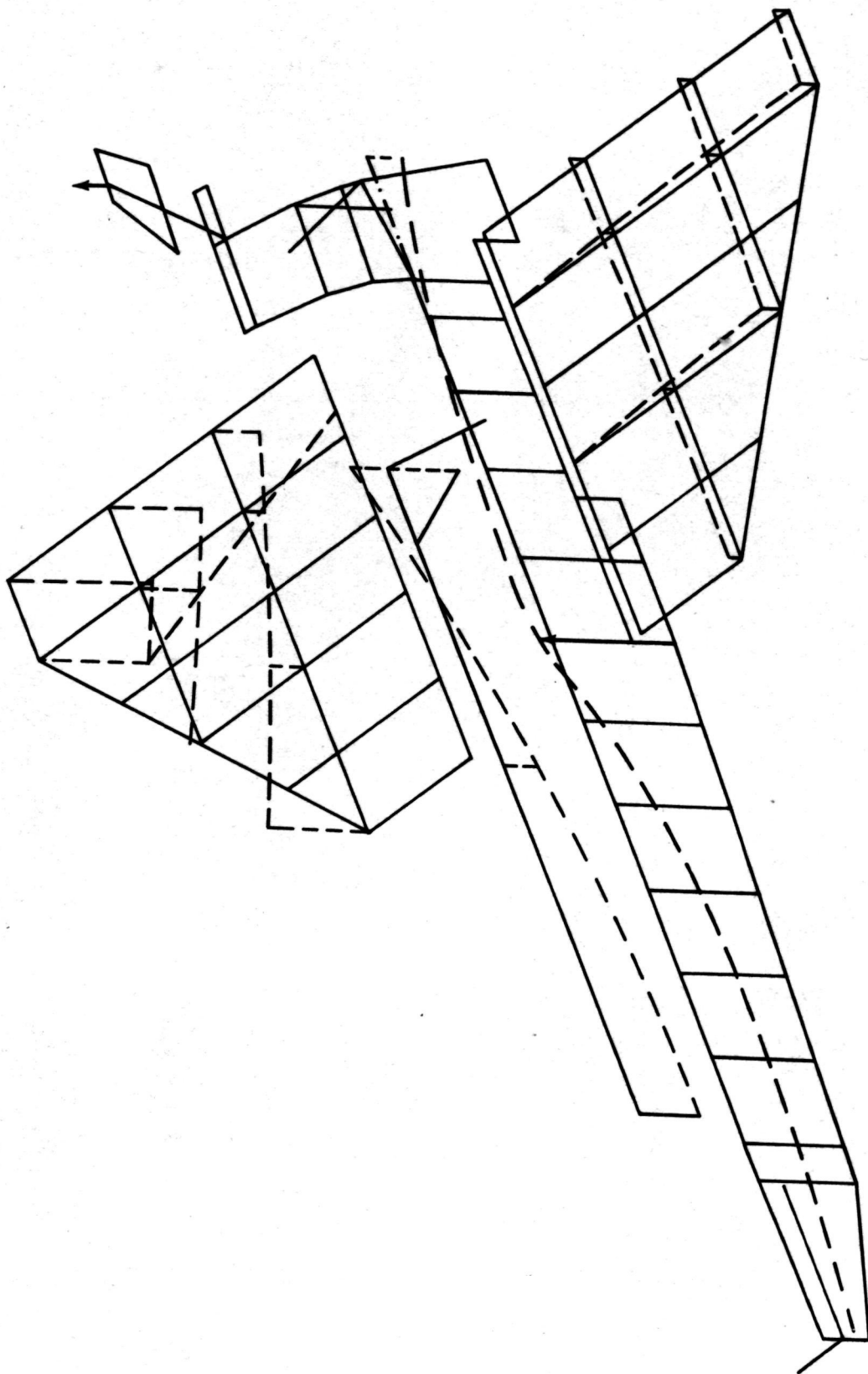
Fig. C-4 Preliminary Mode Survey Data (7-12-73), $f = 58.2$ Hz
Symmetric Z-Excitation



T-132

Ref: NASA Langley Research Center, Structural
Dynamics Research Laboratory

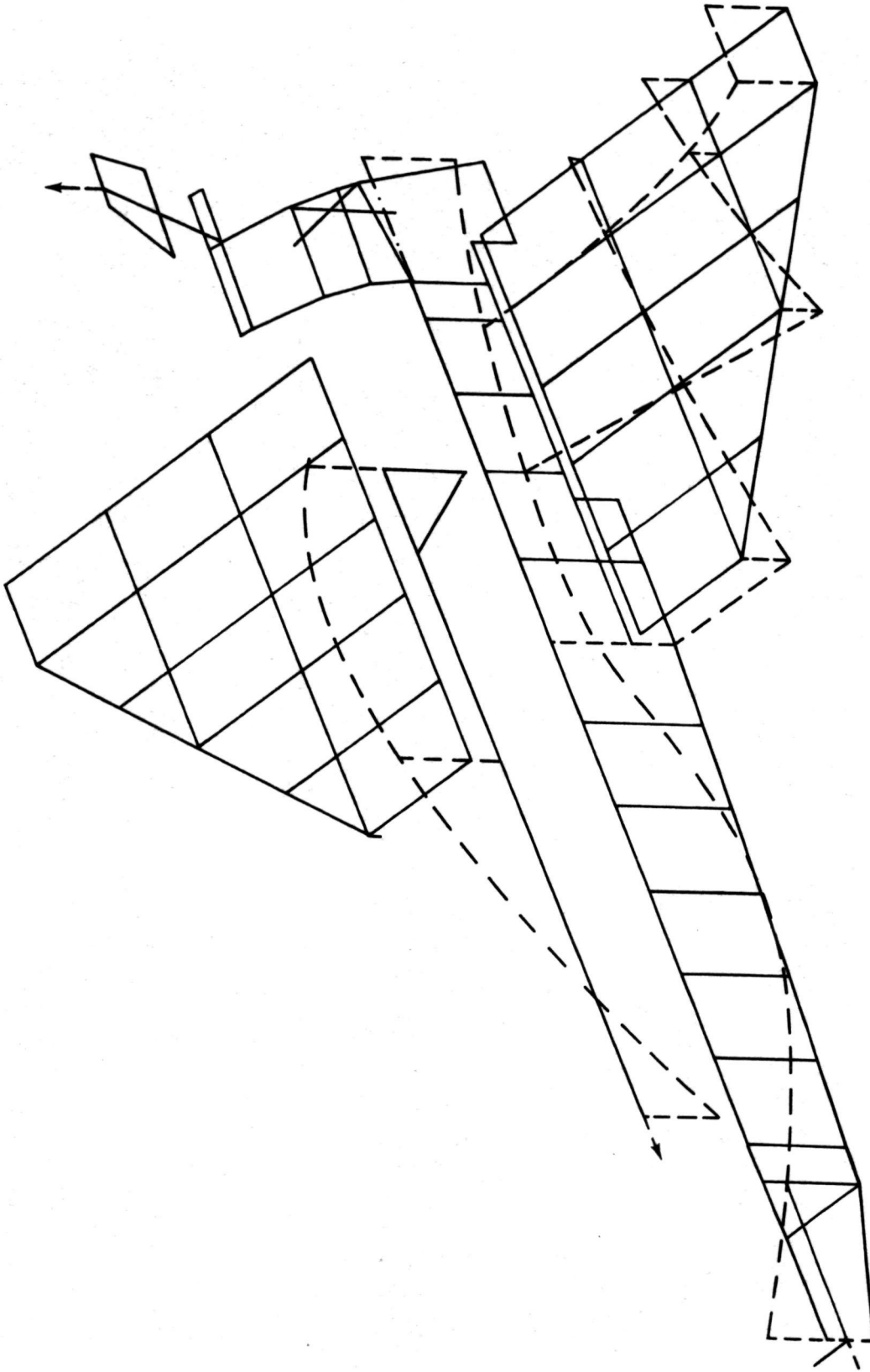
Fig. C-5 Preliminary Mode Survey Data (7-12-73), $f = 80.1$ Hz
Symmetric Z-Excitation



T-133

Ref: NASA Langley Research Center, Structural
Dynamics Research Laboratory

Fig. C-6 Preliminary Mode Survey Data (7-12-73), $f = 95.7$ Hz
Symmetric Z-Excitation

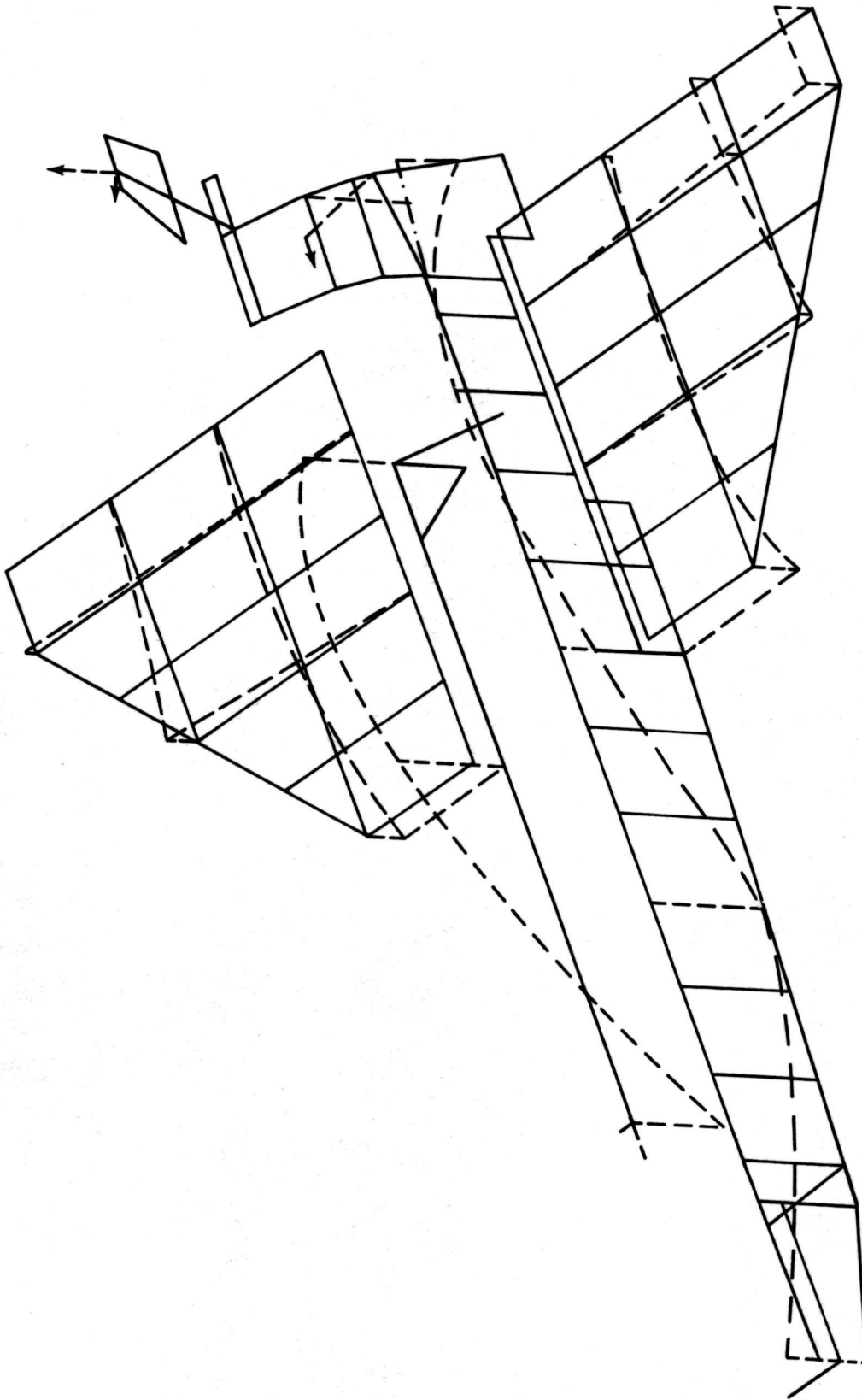


NOTE: RIGHT WING, DATA UNAVAILABLE

Ref: NASA Langley Research Center, Structural
Dynamics Research Laboratory

Fig. C-7 Preliminary Mode Survey Data (7-12-73), $f = 104.1$ Hz
Symmetric Z-Excitation

T-134



Ref: NASA Langley Research Center, Structural
Dynamics Research Laboratory

Fig. C-8 Preliminary Mode Survey Data (7-12-73), $f = 107.0$ Hz
Symmetric Z-Excitation

T-135

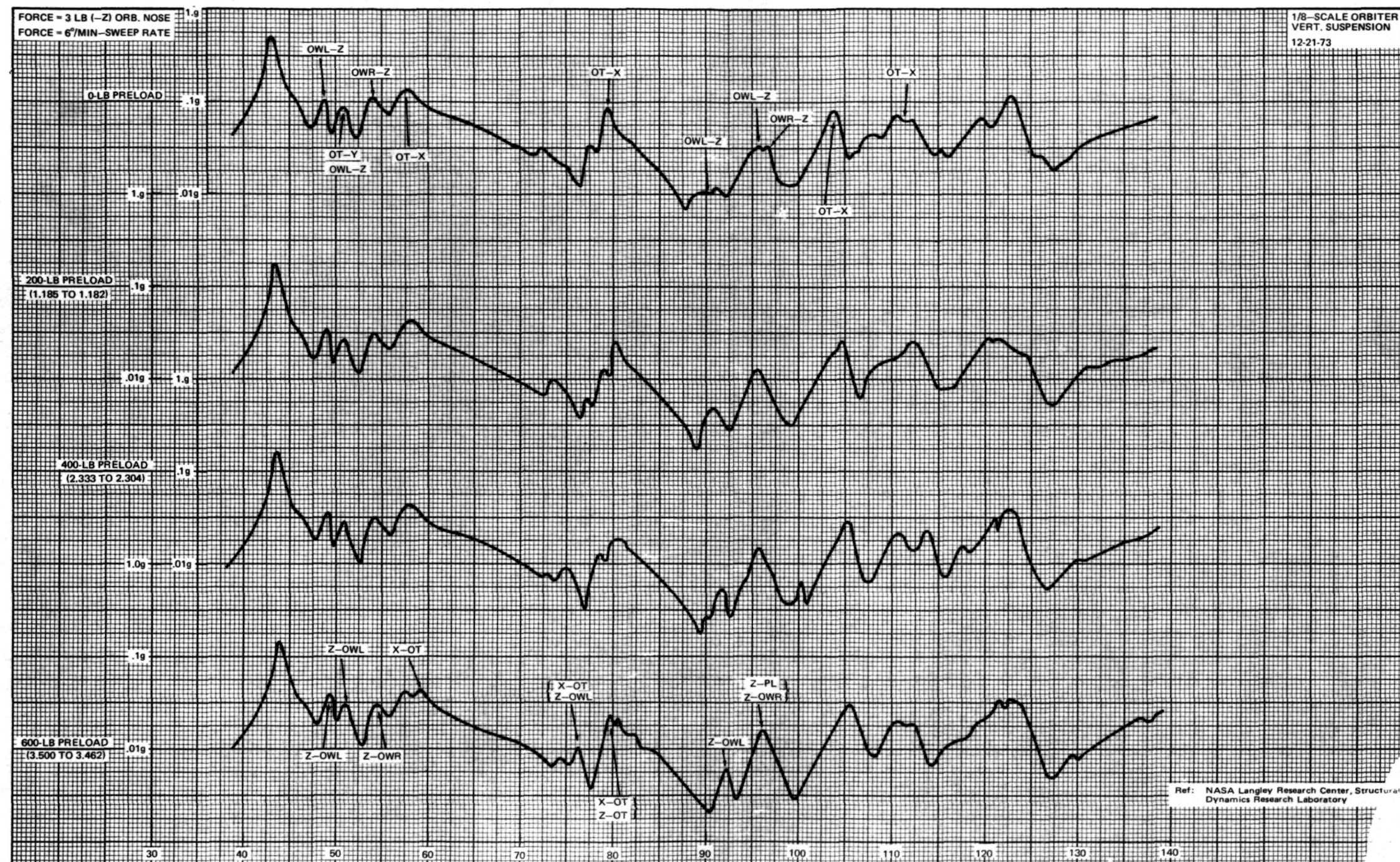
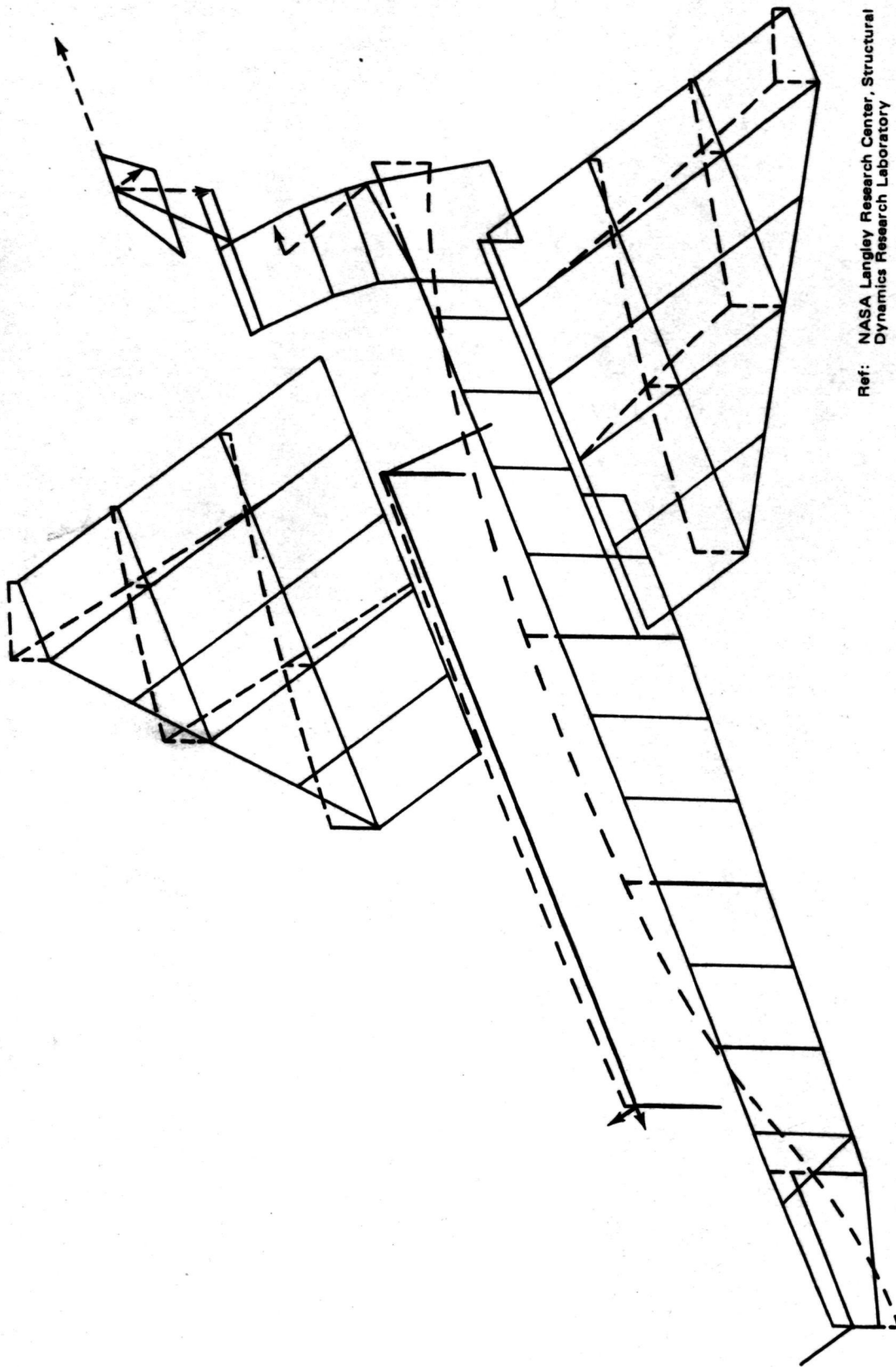


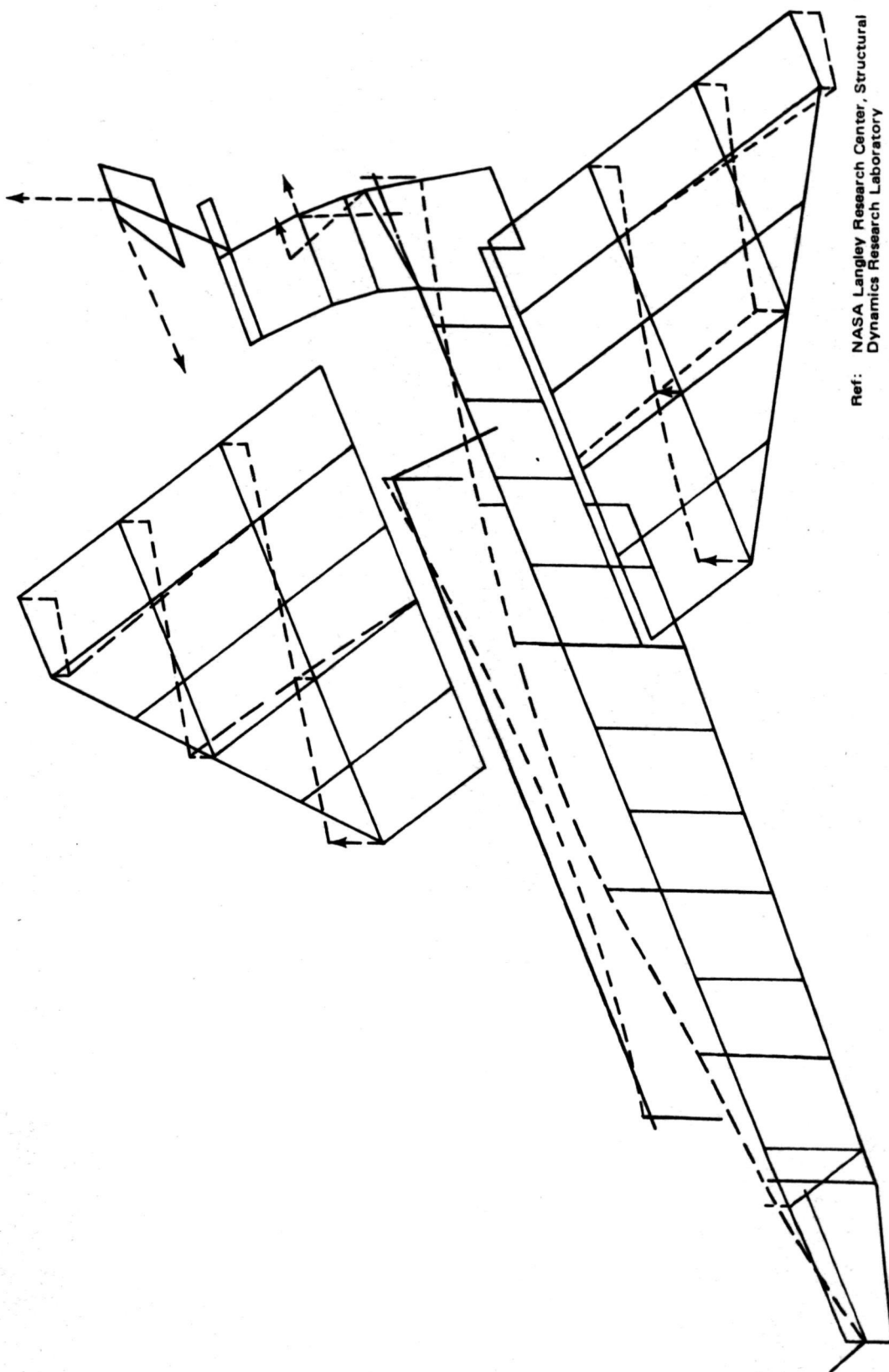
Fig. C-9 Preliminary Vertical Suspension Frequency Sweep - Effect of Preload



Ref: NASA Langley Research Center, Structural
Dynamics Research Laboratory

Fig. C-10 Preliminary Mode Survey Data (1-3-74), 0-lb Static Load, $f=43.67$ Hz
Symmetric Z-Excitation

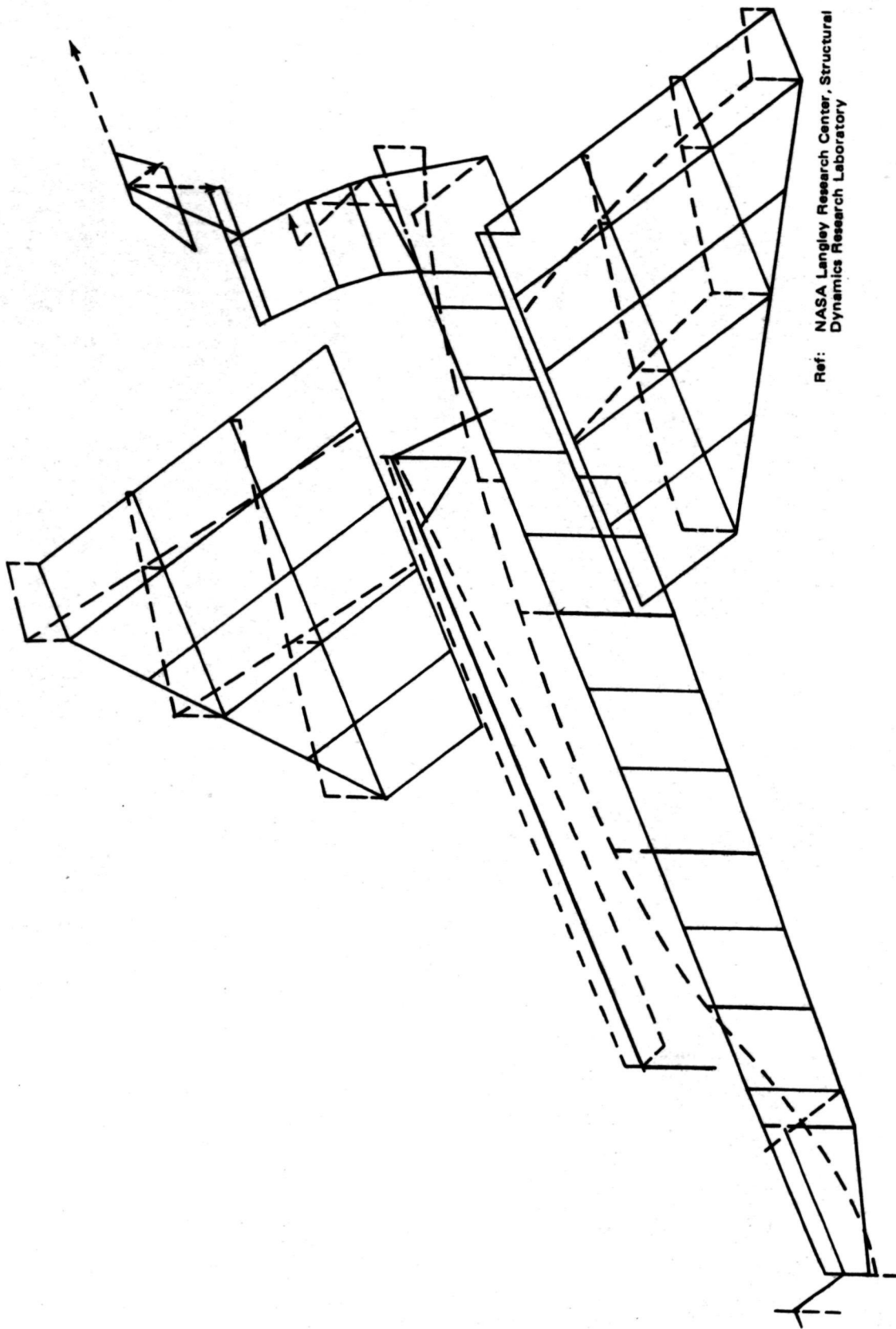
T-137



Ref: NASA Langley Research Center, Structural
Dynamics Research Laboratory

Fig. C-11 Preliminary Mode Survey Data (1-3-74), 0-lb Static Load, $f=80.06$ Hz
Symmetric Z-Excitation

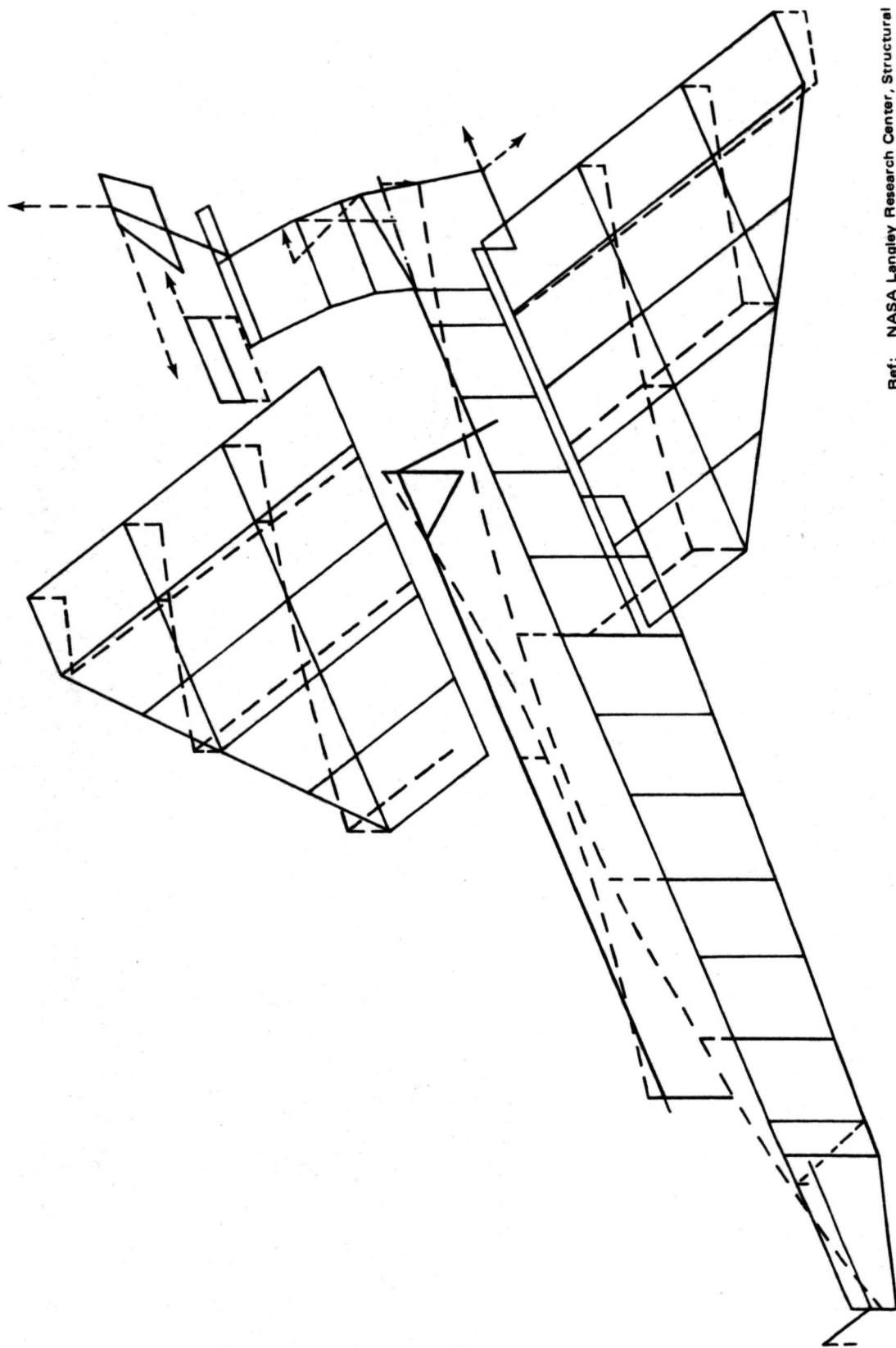
T-138



Ref: NASA Langley Research Center, Structural
Dynamics Research Laboratory

Fig. C-12 Preliminary Mode Survey Data (1-3-74), 600-lb Static Load, $f=44.23$ Hz
Symmetric Z-Excitation

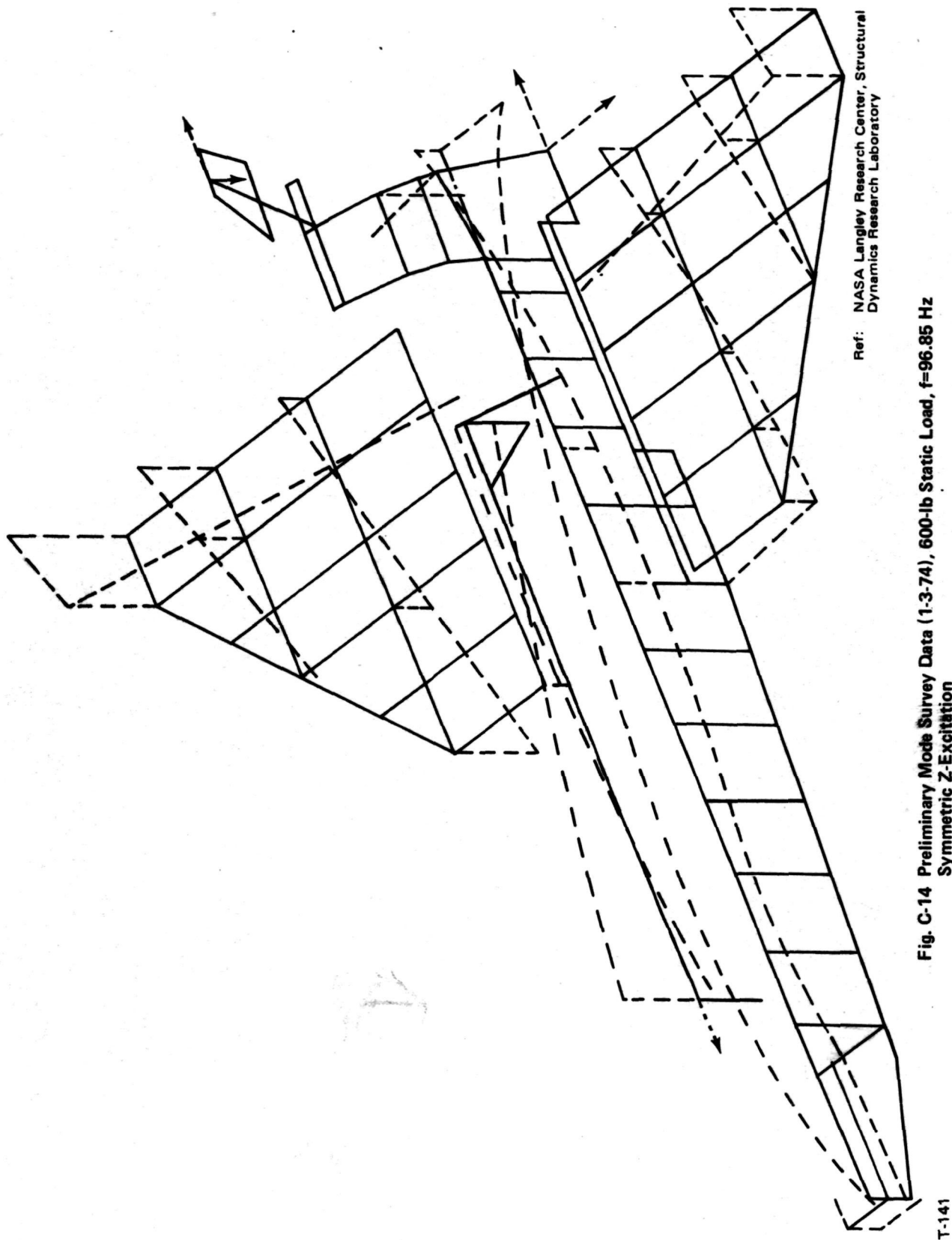
T-139

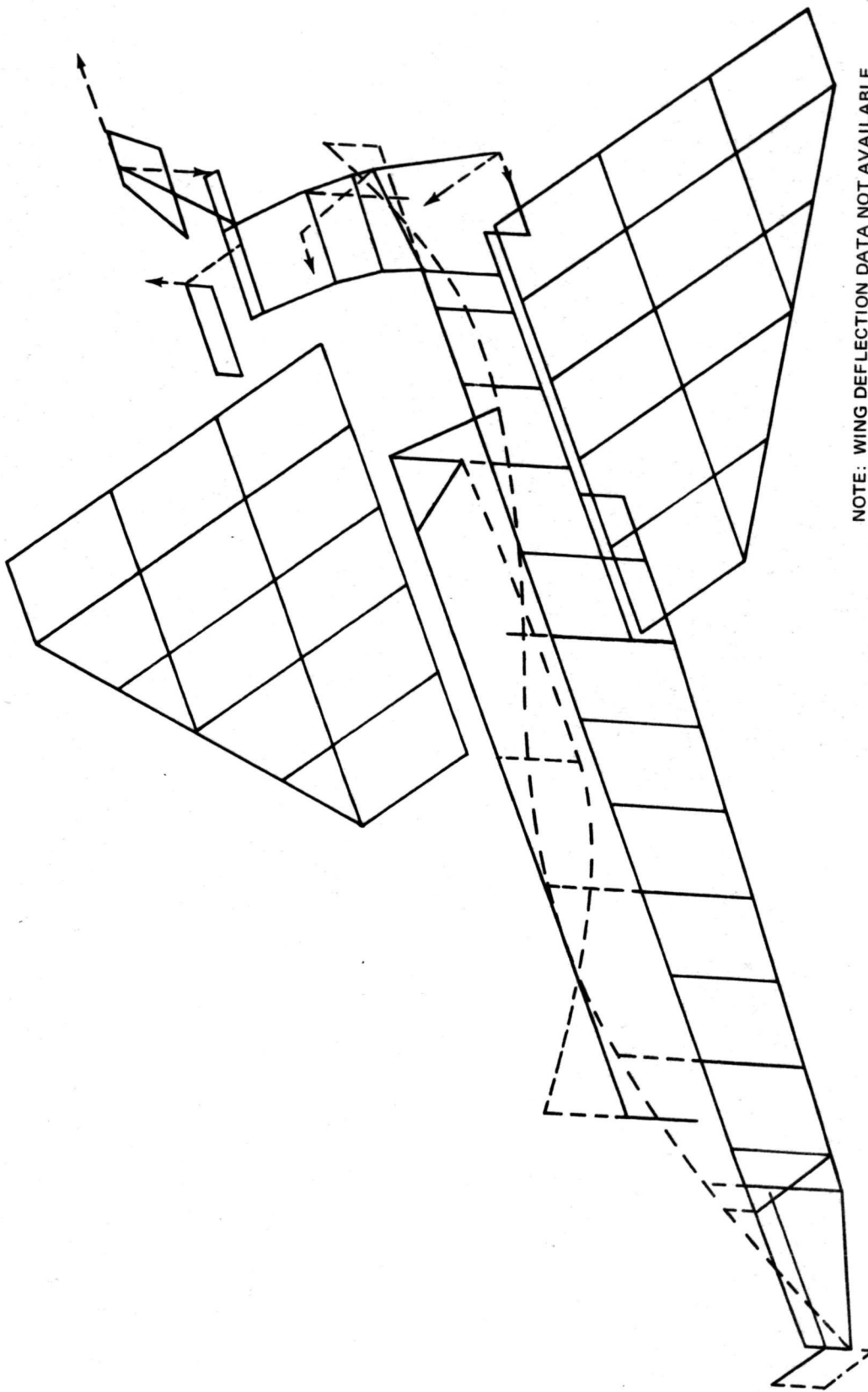


Ref: NASA Langley Research Center, Structural
Dynamics Research Laboratory

T-140

Fig. C-13 Preliminary Mode Survey Data (1-3-74), 600-lb Static Load, $f=80.0$ Hz
Symmetric Z-Excitation



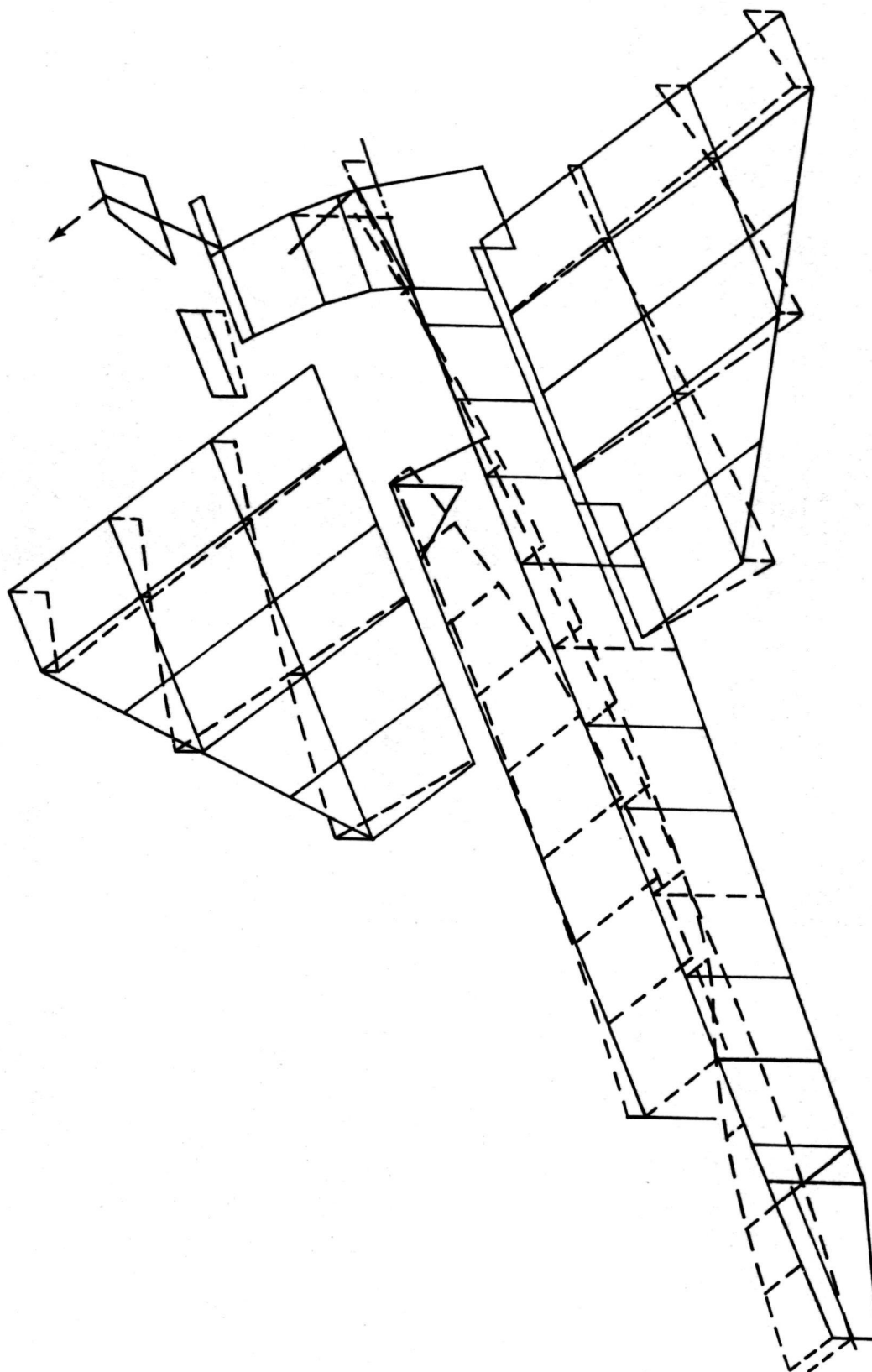


NOTE: WING DEFLECTION DATA NOT AVAILABLE

Ref: NASA Langley Research Center, Structural
Dynamics Research Laboratory

Fig. C-15 Preliminary Mode Survey Data (1-3-74), 600-lb Static Load, $f=106.84$ Hz
Symmetric Z-Excitation

T-142



Ref: NASA Langley Research Center, Structural
Dynamics Research Laboratory

Fig. C-16 Preliminary Mode Survey Data (1-8-74), 0-lb Static Load, $f=43.6$ Hz
Antisymmetric Y-Excitation

T-143

Appendix D
ERROR BOUNDS FOR APPROXIMATE FREQUENCIES OF
FREE-FREE UNDAMPED VIBRATION SYSTEMS

Appendix D

ERROR BOUNDS FOR APPROXIMATE FREQUENCIES OF FREE-FREE UNDAMPED VIBRATION SYSTEMS

In very large dynamic systems, the dynamic degrees of freedom (DOF's) have to be reduced through a reduction scheme. This is necessary if the problem is to be solved economically and within a reasonable time. Therefore, it is important to have a check built into the program that would indicate the deviation of the approximate solution of the reduced system from the exact solution of the unreduced system.

A method for error bounds was suggested by I. U. Ojalvo*; Isaacson and Keller use a similar method**. This method has been extended below so that error bounds for free-free systems can be obtained.

The exact eigenvalue problem is given by

$$[K] \{\varphi_i\} = \lambda_i [M] \{\varphi_i\} \quad (D-1)$$

where λ_i is the exact eigenvalue for the i^{th} exact mode shape $\{\varphi_i\}$.

For free-free systems $[K]$ will be singular. To avoid inversion problems later on, add to each side of Equation D-1 $\epsilon [M] \{\varphi_i\}$, where ϵ is a non zero increment added to the eigenvalue λ_i

$$([K] + \epsilon [M]) \{\varphi_i\} = (\lambda_i + \epsilon) [M] \{\varphi_i\}. \quad (D-2a)$$

or

$$[K_M] \{\varphi_i\} = (\lambda_i + \epsilon) [M] \{\varphi_i\} \quad (D-2b)$$

where

$$[K_M] = [K] + \epsilon [M]. \quad (D-3)$$

Solving Equation D-2b,

$$\{\varphi_i\} = (\lambda_i + \epsilon) [K_M]^{-1} [M] \{\varphi_i\} \quad (D-4a)$$

*Ojalvo, I. U., "An Error Bound For Approximate Modes and Frequencies", Grumman Memorandum No. STMECH 73.66 (November 1973)

**Isaacson, E. and Keller, H. B., Analysis of Numerical Methods, John Wiley & Sons, New York (1966, page 141)

or

$$\left(\frac{1}{\lambda_i + \epsilon} \right) \{\varphi_i\} = [K_M]^{-1} [M] \{\varphi_i\} \quad \text{D-4b}$$

for more than one mode Equation D-4b may be written as:

$$[\Phi] [\Lambda]^{-1} = [K_M]^{-1} [M] [\Phi] \quad \text{(D-5)}$$

where $[\Lambda]$ is the diagonal matrix given by

$$[\Lambda] = \begin{bmatrix} & & \\ & \lambda_j + \epsilon & \\ & & \end{bmatrix}$$

and $[\Phi]$ is the modal matrix whose columns are the vectors $\{\varphi_i\}$.

Since it is always possible to expand an approximate mode, $\{\bar{\Phi}_i\}$, into a linear combination of arbitrarily normalized exact mode shapes, let

$$\{\bar{\Phi}_i\} = [\Phi] \{b_i\}. \quad \text{(D-6)}$$

The k^{th} element, $\bar{\Phi}_{ki}$, for the i^{th} approximate mode would be stated as

$$\bar{\Phi}_{ki} = \sum_j \Phi_{kj} b_{ji}$$

where b_{ji} is the j^{th} element of the vector of constants $\{b_i\}$.

The arbitrary normalization on $[\Phi]$ is taken as

$$[\Phi]^T [M] [\Phi] = [I] \quad \text{(D-7)}$$

where $[I]$ is a unit matrix.

Substituting the approximate mode shape and eigenvalue into the modified, dynamic equilibrium equations will yield residual forces. For the i^{th} mode, the residual forces are

$$\{F_i\} = [K_M] \{\bar{\Phi}_i\} - (\bar{\lambda}_i + \epsilon) [M] \{\bar{\Phi}_i\} \quad \text{(D-8)}$$

where $\bar{\lambda}_i$ is the approximate i^{th} eigenvalue, and $\{\bar{\Phi}_i\}$ the corresponding eigenvector.

Deflections caused by the residual forces are obtained from the equation

$$\{u_i\} = [K_M]^{-1} \{F_i\}. \quad (D-9)$$

Substituting Equation D-8 into D-9, we obtain

$$\{u_i\} = \{\bar{\Phi}_i\} - (\bar{\lambda}_i + \epsilon) [K_M]^{-1} [M] \{\bar{\Phi}_i\}. \quad (D-10)$$

Substituting Equation D-6 into D-10 results in

$$\{u_i\} = [\Phi] \{b_i\} - (\bar{\lambda}_i + \epsilon) [K_M]^{-1} [M] [\Phi] \{b_i\}. \quad (D-11)$$

Using Equation D-5 reduces D-11 to

$$\{u_i\} = [\Phi] \left[[I] - (\bar{\lambda}_i + \epsilon) [\Lambda]^{-1} \right] \{b_i\}. \quad (D-12)$$

Let

$$[E] = [I] - (\bar{\lambda}_i + \epsilon) [\Lambda]^{-1} = \begin{bmatrix} & & & \\ & & & \\ & & \bar{\lambda}_i + \epsilon & \\ & & 1 - \frac{\bar{\lambda}_i + \epsilon}{\lambda_j + \epsilon} & \\ & & & \end{bmatrix} \quad (D-13)$$

and substitute Equation D-13 into D-12

$$\{u_i\} = [\Phi] [E] \{b_i\}. \quad (D-14)$$

The modal mass associated with $\{u_i\}$, using Equation D-14, is

$$\{u_i\}^T [M] \{u_i\} = \{b_i\}^T [E]^T [\Phi]^T [M] [\Phi] [E] \{b_i\}. \quad (D-15)$$

Making use of Equation D-7 and D-13, Equation D-15 reduces to

$$\{u_i\}^T [M] \{u_i\} = \{b_i\}^T \left[\left(1 - \frac{\bar{\lambda}_i + \epsilon}{\lambda_j + \epsilon} \right)^2 \right] \{b_i\} \quad (D-16)$$

Where $j = 1, 2, \dots$, but the i index always refers to the same approximate eigenvalue in Equation D-16.

Equation D-16 can be stated as

$$\{u_i\}^T [M] \{u_i\} = \sum_j (b_{ji})^2 \left(1 - \frac{\bar{\lambda}_i + \epsilon}{\lambda_j + \epsilon}\right)^2 \quad (D-17)$$

Since the terms in the summation are squared and yield positive quantities, it

is possible to select the smallest value of $\left(1 - \frac{\bar{\lambda}_i + \epsilon}{\lambda_j + \epsilon}\right)^2$, which usually occurs

when $j = i$ (exceptions occur when more than one λ_j closely surround $\bar{\lambda}_i$)

$$\sum_j (b_{ji})^2 \left(1 - \frac{\bar{\lambda}_i + \epsilon}{\lambda_j + \epsilon}\right)^2 \geq \left(1 - \frac{\bar{\lambda}_i + \epsilon}{\lambda_i + \epsilon}\right)^2 \sum_j (b_{ji})^2 \quad (D-18)$$

Therefore, Equation D-17 can be stated as

$$\{u_i\}^T [M] \{u_i\} \geq \left(1 - \frac{\bar{\lambda}_i + \epsilon}{\lambda_i + \epsilon}\right)^2 \sum_j (b_{ji})^2 \quad (D-19)$$

The approximate modal mass is $\{\bar{\Phi}_i\}^T [M] \{\bar{\Phi}_i\}$.

Making use of Equations D-6 and D-7,

$$\begin{aligned} \{\bar{\Phi}_i\}^T [M] \{\bar{\Phi}_i\} &= \{b_i\}^T [\Phi]^T [M] [\Phi] \{b_i\} \\ &= \{b_i\}^T \{b_i\} = \sum_j (b_{ji})^2 \end{aligned} \quad (D-20)$$

Substitute Equation D-20 into D-19 to obtain the desired ERROR BOUND equation

$$\frac{\{u_i\}^T [M] \{u_i\}}{\{\bar{\Phi}_i\}^T [M] \{\bar{\Phi}_i\}} \geq \left(1 - \frac{\bar{\lambda}_i + \epsilon}{\lambda_i + \epsilon}\right)^2 \quad (D-21)$$

Change Equation D-21 into matrix form so that the error bounds for more than one mode can be obtained simultaneously by matrix operations

$$([\bar{\Phi}]^T [M] [\bar{\Phi}])^{-1} [U]^T [M] [U] \geq \left[\left(1 - \frac{\bar{\lambda}_i + \epsilon}{\lambda_i + \epsilon}\right)^2 \right] \quad (D-22)$$

where

$[\bar{\Phi}]$ = Approximate mode shapes for any number of modes desired. They are obtained from an analysis using any reduction scheme. Do not include rigid body modes, as they will cause singularities

$[U] = [K_M]^{-1} [F]$ = Deflections caused by residual forces. K_M is defined in Equation D-3

$[F] = [K_M] [\bar{\Phi}] - [M] [\bar{\Phi}] [\bar{\Lambda}]$ = Residual forces

$[\bar{\Lambda}] = \begin{bmatrix} \bar{\lambda}_1 + \epsilon \\ \bar{\lambda}_i + \epsilon \\ \bar{\lambda}_n + \epsilon \end{bmatrix}$ = Diagonal matrix of approximate eigenvalues, incremented by ϵ , obtained from analysis. The rows and columns must correspond to the columns of $[\bar{\Phi}]$.

Let

$$[C] = ([\bar{\Phi}]^T [M] [\bar{\Phi}])^{-1} [U]^T [M] [U] \quad (D-23)$$

substitute Equation D-23 into D-22

$$[C] \geq \left[\left(1 - \frac{\bar{\lambda}_i + \epsilon}{\lambda_i + \epsilon} \right)^2 \right] \quad (D-24)$$

The resulting $[C]$ matrix will not be a diagonal matrix. The off-diagonal or cross mode terms are discarded since they were not used in deriving the error bound Equation D-21. Therefore, the i^{th} error bound equation from Equation D-24 would be

$$C_{ii} \geq \left(1 - \frac{\bar{\lambda}_i + \epsilon}{\lambda_i + \epsilon} \right)^2 \quad (D-25)$$

where C_{ii} is the i^{th} diagonal term corresponding to the i^{th} mode.

Let

$$\epsilon = \alpha_i \bar{\lambda}_i \quad (D-26)$$

Using Equation D-26 in the reduction of D-25 yields

$$\frac{\bar{\lambda}_i}{\lambda_i} \geq \frac{(1 - \sqrt{C_{ii}})}{(1 + \alpha_i \sqrt{C_{ii}})} \quad (D-27)$$

Keep in mind that in computing the error bound for each mode, α_i changes and can be obtained from Equation D-26. In most cases, ϵ can be taken small enough so that α_i can be set to zero.

Changing the eigenvalues to frequencies in Equation D-27 gives

$$\left(\frac{\bar{\omega}_i}{\omega_i} \right)^2 \geq \left(\frac{1 - \sqrt{C_{ii}}}{1 + \alpha_i \sqrt{C_{ii}}} \right)$$

or

$$\left(\frac{\bar{\omega}_i}{\omega_i} \right) \geq \left(\frac{1 - \sqrt{C_{ii}}}{1 + \alpha_i \sqrt{C_{ii}}} \right)^{1/2} \quad (D-28)$$

which is the desired frequency error bound for the i^{th} mode.

Appendix E
LARGE DEFLECTION BEHAVIOR OF INITIALLY IMPERFECT RECTANGULAR PLATES
UNDER UNIFORM END-SHORTENING AND EXTENSION

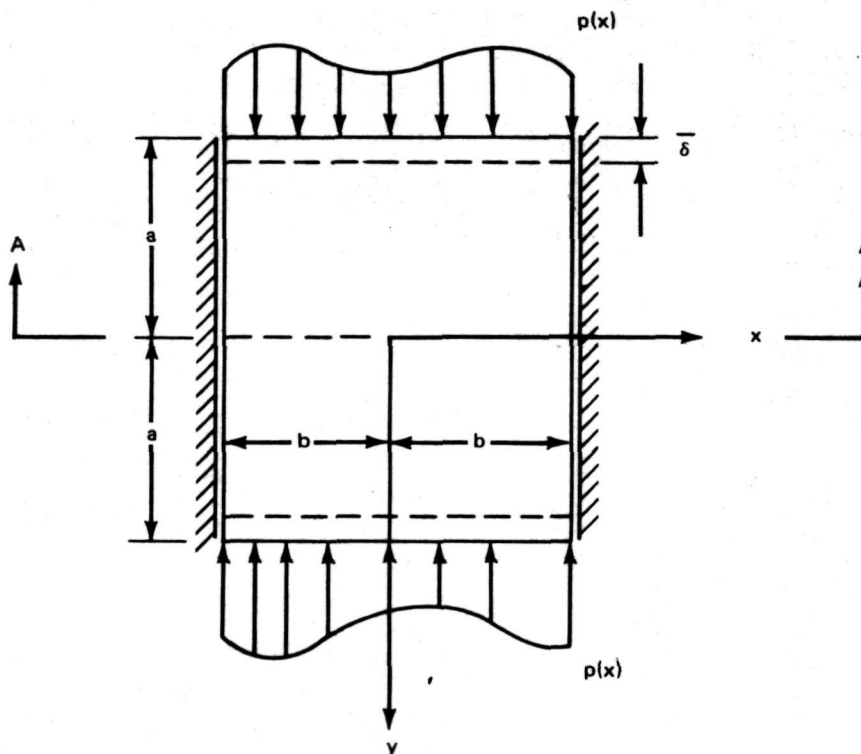
Appendix E

LARGE DEFLECTION BEHAVIOR OF INITIALLY IMPERFECT RECTANGULAR PLATES UNDER UNIFORM END-SHORTENING AND EXTENSION

by

H. Armen, Jr. and E. Saleme

Figure E-1 illustrates the problem under consideration; the edges of a simply supported rectangular plate are loaded so as to cause a uniform shortening or extension. The lateral motion of the plate in the x direction is prevented by rigid supports.



T-144

Fig. E-1 Geometry and Loading of Rectangular Plate

A gross measure of the stiffness of the above panel is represented by the load $p(x)$ associated with a prescribed uniform end-shortening $\bar{\delta}$. For the case of small deformations with no initial imperfections, a uniformly distributed load $p(x)$ will result in a uniform end-shortening, $\bar{\delta}$. The load-deformation relation can be written as

$$P(\text{lbs}) = K\bar{\delta} \quad (\text{E-1})$$

where

$$P = \int_{-b}^b p(x) dx$$

$$\bar{\delta} = ae_0, \quad e_0 \text{ is the end-shortening strain}$$

and

$$K = \frac{2Et}{(1 - \nu^2)} \left(\frac{b}{a}\right)$$

The foregoing expression cannot be expected to remain valid for thin-skin panels having relatively large (of the order of the thickness) initial imperfections. The stiffness influence coefficient, K , for this case will vary not only with the aspect ratio, load distribution (a uniformly distributed load will not necessarily result in a uniform end-shortening), and boundary condition, but also with the applied load level and the amount and shape of the initial imperfection. The method used to determine this coefficient for the large deflection, initial imperfection case, is based on a procedure presented by Timoshenko and Gere,* where assumed displacement functions are used to determine the total potential energy of plate. The energy function is then minimized with respect to the set of generalized displacement coefficients resulting in a set of simultaneous nonlinear algebraic equations. The solution of these equations for the generalized displacement coefficients is obtained and used to determine the load corresponding to a prescribed end-shortening state.

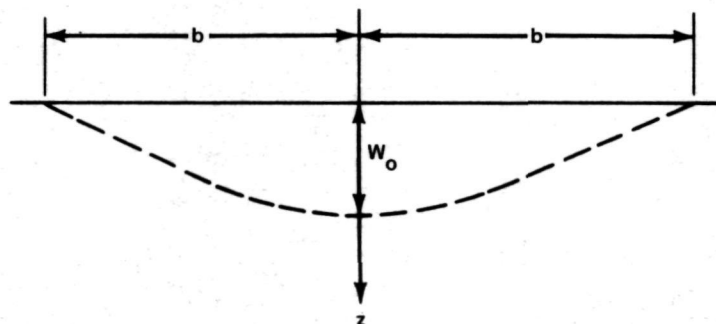
*Timoshenko, S. P. and Gere, J. M., Theory of Elastic Stability, McGraw-Hill, pp. 411-418, 1961

E1 METHOD OF ANALYSIS

Using the coordinate system shown in Fig. E-1, an assumed expression for the initial imperfection is given by the following expression that satisfies the boundary conditions

$$w_o = W_o \cos \frac{\pi x}{2b} \cos \frac{\pi y}{2a} \quad (\text{E-2})$$

where W_o is the magnitude of the initial imperfection at the center of the panel. An illustration of this assumed shape for Section A-A is shown in Fig. E-2. A similar shape exists along the y-axis.



T-145 Fig. E-2 Initial Imperfection Along Section A-A

The application of uniform end-shortening along the edges $y = \pm a$ results in a deformation state that can be described by the displacement components in the x , y , and z -directions as u , v , and w_1 , respectively. As suggested by Timoshenko and Gere, these components of displacement are written in the following form:

$$u = U_1 \sin \frac{\pi x}{b} \cos \frac{\pi y}{2a} \quad (\text{E-3a})$$

$$v = V_1 \sin \frac{\pi y}{a} \cos \frac{\pi x}{2b} - ey \quad (\text{E-3b})$$

and

$$w_1 = W_1 \cos \frac{\pi x}{2b} \cos \frac{\pi y}{2a} \quad (\text{E-3c})$$

where U_1 , V_1 , and W_1 are generalized displacement coefficients to be determined. The form of the above equations for the in-plane displacements u and v were chosen to satisfy the boundary conditions; $u = 0$ along $x = \pm b$ and $y = \pm a$, $v = \delta$ (due to e_y) along $y = \pm a$. The total lateral displacement may be written as

$$w = w_0 + w_1 = (W_0 + W_1) \cos \frac{\pi x}{2b} \cos \frac{\pi y}{2a} \quad (E-4)$$

where, from Equation E-3c, it is assumed that the lateral displacement due to an end-shortening is of the same functional form (shape) as the initial imperfection. This assumption is reasonable for a uniform end-shortening condition only.

The nonlinear strain displacement relations may be written in terms of the bending and stretching components as follows:

$$e_x = e_x^b + e_x^s = \frac{\partial^2 w_1}{\partial x^2} + \frac{\partial u}{\partial x} + 1/2 \left[\left(\frac{\partial w}{\partial x} \right)^2 - \left(\frac{\partial w_0}{\partial x} \right)^2 \right] \quad (E-5a)$$

$$e_y = e_y^b + e_y^s = \frac{\partial^2 w_1}{\partial y^2} + \frac{\partial v}{\partial y} + 1/2 \left[\left(\frac{\partial w}{\partial y} \right)^2 - \left(\frac{\partial w_0}{\partial y} \right)^2 \right] \quad (E-5b)$$

$$\gamma_{xy} = \gamma_{xy}^b + \gamma_{xy}^s = 2 \frac{\partial^2 w_1}{\partial x \partial y} + \frac{\partial u}{\partial y} + \frac{\partial v}{\partial x} + \left[\frac{\partial w}{\partial x} \frac{\partial w}{\partial y} - \frac{\partial w_0}{\partial x} \frac{\partial w_0}{\partial y} \right] \quad (E-5c)$$

The first term e^b in the foregoing equations represents the bending components of the strain, and the remainder e^s is associated with the middle surface strains. The total strain energy (stretching and bending of the sheet) is given by

$$U = \frac{Gh}{1-\nu} \int_A \left[(e_x^s)^2 + (e_y^s)^2 + 2\nu e_x^s e_y^s + \frac{1-\nu}{2} (\gamma_{xy}^s)^2 + \right. \\ \left. + \frac{h^2}{6} \left((e_x^b)^2 + (e_y^b)^2 + 2\nu e_x^b e_y^b + 2(1-\nu) (\gamma_{xy}^b)^2 \right) \right] dA \quad (E-6)$$

For a prescribed uniform end-shortening condition the constants U_1 , V_1 , and W_1 are found by minimizing the total strain energy. The conditions associated with this minimization are

$$\frac{\partial U}{\partial U_1} = 0, \quad \frac{\partial U}{\partial V_1} = 0, \quad \frac{\partial U}{\partial W_1} = 0 \quad (E-7)$$

where

$$\frac{\partial U}{\partial U_1} = \bar{D} \int_A \left[2(e_x^s + \nu e_y^s) \frac{\partial e_x^s}{\partial U_1} + (1-\nu) \gamma_{xy}^s \frac{\partial \gamma_{xy}^s}{\partial U_1} \right] dA = 0 \quad (E-8a)$$

$$\frac{\partial U}{\partial V_1} = \bar{D} \int_A \left[2(e_y^s + \nu e_x^s) \frac{\partial e_y^s}{\partial V_1} + (1-\nu) \gamma_{xy}^s \frac{\partial \gamma_{xy}^s}{\partial V_1} \right] dA = 0 \quad (E-8b)$$

$$\begin{aligned} \frac{\partial U}{\partial W_1} = \bar{D} \int_A \left\{ 2(e_x^s + \nu e_y^s) \frac{\partial e_x^s}{\partial W_1} + 2(e_y^s + \nu e_x^s) \frac{\partial e_y^s}{\partial W_1} + \right. \\ \left. (1-\nu) \gamma_{xy}^s \frac{\partial \gamma_{xy}^s}{\partial W_1} + \frac{h^2}{3} \left[(e_x^b + \nu e_y^b) \frac{\partial e_x^b}{\partial W_1} + \right. \right. \\ \left. \left. (e_y^b + \nu e_x^b) \frac{\partial e_y^b}{\partial W_1} + 2(1-\nu) \gamma_{xy}^b \frac{\partial \gamma_{xy}^b}{\partial W_1} \right] \right\} dA = 0 \quad (E-8c) \end{aligned}$$

and

$$\bar{D} = \frac{Eh}{2(1-\nu^2)} = \frac{Gh}{(1-\nu)}$$

The three conditions represented by Equations E-8a through E-8c may be written in the following form

$$A_{11} U_1 + A_{12} V_1 + C_1 \bar{W}^2 = 0 \quad (E-9a)$$

$$A_{21} U_1 + A_{22} V_1 + C_2 \bar{W}^2 = 0 \quad (E-9b)$$

$$[A_{31} U_1 + A_{32} V_1 + C_3 \bar{W}^2 + E] \bar{W}_1 + F W_1 = 0 \quad (E-9c)$$

where

$$\begin{aligned}
 A_{11} &= 2 + \frac{1-\nu}{4} \left(\frac{b}{a}\right)^2 & C_1 &= -\frac{1}{3a} \left[1 + \frac{1-3\nu}{4} \left(\frac{b}{a}\right)^2 \right] \\
 A_{12} &= \frac{16}{9} \frac{(1+\nu)}{\pi^2} \frac{b}{a} & C_2 &= -\frac{1}{3b} \left[\frac{1-3\nu}{4} + \left(\frac{b}{a}\right)^2 \right] \\
 A_{21} &= A_{12} & C_3 &= \frac{\pi^2}{512a^2} \left[9 \left(1 + \left(\frac{b}{a}\right)^4\right) + 2 \left(\frac{b}{a}\right)^2 \right] \\
 A_{22} &= \frac{1-\nu}{4} + 2 \left(\frac{b}{a}\right)^2 & E &= \frac{\nu + \left(\frac{b}{a}\right)^2}{4} e_o \quad (e_o = + \text{ for } \\
 & & & \text{compression}) \\
 A_{31} &= C_1 & & \\
 A_{32} &= C_2 & F &= \frac{1}{3} \left[\frac{\pi}{8} \left(1 + \left(\frac{b}{a}\right)^2\right) \frac{h}{a} \right]^2
 \end{aligned}$$

and

$$\bar{W}_1 = W_o + W_1$$

$$\bar{W}^2 = \bar{W}_1^2 - W_o^2 = W_1(W_1 + 2W_o)$$

Equations E-9a and E-9b can be used to obtain expressions for U_1 and V_1 in terms of \bar{W}^2 . Substituting these expressions into Equation E-9c, we obtain the following cubic equation in terms of \bar{W}_1

$$\bar{W}_1^3 + pW_1 - qW_o = 0 \quad (E-10)$$

where

$$p = q - \frac{E}{G} - W_o^2$$

$$q = \frac{F}{G}$$

and

$$G = C_3 - \frac{A_{22}C_1^2 - 2A_{12}C_1C_2 + A_{11}C_2^2}{A_{11}A_{22} - A_{12}^2}$$

If we define $Q = (p/3)^3 + (q/2)^2$, then the real root of Equation E-10, for $Q > 0$, is

$$\bar{W}_1 = \sqrt[3]{\sqrt{Q} - \frac{q}{2}} - \sqrt[3]{\sqrt{Q} + \frac{q}{2}} \quad (E-11a)$$

For the case where $Q \leq 0$ then

$$\bar{W}_1 = 2\sqrt{-\frac{p}{3}} \cos \frac{\alpha}{3} \quad (E-11b)$$

where

$$\alpha = \cos^{-1} \left(\frac{q}{2\sqrt{-\left(\frac{p}{3}\right)^3}} \right)$$

E2 STRAINS, STRESSES, AND LOADS

A solution for W_1 and subsequent determination of U_1 and V_1 provides sufficient information to determine the strain and corresponding stress state of the middle plane of the plate. If we define $\alpha \equiv \pi x/2b$ and $\beta \equiv \pi y/2a$ then we can write the strains, Equations E-5a through E-5c, in terms of the displacements Equations E-3a through E-3c as

$$e_x^0 = U_1 \frac{\pi}{b} \cos 2\alpha \cos \beta + 1/2 [\bar{W}_1^2 - W_0^2] \left(\frac{\pi}{2b}\right)^2 \sin^2 \alpha \cos^2 \beta \quad (E-12a)$$

$$e_y^0 = V_1 \frac{\pi}{a} \cos \alpha \cos 2\beta + 1/2 [\bar{W}_1^2 - W_0^2] \left(\frac{\pi}{2a}\right)^2 \sin^2 \alpha \cos^2 \beta - e_0 \quad (E-12b)$$

and the stresses as

$$\sigma_x^0 = \frac{E}{1-\nu} [e_x^0 + \nu e_y^0] \quad (E-12c)$$

$$\sigma_y^o = \frac{E}{1-\nu^2} [e_y^o + \nu e_x^o] \quad (E-12d)$$

The load along the edges $y = \pm a$ can be determined from

$$P(\pm a) = h \int_{-b}^b \sigma_y dx = 2bh \frac{E}{1-\nu^2} \left[\left(-2 \frac{\bar{V}_1}{a} + \frac{\pi^2}{16a^2} \right) (\bar{W}_1^2 - W_o^2) - e_o \right] \quad (E-13)$$

$$\text{where } \bar{V}_1 = \frac{V_1}{\frac{2}{W_1} - W_o}$$

Appendix F
MODEL II FUSELAGE AND WING COVER EFFECTIVE WIDTH CALCULATIONS

TABLE OF CONTENTS

NOTE

Appendix F consists of
the following illustrations:

<u>Figure</u>		<u>Page</u>
F-1	Fuselage Effective Skin Widths	F-2
F-2	Effective Fuselage Width Calculations at Sta. 64	F-3
F-3	Effective Fuselage Width Calculations at Sta. 78	F-4
F-4	Effective Fuselage Width Calculations at Sta. 116	F-5
F-5	Effective Fuselage Width Calculations at Sta. 125.5	F-6
F-6	Effective Fuselage Width Calculations at Sta. 141.75	F-7
F-7	Equivalent Skin Cap Areas in Square Inches	F-8
F-8	Effective Width Modification Factors	F-9
F-9	Moment of Inertia Modification Factors	F-10
F-10	Moment of Inertia Modification Factors	F-11
F-11	Wing Effective Skin Widths When Skin is Half Effective	F-12
F-12	Effective Wing Skin Widths.	F-13
F-13	Effective Skin Width Ratio for Wing.	F-14

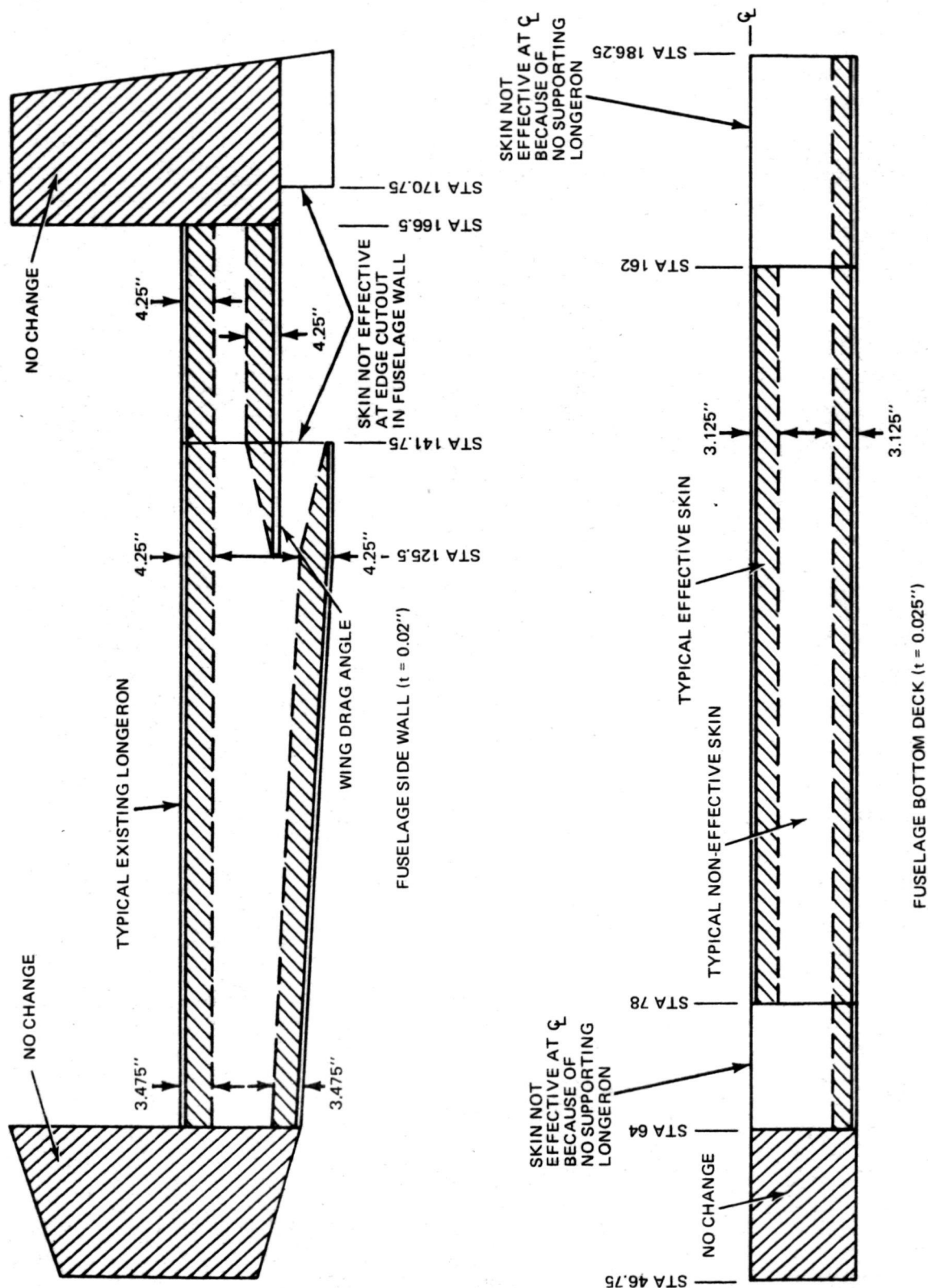
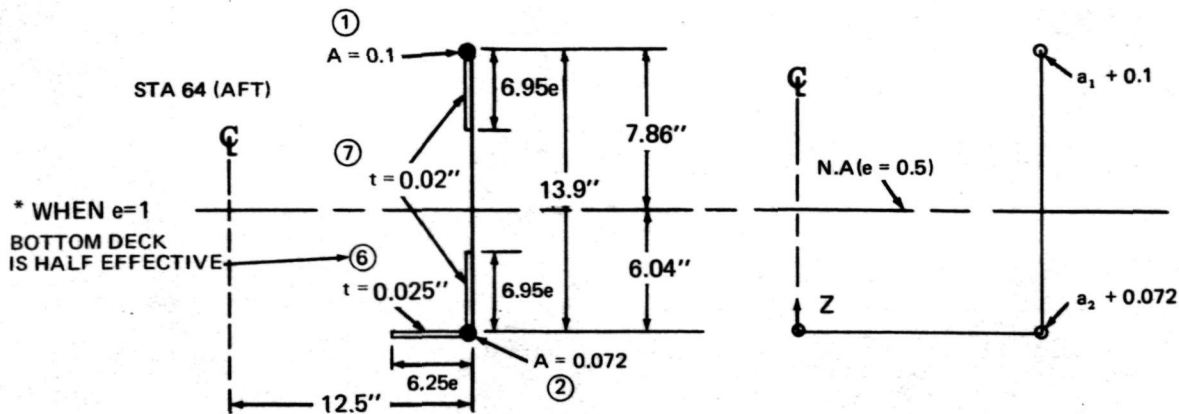


Fig. F-1 Fuselage Effective Skin Widths



	A	z	A x z	\bar{z}	$A(z-\bar{z})^2$	I_{looy}	y	Ay^2	I_{loo_z}	
①	0.100	13.9	1.39	7.86	6.18	—	12.5	15.62	—	
②	0.072	0	0	-6.04	2.62	—	12.5	11.25	—	
⑥	0.156e	0	0	-6.04	5.69e	—	0	0	$16.25[1-(1-\frac{e}{2})^3]$	
⑦	0.278e	6.95	1.93e	0.91	0.23e	$4.48[1-(1-e)^3]$	12.5	43.5e	—	
Σ	0.172 +.434e		1.39 +1.93e		8.8 +5.9e			26.9 +43.5e		
e	ΣA	\bar{z}	$\Sigma A \times z$		$\Sigma A (z-\bar{z})^2$	ΣI_{looy}	I_{yy}	ΣAy^2	ΣI_{looz}	I_{zz}
0.3	0.302	6.52	1.97		10.6	2.9	13.5	39.9	6.3	46.2
0.5	0.389	6.04	2.35		11.8	3.9	15.7	48.6	9.4	58.0
0.7	0.476	5.76	2.74		12.9	4.4	17.3	57.3	11.8	69.1
1.0	0.606	5.47	3.32		14.7	4.5	19.2	70.4	14.2	84.6
*Fully eff.	0.762	4.35	3.32		20.4	4.5	24.9	70.4	16.3	86.7

Determine equivalent cap areas with Neutral Axis assumed unchanged from value circled above

$$1) (a_2 + 0.072)(6.04) = (a_1 + 0.1)(7.86)$$

$$2) (a_2 + 0.072)(6.04)^2 + (a_1 + 0.1)(7.86)^2 = I_{yy}$$

$$(a_1 + 0.1) 7.86 \times 13.9 = I_{yy}$$

$$a_1 = \frac{I_{yy}}{109.2} - 0.1$$

$$a_2 = (a_1 + 0.1) \frac{7.86}{6.04} - 0.072$$

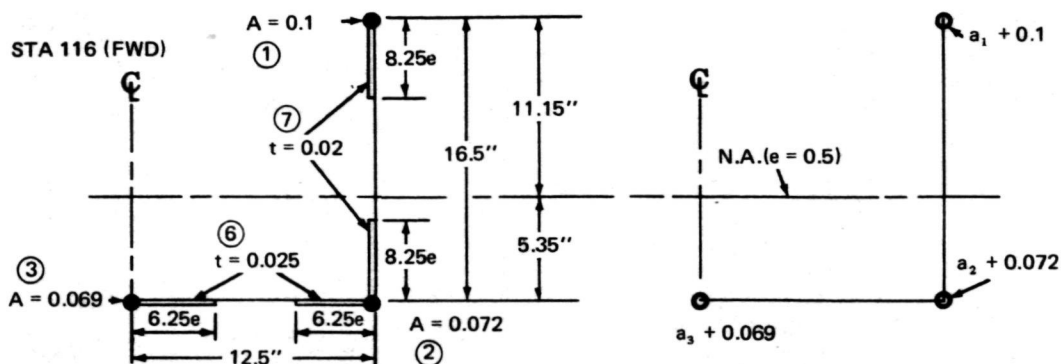
$$a_2 = 1.3(a_1 + 0.1) - 0.072$$

e	a_1	a_2	ΣA^1	I_{zz}^1	$\frac{\Sigma A^1}{\Sigma A}$	$\frac{I_{zz}^1}{I_{zz}}$	$\frac{\Sigma A}{0.762}$	$\frac{I_{yy}}{24.9}$	$\frac{I_{zz}}{86.7}$
0.3	0.024	0.089	0.285	44.5	0.94	0.96	0.40	0.54	0.53
0.5	0.044	0.115	0.331	51.7	0.85	0.89	0.51	0.63	0.67
0.7	0.058	0.140	0.370	57.8	0.78	0.84	0.63	0.70	0.80

$$\Sigma A^1 = (a_1 + a_2 + 0.172)$$

$$I_{zz}^1 = (12.5)^2 (a_1 + a_2 + 0.172)$$

Fig. F-2 Effective Fuselage Width Calculations at Sta 64



	A	z	A x z	z-z̄	A(z-z̄) ²	I _{ooz}	y	Ay ²	I _{ooz}	
①	0.100	16.5	1.65	11.15	12.42	—	12.5	15.62		
②	0.072	0	0	-5.35	2.06	—	12.5	11.25		
③	0.069	0	0	-5.35	1.98	—	0	0		
⑥	0.312e	0	0	-5.35	8.93e	—	6.25	12.19e	4.06[1-(1-e) ³]	
⑦	0.330e	8.25	2.72e	2.9	2.78e	7.5[1-(1-e) ³]	12.5	51.5e		
Σ	0.241 +0.642e		1.65 +2.72e		16.46 +11.71e			26.9 +63.7e		
e	ΣA	z̄	ΣAxz		ΣA(z-z̄) ²	ΣI _{ooz}	I _{yy}	ΣAy ²	ΣI _{ooz}	I _{zz}
0.3	0.434	5.70	2.47		20.0	4.9	24.9	46.0	2.7	48.7
0.5	0.562	5.35	3.01		22.4	6.5	28.9	58.7	3.6	62.3
0.7	0.691	5.14	3.55		24.7	7.2	31.9	71.4	4.0	75.4
0.10	0.883	4.95	4.37		28.2	7.5	35.7	90.6	4.1	94.7

Determine equivalent skin cap areas with Neutral Axis assumed unchanged from value circled above

$$\text{Let } a_2 = a_1 + a_3$$

$$1) (a_1 + 2a_3 + 0.141) 5.35 = (a_1 + 0.1) 11.15$$

$$2) (a_1 + 2a_3 + 0.141) (5.35)^2 + (a_1 + 0.1) (11.15)^2 = I_{yy}$$

$$(a_1 + 0.1) 11.15 \times 16.5 = I_{yy}$$

$$a_1 = \frac{I_{yy}}{184} - 0.1$$

$$2a_3 = (a_1 + 0.1) \left(\frac{11.15}{5.35} - 1 \right) - 0.041$$

$$a_3 = 0.542 (a_1 + 0.1) - 0.021$$

e	a ₁	a ₃	a ₂	ΣA ¹	I _{zz} ¹	$\frac{\Sigma A^1}{\Sigma A}$	$\frac{I_{zz}^1}{I_{zz}}$	$\frac{\Sigma A}{.883}$	$\frac{I_{yy}}{35.7}$	$\frac{I_{zz}}{94.7}$
0.3	0.035	0.052	0.087	0.415	46.0	0.96	0.94	0.49	0.70	0.52
0.5	0.057	0.064	0.121	0.483	54.8	0.86	0.88	0.64	0.81	0.66
0.7	0.073	0.073	0.146	0.533	61.1	0.77	0.81	0.78	0.90	0.80

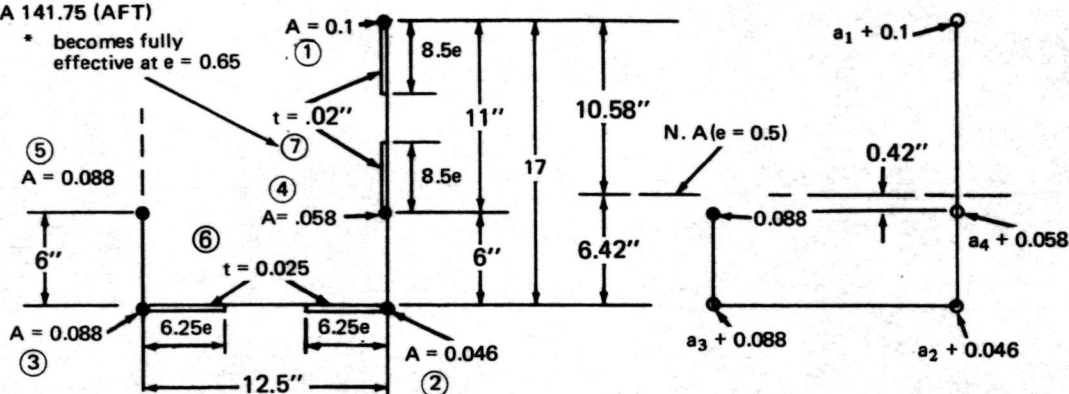
$$\Sigma A^1 = (a_1 + a_2 + a_3 + 0.241)$$

$$I_{zz}^1 = (12.5)^2 (a_1 + a_2 + 0.172)$$

Fig. F-4 Effective Fuselage Width Calculations at Sta 116

STA 141.75 (AFT)

* becomes fully effective at $e = 0.65$



	A	z	Axz	$z - \bar{z}$	$A(z - \bar{z})^2$	I_{ooz}	y	Ay^2	I_{ooz}	
①	0.100	17	1.7	10.58	11.2	—	12.5	15.62		
②	0.046	0	0	-6.42	1.9	—	12.5	7.18		
③	0.088	0	0	-6.42	3.63	—	0	0		
④	0.058	6	0.35	-.42	—	—	12.5	9.05		
⑤	0.088	6	0.53	-.42	—	—	0	0		
⑥	0.312e	0	0	-6.42	12.85e	—	6.25	12.19e	$4.06[1 - (1 - e)^3]$	
⑦	0.34e	11.5	3.9e	5.08	8.78e	$2.22[1 - (1 - 1.55e)^3]$	12.5	53.1e		
Σ	0.38 +0.312e +0.34e*		2.58 +3.9e*		16.7 +12.9e + 8.8e*			31.9 +12.19e +53.1e*		
e	ΣA	\bar{z}	ΣAz		$\Sigma A(z - \bar{z})^2$	ΣI_{ooz}	I_{yy}	ΣAy^2	ΣI_{ooz}	I_{zz}
0.3	0.576	6.50	3.75		23.2	1.9	25.1	51.5	2.7	54.2
0.5	0.706	6.42	4.53		27.6	2.2	29.8	64.6	3.6	68.2
0.7	0.819	6.26	5.12		31.4	2.2	33.6	74.9	4.0	78.9
1.0	0.913	5.61	5.12		35.3	2.2	37.5	78.6	4.1	82.7

Determine Equivalent skin cap areas with Neutral Axis assumed unchanged from value circled above

Let $a_4 = a_1$ & $a_2 = a_3$

$$1) (2a_3 + 0.134) 6.42 = (a_1 + 0.1) 10.58 - (a_1 + 0.058) 0.42$$

$$2) (2a_3 + 0.134) (6.42)^2 + (a_1 + 0.1) (10.58)^2 + (a_1 + 0.058) (0.42)^2 = I_{yy}$$

$$a_1 = \frac{I_{yy} - 177}{-0.1}$$

$$2a_3 = (a_1 + 0.1) \frac{10.58}{6.42} - (a_1 + 0.058) \frac{.42}{6.42} - 0.134$$

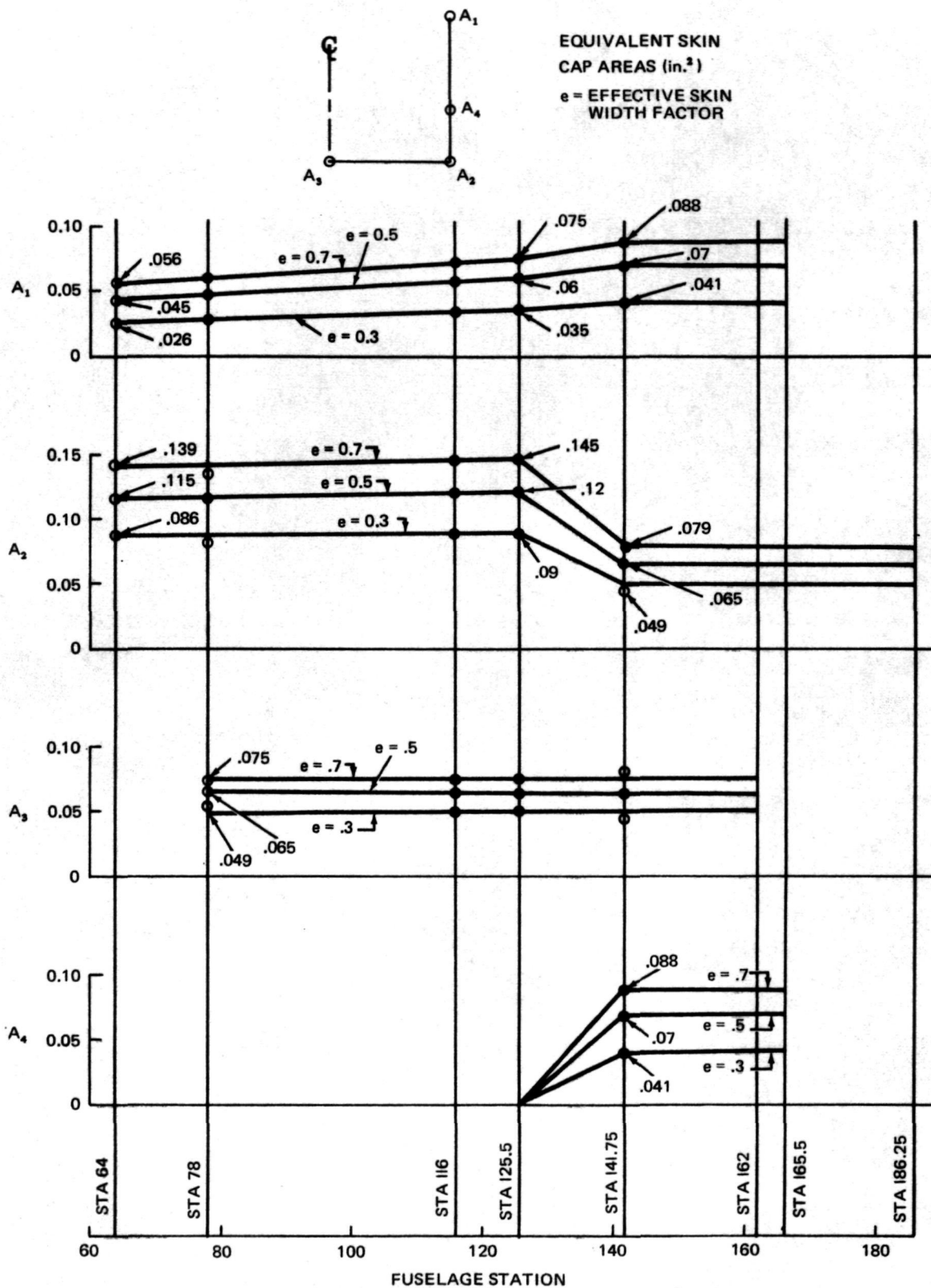
$$a_3 = 0.79 (a_1 + 0.1) - 0.066$$

e	a_1 a_4	a_2 a_3	ΣA^1	I_{zz}^1	$\frac{\Sigma A^1}{\Sigma A}$	$\frac{I_{zz}^1}{I_{zz}}$	$\frac{\Sigma A}{.913}$	$\frac{I_{yy}}{37.5}$	$\frac{I_{zz}}{82.7}$
0.3	0.041	0.045	0.552	51.8	0.96	0.96	0.63	0.67	0.66
0.5	0.069	0.067	0.652	64.0	0.92	0.94	0.77	0.79	0.82
0.7	0.089	0.083	0.724	72.7	0.88	0.92	0.90	0.90	0.95

$$\Sigma A^1 = (a_1 + a_2 + a_3 + a_4 + 0.38)$$

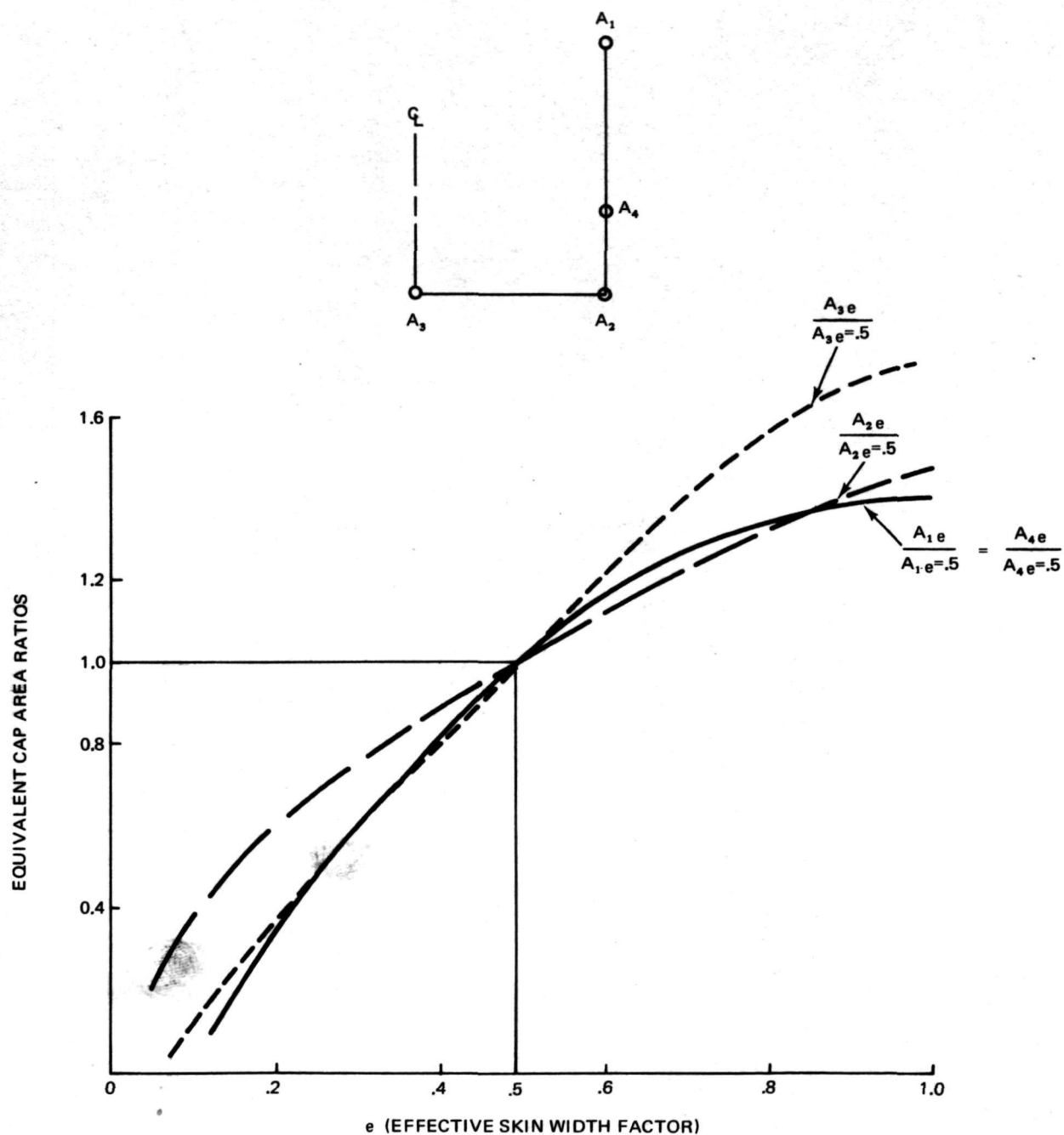
$$I_{zz}^1 = (12.5)^2 (a_1 + a_2 + a_4 + 0.204)$$

Fig. F-6 Effective Fuselage Width Calculations at 141.75

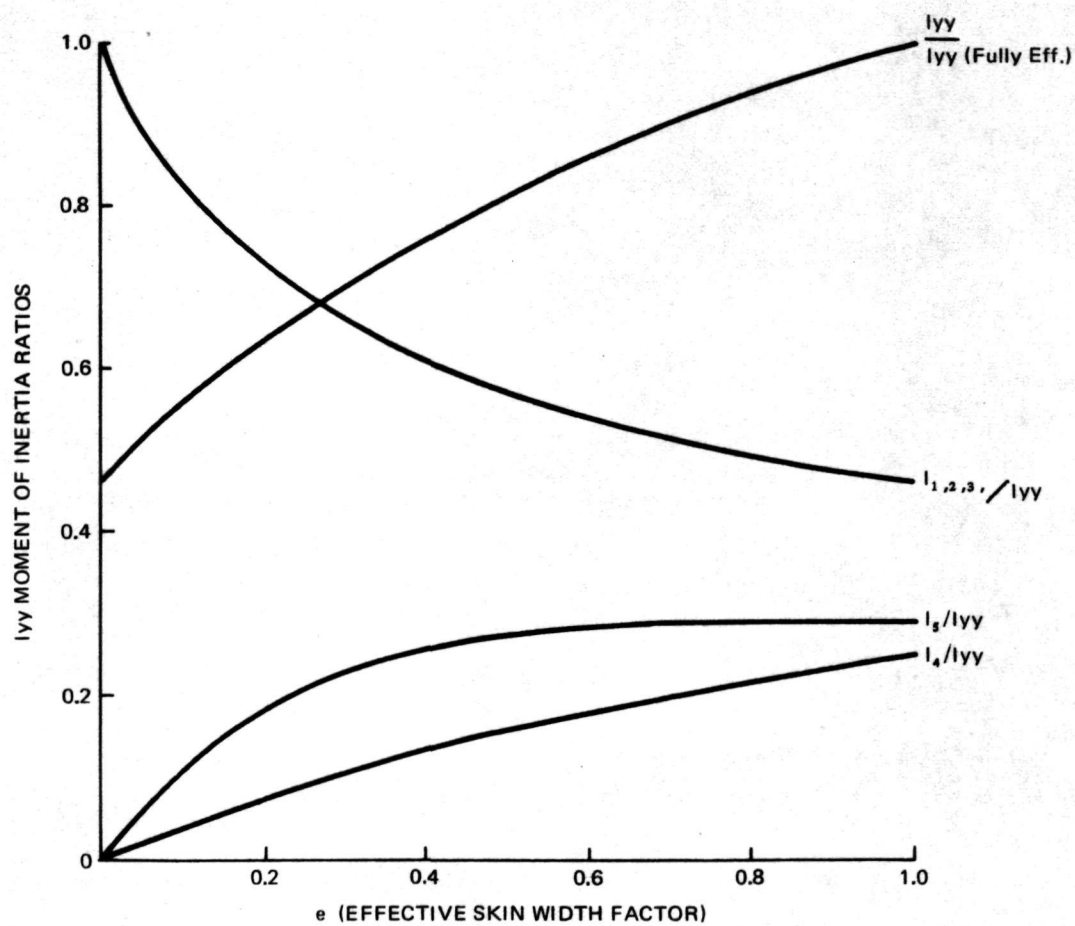
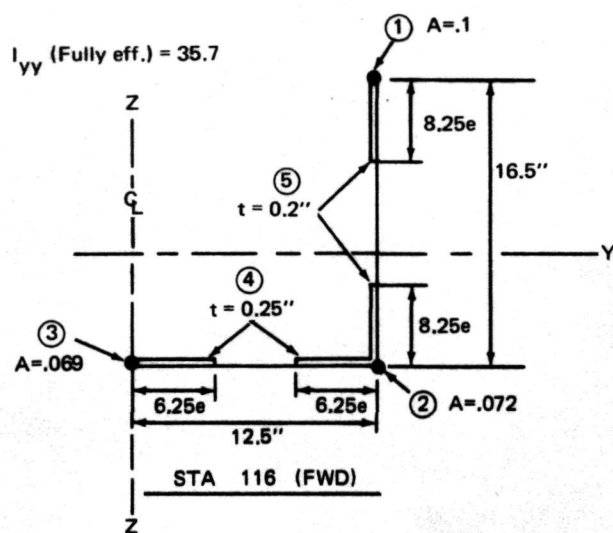


T-151

Fig. F-7 Equivalent Skin Cap Areas in Square Inches



NOTE: Analysis will be set up for $e = .5$. For Re-analysis with a different e , multiply the Modulus of Elasticity (E) for the equivalent caps which are on 4 property cards, by the appropriate area ratio from above curve.

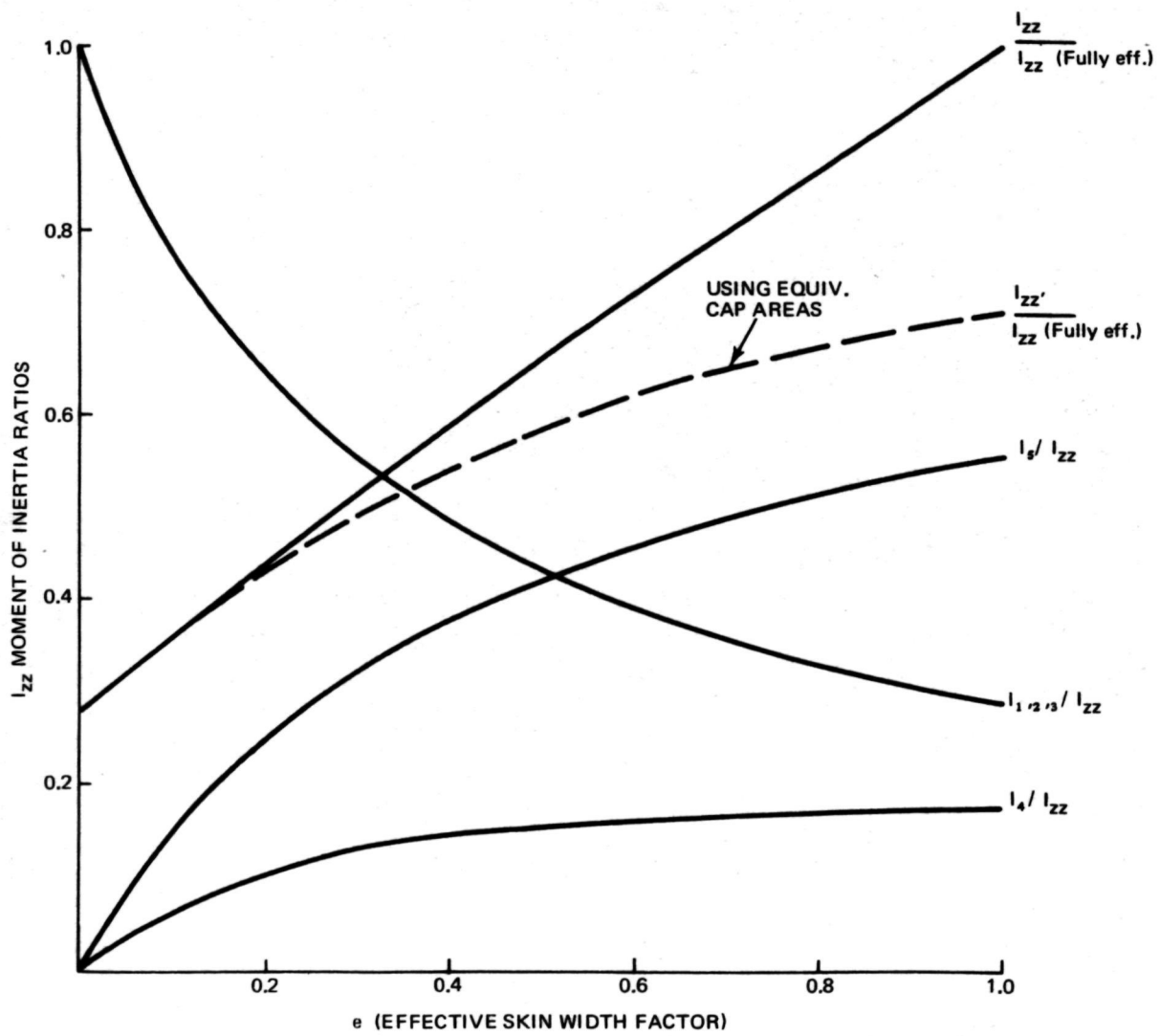


T-153

Fig. F-9 Moment of Inertia Modification Factors – I_{yy} Moment

REFER TO SKETCH ON FIG. F-9 (STA 116)

I_{zz} (Fully Eff.) = 94.7



T-154

Fig. F-10 Moment of Inertia Modification Factors — I_{zz} Moment

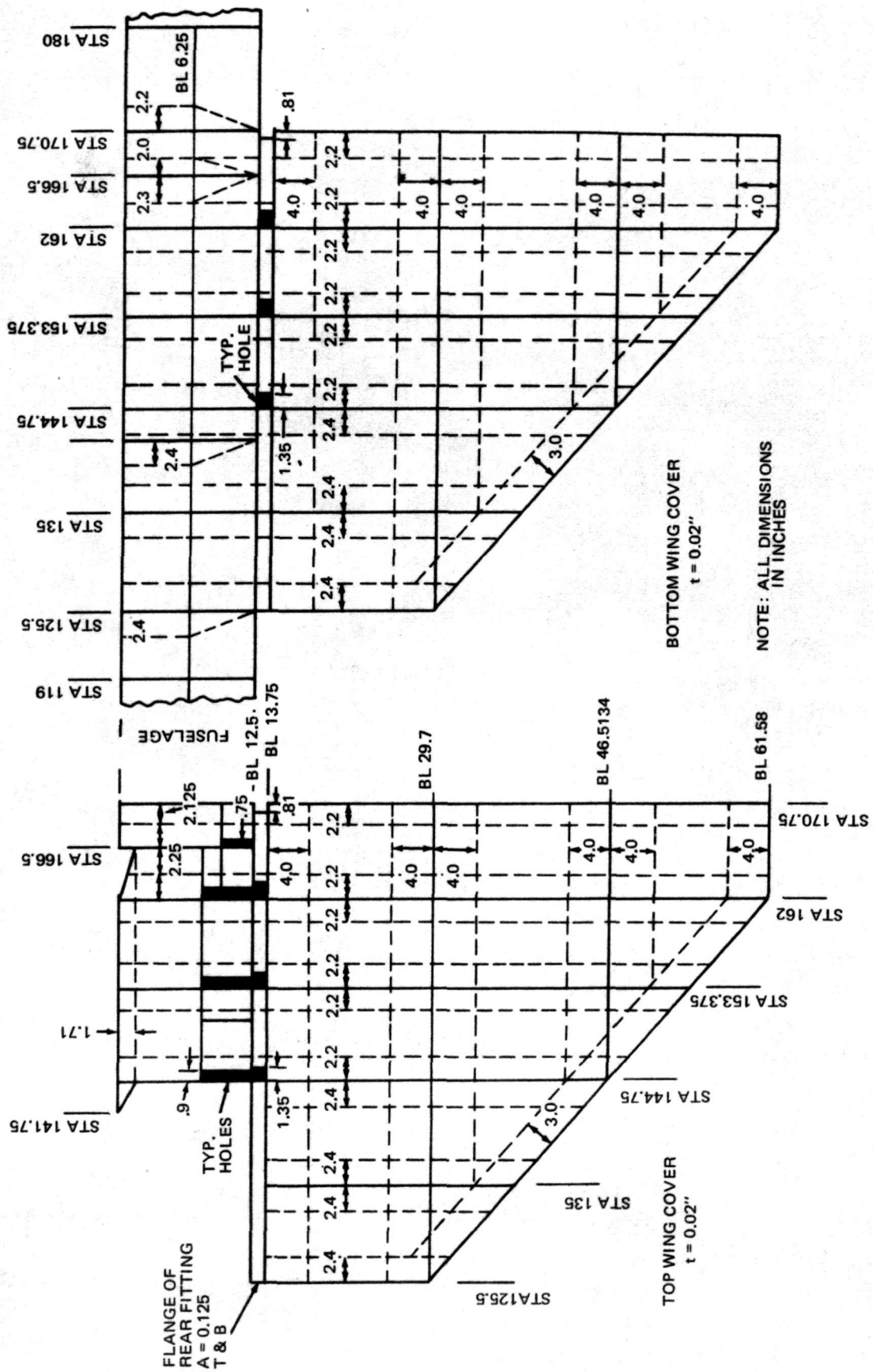


Fig. F-11 Wing Effective Skin Widths When Skin is Half Effective

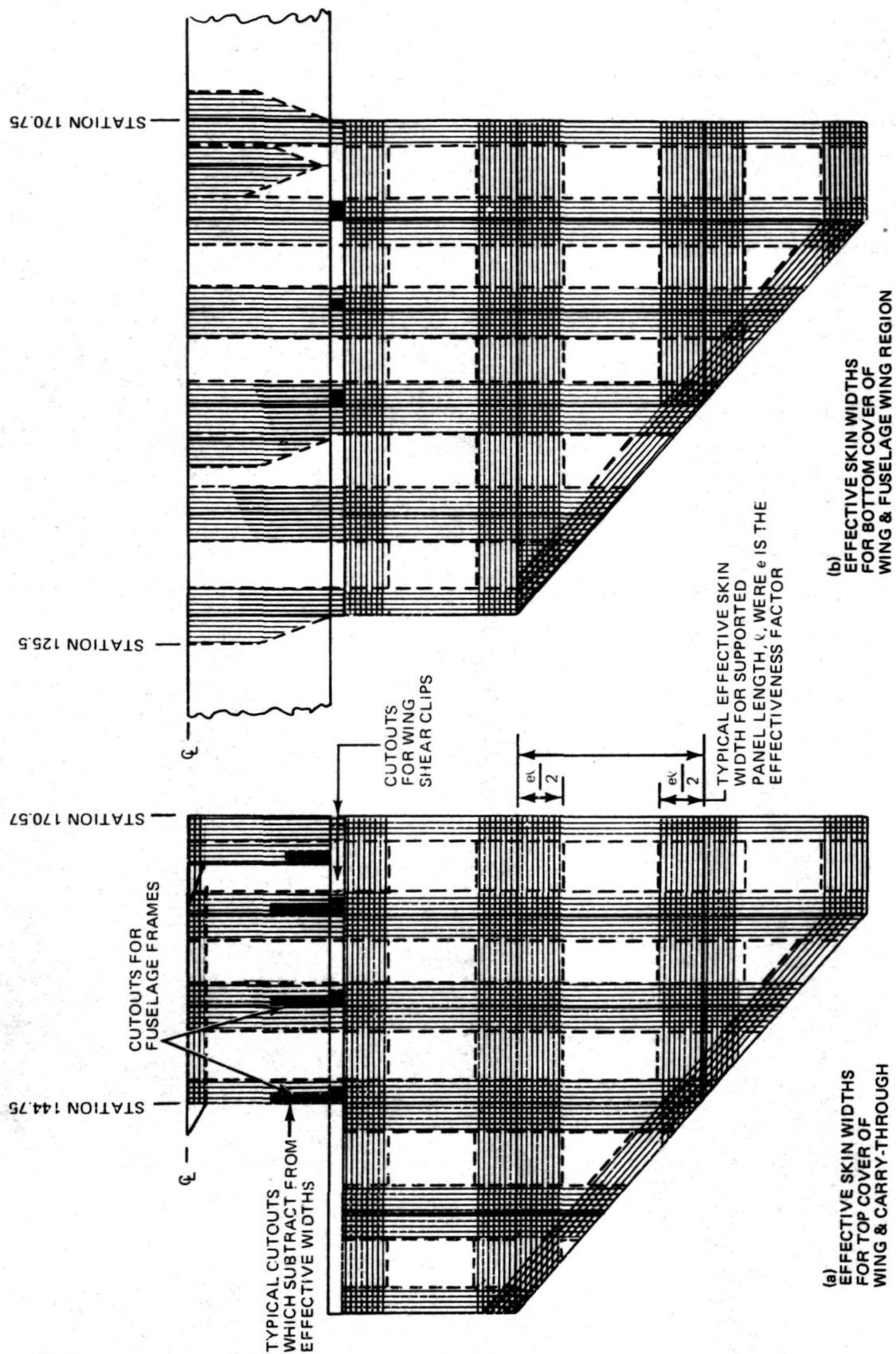
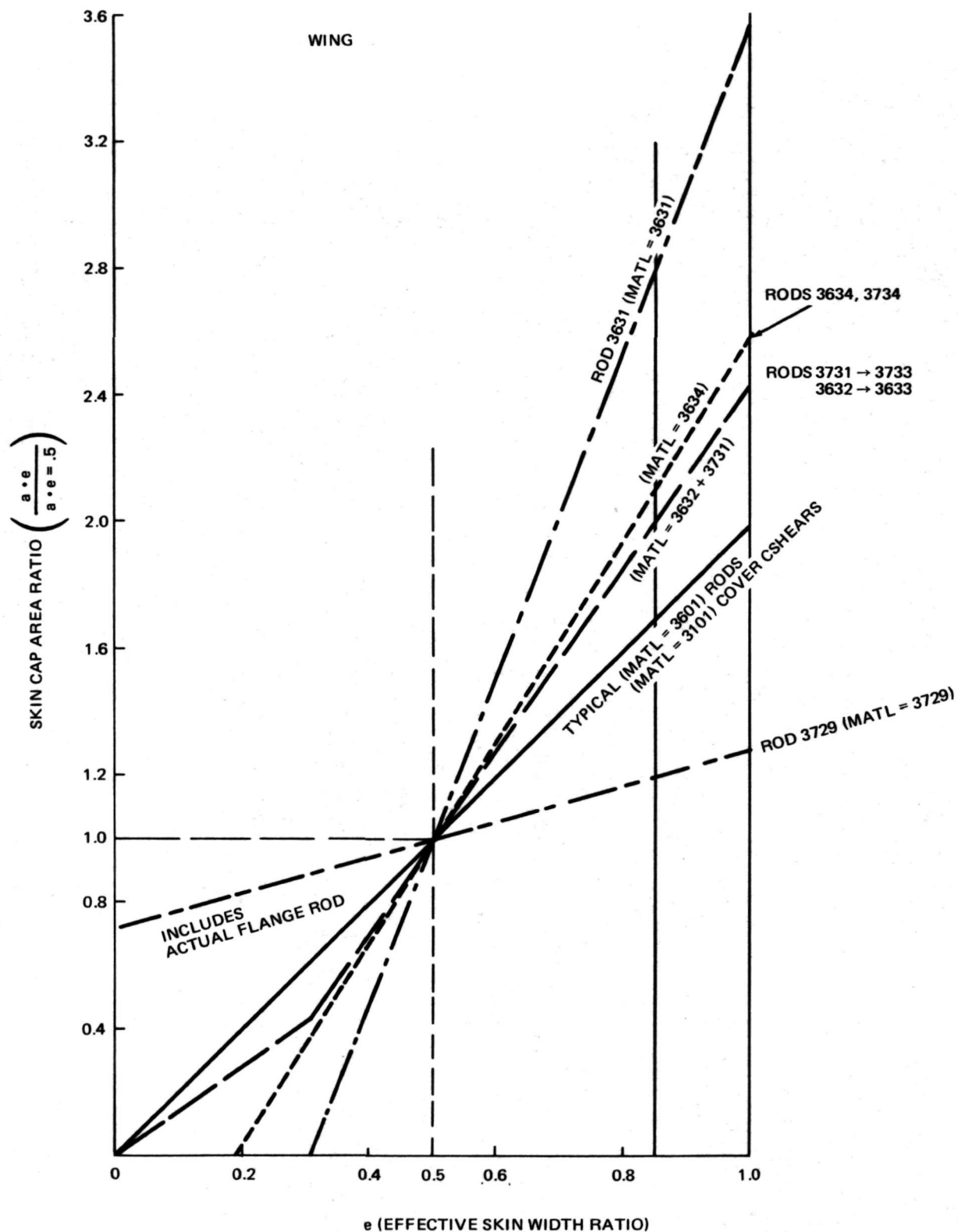


Fig. F-12 Effective Wing Skin Widths



NOTE: Analysis set up for $e = .5$. For re-analysis with different e , multiply the modulus of elasticity (E) on appropriate MAT1 card by area ratio from above curves, rather than changing member areas.

Fig. F-13 Effective Skin Width Ratio for Wing

Appendix G
TEST RESULTS WHICH FORM THE BASIS FOR MODIFICATION OF MODEL I

TABLE OF CONTENTS

NOTE

Appendix G consists of
the following illustrations

<u>Figure</u>		<u>Page</u>
G-1	Static Load-Defl. Curves - Run 18 Fin Ballast Applied Load (+ Px)	G-2
G-2	Static Load - Defl. Curves - Run 18 Fin Ballast Applied Load (+ Px)	G-3
G-3	Static Load - Defl. Curves - Run 18 Fin Ballast Applied Load (+ Px)	G-4
G-4	Static Fin Rotation Relative to Fuselage Run 18 Fin Ballast Applied Load (+ Px)	G-5
G-5	Static Load - Defl. Curves - Run 31 Fin Ballast Applied Load (- Py)	G-6
G-6	Static Load Defl. - Curves - Run 31 Fin Ballast Applied Load (- Py)	G-7
G-7	Static Fin Rotation Relative to Fuselage Run 31 - Fin Ballast Applied Load (- Py)	G-8
G-8	Static Torsion - Rotation Curves Run 30 - Applied Nose Torsion	G-9
G-9	Static Torsion - Rotation Curves Run 30 - Applied Nose Torsion	G-10
G-10	Static Torsion Rotation Curves Run 30 - Applied Nose Torsion	G-11
G-11	Comparison of Test Run 30 with Analysis Nose Torsion Case.	G-12
G-12	Static Load - Defl. Curves - Run 26 Payload Applied Load at Sta. 117.5 (- P _Z)	G-13
G-13	Static Load - Defl. Curves - Run 26 Payload Applied Load at Sta. 117.5 (- P _Z)	G-14
G-14	Static Load - Defl. Curves - Run 26 Payload Applied Load at Sta. 117.5 (P _Z)	G-15

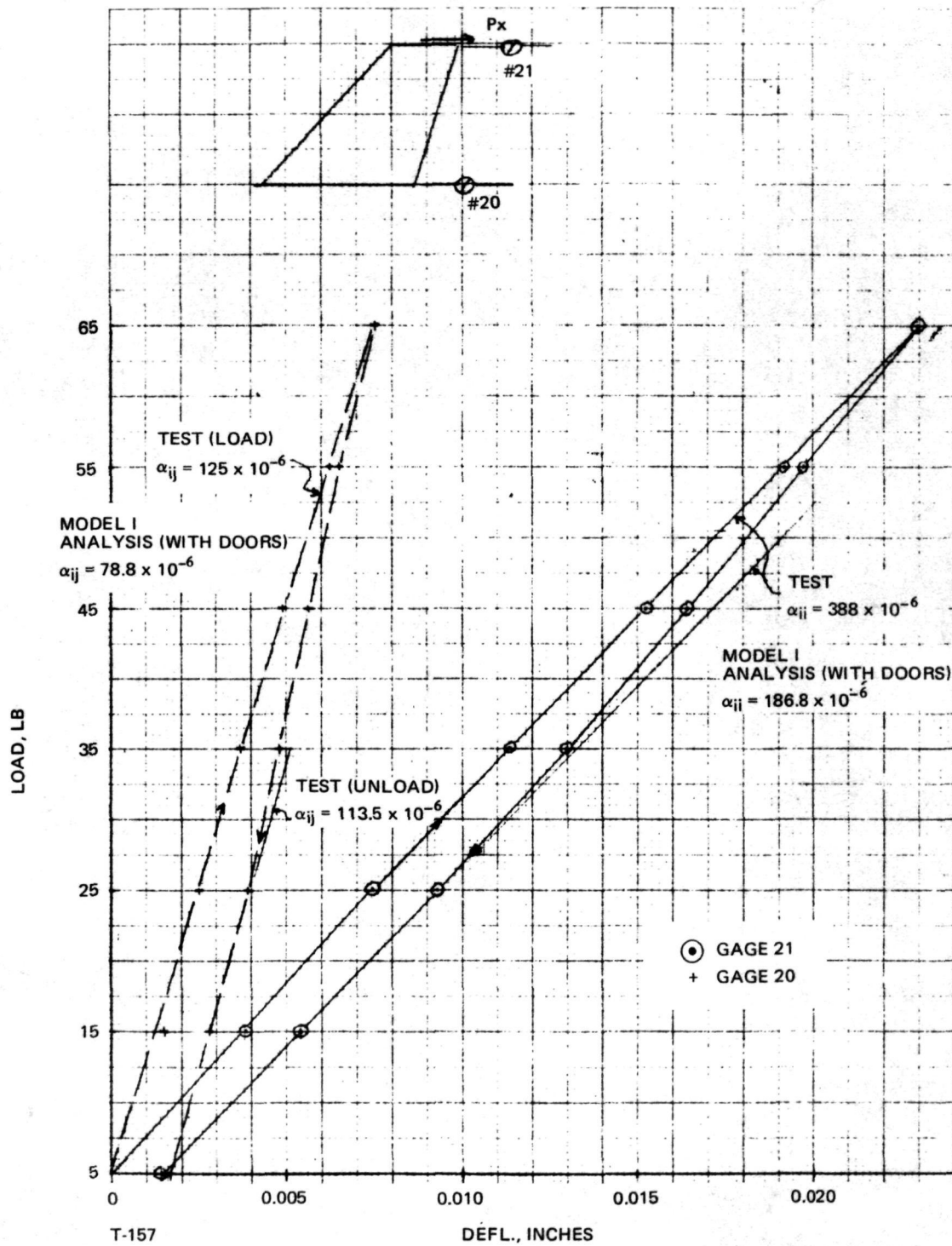


Fig. G-1 Static Load-Defl. Curves — Run 18 Fin Ballast Applied Load (+ P_x)

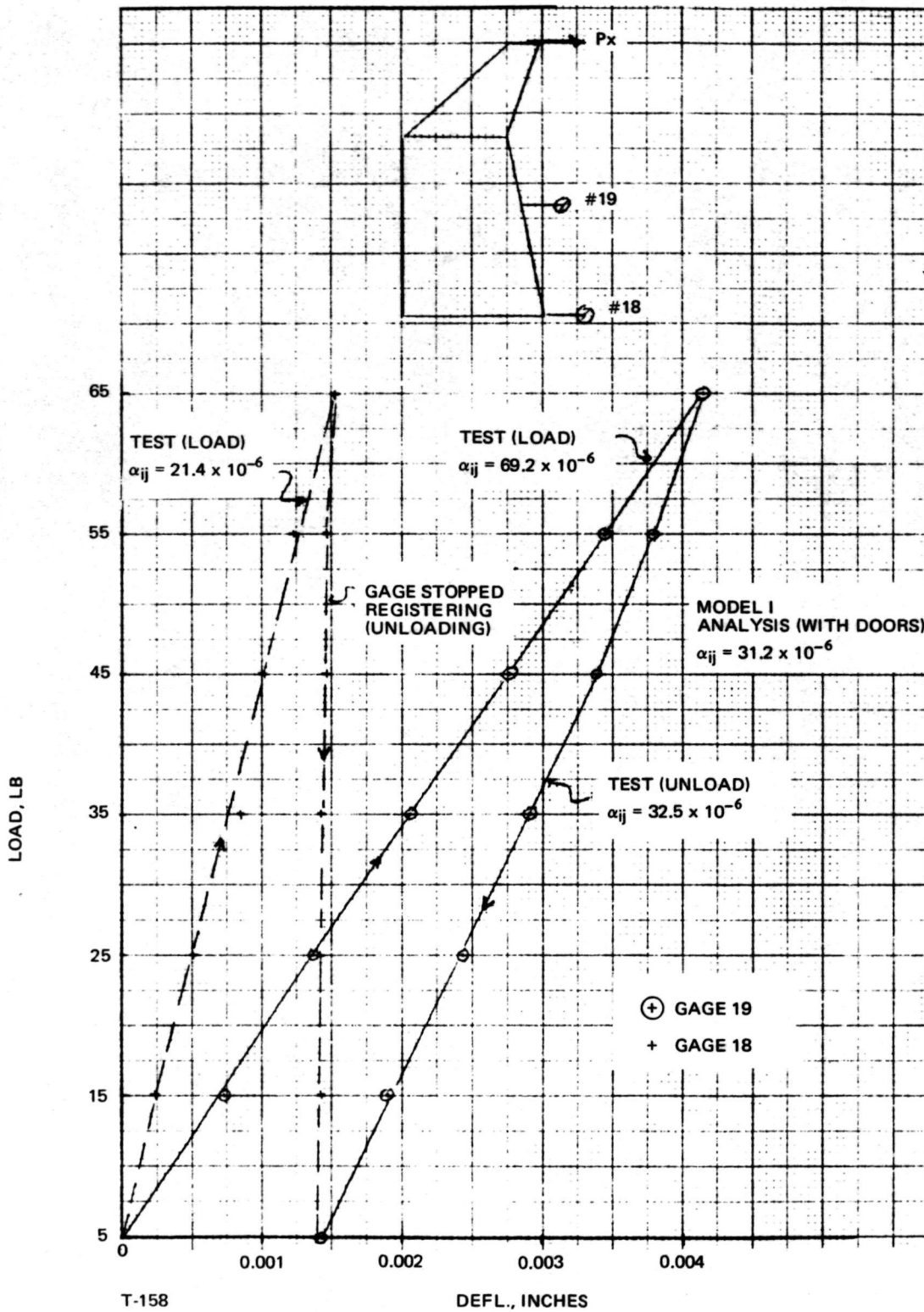


Fig. G-2 Static Load-Defl. Curves — Run 18 Fin Ballast Applied Load (+ Px)

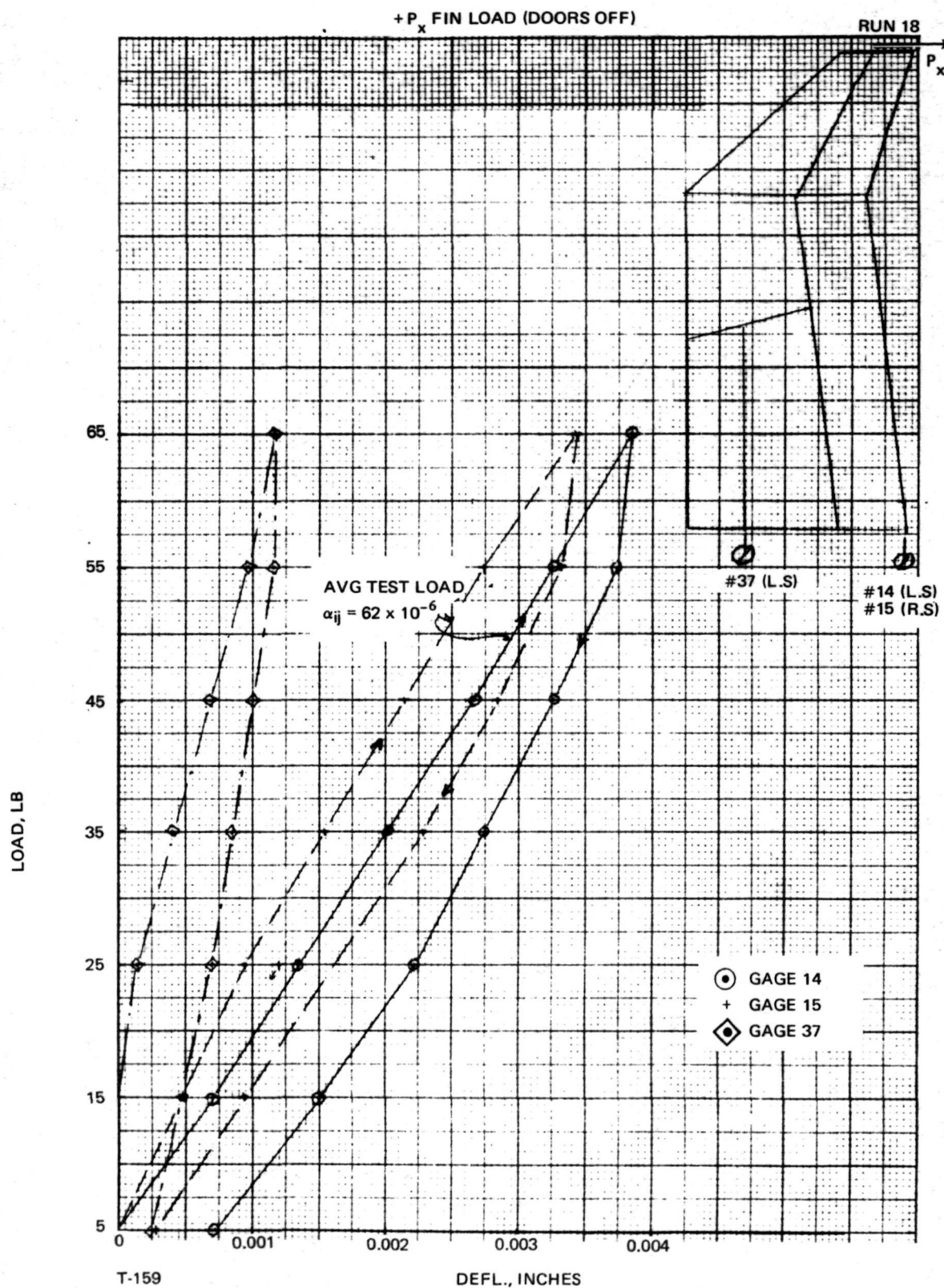
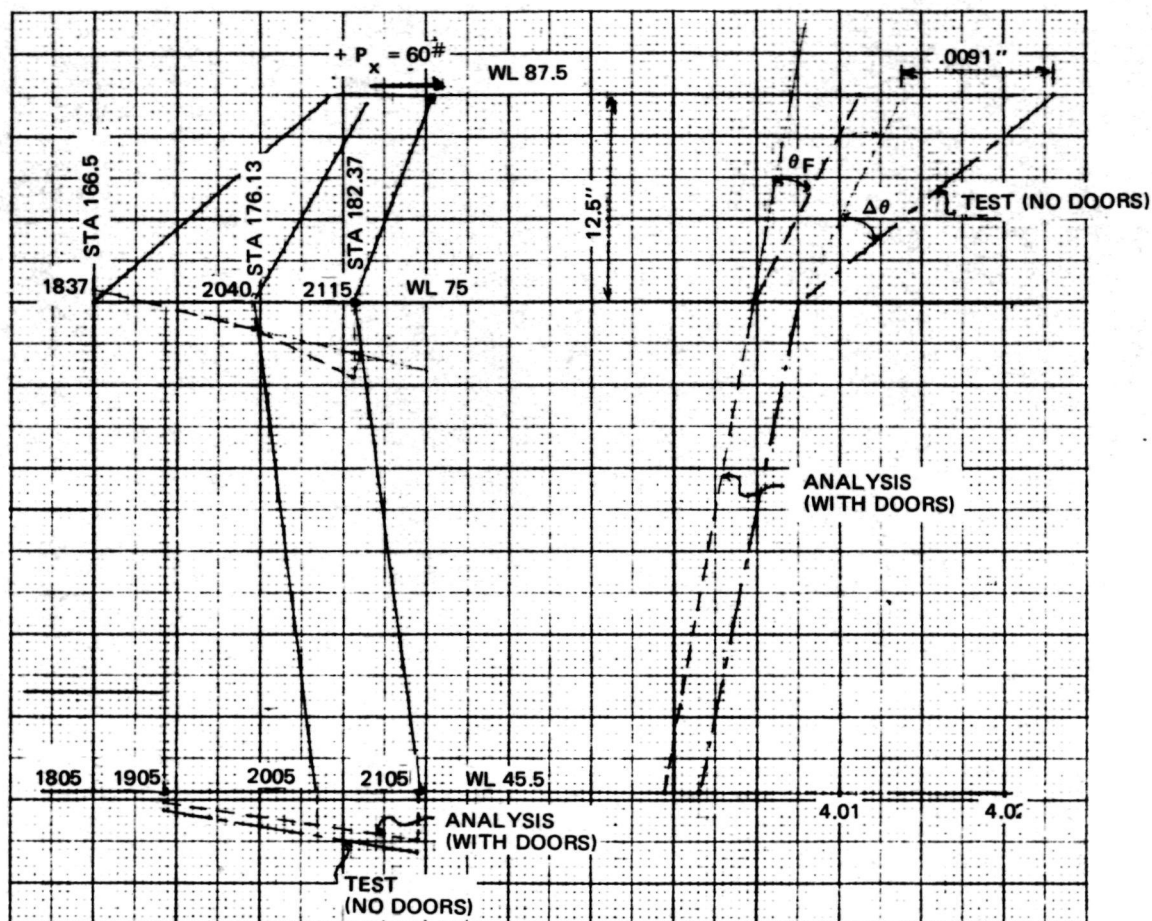


Fig. G-3 Static Load-Defl. Curves — Run 18 Fin Ballast Applied Load (+ P_x)



$$\Delta\theta = \frac{.0091}{12.5} = .00073$$

$$= 12.17 \times 10^{-6} \text{ (P = 1 LB)}$$

MODEL I ANALYSIS FIN ROTATION RELATIVE TO FUS.

$$\theta_F = \frac{.004}{12.5(60)} = 5.34 \times 10^{-6} \text{ (P = 1 LB)}$$

T-160

Fig. G-4 Static Fin Rotation Relative To Fuselage Run 18 Fin Ballast Applied Load (+ P_x)

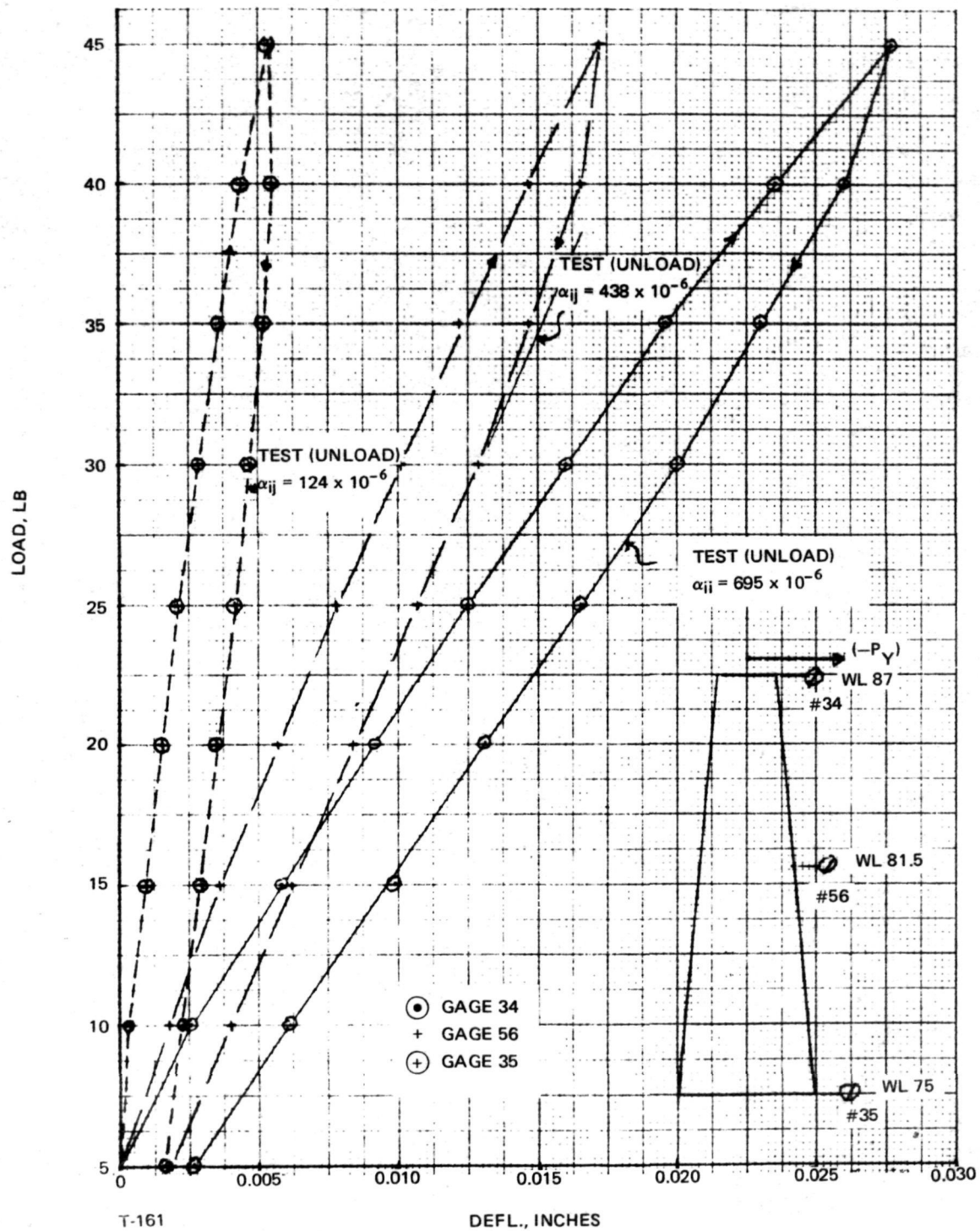


Fig. G-5 Static Load-Defl. Curves – Run 31 Fin Ballast Applied Load ($-P_Y$)

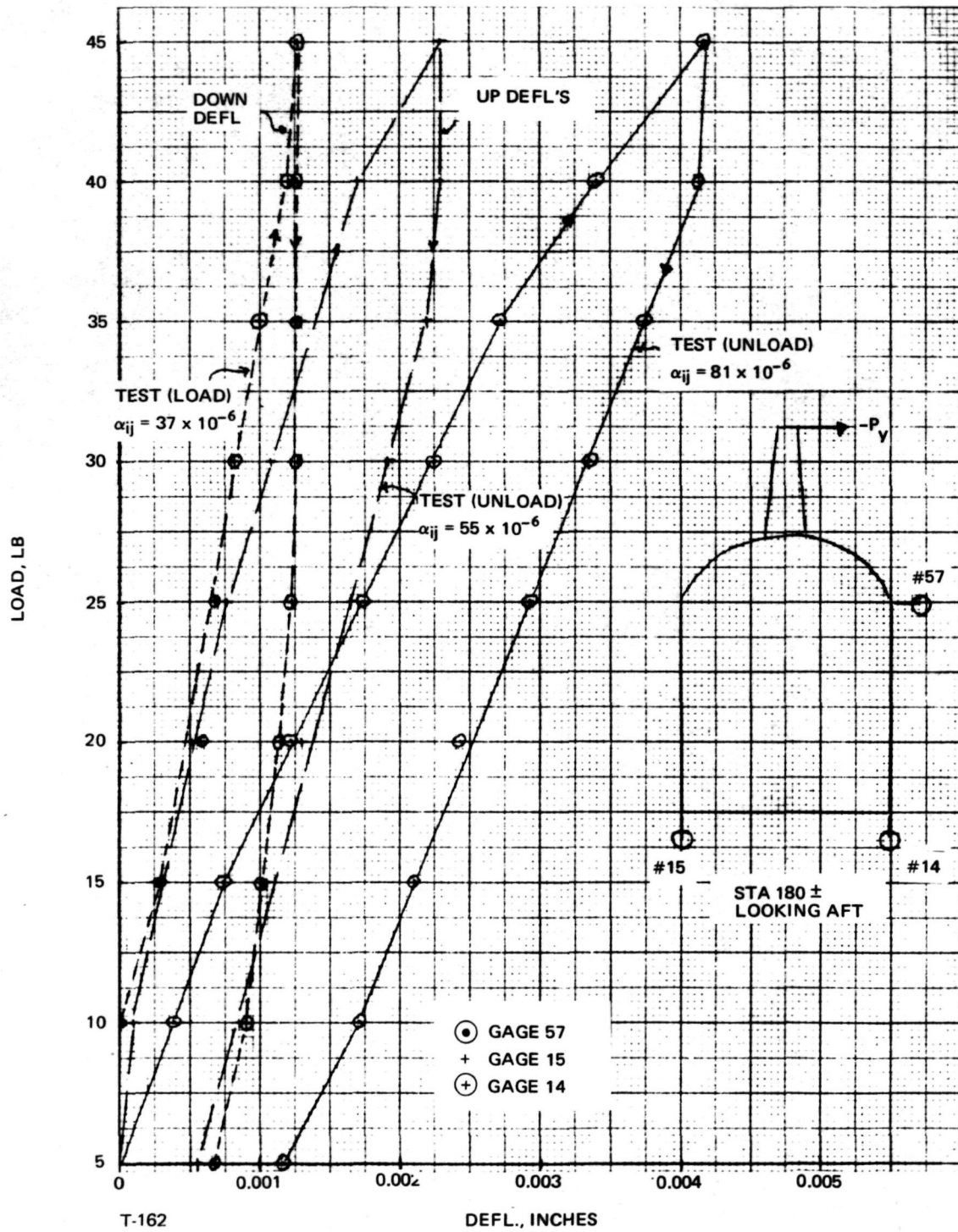
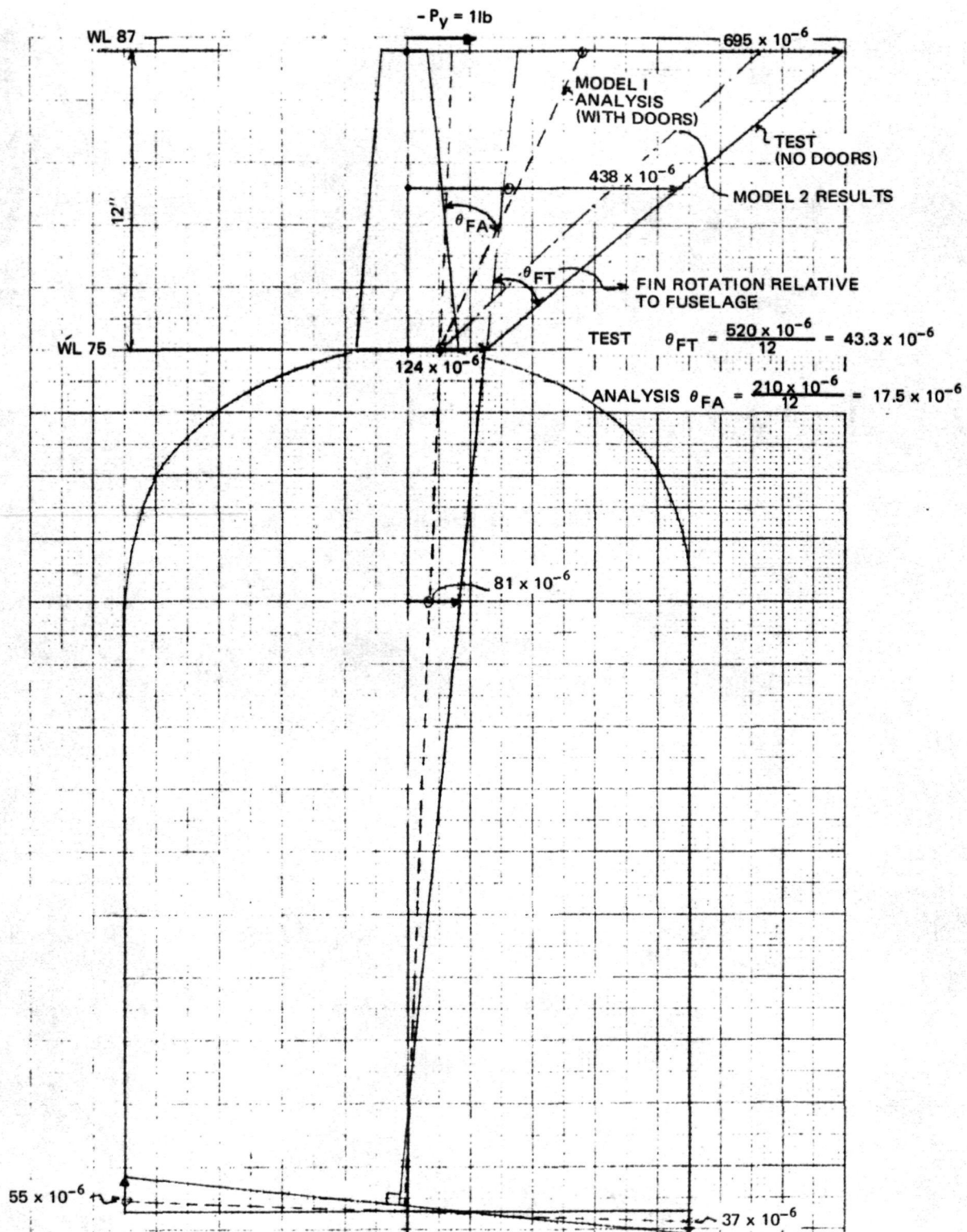


Fig. G-6 Static Load-Defl. Curves — Run 31 Fin Ballast Applied Load ($-P_Y$)



T-163

Fig. G-7 Static Fin Rotation Relative to Fuselage Run 31 – Fin Ballast Applied Load ($-P_y$)

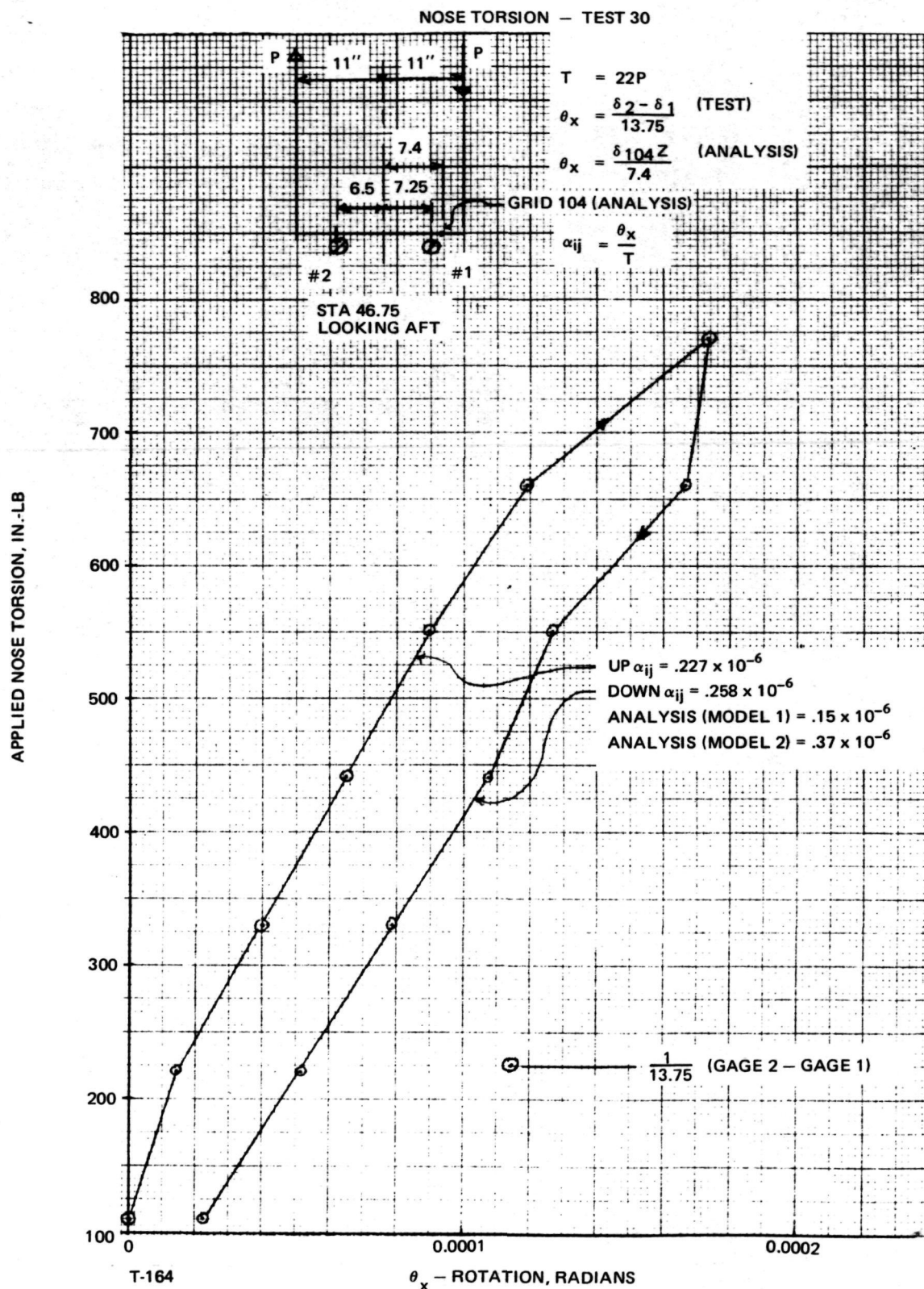


Fig. G-8 Static Torsion-Rotation Curves Run 30 - Applied Nose Torsion

NOSE TORSION — TEST 30

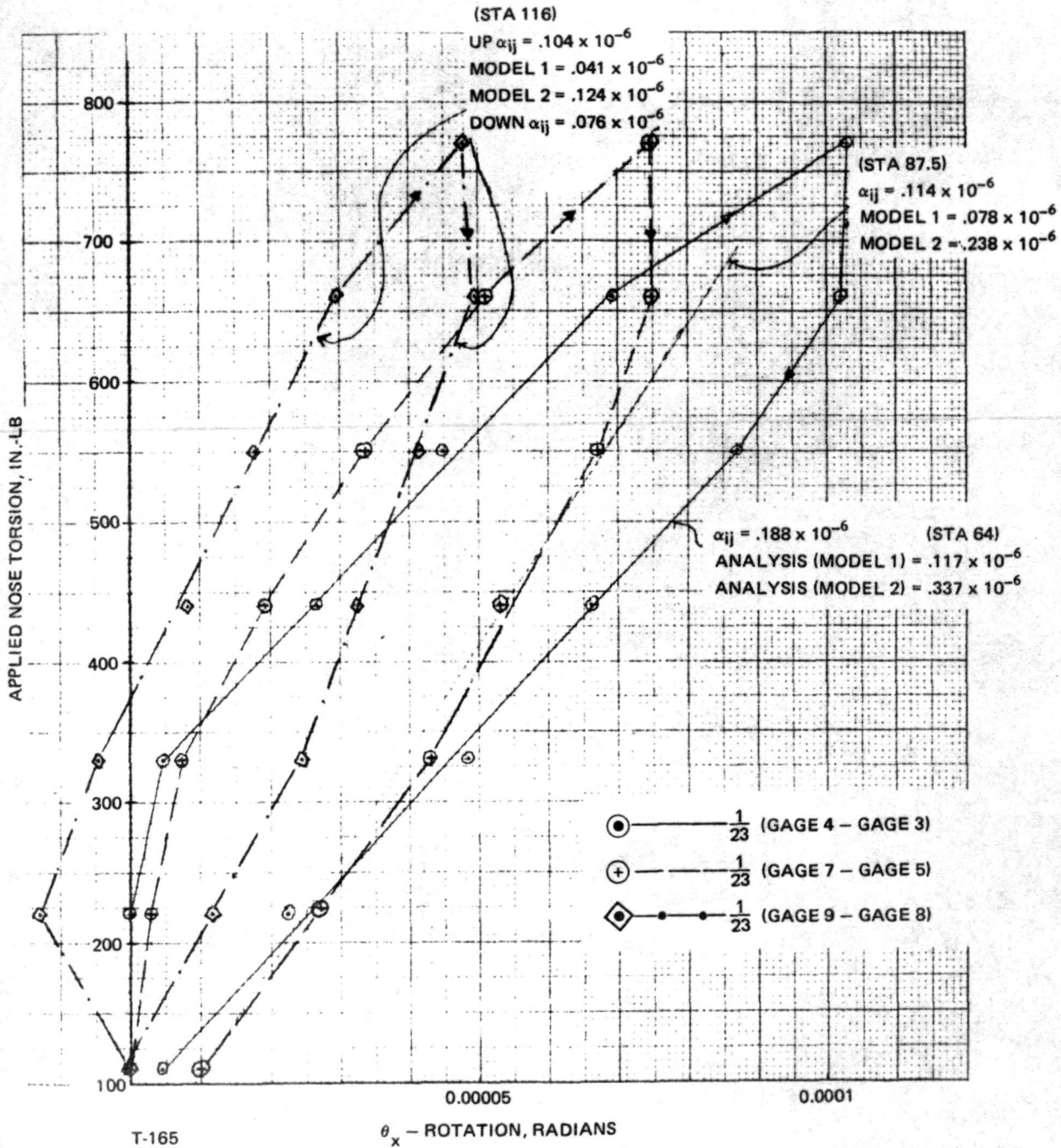


Fig. G-9 Static Torsion — Rotation Curves Run 30 — Applied Nose Torsion

NOSE TORSION - TEST 30

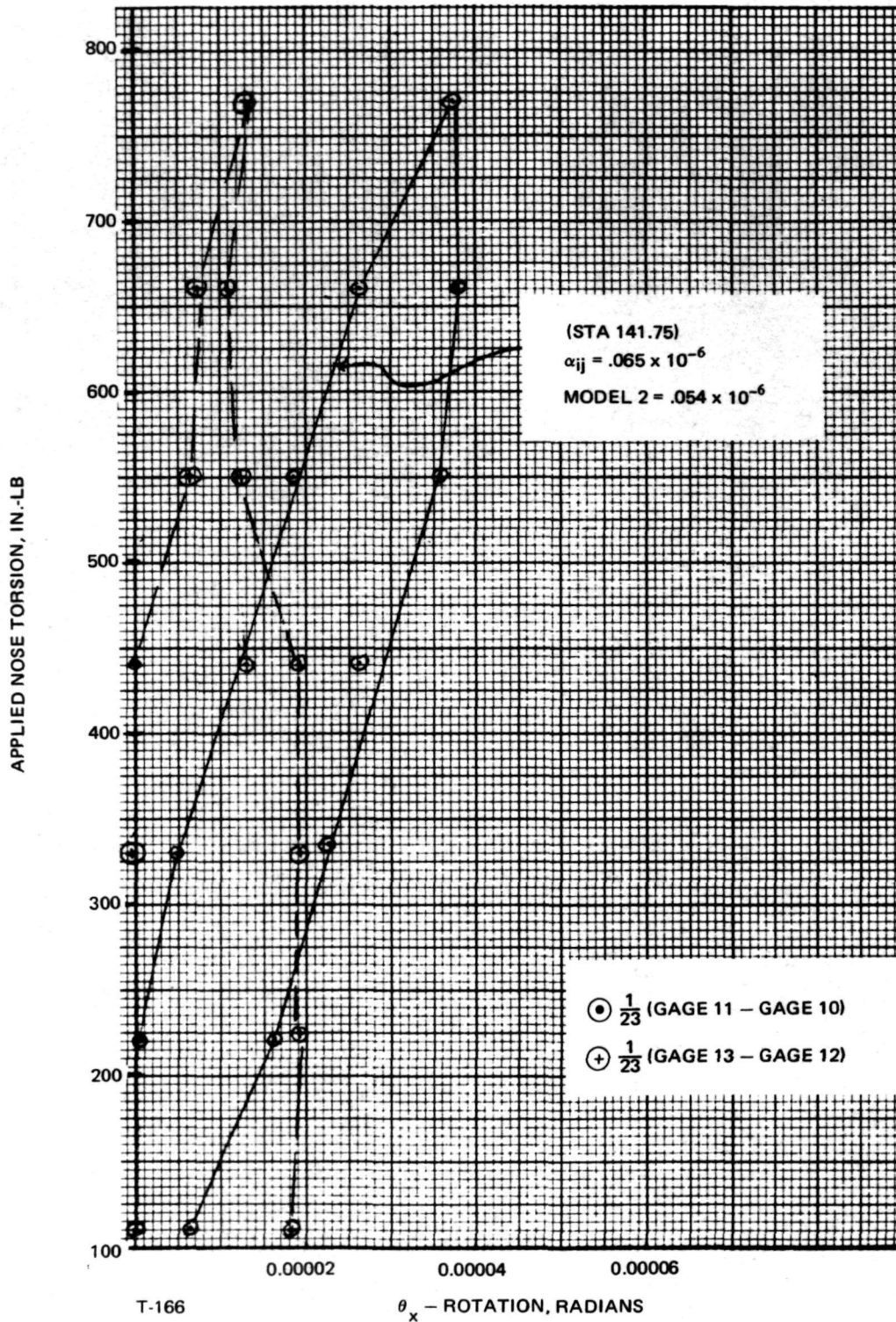


Fig. G-10 Static Torsion-Rotation Curves Run 30 - Applied Nose Torsion

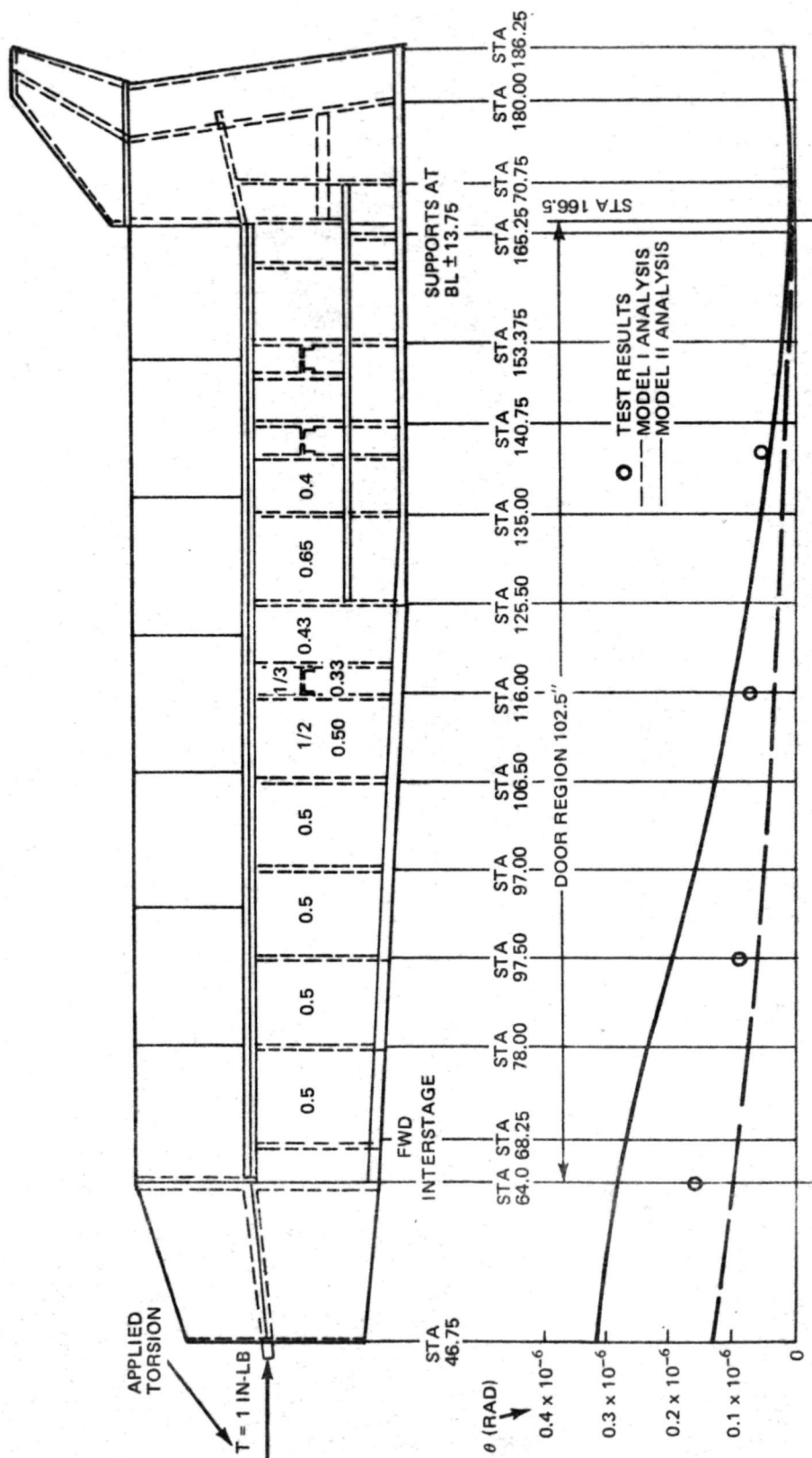
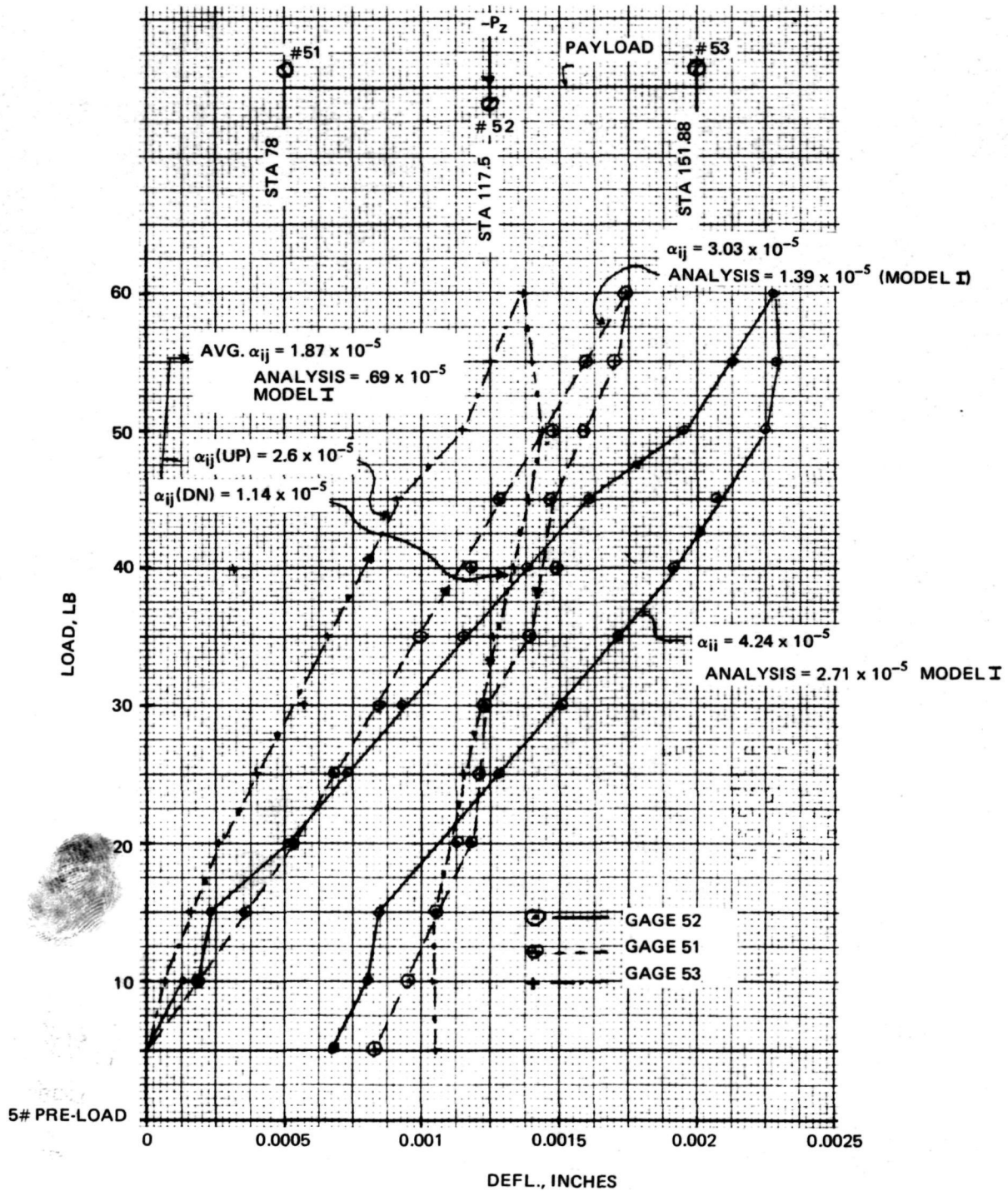


Fig. G-11 Comparison of Test Run 30 With Analyses Nose Torsion Case

T-167

STATIC DEFLECTION (-Z) LOAD AT STA 117.5 ON PAYLOAD RUN 26 (NO DOORS)

ANALYSIS VALUES ARE WITH DOORS



T-168

Fig. G-12 Static Load-Defl. Curves – Run 26 Payload Applied Load at Sta 117.5 ($-P_z$)

STATIC DEFLECTION (-Z) LOAD AT STA 117.5 ON PAYLOAD
RUN 26 (NO DOORS)

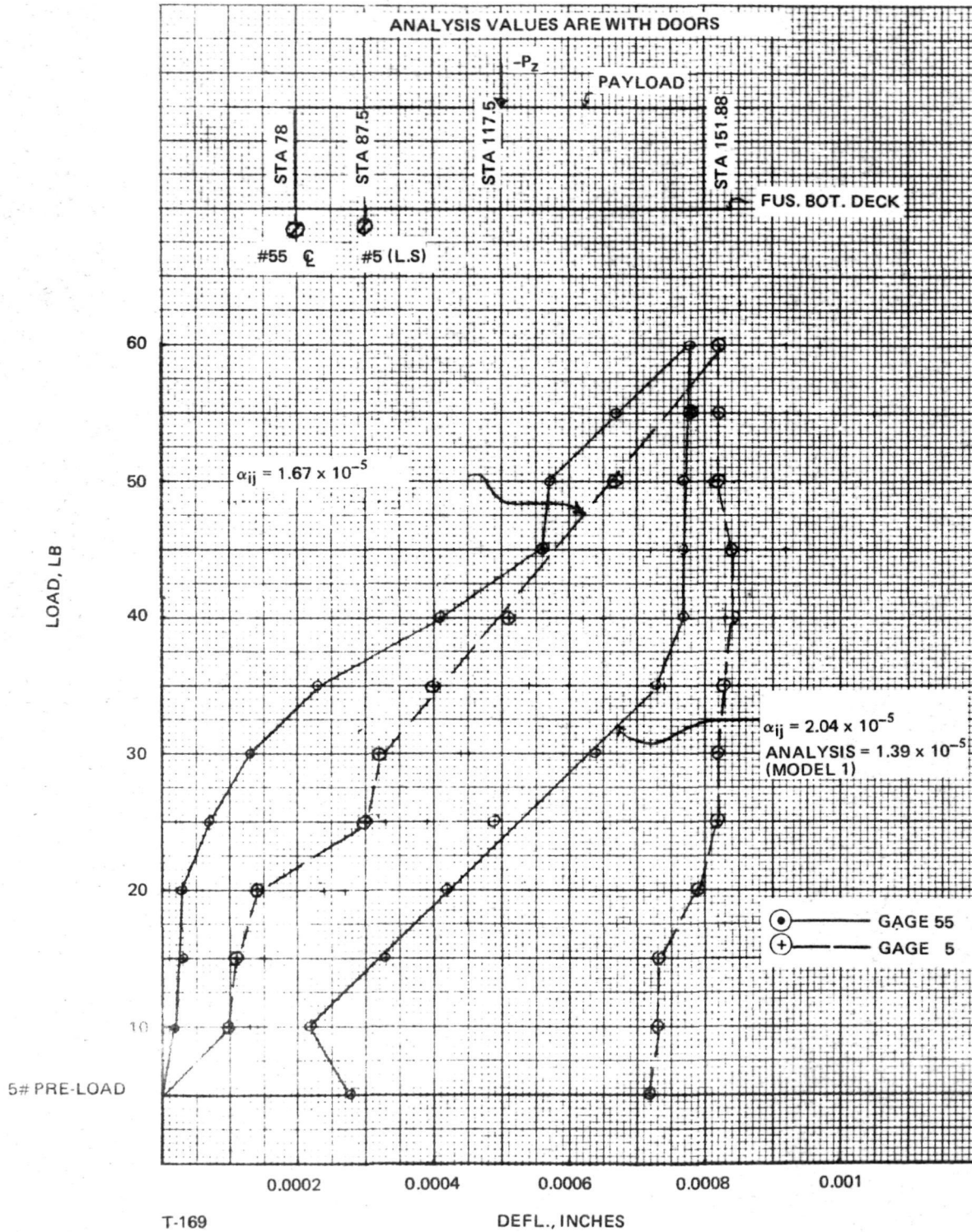


Fig. G-13 Static Load-Defl. Curves — Run 26 Payload Applied Load at Sta 117.5 ($-P_z$)

STATIC DEFLECTION (-Z) LOAD AT STA 117.5 ON PAYLOAD
RUN 26 (NO DOORS)

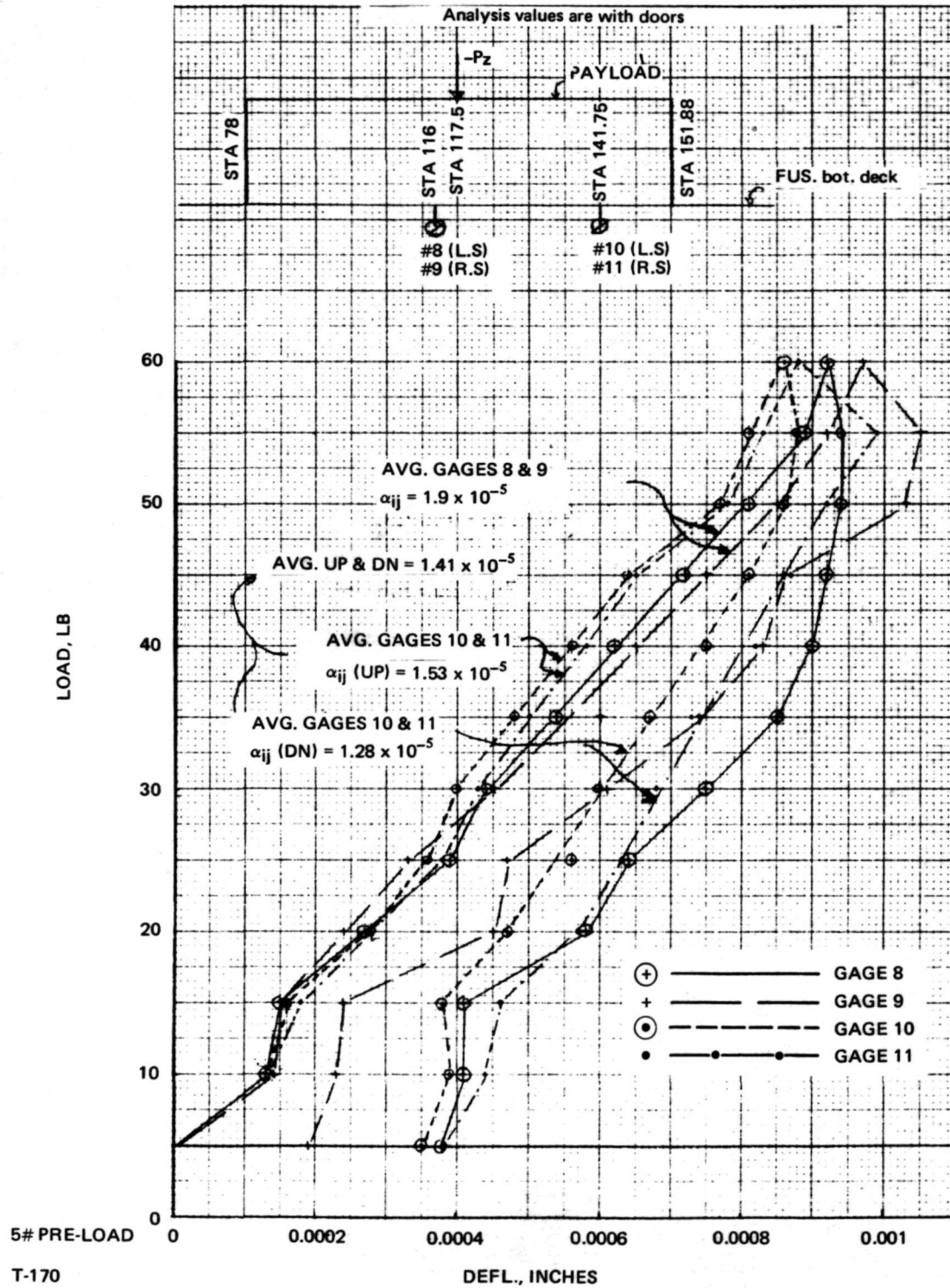


Fig. G-14 Static Load-Defl. Curves — Run 26 Payload Applied Load at Sta 117.5 (P_z)

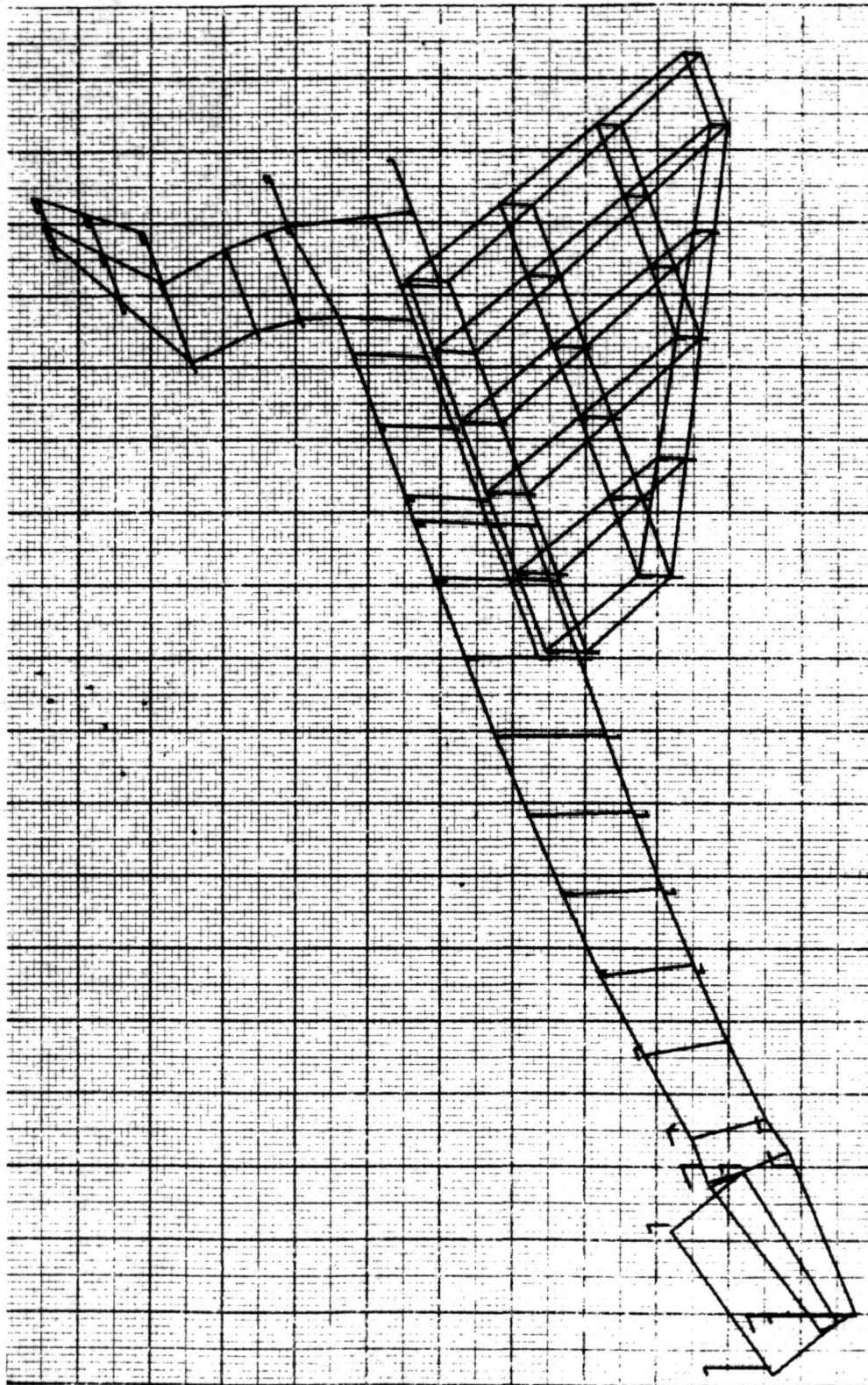
Appendix H
ORBITER STATIC TEST CASE ANALYTICAL DEFLECTIONS FOR MODEL II

TABLE OF CONTENTS

NOTE

Appendix H consists of
the following illustrations:

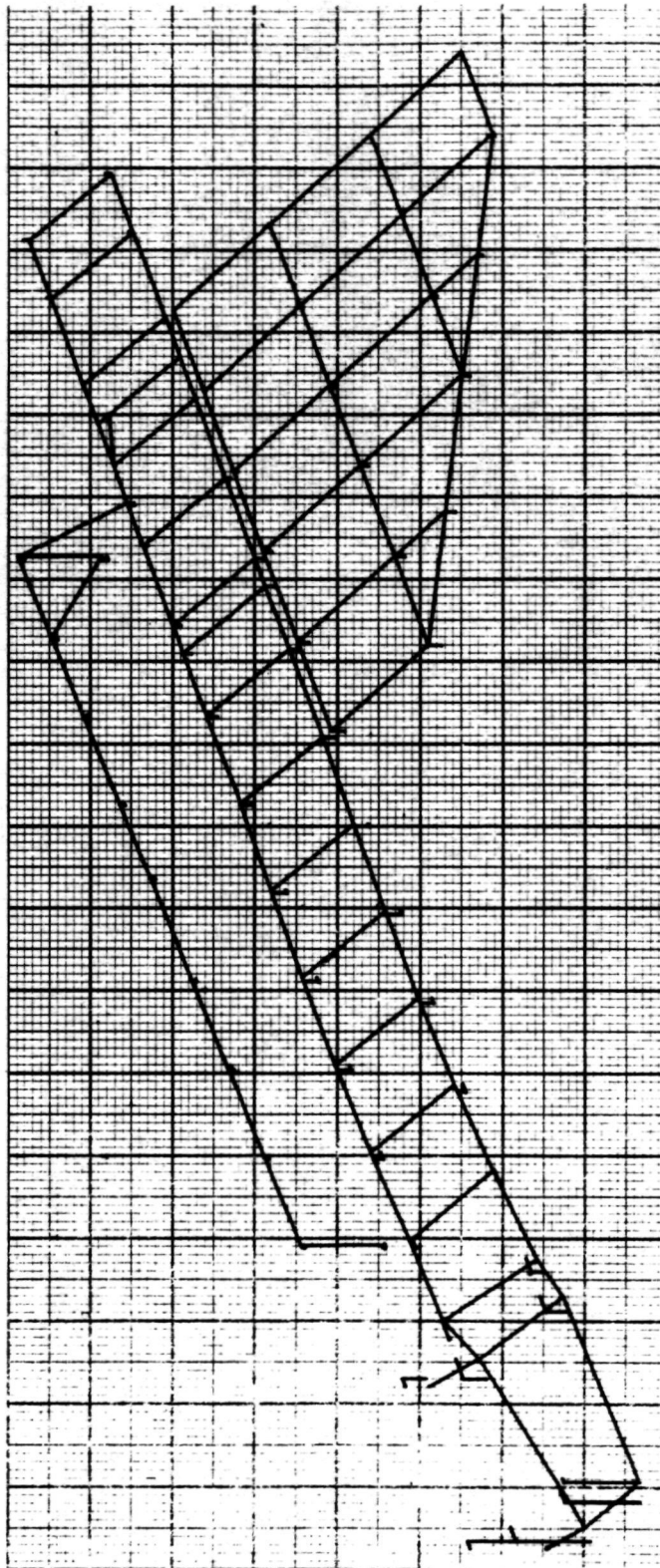
<u>Figure</u>		<u>Page</u>
H-1	Fuselage Nose - Sta 46.75, Grid 120	H-2
H-2	Fuselage Nose - Sta 46.75, Grid 120	H-3
H-3	Mid-Fuselage - Sta 116.0, Grid 905	H-4
H-4	Mid-Fuselage - Sta 116.0, Grid 905	H-5
H-5	Wing Tip - Grid 3017	H-6
H-6	Wing Tip - Grid 3017	H-7
H-7	Fin Ballast - Grid 4400	H-8
H-8	Fin Ballast - Grid 4400	H-9
H-9	OMS Ballast - Grid 2200	H-10
H-10	OMS Ballast - Grid 2200	H-11
H-11	Mid Payload - Sta 117.5, Grid 4886	H-12
H-12	Mid Payload - Sta 117.5, Grid 4886	H-13
H-13	Mid-Fuselage - Sta 116.0, WL 51.5	H-14
H-14	Mid-Fuselage - Sta 116.0, WL 51.5	H-15
H-15	Nose Torsion - Sta 46.75, Grid 120	H-16
H-16	Nose Torsion - Sta 46.75, Grid 120	H-17
H-17	Mid Torsion - Wing Tip, Grid 3017	H-18
H-18	Mid Torsion - Wing Tip, Grid 3017	H-19
H-19	Fin Ballast - Grid 4400	H-20
H-20	Fin Ballast - Grid 4400	H-21



ORBITER STATIC TEST CASES ON INTERSTAGE SUPPORTS
REVISED 5/7/74 SYMM CASE
UNIT PZ DOWN ON FULL ORBITER (FUS. NOSE-STA 46.75-GRID 120)
STATIC DEFOR. SUBCASE 1

T-171

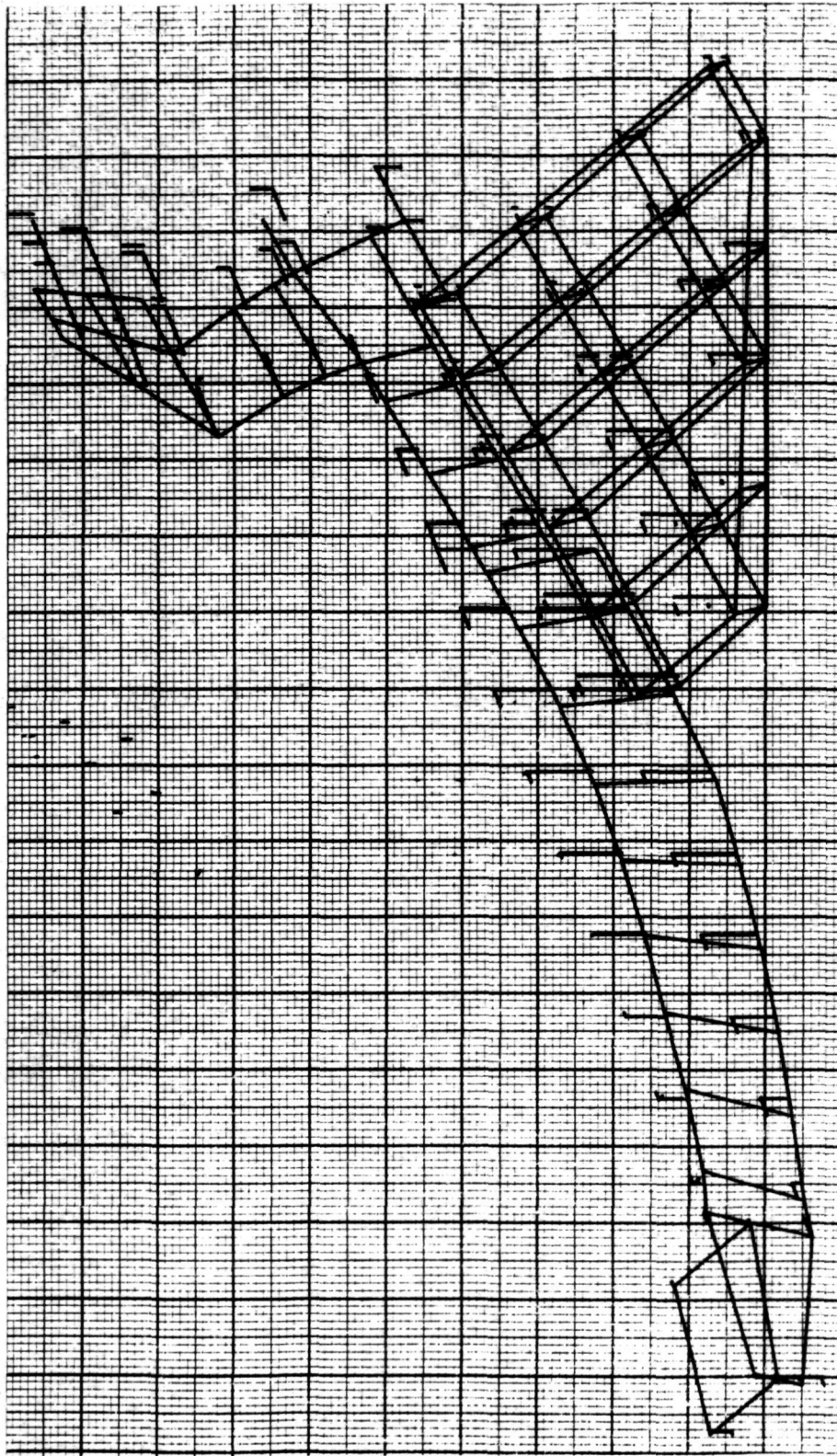
Fig. H-1 Fuselage Nose - Sta 46.75, Grid 120



ORBITER STATIC TEST CASES ON INTERSTAGE SUPPORTS
REVISED 5/7/74 SYMM CASE
UNIT PZ DOWN ON FULL ORBITER (FUS. NOSE-STA 46.75-GRID 120)
STATIC DEFOR. SUBCASE 1

T-172

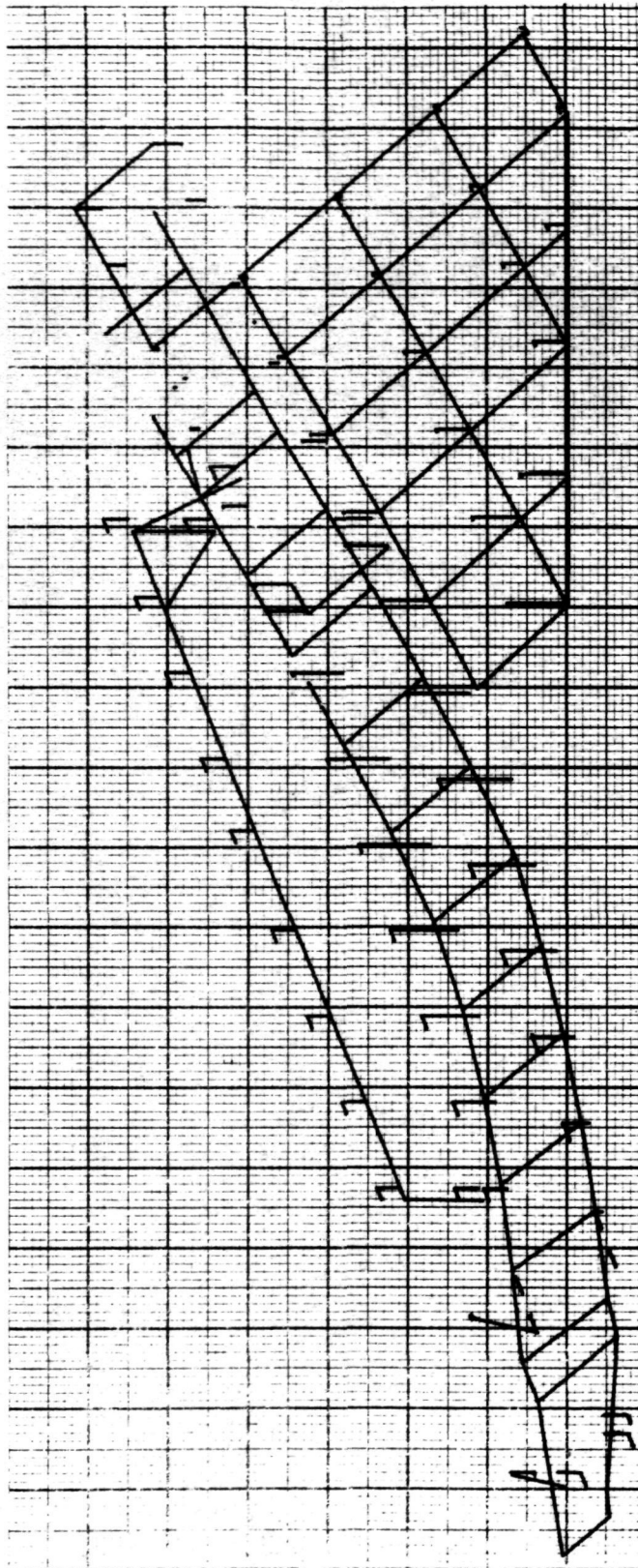
Fig. H-2 Fuselage Nose - Sta 46.75, Grid 120



ORBITER STATIC TEST CASES ON INTERSTAGE SUPPORTS
REVISED 5/7/74 SYMM CASE
UNIT PZ DOWN ON FULL ORBITER (MID FUS. -STA 116.0-GRID 905)
STATIC DEFOR. SUBCASE 2

T-173

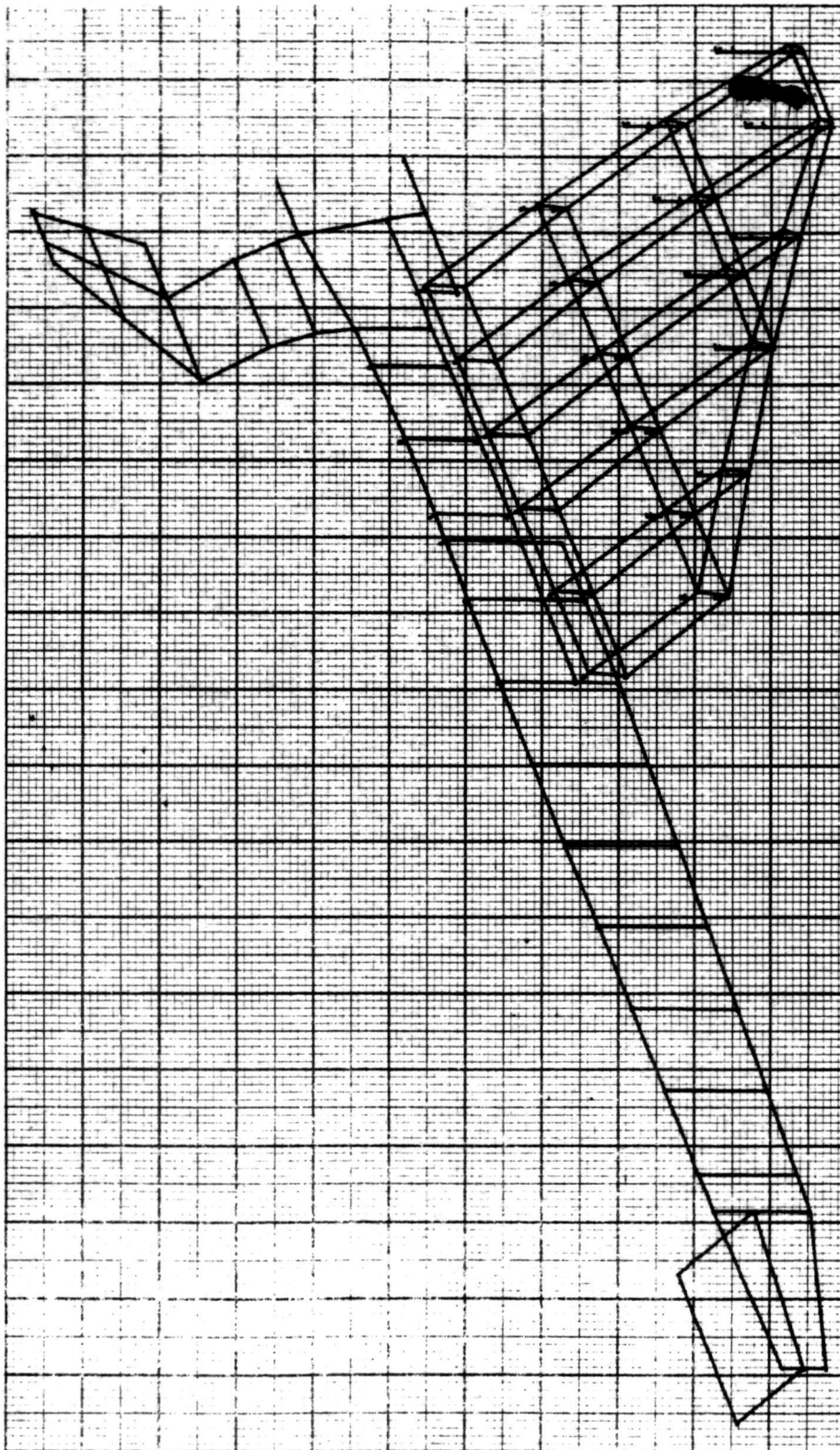
Fig. H-3 Mid-Fuselage - Sta 116.0 Grid 905



ORBITER STATIC TEST CASES ON INTERSTAGE SUPPORTS
REVISED 5/7/74 SYMM CASE
UNIT PZ DOWN ON FULL ORBITER (MID FUS. -STA. 116.0-GRID 905)
STATIC DEFOR. SUBCASE 2

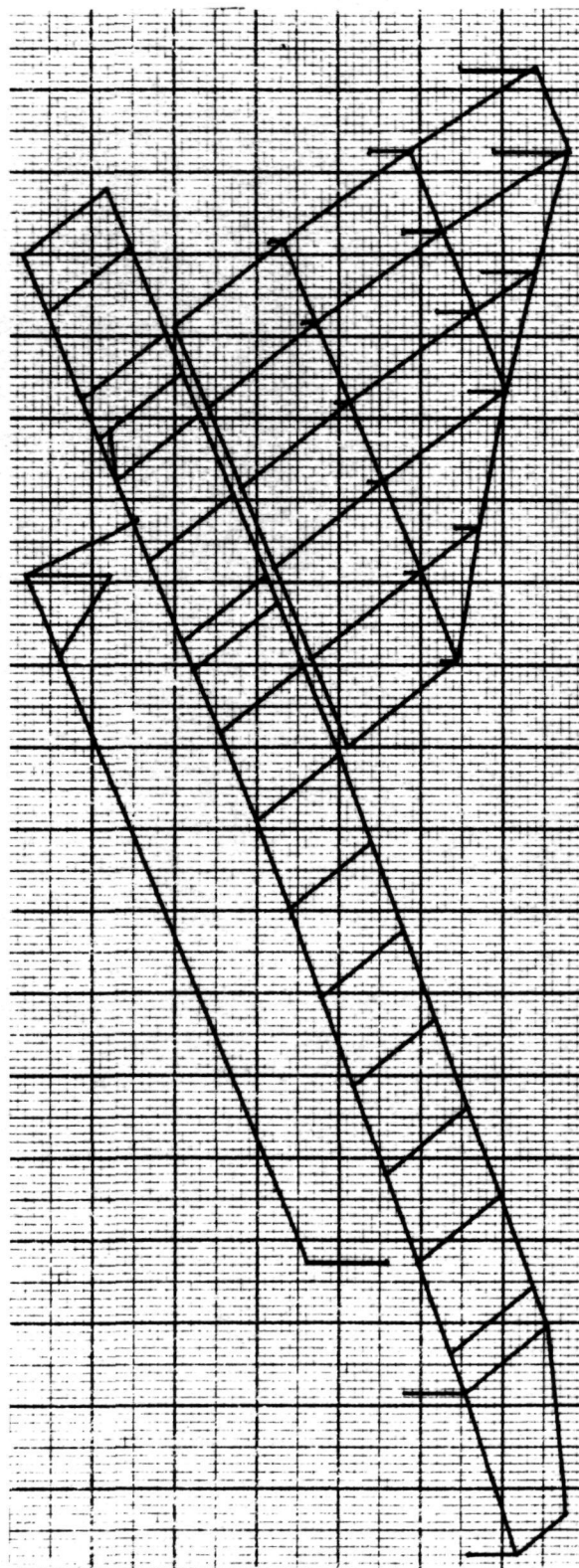
T-174

Fig. H-4 Mid-Fuselage - Sta 116.0, Grid 905



ORBITER STATIC TEST CASES ON INTERSTAGE SUPPORTS
REVISED 5/7/74 SYMM CASE
UNIT PZ DOWN ON FULL ORBITER (WING TIP-GRID 3017)
STATIC DEFOR. SUBCASE 3

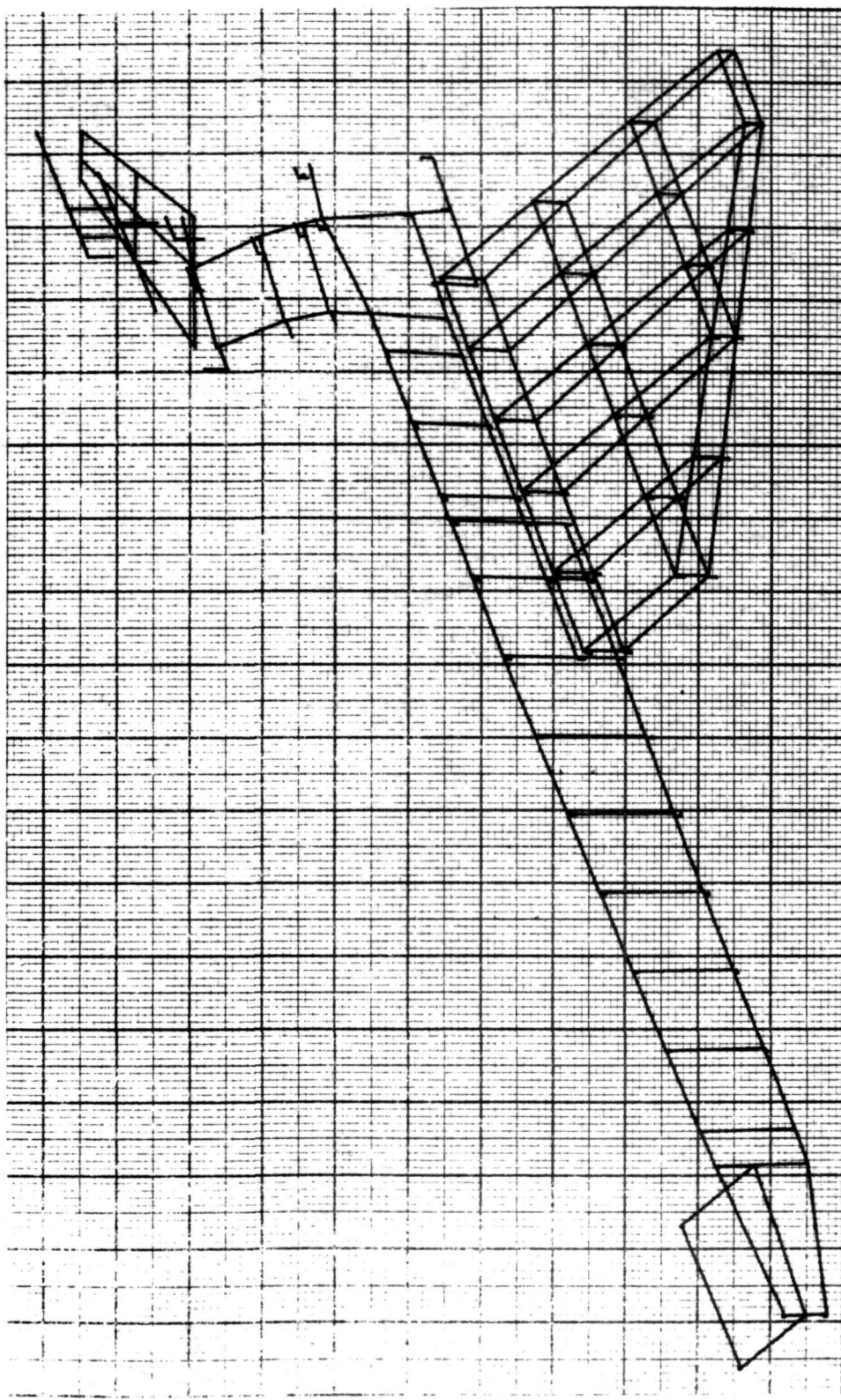
Fig. H-5 Wing Tip - Grid 3017



ORBITER STATIC TEST CASES ON INTERSTAGE SUPPORTS
REVISED 5/7/74 SYMM CASE
UNIT PZ DOWN ON FULL ORBITER (WING TIP - GRID 3017)
STATIC DEFOR. SUBCASE 3

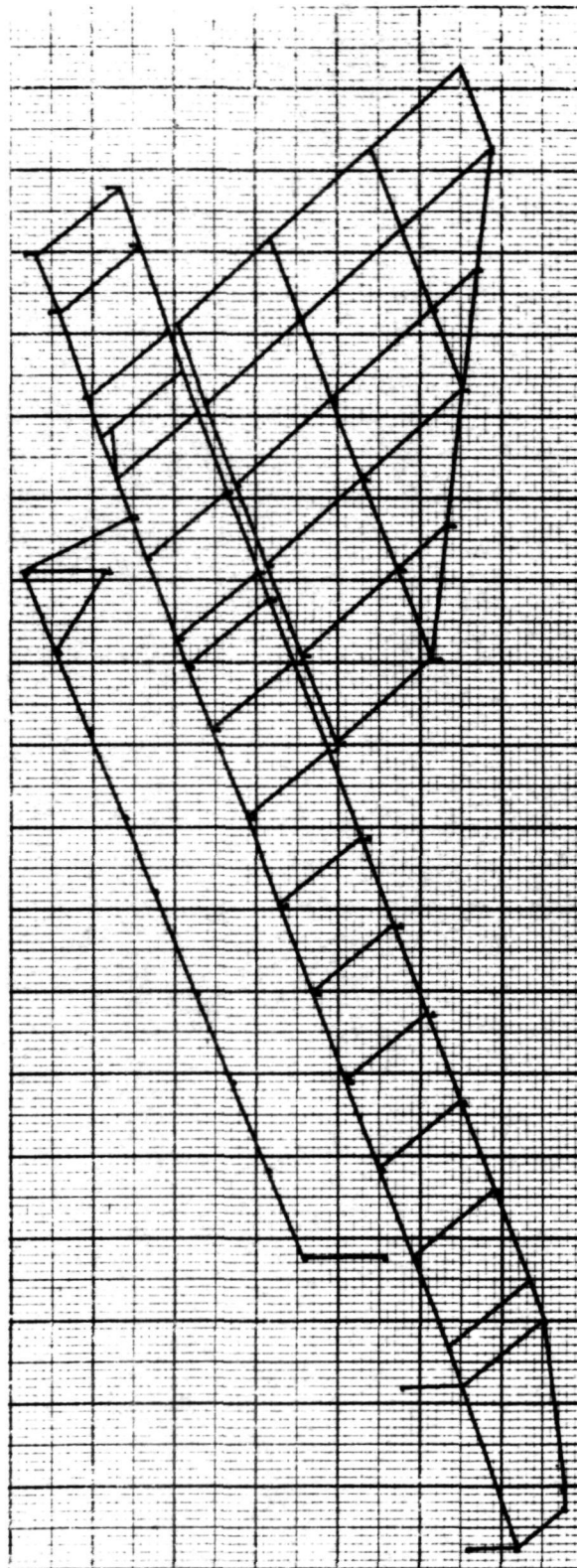
Fig. H-6 Wing Tip - Grid 3017

T-176



ORBITER STATIC TEST CASES ON INTERSTAGE SUPPORTS
REVISED 5/7/74 SYMM CASE
UNIT PX AFT ON FULL ORBITER (FIN BALLAST-GRID 4400)
STATIC DEFOR. SUBCASE 4

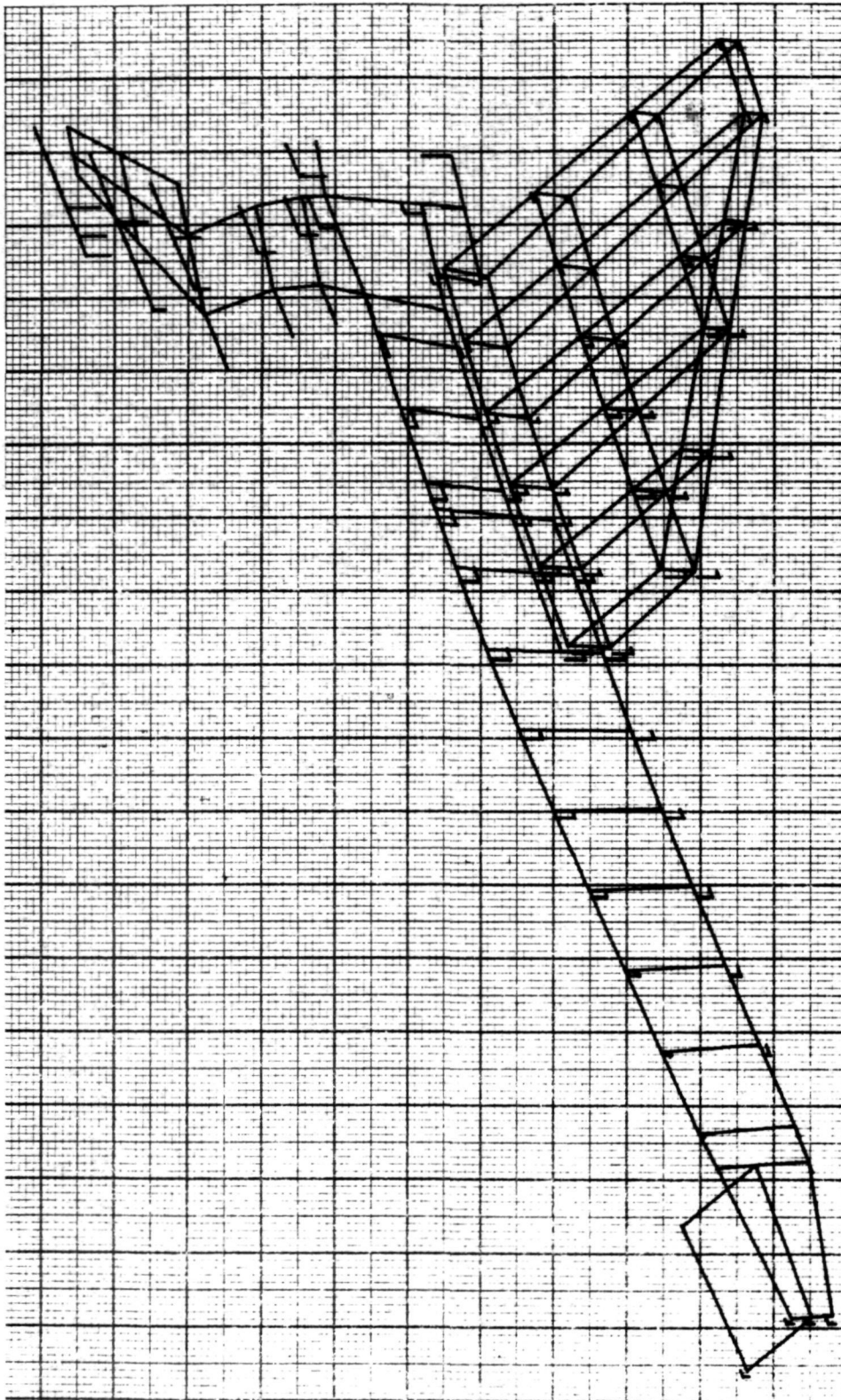
Fig. H-7 Fin Ballast - Grid 4400



ORBITER STATIC TEST CASES ON INTERSTAGE SUPPORTS
REVISED 5/7/74 SYMM CASE
UNIT PX AFT ON FULL ORBITER (FIN BALLAST-GRID 4400)
STATIC DEFOR. SUBCASE 4

T-178

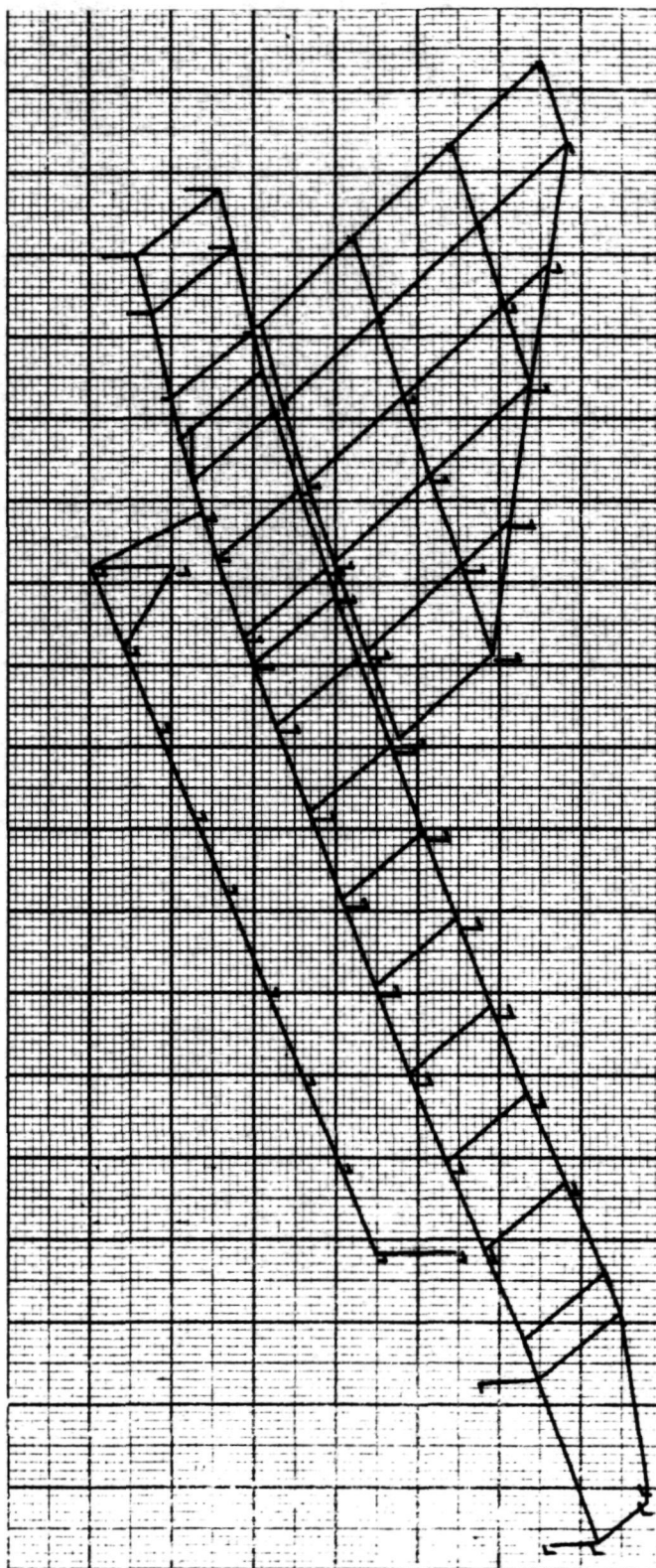
Fig. H-8 Fin Ballast - Grid 4400



ORBITER STATIC TEST CASES ON INTERSTAGE SUPPORTS
REVISED 5/7/74 SYMM CASE
UNIT PX AFT ON FULL ORBITER (OMS BALLAST-GRID 2200)
STATIC DEFOR. SUBCASE 5

T-179

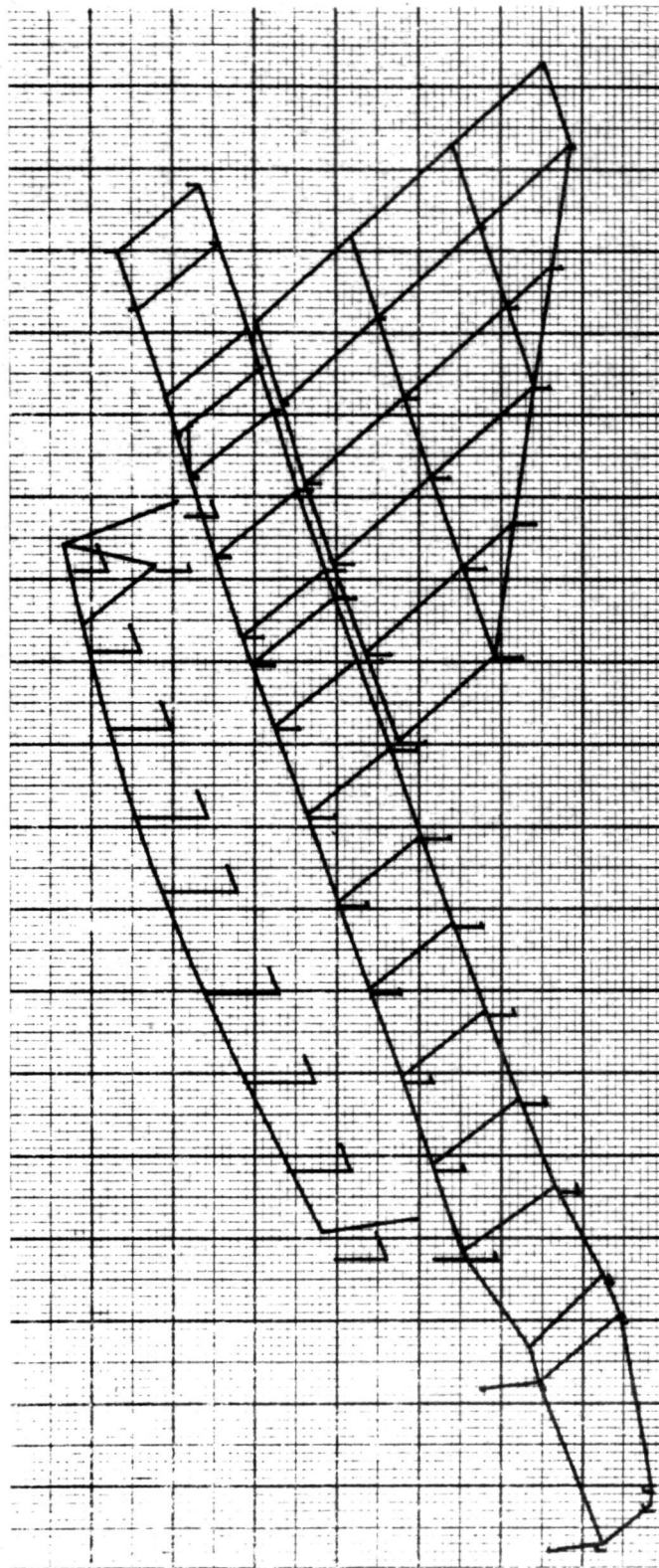
Fig. H-9 OMS Ballast - Grid 2200



ORBITER STATIC TEST CASES ON INTERSTAGE SUPPORTS
REVISED 5/7/74 SYMM CASE
UNIT PX AFT ON FULL ORBITER (OMS BALLAST-GRID 2200)
STATIC DEFOR. SUBCASE 5

Fig. H-10 OMS Ballast - Grid 2200

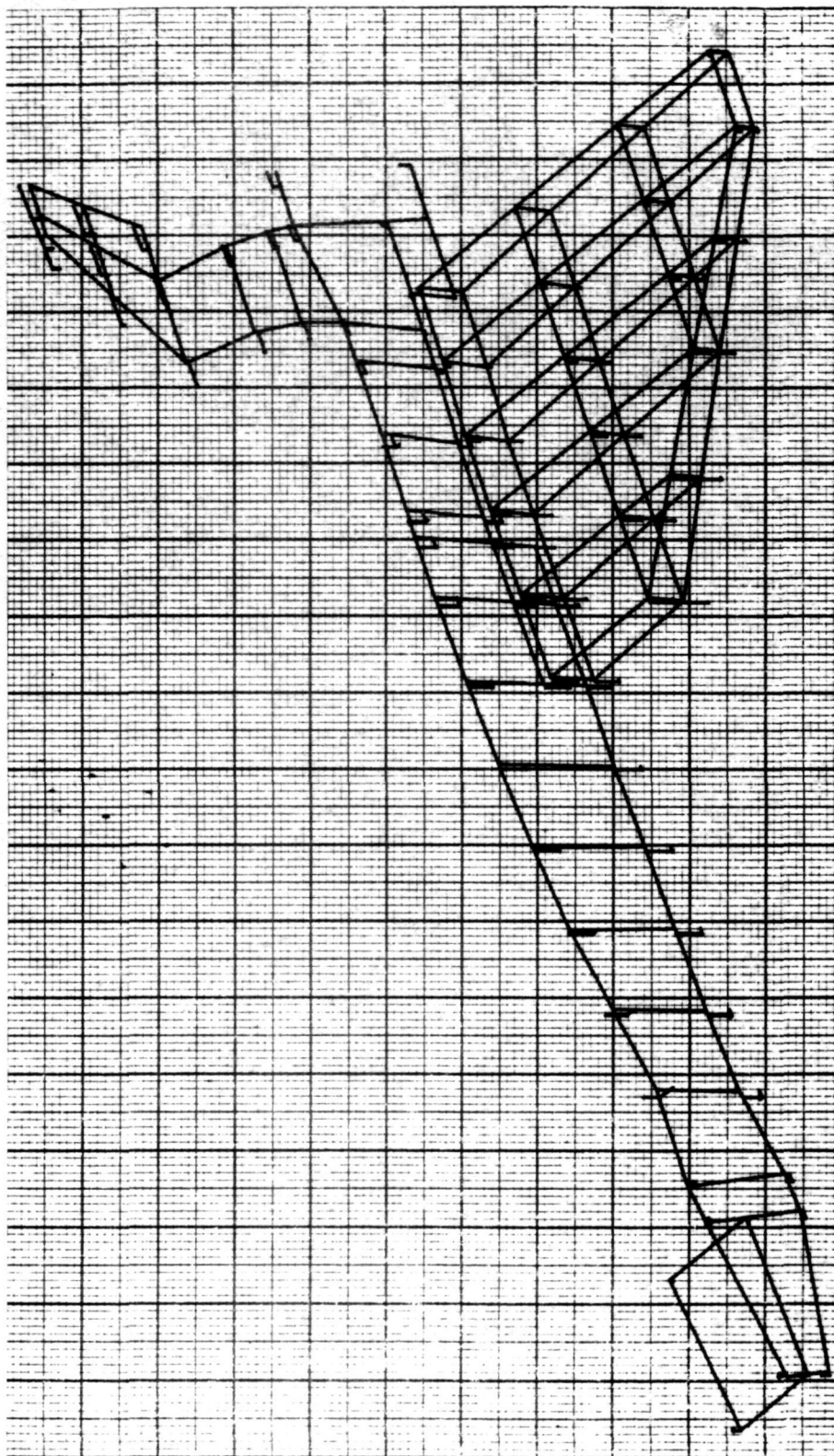
T-180



ORBITER STATIC TEST CASES ON INTERSTAGE SUPPORTS
REVISED 5/7/74 SYMM CASE
UNIT PZ UP ON FULL ORBITER (MID PAYLOAD-STA 117.5-GRID 4886)
STATIC DEFOR. SUBCASE 6

T-182

Fig. H-11 Mid Payload - Sta 117.5, Grid 4886

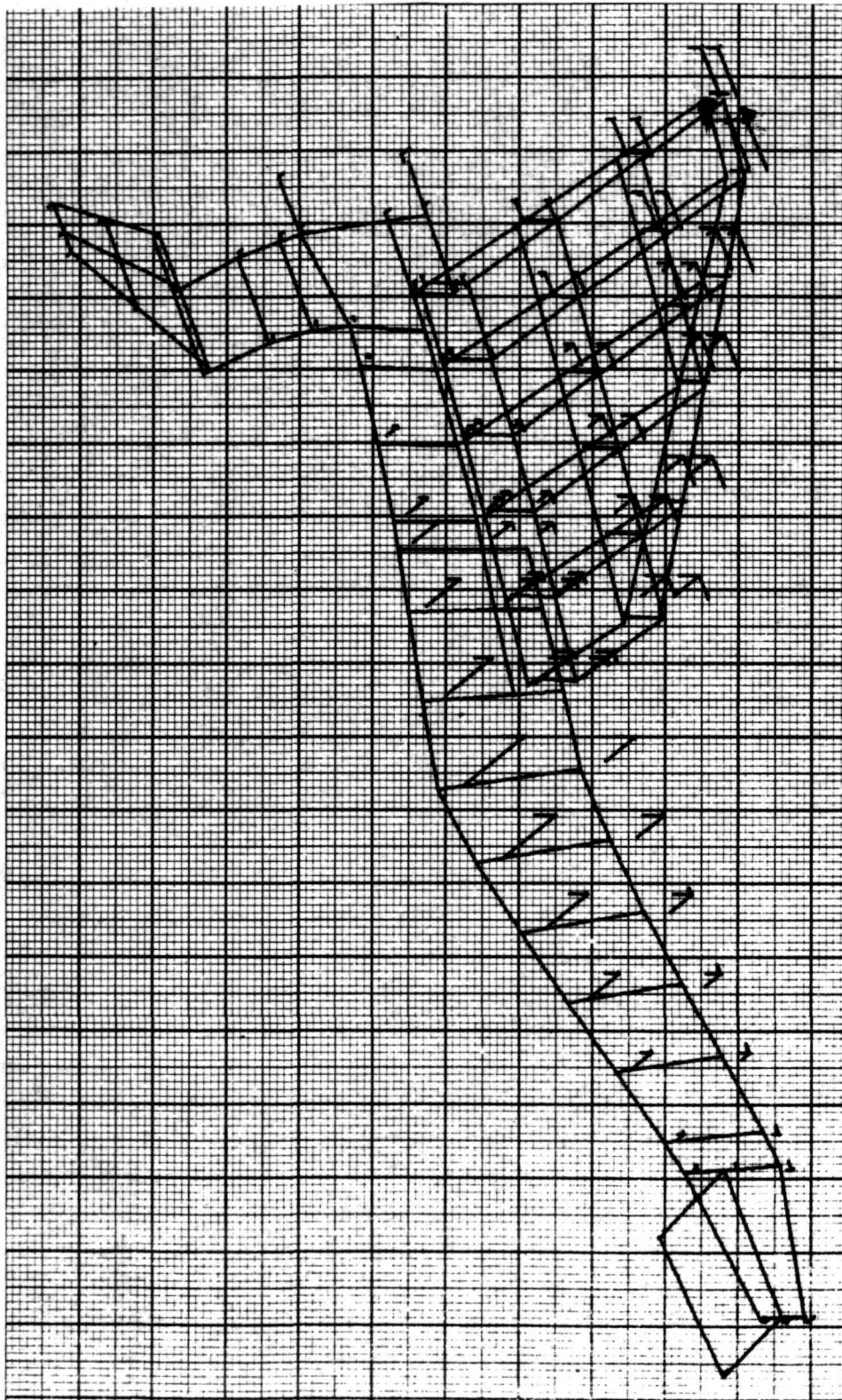


ORBITER STATIC TEST CASES ON INTERSTAGE SUPPORTS
REVISED 5/7/74 SYMM CASE
UNIT PZ UP ON FULL ORBITER (MID PAYLOAD-STA 117.5-GRID 4886)
STATIC DEFOR. SUBCASE 6

T-181

Fig. H-12 Mid Payload - Sta 117.5, Grid 4886

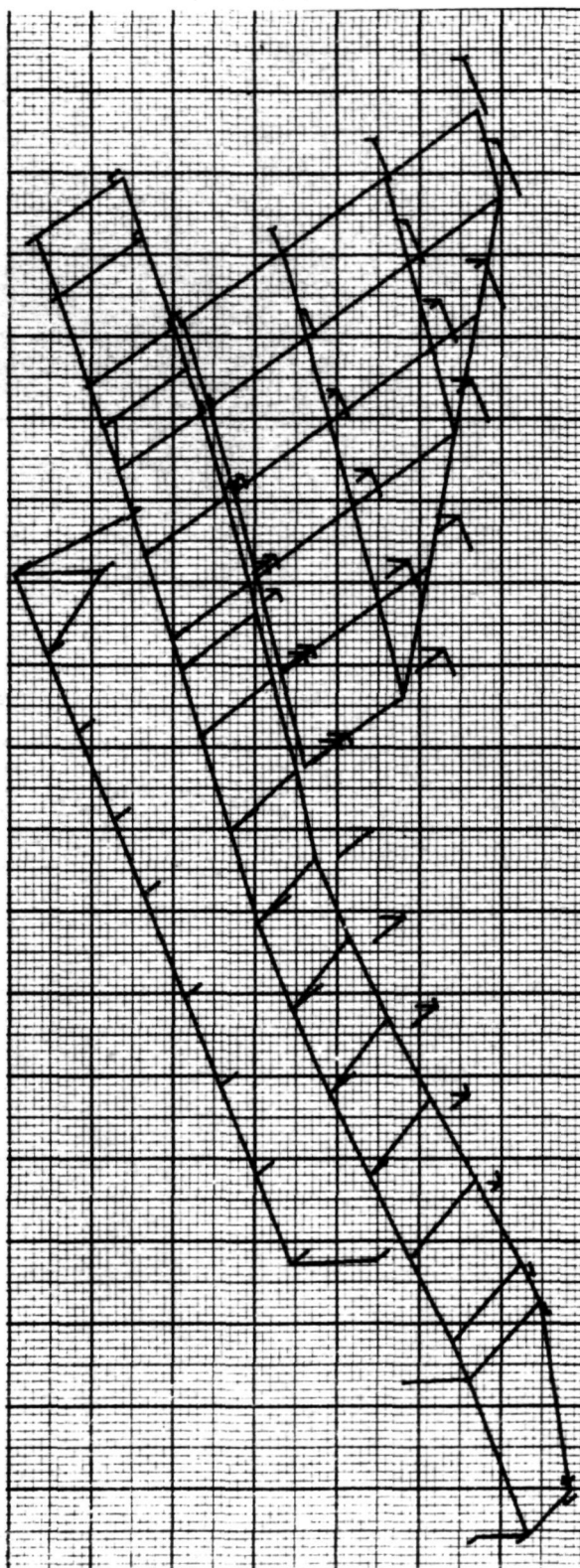
1 5/29/74 MAX-DEF. = 6.87424-05



ORBITER STATIC TEST CASES ON INTERSTAGE SUPPORTS
 REVISED 5/20/74 ANTI CASE
 UNIT PY ON FULL ORBITER (MID FUS.-STA 116.0 WL 51.5)
 STATIC DEFOR. SUBCASE 1

T-183

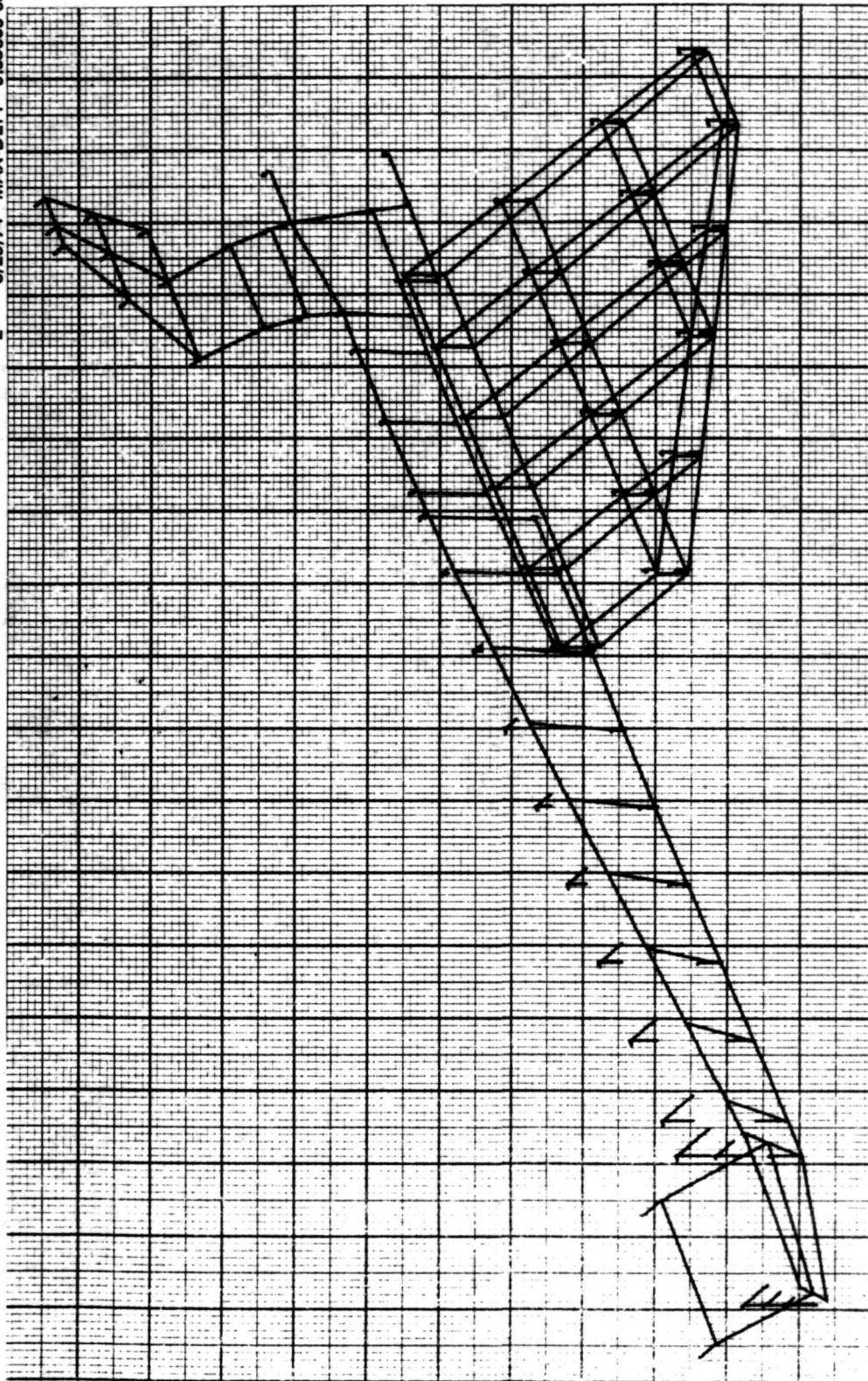
Fig. H-13 Mid-Fuselage - Sta 116.0, WL 51.5



ORBITER STATIC TEST CASES ON INTERSTAGE SUPPORTS
REVISED 5/20/74 ANTI CASE
UNIT PY ON FULL ORBITER (MID FUS.-STA 116.0 WL 51.5)
STATIC DEFOR. SUBCASE 1

T-184

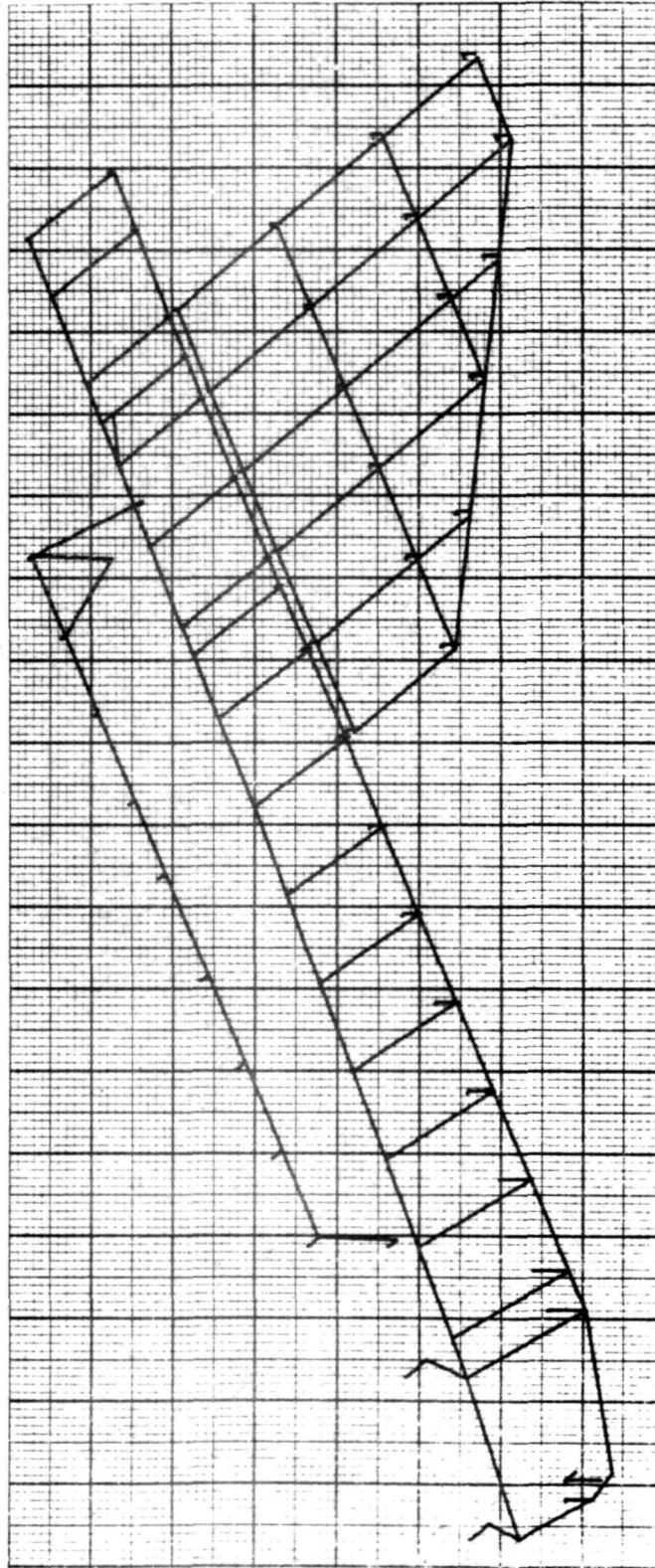
Fig. H-14 Mid-Fuselage - Sta 116.0, WL 51.5



ORBITER STATIC TEST CASES ON INTERSTAGE SUPPORTS
REVISED 5/20/74 ANTICASE
NOSE TORSION, 11 IN.-LB (-PZ = .5 AT STA 46.75-GRID 120)

T-185

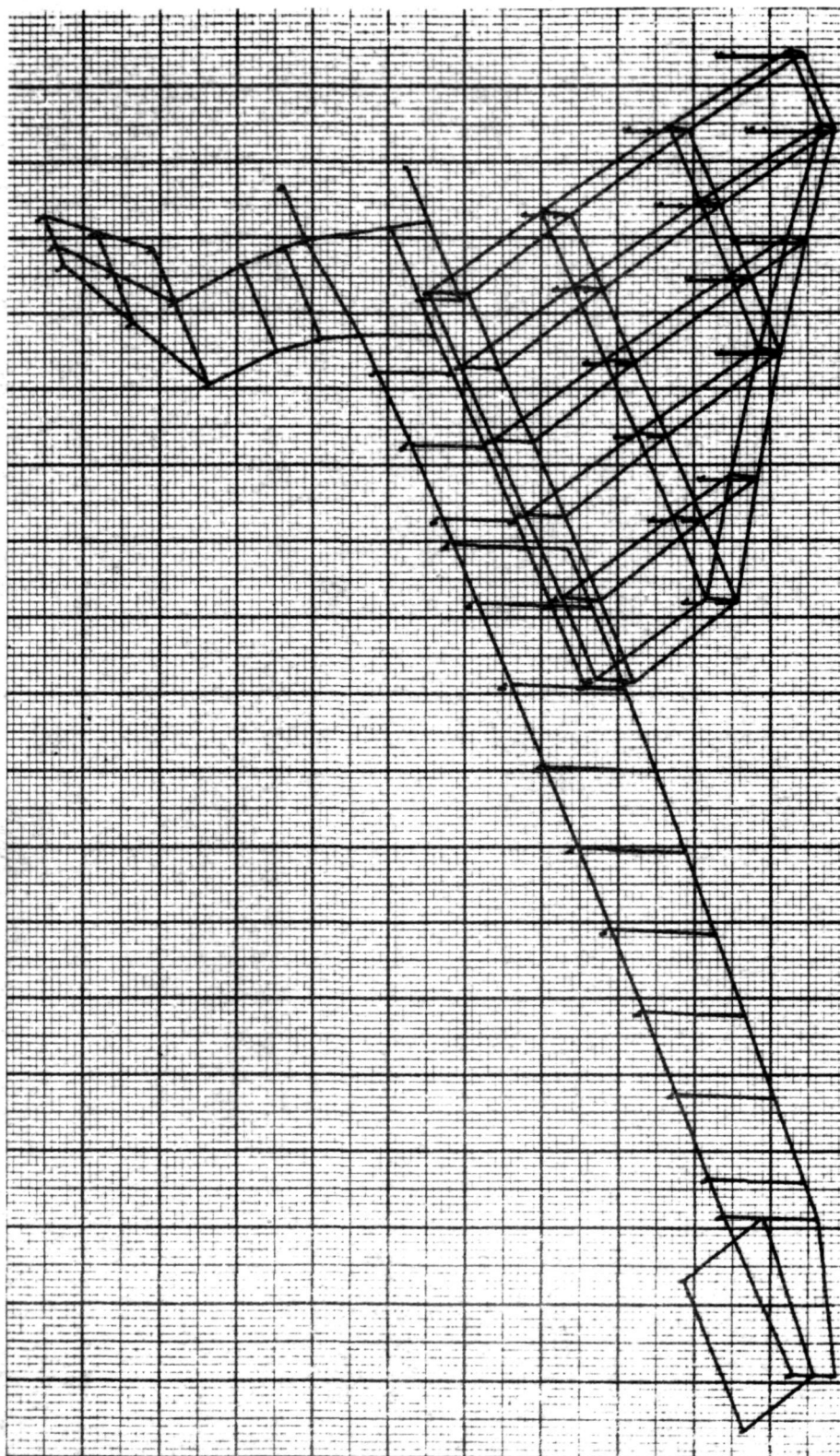
Fig. H-15 Nose Torsion - Sta 46.15, Grid 120



ORBITER STATIC TEST CASES ON INTERSTAGE SUPPORTS
REVISED 5/20/74 ANTI CASE
NOSE TORSION, 11 IN.-LB (-PZ = .5 AT STA 46.75, GRID 120)

T-186

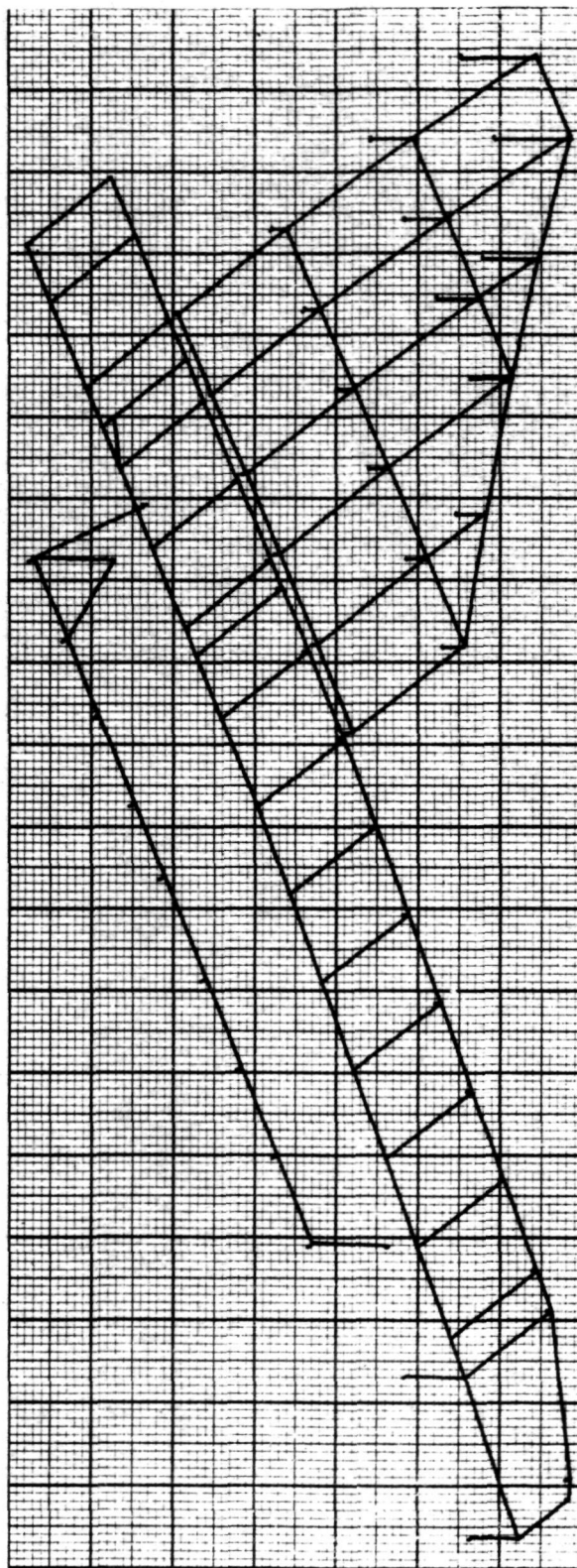
Fig. H-16 Nose Torsion - Sta 46.75, Grid 120



ORBITER STATIC TEST CASES ON INTERSTAGE SUPPORTS
REVISED 5/20/74 ANTI CASE
MID TORSION, 61.6 IN.-LB (-PZ = .5 AT WING TIP, GRID 3017)
STATIC DEFOR, SUBCASE 3

Fig. H-17 Mid Torsion - Wing Tip, Grid 3017

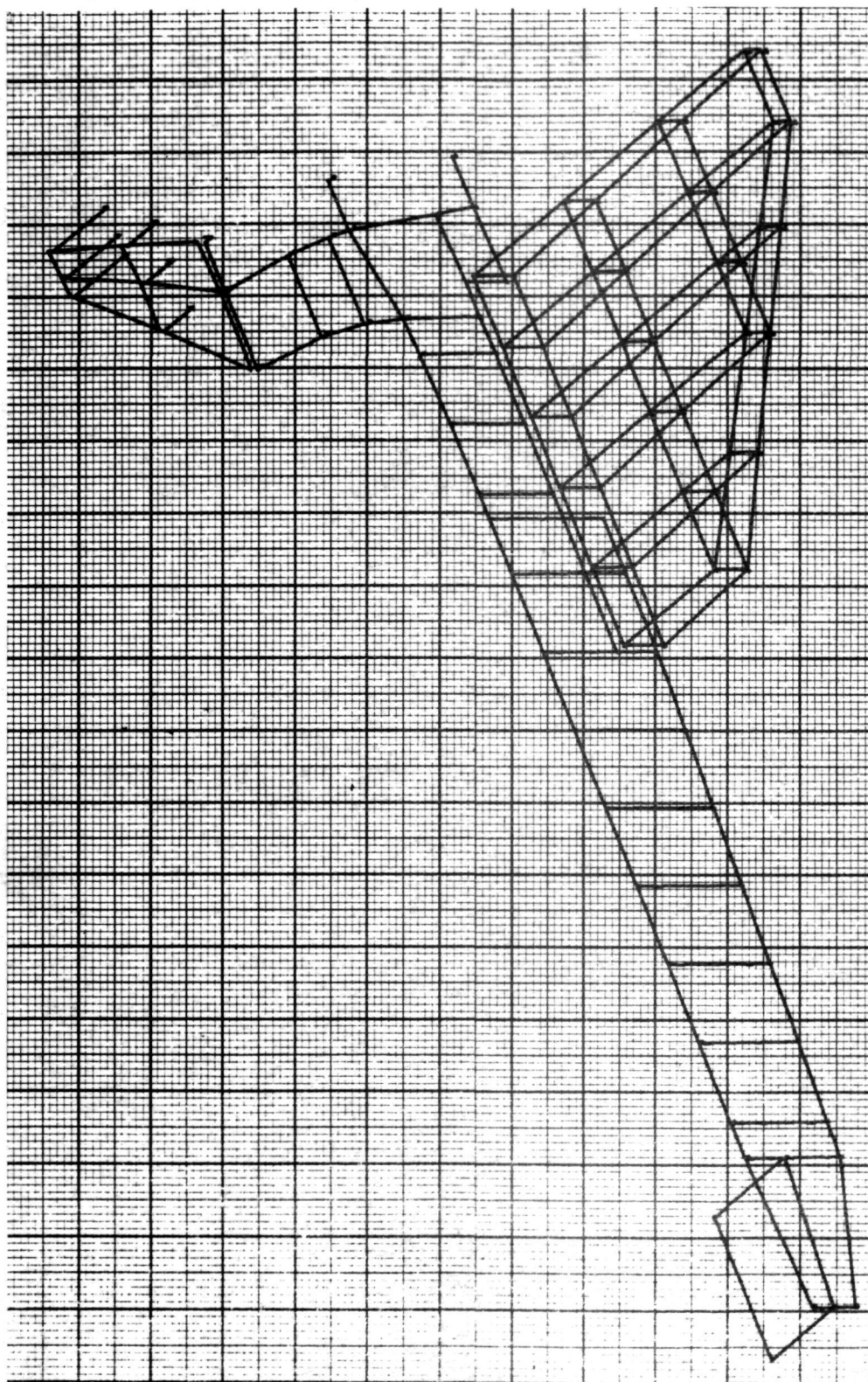
T-187



ORBITER STATIC TEST CASES ON INTERSTAGE SUPPORTS
REVISED 5/20/74 ANTI CASE
MID TORSION, 61.6 IN.-LB (-PZ = .5 AT WING TIP, GRID 3017)
STATIC DEFOR, SUBCASE 3

T-188

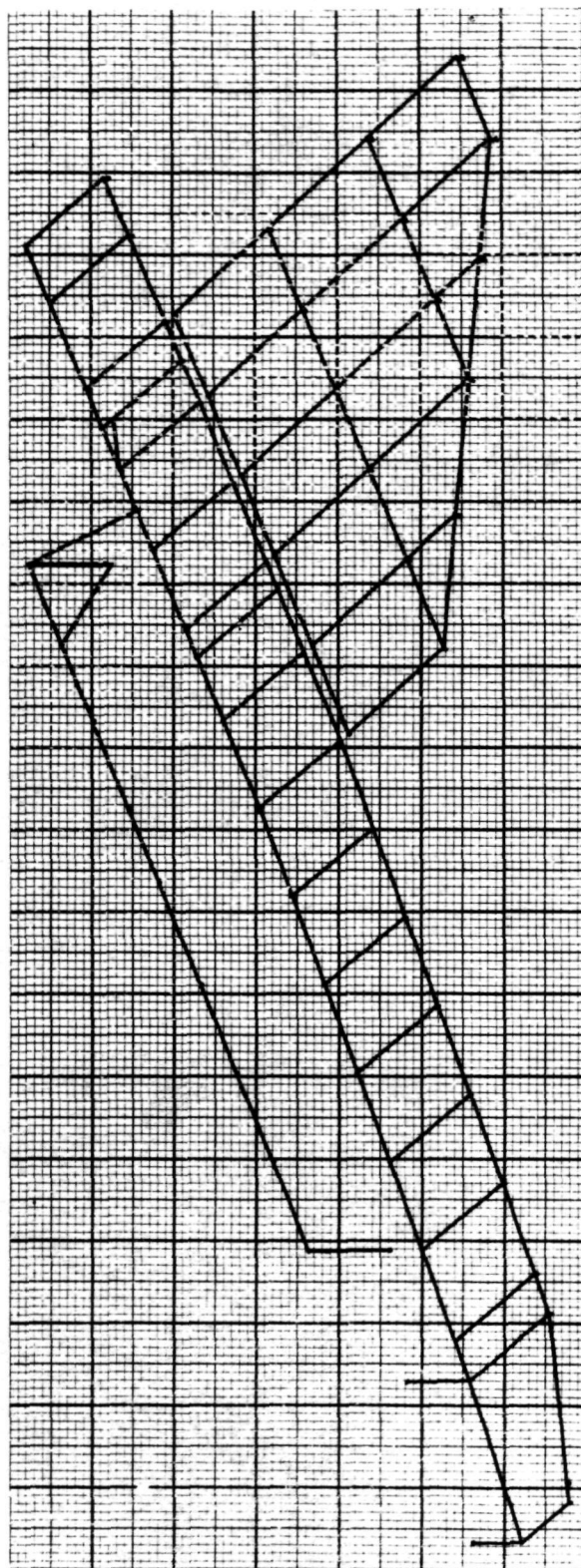
Fig. H-18 Mid Torsion - Wing Tip, Grid 3017



ORBITER STATIC TEST CASES ON INTERSTAGE SUPPORTS
REVISED 5/20/74 ANTI CASE
UNIT PY ON FULL ORBITER (FIN BALLAST, GRID 4400)
STATIC DEFOR. SUBCASE 4

T-189

Fig. H-19 Fin Ballast - Grid 4400



ORBITER STATIC TEST CASES ON INTERSTAGE SUPPORTS
REVISED 5/20/74 ANTI CASE
UNIT PY ON FULL ORBITER (FIN BALLAST, GRID 4400)
STATIC DEFOR. SUBCASE 4

Fig. H-20 Fin Ballast - Grid 4400

T-190

GRUMMAN AEROSPACE CORPORATION
BETHPAGE, NEW YORK 11714

1504-74